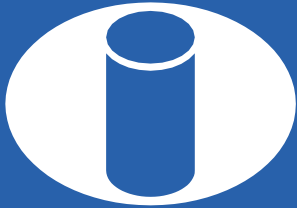


ISSN 1983-4195



**IBRACON**

**IBRACON Structures and Materials Journal**  
Revista IBRACON de Estruturas e Materiais

---

**Volume 14, Number 1**  
February 2021



# IBRACON Structures and Materials Journal

## Revista IBRACON de Estruturas e Materiais

### Contents

*Fracture bi-linear model parameters and brittleness of high-performance concretes for paving: why fatigue tests matters and cannot be spared?..... 14101*  
J. T. BALBO, A. A. SEVERI, T. C. CERVO and A. P. CARGNIN

*Shear friction capacity of self-consolidating concrete ..... 14102*  
G. SAVARIS and R. C. A. PINTO

*Analysis of constructive effect and soil-structure interaction in tall building projects with shallow foundations on sandy soils ..... 14103*  
O. C. MARQUES, L. A. FEITOSA, K. V. BICALHO and E. C. ALVES

*A simplified numerical and analytical study for assessing the seismic response of a gravity concrete lock ..... 14104*  
N. B. MENDES, L. J. PEDROSO and P. M. V. RIBEIRO

*Second-order torsion effects in concrete buildings ..... 14105*  
R. B. ANDRADE and P. G. B. NOBREGA

*Punching shear strength of waffle flat slabs ..... 14106*  
R. J. C. SILVA, D. R. C. OLIVEIRA, N. G. B. ALBUQUERQUE, F. E. S. SILVA JR. and F. S. LEITE

*Numerical analysis of the influence of block geometry on the behavior of piled foundations..... 14107*  
J. R. GARCIA and P. J. R. ALBUQUERQUE

*Numerical analysis of RC wall with opening and strengthened with CFRP ... 14108*  
M. A. SILVA, R. A. S. DIAZ, L. C. ALMEIDA and L. M. TRAUTWEIN

*Influence of recycled concrete aggregates on the shear strength of reinforced concrete beams ..... 14109*  
A. C. CARDOSO, I. G. LIMA, M. P. FERREIRA and R. A. SOUZA

*Numerical evaluation of the slab effective width in steel-concrete composite box girder bridges ..... 14110*  
R. S. NICOLETTI and A. S. C. SOUZA

*Reinforced concrete flat slabs with openings at different distances from the column ..... 14111*  
D. S. LOURENCO, E. A. P. LIBERATI, M. G. MARQUES, L. C. ALMEIDA and L. M. TRAUTWEIN

*Shear failure in reinforced concrete members without transverse reinforcement: analysis of model error of NBR6118:2014..... 14112*  
V. P. BARROS, A. T. BECK and T. N. BITTENCOURT

*Current condition of the exposed concrete façades reinforcement of the Vilanova Artigas building: modern architectural heritage ..... 14113*  
A. ARAUJO, C. A. OLIVEIRA and T. R. S. SIMAO

*Influence of cement type, air-entrained admixture and hydration stabilizing admixture on mortars' setting time..... 14114*  
J. P. ANTONIAZZI, G. MOHAMAD and J. M. CASALI

*Monolithic equivalent stiffness of precast columns with grouted splice sleeve connections ..... 14115*  
M. A. FERREIRA, L. A. BACHEGA and B. CATOIA



Cover: Parametric Tower

Courtesy: Marcela Noronha P. de O. e Sousa



**IBRACON**

IBRACON Structures and Materials Journal is published bimonthly (February, April, June, August, October, and December) by IBRACON.

**IBRACON**  
Instituto Brasileiro do Concreto Founded in 1972

Av. Queiroz Filho, nº 1700 — sala 407/408  
Torre D — Villa Lobos Office Park  
CEP 05319-000 — São Paulo, SP — Brazil  
Phone: +55 11 3735-0202

Fax: +55 11 3733-2190

E-mail: [riem@ibracon.org.br](mailto:riem@ibracon.org.br)

Website: <http://www.ibracon.org.br>

Cover design & Layout: Editora Cubo  
[www.editoracubo.com.br](http://www.editoracubo.com.br)

---

## Aims and Scope

### Aims and Scope

The IBRACON Structures and Materials Journal (in Portuguese: Revista IBRACON de Estruturas e Materiais) is a technical and scientific divulgation vehicle of IBRACON (Brazilian Concrete Institute), published every two months. Each issue has 12 to 15 articles and, possibly, a technical note and/or a technical discussion regarding a previously published paper. All contributions are reviewed and approved by professionals with recognized scientific competence in the area. The IBRACON Structures and Materials Journal is an open access Journal, free of charges for authors and readers.

### Objectives

The IBRACON Structures and Materials Journal's main objectives are:

- Present current developments and advances in concrete structures and materials.
- Make possible the better understanding of structural concrete behavior, supplying subsidies for a continuous interaction among researchers, producers, and users.
- Stimulate the development of scientific and technological research in the areas of concrete structures and materials, through papers peer-reviewed by a qualified Editorial Board.
- Promote the interaction among researchers, constructors and users of concrete structures and materials and the development of Civil Construction.
- Provide a vehicle of communication of high technical level for researchers and designers in the areas of concrete structures and materials.

### Submission Procedure

The procedure to submit and revise the contributions, as well as the formats, are detailed in the Journal Website ([ismj.org](http://ismj.org)).

The papers and the technical notes are revised by at least two reviewers indicated by the editors. Discussions and replies are accepted for publication after a review by the editors and at least one member of the Editorial Board. In case of disagreement between the reviewer and the authors, the contribution will be sent to a specialist in the area, not necessarily linked to the Editorial Board. Conflict of interests is carefully handled by the Editors.

### Contribution Types

The Journal will publish original papers, short technical notes, and paper discussions. Original papers will be accepted if they are in accordance with the objectives of the Journal and present quality of information and presentation. A technical note is a brief manuscript. It may present a new feature of research, development, or technological application in the areas of Concrete Structures and Materials, and Civil Construction. This is an opportunity to be used by industries, companies, universities, institutions of research, researchers, and professionals willing to promote their works and products under development.

A discussion is received no later than 3 months after the publication of the paper or technical note. The discussion must be limited to the topic addressed in the published paper and must not be offensive. The right of reply is granted to the Authors. The discussions and the replies are published in the subsequent issues of the Journal.

The submission file should be in accordance with the paper template available at the Journal Website. It is recommended that the length of the papers does not exceed 25 pages. Where available, URLs for the references should be provided.

The IBRACON Structures and Materials Journal will conduct the review process for manuscripts submitted in English. Titles, abstracts, and keywords are presented in English, and in Portuguese or Spanish. Articles and technical notes are peer-reviewed and only published after approval of the reviewers and the Editorial Board.

Once accepted, an article is typeset according to the journal layout. The author will be required to review and approve the galleys before publishing. At this stage only typesetting errors will be considered.

### Internet Access

The IBRACON Structures and Materials Journal Webpage is available at <http://ismj.org>.

### Sponsors

The funds for the maintenance of the Journal are currently obtained from the IBRACON. The Journal is not supposed to be maintained with funds from private sponsorship, which could diminish the credit of the publications.

### Photocopying

Photocopying in Brazil. Brazilian Copyright Law is applicable to users in Brazil. IBRACON holds the copyright of contributions in the journal unless stated otherwise at the bottom of the first page of any contribution. Where IBRACON holds the copyright, authorization to photocopy items for internal or personal use, or the internal or personal use of specific clients, is granted for libraries and other users registered at IBRACON.

### Copyright

All rights, including translation, reserved. Under the Brazilian Copyright Law No. 9610 of 19th February, 1998, apart from any fair dealing for the purpose of research or private study, or criticism or review, no part of this publication may be reproduced, stored in a retrieval system, or transmitted in any form or by any means, electronic, mechanical, photocopying, recording or otherwise, without the prior written permission of IBRACON. Requests should be directed to IBRACON:

### IBRACON

Av. Queiroz Filho, 1700 – sala 407/408 – Torre D  
Villa Lobos Office Park  
05319-000 – Vila Hamburguesa  
São Paulo – SP  
Phone: +55 (11) 3735-0202  
E-mail: [riem@ibracon.org.br](mailto:riem@ibracon.org.br)

### Disclaimer

Papers and other contributions and the statements made or opinions expressed therein are published on the understanding that the authors of the contribution are the only responsible for the opinions expressed in them and that their publication does not necessarily reflect the views of IBRACON or of the Journal Editorial Board.

---

## Editorial Board

### Editor-in-chief emeritus

José Luiz Antunes de Oliveira e Sousa, Universidade Estadual de Campinas - UNICAMP, Campinas, SP, Brazil, [jls@fec.unicamp.br](mailto:jls@fec.unicamp.br)

### Editor-in-chief

Guilherme Aris Parsekian, Universidade Federal de São Carlos – UFSCAR, São Carlos, SP, Brazil, [parsekian@ufscar.br](mailto:parsekian@ufscar.br)

### Associate Editors

Antônio Carlos dos Santos, Universidade Federal de Uberlândia – UFU, Uberlândia, MG, Brazil  
Bernardo Horowitz, Universidade Federal de Pernambuco - UFPE, Recife, PE, Brazil  
Bernardo Tutikian, Universidade do Vale do Rio dos Sinos – UNISINOS, São Leopoldo, RS, Brazil  
Bruno Briseghella, Fuzhou University, Fujian, China  
David Oliveira, Jacobs Engineering, Sydney, Australia  
Edgar Bacarji, Universidade Federal de Goiás - UFG, Goiânia, GO, Brazil  
Edna Possan, Universidade Federal da Integração Latino Americana – UNILA, Foz do Iguaçu, PR, Brazil  
Fernando Pelisser, Universidade Federal de Santa Catarina – UFSC, Florianópolis, SC, Brazil  
Fernando Soares Fonseca, Brigham Young University – BYU, Provo, UT, USA  
José Marcio Fonseca Calixto, Universidade Federal de Minas Gerais – UFMG, Belo Horizonte, MG, Brazil  
José Tadeu Balbo Universidade de São -Paulo, São Paulo, SP, Brazil  
Leandro Mouta Trautwein, Universidade Estadual de Campinas - UNICAMP, Campinas, SP, Brazil  
Leandro F. M. Sanchez, University of Ottawa, Ottawa, Canada  
Lia Lorena Pimentel, Pontifícia Universidade Católica de Campinas – PUCCAMP, Campinas, SP, Brazil  
Luís Oliveira Santos, Laboratório Nacional de Engenharia Civil, Lisboa, Portugal  
Mark G Alexander, University of Cape Town, Cape Town, South Africa  
Marco Di Prisco, Politecnico di Milano, Milan, Italy  
Mário Jorge de Seixas Pimentel, Universidade do Porto - FEUP, Porto, Portugal  
Maurício de Pina Ferreira, Universidade Federal do Pará - UFPA, Belém, PA, Brazil  
Mauro de Vasconcellos Real, Universidade Federal do Rio Grande – FURG, Rio Grande, RS, Brazil  
Nigel G. Shrive, University of Calgary, Calgary, Canada  
Osvaldo Luís Manzoli, Universidade Estadual Paulista “Júlio de Mesquita Filho” - UNESP, Bauru, SP, Brazil  
Rebecca Gravina, RMIT University, Melbourne, Australia  
Ricardo Carrazedo, Universidade de São Paulo - USP, São Carlos, SP, Brazil  
Samir Maghous, Universidade Federal do Rio Grande do Sul - UFRGS, Porto Alegre, RS, Brazil  
Sérgio Hampshire de Carvalho Santos, Universidade Federal do Rio de Janeiro - UFRJ, Rio de Janeiro, RJ, Brazil  
Túlio Nogueira Bittencourt, Universidade de São -Paulo, São Paulo, SP, Brazil  
Vladimir Guilherme Haach, Universidade de São Paulo - USP, São Carlos, SP, Brazil  
Yury Villagrán Zaccardi, Universidad Tecnológica Nacional Facultad Regional La Plata, Buenos Aires, Argentina

### Editorial Comission

Antônio Carlos R. Laranjeiras, ACR Laranjeiras, Salvador, BA, Brazil  
Emil de Souza Sánchez Filho, Universidade Federal Fluminense, UFF, Rio de Janeiro, RJ, Brazil  
Geraldo Cechella Isaia, Universidade Federal de Santa Maria, UFSM, Santa Maria, RS, Brazil  
Gonzalo Ruiz, Universidad de Castilla-La Mancha - UCLM, Ciudad Real, Spain  
Ivo José Padaratz, Universidade Federal de Santa Catarina - UFSC, Florianópolis, SC, Brazil  
Joaquim de Azevedo Figueiras, Faculdade de Engenharia da Universidade do Porto - FEUP, Porto, Portugal  
Paulo Monteiro, University of California Berkeley, Berkeley, CA, USA  
Pedro Castro Borges, CINVESTAV, Mérida, Yuc., México  
Vladimir Antônio Paulon, Universidade Estadual de Campinas - UNICAMP, Campinas, SP, Brazil

### Former Editors

Américo Campos Filho, Universidade Federal do Rio Grande do Sul - UFRGS, Porto Alegre, RS, Brazil  
Denise C. C. Dal Molin Universidade Federal do Rio Grande do Sul - UFRGS, Porto Alegre, RS, Brazil  
Eduardo Nuno Brito Santos Júlio, Instituto Superior Técnico - IST, Lisboa, Portugal  
Guilherme Sales Melo, Universidade de Brasília, UnB, Brasília, DF, Brazil  
Luiz Carlos Pinto da Silva Filho, Universidade Federal do Rio Grande do Sul - UFRGS, Porto Alegre, RS, Brazil  
Mounir Khalil El Debs, Universidade de São Paulo - USP, São Carlos, SP, Brazil  
Nicole Pagan Hasparyk, Eletrobras Furnas, Aparecida de Goiânia, GO, Brazil  
Paulo Helene, Universidade de São Paulo - USP, São Paulo, SP, Brazil  
Roberto Caldas de Andrade Pinto, Universidade Federal de Santa Catarina - UFSC, Florianópolis, SC, Brazil  
Ronaldo Barros Gomes, Universidade Federal de Goiás - UFG, Goiânia, GO, Brazil  
Romilde Almeida de Oliveira, Universidade Católica de Pernambuco - UNICAP, Recife, PE, Brazil  
Romildo Dias Toledo Filho, Universidade Federal do Rio de Janeiro - UFRJ, Rio de Janeiro, RJ, Brazil  
Rubens Machado Bittencourt, Eletrobras Furnas, Aparecida de Goiânia, GO, Brazil



## **Board of Direction 2019/2021 Biennium**

### **President**

Paulo Helene

### **1<sup>st</sup> Vice-President Director**

Júlio Timerman

### **2<sup>nd</sup> Vice-President Director**

Enio José Pazini Figueiredo

### **Presidency Advisors**

Antônio Domingues de Figueiredo

Iria Lícia Oliva Doniak

Jairo Abud

Jorge Batlouni Neto

Luís Aurélio Fortes da Silva

Mario William Esper

Maurice Antoine Traboulsi

Paula Baillot

Simão Priszkulnik

### **1<sup>st</sup> Director-Secretary**

Cláudio Sbrighi Neto

### **2<sup>nd</sup> Director-Secretary**

Carlos José Massucato

### **1<sup>st</sup> Treasurer Director**

Júlio Timerman

### **2<sup>nd</sup> Treasurer Director**

Hugo S. Armelin

### **Marketing Director**

Jéssika Pacheco

### **Marketing Director Advisor**

Guilherme Covas

### **Publications Director**

Guilherme Parsekian

### **Publications Director Advisor**

Túlio Nogueira Bittencourt

### **Event Director**

Rafael Timerman

### **Event Director Advisor**

Luis César De Luca

### **Technical Director**

José Tadeu Balbo

### **Technical Director Advisor**

Selmo Chapira Kuperman

### **Institutional Relations Director**

César Henrique Daher

### **Institutional Relations Director Advisor**

José Vanderley de Abreu

### **Course Director**

Leandro Moura Trautwein

### **Course Director Advisor**

Antônio Carlos dos Santos

### **Student Activities Director**

Jéssica Andrade Dantas

### **Student Activities Director Advisor**

Sandra Regina Bertocini

### **Personnel Certification Director**

Adriano Damásio Soterio

### **Personnel Certification Director Advisor**

Gilberto Antônio Giuzio

### **Research and Development Director**

Bernardo Tutikian

### **Research and Development Director Advisor**

Roberto Christ

## **Council 2019/2021 Biennium**

### **Individual Members**

Antônio Carlos dos Santos

Antônio Domingues de Figueiredo

Arnaldo Forti Battagin

Bernardo Fonseca Tutikian

Carlos José Massucato

César Henrique Sato Daher

Cláudio Sbrighi Neto

Enio José Pazini Figueiredo

Hugo da Costa Rodrigues Filho

Inês Laranjeira da Silva Battagin

Iria Lícia Oliva Doniak

Jéssika Mariana Pacheco

José Tadeu Balbo

Leandro Moura Trautwein

Luiz Carlos de Almeida

Luiz Prado Vieira Júnior

Mário William Esper

Maurice Antoine Traboulsi

Rafael Timerman

Vladimir Antônio Paulon

### **Past President Members**

Eduardo Antônio Serrano

José Marques Filho

Júlio Timerman

Paulo Helene

Ronaldo Tartuce

Rubens Machado Bittencourt

Selmo Chapira Kuperman

Simão Priszkulnik

Túlio Nogueira Bittencourt

### **Corporate Members**

ABCIC - Associação Brasileira da  
Construção Industrializada de Concreto –  
Iria Lícia Oliva Doniak

ABCP - Associação Brasileira de Cimento  
Portland – Paulo Camilo Penna

ABECE - Associação Brasileira de  
Engenharia e Consultoria Estrutural –  
João Alberto de Abreu Vendramini

ABESC - Associação Brasileira das  
Empresas de Serviços de Concretagem –  
Jairo Abud

EPUSP - Escola Politécnica da  
Universidade de São Paulo – Túlio  
Nogueira Bittencourt

FURNAS Centrais Elétricas S/A – Flávio  
de Lima Vieira

IPT - Instituto de Pesquisas Tecnológicas  
do Estado de São Paulo – José Maria de  
Camargo Barros

L. A. FALCÃO BAUER Centro  
Tecnológico – Patrícia Bauer

PhD Engenharia Ltda – Douglas de  
Andreza Couto

TQS Informática Ltda – Nelson Covas

VOTORANTIM Cimentos S/A –  
Maurício Bianchini

---

## Reviewers List 2019-2020

Aguilar, Maria Teresa Paulino  
Alax, Arthur  
Albuquerque, M. da C. Fonseca de  
Almeida Filho, Fernando Menezes  
Almeida, Fernando do Couto Rosa  
Almeida, Luiz Carlos de  
Almeida, Saulo J. de Castro  
Almeida, Sylvia  
Almeida, Valério  
Altoe, Silvia Paula Sossai  
Alva, Gerson M. Sisnegas  
Alves, Antônio Marcos de Lima  
Alves, Elcio Cassimiro  
Alves, Ricardo Valeriano  
Amorim Júnior, Nilson  
Amorim, David  
Andrade, Jairo José de Oliveira  
Andrade, Jorge  
Ângulo, Sérgio  
Antunes, Elaine Guglielmi  
Arantes, João  
Araújo, Daniel  
Artigas, Laila Valduga  
Assis, Wayne Santos de  
Azevedo, Nuno  
Balbo, José Tadeu  
Baldassino, Nadia  
Bandeira, Alex Alves  
Banting, Bennett  
Barbosa, Claudius de Sousa  
Barbosa, Maria  
Barbosa, Normando Perazzo  
Barbosa, Paola  
Barboza, Aline da Silva Ramos  
Barros, Rodrigo  
Baságli, Cilmar  
Batiston, Eduardo Roberto  
Bauer, Elton  
Beck, André Teófilo  
Beeldens, Anne  
Beraldo, Antônio  
Bernardin, Adriano  
Bernardo, Luis Filipe Almeida  
Betoli, Andrea  
Bianchi, Fernanda  
Bitencourt Júnior, Luís A. Guimarães  
Bolina, Cecília de Castro  
Bolina, Fabricio  
Bono, Giuliana Furtado Franca  
Bonsembiante, Franciele Tiecher  
Borges, Liana Jardim  
Borges, Paulo Henrique  
Bremer, Cynara Fiedler  
Britez, Carlos Amado  
Brito, Jorge de  
Buchaim, Roberto  
Bueno, Jeferson Rafael  
Buratto, Caroline  
Buttignol, Thomaz Eduardo Teixeira  
Cabral, Kleber Cavalcanti  
Caetano, Luciana Fonseca  
Caldas, Rodrigo  
Calixto, José Marcio  
Camarini, Gladis  
Camões, Aires  
Campos, Heloisa Fuganti  
Cardoso, Daniel  
Cargnin, Andrea  
Carneiro, Anselmo  
Carneiro, Arnaldo Manoel Pereira  
Carneiro, Ronaldson J. de F. Mendes  
Carrazedo, Ricardo  
Carrazedo, Rogério  
Carvalho, Hermes  
Carvalho, Roberto Chust  
Castro, Alessandra Lorenzetti  
Cervo, Tatiana Cureau  
Chahud, Eduardo  
Chen, Airong  
Chen, Bing  
Christ, Roberto  
Christoforo, André  
Cincotto, Maria Alba  
Coelho, Antônio Carlos Vieira  
Coelho, Luiz Herkenhoff  
Colombo, Alberto Belotti  
Cordeiro, Luciana de Nazare Pinheiro  
Cordon, Heloisa Cristina Fernandes  
Corrêa, Márcio Roberto Silva  
Correia, José  
Costa e Silva, Ramon Saleno Yure  
Costa Neto, Murilo Limeira da  
Coutinho, Joana Sousa  
Couto, Douglas  
Couto, Eduardo Costa  
Dalfré, Gláucia  
Damineli, Bruno Luís  
De Nardin, Silvana  
Delalibera, Rodrigo Gustavo  
Di Mascio, Paola  
Diaz, Benjamin Ernani  
Diniz, Sofia Maria Carrato  
Domingues, Aline Bensi  
Doz, Graciela Nora  
Ehrenbring, Hinoel  
Einsfeld, Ricardo Amorim  
El Debs, Ana Lúcia Homce de Cresce  
Fabbri, Glauco  
Fairbairn, Eduardo M. R.  
Fakury, Ricardo Hallal  
Feldman, Lisa  
Felipe, Túlio Raunyr Cândido  
Felix, Emerson  
Fenu, Luigi  
Fernandes, Juliana Ferreira  
Fernandes, Robson da Silva  
Ferrari, Vladimir José  
Ferreira, Fernanda Giannotti da Silva  
Ferreira, Gisleiva  
Ferreira, Maurício de Pina  
Ferreira, Régis de C.  
Ferreira, Ruan  
Figueiredo, Antônio Domingues de  
Fonseca, Fernando  
Fonseca, João  
Fontanini, Patrícia Stella Pucharelli  
Formagini, Sidiclei  
Forti, Tiago Luís Duarte  
França Filho, Wanderson Luiz  
Futai, Marcos Massao  
Gachet, Luísa Andréia  
Gama, João Luiz Calmon N.  
Garcez, Estela Oliari  
Garcez, Mônica Regina  
Garcia, Jean  
Gaspar, Ricardo  
Ghorbel, Elhem  
Gidrão, Gustavo de Miranda Saleme  
Gil, Augusto  
Girardi, Ricardo  
Gleize, Philippe Jean Paul  
Gomes João Paulo  
Gomes, Helder Pontes  
Gomes, Henrique Campelo  
Gomes, Ronaldo  
Gouveia, Fernanda Pereira  
Greco, Marcelo  
Guimarães, Gilson Natal  
Guimarães, Giuseppe  
Guindani, Eduardo  
Gumieri, Adriana  
Haach, Vladimir Guilherme  
Helene, Paulo R. L.  
Hentges, Tatiane Isabel  
Holanda, José Nilson Franca de  
Hotza, Dachamir  
Houmard, Manuel  
Huespe, Alfredo  
Jacintho, Ana Elisabete P. G. de Ávila  
John, Vanderley Moacyr  
Jordani, Bárbara  
Justino Filho, Manoel Rodrigues  
Kataoka, Marcela Novischi  
Kautzmann, Vanessa  
Kazmi, Syed  
Kazmierczak, Cláudio de Souza  
Kimura, Alio Ernesto  
Kimura, Erica Fernanda Aiko  
Koppe, Angélica  
Krahl, Pablo  
Kremer, Bruna Maria  
Kulakowski, Marlova Piva  
Ladeira, Luiz Orlando  
Lages, Eduardo Nobre  
Lautenschläger, Carlos  
Lemes, Ígor  
Lemonge, Afonso Celso de Castro  
Leonel, Edson Denner  
Liberati, Elyson  
Lima, Flávio  
Lima, Flávio Barboza de  
Lima, Maria Cristina Vidigal  
Lima, Paulo Roberto Lopes  
Lima, Silvio de Souza  
Lintz, Rosa Cristina Cecche  
Lisserre, Andréa Prado Abreu Reis  
Longhi, Marlon  
Lopes, Raduan Krause  
Lopez, Rafael  
Lubeck, André  
Ludvig, Péter  
Luz, Caroline Angulski da  
Maedo, Michael  
Magalhães, Aldo Giuntini de  
Malite, Maximiliano  
Mancio, Mauricio  
Mappa, Paulo César  
Marangon, Ederli  
Mari, Antônio R.  
Marin, Marcelo Cuadrado  
Marques Filho, José  
Marques, Marília  
Martins, Carlos Humberto  
Marvila, Markssuel Teixeira

---

## Reviewers List 2019-2020

Mata, Rodrigo da  
Matos, Paulo de  
Mazer, Wellington  
Medeiros Júnior, Ronaldo A  
Medeiros, Arthur  
Medeiros, Marcelo  
Meira, Gibson  
Melges, José Luiz Pinheiro  
Melo, Antônio Macário Cartaxo de  
Melo, Guilherme  
Melo, Wesley Imperiano Gomes de  
Mendes, Julia Castro  
Mendes, Paulo  
Meneghetti, Leila Cristina  
Mennucci, Marina Martins  
Menon, Nara Villanova  
Mesquita, Esequiel  
Milani, Ana Paula da Silva  
Mohamad, Gihad  
Moita, Gray  
Monte, Renata  
Morsch, Inácio  
Motta, Leila A. Castro  
Moura, Márcio Wrague  
Munaiar Neto, Jorge  
Munhoz, Fabiana Stripari  
Nascimento, Aderson  
Neto, Joel  
Neves Júnior, Alex  
Noaman, Ahmed Tareq  
Nóbrega, Petrus Gorgônio Bulhões da  
Nogueira, Caio Gorla  
Novais, Rui Miguel  
Nunes, David Brandão  
Oliveira Neto, Lutgardes de  
Oliveira, Andrielli Moraes de  
Oliveira, Dênio Ramam Carvalho de  
Oliveira, Luiz Antônio Pereira de  
Oliveira, Marco Antônio Barbosa de  
Oliveira, Marcos  
Oliveira, Marcos Honorato de  
Oliveira, Mateus Antônio  
Oliveira, Romilde Almeida de  
Oliveira, Tiago  
Ortolan, Vinicius  
Paccola, Rodrigo Ribeiro  
Pachêco, Admilson da Penha  
Pachêco, Alexandre Rodrigues  
Pachêco, Fernanda  
Paes, José Luiz Rangel  
Pagnussat, Daniel  
Palermo Júnior, Leandro  
Paliga, Charlei Marcelo  
Pantoja, João da Consta  
Parente Júnior, Evandro  
Parsekian, Guilherme  
Passuello, Alexandra Cruz  
Paula, Júnia de  
Pauletti, Ruy Marcelo de Oliveira  
Pavan, Roberto Carlos  
Pavanello, Renato  
Paz, Gumersinda Seara  
Peixoto, Ricardo André Fiorotti  
Pelisser, Fernando  
Pellegrino Neto, Januario  
Pereira, Eduardo  
Pereira, Mauro Real  
Pereira, Sebastião Salvador Real  
Perlin, Lourenço  
Pessoa, José Renato Castro  
Pfeil, Michèle Schubert  
Pieralisi, Ricardo  
Pimenta, Roberval J.  
Pimentel, Lia Lorena  
Pimentel, Roberto  
Pinto, Roberto Caldas de Andrade  
Pituba, José Julio de Cerqueira  
Portela, Enson de Lima  
Positieri, Maria Ajosefina  
Possan, Edna  
Posterli, Mariana  
Pravia, Zacarias Martin Chamberlain  
Proença, Sérgio Persival Baroncini  
Quinino, Uziel Cavalcanti de Medeiros  
Ramos, Antônio Pinho  
Ramos, Violeta  
Ranzi, Gianluca  
Real, Mauro de Vasconcellos  
Rebelo, Carlos  
Ribeiro, Daniel Veras  
Ribeiro, Diogo  
Ribeiro, Paula de Oliveira  
Ribeiro, Paulo Marcelo Vieira  
Rocha, Fábio  
Rocha, Janaide Cavalcante  
Rodrigues Júnior, Sandoval José  
Rodrigues, Eduardo Alexandre  
Rohden, Abrahão Bernardo  
Romano, Roberto Desar Oliveira  
Ruan, Xin  
Ruthes, Heloiza Candeia  
Sales, Almir  
Sales, Maurício Martines  
Salles, Lúcio Salles de  
Salvador Filho, José Américo Alves  
Sanchez, Emil  
Santos, Ana Carolina  
Santos, Ana Carolina Parapinski dos  
Santos, Antônio Carlos dos  
Santos, Caio  
Santos, Carol Ferreira Rezende  
Santos, Daniel Miranda dos  
Santos, Pablo Juan Lopes e Silva  
Santos, Robson Arruda dos  
Santos, Sérgio Hampshire de Carvalho  
Santos, White José dos  
Savaris, Gustavo  
Sbrighi Neto, Cláudio  
Scherer, Mailson  
Schulz, Mauro  
Scott, Allan  
Seiffert, Henrique Luiz de Lima  
Severi, Andrea Arantes  
Shehata, Lidia  
Shi, Jinjie  
Shrive, Nigel  
Siacara, Adrian Torrico  
Silva Filho, José Neres  
Silva, Adriano de Paula e  
Silva, Arthur Leandro  
Silva, Bruno do Vale  
Silva, Fernando Artur Nogueira  
Silva, Jordlly Reydson de Barros  
Silva, José Guilherme Santos da  
Silva, Maria Cecília Amorim Teixeira  
Silva, Matheus Fernandes de Araújo  
Silva, Ricardo  
Silva, Roberto Marcio da  
Silva, Valdir Pignatta e  
Silva, Wellington Andrade da  
Simão, Tatiana Regina da Silva  
Simonetti, Camila  
Siqueira, Gustavo Henrique  
Sousa Júnior, João Batista Marques de  
Sousa, José  
Souza, Alex Sander  
Souza, Beatriz Ferreira  
Souza, Diego Jesus de  
Souza, Flávio Teixeira de  
Souza, Rafael Alves de  
Souza, Regina H.  
Specht, Luciano  
Strauss, Alfrede  
Tamashiro, Jacqueline Roberta  
Tamayo, Jorge  
Tanesi, Jussara  
Tavares, Danusa  
Teixeira, Ritermayer Monteiro  
Thives, Liseane  
Thomas, Carlos  
Titotto, Silvia Lenyra Meirelles Campos  
Torralles, Berenice  
Torres, Ariela da Silva  
Trautwein, Leandro Mouta  
Trindade, Guilherme Höehr  
Tsavdaridis, Konstantinos Daniel  
Tutikian, Bernardo  
Ulsen, Carina  
Vellasco, Pedro Colmar G. da Silva  
Velo, Luis Augusto  
Veríssimo, Gustavo  
Vieira, Gregorio Sandro  
Villegas, Noé  
Vizotto, Isaías  
Waimberg, Marcelo  
Wally, Gustavo Bosel  
Wolenski, Anderson  
Xie, Tianyu (Anson)  
Xin Lu, Jian  
Yalcin, Omer  
Yanez, Pablo Anibal Lopez  
Zaccardi, Yury Andrés Villagrán  
Zuchetti, Laís.



ORIGINAL ARTICLE

## Fracture bi-linear model parameters and brittleness of high-performance concretes for paving: why fatigue tests matters and cannot be spared?

*Parâmetros do modelo bilinear de fratura e fragilidade de concretos de alto desempenho para pavimentação: por que estudos de fadiga interessam e não podem ser dispensados?*

José Tadeu Balbo<sup>a</sup>

Andrea Arantes Severi<sup>b</sup>

Tatiana Cureau Cervo<sup>c</sup>

Andréia Posser Cargnin<sup>a</sup>

<sup>a</sup>Universidade de São Paulo – USP, Escola Politécnica, Departamento de Engenharia de Transportes, Laboratório de Mecânica de Pavimentos – LMP, São Paulo, SP, Brasil

<sup>b</sup>Ecoworld, São Paulo, SP, Brasil

<sup>c</sup>Universidade Federal de Santa Maria – UFSM, Centro de Tecnologia, Departamento de Transportes, Grupo de Estudos e Pesquisas em Pavimentação e Segurança Viária – GEPASV, Santa Maria, RS, Brasil

Received 24 April 2018

Accepted 14 May 2020

**Abstract:** Fracture tests on two high-performance concrete for pavements were performed using the wedge-split test. The results allowed perceiving the same specific fracture energy for both concrete. However, the crack opening during the tests as well as the characteristic length of the materials resulted in roundly distinct behaviors in terms of brittleness. Previous fatigue studies for both concretes are then fairly readdressed pointing out the unavoidable needs for studying the concrete brittleness as a parametric way for selecting suitable concrete proportions and materials as well as to reach its microstructural behavior in order to acquire an appropriate judgment about its fatigue performance.

**Keywords:** concrete, fracture, fatigue, brittleness.

**Resumo:** Estudos de fratura sobre dois concretos de alto desempenho para pavimentação foram realizados empregando-se o wedge-split test. Com base nos ensaios foi possível observar que a energia de fratura específica era semelhante para ambos os concretos estudados. Na realidade, apenas a medida de taxa de abertura de fissuras durante os ensaios, bem como a determinação do comprimento característico e o número de fragilidade dos materiais permitiu a sua diferenciação com clareza, apontando a relevante fragilidade de um concreto em relação ao outro. Estudos anteriores de fadiga para ambos os concretos são revisitados, permitindo concluir pela necessidade da caracterização da fragilidade de concretos como meio paramétrico de seleção de dosagens, bem como para o correto entendimento de sua microestrutura que resulta em seu comportamento à fadiga.

**Palavras-chave:** concreto, fratura, fadiga, fragilidade.

**How to cite:** J. T. Balbo, A. A. Severi, T. C. Cervo, and A. P. Cargnin, “Fracture bi-linear model parameters and brittleness of high-performance concretes for paving: why fatigue tests matters and cannot be spared?,” *Rev. IBRACON Estrut. Mater.*, vol. 14, no. 1, e14101, 2021, <https://doi.org/10.1590/S1983-41952021000100001>

Corresponding author: José Tadeu Balbo. E-mail: jotbalbo@usp.br

Financial support: CAPES.

Conflict of interest: Nothing to declare.



This is an Open Access article distributed under the terms of the Creative Commons Attribution License, which permits unrestricted use, distribution, and reproduction in any medium, provided the original work is properly cited.

## 1 INTRODUCTION

### 1.1 Background and motivation

In 2015, during the discussion of a doctorate thesis at the University of Delft [1] which included several fatigue tests on cementitious design mixtures for pavement bases, one member of the board (American university professor) asked the candidate why not perform fracture tests to decide about the material mixture design and about its durability potential in the field in clear opposition to the time-consuming and costly flexural fatigue tests [2].

Considering this frequent thinking, this study presents fracture tests for two concrete types, which are similar to ones previously studied [3]. So, this paper brings up this old discussion, seeking to point out the ability of some parameters to, indeed, distinguish the utility of these tests in a comparative and complementary way considering the concrete pavements issues. For this purpose, fracture tests parameters for identical specimens of two concretes are presented, addressed and compared to fatigue tests carried out on the same concretes, in order to indicate their value to make it clear the different fatigue behavior of such materials and in the case of Pavement Mechanics, especially for pavement structural designers, regarding the current normative context whether Brazilian, American or European.

### 1.2 Fracture Energy Concept and the Crack Coalescence

The specific fracture energy ( $G_f$ ) is a parameter of paramount relevance to the characterization of fractured structures and it is affected by the specimen size used for its measurement [4]; in other words, there is a scale factor continuously influencing the results. There are specific recommendations from RILEM [5], for instance, for computing this energy: The full fracture work shall be divided by the fractured area (the area originally without notches), and the test formats commonly used are prismatic samples with a central notch and vertical load over its surface in the same direction of the notch; or using methods of splitting by a wedge forcing the crack under the notched area (using cubic or cylindrical samples). The specific fracture energy, given by the load-displacement or load-crack opening curves is defined by Equation 1:

$$G_f = \frac{1}{A} \int_0^{\delta_{ult}} F_H \cdot d\delta \quad (1)$$

where  $A$  is the area under fracture during the test,  $F_H$  is the horizontal force (in the wedge test over cubes, for instance),  $\delta$  is the displacement and  $\delta_{ult}$  is the final displacement during the test when  $F_H = 0$ . It is convenient to remark that the force-displacement curve for  $G_f$  calculation is taken from the force peak, when the relaxation and catastrophic regimen starts [6], inducing the crack propagation within the entire area of the sample. The zone between the zero initial force and the peak is admitted, for practical purposes, as the elastic zone where there is no material plastification. The size of the tested specimen does not seem to be a worthless geometric aspect in the fracture analysis (elastic-linear fracture mechanics) as stated by several authors [7].

The fracture tests for road materials analysis and mixture design, especially brittle materials, such as concretes and bases as cement treated crushed stones and roller compacted concretes, although rarely used, has the great advantage of allowing the prediction of the material behavior from the strain's approach (microstructural).

In fracture toughness tests, at the same concrete beam is notched causing a vertical flat section with a height lower than all the others vertical sections of the sample; the vertical loading is applied on the same direction of the notch, in such a way that the stress lines are concentrated in the notch tip, making the sample starts cracking in this zone, forcing the fracture always in that vertical plan or very close to it (Figure 1). That should reduce or even eliminate the test dispersion, avoiding the fracture zones randomness like in fatigue tests. Rots et al. [8] state that as the deformation position in the fracture zone is defined, the surrounding zone unloaded, which means the micro-cracking in the surrounding area is captured or even blocked.

Nevertheless, the authors recommend five to ten tests that should be run to calculate the mean fracture toughness parameters (for example, Karihaloo et al. [4]).

The elastic energy stored in the specimen tested is proportional to the material volume, whereas the fracture energy is related to the fracture area [9]. So, the relation between both suggests a characteristic linear length which distinguishes them, namely characteristic length ( $l_{ch}$ ), as shown in Equation 2:

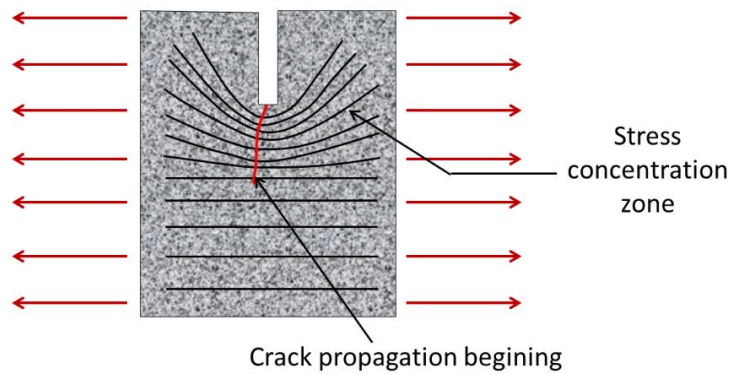


**Figure 1.** Stress concentration in the notch tip of cubic concrete specimens (adapted from Balbo, 2009).

$$I_{ch} = \frac{G_f \times E}{f_t^2} \quad (2)$$

where  $E$  is the material elastic-linear modulus of elasticity,  $f_t$  is the tensile strength and  $G_f$  is the specific fracture energy. The brittleness of a certain material is reduced for longer characteristic lengths [10], [11], allowing material comparisons regarding this parameter. Equation 3 defines the brittleness number, which is proportional to the characteristic length ( $L$ ) and is related to the material tensile strength ( $f_t$ ), its modulus of elasticity ( $E$ ) and specific fracture energy ( $G_f$ ) as well:

$$B = \frac{f_t^2 \times L}{G_f \times E} \quad (3)$$

Considering the two concretes for pavements assessed in this paper, which were also studied by Cervo [12] and Cervo and Balbo [3] under the fatigue approach, it was observed that the high strength concrete (HSC) (with high cement consumption and micro-silica addition, with a smaller maximum aggregate size) fails under lower fatigue cycles. However, due to the reasons aforementioned, and the fatigue response during the tests, microstructural parameters such as energy, fracture deformation and brittleness are not obtained directly, hindering the objective interpretation of such parameters. So, in this paper, the same concrete mixes former studied regarding their fatigue behavior, are studied seeking to make it clearer their behavior in the light of the most important fracture parameters. Finally, the concretes are compared by the cohesive zone model, using the graphic approach proposed by Petersson [13].

### 1.3 The Fatigue Strength concepts and the Crack Coalescence

Traditional fatigue tests on pavement materials are usually performed on beams by the third-point beam tests (flexural) and present great results dispersion, at most, due to the randomness of the fracture planes; the flexural stresses cause gradual microstructural breaks, but following random planes since in the middle third the bending moment is constant, making the crack coalescence starts in the weaker planes following through the surrounding zones where the crack progress is facilitated point to point. It means that each sample tested has a specific fracture geometry which usually does not follow a planar state, in contrast to what normally happens in fracture tests.

An explanation [14] to fatigue behavior can be “is a phenomenon or process of damaging or deteriorating the mechanical characteristics of certain materials causing its failures as a structural component. Consequently, fatigue is a behavior change sign, in other words, it is the material failure over an initial pattern; this change is harmful and sometimes catastrophic. As the fatigue process goes forward there is the crack coalescence in the material microstructure and when the crack length is longer than the namely critical length, the material breaks. It happens under cyclic loadings when the strains experienced by the material are slower than its strain capacity; therefore, it cannot be confused with a static strength rupture.”

Considering  $N_f$  as the number the loading cycles until failure (crack) and  $2N_f$  the reversal number during the test to happen the same failure, the strain elastic component is given by Equation 4:

$$\frac{\Delta}{2} = \frac{\sigma_a}{E} = \left( \frac{\sigma'_f}{E} \right) \cdot (2N_f)^b \tag{4}$$

where  $\Delta\varepsilon/2$  is the elastic strain amplitude,  $\sigma'_f$  is the stress coefficient or stress at  $2N_f = 1$  cycle, E is the material modulus of elasticity and b is an experimental coefficient, namely *fatigue strength coefficient*, normally admitted as linear in the log-log representation, where b is the slope of the fatigue curve obtained through the tested specimens ( $\varepsilon$  as a function of  $N_f$ ).

Regarding the plastic component ( $\varepsilon_p$ ), it is expressed by Equation 5:

$$\frac{\Delta\varepsilon_p}{2} = \frac{\sigma_a}{E} = \varepsilon'_f \cdot (2N_f)^c \tag{5}$$

where  $\varepsilon'_f$  is the ductility coefficient, equivalent to the plastic strain for  $2N_f = 1$  cycle and c is the *fatigue ductility exponent* (Figure 2). The lower the c value, the greater the fatigue ductility of the material studied, i.e., the lower its brittleness, breaking under plastic strain higher levels.

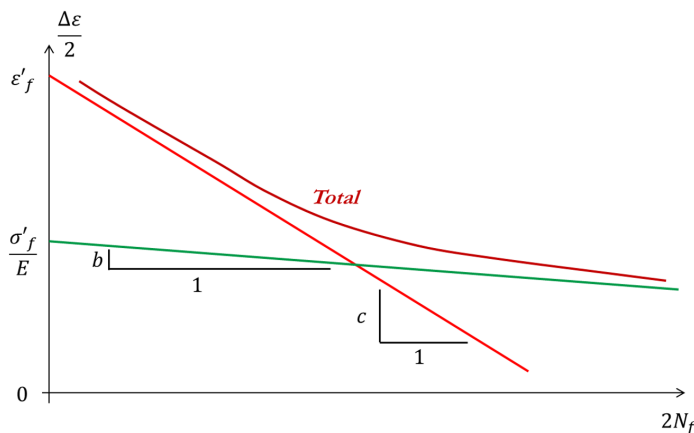


**Figure 2.** Elasto-plastic components fatigue behavior (Adapted from Balbo, 2009).

Fatigue flexural tests with concrete beams are usually described by statistic models or transfer functions which relate the flexural stress applied ( $\sigma_{ff}$ ), the flexural concrete strength ( $f_{ct,f}$ ) and the fatigue strength ( $N_f$ ), through the “S-N” curves, as presented in Equation 6 for tests conducted under controlled stress, with a and b called experimental coefficients.

$$\log_{10} N_f = a + b \cdot \left( \frac{\sigma_{ff}}{f_{ct,f}} \right) \tag{6}$$

## 2 EXPERIMENTAL METHOD FOR FRACTURE STUDIES

In order to assess the specimen’s fracture on Mode I (pure tensile), the wedge splitting test was conducted with cubic concrete specimens of  $150 \times 150 \times 150 \text{ mm}^3$ . Ten identical specimens from the same concrete batching produced

in the lab were prepared for each concrete (Table 1). The wedge splitting test requires the use of cubic specimens with a size of 150 mm, which must be notched.

**Table 1.** Materials employed and concrete characteristics

Materials and characteristics	Conventional concrete	High strength concrete
Cement consumption (kg/m <sup>3</sup> )	396	420
Cement type	CP II 32	CP V
Coarse aggregate 19 mm (kg/m <sup>3</sup> )	483	1029
Coarse aggregate 25 mm (kg/m <sup>3</sup> )	724	-
Fine aggregate – medium sand (kg/m <sup>3</sup> )	620	641
Water (L/m <sup>3</sup> )	180	204
Plasticizer (L/m <sup>3</sup> )	1.388	1.428
Superplasticizer (L/m <sup>3</sup> )	-	2.38
Silica fume (kg/m <sup>3</sup> )	-	42
Water/cement ratio	0.455	0.442
Compressive strength (MPa) – 24 hours	-	22.6
Compressive strength (MPa) – 7 days	-	35.1
Compressive strength (MPa) – 28 days	37.6	53.2
Flexural strength (MPa) – 24 hours	-	3.5
Compressive strength (MPa) – 110 days	48.0	76.7
Flexural strength (MPa) – 24 hours	-	3.5
Flexural strength (MPa) – 7 days	-	7.0
Flexural strength (MPa) – 28 days	5.14	7.2
Indirect tensile strength (estimated – MPa)	4.0	5.3
Modulus of Elasticity – E (MPa)	32,000 (55 days)	38,000 (29 days)
Modulus - E (MPa) – fracture tests	36,200 (100 days)	42,900 (100 days)

Figure 3 depicts the schematic representation employed for type I fracture tests through the wedge splitting test; on the top of the concrete cube is made a notch (concrete is cutout) along the specimen length. On this wide upper notch are positioned two metallic segments along the specimen length; such segments have two downright faces that are thoroughly fitted to the lateral and bottom surfaces of the notch. Then a wedge is introduced between those metallic segment’s diagonal faces, slipping on small metal cylinders. As the applied vertical force on the wedge increases, horizontal deformations trend to separate both sides of the specimen, resulting in its fracture underneath the thin vertical notch below the top wide notch [15].

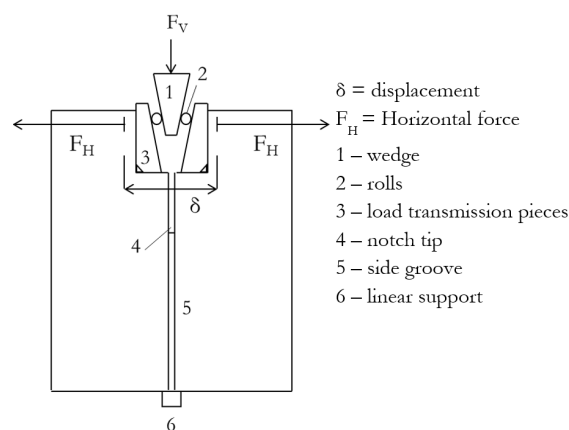


**Figure 3.** Test arrangement: fracture zone between points 4 and 6; horizontal pieces for application wedge with devices 1 and 3; 5 represents the height of the face initially linked.

Figure 4 details the test arrangement and the specimen positioned to be tested. The machine employed is a universal Hydropulse test adjusted for static constant load application; tests were conducted at 0.4 kN/s. Two Linear Variable

Differential Transformer (LVDT) were installed at the top of the device arrangement on the concrete cube in order to measure displacements while the wedge moves entering the large superior notch when force actuates; both LVDT are placed in opposed faces and oppositely at surface extremities, but at the same horizontal plane (see Figure 4 top).

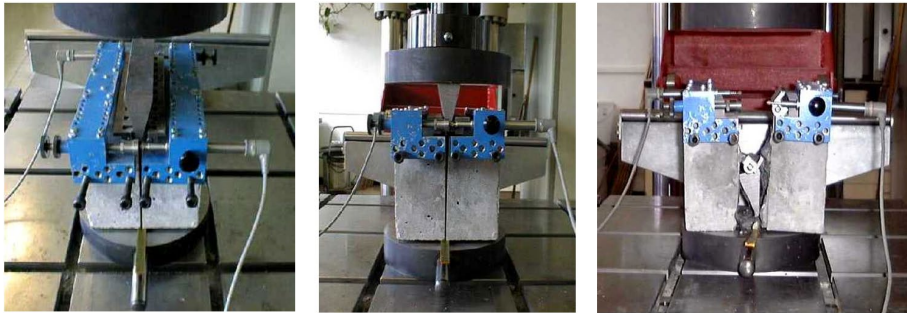


**Figure 4.** Test arrangement: at left the wedge is seen in the whole concrete cube extension; at the center it is seen the vertical notch; at right it is seen the fractured concrete cube.

At last, Figure 5 illustrates the cuts and notches made in the cubic specimen and the linking zone before the test. Figure 6 shows the fractured faces for conventional concrete and the HSC for two cubes after the test; the images make it clear the different maximum diameters of aggregates for the two concrete mixtures.

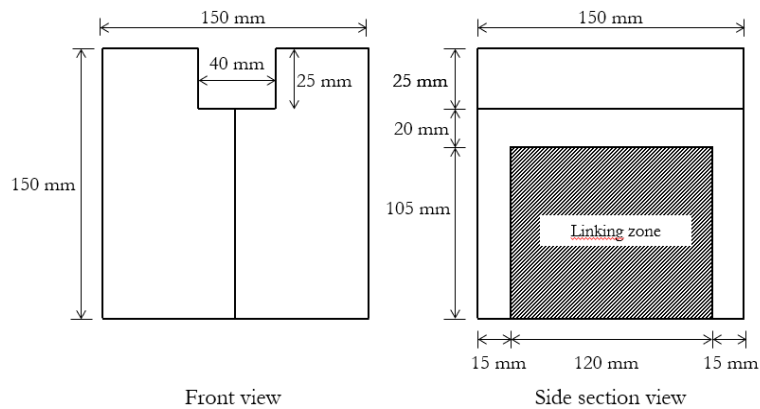


**Figure 5.** Cut zones sizes at the concrete cube (notches).



**Figure 6.** Conventional concrete (left) and high strength concrete (right) fractured faces.

Tests on the modulus of elasticity for both the conventional and HSC mixes were performed to determine the fracture parameters. Therefore, following to the fracture tests, cylindrical specimens with 50 mm of diameter were cored from both non-fractured sizes of the specimens to measure the compressive modulus of elasticity; it is an approximate value related to the concrete flexural modulus of elasticity and differences around 10% are recorded for both tests [16]. The fracture tests were performed at the ages of 97 and 95 days for conventional concrete and 84 and 92 days for the HSC. All these tests were held in the TFB (*Technische und Forschung Beratungsstelle*, Wildegg) facilities.

Modulus of elasticity was measured by simple arrangements of cylindrical specimens cored from the non-fractured parts of the concrete cubes (50 mm x 150 mm), using uniaxial compression tests on a universal testing machine and employing LVDTs for measuring vertical strains during the tests, conducted at the same aforementioned rate of force application. This parameter in compression tests is commonly affected by aggregate type and size while the interfacial transition zone phase is critical for measuring the modulus of elasticity in tensile. Due to aggregate type (mineral structure and origin), for instance, multiplicative correction factors for modulus of elasticity measured over basalt and limestone aggregate are, respectively close to 0.90 and 1,20 [17]. One should note that the magmatic rocks tend to be harder and stiffer than some sedimentary ones; this study employed limestone aggregates for the conventional concrete and granitic aggregates for the high strength concrete, which contributes somehow to improve results for the high strength concrete.

Though the parameter is also affected by the maximum coarse aggregate size, complexity on establishing the degree of comparison among the different concretes where really affected not only by the own aggregate model phase of a multiphase material but also by the sharp differences on the paste-mortar phases of both concrete mixes: (1) high strength concrete using 66 kg/m<sup>3</sup> in excess of different nature of hydraulic binders (including 40 kg/m<sup>3</sup> of highly fine silica fume); (2) conventional concrete employing 1,207 kg/m<sup>3</sup> of coarse aggregates (a blend of 19 mm and 25 mm diameters), i.e., circa 200 kg/m<sup>3</sup> in excess than the high strength concrete. If now one considers that the compressive strength at 100 days is circa 63% greater for the HSC and its modulus of elasticity is 84% greater, the issue of maximum diameter becomes a little bit hard to discuss, if one expects higher compressive moduli when higher diameters are presented. Therefore, the bottom line of the discussion to be done is whether fracture or fatigue parameters are able to explain the mixtures' performances in macro and microstructural points of view. Fracture tests will suggest very different concrete performances as suggested from former fatigue studies for the mixtures?

### 3 RESULTS

Table 2 presents the average results obtained for ten tests for each concrete, for a parameter such as the critical load applied, the crack width, the fracture energy, and the specific fracture energy. The load when the fracture starts (peak) is higher for the HSC than the conventional concrete; note that when this force occurs the notched width is the same for both concretes and it is about five-hundredths of a millimeter (Figure 7 and 8). However, when the maximum dissipated energy is reached, although the energies are similar for both the concrete (see  $G_f$  in Figures 9 and 10), the crack width in the conventional concrete notch is twice the crack width in the HSC denoting the greater brittleness of the HSC.

**Table 2.** Fracture test parameters, crack length and energy

Type	Value	Dimensions			At maximum force		At maximum energy			$G_f$ (N/m)
		L (mm)	H (mm)	Area (m <sup>2</sup> )	Force (kN)	Crack width (mm)	Force (kN)	Crack width (mm)	Fracture energy (N/m)	
	Mean	128.5	114.3	0.015	5.571	0.044	0.019	3.380	1.45	97.91
CV	SD	8.0	5.5	0.001	0.670	0.003	0.009	1.455	0.41	21.09
	CoV (%)	6.2	4.8	7.025	12.030	7.528	45.829	43.054	27.91	21.54
	Mean	126.9	112.7	0.014	7.780	0.046	0.026	1.672	1.39	97.39
HSC	SD	2.6	1.2	0.000	0.608	0.003	0.011	0.334	0.16	12.71
	CoV (%)	2.0	1.1	2.138	7.816	5.619	43.020	19.982	11.83	13.05

Figures 7 and 8 show the curves force versus strain (crack width) for both conventional and HS concretes. The graphs detail the differences between the peak forces for the crack coalescence beginning and the crack width at the

end of the test, as well. These are the highlighted differences between the set of tests conducted since there is not much difference in the total energy where the areas are compensated regarding the curvature for crack width around 0.5 mm.

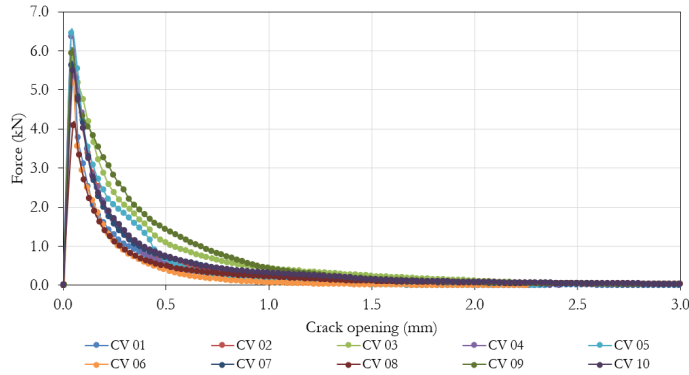


Figure 7. Force versus crack width curves for conventional concrete.

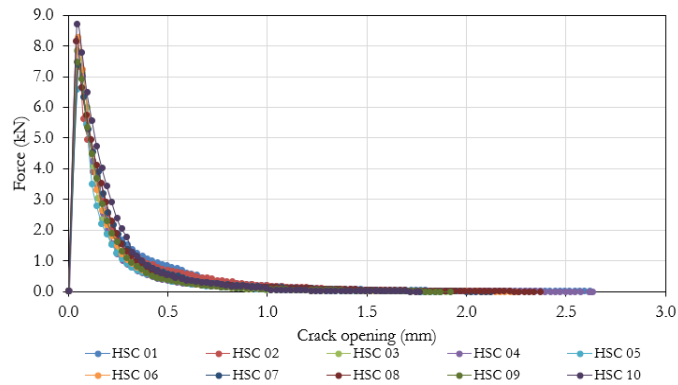


Figure 8. Force versus crack width curves for the high strength concrete.

In Figure 7 is worth noting to remember that specimen CV5 presented some unstable post-peak behavior. During the discussion with the lab technicians it was clarified that in face of daily fracture tests performed at TFB and considering that the other 19 tests for this study with no signals regarding instability, possible small and non-detected displacement of the testing table was imputed for such a specific misbehavior, though not affecting the fully coherence of the CV5 test. There is no reason for the possible failure to be omitted or discharged on the results in Figure 7.

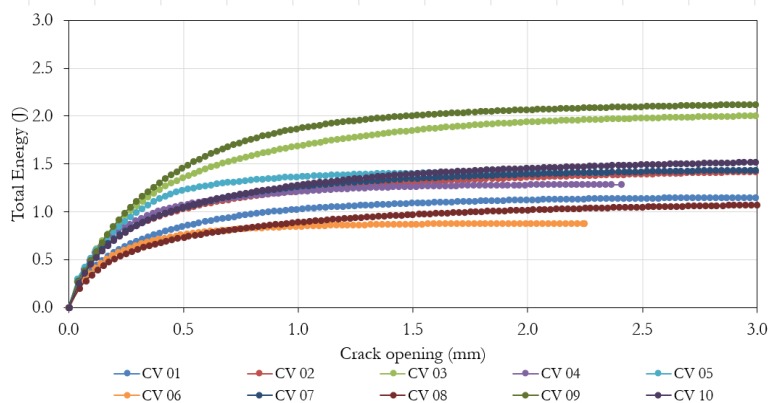


Figure 9. Fracture energy curves for conventional concrete.

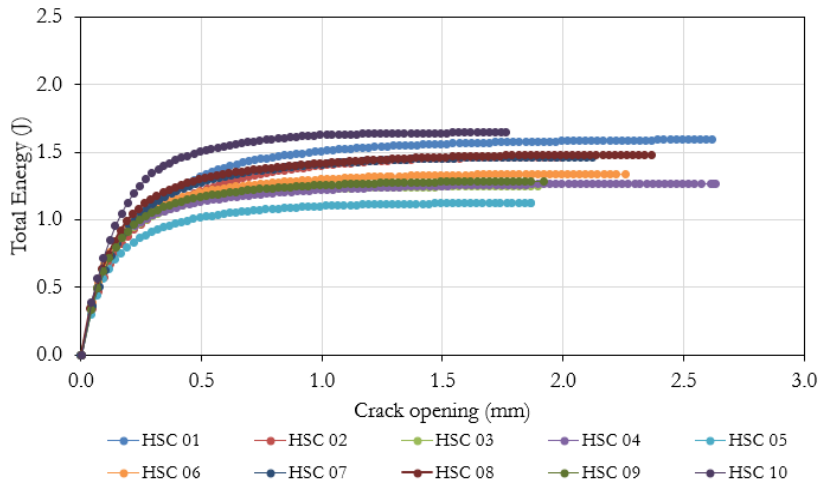


Figure 10. Fracture energy curves for high strength concrete.

The total energy versus crack width curves (Figures 9 and 10), also with absolute values close, show greater dispersion on tests performed with conventional concrete than tests with HSC. During the tests, the conventional concrete presented energy individual values wider than the HSC, in both upper and lower limits.

#### 4 CRITICAL ANALYSIS OF THE FATIGUE TESTS IN VIEW OF THE FRACTURE TESTS

Studies conducted by Cervo [12] and Cervo and Balbo [3] resulted in the S-N models for fatigue characterization of the same concretes here assessed regarding their fracture behavior. Figure 11 shows the fatigue test results for both concrete; regarding the conventional concrete, it was evaluated results obtained on 21 concrete beams, which presented standard error of 0.18 and coefficient of determination ( $R^2$ ) of 0.91; for the HSC, 30 concrete beams were assessed, resulting in a standard error of 0.16 and coefficient of determination ( $R^2$ ) of 0.96. The results also show that the HSC has lower fatigue performance than conventional concrete, which is described by the correlation logarithmic slopes. Figure 12 presents several concrete specimens after ending the flexural fatigue tests.

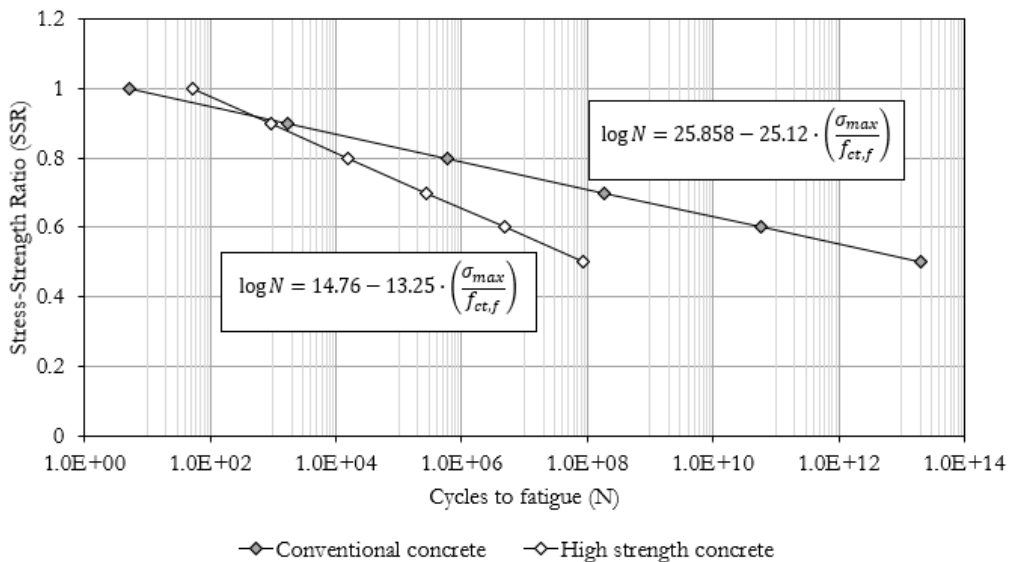


Figure 11. S-N curves for conventional and high strength concrete.



**Figure 12.** Fractured sections for the high strength concrete during fatigue tests.

It is clearly observed the fatigue rupture rarely happens in the middle third of the span, not even on a specific vertical plan, but on non-flat and usually non-centered surfaces, one of the reasons for the common dispersion of results during tests of such nature. When the specimens are instrumented with LVDT, it is only indicated the vertical strain growth when the fatigue cycle is close to the end. The evident information from the fatigue tests is the HSC smaller capacity to support cyclic loadings compared to a conventional concrete for pavements.

Fracture studies bring new lights to the behavior former recorded, based on fracture parameter determined by tests presented in item 3, as follows. Firstly, in Figure 13 are shown the mean curves force versus crack width for each concrete studied. The overlap of such curves makes clear the energy compensation between curves for  $\delta = 0.25$  mm and greater than this value. Ignoring the observed discrepancies, the small concrete toughness is very clear in the zones after the peak of the vertical force. The energy dissipation is faster for the HSC (Figure 14), which is greater than conventional concrete until crack width of 1 mm, stabilizing, when there is still some dissipation in the conventional concrete until it breaks, happening when the crack with is twice the HSC crack width.

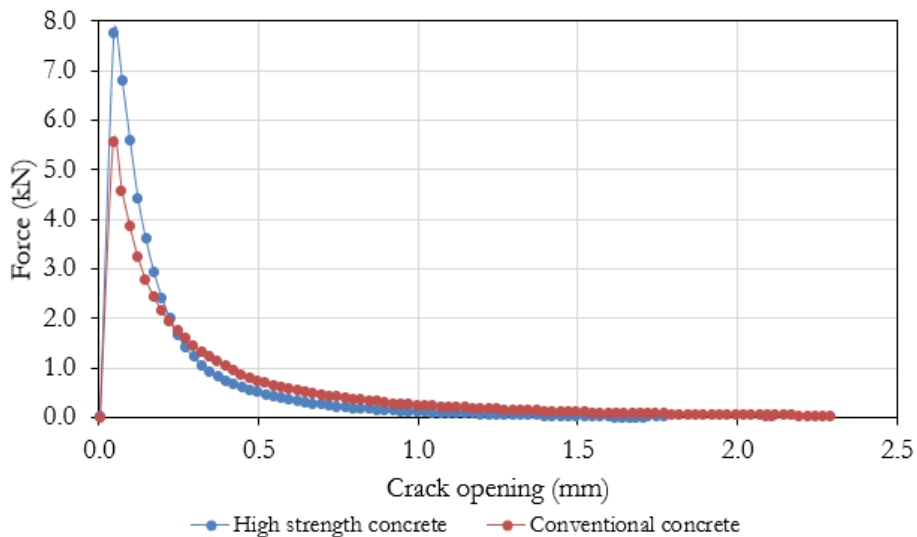


**Figure 13.** Overlap of the force versus crack width means curves for conventional and HS concrete.

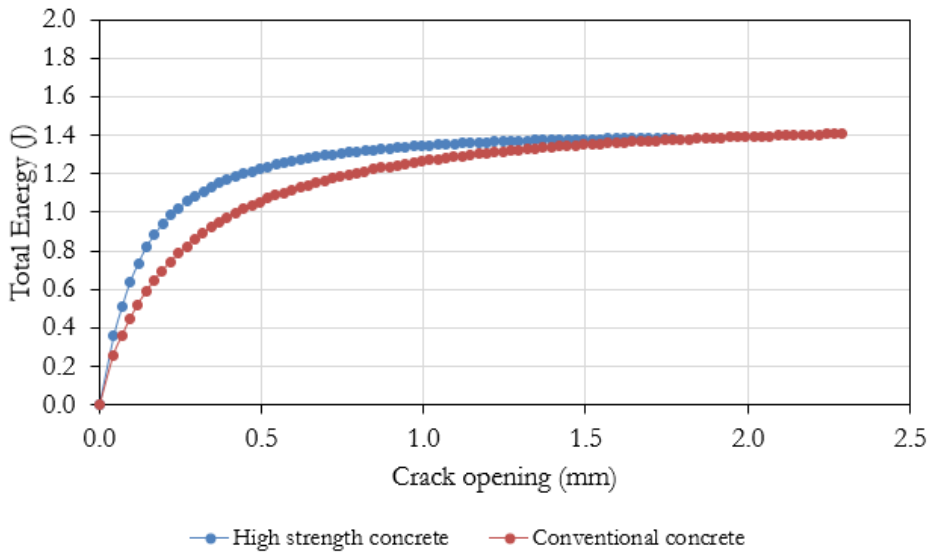


**Figure 14.** Overlap of the total energy curves along the concrete fracture tests.

In order to compare properties, the concretes compressive strength at 90 days were assessed as 13% higher than the strength measured at 28 days. Subsequently, the indirect tensile strength was estimated by Equation 7, for values in MPa:

$$f_t = 0.3 \times \sqrt[3]{f_c^2} \tag{7}$$

Tables 3 and 4 show the parameters for tests conducted in individual specimens, as well as the characteristic length ( $I_{ch}$ ) results and their brittleness number (B). As seen, the brittleness is reduced for characteristic lengths longer [9], [10], [18], and it is observed from this fracture test numeric parameter that the HSC is weaker than conventional concrete, despite their total fracture energy are similar. In absolute values, the brittleness observed for both concretes, close to each other (0.24 and 0.34) are comparable to that of carbon ally refractories [18].

**Table 3.** Conventional concrete characteristic length and brittleness

Specimen	$G_f$ (N/mm)	$I_{ch}$ (mm)	B
CV 01	0.00083	0.18	0.272
CV 02	0.000103	0.23	0.219
CV 03	0.000125	0.28	0.180
CV 04	0.000089	0.20	0.253
CV 05	0.000098	0.22	0.230
CV 06	0.000061	0.14	0.370
CV 07	0.000100	0.22	0.225
CV 08	0.000078	0.17	0.289
CV 09	0.000130	0.29	0.173
CV 10	0.000112	0.25	0.201
Mean	0.000096	0.22	0.241
Standard deviation	0.000021	0.05	0.058
Coefficient of variation (%)	22.0	21.5	24.2

Note: E= 36.200 MPa;  $f_t$ = 4.04 MPa; L=0.05 mm

**Table 4.** High strength concrete characteristic length and brittleness

Specimen	$G_f$ (N/mm)	$I_{ch}$ (mm)	$B$
HSC 01	0.00011	0.17	0.301
HSC 02	0.00010	0.16	0.331
HSC 03	0.00009	0.13	0.368
HSC 04	0.00009	0.13	0.368
HSC 05	0.00008	0.12	0.414
HSC 06	0.00009	0.14	0.368
HSC 07	0.00010	0.16	0.331
HSC 08	0.00010	0.16	0.331
HSC 09	0.00009	0.13	0.368
HSC 10	0.00015	0.17	0.221
Mean	0.000100	0.15	0.340
Standard deviation	0.000019	0.02	0.052
Coefficient of variation (%)	19.4	13.1	15.4

Note:  $E=42,900$  MPa;  $f_t=5.33$  MPa;  $L=0.05$  mm

Hypothesis tests (T-test) for paired samples (data set for CV and HSC) were held in order to analyze the numeric parameters obtained for  $G_f, I_{ch} \in B$ , for a confidence level of 95%, point out in the following important comments. In the fracture energy test, the hypothesis of equality between the average samples was confirmed, with  $stat-t$  equal to -0.245 and  $t-critical$  for the two-tailed test equal to 2.262, showing  $stat-t$  between the limits of the test. However, regarding the critical length, the null hypothesis for the samples is rejected, indicating the mean values are different, with  $stat-t$  equal to 4.048 and  $t-critical$  for the two-tailed test equal to 2.262. The same trend is observed for the brittleness number, with the rejection of the null hypothesis, i.e., the samples mean values are different, with  $stat-t$  equal to -4.22 and  $t-critical$  equal to 2.262 for the two-tailed test.

From the concrete tensile strengths, calculated as previously described, it is possible to determine the bilinear graphic model [13] to describe and compare the mechanical parameters for both concretes. The draft of the bilinear model after peak requires the following parameters:

- The abscissa of the center of gravity ( $s_1$ ) of the first triangle as  $s_1 = f_t/3$
- The abscissa of the first interception in the crack opening (displacement)  $w_1 = 0.8 G_f/f_t$
- The abscissa of the second interception in the crack opening (displacement)  $w_1 = 3.6 G_f/f_t$ .

Figure 15 represents the bilinear models for both conventional and HSC. The models allow clearly see the fracture parameter of such concretes: comparable fracture energy; stress peak higher in the HSC; fracture rate higher for the HSC; and fracture strain smaller for the HSC.

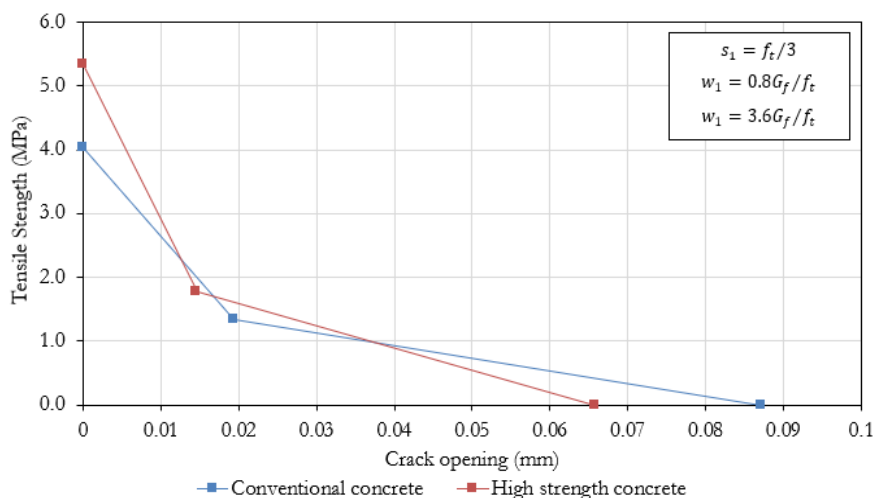


**Figure 15.** Fracture bilinear mean model for conventional and high strength concrete.

Taking up the fatigue models obtained for the conventional and HSC, it can be said that the answer on the lower fatigue strength capacity to dynamic and monotonic loading (stress-controlled) is not established based on the specific fracture energy  $G_f$ . Fatigue is a process of micro-cracking coalescence in the concrete microstructure, and in the case of HSC the rupture happens faster due to its greater brittleness, which presents characteristic length shorter than conventional concrete. So, the faster cracking coalescence combined to the slower strain levels required for the same coalescence justify the HSC's poor performance regarding the fatigue process, which is a typical process of strain increasing until cracks reach a critical length, resulting in a catastrophic rupture.

Therefore, the fracture tests are excellent to explain the microstructural cracking phenomenon considering the clarification and better understanding of the HSC smaller strength compared to conventional concrete. However, unlike an S-N model, the fracture tests, although based on linear fracture, still do not allow to establish directly cause-effect relationships which could simply allow structural evaluations related to the geometry and strength of concrete slabs for pavements.

## 5 CONCLUSIONS

The fracture tests with two typical concrete for pavement allow summarizing the main findings as follows:

- The high strength concrete (HSC), despite its modulus of elasticity and tensile strength higher than conventional concrete, presented specific fracture energy similar to the conventional concrete, which does not allow singly to distinguish them. Thus, the performed fracture tests do not have enough potential for distinction for the studied cases;
- Otherwise, the critical length and brittleness number were well distinguished by the fracture studies, indicating that such parameters calculated by the described tests (fracture and modulus of elasticity) are good indicators for the desired comparisons;
- The HSC presents rupture strains significantly lower than conventional concrete, which is associated with the HSC highest relaxation rate;
- The HSC has a characteristic length markedly shorter than the conventional concrete, highlighting its brittleness in numeric and objective terms, explaining its worse fatigue behavior;
- What the fatigue tests were not capable to explain from the microstructure point of view and why the HSC fatigue strength is slower than the conventional concrete is well explained by the fracture parameters: the high-performance concrete presented poorer fracture and fatigue performance than conventional concrete for pavements regarding the microstructural indexes and observed parameters.

The future connection between both kinds of test results may allow distinguishing clearer the concretes with different mixing designs as a way of selection for pavement concretes regarding performance criteria much more realistic than the strength tests commonly used as a reference for pavement projects. It is evident the importance of the concrete modulus of elasticity control for the advancement in the mixing design and technologic control criteria since without this parameter would not be possible to discuss tests and conclusions previously addressed.

However, fracture tests alone, considering the current state of the knowledge about mechanistic models for the analysis of concrete pavements structure degradation, whether road, airport or port, do not provide yet elements capable to directly relating the cause and effect of immediate application in daily projects; those tests are not even standardized or specified for studies in this field of knowledge, as a non-encouraging aspect. Nevertheless, the fracture parameters allow an understanding of the microstructural behavior which fatigue tests alone do not provide to the designer/technologist.

## ACKNOWLEDGEMENTS

The authors thank to Dr. Maher Badawy by the support on tests and their interpretation in the *Technische Forschungs und Beratungstelle der Schweizer Zement Industry* facilities, TFB, Wildegg, Switzerland.

## REFERENCES

- [1] P. Wu, "Cement stabilized materials with use of RoadCem Additives," Ph.D. dissertation, Civ. Eng. Dept., Delft Univ. Technol., Delft, 2015.
- [2] J. T. Balbo, *Personal communication: i was member of this doctoral board and witnessed the questioning, which is very common for technologists who ignore the theoretical, empirical and practical aspects of the pavement mechanics regarding the fatigue degradation of such structures.* Delft Univ. Technol., 2015.

- [3] T. C. Cervo and J. T. Balbo, "Calibration of a shift-factor for the fatigue prediction of high strength concrete pavement in the field," *Int. J. Pavement Res. Technol.*, vol. 5, no. 3, pp. 153–160, 2012.
- [4] B. L. Karihaloo, H. M. Abdalla, and T. Imjai, "A simple method for determining the true specific fracture energy of concrete," *Mag. Concr. Res.*, vol. 55, no. 5, pp. 471–481, 2003.
- [5] RILEM, "Determination of the fracture energy of mortar and concrete by means of three-point bend on notched beams," *Mater. Struct.*, vol. 18, no. 6, pp. 285–290, 1985.
- [6] A. Carpentieri and G. A. Ferro, "Scaling behaviour and dual renormalization of experimental tensile softening responses," *Mater. Struct.*, vol. 31, no. 209, pp. 303–309, 1996.
- [7] M. Elices, G. V. Guinea, J. Gómez, and J. Planas, "The cohesive zone model: advantages, limitations and challenges," *Eng. Fract. Mech.*, vol. 69, no. 2, pp. 137–163, 2002.
- [8] J. G. Rots, P. Nauta, G. M. A. Kusters, and J. Blaauwendraad, "Smearred crack approach and fracture localization in concrete," *Heron*, vol. 30, no. 1, 1985.
- [9] H. Harmuth and R. C. Bradt, "Investigation of refractory brittleness by fracture mechanical and fractographic methods," *Inter-ceram*, pp. 6–10, 2010.
- [10] D. P. H. Hasselman, "Unified theory of thermal shock fracture initiation and crack propagation in brittle ceramics," *J. Am. Ceram. Soc.*, vol. 52, no. 11, pp. 3600–3604, 1969.
- [11] Z. P. Bazant and M. T. Kazemi, "Determination of fracture energy, process zone length and brittleness number from size effect, with application to rock and concrete," *Int. J. Fract.*, vol. 44, no. 2, pp. 111–131, 1990.
- [12] T. C. Cervo, "Study of fatigue strength of Portland cement concrete for paving," Ph.D. dissertation, Esc. Politec., Univ. São Paulo, 2004.
- [13] P. Petersson, "Crack growth and development of fracture zones in plain concrete and similar materials," *Rep. TVBM*, vol. 1006, pp. 174, 1981.
- [14] J. T. Balbo, *Pavimentos de Concreto*. São Paulo: Oficina de Textos, 2009.
- [15] K. Tschegg, M. Elser, and S. E. Stanzl-Tschegg, "Biaxial fracture tests on concrete – development and experience," *Cement Concr. Compos.*, vol. 17, no. 1, pp. 57–75, 1995.
- [16] J. T. Balbo, "Estudo das propriedades mecânicas das misturas de brita e cimento e sua aplicação aos pavimentos semirrígidos," Ph.D. dissertation, Dep. Eng. Transp., Esc. Politec., Univ. São Paulo, 1993.
- [17] T. Noguchi, F. Tomosawa, K. M. Nematí, B. M. Chaia, and A. P. Fantilli, "A practical equation for elastic modulus of concrete," *ACI Struct. J. Title*, vol. 64, no. 106-S, pp. 690–696, 2009.
- [18] H. Harmuth and E. K. Tschegg, "A fracture mechanics approach for the development of refractory materials with reduced brittleness," *Fatigue Fract. Eng. Mater. Struct.*, vol. 20, no. 11, pp. 1585–1603, 1997.

---

**Author contributions:** JTB: writing, conceptualization, formal analysis; modeling; literature review; AAS: testing runner, data acquisition; TCC: testing runner, data acquisition; APC: statistical analysis, writing.

**Editors:** Osvaldo Luís Manzoli, José Luiz Antunes de Oliveira e Sousa, Guilherme Aris Parsekian.



ORIGINAL ARTICLE

# Shear friction capacity of self-consolidating concrete

## *Resistência atrito cisalhamento do concreto autoadensável*

Gustavo Savaris<sup>a</sup> Roberto Caldas de Andrade Pinto<sup>b</sup> <sup>a</sup>Universidade Tecnológica Federal do Paraná – UTFPR, Coordenação de Engenharia Civil, Toledo, PR, Brasil<sup>b</sup>Universidade Federal de Santa Catarina – UFSC, Departamento de Engenharia Civil, Florianópolis, SC, Brasil

Received 23 December 2018

Accepted 18 May 2020

**Abstract:** An experimental research was developed to evaluate shear transfer in self-consolidating. Three concrete mixes were prepared, one conventional and two self-consolidating, differing on the proportion of the coarse and fine aggregate used. Nine push-off specimens, containing steel reinforcement passing through the shear plane, were tested, to evaluate the ultimate shear stress and shear plane displacements. Shear strength of self-consolidating concrete specimens were higher than conventionally vibrated concrete. The experimental results were compared to the shear strength estimated by literature and code based equations, yielding conservative results of these equations for both types of concrete, especially the models that disregard the compressive strength of concretes.

**Keywords:** self-consolidating concrete. shear friction. aggregate interlock. push-off.

**Resumo:** Um programa experimental foi desenvolvido para avaliar o atrito cisalhamento no concreto autoadensável. Três misturas de concreto foram preparadas, uma convencional e duas autoadensáveis, diferenciadas pela proporção de agregados miúdo e graúdo utilizada. Nove exemplares para ensaios do tipo *push-off*, contendo armadura transversal ao plano de cisalhamento, foram ensaiados para avaliar a tensão cisalhante última e os deslocamentos do plano de cisalhamento. A resistência ao cisalhamento do concreto autoadensável foi superior aos de concreto convencionalmente vibrado. Os resultados experimentais foram comparados com estimativas calculadas com equações da literatura e de normas de dimensionamento, demonstrando estas equações serem conservadoras para os dois tipos de concreto, especialmente em modelos que desconsideram a resistência à compressão do concreto.

**Palavras-chave:** concreto autoadensável. atrito cisalhamento. engrenamento do agregado. *push off*.

**How to cite:** G. Savaris and R. C. A. Pinto, “Shear friction capacity of self-consolidating concrete,” *Rev. IBRACON Estrut. Mater.*, vol. 14, no. 1, e14102, 2021, <https://doi.org/10.1590/S1983-41952021000100002>

## 1 INTRODUCTION

The shear transfer consists on different components that contribute to the shear resistance in reinforced concrete structures, involving the adhesion originated from a chemical bond between the cement paste and aggregates, friction between the interfaces of a crack, the aggregate interlock, the dowel effect caused by the reinforcement that is placed across the interfaces and external clamping force on the concrete [1]–[5].

Evaluating connections in precast concrete buildings, Birkeland and Birkeland [1] proposed the Equation 1 to determine the ultimate shear capacity across an interface, as well as potential cracks, for monolithic concrete, assuming that shear strength is proportional to reinforcement ratio placed across the interface and yield strength of reinforcement.

$$\tau_u = 1.7 \rho_y f_y \quad (1)$$

**Corresponding author:** Gustavo Savaris. E-mail: [gsavaris@utfpr.edu.br](mailto:gsavaris@utfpr.edu.br)

**Financial support:** This research was supported by the Coordination for the Improvement of Higher Education Personnel (CAPES) and Federal University of Technology - Paraná.

**Conflict of interest:** Nothing to declare.



This is an Open Access article distributed under the terms of the Creative Commons Attribution License, which permits unrestricted use, distribution, and reproduction in any medium, provided the original work is properly cited.

Where  $\tau_u$  = ultimate shear stress (MPa);  $\rho_v$  = reinforcement ratio ( $A_s/A_c$ );  $f_y$  = yield strength of reinforcing (MPa).

The push-off test is a nonstandard, but widely recognized, test used in the testing of shear in concrete. Using this kind of test Hofbeck et al. [2] demonstrated the influence of the cohesion of the material particles and of the friction between the surfaces of the cracks in push-off tests. Concrete failure on the shear plane was dependent on the combination of normal and shear stresses. Thus, the authors proposed that the failure envelope resembled to the Mohr-Coulomb rupture failure criterion.

Evaluating the results from several experimental push-off tests, with and without pre-cracking of the shear plane, Mattock [3] quantified the ultimate shear stress considering the Mohr-Coulomb rupture failure criteria, as shown in Equation 2 (in MPa). The first term of the equation corresponds to the cohesion of material particles, estimated at 2.76 MPa, while the second term is related to the friction between the surfaces of the cracks, considering the externally applied normal stress acting across the shear plane and a coefficient of friction equal to 0.8:

$$\tau_u = 2.76 + 0.8(\rho_v f_y + \sigma_n) \leq 0.3 f_c \quad (2)$$

Where  $f_c$  = compressive strength of the concrete (MPa);  $\sigma_n$  = externally applied normal stress across the shear plane (MPa).

A theoretical model for the transfer of forces through the crack interfaces, considering that cracks originate in the mortar phase, was developed by Walraven [4]. This model considers concrete as a combination of coarse aggregate, with high strength and stiffness, and mortar with low strength and stiffness. Vecchio and Collins [5] used this model to determine the ultimate tensile strength of reinforced concrete elements submitted to shear and normal stresses, considering the crack width, the stress of the crack surfaces, the compressive strength of the concrete and the maximum aggregate size employed, proposing the Equation 3:

$$\tau_u = 0.18 \tau_{cimax} + 1.64 \sigma_n - 0.82 \frac{\sigma_n^2}{\tau_{cimax}} \quad (3)$$

$$\tau_{cimax} = \frac{\sqrt{f_c}}{\left(0.31 + \frac{24 w}{a_g + 16}\right)} \quad (4)$$

Where  $\tau_{cimax}$  = maximum shear stress on the shear plane in the cracked concrete (MPa);  $w$  = crack width (mm);  $a_g$  = maximum coarse aggregate size (mm).

Walraven et al. [6] related the ultimate shear strength to the compressive strength of concrete, to the transverse reinforcement ratio, and to the steel yield strength, resulting in Equation 5, which was obtained by statistical analysis of a large number of experimental tests:

$$\tau_u = 0.878 f_c^{0.406} (\rho_v f_y)^{0.167 f_c^{0.303}} \quad (5)$$

In the discussion of Walraven et al. [6], Mattock [7] presented a modified expression, that related the frictional shear resistance to compressive strength of concrete, obtained from push-off tests using concrete with compressive strength lower than 45 MPa:

$$\tau_u = 0.467 f_c^{0.545} + 0.8(\rho_v f_y + \sigma_n) \leq 0.3 f_c \quad (6)$$

Sonnenberg et al. [8] performed an experimental program using a shear box and compared the results with the Mohr-Coulomb frictional hypothesis, demonstrating that for normal stresses greater than 0.15  $f_c$ , a Mohr-Coulomb model with cohesion of 0.22  $f_c$  and a friction angle of 35° could be used to predict the results.

Lin et al. [9] presented the results of an experimental program with push-off and direct shear tests aiming to reveal the components of shear resistance. Based on results the authors defined that, for initially uncracked reinforced concrete, the shear components: friction between concrete and aggregate interlock, cement paste–aggregate adhesion, shear dilation and dowel action corresponds to 20%, 25%, 40% and 15% of the ultimate shear transfer capacity, respectively.

Self-consolidating concrete (SCC) is a concrete that can flow under its own weight, completely filling formwork and achieving full compaction, even in the presence of congested reinforcement. The mix proportioning of SCC requires smaller aggregate content and higher ratios of fine aggregate volume, besides mineral additions, and the use of superplasticizer. These mixture characteristics can affect the shear strength mechanisms and several researches have been carried out to evaluate the shear strength of self-consolidating concrete (SCC) and compare to conventional concrete, but there is not a consensus.

Sells et al. [10] performed push-off tests with conventional and self-consolidating concretes, varying coarse aggregate type and coarse aggregate to fine aggregate volume ratios, finding that concrete type (CC or SCC) and coarse aggregate content makes little difference to the aggregate interlock capability of the concrete, resulting similar shear strengths.

However, the results presented by Desnerck et al. [11] demonstrated higher shear strength of self-consolidating concrete than the conventional concrete, even though SCC contains a lower coarse aggregate volume fraction. The increase on shear strength was associated to an improve on the mortar matrix, due to the addition of fine materials to the concrete mixture, such as filler and silica fume.

Kim et al. [12] performed push-off tests to investigate the influence of SCC aggregate and paste volumes on the shear capacity and these results were compared with those obtained from similar CC samples. The test results confirmed that the volume of aggregate influences the contribution of aggregate interlock to the shear capacity, so that SCC samples presented lower maximum shear stresses at a given crack width as compared to the CC samples.

Savaris and Pinto [13] investigated the influence of the reduction in volume content and the nominal size of coarse aggregate on the SCC and CC shear strength. Six concrete mixes were used for casting beams with longitudinal reinforcement and without shear reinforcement under four-point loading condition. The results demonstrated a lower shear resistance of self-consolidating concrete beams, caused mainly due to the reduced aggregate size.

Current design codes do not take account of the particularities of self-consolidating concrete mixtures and possible effects on shear strength. American building code requirements for structural concrete ACI 318 [14] estimates the shear friction resistance in a plane with or without a crack through Equation 7, based on Birkeland and Birlekand theory [1]. ACI 318 considers the existence of transverse reinforcement perpendicular to the surface with a coefficient of friction ( $\mu$ ) of 1.4 for concrete produced with aggregate of normal specific weight and placed monolithically.

$$V_n = \mu A_{vf} f_y \quad (7)$$

Where  $A_{vf}$  = area of reinforcement crossing the assumed shear plane to resist shear ( $\text{mm}^2$ ).

The Canadian code for design of concrete structures, CAN A23.3 [15], considers that for a crack occurring along the shear plane, the relative displacement of this plane must be resisted by cohesion and friction, maintained by the reinforcement crossing the crack. The shear strength across the assumed shear plane shall be computed by the Equation 8 for normal weight concrete placed monolithically and with reinforcement perpendicular to the crack:

$$\tau_n = 0.6 \sqrt{\sigma f_c} \quad (8)$$

$$\sigma = \rho_v f_y + \frac{N}{A_g} \quad (9)$$

Where  $N$  is the unfactored permanent load perpendicular to the shear plane, positive for compression and negative for tension, and  $A_g$  is the gross area of the concrete section.

The equations presented at codes described above are based on test results with conventional concrete. Considering that it is important to evaluate the shear strength to better understand how changes in concrete composition can influence the shear transfer mechanism, this paper presents the results of an experimental investigation dealing with the shear strength of self-consolidating and conventionally vibrated concrete under push-off tests. The literature and code-based

design equations in predicting the shear strength are also evaluated and their estimates are compared to the experimental results.

## 2 EXPERIMENTAL PROGRAM

To evaluate the shear friction strength of self-consolidating concrete, an experimental program was performed. Nine reinforced concrete specimens, all of them with the same dimensions and reinforcement ratio were submitted to push-off tests. The concrete mixtures differ on their workability/fluidity and their coarse aggregate volume fraction in the mixture.

### 2.1 Mix design and materials

Three concrete mixes were used, one conventional vibrated concrete and two self-consolidating concrete. Table 1 presents the mixture proportions. Conventional concrete specimens were denoted as CC and self-consolidating concrete specimens were denoted as SC followed by N for mixture with the same coarse aggregate content as conventional concrete or R for mixture with coarse aggregate content reduced by 30%.

**Table 1.** Mix proportions (kg/m<sup>3</sup>).

Concrete mixture	Cement	Filler	Natural sand	Artificial sand	Coarse aggregate	Water	Superplasticizer
CC	385.2	-	418.5	417.4	964.6	200.3	-
SCN	385.2	214.7	312.9	312.0	964.6	200.3	0.87
SCR	385.7	215.1	456.5	455.3	676.0	200.6	1.15

High early-strength cement CP-V ARI, similar to ASTM Type III, was used for all mixtures. Fine aggregate consisted of a mix of 50% natural quartz sand, and 50% crushed granite stone, with the former material being much finer than the latter. A granite coarse aggregate with nominal maximum size of 19.0 mm was used. In self-consolidating concrete mixtures, fine aggregate was partially replaced by limestone filler to promote higher viscosity. A polycarboxylate-based superplasticizer was used in the SC mixtures.

Table 2 presents the fresh properties and 28-day compressive strength of the concrete mixtures investigated. The traditional slump test was conducted for the conventional concrete, while slump flow, L-Box and V-Funnel tests were conducted for self-consolidating concretes. The compressive strengths were determined using three cylindrical specimens (10 x 20 cm) for each mixture.

**Table 2.** Fresh and hardened properties of self-consolidating and conventional vibrated mixtures.

Concrete mixture	Slump (mm)	Slump flow (mm)	V-funnel (s)	L-Box	f <sub>c,m</sub> (MPa)
CC	105	-	-	-	36.3
SCN	-	665	19.63	0.87	41.2
SCR	-	690	11.94	0.87	47.0

### 2.2 Specimens details

The dimensions and reinforcement details of the tested specimens are shown in Figure 1. Three specimens were cast for each concrete mixture, being denoted by letters A, B or C.

Ribbed steel bars of 5 mm in diameter (CA-60) were used as closed stirrups through the shear plane, corresponding to a transverse reinforcement ratio of 0.181%, and an additional reinforcement L-shaped with bars of 10 mm in diameter (CA-50) and 5 mm (CA-60) closed stirrups were used to prevent premature failure outside the shear plane during load application, as can be seen in Figure 1. The steel bars were tested in tension, resulting in yield stresses of 538 and 658 MPa for CA-50 and CA-60 reinforcing bars, respectively.

The shear plane cross section was reduced to 100 mm x 220 mm, as detailed in Figure 1, by inserting thin wood sheets of 10 mm in width, prior to casting, at each side of shear plane. Three push-off specimens were cast for each batch. Mechanical vibration was used only for the conventional concrete mix. After 24 h, the specimens and cylinders were demolded, placed under plastic canvas, and moistened during the first seven days, after which they remained in laboratory conditions.

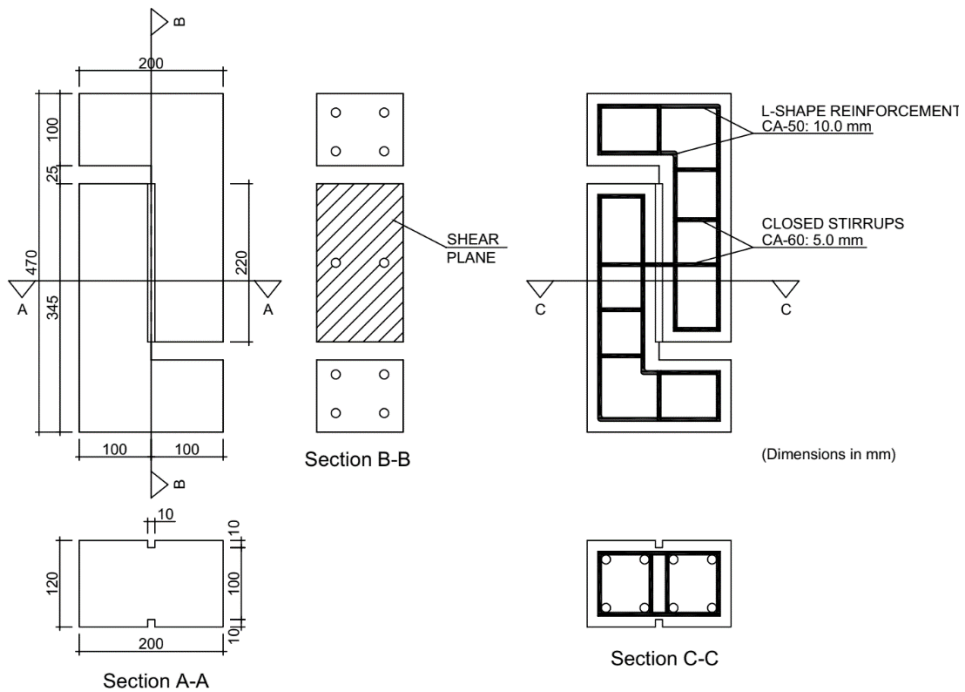


Figure 1. Specimens dimensions and reinforcement details.

### 2.3 Test instrumentation and procedure

Push-off tests were conducted at 28 days after casting. Vertical loading was applied using a hydraulic actuator with a capacity of 500 kN, at an average load rate of 50 N/s (Figure 2), until the specimen rupture. The specimens were instrumented using four 50 mm stroke linear variable displacement transducers, two of them installed vertically to measure the vertical displacement of the shear plane, whereas the others horizontally to measure crack width.

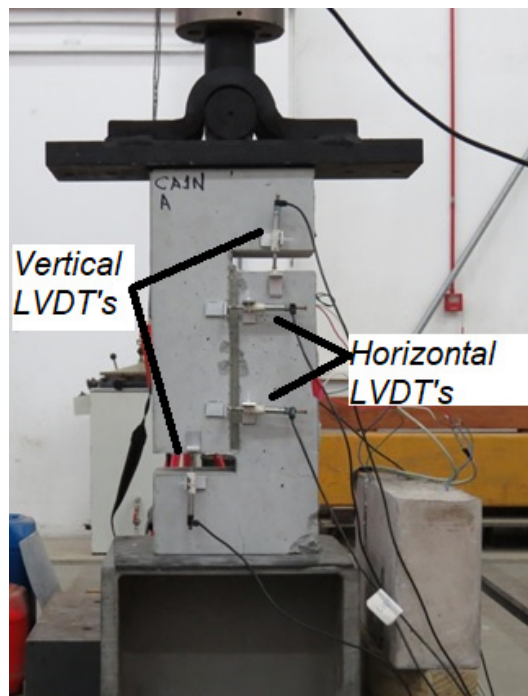


Figure 2. Specimen set-up and instrumentation.

The steel bars that crossed the shear plane in the specimens denoted by letter “A” were instrumented using strain gauges located approximately 10 mm from the shear plane (Figure 3). This distance was necessary to ensure that the strain gauge would not be damaged during the test. The load cell installed in the hydraulic actuator, the displacement transducers and the strain gauges were connected to a data acquisition system.



Figure 3. Steel bar instrumentation using strain gauge.

### 3 RESULTS AND DISCUSSION

#### 3.1 General cracking and failure behavior

In general, a similar behavior was observed for all push-off tests. The shear friction mechanism could be divided into three distinct stages, similar as showed by Harries et al. [16], and illustrated in Figure 4, for the three specimens of each concrete type.

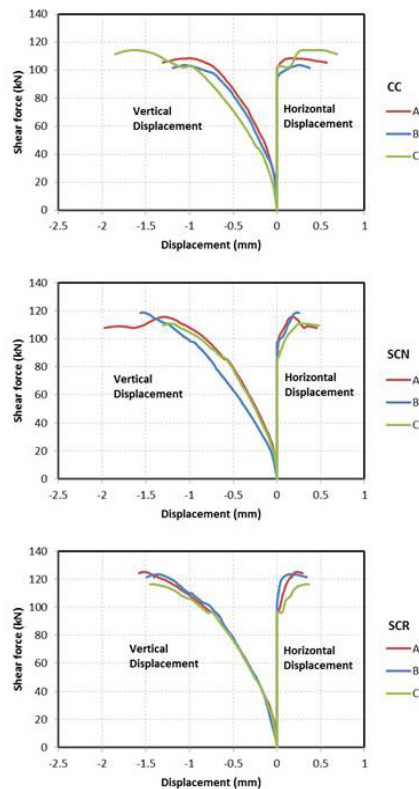


Figure 4. Shear plane displacements measured during loading.

The first stage, from the beginning of the loading until the formation of the crack in the shear plane, was characterized by vertical displacement, due to concrete deformation under compression, and small horizontal displacements, with the applied load being resisted only by the concrete. The strength at this stage would be the result of the cohesion forces before cracking.

The second stage began with the formation of the crack in the shear plane, when an increase in the reinforcement strain was observed, as showed at Figure 5, with shear force around 80 kN. At this stage, shear forces were initially resisted by the friction between the crack surfaces, resulting from the surface roughness of the interface and by the normal force generated by the reinforcement, which restricted crack opening. Nonetheless, with the increase of reinforcement strain, the crack opening increased and a subsequent reduction of aggregate interlock occurred, until the ultimate resistance was reached.

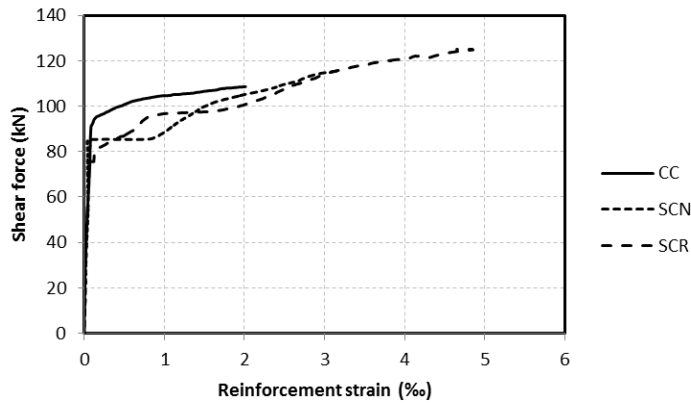


Figure 5. Reinforcement strain measured during loading.

At final stage, an increase of the vertical and horizontal displacements was observed with the decrease of the applied load, indicating the yield of the reinforcement, resulting in the rupture of one or both reinforcement bars that crossed the shear plane (Figure 6).



Figure 6. Rupture of specimen CC-A.

### 3.2 Shear resistance

Table 3 presents the ultimate shear stresses ( $\tau_u$ ) at the shear plane area (100mm x 220mm) for each specimen, as well as the average stresses and the standard deviation for each mixture. To take into account differences in compressive strength among the concrete mixtures, normalized shear stresses ( $\tau_{un}$ ) were calculated according to Equation 10, being also shown in Table 3.

**Table 3.** Ultimate shear stresses

Concrete mixture	Specimen	$\tau_u$ (MPa)	$\tau_{u,m}$ (MPa)	Standard deviation (MPa)	$\tau_{un}$ (MPa <sup>0.5</sup> )
CC	A	4.94			0.82
	B	4.71	4.95	0.25	0.78
	C	5.20			0.86
SCN	A	5.25			0.82
	B	5.39	5.23	0.18	0.84
	C	5.04			0.79
SCR	A	5.69			0.83
	B	5.62	5.53	0.21	0.82
	C	5.29			0.77

$$\tau_{un} = \frac{\tau_u}{\sqrt{f_c}} \tag{10}$$

The statistical F-test for equality of means of the normalized shear stress of the mixtures was performed. The results indicated that there was not a significant difference between these values at a 95% confidence level.

The normalized shear stress vs. reinforcement strain plots for the specimens are shown in Figure 7, where it can be verified that before cracking, the three mixtures presented similar shear strength. After cracking it seems to exist a little time interval until the cracks begins to increase its opening, when the aggregate interlock mechanisms occur. The CC presented higher normalized shear stress until cracking, around 0.7 MPa<sup>0.5</sup>, probably due to higher aggregate interlock, considering that this concrete had lower content of fine materials. Despite self-consolidating concrete presented normalized shear stress between 0.55 and 0.6 MPa<sup>0.5</sup> when the crack started to open, a higher reinforcement strain after cracking was observed, that may be associated to a better bond of self-consolidating concrete to the reinforcement bars [17] [18]. This possible improve in bond strength would increase the compression forces transverse to the shear plane with a consequently higher friction between the surfaces, which would result in similar ultimate shear stresses to all concretes.

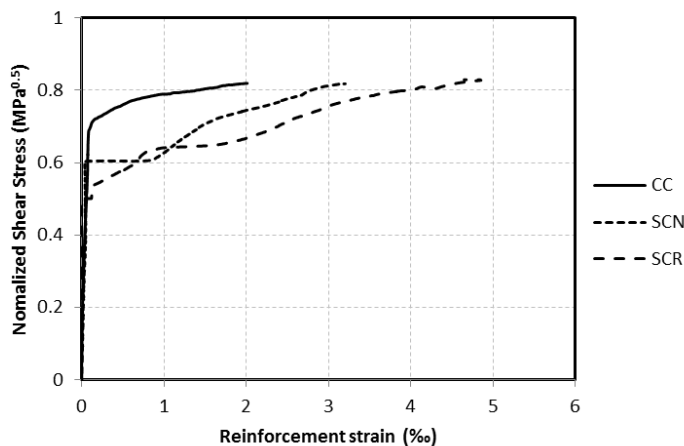


**Figure 7.** Normalized shear stress vs. reinforcement strain.

Considering that the specimens used in this study presented low transverse reinforcement ratio, this result may indicate that the increase in the transverse reinforcement ratio may result in higher shear strength for self-consolidating concrete, due to a better bond to the reinforcement, increasing the compression force transverse to the shear plane and consequently higher friction between the surfaces.

### 3.3 Vertical displacement and cracking width

Table 4 shows the average vertical displacements of shear plane and the crack widths measured at ultimate normalized stresses. Although the ultimate normalized shear stresses presented similar results, small variations in the vertical displacements and in the crack width values were observed. Comparing mean values, SCC mixtures presented higher vertical displacements than the CC mix, probably because of its higher amount of fine material, but more samples must be tested to allow a statistical analysis.

**Table 4.** Average vertical displacements and crack width at ultimate normalized stress.

Concrete mixture	$\tau_{un}$ (MPa <sup>0.5</sup> )	$\tau_{un,m}$ (MPa <sup>0.5</sup> )	$\Delta_u$ (mm)	$\Delta_{u,m}$ (mm)	$w_u$ (mm)	$w_{u,m}$ (mm)
	0.82		0.989		0.167	
CC	0.78	0.82	1.056	1.23	0.255	0.24
	0.86		1.641		0.301	
	0.82		1.302		0.296	
SCN	0.84	0.81	1.541	1.35	0.234	0.28
	0.79		1.22		0.295	
	0.83		1.523		0.332	
SCR	0.82	0.81	1.367	1.44	0.164	0.28
	0.77		1.421		0.33	

Kim et al. [12] and Harries et al. [16] demonstrated that shear strength reduces when the volume of aggregate size is reduced in concretes and this reduction has been attributed to a lower aggregate interlock in SCC. However, in this work the three mixtures showed similar normalized shear stresses for crack widths of 0.10 mm and 0.15 mm, as presented in Table 5. As discussed before, similar shear strength may be associated to a higher bond to the reinforcing bars in self-consolidating concrete, that would increase the compressive force applied by the reinforcement to the crack surfaces, increasing shear transfer by friction, and therefore, compensating the lower aggregate interlock. This effect was also observed in Savaris and Pinto [19] were self-consolidating beams with stirrups presented similar shear strength to conventional concrete, compensating lower shear strength presented by beams without stirrups.

**Table 5.** Normalized shear stresses at crack width of 0.10 and 0.15 mm.

Concrete mixture	Specimen	$\tau$ (MPa)			
		w=0.10 mm		w=0.15 mm	
	A	0.81		0.82	
CC	B	0.72	0.77	0.73	0.79
	C	0.78		0.81	
	A	0.78		0.81	
SCN	B	0.75	0.74	0.80	0.78
	C	0.71		0.74	
	A	0.77		0.80	
SCR	B	0.81	0.76	0.82	0.78
	C	0.70		0.71	

The relationship between reinforcement stresses, calculated based on measured strains, with measured crack widths is plotted in Figure 8 for all mixtures. The tested specimens showed a low variation on reinforcement stresses for crack width close to 0.1 mm.

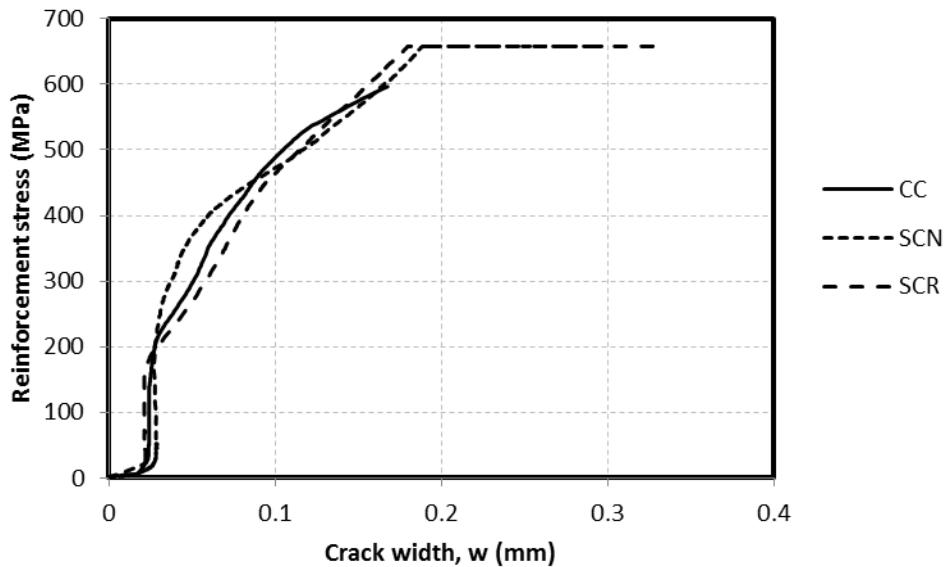


Figure 8. Reinforcement stresses vs. crack width.

Figures 9 to 11 show the relationship between shear forces and crack widths for all specimens. Also, the theoretical shear forces resisted by the cohesion of concrete and by the reinforcement are presented. As proposed by Harries et al. [16], the shear force resisted by the reinforcement was calculated from the reinforcement strains, measured during the test, assuming a coefficient of friction ( $\mu$ ) equal to 1.4. The theoretical shear stress component resisted by the cohesion of concrete consisted of the subtraction of the shear force resisted by reinforcement from the total shear force applied. The vertical straight line indicates the crack width corresponding to the ultimate shear force and the horizontal line indicates the shear force corresponding to yielding of the reinforcement.

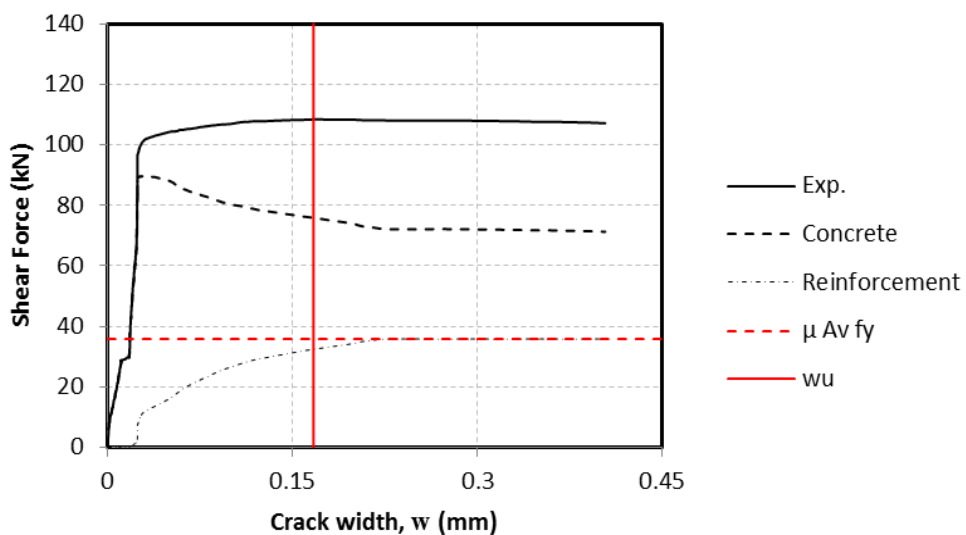


Figure 9. Experimental and theoretical shear strengths of CC-A specimen.

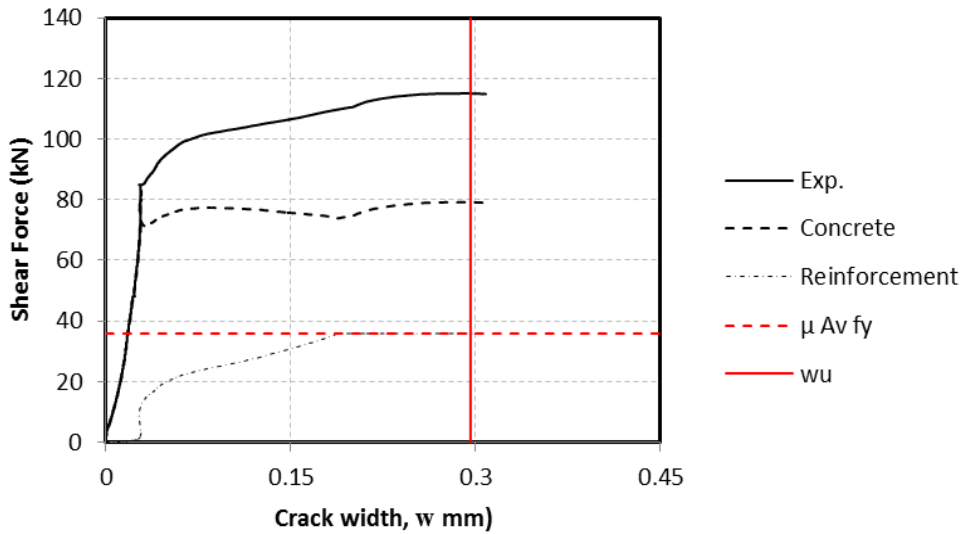


Figure 10. Experimental and theoretical shear strengths of SCN-A specimen.

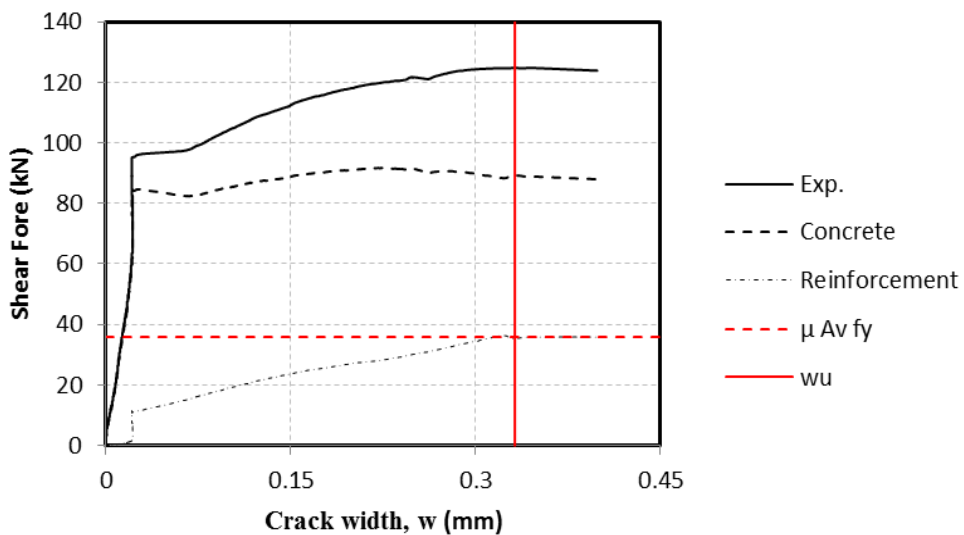


Figure 11. Experimental and theoretical shear strengths of SCR-A specimen.

From Figures 9 to 11 it can be observed that there was a distinct behavior between the CC and SCC mixes. In CC specimen, the compression force generated by the reinforcement after crack formation did not increase the total shear force resisted; instead the total shear remain approximately constant which led to a decrease in the cohesion forces (as can be seen by the decrease in the dashed lines). This behavior may have happened since as the crack opened, the aggregate interlock forces decreased while reinforcement strain increased. On the other hand, the SCC mixes showed an increase of the shear forces proportional to the resistance attributed to the reinforcement while the cohesion forces remained constant (as can be seen by the almost no variation on the dashed lines). This latter behavior justifies the observed largest post-cracking shear resistance of the SCC mixes.

### 3.4 Comparisons of experimental and theoretical shear strength

Table 6 shows the experimental results and the estimates based on equations proposed in the literature by Birkeland and Birkeland [1], Mattock [3], Vecchio and Collins [5], Walraven et al. [6] and Mattock [7], (Equations 1, 2, 3, 5 and 6, respectively).

**Table 6.** Experimental ultimate stress and estimates based on literature equations.

Concrete mixture	$\tau_{u,exp}$ (MPa)	Birkeland and Birkeland [1] (MPa)	Mattock [3] (MPa)	Vecchio and Collins [5] <sup>(1)</sup> (MPa)	Walraven et al. [6] (MPa)	Mattock [7] (MPa)
CC	4.95			4.11	4.07	4.24
SCN	5.23	1.98	3.69	4.14	4.30	4.48
SCR	5.53			4.31	4.55	4.74

<sup>(1)</sup> Calculated considering crack width measured at ultimate shear stress and compression force perpendicular to shear plane related to reinforcement yield strength.

The equations presented ultimate shear stress estimates lower than the experimental results. This lower estimate is a consequence of their formulation, since they resulted mainly from experimental tests with pre-cracked specimens, in which the strength attributed to cohesion is lower than the specimens tested here.

Comparing the performance among these equations, it can be observed that Birkeland and Birkeland [1] presented the most conservative values, justified by a simplified model that considers only the friction coefficient and the transverse reinforcement ratio, while the equation proposed by Walraven et al. [6] presents less conservative results than the other models evaluated, even disregarding the portion resisted by the concrete cohesion.

Even though the equation proposed by Vecchio and Collins [5] considers aggregate size, crack width and compression force perpendicular to the crack plane, its estimates were still lower than the experimental values.

Since the ultimate shear stress was influenced by the compressive strength of the mixes, the equations proposed by Walraven et al. [6] and by Mattock [7], which considered this concrete property, fitted best to the experimental results than the others, with ratio ranges between 0.75 and 0.90.

The ACI and CSA based design equations to estimate the ultimate shear friction resistances of experimental self-consolidating and conventional concrete were also evaluated. Table 7 shows the experimental results and those calculated using Equations 7 and 8, corresponding to ACI 318 and CAN A23.3, respectively, and the ratio between these values.

**Table 7.** Ultimate shear strength – experimental results and code predictions.

Concrete mixture	$\tau_{u,exp}$ (MPa)	ACI 318 [14] (MPa)	CAN A23.3 [15] (MPa)	ACI/ $\tau_{u,exp}$ (MPa)	CAN/ $\tau_{u,exp}$ (MPa)
CC	4.95		3.90	0.34	0.79
SCN	5.23	1.67	4.16	0.32	0.80
SCR	5.53		4.44	0.30	0.80

In general, CAN A23.3 [15] presented fewer conservative values with an estimated value near 0.80 of the experimental one. This better approximation is due since it considers the cohesion of the particles, associated to the concrete compressive strength, the friction between the surfaces and the transverse reinforcement ratio for monolithically concreted specimens. ACI 318 [14], however, presented the most conservative values due to its simple approach, which considers only the friction between surfaces, with a friction coefficient lower than the one proposed by the original authors.

## 4 CONCLUSIONS

The shear friction strength of conventional and self-consolidating concretes produced with different volume fraction of aggregate in the mixes were compared in this paper. The analysis of the experimental results obtained in concrete specimens submitted to push-off tests led to the following conclusions:

- The tested specimens showed the same failure mode, regardless the differences on the concrete mixtures, with a crack formation in the shear plane, followed by vertical displacement of this plane and crack opening, resulting in rupture of the transverse reinforcement.
- Self-consolidating concrete mixtures with reduced coarse aggregate content showed lower shear cracking strength, which may have been caused by the replacement of fine aggregate by limestone filler and the reduction of coarse aggregate content resulting in a reduction of aggregate interlock.
- The ultimate shear stresses of the self-consolidating concrete mixes were slightly higher than the one for the conventional concrete mix, however, when the variation of concretes compressive strength were considered, the normalized shear stress of the mixtures indicated that there was not a significant difference between these values.
- Considering that the specimens tested had low reinforcement ratio, self-consolidating concrete mixes may present higher shear strength compared to conventional concrete when used higher transverse reinforcement ratio. This possible increase in shear strength may be due to the higher bond of self-consolidating concrete to reinforcement, raising the compression force perpendicular to shear plane and increasing friction between the crack surfaces.
- The ultimate shear stresses equations proposed in the literature that consider the concrete compressive strength provided estimates of around 80% of the experimental results, while the numerical models that disregard the cohesion between the concrete particles or the contribution of the transversal reinforcement presents estimates around 40% of experimental results.

## ACKNOWLEDGEMENTS

The authors gratefully acknowledge the Coordination for the Improvement of Higher Education Personnel (CAPES), the Federal University of Santa Catarina and the Federal University of Technology – Paraná for their great support.

## REFERENCES

- [1] P. W. Birkeland, and H. W. Birkeland, "Connections in precast concrete construction," *J. Am. Concr. Inst.*, vol. 63, no. 3, pp. 345–368, 1966.
- [2] J. A. Hofbeck, I. O. Ibrahim, and A. H. Mattock, "Shear transfer in reinforced concrete," *J. Am. Concr. Inst.*, vol. 66, no. 2, pp. 119–128, 1969.
- [3] A. H. Mattock, "Shear transfer in concrete having reinforcement at an angle to the shear plane," *ACI SP-42: Shear in Reinforced Concrete*, vol. 1, pp. 17–42, 1974.
- [4] J. C. Walraven, "Aggregate interlock: a theoretical and experimental analysis," Doctoral thesis, Technische Hogeschool Delft, The Netherlands, 1980.
- [5] F. J. Vecchio, and M. P. Collins, "The modified compression field theory for reinforced concrete elements subject to shear," *ACI J.*, vol. 83, pp. 219–231, 1986.
- [6] J. C. Walraven, J. Frenay, and A. Pruijssers, "Influence of concrete strength and load history on the shear friction capacity of concrete members," *PCI J.*, vol. 32, no. 1, pp. 66–84, 1987.
- [7] A. H. Mattock, "Reader comments of paper Influence of concrete strength and load history on the shear friction capacity of concrete members," *PCI J.*, vol. 33, no. 1, pp. 165–166, 1988.
- [8] A. M. C. Sonnenberg, R. Al-Mahaidi, and G. Taplin, "Behaviour of concrete under shear and normal stresses," *Mag. Concr. Res.*, vol. 55, no. 4, pp. 367–372, 2003.
- [9] F. Lin, H. Lu, and Y. Dong, "Component model for shear transfer in reinforced concrete," *Mag. Concr. Res.*, vol. 68, no. 15, pp. 755–767, 2016., <http://dx.doi.org/10.1680/jmacr.15.00269>.
- [10] E. Sells, J. J. Myers, and J. S. Volz, "Aggregate interlock push-off test results of Self-Consolidating Concrete (SCC) for use in infrastructure elements," in *Proc. ISEC-7*, Honolulu, Hawaii, 2013, <http://dx.doi.org/10.3850/978-981-07-5354-2>.
- [11] P. Desnerck, G. De Schutter, and L. Taerwe, "Shear friction of reinforced self-consolidating concrete members," in *ACI Special Publication 261-9*, Farmington Hills, Michigan, 2009, pp. 133-141.
- [12] Y. H. Kim, M. B. D. Hueste, D. Trejo, and D. B. H. Cline, "Shear characteristics and design for high-strength self-consolidating concrete," *J. Struct. Eng.*, vol. 136, no. 8, pp. 989–1000, 2010, [http://dx.doi.org/10.1061/\(ASCE\)ST.1943-541X.0000194](http://dx.doi.org/10.1061/(ASCE)ST.1943-541X.0000194).
- [13] G. Savaris, and R. C. A. Pinto, "Influence of coarse aggregate on shear resistance of self-consolidating concrete beams," *IBRACON Struct. Mater. J.*, vol. 10, no. 1, pp. 30–52, 2017, <http://dx.doi.org/10.1590/S1983-41952017000100003>.
- [14] American Concrete Institute, *Building code requirements for structural concrete and commentary*, ACI 318R-14, 2014.
- [15] Canadian Standards Association, *Design of concrete structures*, CAN A23.3, 2004.

- [16] K. A. Harries, G. Zeno, and B. Shahrooz, "Toward an improved understanding of shear friction behavior," *ACI Struct. J.*, vol. 109, no. 6, pp. 835–844, 2012.
- [17] A. A. A. Hassan, K. M. A. Hossain, and M. Lachemi, "Strength, cracking and deflection performance of large-scale self-consolidating concrete beams subjected to shear failure," *Eng. Struct.*, vol. 32, pp. 1262–1271, 2010, <http://dx.doi.org/10.1016/j.engstruct.2010.01.002>.
- [18] T. J. Looney, M. Arezoumandi, J. S. Volz, and J. J. Myers, "An experimental study on bond strength of reinforcing steel in self-consolidating concrete international," *J. Concr. Struct. Mater.*, vol. 6, no. 3, pp. 187–197, 2012, <http://dx.doi.org/10.1007/s40069-012-0017-9>.
- [19] G. Savaris, and R. C. A. Pinto, "Experimental investigation on shear resistance of self-consolidating concrete beams," *IBRACON Struct. Mater. J.*, vol. 12, no. 6, pp. 1305–1326, 2019, <http://dx.doi.org/10.1590/S1983-41952019000600005>.

---

**Author contributions:** GS: conceptualization, methodology, experimental results, formal analysis, writing; RCAP: conceptualization, supervision, formal analysis, writing.

**Editors:** Jose Tadeu Balbo, José Luiz Antunes de Oliveira e Sousa, Guilherme Aris Parsekian.



## ORIGINAL ARTICLE

# Analysis of constructive effect and soil-structure interaction in tall building projects with shallow foundations on sandy soils

## *Análise do efeito incremental e interação solo-estrutura em edifícios altos com fundações superficiais em solos*

Olivia Catelan Marques<sup>a</sup> Leonardo Almeida Feitosa<sup>a</sup> Katia Vanessa Bicalho<sup>a</sup> Elcio Cassimiro Alves<sup>a</sup> <sup>a</sup>Universidade Federal do Espírito Santo – UFES, Departamento de Engenharia Civil, Vitória, ES, Brasil

Received 01 March 2019

Accepted 20 May 2020

**Abstract:** The influence of incremental constructive effects (IE) and soil-structure interaction (SSI) on high-rise buildings of reinforced concrete with shallow foundations on sandy soils were analyzed. IE and SSI evaluations were carried out by the parameters of global instability, maximum horizontal displacements, foundation loads, and settlements of a symmetrical and non-symmetrical plant of a 23-storey building. For the analysis of the IE, the variation of the modulus of elasticity was considered over time along with the phases of application of loads in the building. For ISS analysis, the continuous medium was considered, and the calculation model considers a multi-spring-mass system under the foundation of the building. The results show a significant redistribution in the foundation efforts and suggest that a failure in considering these effects along with the structure can lead to projects that do not meet the standard specifications regarding stability parameters and overall structure displacements.

**Keywords:** global stability, constructive effects, soil-structure interaction, shallow foundations, reinforced concrete.

**Resumo:** Neste artigo analisa-se a influência dos efeitos construtivos incrementais (EI) e da interação solo-estrutura (ISE) em edifícios altos de concreto armado com fundações superficiais assentes sobre solos arenosos. Foram realizadas avaliações dos EI e ISE nos parâmetros de instabilidade global, deslocamentos horizontais máximos, cargas de fundação e recalques de uma planta simétrica e uma não simétrica de um edifício com 23 pavimentos. Para análise do EI considerou-se a variação do módulo de elasticidade ao longo do tempo, bem como as fases de aplicação de cargas na edificação. Para análise do ISE foi considerado o meio contínuo e o modelo de cálculo considera uma série de molas discretas sob a base da fundação da edificação. Os resultados mostram uma redistribuição significativa nos esforços da fundação e sugerem que a não consideração desses efeitos em conjunto na estrutura pode levar a projetos que não atendam as especificações de norma quanto aos parâmetros de estabilidade e deslocamentos globais da estrutura.

**Palavras-chave:** estabilidade global, efeito incremental, interação solo-estrutura, fundação superficial, concreto armado.

**How to cite:** O. C. Marques, L. A. Feitosa, K. V. Bicalho, and E. C. Alves, “Analysis of constructive effect and soil-structure interaction in tall building projects with shallow foundations on sandy soils,” *Rev. IBRACON Estrut. Mater.*, vol. 14, no. 1, e14103, 2021, <https://doi.org/10.1590/S1983-41952021000100003>

## 1 INTRODUCTION

With use of expensive land located in the central area of Brazilian cities, a verticalization is observed with the frequent construction of tall buildings with more than 20 stories high. The analysis of the load redistribution in the

Corresponding author: Olivia Catelan Marques. E-mail: [oliviacmarques@gmail.com](mailto:oliviacmarques@gmail.com)

Financial support: None.

Conflict of interest: Nothing to declare.



This is an Open Access article distributed under the terms of the Creative Commons Attribution License, which permits unrestricted use, distribution, and reproduction in any medium, provided the original work is properly cited.

structure, as well as the structure overall stability evaluation, become important in the building conception, since it ensures the safety of the structure through the loss of its resistant capacity caused by the increase of deformations due to actions on the building.

Generally, the dimensions of the projects are done in a simplified way and do not always represent the physical reality of the work. Thus, important factors that are not normally considered, such as the constructive (or incremental) effect and the soil-building interaction is disregarded in the design.

One of the points that is important to be considered in these analyses are the efforts produced during the construction process, since most shipments happen even before the structure is complete. The Incremental Constructive Effect, called in this work Incremental Effect (IE) contemplates the consideration of these steps in the calculation process. Studies such as Prado [1] and Gorza [2] consider this analysis.

Another relevant point is an integrated analysis of the three parts that constitutes the edifications: superstructure, infrastructure and foundation ground, on a mechanism called Soil-Structure Interaction (SSI) where the rigidity of the whole building is considered in its analysis of stability, loads and pressurized system.

The study of the effect of SSI can be observed for different types of projects and load states. Ge et al. [3], Saragi et al. [4], Galvín et al. [5] present in their studies the importance of soil-structure interaction considering effects of dynamic loads at different scales.

Damgaard et al. [6], Lombardi et al. [7], Bhattacharya et al. [8] present various analyses for different types of projects where the importance of considering soil-structure interaction for the structural models studied was pointed out. Su and Wang [9] present a finite element model for a study with equivalent dynamic load considering the soil-structure interaction and Papadopoulos et al. [10] present in their study the determination of the modal characteristics of structures considering the soil-structure interaction.

Ge et al. [11] analyze the soil-structure interaction considering the movement of soil in building projects and the impacts on neighboring buildings.

On the other hand, Alves and Feitosa [12], Danziger et al. [13], Feitosa and Alves [14], Gusmão [15], Savaris et al. [16], Pavan et al. [17], Agrawal and Harne [18] study (SSI) for buildings, but don't consider the influence of the incremental effect on the analyses performed.

In this context, the study is based on the analysis of the overall stability of the building, associated with the redistribution of efforts in the foundations. Consideration of EI and SSI analyses is expected to lead to changes in these parameters.

Previous studies allow us to conclude that the models that consider both analyses will be more unstable when compared to those that disregard. Works such as Marques et al. [19] and Jucá et al. [20] show this variation studied.

The objective of this paper is to evaluate the influence and relevance of incremental effects associated with the soil-structure interaction in buildings with shallow foundations based on sandy soils. The focus is to verify whether using a more refined model can lead to more critical design considerations of the analyses without them.

It is important to evaluate whether this analysis will generate values relevant to the project parameters, such as global instability and effort redistribution. Thus, the cost-benefit analysis of this new form of analysis is especially important.

For this study, two models of reinforced concrete buildings are analyzed, both with shallow foundation, but one model with symmetrical structure and another with asymmetric structure (insertion of balconies). Cad/TQS v19 [21] software that considers the building as a spatial gantry, composed of elements that will simulate beams, pillars and slabs of the structure, is used as an analysis tool. The floors are defined by grid model on the slabs.

## 2 INCREMENTAL EFFECT (IE)

The structural analysis should consider the sequence of applied load history. As the self weight load of a floor is given immediately after its installation, it does not affect the deformation of the upper floors that do not exist yet.

The Incremental Effect (or incremental analysis) is defined as being the consideration of the construction steps influence in a building.

Prado [1] concluded that introducing loads in an incremental form on the structure results in different values from those obtained by usual calculating methods. He emphasizes that it is necessary to consider premature shipments, since they increase deformations and endanger safety.

Gorza and Coelho [22] evaluate the influence of the transversal rigidity to the bending of the slabs and the construction and loading sequence in a building with metallic structure. And they conclude that the consideration of the transversal rigidity of the slab results in a more realistic analysis of each floor, in that way, it is possible to reduce dimensions of structural parts. In incremental analysis, it was possible to prove that its consideration generates different

values, when it is compared to conventional analysis, of efforts and shifts. In relation to the efforts it was possible to verify the reduction, and in relation to the shifts, the maximum different shifts were found approximately half height of the building and not at the top as normally.

In this work, the analysis model used in IE was based on calculation of the variation of the modulus of elasticity. The axial rigidity of the pillars is increased in the space gantry, considering an analysis closer to physics reality of the behavior of the structure. At each stage of construction (07 days), a portion of the load's acts on the floor, thus creating the stages of construction regarding the shipments, and 01 floor is built at the same time. These data are presented in Table 1.

**Table 1** Incremental Effect Load History

Shipments Cases	Portion (%)	Phase
All permanent and accidental pavements	0	0
	100	Final
Own weight	100	0
	0	Final
Dead loads	0	0
	30	1
	60	2
	10	Final
Live loads	0	0
	50	1
	15	2
	35	Final
Wind 90°	0	0
	100	Final
Wind 270°	0	0
	100	Final
Wind 0°	0	0
	100	Final
Wind 180°	0	0
	100	Final
Wind 45°	0	0
	100	Final
Wind 135°	0	0
	100	Final
Wind 225°	0	0
	100	Final
Wind 315°	0	0
	100	Final

### 3 SOIL-STRUCTURE INTERACTION (SSI)

A building is divided into three parts, superstructure, infrastructure and foundation ground, integrated by the mechanism called soil-structure interaction. However, in practice, this factor is usually not analyzed, and may generate results that do not match the reality of the structure in the service boundary state.

The soil-structure interaction is defined by the consideration of the parts working together. That is, the building is considered in a complete and unified way. In the CAD/TQS model [21], the program generates a stiffness matrix based on the characteristics of the modeled soil, and thus calculates the deformations in the foundation. With this data, the software returns to the spatial portico a model of springs that will be used in the calculation of the additional efforts generated in the building due to soil deformation.

According to ABNT NBR 6118 [23], soil-structure interaction should only be considered in more complex cases of structural analysis. Apart from this orientation, the standard does not contemplate the subject, leaving it up to the designer to choose or not to use the method of analysis.

Albuquerque and Gusmão [24] studied the soil-structure interaction for building in reinforced concrete with shallow foundation. The researchers show that for most buildings with monitoring, the estimated displacements are greater than those measured. This is due to the standardization of the settlements and a redistribution of the loads of the pillars, where the most loaded tend to settle less than expected and the less, more than expected.

Alves and Feitosa [12], concluded that the consideration of the soil-structure interaction leaves the structure more flexible, increasing the parameter  $\gamma_z$  (parameter of instability defined by ABNT NBR 6118 [23] that represents the stability of the structure for the analysis of 2nd order efforts) The analysis of global stability considering soil-structure interaction showed that this influence should be taken into account in daily life, such importance. The results were for symmetrical buildings in reinforced concrete formed by flat slabs and rigid cores, modeled on Cad/TQS software [21].

In their comparison of a real building with a numerical simulation, Savaris et al. [16] verify the importance of joint consideration of structure and foundations. The simulation was able to prove the redistribution of the loads, and the settlements monitoring equipment was effective in its verification. In addition, the results of the analysis proved that the effects of SSI are more significant for calculations on the first floors.

Danziger et al. [13], confirm that loads are redistributed to the peripheral pillars when considering SSI, relieving the central pillars for an analysis of symmetrical buildings with shallow foundation, in reinforced concrete.

Souza and Reis [25] found that the consideration of SSI introduced differences for the efforts working on the pillars, always presenting average values greater than 20% in relation to the model that disregards. The researchers mention that the consideration of SSI can be of great importance in cases that have great normal strength concentrated in certain pillars or in shoes seated on stratified soils. The analysis of the models proved that CAD/TQS software represents a very effective tool, providing a more realistic analysis than that usually practiced (without SSI), in symmetrical models in reinforced concrete.

Passos et al. [26] concluded that the use of SSI should be done by the structural calculation offices, since it increases the value of the parameter  $\gamma_z$ . The analysis was based on a study of a symmetrical building with deep foundation in reinforced concrete, with the aid of CAD/TQS software [21].

Pavan et al. [17] proved that the soil-structure interaction generates variations in the active efforts. And, they mention that disregarding the influence of support displacements can lead to unrealistic efforts, which can impair the safety and durability of buildings. These conclusions commend buildings built of symmetrical reinforced concrete and with shallow foundations.

Rosa et al. [27] performed an analysis of the soil-structure interaction focused on creep and retraction, where they compared a real building with a modeling in Sap2000 software. The non-symmetrical construction, in reinforced concrete, with mixed foundation, presented calculated results consistent with those measured in the field. They conclude that the consideration of fluency and retraction in numerical analysis indicates for an evaluation more than its real significance when compared only to the effect of the interaction.

In this work, the calculation of the soil-structure interaction considers the unset foundation and quantifies the effect of the deformability of the foundation soil considering the continuous medium. The calculation model is represented by a multi-spring-mass system under the foundation base. The vertical settlement coefficient is estimated based on the results of the in-situ standard penetration tests (SPT), whose geotechnical profile is shown in Figure 1.

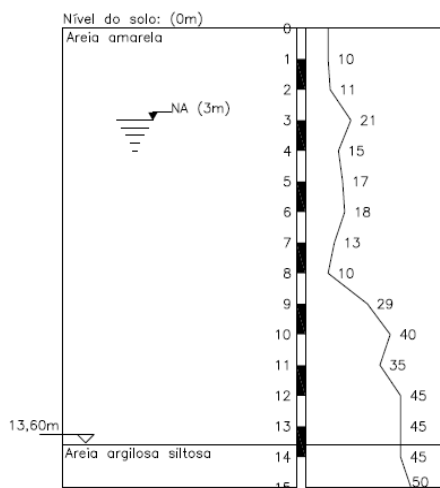


Figure 1 Geotechnical profile with subsurface SPT survey results

The model for analysis of the settlement of shallow footings on sandy soil was proposed by Schmertmann et al. [28], who uses the calculation of the modulus of elasticity estimated by the in-situ tests results. The vertical reaction coefficient represents the resistance of the soil in relation to an imposed displacement, analogous to a spring coefficient.

#### 4 INCREMENTAL EFFECT X SOIL-STRUCTURE INTERACTION

In building projects, usually the analysis of incremental effects, as well as soil-structure interaction is not routine, in view of the difficulties to understand these models. Models involving the analysis of the two parameters together, makes the analysis of the building somewhat more sophisticated and with a higher computational cost, so that few studies are found for this project model.

Jucá et al. [20] compared models considering or not the soil-structure interaction, and evaluated the settlement of footings on sands. The results showed that the model that disregards the soil-structure interaction overestimates the prediction of differential settlements, since it does not consider the stiffness of the structure. The model that considers SSI, but applies instant loading to the complete structure, without the incremental effect, ended up underestimating the prediction of footing settlements. This was due to the non-consideration of the gradual loading in the structure and the increase in stiffness, which leads to the consideration of a greater stiffness than the actual one. The closest result to that found in the field was the one in which the soil-structure interaction was considered associated with the incremental effect.

Albuquerque and Gusmão [24] show that the constructive sequence has greater importance in the first floors, increasing the stiffness in them.

Marques et al. [19] suggest that the use of CAD/TQS software [21] considering SSI showed relevant values in global stability: there was an increase in all wind models analyzed. For the incremental effect, they did not observe any change in the resulted values, when compared with the simple model of the software. The conclusion was based on a study of a building in symmetrical reinforced concrete, with shallow foundations as footings.

#### 5 METHODOLOGY

For the combined analysis of the incremental effect (IE) and the soil-structure interaction (SSI) on the global stability, 4 models were analyzed considering the same symmetrical building and 4 models considering non symmetric building were analyzed, with the models 1.1 -1.4 and 2.1-2.4 respectively.

The starting point for the analysis of the models of each group was the development of a model that presented the value of the parameter of instability  $\gamma_z$  as close as possible to the limit value indicated by ABNT NBR 6118 [23], which is 1.3. The calculation of the instability parameter was performed by the P-Delta simplified method.

To point out the influence of IE and SSI, models 1.1 and 2.1 were defined as reference models. Models 1.2 and 2.2 used the IE analysis only. On the other hand, in models 1.3 and 2.3, the SSI analysis was applied. Finally, models 1.4 and 2.4 are those that use both IE and SSI analyses.

The reinforced concrete building with shallow foundations on sandy soils considered in analysis has 23 floors: Ground floor, Garage, Type (20 floors) and Penthouse, with the ceiling height of 4.14 meters. The characteristics of the structural elements considered in the analyzed models are presented in Table 2 and loads in Table 3.

**Table 2** Characteristics of structural elements considered in the models analyzed

Beams:	30	MPa
Slabs:	30	MPa
Columns:	40	MPa
Foundation	40	MPa
Wind	30	m/s
Terrain topographic factor	1	
Roughness Category	IV	
Height Relation	h/4	

**Table 3** Loads distributed by area in the building considered in the analysis

FLOOR	PERMANENT	ACCIDENTAL
-	kN/m <sup>2</sup>	kN/m <sup>2</sup>
Type	1.0	1.5
Garage	1.0	3.0
Common area	1.0	3.0

For the considered models, the criteria of the physical nonlinearity coefficient remained the same, with 0.8 for columns, 0.3 for slabs and 0.4 for beams. In addition, the buildings have H/4 ratio.

Figure 2 shows the plan used for symmetrical models 1, as well as the 3D building representation of the modeling. Figure 3 shows the plan and the 3D view for non-symmetrical models. Garage and Ground floor have beam elements that vary the beam dimensions from 25x25 cm to 30x60cm; the slabs ranged from 15 to 20 cm in thickness; the pillars were dimensioned with 25x25cm for the areas not related to the projection of the type, the others followed the dimensions related to this one.

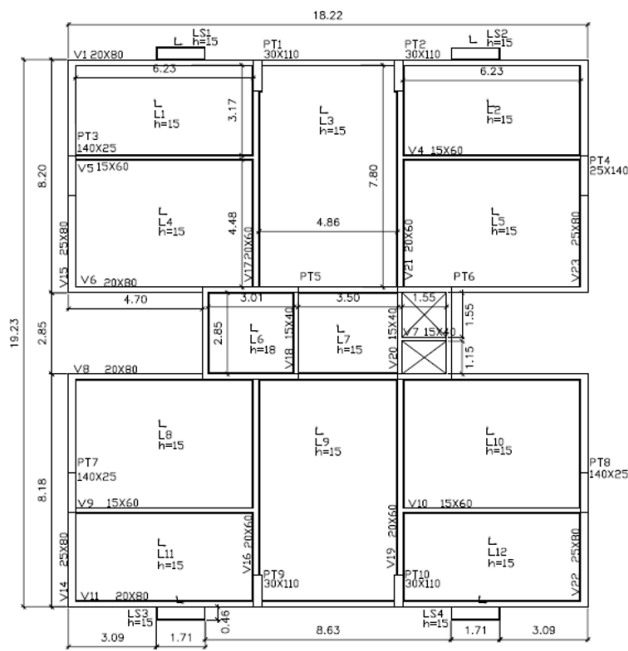


Figure 2 Structural launch layout and 3D view, symmetrical models

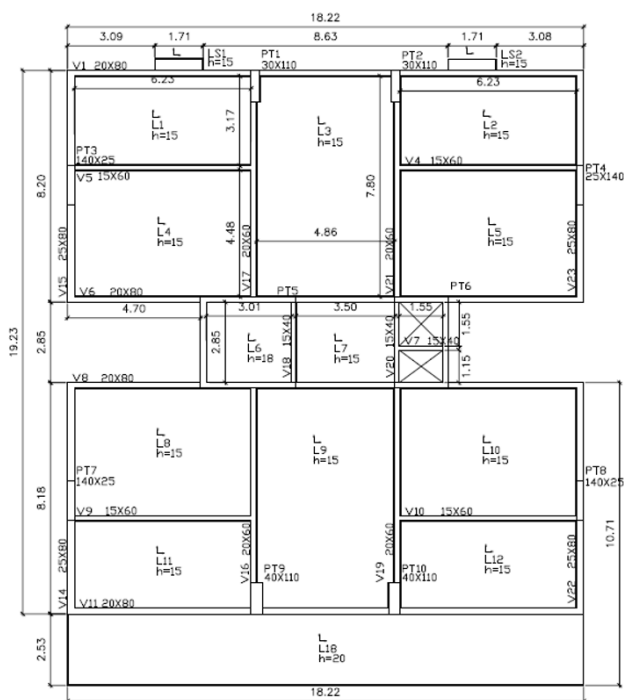


Figure 3 Structural launch layout and 3D view, non-symmetrical models

Foundation loads and settlements were evaluated according to the combination provided by the software that considers the own limit weight, permanent loads and reduced accidental loads, of the Ultimate Limit State (ULS), for columns and foundation.

## 6 RESULTS AND DISCUSSIONS

### 6.1 Instability parameters and maximum horizontal displacements

In relation to the parameter  $\gamma_z$  and maximum horizontal displacements, the results of the first group are presented in Table 4. The use of the IE generated change in the parameter, even in small values in some cases (Wind 90° and 270°). All cases which SSI was used exceeded the standard limit of 1.3, which did not happen when the analysis was not considered. The most altered model was the one that considered the analysis with both parameters simultaneously (models 1.4 and 2.4).

**Table 4** Instability parameters  $\gamma_z$  and maximum horizontal displacements

MODEL	$\gamma_z$		HORIZONTAL DISPLACEMENTS		
	Wind		90°-270°	0° -180°	
	90°-270°	0° -180°			
SYMMETRICAL	1.1	1.150	1.090	1.65	1.00
	1.2	1.151	1.090	1.66	1.00
	1.3	1.305	1.306	2.72	2.74
	1.4	1.311	1.306	2.61	2.85
NON-SYMMETRICAL	2.1	1.162	1.098	1.62	1.36
	2.2	1.162	1.098	1.63	1.38
	2.3	1.323	1.314	2.64	3.11
	2.4	1.327	1.315	2.53	3.23

For the symmetrical models the maximum changes occurred in the SSI models for 0° and 180° Wind cases, with a 19.82% increase. Model 1.2 showed a minimum difference of 0.09% compared to 1.1, so there was no considerable percentage increase. Although the model with SSI and IE showed change in value, it was not relevant in comparative values. Similarly, for the non-symmetric models the largest changes occurred in the SSI models for 0° and 180° Wind cases, with a 19.76% increase. Model 2.2 showed no difference when compared to 2.1, so there was no percentage increase. All models with SSI varied between 10 and 20%. Comparatively, both groups of models showed similar results.

For maximum horizontal displacements, the models with IE (1.2 and 2.2) show smaller changes when compared to the base models. Those using SSI had the greatest values.

ABNT NBR 6118 [23], according to table 13.3, determines that the maximum displacement is:

$$DeslH = \frac{H}{1700} \tag{1}$$

Where: DeslH -- Maximum displacement allowed by norm; H - Total height of the building.

For the studied cases, all the values found are in the limit proposed by the 40.2 mm norm, even those models that present  $\gamma_z$  beyond the norm.

Symmetrical models that used SSI more than doubled the value, for the most part. The addition to using IE was only negligible. The largest variations were for 0° and 180° Wind cases in model 1.4, with a 185% increase compared to the base model. For the non-symmetrical models, model 2.2 presents alteration when compared to 2.1, for two Wind cases, but variations less than 1%. Models 2.3 and 2.4, which use SSI, had the greatest values, with a maximum displacement of 4.30 cm, that means in some cases displacements were greater than the value imposed by the standard. Model 2.4 presented the greatest values of all wind cases.

The introduction of an asymmetry in the building made the maximum horizontal displacements a little more sensitive to IS and SSI. All wind cases generated greater changes than 90° and 270° cases. For the most critical situation

there was a 38% increase from the asymmetric structure to the symmetrical structure for 0° and 180° wind cases in models 2.1 and 2.2.

Symmetric models that used SSI more than doubled the value, mostly. The addition to using IE was only negligible. The greatest variations were for 0° and 180° Wind cases in model 1.4, with a 185% increase compared to 1.1. Non-symmetrical models that used SSI more than doubled the value for some Wind cases. The maximum variation occurred for 0° and 180° Wind cases and was 134.06%.

### 6.2 Loads and settlements of shallow foundations on sand

The shallow foundations (i.e., footings) were identified in: central, peripheral and garage. This separation facilitates understanding of loads distribution. Figure 4 shows a schematic that represents how this classification was made. In this model, the central shallow foundation was characterized as the footing foundation 20, the peripheral one related to the main building (11, 12, 13, 23, 24, 29) and the others as garage. This separation facilitates the understanding of loads distribution.

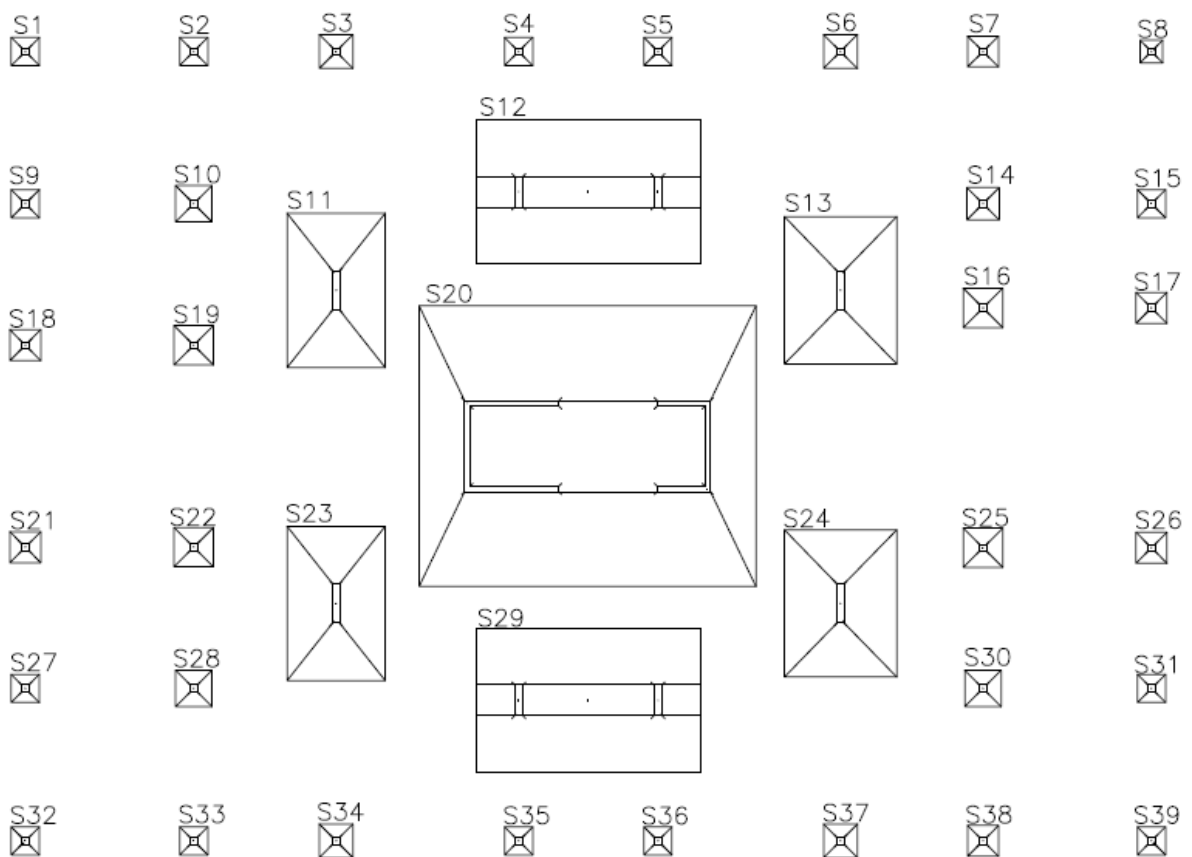


**Figure 4** Structural layout of the shallow foundation

The results of the foundation load analysis are presented in Table 5. For both symmetrical and non-symmetrical models, the garage shallow foundation showed slight changes when compared to the model with IE as a base. All the peripheral shallow foundation of 1.2 and 2.2 suffered a decrease in loading, and the central one increased. For the use of SSI, models 1.3 and 2.3, in relation to effort redistribution, when compared to the base models, the garage shallow foundation have undergone more relevant changes. The peripheral ones suffered different variations, with 12 and 29 with decrease of the loads and the others with increase; the central shoe had a decrease in load. The most relevant variations were in the garage shallow foundation. The use of IS in conjunction with SSI, model 1.4 and 2.4 showed a smaller redistribution when compared to 1.3 and 2.3 respectively, that means, the model showed smaller differences in the periphery and larger shallow foundation in the central shoe, but following the model logic with only SSI for the most part.

**Table 5** Loads in the foundation in the building considered in the analysis (kN)

SHALLOW FOUNDATION POSITION	SHALLOW FOUNDATION	SYMMETRICAL				NON-SYMMETRICAL				
		1.1	1.2	1.3	1.4	2.1	2.2	2.3	2.4	
GARAGE	1	113	113	118	116	113	113	117	115	
	2	235	235	237	237	235	235	236	235	
	3	284	285	308	310	284	284	305	307	
	4	186	190	300	306	185	189	291	297	
	5	186	191	299	305	186	190	290	296	
	6	280	280	301	303	280	280	298	301	
	7	248	248	251	251	247	248	250	249	
	8	121	121	120	120	121	121	119	118	
	9	225	224	206	306	225	225	208	207	
	10	550	552	589	590	550	551	586	587	
	14	405	406	429	428	405	406	426	426	
	15	162	161	149	148	162	161	150	148	
	16	431	435	505	502	431	435	508	506	
	17	185	185	173	175	185	185	174	175	
	18	262	260	239	238	262	260	239	238	
	19	602	606	688	686	602	607	691	690	
	21	266	265	242	242	266	265	238	238	
	22	611	616	698	693	611	617	711	706	
	25	562	567	628	625	562	568	639	637	
	26	231	230	216	216	231	230	212	212	
	27	225	224	206	206	225	224	201	202	
	28	545	547	590	587	544	548	600	595	
	30	548	550	578	575	548	551	587	583	
	31	228	227	207	207	228	226	202	202	
	32	116	116	121	119	116	116	122	121	
	33	241	241	242	242	241	241	243	243	
	34	288	289	316	314	288	289	328	327	
	35	192	198	321	316	194	200	366	364	
	36	183	198	319	315	194	201	365	365	
	37	283	284	306	306	284	284	318	318	
	38	240	241	246	246	241	241	247	246	
	39	116	116	121	120	116	117	122	121	
	PERIPHERAL	11	6707	6607	6988	7079	6678	6580	6845	6995
		12	14148	13933	13727	14567	13989	13805	13316	14291
		13	6823	6765	7123	7206	6796	6732	6972	7109
		23	6937	6840	7217	7013	8180	7982	8488	8167
		24	6957	6904	7324	7075	8244	8100	8659	8333
		29	15151	14897	14641	14454	20651	20438	19370	19439
	CENTRAL	20	32375	33109	31162	32059	30839	31693	30698	31277

In percentage values, the large variation for model 1.2 happened for the garage footing, with an increase of 8%. The others had minimum variations of -1% and the central shallow foundation suffered a load increase of 2%. The model 1.3 obtained more expressive values. The largest variation happens for the same footing as model 1.2, but with maximum values of 74%. Peripheral shallow foundations ranged from -3% to 5% and the center shallow foundation decreased the load value by 4%. In turn, model 1.4 followed the logic of 1.3, but with smaller values: garage shallow foundations varied by a maximum of 72%, peripherals from -5% to 6% and central -1%.

For non-symmetrical models, the largest variation for model 2.2 was for the garage shallow foundation, with a 4% increase. The others had minimum variations of -1% and the central shallow foundation suffered a load increase of 3%. The model 2.3 obtained more expressive values. The largest variation happens for the same shallow foundation as 2.2, but with maximum values of 89%. The periphery shallow foundation ranged from -6% to 5%, while the central shallow foundation did not vary the load value. Model 2.4 followed the logic of 2.3, but with smaller values: garage shallow

foundations varied by a maximum of 88%, peripherals from -6% to 5%, and central 1%. Unlike the symmetrical model, shallow foundations 3, 4, 34 and 35 did not show coherence in the variation of values. Shallow foundations 34 and 35 showed larger changes due to the asymmetry of the building.

The analysis of settlements was performed only in the models that used SSI, since the others consider the supports set. Therefore, Table 6 shows the settlement results for models 1.3, 1.4, 2.3, and 2.4.

**Table 6** Settlements in the building considered in the analysis (cm)

SHALLOW FOUNDATION POSITIONS	SHALLOW FOUNDATION	SYMMETRICAL		NON-SYMMETRICAL		
		1.3	1.4	2,,3	2.4	
GARAGE	1	0.17	0.17	0.17	0.17	
	2	0.32	0.32	0.32	0.32	
	3	0.36	0.36	0.35	0.36	
	4	0.43	0.45	0.42	0.43	
	5	0.43	0.44	0.41	0.43	
	6	0.35	0.35	0.34	0.35	
	7	0.29	0.31	0.31	0.31	
	8	0.2	0.2	0.2	0.2	
	9	0.27	0.27	0.27	0.27	
	10	0.62	0.62	0.61	0.61	
	14	0.51	0.51	0.5	0.51	
	15	0.2	0.2	0.21	0.2	
	16	0.51	0.51	0.51	0.51	
	17	0.22	0.22	0.22	0.22	
	18	0.29	0.29	0.29	0.29	
	19	0.68	0.68	0.68	0.68	
	21	0.29	0.29	0.29	0.29	
	22	0.68	0.69	0.7	0.7	
	25	0.62	0.62	0.63	0.63	
	26	0.27	0.27	0.26	0.26	
	27	0.27	0.27	0.27	0.27	
	28	0.62	0.62	0.63	0.62	
	30	0.6	0.6	0.61	0.61	
	31	0.27	0.27	0.27	0.27	
	32	0.17	0.17	0.17	0.17	
	33	0.32	0.32	0.33	0.33	
	34	0.37	0.37	0.38	0.38	
	35	0.46	0.46	0.53	0.53	
	36	0.46	0.46	0.52	0.53	
	37	0.36	0.36	0.37	0.37	
	38	0.31	0.31	0.31	0.31	
	39	0.17	0.17	0.17	0.17	
	PERIPHERAL	11	2.24	2.28	2.2	2.24
		12	2.46	2.58	2.38	2.5
		13	2.08	2.11	2.03	2.07
		23	2.31	2.26	2.59	2.51
		24	2.13	2.09	2.42	2.34
		29	2.61	2.56	3.26	3.23
	CENTRAL	20	2.7	2.77	2.54	2.63

For all studied models, most values found were similar for garage shallow foundations. All periphery shallow foundations changed their values: footings 11, 12, and 13 increased their displacements with the use of the IE, and footings 23, 24, and 29 decreased, as did the center footing.

The greatest settlement found for symmetrical models was in the 2.77cm center footing, and for 2.63 cm non-symmetrical footings for cases 1.4 and 2.4, respectively. The periphery footings presented smaller values, but in this order of magnitude. As for the garage, none of them reached 1.00 cm.

In garage footings of symmetrical models, the largest change in percentage value was 6%. The peripheral footings ranged from -2% to 5%. For the plant, there was a 3% change in its value. In the case of non-symmetrical models, the largest change in percentage value was 5% for the garage, the peripheral footings ranged from -3% to 5%, while for the central, there was a change of 3% in its value.

## 7 CONCLUSIONS

The objective of this paper was to evaluate the influence of Incremental Effect and Soil-Structure Interaction on overall stability analyses of a reinforced concrete structure with shallow foundations on sandy soils. For such, the instability  $\gamma_z$  parameters were analyzed, in addition to foundation loads, settlements and quantity of materials, to complement the analysis and understand how these parameters can influence the design of the building.

Thus, in general, the use of SSI presented more relevant variations, showing to be the most complex tool and requiring more attention from the designer, which is in agreement with the studies of Alves and Feitosa [12] and Marques et al. [19], which draw attention to the variations found in the parameters analyzed.

For SSI and EI, the models presented: great variation in stability and displacement and an intermediate redistribution of loads, demonstrating that they alter the efforts in which the building is submitted in the calculation process.

The results agree with Jucá et al. [20], since the model that considers SSI and IE (models 1.4 and 2.4) increases the instability of the building when compared to without the IE (models 1.3 and 2.3). In relation to the case without the use of ISE, it is not possible to evaluate it, because it was considered the foundation set. Considering that the study done by the authors was compared to a real building, the agreement of the values found highlights the importance of considering these calculation models in the project.

In summary, it is possible to conclude that the joint use of the Incremental Effect and Soil-Structure Interaction parameters are relevant to the final design of the building, especially when these effects are considered in combination.

## ACKNOWLEDGEMENTS

The authors acknowledge TQS Informática for providing the program in its full version for the development of the work, as well as to PPGEC UFES for their support. At the same time, we acknowledge Profa. Cristina Helena Carneiro from IFES for English translations. The third author thanks CNPq for the research grant called scientific productivity fellowship.

## REFERENCES

- [1] J. F. M. A. Prado, "Structures of reinforced concrete buildings subjected to construction actions," Ph.D. dissertation, Univ. Fed. São Carlos, São Carlos, 1999.
- [2] L. S. Gorza, "Constructive incremental analysis of multi-story metallic building using the finite element method," M.S. thesis, Univ. Fed. Espírito Santo, Vitória, 2000.
- [3] O. Ge, F. Xiong, L. Xie, J. Chen, and M. Yu, "Dynamic interaction of soil – structure cluster," *Soil. Dyn. Earthquake Eng.*, vol. 123, pp. 16–30, 2019.
- [4] Y. Saragi, M. Irsyam, and H. Roesyanto, "Nonlinear dynamic soil structure interaction in adjacent basement," *IOP Conf. Series Mater. Sci. Eng.*, 2019.
- [5] P. Galvín, A. Romero, and J. Domínguez, "Fully three-dimensional analysis of tall-speed train-track-soil-structure dynamic interaction," *J. Sound Vibrat.*, vol. 329, no. 24, pp. 5147–5163, 2010.
- [6] M. Damgaard, L. V. Andersen, and L. B. Ibsen, "Computationally efficient modelling of dynamic soil-structure interaction of offshore wind turbines on gravity footings," *Renew. Energy*, vol. 68, pp. 289–303, Aug 2014.
- [7] D. Lombardi, S. Bhattacharya, and D. M. Wood, "Dynamic soil-structure interaction of monopile supported wind turbines in cohesive soil," *Soil. Dyn. Earthquake Eng.*, vol. 49, no. 16, pp. 165–180, Jun 2013.
- [8] S. Bhattacharya et al., "Observed dynamic soil-structure interaction in scale testing of offshore wind turbine foundations," *Soil. Dyn. Earthquake Eng.*, vol. 54, no. 14, pp. 47–60, Nov 2013.
- [9] J. Su and Y. Wang, "Equivalent dynamic infinite element for soil-structure interaction," *Finite Elem. Anal. Des.*, vol. 63, pp. 1–7, Jan 2013.
- [10] M. Papadopoulos, R. Van Beeumen, S. François, G. Degrande, and G. Lombaert, "Modal characteristics of structures considering dynamic soil-structure interaction effects," *Soil. Dyn. Earthquake Eng.*, vol. 105, pp. 114–118, Feb 2018.

- [11] Q. Ge, F. Xiong, J. Chen, and Z. Yao, "Effects of soil-structure cluster interactions on ground motions," *Struct. Des. Tall Spec. Build.*, vol. 29, no. 1, 2020.
- [12] E. C. Alves and L. A. Feitosa, "Analysis of the overall stability of tall buildings on flat slabs considering the soil-structure interaction," *Int. J. Struct. Mater.*, vol. 13, pp. 183–199, Feb 2020.
- [13] B. R. Danziger, E. M. L. Carvalho, R. V. Costa, and F. A. B. Danziger, "Study of case work with interaction analysis soil-structure," *Civ. Eng. Mag.*, no. 23, pp. 43–54, 2005.
- [14] L. A. Feitosa and E. C. Alves, "Study of global stability of tall buildings with prestressed slabs," *Int. J. Struct. Mater.*, vol. 8, no. 2, pp. 196–224, Apr 2015.
- [15] A. D. Gusmão, "Study of soil-structure interaction and its influence on building settlements," M.S. thesis, Univ. Fed. Rio de Janeiro, Rio de Janeiro, 1990.
- [16] G. Savaris, P. H. Hallak, and P. C. A. Maia, "Influence of foundation settlements in load redistribution on columns in a monitoring construction – case study," *Int. J. Struct. Mater.*, vol. 3, no. 3, pp. 346–356, 2010.
- [17] R. C. Pavan, M. F. Costella, and G. Guarnier, "Soil-structure interaction for frame structures on shallow foundations," *Int. J. Struct. Mater.*, vol. 7, no. 2, pp. 260–285, 2014.
- [18] N. S. Agrawal and V. R. Harme, "Analysis of reinforced concrete structure considering the influence of soil structure interaction," *Helix*, vol. 10, no. 1, pp. 98–104, 2020.
- [19] O. C. Marques, E. C. Alves, and L. A. Feitosa, "Analysis of instability parameters considering constructive effect and solo-structure interaction in tall-rise design," in *Proced. 60th Brazilian Concr. Congr.*, Foz do Iguaçu, 2018. (In Portuguese).
- [20] J. F. T. Jucá, A. O. C. Fonte, and I. D. S. Pontes Fo., "Building performance founded on an improved sand in Recife, Brazil," in *Vertical and Horizontal Deformations of Foundations and Embankments*, A. T. Yeung and G. Y. Fêlio, Eds., New York: ASCE, 1994, pp. 1202-1213.
- [21] TQS Informática, *Theoretical Manual – Soil-structure Interaction System*. São Paulo: TQS Informática Ltda., 2018.
- [22] L. S. Gorza and L. H. Coelho, "Constructive incremental analysis of multi-story metal buildings – case study," *Eng. Sci. Technol. Mag.*, vol. 3, no. 17, pp. 33–41, 2000.
- [23] Associação Brasileira de Normas Técnicas, *Design of Concrete Structures – Procedures*, NBR 6118, 2014.
- [24] R. C. B. L. Albuquerque and A. D. Gusmão, "Considerations on the relevance of soil-structure interaction in settlements: case of a building in the city of Recife," in *2nd Brazilian Symp. Young Geotech.*, Nova Friburgo, 2006. (In Portuguese).
- [25] R. A. Souza and J. H. C. Reis, "Solo-structure interaction for buildings under shallow foundation," *Min. Sci. Technol.*, vol. 30, no. 2, pp. 161–171, 2008.
- [26] V. M. Passos, E. C. Alves, and L. A. Feitosa, "Stability analysis of tall buildings on smooth and ribbed slabs with the effect of soil-structure interaction," in *Proced. 58th Brazilian Concr. Congr.*, Belo Horizonte, 2016.
- [27] L. M. P. Rosa, B. R. Danziger, and E. M. L. Carvalho, "Soil-structure interaction analysis considering concrete creep and shrinkage," *Int. J. Struct. Mater.*, vol. 11, no. 3, pp. 564–585, Jun 2018.
- [28] J. H. Schmertmann, J. P. Hartman, and P. R. Brown, "Improved strain influence factor diagrams," *J. Geotech. Eng. Div.*, vol. 104, no. 8, pp. 1131–1135, 1978.

---

**Author contributions:** OCP: conceptualization, data curation, formal analysis, methodology, writing; LAF: conceptualization, data curation, formal analysis; KVB: conceptualization, writing; ECA: conceptualization, data curation, methodology, supervision, writing.

**Editors:** Bernardo Horowitz, José Luiz Antunes de Oliveira e Sousa, Guilherme Aris Parsekian.



ORIGINAL ARTICLE

# A simplified numerical and analytical study for assessing the seismic response of a gravity concrete lock

*Um estudo numérico e analítico simplificado para a avaliação da resposta sísmica de uma eclusa em concreto gravidade*

Neander Berto Mendes<sup>a</sup>

Lineu José Pedroso<sup>a</sup>

Paulo Marcelo Vieira Ribeiro<sup>b</sup>

<sup>a</sup>Universidade de Brasília – UnB, Departamento de Engenharia Civil e Ambiental, Programa de Pós-graduação em Estruturas e Construção Civil – PECC, Grupo de Dinâmica e Fluido-Estrutura – GDFE, Brasília, DF, Brasil

<sup>b</sup>Universidade Federal de Pernambuco – UFPE, Departamento de Engenharia Civil, Recife, PE, Brasil

Received 02 May 2019

Accepted 12 May 2020

**Abstract:** This work presents the dynamic response of a lock subjected to the horizontal S0E component of the El Centro earthquake for empty and completely filled water chamber cases, by coupled fluid-structure analysis. Initially, the lock was studied by approximation, considering it similar to the case of a double piston coupled to a two-dimensional acoustic cavity (tank), representing a simplified analytical model of the fluid-structure problem. This analytical formulation can be compared with numerical results, in order to qualify the responses of the ultimate problem to be investigated. In all the analyses performed, modeling and numerical simulations were done using the finite element method (FEM), supported by the commercial software ANSYS.

**Keywords:** lock, seismic analysis, fluid-structure, finite elements, analytical solutions.

**Resumo:** Este trabalho apresenta a resposta dinâmica de uma eclusa submetida à componente horizontal S0E do terremoto ocorrido em El Centro, para os casos de câmara de água vazia e completamente cheia, por meio de uma análise acoplada fluido-estrutura. Inicialmente, estudou-se a eclusa de forma aproximada, considerando-a semelhante ao caso de um pistão duplo acoplado a uma cavidade acústica bidimensional (tanque), que representa um modelo analítico simplificado do problema fluido-estrutura. Esta formulação analítica pode ser comparada com resultados numéricos, com vistas a qualificar as respostas do problema final a ser investigado. Em todas as análises realizadas, o modelamento e as simulações numéricas foram feitos pelo método dos elementos finitos (MEF), com apoio do software comercial ANSYS.

**Palavras-chave:** eclusa, análise sísmica, fluido-estrutura, elementos finitos, soluções analíticas.

**How to cite:** N. B. Mendes, L. J. Pedroso, and P. M. V. Ribeiro, “A simplified numerical and analytical study for assessing the seismic response of a gravity concrete lock” *Rev. IBRACON Estrut. Mater.*, vol. 14, no. 1, e14104, 2021, <https://doi.org/10.1590/S1983-41952021000100004>

## 1 INTRODUCTION

Locks are hydraulic structures used to transpose vessels in channels where there is sharp natural unevenness, such as rapids, or artificial unevenness, such as dams. The locks consist basically of a chamber, upstream and downstream gates, filling and emptying system and upstream and downstream accesses. The locks can be submitted to various types of actions, such as, for example, the seismic stresses. There is an interesting case in the event of dynamic interaction between the lock walls and the chamber fluid, during an earthquake. It is a fluid-structure phenomenon, where the movement of the structure produces stresses on the fluid, which in turn interacts, producing hydrodynamic pressures on the structure. If the fluid is considered to be acoustic, the problem will be treated as an acoustic-structural interaction,

Corresponding author: Neander Berto Mendes. E-mail: [neanderberto@hotmail.com](mailto:neanderberto@hotmail.com)

Financial support: None.

Conflict of interest: Nothing to declare.



This is an Open Access article distributed under the terms of the Creative Commons Attribution License, which permits unrestricted use, distribution, and reproduction in any medium, provided the original work is properly cited.

where the lock walls will function as a flexible wall and the chamber fluid will be associated with an acoustic compartment.

On locks, Ables [1] investigated the lock filling and emptying system in Bay Springs, Tennessee-Tombigbee waterway, in Mississippi, USA, using a reduced model. Novak and Cábélka [2] presented models in hydraulic engineering, their physical principles and applications thereof in design. Studies on characteristics and seismic responses of a lock through a 3-D dynamic analysis, taking into account the soil-structure interaction by the finite element method, were conducted by Ming [3]. The influence of soil stiffness, variation, and non-linearity on the dynamic characteristics and seismic responses of the lock system is discussed. The following conclusions are drawn: (1) the influence of soil-structure interaction on the dynamic characteristics and seismic responses of the lock is quite significant and (2) the lock system can generally be analyzed as a linearly elastic system, unless the lock is on soft ground or subjected to a strong earthquake. According to Novak [4], the headwaters of channeled rivers and waterways are usually surpassed by navigation locks. The main components of the locks are the lock gates, the crosspiece, the lock valves, and the filling systems. Trentini et al. [5] presented the result of the finite element modeling of one of the most complex structures of the Tucuruí unevenness transposition system, which is the lock downstream head 1. The modeling was carried out with the help of the ANSYS program, which allowed high quality and fidelity in the structure discretization. With 3D structure modeling to the smallest detail, it was possible to make both global and local assessments, allowing the verification of global stability and stress concentrations in the most critical regions of the structure, resulting from the interaction across all the elements and the foundation. Based on the structure of a lock, Lin and Yong-he [6] adopted a porch structural model and used the elastic foundation model of the ground behavior proposed by Winkler, characterizing the ground as a series of springs. A reverse iteration method is used to calculate the vibration frequency of the lock structure. With finite element programming, the Xinming lock in Shanghai is analyzed. The results are close to the measurements. Novak et al. [7] presented general studies on locks – locks with direct filling and indirect filling and emptying, the hydraulics of the locks, etc. Modeling is a vital part of all engineering projects and Novak et al. [8] provide guidance on simulations of hydraulic models, such as locks, and how they should be related to the prototype. By investigating the damage caused by the Wenchuan earthquake on the GuansongPeng lock, Xiao [9] summarized the main anti-earthquake measures in force in China. For reinforced concrete locks, when earthquake intensity was less than 8 degrees, a minor seismic damage can occur. The work also analyzes the specifications for the seismic design of hydraulic structures of the lock and points out possible serious secondary disasters, indicating that the anti-earthquake criteria are insufficient and should be changed in the future. Maltidis [10] investigated the seismic loading of hydraulic structures, with an emphasis on the dynamic pressures of water and ground and provided information for the design and analysis of navigation locks, considering the ground-structure and fluid-structure interactions.

In the context of studies on gravity structures, Oliveira [11] analyzed the stresses and the global stability of concrete gravity dams. Ribeiro [12] developed an analytical methodology for assessing the stress field in concrete gravity dams during earthquakes. Silva [13] studied the dynamic dam-reservoir interaction using analytical and numerical models. Melo [14] studied reservoir-gate coupling under seismic actions.

In the scope of the simplified model used here, Pedroso [15], [16] presented the complete development of the formulation for the uncoupled and coupled free vibrations of the 2D double-piston-acoustic cavity case. Souza [17] showed an application of finite element and finite differences methods to the fluid-structure interaction. Souza [18] developed a fluid-structure coupled analysis methodology for acoustic cavities with flexible walls. Ribeiro [19] developed analytical solutions for two-dimensional acoustic cavities applicable to the study of dam-reservoir dynamic interaction problems. Intartaglia et al. [20] studied the flexural vibrations of two thin beams coupled through a quiescent viscous fluid. Rezaiee-Pajand et al. [21] provided a brief bibliographic review on the dynamic behavior of liquid storage containers. The free vibration of two-dimensional, deformable rectangular tanks completely filled with a compressible fluid was analytically investigated, and exact solutions were obtained by them. A closed solution was also developed by them to assess the fundamental frequency of flexible 2D rectangular tanks filled with compressible liquid and an approximate formula to determine the corresponding pressure distribution on the tank walls was suggested.

As previously mentioned, “hydraulic structures” refer to a particular set of structures, such as dams, dikes, locks, quay walls, port entrance towers, etc. However, when referring to the navigation locks themselves, there is very limited number of technical-scientific engineering publications, in comparison with other hydraulic structures.

But the number of scientific contributions on the analysis of locks can be significantly increased if they are treated as retention structures and/or as tanks with fluids or water reservoirs. On the other hand, despite the large number of publications related to the analysis and design of those structures, addressed as such, there are few of these contributions related to the analysis of seismic fluid-structure behavior, if they are not considered similar to retention structures but

are effectively treated as navigation locks. This is an aspect that highlights a significant gap in scientific activities in this field of knowledge, to which our work intends to pay a modest contribution.

Thus, the purpose of this work is to investigate the uncoupled and coupled fluid-structure (walls-water chamber) dynamic behavior of a navigation lock, when subjected to seismic action, under the conditions of the empty and completely filled water chamber. Initially, the lock was studied in an approximate way, considering it similar to the case of a double piston coupled to a two-dimensional acoustic cavity (tank), which represents a simplified analytical model of the coupled fluid-structure problem, but which sheds light on important aspects of the phenomenology involved, providing preliminary relevant information for the design and analysis of those structures. This analytical formulation is compared with numerical results, to qualify the answers to the ultimate problem that shall be investigated. In all the analyses performed, modeling and numerical simulations were done using the finite element method (FEM), with the support of the commercial software ANSYS. The analytical solution, although limited to predict the upper coupled modes of additional mass, is capable of satisfactorily responding to the first coupled modes and vibration frequencies, which represent the most significant part of the responses sought in the dynamic analysis of those structures.

## 2 MATHEMATICAL FORMULATION

The fluid-structure interaction problem under study is subject to some considerations: the solid has a linear elastic behavior, consisting of isotropic, homogeneous material, with a constant elasticity module and subjected to small displacements, when compared with the dimensions of the structure. It is also assumed that the fluid is invisible, compressible, and that the process is adiabatic.

The numerical analysis of the fluid-structure coupling by the finite element method is based on the acoustic formulation (U-P), with pressure being the variable in the fluid domain and displacement being the unknown factor of the structure.

The equation of the structure motion for the coupled problem is given by the Formula 1, whose vector of forces  $\{F\}$  can be broken down into two other vectors: a vector of generic forces  $\{F^E\}$  and another vector of forces at the interface  $\{F^I\}$ , which corresponds to the pressures of the fluid on the region contacting the solid.

The equation of solid motion is given by:

$$[M_s]\{\ddot{U}\} + [C_s]\{\dot{U}\} + [K_s]\{U\} = \{F^E\} + \{F^I\} \tag{1}$$

where:

$$[K_s] = \int_{V_s} [Bu]^T [C_s] \cdot [Bu] \cdot dV_s \text{ Solid stiffness matrix} \tag{2}$$

$$[M_s] = \int_{V_s} \rho [Nu]^T \cdot [Nu] \cdot dV_s \text{ Solid mass matrix} \tag{3}$$

where:  $[Bu]$  = element shape functions derivatives matrix;  $[C_s]$  = elastic stiffness matrix or stress-strain matrix;  $\rho$  = specific mass of the structure;  $[Nu]$  = structural element shape functions matrix.

The vector of forces at the interface  $\{F^I\}$  applied in the region of the coupling is obtained by integrating the pressure on the fluid-structure interface surface, as follows:

$$\{F^I\} = \int_S \{N_u\} P \{n\} dS \tag{4}$$

where:  $\{N_u\}$  = vector of shape functions used to discretize the displacement components u, v, w;  $\{n\}$  = vector in the normal direction.

The displacement field of the solid element is given by the Equation 5:

$$U = \{N_u\}^T \{U_e\} \tag{5}$$

For the fluid element, the pressure at a certain point in the element can be expressed by:

$$P = \{N_p\}^T \{P_e\} \tag{6}$$

where the vector  $U_e = [u_i \ v_i \ w_i \ u_2 \ v_2 \ w_2 \ \dots \ u_N \ v_N \ w_N]$  represents the nodal displacements, where  $u_i$ ,  $v_i$  and  $w_i$  correspond to the displacements of node  $i$ , in the  $x$ ,  $y$  and  $z$  directions, respectively. While  $P_e = [p_1 \ p_2 \ p_3 \ \dots \ p_N]$  represents the pressures and is associated with the nodal variables of the fluid.

Substituting Equation 6 in the force equation in the interface region (4), we obtain:

$$\{F^f\} = \int_S \{N_p\} \{N_u^T\} \{n\} dS \{P_e\} \tag{7}$$

It is observed that  $\int_S \{N_p\} \{N_u^T\} \{n\} dS$  represent the fluid-structure matrix  $\{FS\}$  for the coupled system, as also shown in Sousa [17] and in the summary of the method in the ANSYS program manual, then:

$$\{F_e^f\} = [FS] \{P_e\} \tag{8}$$

Substituting Equation 8 in Equation 1 the outcome is the structure motion equation for the coupled problem:

$$[M_s] \{\ddot{U}\} + [C_s] \{\dot{U}\} + [K_s] \{U\} - [FS] \{P_e\} = \{F^s\} \tag{9}$$

Applying the Galerkin method to the wave equation and using finite element discretization, the outcome is the dynamic equation for the acoustic cavity of the coupled problem, according to Sousa [17]).

$$[M_f] \{\ddot{P}\} + [C_f] \{\dot{P}\} + [K_f] \{P\} + \rho [FS] \{\ddot{U}\} = \{0\} \tag{10}$$

where:

$$[K_f] = \int_{\Omega_f} [Bp]^T \cdot [Bp] \cdot d\Omega_f \text{ Fluid stiffness matrix} \tag{11}$$

$$[M_f] = \int_{\Omega_f} [Np]^T \cdot [Np] \cdot d\Omega_f \text{ Fluid mass matrix} \tag{12}$$

$$[C_f] = \frac{I}{c} \int_{\Gamma_d} [Np]^T \cdot [Np] \cdot d\Gamma_d \text{ Fluid damping matrix} \tag{13}$$

$$[FS]^T = \oint_{\Gamma_f} [Nu]^T \cdot \bar{n} \cdot [Np] \cdot d\Gamma_f \text{ Fluid-structure coupling matrix} \tag{14}$$

being  $[Bp] =$  matrix operator (gradient) applied to the fluid element shape functions;  $[Np] =$  fluid element shape function for pressure.

The shape functions used are for 2-D solid quadrilateral 4-node and axisymmetric elements, both for the structure and the fluid.

Equations 9 and 10 describe the problem of fluid-structure interaction and when placing them in the matrix form, the formulation presented in the ANSYS program is reproduced in an analogous way, as follows:

$$\begin{bmatrix} [M_s] & [0] \\ \rho[FS] & [M_f] \end{bmatrix} \begin{Bmatrix} \ddot{U} \\ \dot{P} \end{Bmatrix} + \begin{bmatrix} [C_s] & [0] \\ [0] & [C_f] \end{bmatrix} \begin{Bmatrix} \dot{U} \\ \dot{P} \end{Bmatrix} + \begin{bmatrix} [K_s] & -[FS] \\ [0] & [K_f] \end{bmatrix} \begin{Bmatrix} U \\ P \end{Bmatrix} = \begin{Bmatrix} F^E \\ 0 \end{Bmatrix} \quad (15)$$

Or yet:

$$M \ddot{X} + C \dot{X} + KX = F \quad (16)$$

Equation 16 corresponds to the complete system for the fluid-structure interaction problem and represents the classic form of the equation of motion in forced vibrations.

### 3 APPROXIMATE ANALYTICAL SOLUTION FOR THE SIMPLIFIED LOCK MODEL

This development is based on the formulation of Pedroso [16] apud Souza [18], who presents the complete theoretical foundation for the case of the 2D double-piston-acoustic cavity problem in free vibrations. This study presents a consistent and reference methodology for understanding and comprehension of the phenomena associated with the fluid-structure coupling problem, in addition to providing an analytical formulation for the uncoupled structure, uncoupled fluid and coupled fluid-structure cases. Figure 1 shows the 2D double-piston-acoustic cavity system superimposed on the real lock-tank system, assumed in a 1<sup>st</sup> approach as a rigid-mobile structure.

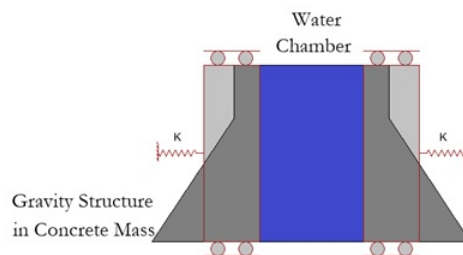


Figure 1. 2D double piston-acoustic cavity system superimposed on the supposed rigid-mobile lock-tank system

#### 3.1 Uncoupled structure

In a first approach, the behavior of the rigid-mobile lock can be compared to a “piston” (straight beam) on an elastic base, represented in Figure 2a that works as if it was a beam on springs with elastic constant  $k_f$  separated by  $\Delta$ .

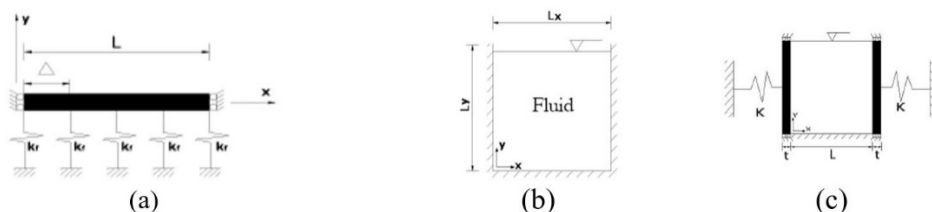


Figure 2. (a) Schematic of the structure (piston) on an elastic base, (b) Short rigid cavity with open upper end. (c) 2D double piston-cavity model with open boundary.

The analytical frequencies of the structure in Figure 2, in Hz, can be obtained by combining the dynamic behavior of a rectangular section beam on an elastic base - springs (m) - considering the bending (f) and shear (c) deformations. Equation 17 provides these frequencies for the uncoupled structure.

$$f_{m+f+c} = \sqrt{f_m^2 + f_{f+c}^2}; i = 1, 2, 3, \dots \tag{17}$$

where,

$$f_m = f_{i=0} = (1/2\pi)\sqrt{\bar{k}/\bar{m}} = \text{frequency of the springs}; \tag{18}$$

$$f_{f+c} = \frac{1}{(1/f_f)^2 + (1/f_c)^2}, \text{ beams with comparable bending and shear deformations}; \tag{19}$$

$$f_f = (i^2\pi/2)\sqrt{EI/(\bar{m}L^4)} = \text{beam bending frequencies}; \tag{20}$$

$$f_c = (i/2)\sqrt{KGA/(\bar{m}L^2)} = \text{beam shear frequencies}; \tag{21}$$

$\bar{k} = K/L$  = spring stiffness per elastic base length unit;  $\bar{m} = m_e/L$  = mass per beam length unit;  $K = Nk_f$  = spring stiffness; N = number of springs; L = beam/elastic base length;  $m_e$  = mass of the structure; b = base of the beam cross-section (equal to 1m); E = Young's modulus of the material;  $\nu$  = Poisson's ratio of the material;  $I = bt^3/12$  = moment of inertia of the beam cross-section; EI = stiffness to the part bending; t = thickness/height of the beam cross-section;  $K = 10(1+\nu)/(12+11\nu)$  = shear coefficient;  $A = bt$  = cross-section area of the beam;  $G = E/[2(1+\nu)]$  = transverse elasticity modulus of the material; KGA = transverse stiffness of the part.

The analytical frequencies of the structure, considering the normal deformations (n) of tension and compression are given by:

$$f_n = (i/2)\sqrt{EA/(\bar{m}L^2)}; i = 1, 2, 3, \dots \tag{22}$$

where, EA = axial stiffness of the part.

### 3.2 Uncoupled cavity

To obtain the natural frequencies of a one-dimensional acoustic cavity, the transfer matrix method (MMT), Pedroso [15], is used, which is developed based on the wave equation, in terms of pressure:

$$\frac{\partial^2 p}{\partial x^2} + (\omega/c)^2 p = 0 \tag{23}$$

where, p = pressure;  $\omega = 2\pi f$  = natural frequency, in rad/s; c = speed of sound.

The solution of Equation 23 is given by:

$$p(x) = A\cos(\omega x/c) + B\sin(\omega x/c) \tag{24}$$

With the acoustic flow being equal to

$$q = -(S / (i\omega)) \frac{\partial p}{\partial x} \tag{25}$$

where, S = cross-section area; i = imaginary unit.

Thus:

$$q(x) = (iS / c) [-A \operatorname{sen}(\omega x / c) + B \cos(\omega x / c)] \tag{26}$$

For x = 0, at the input of the cavity, the result is:

$$A = p_e \tag{27}$$

$$B = (c / (iS)) q_e \tag{28}$$

And for x = L, at the output of the cavity, the result is:

$$p_s = p_e \cos(\omega L / c) + [c / (iS)] q_e \operatorname{sen}(\omega L / c) \tag{29}$$

$$q_s = -(iS / c) p_e \operatorname{sen}(\omega L / c) + q_e \cos(\omega L / c) \tag{30}$$

Where L = length of the cavity; p<sub>e</sub> = pressure at the input of the cavity; q<sub>e</sub> = flow at the input of the cavity; p<sub>s</sub> = pressure at the output of the cavity; q<sub>s</sub> = flow at the output of the cavity.

Associating Equations 29 and 30 in a matrix form, we have:

$$\begin{bmatrix} p_s \\ q_s \end{bmatrix} = A \begin{bmatrix} p_e \\ q_e \end{bmatrix} \tag{31}$$

where,

$$A = \begin{bmatrix} \cos(\omega L / c) & (c / (iS)) \operatorname{sen}(\omega L / c) \\ -(iS / c) \operatorname{sen}(\omega L / c) & \cos(\omega L / c) \end{bmatrix} \tag{32}$$

this is the so-called transfer matrix.

In the case of open boundary, there is zero pressure and in the case of closed boundary, zero flow. Thus, the natural frequencies, in Hz, of closed-open and closed-closed 1D cavities filled with fluid are those given in Table 1.

**Table 1.** Natural Frequency of Acoustic Cavities

Cavity	Natural Frequency, <i>f</i> (Hz)	Cavity	Natural Frequency, <i>f</i> (Hz)
Closed-Open	$\frac{ci}{4L}, i = 1, 3, 5, \dots$	Closed-Closed	$\frac{ci}{2L}, i = 0, 1, 2, \dots$

c = speed of sound; L = width of the cavity.

For the rectangular geometry of the 2D cavity, the resulting frequency uncoupled from the cavity is obtained by combining the natural frequencies uncoupled in x and y (1D), which can be expressed as follows:

$$f = \sqrt{f_x^2 + f_y^2} \tag{33}$$

For the case closed-closed in x and closed-open in y, which are the boundary conditions of the model used in this article, shown in Figure 2b, we have:

$$f = c \sqrt{\left(\frac{i}{2L_x}\right)^2 + \left(\frac{j}{4L_y}\right)^2}; \begin{cases} i = 0, 1, 2, \dots \\ j = 1, 3, 5, \dots \end{cases} \tag{34}$$

### 3.3 Coupled structure-cavity

This section presents the theoretical basis for the coupled free vibrations in the case of a “2D Double-Piston-Acoustic Cavity” (a simplified representation of the lock) for the first phase (F) mode of the pistons, which are characterized by the additional mass effect (fluid incompressibility) and for all the cavity mastery modes, which induce additional stiffness in the system.

The additional mass (MA) effect reduces the natural frequency of the coupled fluid-structure system in relation to the natural frequency of the corresponding uncoupled structural system, with the coupled mode being a structure dominant (DE) mode. The effect of additional stiffness (RA) increases the natural frequency of the coupled fluid-structure system in relation to the natural frequency of the corresponding uncoupled fluid system, with this coupled mode being a cavity dominant (DC) mode.

The referred case is characterized vertically because it has a boundary of the cavity opened to the atmosphere ( $p = 0$ ) and the other rigid (bottom). The left and right ends have two rigid-mobile plates, supported by springs with elastic constant K. The structure has freedom of movement in the x-direction, as shown in Figure 2c.

Equation 35 allows, in a simplified way, the calculation of the first two fundamental frequencies of additional mass and incompressible fluid (i.e., with a compressibility parameter  $\lambda$  less than 1) for the two moving plates:

$$f = (1 / 2\pi) \sqrt{K / (m_e + m_{ad})} \tag{35}$$

on what:  $m_{ad}$  = additional mass of the chamber fluid; L = horizontal length of the cavity.

Equation 35 is for the first phase (F) mode, where each piston drags half the total mass of the fluid ( $m_f$ ) in the chamber ( $m_{ad} = m_f / 2$ ). In this case, with the movement in phase opposition (OF) of the cavity walls, there is a confinement of the fluid without compressing it, which adds more mass to each piston than  $m_f / 2$ . Equation 35 is still valid, but the additional mass needs to be evaluated by another process. As the fluid is incompressible, and there is the piston movement in OF, the movement of each piston in the opposite direction works as if more mass (virtual mass) was added to the opposite piston, an aspect not captured by the adopted double-piston model.

For the cavity domain modes, which generate additional stiffness in the coupled system, another formulation must be used, Pedroso [15]. Displacement of the  $x_s$  piston imposes a mass flow source, given by:

$$q = i\omega\rho_f Sx_s \tag{36}$$

Applying the coupled piston boundary condition in Equation 31 with the input being ( $q_e = i\omega\rho_f Sx_{s_e}$ ) and the output being ( $q_s = i\omega\rho_f Sx_{s_s}$ ), we obtain:

$$p_e = \omega\rho_f c [x_{s_e} \cot(\omega L / c) - x_{s_s} \operatorname{cosec}(\omega L / c)] \tag{37}$$

$$p_s = \omega \rho_f c [x_{S_e} \cos(\omega L / c) - x_{S_s} \cot(\omega L / c)] \tag{38}$$

The equations for the dynamic balance of the two pistons are given by:

$$(K_e - \omega^2 m_e) x_{S_e} = -p_e S \tag{39}$$

$$(K_e - \omega^2 m_e) x_{S_s} = p_s S \tag{40}$$

where,  $K_e$  = stiffness of the structure;  $m_e$  = mass of the structure.

Observing that for pistons in phase,  $x_{S_e} = x_{S_s}$  and for pistons out of phase,  $x_{S_e} = -x_{S_s}$ , Equation 39, results in:

$$\lambda^2 [\mu - (1 / \lambda) (\cot \lambda \mp \cos \sec \lambda)] = \alpha \tag{41}$$

where,  $\mu = m_e / m_f$  = ratio between the mass of the structure and the mass of the fluid;  $\alpha = K / K_f$  = ratio between the stiffness of the structure and the stiffness of the fluid;  $\lambda = \omega L / c = 2\pi f L / c$  = compressibility parameter;  $K_f = \rho_f c^2 S / L$  = cavity stiffness with fluid;  $L$  = width of the cavity;  $\rho_f$  = fluid density;  $S$  = cavity area.

Therefore, for the cavity domain modes, which generate additional stiffness, Equation 41 allows the calculation of the natural frequencies of the problem coupled in phase (F) (- signal), except the first root; and phase opposition (OF) (+ signal), Pedroso [16]. For the 1st mode in phase (F),  $x_{S_e} = x_{S_s}$ , with  $\lambda \lll 1$ , Equation 41 results in Equation 35.

The resulting frequency coupled for the 2D double-piston-cavity case with the open upper end (Figure 2c) is the combination of the natural frequency coupled in the x-direction with the natural frequency uncoupled in the y-direction. It is given by Equation 42. Therefore, the analytical frequency of the coupled system for the case of Figure 2c can be expressed as follows, Pedroso [16]:

$$f = \sqrt{f_{acop,x}^2 + f_{des,y}^2} \tag{42}$$

with, for the closed-open case,

$$f_{des,y} = (j / 4) (c / L); j = 1, 3, 5, \dots \tag{43}$$

The larger frequencies and modes of additional mass (structure deformational modes) in this simplified analytical formulation cannot be calculated (the theory does not foresee this possibility, since the formalism used is for a 1D acoustic cavity problem, and the rigid-mobile structure); however, this case could be supported by a more comprehensive theory (additional mass dependent on the deformation mode structure, Silva [13], Ribeiro [19]), which will not be used in this work.

However, if the additional mass is calculated by the frequency reduction, obtained by the numerical analysis via FEM, and introduced in the frequency formulas of the structure, making it similar to a deformed one that produces a fluid displacement equivalent to the mass displaced by the coupled deformed one, we will have the analytical results marked by  $\bar{A}$ , for being analyzed by this process. It is a hybrid process in which the additional mass is calculated by reducing the frequencies of the structure by the presence of the fluid via FEM and then introduced in the analytical equation. However, it is important to clarify that the procedure indicated above was performed to prove the potential of the simplified model adopted, in capturing the coupled frequencies of the reservoir dominant, and with very good precision the 1st coupled frequency of the mode in phase, of additional mass of the structure, which is the one of interest for a previous evaluation of the designer. Therefore, it is not a matter of recommending a more complex and difficult calculation via FEM, to find the additional mass, and then inject it into the analytical model to obtain the modal frequencies and deformed of the relevant system, which would not be an adequate and rational procedure.

The additional mass is given by the following Equation:

$$\bar{m}_{ad} = \bar{m} \left[ \left( f / f^{fe} \right)^2 - 1 \right] \tag{44}$$

where  $f^{fe}$  is the numerical fluid- structure frequency.

The frequencies of additional mass (structure deformation modes) are calculated based on Equations 17, 18, 19, 20, 21 and 22, adding the additional mass portion due to the fluid per unit of beam length ( $\bar{m}_{ad}$ ) to the mass portion of the structure per unit of beam length ( $\bar{m}$ ). The fluid-structure (fe) spring (m), bending (f), shear (c) and normal (n) frequencies are, therefore, given by:

$$f_m^{fe} = (1 / 2\pi) \sqrt{k / (\bar{m} + \bar{m}_{ad})} \tag{45}$$

$$f_f^{fe} = (i^2 \pi / 2) \sqrt{EI / [(\bar{m} + \bar{m}_{ad}) L^4]} \tag{46}$$

$$f_c^{fe} = (i / 2) \sqrt{KGA / [(\bar{m} + \bar{m}_{ad}) L^2]} \tag{47}$$

$$f_n^{fe} = (i / 2) \sqrt{EA / [(\bar{m} + \bar{m}_{ad}) L^2]} \tag{48}$$

## 4 RESULTS AND DISCUSSIONS

### 4.1 Description of the model and resulting actions

The results presented in this article are the outcome of a case study little addressed and explored in the technical literature: the problem of the dynamic behavior of a navigation lock in free and forced vibrations.

Due to the importance of the work and the rare studies found on this topic, this numerical simulation accompanied by a simplified solution is intended to provide designers with a simple way of approaching the issue.

The dimensions used in the concrete structure of the lock correspond to data from real life structures, namely: crest width, 8.00 m, base width, 34.00 m, total height, 55.00 m and height of the vertical wall in the dry part, 16.50 m. The width of the chamber is equal to 33.00 m. Figure 3a represents the left part of the lock-tank system, which is symmetrical in its dimensions.

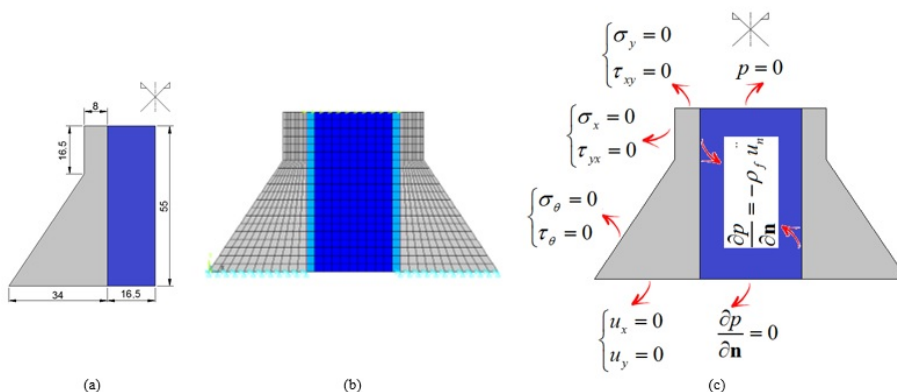


**Figure 3.** (a) Left part of the symmetrical lock-tank system. Measured in meters. (b) Model of the lock system. (c) Boundary conditions adopted in the lock model.

Numerical modeling using the finite element method (MEF) was performed using the ANSYS software. Figure 3b shows the discretized two-dimensional model of the complete system.

The physical properties adopted are: Young’s modulus  $E = 25 \text{ GPa}$ , Poisson’s ratio  $\nu = 0.25$  and specific mass  $\rho = 2400 \text{ kg/m}^3$  for gravity structures in concrete mass and speed of sound  $c = 1500 \text{ m/s}$  and specific mass  $\rho_f = 1000 \text{ kg/m}^3$ , for the fluid (water).

The boundary conditions adopted are: for the structures, clamped on the base and free on the top and dry side faces; for the cavity, closed at the base and open at the top, and the wall-chamber interface, fluid-structure condition. Figure 3c indicates the boundary conditions of the model.

The models were discretized so that the length of the elements at the edges of the structure and acoustic cavity in contacts, in general, would be 3.0 m (at the base of the gravity structures and water chamber), totaling 440 (220 + 220) PLANE182 elements for the structures and 220 FLUID29 elements for the cavity. The finite elements mentioned are from the library of the ANSYS program.

The ground movement selected for the dynamic analysis of the system was the S0E horizontal component of the ground movement recorded in El Centro, California, USA, during the earthquake verified in the Imperial Valley irrigation district, California, USA on May 18, 1940. The component of the ground movement and its peak acceleration are shown in Figure 4. The acceleration is given in g, where  $g \approx 9.81 \text{ m/s}^2$ .

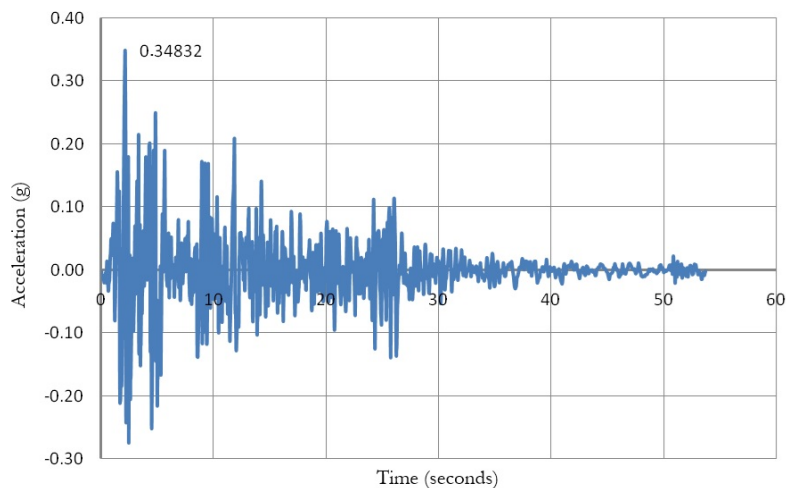


**Figure 4.** S0E component of the El Centro earthquake [22].

The natural frequencies, the free vibration modes and the time variations of the horizontal displacement at a point on the lock crest, where the maximum horizontal displacement and the envelopes of maximum normal vertical stress of tension and compression, due to the earthquake, are analyzed for the cases of empty and totally full water chamber.

In this work, for the numerical-computational structural analysis, transient dynamic analysis was used, which is a technique used to determine the dynamic response of a structure, under the action of any general time-dependent loads. Two methods of analyzing the transient response are available in ANSYS. We have applied the full method, which uses the complete matrices of the system to calculate the transient response (without matrix reduction).

## 4.2 Case studies

In this section, two cases that have similarities will be studied:

1<sup>st</sup>) Simplified lock and made comparable (modeled with the closest possible characteristics to the original lock) to a rigid-mobile structure (double-piston) of constant thickness (simplified method presented). 2<sup>nd</sup>) The Lock itself (actually modeled by the FEM).

### Case 1 - Free Vibration of the Simplified Lock (Straight Thick Beam)

To qualify the results of the free vibrations of the lock system, a preliminary analytical-numerical study (2D double-piston-cavity) was carried out, considering the following dimensions: piston height, 55.00 m; piston thickness, 17.10 m

(in order to maintain the same cross-section area as the gravity structure, 940.50 m<sup>2</sup>) and cavity width, 33.00 m. The physical properties of the materials are the same as the lock.

The spring stiffness adopted is equal to 2.1 x 10<sup>9</sup> N/m. This value was reached by applying a horizontal unit load (P = 1N) at the end of a free-standing clamped vertical Timoshenko beam, with the physical and geometric properties of the piston (Figure 5a), obtained through analytical formula for beam deflection (Equation 49) the value of its horizontal displacement (w = 4.8 x 10<sup>-10</sup> m) at that point (x = 0 m), resulting in a stiffness (K = P/w) of 2.1 x 10<sup>9</sup> N/m, so that the spring stiffness approximately represents the stiffness of the lock.

$$w(x) = P(L-x)/(KAG) - Px/(2EI)(L^2 - x^3/3) + PL^3/(3EI) \tag{49}$$

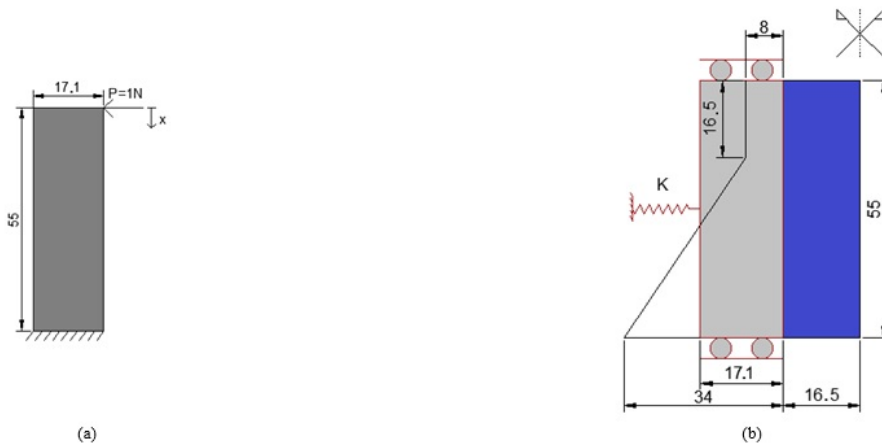


**Figure 5.** (a) Timoshenko beam clamped-free of unitary width, with its dimensions in meters. (b) Left part of the 2D double-piston-acoustic cavity system superimposed on the left part of the lock-tank system, with its dimensions. Both systems are symmetrical. Measured in meters.

Figure 5b shows the left part of the 2D double-piston-acoustic cavity system superimposing the left part of the lock-tank system, with its dimensions, both systems being symmetrical.

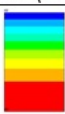
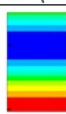
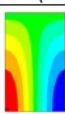
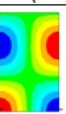
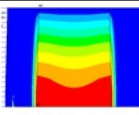
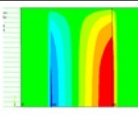
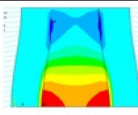
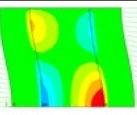
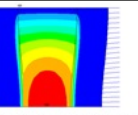
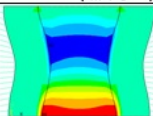
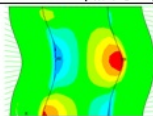
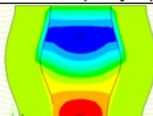
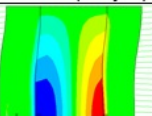
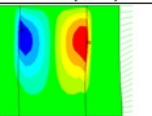
Figure 6 shows the first five modes of vibration of the uncoupled structure (a), of the uncoupled cavity (b) and the first ten modes of the 2D coupled double-piston-cavity system (c). The numerical and analytical results of the natural frequencies are presented, in Hz, the percentage difference between the analytical and numerical values in relation to the analytical values and the numerical modes of vibration obtained by the FEM via ANSYS, where i and j represent the modal indices, the sub-indices m, f, c and n mean spring, bending, shearing and normal, respectively, MA, additional mass, RA, additional stiffness, DE, dominant structure, DC, dominant cavity, F, phase and OF, opposed phase. The analysis by the MEF of the simplified system is carried out in order to compare these results with the analytical results obtained by the presented formulas.

Analyzing these results, there is good match between the analytical and numerical results with maximum differences of 2.31% for the third uncoupled structural mode, 0.65% for the fifth uncoupled fluid mode and 8.54% for the fifth coupled fluid-structure mode.

In the coupled case, among the presented modes that have analytical solution, mode 2 is the first mode, in phase (F), of the pistons (additional mass effect with fluid incompressibility ( $\lambda_{numeric} = 0.58$ )), and the mode 5 is the first cavity domain and structure in opposed phase (OP) mode. Once the simplified analytical formulation has been validated, with the numerical model for these modes, it is possible to show the other modes (1, 3, 4, 6, 7 and 10) obtained by ANSYS to complement the sequence.

From the numerical values, it is observed that the coupled modes 1 and 2 are fundamental modes of additional mass with the incompressible fluid ( $\lambda = 0.39$  and  $0.58$ ), at opposed phase (OF) and phase (F), reducing the first uncoupled frequency of the structure by 42.2% and 13.9%, respectively. Coupled modes 3 and 4 are modes of additional mass, dominant of the structure and compressible fluid ( $\lambda = 1.01$  and  $1.09$ ), at opposed phase (OF) and phase (F) reducing the second uncoupled frequency of the structure by 16.6% and 9.84%, respectively. Mode 5 is an additional stiffness mode,

caused by a certain compressibility of the fluid. It is a dominant mode of the cavity and the structure is opposed phase (OF), raising the first uncoupled frequency of the cavity by 72.1%. Coupled modes 6 and 7 are modes of additional mass, dominant of the structure and compressible fluid ( $\lambda = 2.73$  and  $2.97$ ), at opposed phase (OF) and phase (F), reducing the third uncoupled frequency by 16.7% and 9.32%, respectively. Mode 8 is an additional stiffness mode, caused by the compressibility of the fluid. It is a dominant mode of the cavity and the structure is opposed phase (OF), raising the second uncoupled frequency of the cavity by 17.2%. Mode 9 is an additional stiffness mode, dominant cavity, with the structure in phase (F) following the deformed modes of the fluid, raising the third uncoupled frequency of the cavity by 10.6%. Coupled mode 10 is an additional mass mode, dominant of the structure and compressible fluid ( $\lambda = 4.04$ ), normal, reducing the fourth uncoupled frequency of the structure by 0.29%.

(a)	Mode 1 ( $i_m = 0$ )	Mode 2 ( $i_{m+f+c} = 1$ )	Mode 3 ( $i_{m+f+c} = 2$ )	Mode 4 ( $i_n = 1$ )	Mode 5 ( $i_{m+f+c} = 3$ )
					
(b)	Mode 1 ( $i=0, j=1$ )	Mode 2 ( $i=0, j=3$ )	Mode 3 ( $i=1, j=1$ )	Mode 4 ( $i=1, j=3$ )	Mode 5 ( $i=0, j=5$ )
					
(c)	Mode 1 ( $i_m=0$ )	Mode 2 ( $i_m=0$ )	Mode 3 ( $i_{m+f+c}=1$ )	Mode 4 ( $i_{m+f+c}=1$ )	Mode 5 ( $i=0, j=1$ )
					
	N: 2.79 Hz (MA/OF) $\bar{A}$ : 2.80 Hz D: 0.49% $\lambda = 0.39$	N: 4.16 Hz (MA/F) A: 4.10 Hz D: 1.46% $\lambda = 0.58$	N: 7.29 Hz (DE/MA-OF) $\bar{A}$ : 6.81 Hz D: 7.05% $\lambda = 1.01$	N: 7.88 Hz (DE/MA-F) $\bar{A}$ : 7.91 Hz D: 0.38% $\lambda = 1.09$	N: 11.74 Hz (DC/OF) A: 11.01 Hz D: 8.54% $\lambda = 1.62$
	Mode 6 ( $i_{m+f+c}=2$ )	Mode 7 ( $i_{m+f+c}=2$ )	Mode 8 ( $i=0, j=3$ )	Mode 9 ( $i=1, j=1$ )	Mode 10 ( $i_n=1$ )
					
N: 19.74 Hz (DE/MA-OF) $\bar{A}$ : 20.00 Hz D: 1.30% $\lambda = 2.73$	N: 21.49 Hz (DE/MA-F) $\bar{A}$ : 21.96 Hz D: 2.14% $\lambda = 2.97$	N: 24.02 Hz (DC/OF) A: 22.20 Hz D: 8.20% $\lambda = 3.32$	N: 26.32 Hz (DC/F) A: 26.81 Hz D: 1.83% $\lambda = 3.64$	N: 29.22 Hz (DE) $\bar{A}$ : 29.26 Hz D: 0.14% $\lambda = 4.04$	

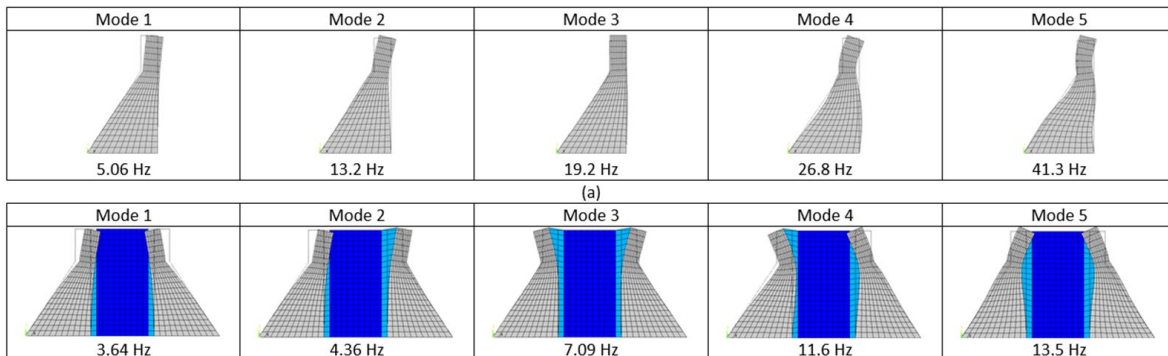
**Figure 6.** Natural numerical (N) and analytical (A) frequencies, in Hz, the percentage difference between the values (D) and the corresponding vibration modes of the 2D acoustic cavity piston case: (a) uncoupled structural system, (b) uncoupled fluid system and (c) coupled fluid-structure system.  $\lambda$  is the compressibility parameter.  $\bar{A}$  is the coupled frequency obtained by the hybrid process.

As it can be seen in these results, the simplified analytical model can predict all the dominant cavity coupled modes (with additional stiffness and fluid compressibility - modes 5, 8 and 9) regardless of the deformed mode of the structure, which in these cases accompanies the deformed mode of the fluid. To make the explanations clearer, dominant modes (structure or cavity), are the modes of the media (solid and/or fluid) that control (dominate) the response, and the other medium adapts, fits, follows the deformed mode that predominates in the process. The coupled deformed modes corresponding to the simplified analytical formulation are not presented in this article but can be found in Pedroso [16], apud Souza [18].

Figure 6c depicts a greater number of coupled modes than in uncoupled cases (a) and (b), to show the effectiveness of the simplified formulation in predicting the coupled modes of the cavity (5, 8, 9) for additional stiffness. These dominant cavity modes reproduce the uncoupled cavity modes at a larger frequency ( $f_1^{des} \rightarrow f_5^{acop}$ ,  $f_2^{des} \rightarrow f_8^{acop}$ ,  $f_3^{des} \rightarrow f_9^{acop}$ ). In this figure, the match between the uncoupled and coupled modal form can be seen, a fact that makes it possible to highlight the modal form mobilized by the structure in the coupled problem.

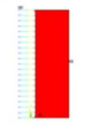
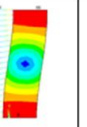
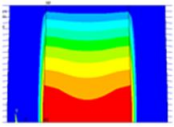
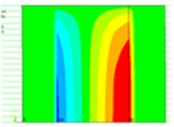
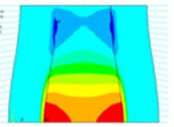
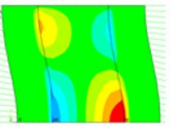
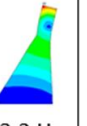
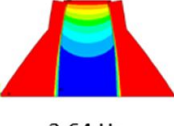
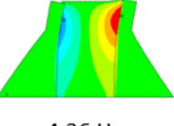
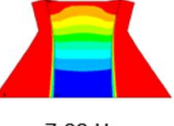
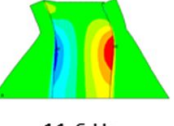
**Case 2 - Free Vibrations of the Lock**

Figure 7 shows the first five modes of vibration in this case. The numerical results of natural frequencies, in Hz, and the numerical modes of vibration obtained by the MEF via ANSYS are presented.



**Figure 7.** Vibration modes of the lock: (a) uncoupled structural system (left structure) and (b) coupled fluid-structure system.

Figure 8 shows a view with the first two modes of vibration of the double-piston system compared to those of the real life lock for the uncoupled structural case and the first four modes of vibration of the double-piston-acoustic cavity system compared with those of the lock-tank for the coupled fluid-structure case. The natural frequencies, in Hz, and the numerical modes of vibration obtained by the FEM via ANSYS are presented.

System	Structure		Fluid -Structure			
	Mode 1	Mode 2	Mode 1	Mode 2	Mode 3	Mode 4
Piston	 5.57 Hz	 9.15 Hz	 3.14 Hz	 4.78 Hz	 7.65 Hz	 8.24 Hz
Lock	 5.06 Hz	 13.2 Hz	 3.64 Hz	 4.36 Hz	 7.09 Hz	 11.6 Hz

**Figure 8.** Natural frequencies, in Hz, and numerical vibration modes of the Piston compared to the lock.

The analytical study of the 2D double-piston-acoustic cavity system is done to show the relevance of the simplified model. Although a closed analytical formulation for the frequencies and modal deformations of the lock-tank system has not been presented, it is possible “as an approximation” (preliminary assessment), to use the 2D double-piston-acoustic cavity model. As it is a simplified and easy to apply model, it cannot be expected that it reproduces with great precision the numerical results obtained with a sophisticated program based on FEM. However, for the first frequencies (in particular the 1<sup>st</sup> one, the most important for this problem category), the simplified model presents results within the

magnitude of 10%, which is one of the characteristics expected for a quick assessment on practical design problems in engineering, especially when a preliminary estimate of the case is sought. Thus, the methodology developed here becomes applicable to a preliminary study of the tank-lock problem.

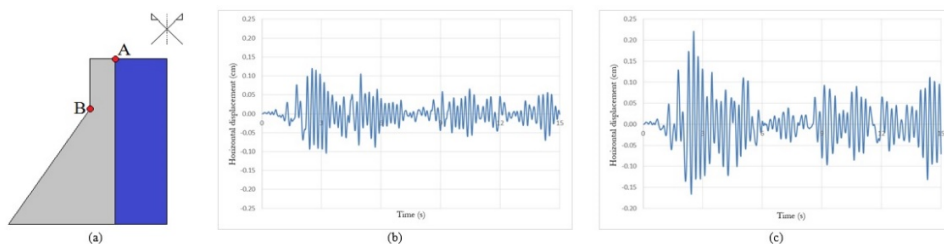
Further analyzing the presented results, it is observed that the natural frequencies and the modes of vibration of the simplified model present good correlation with those obtained for the real life lock, concluding, therefore, that the two studied models do match.

### Case 3 - Forced Excitation (Seismic) of the Lock

In this section, the dynamic response of the lock to a seismic request will be studied. In this case, the El Centro earthquake (component SOE) was adopted.

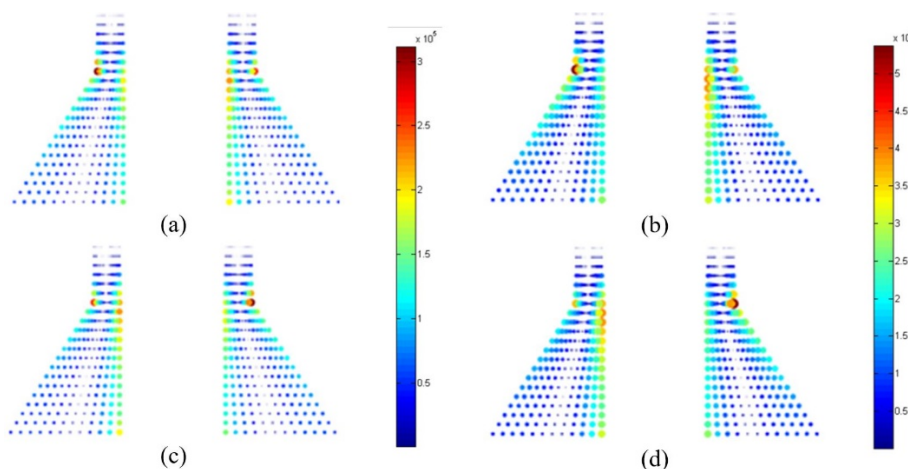
For the calculation of the parameters that relate frequencies to the damping rates, in the analysis in forced vibration with seismic load,  $\zeta = 5\%$  was considered for  $\omega_1 = 31.80$  rad/s and  $\omega_2 = 82.94$  rad/s (1<sup>st</sup> and 2<sup>nd</sup> modes), resulting in Rayleigh's damping constants,  $\alpha = 2.30$  and  $\beta = 8.72 \times 10^{-4}$ , for the uncoupled structural case and also  $\zeta = 5\%$  for  $\omega_1 = 22.87$  rad/s and  $\omega_2 = 27.39$  rad/s (1<sup>st</sup> and 2<sup>nd</sup> modes), resulting in Rayleigh's damping constants,  $\alpha = 1.25$  and  $\beta = 1.99 \times 10^{-3}$ , for the coupled fluid-structure case.

Figure 9a shows the points chosen for observing responses in the seismic analysis of the lock. Figure 9b shows the relative horizontal displacement in time of the upper extreme point of the left side of the inner (wet) wall (Point A of Figure 9a) of the lock, for the uncoupled (a) and coupled (b) problem.



**Figure 9.** (a) Chosen points for the responses in the seismic analysis of the lock. Horizontal displacement in time (in cm) of the upper extreme point of the wall on the inner side of the left gravity structure of the lock (Point A) for the (b) uncoupled structural and (c) coupled fluid-structure cases.

Figure 10 show the envelopes of the maximum vertical tension and compression normal stresses in the lock structures, respectively, for the uncoupled (a) and coupled (b) case. The diameters of the circles represent the magnitude of the stresses, the values of which can be taken from the color palettes (vertical scale) also shown in the figures.



**Figure 10.** The envelope of the maximum normal vertical stresses of tension (a, b) and compression (c, d) in the gravity structures of the lock for the (a, c) uncoupled structural and (b, d) coupled fluid-structure cases, in Pa.

The maximum horizontal displacement at the upper point of the wet side of the lock gravity structure (Point A) in Figure 9 was 0.12 cm for the uncoupled structural case and 0.22 cm for the fluid-structure coupled case, as shown in Figure 9b. For the design of gravity structures, the magnitude of normal stresses in the vertical direction will be critical. The maximum value of the normal tension and compression stresses was 311.65 kPa for the uncoupled structural case and 537.13 kPa for the coupled fluid-structure case, both in the transition between the vertical and inclined outer (dry) sides of the concrete structures of the lock (Point B) of Figure 9a, as shown in Figure 10. The fluid-structure coupled case presents a displacement, 84.8%, and stresses, 72.4% greater than the uncoupled structural case. Thus, a significant increase in responses to the earthquake is observed when the lock water chamber is completely full; this aspect emphasizes the importance of taking into account the coupled calculation when assessing the dynamic response in this type of problems.

The apparently significant tension stress values for a concrete mass structure need to be relativized due to some aspects, such as load combination and the weighting coefficients to consider, the probabilistic nature of earthquakes, among others. In any case, the values obtained in this preliminary analysis would be lower than the design values used in such a structure.

## 5 CONCLUSIONS AND PERSPECTIVES

This work aimed to perform a preliminary dynamic analysis (uncoupled and coupled) of a lock subjected to a reference earthquake (El Centro earthquake). The studies were done with numerical modeling by FEM from results obtained via ANSYS. In addition, the use of a simplified model (2D double-piston-cavity) was proposed, which presents an analytical solution to address the coupled lock-tank problem in its first natural frequencies.

In numerical analysis, the verification and validation of a problem could be described as processes that develop and present evidence of the accuracy of the results. To measure accuracy, accurate reference values are required. Within this perspective, it should be noted that a critical element in certain cases is the precision estimate when no reference value is available. Thus, simplified models, such as the one presented here, contribute significantly so that the designer has, in principle, the magnitude of the expected results. It has been shown that the 2D double-piston-cavity model consistently targets the results of the lock-tank system. To do this, the height of the pistons must be set equal to the height of the lock; the thickness of the pistons has to be determined in order to maintain the same cross-section area of the gravity structures and the width of the cavity equal to the width of the chamber. Of course, the physical properties of the materials must be the same as those of the lock. The determination of the spring stiffness was obtained by applying a horizontal unit load to the free end of a free-clamped beam, obtaining the value of its horizontal displacement at that point by using the analytical Timoshenko beam displacement formula, thereby calculating the stiffness of the relevant structure.

As for the forced excitation, the response results presented were: the variations in the time of the horizontal displacement at the point of the crest of the structure where the maximum horizontal displacement occurred and the maximum stress envelopes, due to the earthquake, for the cases of the empty completely and completely full of water. It was concluded that the maximum horizontal displacement occurs at the upper point of the wet side of the lock structure, and for the coupled fluid-structure case the displacement was 83.3% greater than for the uncoupled structural case. For the design of gravity structures, the magnitude of normal stresses in the vertical direction will be critical. The maximum value of normal tension and compression stresses occurs at the transition between the vertical and inclined walls of the outer (dry) side of the concrete structures of the lock (known as the bottleneck), and for the coupled fluid-structure case, the stress was 72.4% higher than for the uncoupled structural case. The results highlight the importance of considering fluid-structure coupling when analyzing this type of problems.

The relevance of this study lies in the fact that it highlights the influence of aspects of fluid-structure interactions on the dynamic behavior of a gravity structure system - water chamber subjected to an earthquake, thus contributing to an expansion of the limited bibliography available on this theme, and for the development of an appropriate methodology that provides technical support for the practice of safe and reliable projects.

Continuing this work, it is still possible to consider the interaction across the 3 media: structures (lock)-tank-foundation, considering in the modeling of the latter its inertia, damping and flexibility, an aspect that leads to a complex problem of wave propagation in unlimited domains, with reflection in the boundary.

As for the analytical solutions for the relevant case and which translate the additional masses associated with the modes of deformation of the dominant modes of the structure, these can be obtained through solving the wave equation with flexible boundaries that represent the appropriate modes of the vibrant structure in a fluid medium.

## ACKNOWLEDGEMENTS

The authors thank CNPq for supporting this research.

## REFERENCES

- [1] J. H. Ables Jr., *Filling and Emptying System for Bay Springs Lock, Tennessee-Tombigbee Waterway, Mississippi. Technical Report h-78-19*. Vicksburg, Miss.: US Army Corps of Engineers Waterways Experimental Station, 1978.
- [2] P. Novak and J. Cábalka, *Models in Hydraulic Engineering – Physical Principles and Design Application*. London: Pitman, 1981.
- [3] M. G. G. Ming, "Seismic response analysis of sluice taking into consideration of structure-soil interaction," *Hydro-Science and Engineering*, vol. 3, pp. 297–306, 1991.
- [4] P. Novak, "Inland waterways," in *Kempe's Engineering Yearbook*, C. Sharpe, Ed., Tonbridge: Benn, 1994, ch. L2.
- [5] L. Trentini, G. S. Corrêa, J. G. Ferrer, and L. M. Bezerra, "Sistema de transposição de desnível de Tucuruí Eclusa 1 – Análise em elementos finitos da cabeça de jusante – Bloco 9," in *XXIV Sem. Nac. Grandes Barragens. Tema 3 – Projeto e Construção*, 2003.
- [6] Y. Lin and L. Yong-he, "Analysis of sluice vibration based on the frame structure," *J. Shanghai Univ.*, vol. 10, no. 1, pp. 96–97, 2004.
- [7] P. Novak, A. I. B. Moffat, C. Nalluri, and R. Narayanan, *Hydraulic Structures*, 4th ed. New York: Taylor & Francis, 2007.
- [8] P. Novak, V. Guinot, A. Jeffrey, and D. E. Reeve, *Hydraulic Modelling - An Introduction: Principles, Methods and Applications*, 1st ed. Baton Rouge: CRC Press, 2010.
- [9] H. Xiao, "Investigation and analysis of sluice damage by earthquake," *Water Power*, 2009.
- [10] G. Maltidis, *Seismic Soil Structure Interaction of Navigation Locks*. Karlsruhe: Karlsruher Institut für Technologie, 2017.
- [11] F. F. Oliveira, "Análise de tensões e estabilidade global de barragens de gravidade de concreto," M.S. thesis, Dep. Eng. Civ. Amb., Univ. Brasília, Brasília, 2002.
- [12] P. M. V. Ribeiro, "Uma metodologia analítica para a avaliação do campo de tensões em barragens gravidade de concreto durante terremotos," M.S. thesis, Dep. Eng. Civ. Amb., Univ. Brasília, Brasília, 2006.
- [13] S. F. Silva, "Interação dinâmica barragem-reservatório: modelos analíticos e numéricos," Ph.D. dissertation, Dep. Eng. Civ. Amb., Univ. Brasília, Brasília, 2007.
- [14] C. A. E. Melo, "Estudo do acoplamento comporta-reservatório sob ações sísmicas," M.S. thesis, Dep. Eng. Civ. Amb., Univ. Brasília, Brasília, 2009.
- [15] L. J. Pedroso, "Método da matriz de transferência e suas aplicações em problemas acústicos de interação fluido-estrutura," in *Notas de Curso e Apostila Didática*. Brasília: UnB-FT/ENC, 1992.
- [16] L. J. Pedroso, "Interação fluido-estrutura," in *Notas de Curso e Apostila Didática*. Brasília: UnB-FT/ENC, 2003, Vs.3.
- [17] L. C. Sousa Jr., "Uma aplicação dos métodos dos elementos finitos e diferenças finitas à interação fluido-estrutura," M.S. thesis, Dep. Eng. Civ. Amb., Univ. Brasília, Brasília, 2006.
- [18] S. M. Souza, "Contribuição para uma metodologia de análise acoplada fluido-estrutura para cavidades acústicas de paredes flexíveis," M.S. thesis, Dep. Eng. Civ. Amb., Univ. Brasília, Brasília, 2007.
- [19] P. M. V. Ribeiro, "Soluções analíticas para cavidades acústicas bidimensionais com aplicação ao estudo de problemas de interação dinâmica barragem-reservatório," Ph.D. dissertation, Dep. Eng. Civ. Amb., Univ. Brasília, Brasília, 2010.
- [20] C. Intartaglia, L. Soria, and M. Porfiri, "Hydrodynamic coupling of two sharp-edged beams vibrating in a viscous fluid," *Proc. R. Soc. A*, vol. 470, pp. 20130397, 2014, <http://dx.doi.org/10.1098/rspa.2013.0397>.
- [21] M. Rezaiee-Pajand, S. A. Aftabi, and M. S. Kazemiyan, "Analytical solution for free vibration of flexible 2D rectangular tanks," *Ocean Eng.*, vol. 122, pp. 118–135, 2016.
- [22] A. K. Chopra, *Dynamics of Structures – Theory and Applications to Earthquake Engineering*. Berkeley: Univ. California, 1995.

---

**Author contributions:** LJP: conceptualization, formal analysis, methodology, supervision; PMVR: supervision.

**Editors:** Osvaldo Luís Manzoli, José Luiz Antunes de Oliveira e Sousa, Guilherme Aris Parsekian.



ORIGINAL ARTICLE

## Second-order torsion effects in concrete buildings

*Efeitos de torção de segunda-ordem em edifícios de concreto*

Rodrigo Bezerra Andrade<sup>a</sup> Petrus Gorgônio Bulhões da Nóbrega<sup>a</sup>

<sup>a</sup> Universidade Federal do Rio Grande do Norte – UFRN, Centro de Tecnologia, Campus Universitário, Lagoa Nova, Natal, RN, Brasil

Received 22 March 2019

Accepted 25 May 2020

**Abstract:** The internal forces due to torsion in global analysis of buildings, and its second-order effects, usually are not properly considered in structural design or even in design code's prescriptions. Although the  $\gamma_z$  coefficient, which is used to the evaluation of global second-order effects, has a wide, useful and consolidated application, it is true that specific torsional aspects are not well considered by it. This paper discusses the little-known  $\gamma_\theta$  coefficient, an analogous proposition to the  $\gamma_z$  coefficient, but focused specifically on the consideration of torsional effects. After the discussion on the concepts and the design methodology, several buildings are evaluated and their displacements and the coefficients  $\gamma_z$  and  $\gamma_\theta$  are calculated. Comparing these parameters, and also the results obtained by the P- $\Delta$  method, it is demonstrated the importance and the reliability of the  $\gamma_\theta$  coefficient.

**Keywords:** torsion, second-order effect, global analysis.

**Resumo:** Os esforços torcionais na análise global de edifícios, e seus respectivos efeitos de segunda-ordem, usualmente não são adequadamente considerados, seja na prática de projetos ou mesmo nas prescrições normativas. Embora o coeficiente  $\gamma_z$  de avaliação dos esforços globais de segunda-ordem tenha uma larga, útil e consolidada aplicação, é fato que os aspectos específicos de torção não são bem representados por este parâmetro. Este artigo discute o pouco difundido coeficiente  $\gamma_\theta$ , proposta análoga ao  $\gamma_z$ , voltado especificamente para a consideração dos efeitos rotacionais. Após a discussão dos conceitos e da metodologia de cálculo, diversos edifícios são avaliados, calculando-se seus deslocamentos e os parâmetros  $\gamma_z$  e  $\gamma_\theta$ , comparando-os entre si e com os resultados obtidos pelo método P- $\Delta$ , demonstrando, dessa forma, a importância e a confiabilidade do coeficiente  $\gamma_\theta$ .

**Palavras-chave:** torção, efeito de segunda-ordem, análise global.

**How to cite:** R. B. Andrade, and P. G. B. Nóbrega, "Second-order torsion effects in concrete buildings", *Rev. IBRACON Estrut. Mater.*, vol. 14, no. 1, e14105, 2020, <https://doi.org/10.1590/S1983-41952021000100005>

### 1 INTRODUCTION

The classical structural analysis, as generally used in civil engineering applications, considers the first-order effects to simplify its evaluation. Based on this assumption, the analysis of the structure occurs at its original configuration (Fusco and Onishi [1]). However, it is evident that the structural element's deformation cause new internal forces, the so-called second-order effects. These are unavoidable, and for slender structures they should not be neglected, that is, the structure's final configuration should not be regarded as the same as its initial configuration (Wight and MacGregor [2]).

Kimura [3] affirms that the global stability of a structure is inversely proportional to its sensitivity to second-order effects. Obviously, in many usual concrete-made buildings with relatively small height and beam spans, the second-order effects tends to be insignificant when compared with those of first-order. In such cases, they may be neglected.

In tall concrete buildings, typical second-order effects essentially derive from the horizontal actions, especially wind and earthquakes. Furthermore, the geometrical imperfections result in two types of second-order effects: the local and

Corresponding author: Petrus Nóbrega. E-mail: [petrus@ufrn.edu.br](mailto:petrus@ufrn.edu.br)

Financial support: None.

Conflict of interest: Nothing to declare.



This is an Open Access article distributed under the terms of the Creative Commons Attribution License, which permits unrestricted use, distribution, and reproduction in any medium, provided the original work is properly cited.

the global ones. Local effect refers to a specific structural element which presents a geometric deviation (columns, essentially), and the global effect concerns to the whole structure out-of-plumbness.

It is important to notice that other factors, besides horizontal actions, may give rise to the second-order effects. Vertical actions are also capable of causing horizontal displacements in some cases, such as: (a) when buildings are non-symmetrical, either by geometry or stiffness distribution (irregular placement of columns in the horizontal plane and/or asymmetrical shear walls); (b) when there are non-symmetrical elements acting as cantilevers at one side of the building (which impose unilateral displacements); or (c) when there are floating columns or columns with a great cross-section change, which also modifies the whole system's stiffness (Moncayo [4]). All these cases may present relevant horizontal displacements and, consequently, second-order effects.

The importance of the global second-order effects in tall concrete buildings can be determined by the use of the  $\gamma_Z$  coefficient, whose design procedure is already established in ABNT NBR 6118:2014 prescriptions [5]. This is a dimensionless term, developed and originally presented in English by the celebrated Brazilian engineers Franco and Vasconcelos [6]. Its first version in Portuguese was published several years later (Franco and Vasconcelos [7]). This coefficient, of admirable simplicity and representativeness, is widely spread and consolidated in literature, and it is a function of the building's fundamental characteristics, such as height, stiffness and internal forces amplitude, being used to determine approximately the magnitude of global second-order effects.

The  $\gamma_Z$  coefficient is absolutely useful as an indicator of instability, as it is especially practical to obtain and to use. However, as a simplified parameter, it may present a variable accuracy in its representation of the global second-order effects when compared to results obtained by applying more rigorous and precise methods.

In the last few years, some studies have compared the  $\gamma_Z$  coefficient with other variables that were idealized for the same purpose. Vieira et al. [8] verify the  $\gamma_Z$  efficacy as a global stability parameter, relating it to the critical global buckling load factor ( $\lambda$ ) and its respective critical instabilities modes. Generally, satisfactory results were obtained, but the  $\gamma_Z$  coefficient inefficacy becomes clear when the critical mode is a torsional configuration.

Following another idea, Mamone et al. [9] define a  $\chi_t$  parameter, based on the natural vibration period and on the geometrical characteristics of the building, which is used as an indicator of susceptibility to second-order effects and as a factor of amplification of first-order moments in the structure, in the same way as the  $\gamma_Z$  coefficient. Reis et al. [10] expand and modify Mamone et al. [9] work, using the denomination  $\chi_T$  for the amplification parameter proposed to substitute the  $\gamma_Z$  coefficient.

Leitão et al. [11] follow the development of the  $\chi_T$  parameter, focusing specially in structures with geometric asymmetry and with vibration fundamental mode of torsional shape. The results of the simplified analysis are compared with those obtained through non-linear numerical analysis considering the P- $\Delta$  effect.

Recently, Cunha et al. [12] proposed a new simplified parameter ( $\zeta_g$ ) in order to consider the global second-order effects, based on the Galerkin Method, and with the same application of the  $\gamma_Z$  coefficient.

Clearly, the  $\gamma_Z$  coefficient considers essentially the second-order effects due to the building flexure behavior, which result in translation of its floors. However, it is known that, besides the translational displacements, the building is also subjected to rotational effects, generated by factors such as asymmetrical horizontal forces acting on its sides, the unavoidable misalignment between the center of loadings and the center of stiffness of the structure, among others. Such rotational displacements are also capable of producing second-order effects, which are not completely encompassed by the  $\gamma_Z$  coefficient.

An alternative for the consideration of the torsional global second-order effects, in a simplified and efficient manner, was proposed by Franco [13], [14]: the  $\gamma_\theta$  coefficient. This is a parameter analogous to the  $\gamma_Z$  coefficient, but specifically used to measure the global second-order effects caused by rotational displacements of the building. It is surprising that, despite the elapsed time since it was originally proposed, this parameter is still relatively unknown, especially when considering its potential application. There is no related study that has researched the  $\gamma_\theta$  coefficient, whether in technical literature or in design standards, besides the two already mentioned papers written by Mario Franco, one of the geniuses behind the  $\gamma_Z$  coefficient, who recently passed away on September 2019.

The main purpose of this paper is to rescue and to divulgate this important contribution of a simplified formulation whose features are the precision and the reliability. After the discussion on the concepts and the design methodology, several regular and irregular buildings are evaluated. Their displacements,  $\gamma_Z$  and  $\gamma_\theta$  coefficients are calculated, and the results are compared to each other and to those obtained from the P- $\Delta$  method.

In Franco's own words [14], structural engineers take a concerned look to ensure, in two orthogonal directions, the required strength and flexural stiffness to the building. However, not always these panels provide the necessary torsional stiffness. Evidently, such cases should be investigated with the same rigor as commonly applied in flexural analysis.

## 2 EXPRESSIONS FOR $\gamma_z$ AND $\gamma_\theta$ , CONCEPTS AND CORRELATION

### 2.1 $\gamma_z$ coefficient

As already mentioned, the  $\gamma_z$  coefficient is used for the evaluation of global second-order effects in tall buildings, and it represents the ratio between final internal forces in the structure and those obtained in a first-order linear analysis. This relation can be used as an amplification factor to the first-order effects to obtain the final results.

This term was developed by Franco and Vasconcelos [6], [7] considering that, in successive iterations of the second-order analysis, the proportion between forces is constant, that is, these forces grow according to a geometric progression. Based on this premise, the coefficient is given by Equation 1:

$$\gamma_z = \frac{M_2}{M_1} = \frac{1}{1 - \frac{\Delta M_1}{M_1}} \tag{1}$$

where:

$M_1$  = Global first-order bending moment;

$M_2$  = Global total bending moment;

$\Delta M_1$  = Increment of global bending moment, due to first-order displacements.

Equation 1 is an exact numerical expression for  $M_2$  if the ratio between the incremental force  $\Delta M_1$  and the first-order force  $M_1$  is kept proportional for any of the additional forces  $\Delta M_i$  and its respective term  $\Delta M_{i-1}$  in any iteration. This is a particular property of framed structures in linear analysis (without cracking effects) where the geometric proportionality is observed between bending moments of two consecutive steps of the process.

The  $\gamma_z$  coefficient application may be illustrated in the classical problem of a cantilever beam subjected to vertical and horizontal forces, according to Figure 1. In this case, the bending moment increment  $\Delta M_1$  in the structure's base is the product of the eccentricity  $e_1$ , due to the displacement produced by the horizontal force  $V$ , and the vertical force  $P$ . The relation between  $\Delta M_1$  and  $M_1$  expresses the proportion between the increment of internal forces and the global first-order moment, as in Equation 1.

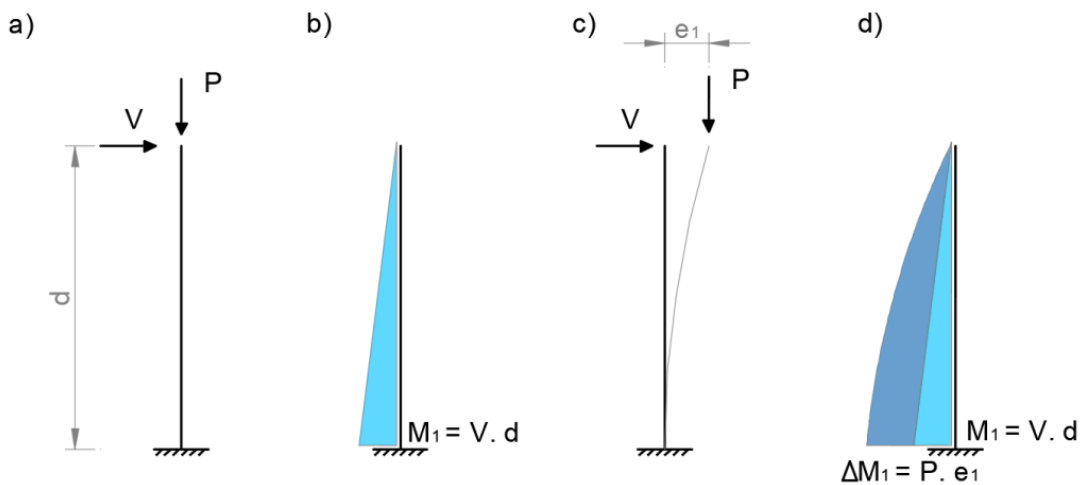


Figure 1. a) Cantilever beam. b) First-order internal forces. c) Beam displacement. d) Internal forces considering second-order effects.

### 2.2 $\gamma_\theta$ coefficient

After the development of the  $\gamma_z$  coefficient, Franco [13], [14] proposed another parameter for the precise evaluation of torsion, analogous to the  $\gamma_z$  coefficient, towards estimating the importance of the global second-order effects due to rotation of the building floors, as well as the magnitude between the first-order and the total rotation displacement of the building. This is the  $\gamma_\theta$  coefficient, given by Equation 2.

$$\gamma_\theta = \frac{\theta_{II}}{\theta_I} = \frac{I}{I - \frac{\Delta M_t}{M_{t,I}}} \tag{2}$$

where

$\theta_I$  = First-order rotation (due to torsion) of the building, around a vertical axis;

$\theta_{II}$  = Final rotation (due to torsion) of the building;

$M_{t,I}$  = Global first-order torsion moment;

$\Delta M_t$  = Increment of global torsion moment due to the first-order torsional displacements.

It is noticeable that the Equations 1 and 2 are similar, and so are the physical and mathematical concepts. An important difference, however, is that the  $\gamma_z$  coefficient may be considered as a simplified amplification factor for the internal forces (relating  $M_1$  e  $M_2$ ), while the coefficient  $\gamma_\theta$  may be a simplified amplification factor for the displacements (specifically to the rotation, relating  $\theta_I$  and  $\theta_{II}$ ).

The way  $\Delta M_t$  is calculated, however, requires a special attention. The second-order internal forces due to the rotation of the building's horizontal planes are functions of the eccentricities between the top and the bottom of each column, which are misaligned after rotation. Figure 2 illustrates one column in the situation of floor rotation.

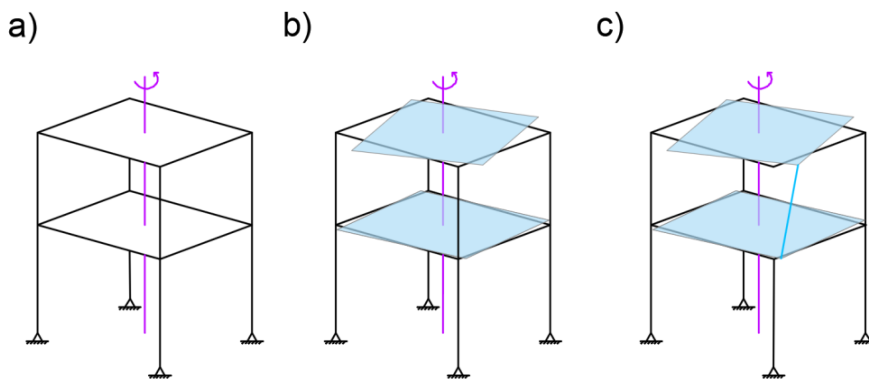


**Figure 2.** a) Torsional moment applied at a building. b) Rotation of the building's floor. c) Displacement of the highlighted column.

Considering the eccentricity and the vertical load at the ends of a column (Figure 3), it is noticeable that an incremental internal force takes place due to the floor rotation. This is the flexural moment observed through the column length and its associated second-order internal force is due to the building displacement. This internal force can also be considered as an increment of the first-order internal force.

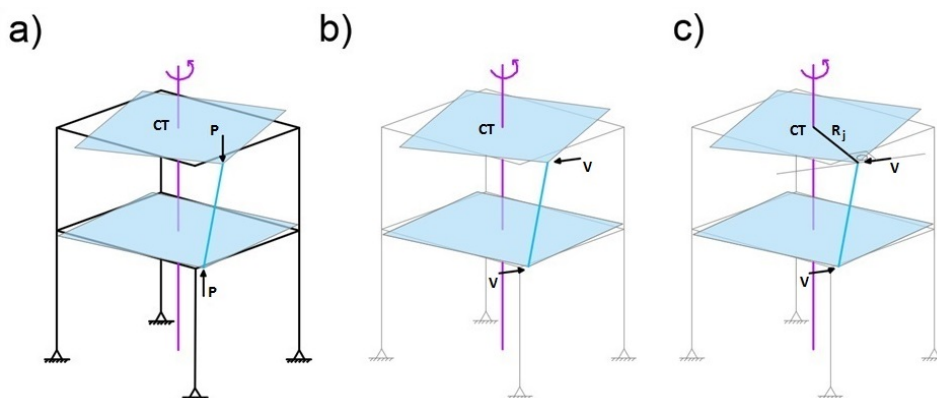


**Figure 3.** a) Eccentricity between vertical forces. b) Notional forces V. c) Distance R between the column and the CT.

For the purpose of taking in account the internal forces in all column elements, Franco [13] uses the term  $\Delta M_t$ . This is done employing the P- $\Delta$  method, when considering that the flexural moment in each column, caused by the eccentricity between vertical loads P, can be replaced by a horizontal force couple, defined as notional forces V, that causes an equal flexural moment in that element. Furthermore, for each force V, there is a term  $\Delta M_t = V \times R_j$ , where  $R_j$  is the distance between the column j position to the center of twist (CT) of the floor, as illustrated in Figure 3. The expression “center of twist”, or “twist center”, is used by Franco, differently from others authors, for example Wight and MacGregor [2], that define it as “center of rotation”. The sum of these terms, for every column, results in the total  $\Delta M_t$  of the building.

Franco [14] formulated an expression for  $\Delta M_t$  as a function of the building global characteristics, given by Equation 3.

$$\Delta M_t = \frac{\bar{P}R^2\theta_1}{H} \tag{3}$$

where:

$\bar{P}$  = Total vertical load of the building;

R = Radius of gyration of the floor masses, related to the CT of that floor;

$\theta_1$  = Global first-order rotation at the top of the building;

H = Total building height.

Equation 3 allows the calculation of the internal forces increment due to the rotation of the building as a function of its total vertical loading  $\bar{P}$ , its total height H, the R parameter, and the first-order rotation  $\theta_1$ . Employing all these variables, it is possible to obtain  $\gamma_\theta$ .

Note the term  $\theta_1$ , as defined above, is a result of the first-order structural analysis of the building. This depends not only on the torsional stiffness of each column, shear cores, shear walls, or any other structural element, but also on the interaction of these elements themselves and those in each floor of the building, in a global sense. This means that the  $\theta_1$  result reflects the structural model used.

Furthermore, it should be emphasized that the denomination “radius of gyration” was originally used by Franco [13], but should not be confused with the traditional definition of radius of gyration of a surface, which mathematically is the square root of the ratio between the inertia moment and the area of the surface. The definition used here refers to a body composed of various discrete particles (in this case, the particles are the points associated with each column in the building).

In the analytical development presented by Franco [13], the radius of gyration of the system is calculated for a given floor.  $P_j$  is the normal force in each column j, and  $R_j$  is the distance of each column to the CT of the floor, calculated by Equation 4.

$$R = \sqrt{\frac{\sum P_j \cdot R_j^2}{\sum P_j}} \tag{4}$$

The center of twist (CT) of a floor, in turn, is defined as the geometric point of the building’s floor that does not undergoes as translational movement when there is a global twisting displacement. If a horizontal force is applied at this point, there will be only translational displacement, with no rotation. If the floor is symmetrical in two orthogonal directions (regarding geometry and structural elements), it is easy to conclude that the CT will be at the geometrical center of the floor. In non-symmetrical buildings, the CT may be calculated with the stiffness of each bracing structural element, or through the interpretation of the displacements in the case of a pure torsional loading of the structure.

After determining the CT position in each floor, there could be defined a vertical twist axis, if the building is regular (that is, the building has the same story plan repeated along its height). If it is irregular (different story plans in different floors), an averaged vertical twist axis may be considered as an approximation.

The position of the CT will depend on the geometric and stiffness characteristics of the building. It may be estimated analytically, using some hypotheses as simplification, through a weighted average between the position of each element and their stiffness, in each direction, considering all bracing elements. This is sometimes done in buildings with shear walls and shear cores, ignoring the contribution from beam-columns frames (Wight e MacGregor [2]).

On the other hand, if all the aforementioned structural elements are considered, the analytical calculation of the CT position may be highly complex. Franco [14] indicates a second way to determine this point location: through the

geometric interpretation of the displacements of the building in a pure torsional loading situation. In this case, with the nodal displacements obtained by the structural analysis, it is possible to determine the geometrical point that did not present translational movement, considering the influence of all structural elements in the model. A more detailed description of this methodology, which may be regarded as more adequate than the one presented by Wight e MacGregor [2], may be found in Andrade et al. [15].

### 3 ON THE RESTRICTION USAGE OF THE $\gamma_z$ COEFFICIENT REGARDING TORSION IN BUILDINGS

The use of the  $\gamma_z$  coefficient in current Brazilian design practice is a procedure already established and guided according to ABNT NBR 6118:2014 [5]. As pointed previously, its main hypothesis is the consideration of geometrical progression among the increments of second-order forces.

According to Vasconcelos [16], this premise is valid for  $\gamma_z$  coefficient values up to 1.3. However, the author also discusses some exception cases, where such hypothesis may be only partially valid, or even not applicable. Among those situations, one is especially relevant for this study: frames submitted to torsion.

As discussed by Covas [17], the  $\gamma_z$  coefficient was originally formulated considering regular structures, that is, multi-story buildings with regular floor height, the same inertia and stiffness for columns, equal cross-section for beams, and the same boundary condition. The author also comments on the importance to design the building so that the resulting forces are aligned with the twist center, but recognize that this is not always possible. Furthermore, he additionally highlights that a precise limit to the building rotation for the admissible use of the  $\gamma_z$  coefficient might be hard to define.

It is notorious that the non-regularity cases listed before will make the  $\gamma_z$  values gradually deviate from a more accurate result. Hence, the effects due to the building rotation are not completely considered by the  $\gamma_z$  coefficient, especially if they are particularly relevant.

When there is a rotation about the vertical axis of a building, the eccentricity between the top and bottom of the structure will not be in the same direction as the external resultant force (Figure 4). This means that each column will present a different eccentricity. Vasconcelos [16] affirms prominently that, because of this rotation, it will not be possible to guarantee that a magnification factor between the first and second-order internal forces will be constant throughout the whole structure. Vieira et al. [8], as already mentioned, explicitly indicate the inefficiency of the  $\gamma_z$  coefficient when the critical instability mode has a torsional shape.

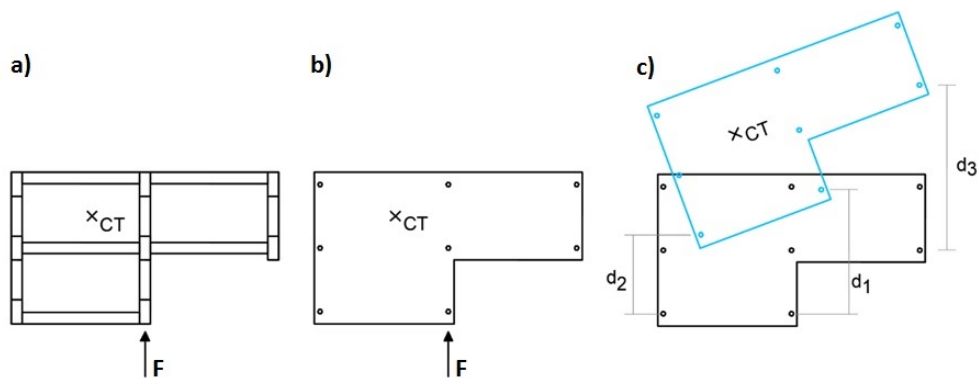


**Figure 4.** a) Force F at a building's floor with center of twist CT. b) Simplification of the building's floor. c) Structural elements presenting different eccentricities.

Finally, it should be noticed that even a symmetrical and trivial building might be subjected to torsion because the ABNT NBR 6123:1988 [18] code states the need to verify the effects due to eccentricities considering the direction of the resultant wind forces related to the geometrical axis of the building.

In addition to the discussion above, some numerical examples regarding the representation of torsional effects with the  $\gamma_z$  coefficient are presented in section 5.5 of this paper.

## 4 METHODOLOGY

### 4.1 Model description

As explained previously, the main purpose of this work is to discuss the torsional effects in concrete buildings, to evaluate the  $\gamma_\theta$  coefficient as an estimating parameter of the global second-order effects due to torsion, and to measure the sensitivity of the  $\gamma_z$  coefficient to these effects. The analyses used seven different buildings, divided in two categories:

- a) Regular buildings: five models, named Buildings 1 to 5 (Figure 5);
- b) Irregular buildings: two models, named Building 6 and 7 (Figure 6).

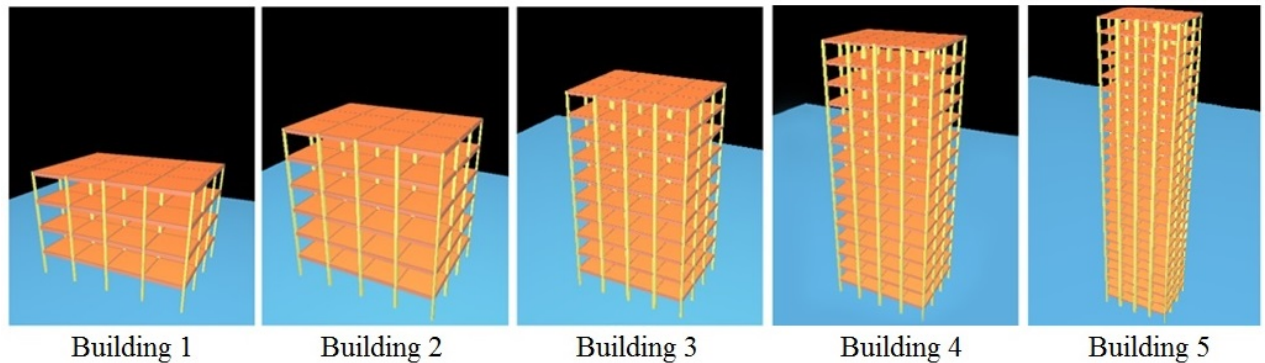


Figure 5. Regular buildings.

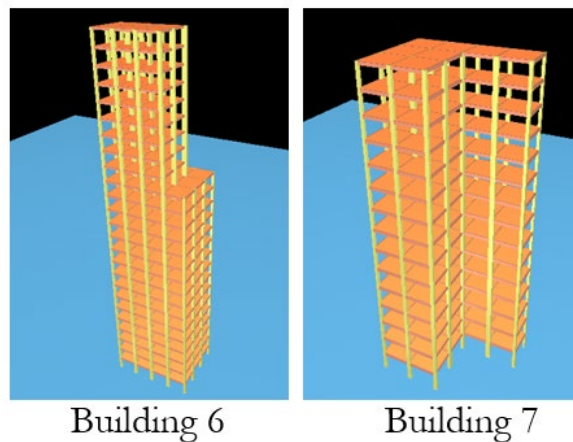


Figure 6. Irregular buildings.

The five regular buildings have similar geometry, but different height and number of stories. Each story has a rectangular shape, measuring 13 m x 17 m, with double symmetry. The story height is 3 m, beams have uniform cross-section and slabs, the same thickness. However, columns present different cross-sections according to each building total height. All structural elements present sections that are design-compatible to dead, live and wind loads. Each regular building has the following height: Building 1 has 4 stories (12 m tall); Building 2 has 6 stories (18 m tall); Building 3 has 10 stories (30 m tall); Building 4 has 15 stories (45 m tall); and the Building 5 has 25 stories (75 m tall).

The two irregular buildings, in turn, present the following characteristics: Building 6 has 25 stories (75 m tall, with a reduced story size starting at the 16<sup>th</sup> floor); and the Building 7 has 15 stories (45 m tall, with an L-shaped floor).

Initially, the final rotation obtained by the  $\gamma_\theta$  coefficient, which is a simplified approach, was compared with the final rotation obtained by the P- $\Delta$  method. The later was considered as the reference value, as it was calculated from a more precise method.

## 4.2 Remarks on the torsional load

All the five regular building models were submitted to two distinct torsional loading cases, simultaneously to the usual dead and live loads (Figure 7): (a) Distributed torsional force couples (applied to each floor); and (b) Single torsional force couple (applied at the top).

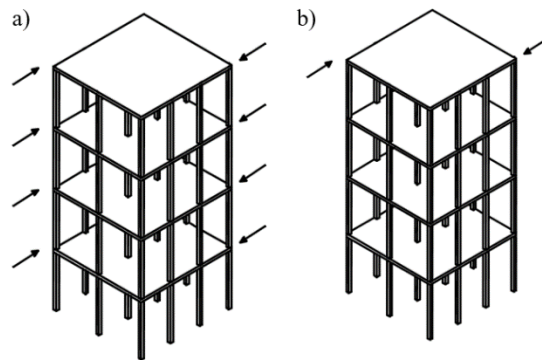


Figure 7. a) Distributed torsion couples. b) Single torsion couple.

The structural analysis considering the first torsional loading situation (distributed couples) will henceforth be referred as first analysis, and the second torsional loading type will be referred as second analysis.

An important remark is that second-order effects are tightly connected to the structure's nodal displacements, which are different according to the torsional loading condition. A single torsional moment (or, equivalently, a couple) applied at the top floor is more consistent with the hypothesis of proportional increments of internal forces (as already discussed in the context of the  $\gamma_z$  coefficient). However, this was not the procedure followed by Franco [13], [14], that applied distributed couples.

Because of that, it is proposed the investigation of how the change in couples' distribution and the consequent displacement of the building will affect the  $\gamma_0$  coefficient. Furthermore, by observing the changes in the frame's structure at the façade of the building studied by Franco [14], it seems that as the frame's displacement modifies, so does the error (the difference between the  $\gamma_0$  coefficient and the P- $\Delta$  method results), even if only slightly.

Consequently, this observation has inspired the investigation of how the models would respond to a change in its displacement because of the different torsional loading applied. Thus, all regular buildings were analyzed twice, by changing the acting torsional couple.

## 4.3 Software used

The CAD/TQS software package, which is widely known and utilized by professional offices in Brazil, was used in this work and presents many computational modules for different steps of structural design (modeling, analysis, detailing and BIM). However, its use in this study was restricted to the structural analysis. It is fact that several other structural analysis softwares might have been used, especially those based on Finite Element Method, but CAD/TQS was chosen due to its reliability and ease of use when dealing with concrete framed buildings.

It should be observed that the  $\gamma_z$  coefficient determination is an automated process in CAD/TQS, which is not the case for the  $\gamma_0$  coefficient. In fact, no structural analysis software contains such feature, and all the necessary calculation presented on this work was done through the evaluation of the analysis output results and subsequent manual treatment of the necessary values. The process, although arduous, is relatively simple, and may be easily automated. Andrade et al. [15] describe this process in detail.

Others important aspects were subjected to complementary investigations, such as the displacement profile of the buildings, and the sensitivity of the  $\gamma_z$  coefficient to the torsional couple distribution. The following section presents and discusses the results.

## 5 RESULTS AND COMMENTS

### 5.1 $\gamma_\theta$ coefficient evaluation of regular buildings

The  $\gamma_\theta$  coefficient was calculated for each regular building (Models 1 to 5) by using Equations 2 to 4. The structure's final rotation will be the product between the first-order rotation and the  $\gamma_\theta$  coefficient. This is the proposed simplified approach. The final rotation will also be evaluated and compared by the P- $\Delta$  method, which is accepted as a more accurate process.

Once more, it is relevant to emphasize a remark about the radius of gyration (R) and the twist center (CT) of the floor, which are essential to the  $\gamma_\theta$  coefficient determination. For each building, the R variable was obtained considering the axial force of each column and its positions relative to the CT of the building. As the stories of buildings 1 to 5 are symmetrical, the CT will be positioned at the geometrical center of the floor (and the twist axis will be a vertical line along all the structure). For a better understanding, the calculations associated to the building 1 will be presented. For the others, a summary of the results is provided.

Because all the floors of the building are identical (regarding to loadings and to the position of structural elements, due to its double symmetry), it is possible to obtain R with the information of only one of the stories (if all the stories were considered, the numerator and the denominator would change proportionally). Thus, R will be calculated, for building 1, by using Equation 4 and the data provided in Table 1:

$$R = \sqrt{\frac{\sum_{j=1}^r P_j R_j^2}{\sum_{j=1}^r P_j}} = \sqrt{\frac{394067,249}{8951,3}} = 6.635 \text{ m}$$

**Table 1.** Column loading and column position relative to the floor's CT– Building 1.

Column	$P_j$ (kN)	$R_j$ (m)	$P_j R^2$
1	190.4	10.53	21095.480
2	380.9	7.59	21957.363
3	345.6	6.28	13638.401
4	390.4	7.52	22080.996
5	201.1	10.42	21844.173
6	383.2	8.70	28999.346
7	760.9	4.71	16902.444
8	682.3	2.01	2750.157
9	758.6	4.60	16027.456
10	377.1	8.57	27718.600
11	369.1	8.76	28303.693
12	763.9	4.82	17737.725
13	682.6	2.24	3438.201
14	754.9	4.70	16708.868
15	390.6	8.63	29103.936
16	198.5	10.67	22592.119
17	393.4	7.79	23870.118
18	347.5	6.52	14766.463
19	386.7	7.70	22917.809
20	193.6	10.57	21613.901
<b>Total</b>	<b>8951.3</b>	<b>-</b>	<b>394067.249</b>

The first-order rotation obtained through the structural analysis of building 1 in CAD/TQS is  $\theta_1 = 1.46 \times 10^{-3}$  rad with a respective total torsional moment loading (as distributed couples) of  $M_{t,1} = 672$  kN.m. Hence, considering the complementary information:

$$H = 12 \text{ m}$$

$$\bar{P} = 8951.3 \text{ kN}$$

$$\theta_{1,n} = 1.46 \times 10^{-3} \text{ rad}$$

$$\Delta M_t = \frac{\overline{PR}^2 \theta_{I,N}}{H} = \frac{8951.3 \cdot 6.635^2 \cdot 0.00146}{12} = 47.945 \text{ kN.m}$$

This is the expected increment of torsional moment  $\Delta M_t$ .

Admitting the applied first-order moment  $M_{t,I} = 672 \text{ kN.m}$ , the  $\gamma_\theta$  coefficient is obtained:

$$\gamma_\theta = \frac{I}{I - \left( \frac{\Delta M_t}{M_{t,I}} \right)} = \frac{I}{I - \left( \frac{47.945}{672} \right)} = 1.0768$$

The  $\gamma_\theta$  coefficient indicates that the final rotation (taking into account second-order effects) is approximately 1.0768 times larger than the first-order rotation. The value for the rotation obtained by the P- $\Delta$  method, also performed in CAD/TQS, is  $\theta_{II \text{ P-}\Delta} = 1.637 \times 10^{-3} \text{ rad}$ . The following comparison is presented:

Final rotation at the top, provided by  $\gamma_\theta$ :  $\theta_{I,n} \cdot \gamma_\theta = 0.00146 \times 1.0768 = 1.572 \times 10^{-3} \text{ rad}$

Final rotation at the top, provided by P- $\Delta$  method:  $\theta_{II \text{ P-}\Delta} = 1.637 \times 10^{-3} \text{ rad}$

$$\text{Error} = (0.001572 - 0.001637) / 0.001637 \cong -4.0 \%$$

The same methodology is used for the remaining four regular buildings. Table 2 summarizes the results. Notably, the second-order rotation values obtained using the  $\gamma_\theta$  coefficient were similar to the rotation presented by the P- $\Delta$  method. The maximum error found was 10.3% (on the nonconservative side) and the average error was 6.06%. Franco [14] also compares the values of the same parameter analyzing one building (with modifications on frames in its façade) with the P- $\Delta$  method and indicates error values of -0.6%, -1.6% and -5.5%.

**Table 2.**  $\gamma_\theta$  coefficient calculation and comparison with P- $\Delta$  method (first analysis).

	Building 1	Building 2	Building 3	Building 4	Building 5
n (number of stories)	4	6	10	15	25
H (m)	12	18	30	45	75
P Total (kN)	8951.3	13614.3	23182.8	35919.92	64310.2
R (m)	6.635	6.672	6.674	6.716	6.726
$\theta_I$ (rd)	$1.46 \times 10^{-3}$	$1.88 \times 10^{-3}$	$3.04 \times 10^{-3}$	$5.24 \times 10^{-3}$	$1.052 \times 10^{-2}$
$\Delta M_t$ (kN.m)	47.945	63.293	104.645	188.631	408.028
$M_{t,I}$ (kN)	672	1008	167	2497.5	4162.5
$\gamma_\theta$	1.0768	1.0670	1.0669	1.0817	1.1087
$\theta_{II}$ (rad) ( $\gamma_\theta$ method)	$1.572 \times 10^{-3}$	$2.006 \times 10^{-3}$	$3.243 \times 10^{-3}$	$5.668 \times 10^{-3}$	$1.166 \times 10^{-2}$
$\theta_{II}$ (rad) (P- $\Delta$ method)	$1.637 \times 10^{-3}$	$2.092 \times 10^{-3}$	$3.406 \times 10^{-3}$	$6.100 \times 10^{-3}$	$1.300 \times 10^{-2}$
Error	-4.0%	-4.1%	-4.8%	-7.1%	-10.3%

Bueno [19], in an analogous procedure, compares the second-order moments obtained applying the  $\gamma_z$  coefficient and the P- $\Delta$  method for three buildings. For this purpose, the author adopts a ratio named RM2M1, which is available in CAD/TQS software, and provides a comparison between the first and the second-order moments. The first building shows small error values such as +0.1% up to +1% (on the conservative side). For the second one, that presents torsional effects, there are greater error values such as 4.9%. And for the last one, which  $\gamma_z$  parameter is greater than 1.3 (the limit value recommended by the standard code ABNT NBR 6118:2014 [5]), the error is 14.5%.

So, the error values obtained in the present study were considered acceptable, taking into account the simplified nature of the method for the determination of the second-order rotation. Thus, the  $\gamma_\theta$  coefficient may be regarded as an adequate parameter for the evaluation of susceptibility to second-order rotations.

### 5.2 $\gamma_\theta$ coefficient evaluation of regular buildings with different torsional loading

As described before, buildings 1 to 5 are analyzed twice, now with a single torsion couple applied at the top floor. This procedure would be expected as the most consistent with the fundamental premises of the  $\gamma_\theta$  coefficient. As before, the results are compared with those obtained by the more accurate P- $\Delta$  analysis.

Table 3 summarizes the results from the second analysis, similarly to Table 2. It is important to highlight that the rotation displacements magnitude continues in the same level as in previous analysis, but the results are now closer to the reference values of the P- $\Delta$  method. Now, the greatest error is 4.0%. These results confirm the  $\gamma_\theta$  coefficient applicability and accuracy as an evaluation procedure for torsional effects.

The dependence of the  $\gamma_\theta$  coefficient on the loading distribution is discussed again in the next section, devoted to the angular displacement profile of the building.

**Table 3.**  $\gamma_\theta$  coefficient calculation and comparison with P- $\Delta$  method (second analysis).

	Building 1	Building 2	Building 3	Building 4	Building 5
$\gamma_\theta$	1.0768	1.0670	1.0669	1.0817	1.1087
$\theta_{II}$ (rad) ( $\gamma_\theta$ method)	$1.407 \times 10^{-3}$	$1.913 \times 10^{-3}$	$3.294 \times 10^{-3}$	$6.020 \times 10^{-3}$	$1.313 \times 10^{-2}$
$\theta_{II}$ (rad) (P- $\Delta$ method)	$1.374 \times 10^{-3}$	$1.865 \times 10^{-3}$	$3.189 \times 10^{-3}$	$5.830 \times 10^{-3}$	$1.263 \times 10^{-2}$
Error	2.4%	2.5%	3.3%	3.3%	4.0%

### 5.3 Evaluation of the angular displacement profile

The angular displacement (rotation) profiles of buildings 1 to 5 were analyzed in order to investigate if the different loading distributions produce modification on them. All the buildings of the first analysis (with distributed torsion couples) present a similar behavior: a variation of the inter-story rotation displacement along the height. For the second analysis (with torsion couples applied only at the top floor), all the buildings presented a quasi-constant increment in rotation between any two floors. Figures 8 and 9 show the plots of the angular displacement per floor, resulting from the two analyses of building 4.

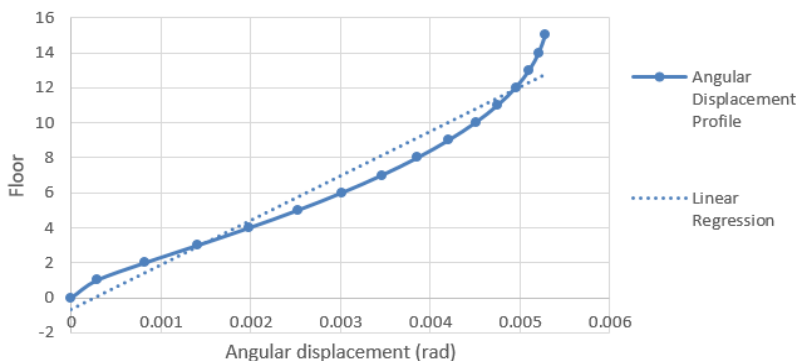


**Figure 8.** Angular displacement at each floor (building 4 and first analysis).

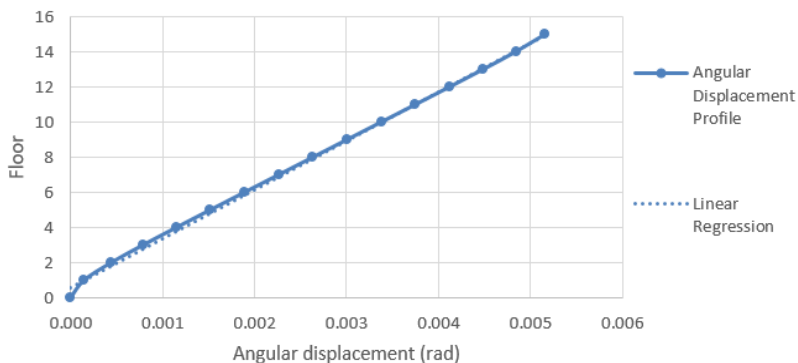


**Figure 9.** Angular displacement at each floor (building 4 and second analysis).

At first sight, this can be an influence factor on  $\gamma_\theta$  coefficient values, because the angular displacements between floors, for a given second-order analysis iteration, are closely related with the distribution of new internal forces in the structure and with the consideration of the geometrical progression (as invariable) between iterations.

The  $\gamma_\theta$  coefficient makes use of the hypothesis that the ratio of the increment in internal forces is constant between two successive second-order iterations. This is expected only if, for each story, the current distribution of the addition of internal forces is similar as that obtained in the previous iteration. The P- $\Delta$  method, on the other hand, is fully capable of considering different distribution of internal forces at each iteration, even if those may not follow exactly this hypothesis of constant geometrical progression.

Unchanged variations of angular displacements along the height for each building in the second analysis are probably closer to the situation of similar distributions of incremental internal forces between iterations (eccentricities are almost the same between each floor). At the other hand, the greater variation in displacements between floors in the first analysis are tied to different increment in internal forces between each floor, giving rise to a new distribution of displacement (and internal forces) in the next iteration.

It should be observed that a usual design situation would involve not a single force couple at the top floor, or identical force couples in each story, but different torsion intensities according to the wind action, out-of-plumb horizontal forces and their respective eccentricities to the CT. In reality, the design practice faces an intermediate situation between the first and second analyses discussed previously.

In addition, it should be noticed that even for usual horizontal forces loadings, different buildings may present different profile displacement shapes. Hence, it is important to study how this may be related to the variation in error values between the  $\gamma_\theta$  coefficient and the P- $\Delta$  method.

#### 5.4 $\gamma_\theta$ coefficient evaluation of irregular buildings

Sections 5.1 and 5.2 covered the regular buildings (models 1 to 5) to evaluate the response of the  $\gamma_\theta$  coefficient. At this point, the results from irregular buildings (models 6 and 7) are presented. Table 4 shows the values of the second-order final rotation of the structure, using the  $\gamma_\theta$  coefficient procedure and the P- $\Delta$  method. Once again, a good convergence between the results is evident, with a maximum error of 5.3%.

For all the previous analyses, it is possible to conclude that the evaluation procedure considering the  $\gamma_\theta$  coefficient presented an adequate estimate regarding both regular and irregular buildings.

**Table 4.**  $\gamma_\theta$  coefficient calculation and comparison with P- $\Delta$  method (irregular buildings).

	<b>Building 6</b>	<b>Building 7</b>
$\gamma_\theta$	1.1001	1.0950
$\theta_{II}$ (rad) ( $\gamma_\theta$ method)	$1.221 \times 10^{-2}$	$6.910 \times 10^{-3}$
$\theta_{II}$ (rad) (P- $\Delta$ method)	$1.290 \times 10^{-2}$	$7.230 \times 10^{-3}$
Error	-5.3%	-4.5%

#### 5.5 $\gamma_z$ coefficient behavior under extra torsional load action

The behavior of the  $\gamma_z$  coefficient is now investigated analyzing the model 4, in the absence or presence of distributed torsional couples acting simultaneously with the usual design loads (live, dead and wind loads). Table 5 summarizes the results.

**Table 5.**  $\gamma_z$  coefficient values in absence or presence of torsional couples.

	<b><math>\gamma_z</math> in absence of couples</b>	<b><math>\gamma_z</math> in presence of couples</b>
Case 1 (90° wind)	1.174	1.174
Case 2 (270° wind)		
Case 3 (0° wind)	1.153	1.153
Case 4 (180° wind)		

There was no difference in  $\gamma_z$  coefficient values in the presence of an extra rotation due to torsion. This happens because the building has symmetrical floors, and the “extra” eccentricity caused by the rotation in one side of the

building is balanced by the other detected on the opposite side, that has an eccentricity in the reverse direction. Then, the “extra” displacements due to torsion cancel each other.

Despite that the  $\gamma_Z$  coefficient is a term used to measure the magnitude of global second-order effects, in this case, with the presence of the torsional couples that cause greater global second-order effects and a top story rotation increment of approximately 8% (according to the  $\gamma_\theta$  coefficient), the  $\gamma_Z$  coefficient is incapable to detect these effects.

However, the building’s floors rotations due to torsional moment (caused either by horizontal couples or, equivalently, by an eccentricity between resultant external forces and the twist center) will cause a force redistribution on the elements of bracing frames to resist the new load. This means that greater moments in the structural elements, due to the rotation and its respective second-order effects, may occur without significant change of the  $\gamma_Z$  coefficient. This clearly shows the importance of examining specifically the global second-order effects due to torsion and the use of the  $\gamma_\theta$  coefficient.

Finally, it is important to highlight that the discussion of the preceding paragraphs refers to buildings with uniform distributed loading in the area of the floors (especially the idea about the displacements equilibrium due to eccentricities). When the floors have different vertical gravity loads, depending on the area, the  $\gamma_Z$  coefficient will change more prominently, because the opposite sides’ eccentricity will not compensate each other. As discussed in section 3, effects due to torsion may not be adequately considered by the  $\gamma_Z$  coefficient, and its use as an amplification factor in cases where torsion is significant, may result inaccurate and unsatisfactory.

To better understand this inadequate sensitivity of the  $\gamma_Z$  coefficient due to rotations, Table 6 shows the values of  $\gamma_Z$  ( $\gamma_{ZX}$  in the X direction and  $\gamma_{ZY}$  in the Y direction) and  $\gamma_\theta$  for each one of the five buildings studied in section 5.1, besides the values of  $\theta_I$  (first-order rotation),  $\theta_{II P-\Delta}$  (second-order rotation calculated by the P- $\Delta$  method) and the ratio  $\theta_I/\theta_{II P-\Delta}$ .

**Table 6.**  $\gamma_\theta$  coefficient calculation and comparison with P- $\Delta$  method (second analysis).

	Building 1	Building 2	Building 3	Building 4	Building 5
$\gamma_{ZX}$	1.133	1.190	1.180	1.153	1.219
$\gamma_{ZY}$	1.134	1.170	1.145	1.174	1.259
$\gamma_\theta$	1.0768	1.067	1.0669	1.0817	1.1087
$\theta_I$ (rad)	$1.460 \times 10^{-3}$	$1.880 \times 10^{-3}$	$3.040 \times 10^{-3}$	$5.240 \times 10^{-3}$	$1.052 \times 10^{-2}$
$\theta_{II}$ (rad) (P- $\Delta$ method)	$1.640 \times 10^{-3}$	$2.092 \times 10^{-3}$	$3.406 \times 10^{-3}$	$6.100 \times 10^{-3}$	$1.300 \times 10^{-2}$
$\theta_I / \theta_{II}$	1.1211	1.1126	1.1204	1.1640	1.2361

Figure 10 presents the curves of each of these variables in the first analysis (distributed couples along the height). The  $\gamma_\theta$  coefficient curve exhibits a similar tendency as the ratio  $\theta_I/\theta_{II P-\Delta}$ . The profile of the  $\gamma_Z$  coefficient, however, is considerably different.

Similarly, Figure 11 shows the curves for the second analysis (single couple at the top). The general conclusion is the same: the  $\gamma_\theta$  coefficient curve is the only one with a similar shape as the results from the P- $\Delta$  method, differently from the  $\gamma_Z$  coefficient values.

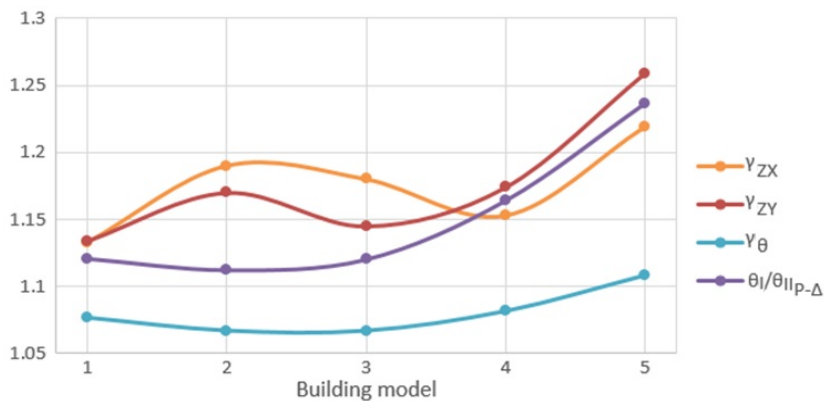


**Figure 10.** Comparison on the parameters behavior (first analysis).

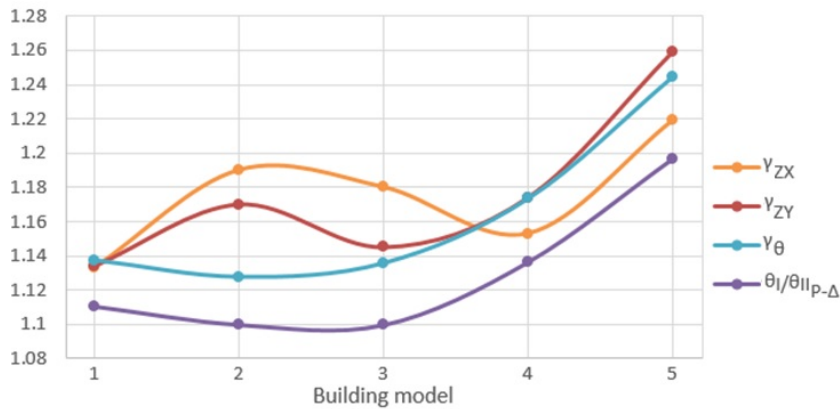


Figure 11. Comparison on the parameters behavior (second analysis).

As a final note, it is important to emphasize that the numerical comparison of internal forces in structural elements, in the presence or absence of torsional moments, was not discussed in this study. Obviously, there is a significant modification in the internal forces distribution between these two cases. This paper did not aim to study the change in internal forces distribution, but to investigate the global behavior of the structure and the instability parameters evaluated.

## 6 CONCLUSIONS

This paper discusses the  $\gamma_{\theta}$  coefficient use and its calculation, another ingenious development from Professor Engineer Mario Franco, as estimator criteria for the magnitude of the second-order global rotation of buildings due to torsion effects. This is a parameter analogous to the  $\gamma_Z$  coefficient, but differently from the latter, has been neglected by the technical literature.

The global second-order angular displacements from seven different building analyses were evaluated with the use of the software CAD/TQS. They had regular and irregular geometries, and were submitted to two different torsion loadings. The buildings' final rotation (estimated by the  $\gamma_{\theta}$  coefficient) was compared with the values obtained using a more accurate analysis, the P- $\Delta$  method. The error found between both procedures ranged from 1.7% to 10.6%, which is regarded as acceptable for a simplified method.

Other complementary analyses were done, evaluating the rotation displacement profile of the buildings according to the torsional loading distribution. The objective was to verify the sensibility and the completeness (in the sense of the capability to assess any global second-order effect) of the  $\gamma_Z$  coefficient to rotation displacements, especially when considered regular structures.

Finally, the importance of a measure criteria related to the rotation of structures is highlighted, as a complement to the flexural effects. Currently, the rotation due to torsion is sometimes neglected in the design practice, even if it is always present in buildings, in a high or low level of magnitude.

## ACKNOWLEDGMENTS

The authors are grateful to the TQS Informática Ltda. for providing the software CAD/TQS academic version for UFRN.

## REFERENCES

- [1] P. B. Fusco and M. Onishi, *Introdução à engenharia de estruturas de concreto*. São Paulo: Cengage, 2017.
- [2] J. K. Wight and J. G. Macgregor, *Reinforced concrete: mechanics and design*, 5th ed. Upper Saddle River: Pearson Prentice Hall, 2009.
- [3] A. Kimura, *Informática aplicada a estruturas de concreto armado*, 2. ed. São Paulo: Oficina de Textos, 2018.
- [4] W. J. Z. Moncayo, "Análise de segunda ordem global em edifícios com estrutura de concreto armado," M.S. thesis, EESC, USP, São Carlos, SP, 2011. <http://dx.doi.org/10.11606/D.18.2011.tde-19042011-085946>.

- [5] Associação Brasileira de Normas Técnicas. *NBR 6118:2014: Projeto de Estruturas de Concreto – Procedimento*. Rio de Janeiro: ABNT, 2014.
- [6] M. Franco and A. C. Vasconcelos, “Practical assessment of second order effects in tall buildings,” in *Colloq. CEB-FIP MC90*, Rio de Janeiro, 1991, pp. 307-323.
- [7] M. Franco and A. C. Vasconcelos, “Avaliação prática dos efeitos de 2ª ordem em edifícios altos,” in *Coletânea de Trabalhos Sobre Estabilidade Global e Local das Estruturas de Edifícios*, Instituto de Engenharia de São Paulo, São Paulo: Instituto de Engenharia de São Paulo, 1997, pp. 41-54.
- [8] V. V. S. Vieira, S. J. Rodrigues Jr., and L. A. C. M. Veloso, “Análise da estabilidade global de edifícios de concreto armado usando o coeficiente  $\gamma Z$ ,” *Rev. IBRACON Estrut. Mater.*, vol. 10, no. 5, p. 1113-1140, Sept./Oct. 2017, <http://dx.doi.org/10.1590/S1983-41952017000500010>.
- [9] R. G. Mamone, G. H. Siqueira, and L. C. M. Vieira Jr, “The use of natural period of vibration as a simplified indicator of second-order effects for RC frames,” *Int. J. Struct. Civ. Eng. Res.*, vol. 7, no. 1, pp. 15-21, Feb. 2018, <http://dx.doi.org/10.18178/ijscer.7.1.15-21>.
- [10] D. G. Reis, G. H. Siqueira, L. C. M. Vieira Jr, and R. D. Ziemian, “Simplified approach based on the natural period of vibration for considering second-order effects on reinforced concrete frames,” *Int. J. Struct. Stab. Dyn.*, vol. 18, no. 5, p. 1-22, Jan. 2018, <http://dx.doi.org/10.1142/S0219455418500748>.
- [11] F. F. Leitão, G. H. Siqueira, L. C. M. Vieira Jr, and S. J. C. Almeida, “Análise dos efeitos globais de segunda ordem em estruturas irregulares em concreto armado utilizando o período natural de vibração,” *Rev. IBRACON Estrut. Mater.* vol. 12, n. 2, p. 408-428, Mar./Apr. 2019, <http://dx.doi.org/10.1590/S1983-41952019000200012>.
- [12] R. N. Cunha, L. A. Mendes, and D. L. N. F. Amorim, “Proposta de critério simplificado para estimar efeitos de segunda ordem em edifícios de concreto armado,” *Rev. IBRACON Estrut. Mater.*, vol. 13, n. 2, p. 200-211. 2020, <http://dx.doi.org/10.1590/S1983-41952020000200002>.
- [13] M. Franco, “Torsion in tall buildings,” in *3rd International Conference of High-Performance Concrete, and Performance and Quality of Concrete Structures*, Recife, 2002.
- [14] M. Franco, “A torção nos edifícios altos,” in *Simpósio EPUSP Sobre Estruturas de Concreto*, São Paulo, 2003.
- [15] R. B. Andrade, P. G. B. Nóbrega, and S. H. S. Nóbrega, “Metodologia para o cálculo de um coeficiente de avaliação dos efeitos de segunda ordem globais de torção,” in *61º Congresso Brasileiro do Concreto CBC2019*, Fortaleza, 2019. Accessed: Mar. 22, 2019. [Online]. Available: <https://www.researchgate.net/publication/336672173>.
- [16] A. C. Vasconcelos, “Em que casos não se deve aplicar o Gamaz?,” *TQS Docs*. 2000. Accessed: Mar. 30 2020. [Online]. Available: <http://docs.tqs.com.br/Docs/Details?id=3300&search=Gamaz&language=pt-Br>
- [17] N. Covas, “GamaZ,” *TQS Docs*. 2009. Accessed: Mar. 30 2020. [Online]. Available: <http://docs.tqs.com.br/Docs/Details?id=3306&search=Gamaz&language=pt-Br>
- [18] Associação Brasileira de Normas Técnicas, *NBR 6123:1988: Forças devidas ao vento em edificações*. Rio de Janeiro: ABNT, 1988.
- [19] M. M. E. Bueno, “Avaliação dos parâmetros de instabilidade global em estruturas de concreto armado,” M.S. thesis, ENC, UnB, Brasília, DF, 2009. [Online]. Available: <http://www.pecc.unb.br/wp-content/uploads/dissertacoes/M09-2A-Mônica-Bueno.pdf>

---

**Author contributions:** R. B. Andrade: conceptualization, formal analysis, writing; P. G. B. Nóbrega: conceptualization, methodology, writing, supervision.

**Editors:** Edgar Bacarji, José Luiz Antunes de Oliveira e Sousa, Guilherme Aris Parsekian.



ORIGINAL ARTICLE

# Punching shear strength of waffle flat slabs

## *Estudo da resistência à punção em lajes lisas nervuradas*

Ricardo José Carvalho Silva<sup>a</sup> Dênio Ramam Carvalho de Oliveira<sup>b</sup> Nívea Gabriela Benevides de Albuquerque<sup>b</sup> Francisco Eudázio Suriano da Silva Júnior<sup>a</sup> Felipe da Silva Leite<sup>b</sup> <sup>a</sup>Universidade Estadual do Vale do Acaraú – UVA, Faculdade de Engenharia Civil, Sobral, CE, Brasil<sup>b</sup>Universidade Federal do Pará – UFPA, Faculdade de Engenharia Civil, Belém, PA, Brasil

Received 07 January 2020

Accepted 25 May 2020

**Abstract:** This research aimed to compare the ultimate load of 10 waffle flat slabs with different sizes of solid area and spacing between ribs. For this, a non-linear computational simulation of the slabs was carried out until their failure using the engineering software ANSYS. The failure modes and loads were analyzed, and the results showed that the models with less solid area presented less bearing capacity in comparison to the models with greater solid area when the failure mode was shearing of the ribs. The slabs with the largest solid regions experienced punching shear and behaved in a similar way as solid flat slabs, indicating compliance with the codes in relation to their punching shear strength provisions, especially with the NBR 6118. The results show that a square solid area whose length is 15% of the span is reasonable and that the ACI, Eurocode 2 and NBR 6118 provisions underestimate the shear strength of the ribs.

**Keywords:** waffle flat slab, punching shear, solid area, Ansys.

**Resumo:** Esta pesquisa teve o objetivo de comparar computacionalmente a resistência de 10 lajes lisas nervuradas com diferentes tamanhos de área maciça e diferentes espaçamentos das nervuras. Para isso, os ensaios das lajes foram simulados no programa computacional ANSYS até a ruptura. Foram observados os modos e as cargas de ruptura, e, através dos resultados, observou-se que os modelos com menor região maciça apresentaram menor resistência em comparação aos modelos de maior área maciça, pois sua ruptura se deu por cisalhamento nas nervuras. As lajes com maiores regiões maciças sofreram punção e se comportaram de forma semelhante a lajes lisas maciças, apresentando conformidade com as normas em relação às suas estimativas de resistência à punção, especialmente com a NBR 6118. Desta forma, a regra prática de se determinar a região maciça com 15% do vão se mostrou razoável, e observou-se que o ACI, o Eurocode 2 e a NBR 6118 subestimam as resistências ao cisalhamento das nervuras.

**Palavras-chave:** laje lisa nervurada, punção, área maciça, Ansys.

**How to cite:** R. J. C. Silva, D. R. C. Oliveira, N. G. B. Albuquerque, F. E. S. Silva Júnior, and F. S. Leite, “Punching shear strength of waffle flat slabs,” *Rev. IBRACON Estrut. Mater.*, vol. 14, no. 1, e14106, 2021, <https://doi.org/10.1590/S1983-41952021000100006>

## 1 INTRODUCTION

Punching shear is a type of brittle failure that occurs in slabs supported directly on a column and when flexural strength of the slab is greater than its shear strength. This type of failure can lead to progressive collapse of the structure.

Currently, the waffle slab system without beams and with a solid area around the column is one of the most used structural system in Brazil. The simplicity of the construction of this system and the lesser use of concrete in relationship to that of the solid flat slab made this type of slab popular for construction of medium height and tall buildings.

Corresponding author: Ricardo José Carvalho Silva. E-mail: [ricardo.carvalho222@gmail.com](mailto:ricardo.carvalho222@gmail.com)

Financial support: None.

Conflict of interest: Nothing to declare.



This is an Open Access article distributed under the terms of the Creative Commons Attribution License, which permits unrestricted use, distribution, and reproduction in any medium, provided the original work is properly cited.

However, the strength of the waffle flat slab is directly linked to the size of the solid area around the column and very small areas can promote the formation of the punching shear cone beyond the solid area and induce shearing of the ribs.

Al-Bayati et al. [1], [2], Arunkumar et al. [3] and Sacramento et al. [4] observed that some tested waffle slabs had their strength reduced when the punching shear cone reached the ribbed region. That is, in order to avoid a bearing capacity reduction of the slab, it is of fundamental importance that the punching shear cone is located within the solid area of the slab. The problem is that NBR 6118 [5], EC2 [6] and ACI 318 [7] are silent on this point. These codes don't have any recommendation to the dimension of this solid area. Although there is no normative prescription, it is common among designers to adopt the dimensions of the solid area to be around 15% of the span in each direction.

### 1.1 Objective

The aim of this work was to investigate, using the Ansys computer program, the ultimate strength and the failure mode of waffle flat slabs without shear reinforcement and with a solid area of different sizes around the column. In addition, the size of the solid area around the column was also correlated with the failure mode (Punching shear in the solid area or Shearing of the ribs with the punching shear cone extending beyond the solid area).

### 1.2 Justification

Experimental studies such as those by Al-Bayati et al. [1], [2], Arunkumar et al. [3] and Sacramento et al. [4] showed that the reduction of the solid area in waffle flat slabs can reduce their ultimate strength, leading to the punching shear cone extending beyond the solid area. There is a rule of thumb among designers to use the length of the solid area to be at least equal to 15% of the clear span between columns, but there is no scientific basis for this rule.

Building codes are silent on the subject on the dimensions of the solid area around the column, as well as not providing clear methods to determine the punching shear strength of this type of slab. The only specific recommendation concerns the necessity to check the shear capacity of the ribs, and this recommendation is significantly conservative.

With so many uncertainties and omissions on this subject by the codes, the study of waffle flat slabs has great relevance. The subject is still of great technical and scientific importance, given the existing knowledge gap.

The research presented herein is fundamentally computational, although 2 experimental results from Albuquerque and Oliveira [8] have been used to validate the numerical models.

## 2 CODE RECOMMENDATIONS

The ACI 318 [7], Eurocode 2 [6] and NBR 6118 [5] formulations are presented below, with the safety factors removed, in order to compare the calculated values to the computational results.

### 2.1 ACI 318 [7]

According to the American code, the estimated punching shear load ( $V_{ACI,p}$ ), for slabs without shear reinforcement, is the lowest among Equations 1, 2 and 3.

$$V_{ACI,p} = 0.33\sqrt{f'_c} u_1 d \quad (1)$$

$$V_{ACI,p} = 0.17\left(1 + \frac{2}{\beta_c}\right)\sqrt{f'_c} u_1 d \quad (2)$$

$$V_{ACI,p} = 0.083\left(2 + \frac{\alpha_s d}{u_1}\right)\sqrt{f'_c} u_1 d \quad (3)$$

Where:

$f'_c$  = compressive strength of concrete limited to 70 MPa;

$\beta_c$  = ratio between the largest and smallest column dimensions;

$\alpha_s$  = constant that assumes a value equal to 40 for internal columns, 30 for edge columns and 20 for corner columns;

$d$  = section effective depth;

$u_1$  = control perimeter according to ACI 318 [7] (Figure 1).

For waffle slabs, the American code recommends that the ribs should have a minimum width ( $b_w$ ) of 100 mm, a maximum height ( $h_b$ ) of 3.5 times the minimum width of the rib and a maximum spacing between the faces of the ribs ( $s$ ) of 750 mm. The thickness of the topping slab ( $h_f$ ) must be at least 37.5 mm and at most  $s/12$  ratio (Figure 1). For ribs without shear reinforcement, ACI 318 [7] allows the shear strength to be estimated by Equation 4.

$$V_{ACI,s} = \frac{1}{6} \sqrt{f'_c} b_w d \quad (4)$$

Where,

$f'_c$  = compressive strength of concrete limited to 70 MPa;

$b_w$  = rib width considered;

$d$  = rib effective depth.

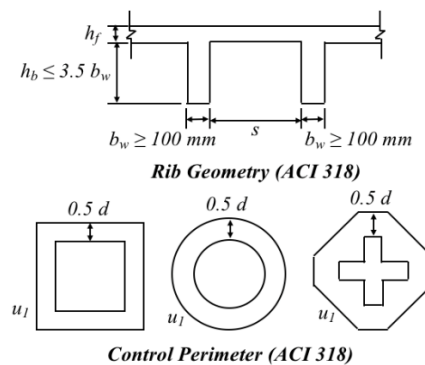


Figure 1. Rib geometry and control perimeter according to ACI 318 [7]

## 2.2 Eurocode 2 [6]

According to the European code, the estimated punching shear load ( $V_{EC,p}$ ) for slabs without shear reinforcement is given by Equation 5.

$$V_{EC,p} = 0.18 \xi (100 \rho_l f_{ck})^{\frac{1}{3}} u_1 d \quad (5)$$

Where,

$f_{ck}$  = compressive strength of concrete in MPa;

$\rho_l$  = longitudinal reinforcement rate, not greater than 0.02;

$\xi = (1 + \sqrt{200/d}) \leq 2.0$  ;

$d$  = section effective depth;

$u_1$  = control perimeter according to Eurocode 2 [6] (Figure 2).

For waffle slabs, EC2 [6] recommends that the topping slab and the ribs do not need to be analyzed separately when there is sufficient torsional stiffness between these two elements, and the waffle slab can be analyzed as solid slab. However, this condition is only acceptable if the spacing between the faces of the ribs ( $s$ ) does not exceed 1500 mm, if the height of the rib ( $h$ ) does not exceed 4 times its width ( $b_w$ ) and if the height of the table ( $h_f$ ) is at least the greater of these two factors: ( $s/10$ ) or (50 mm) (Figure 2). For ribs without shear reinforcement, EC2 [6] allows the shear strength to be estimated using Equation 6.

$$V_{EC,s} = 0.18 \xi (100 \rho_l f_{ck})^{\frac{1}{3}} b_w d \tag{6}$$

With,

$\rho_l$  = longitudinal reinforcement rate, not greater than 0.02;

$f_{ck}$  = compressive strength of concrete in MPa;

$b_w$  = rib width considered;

$d$  = rib effective depth.

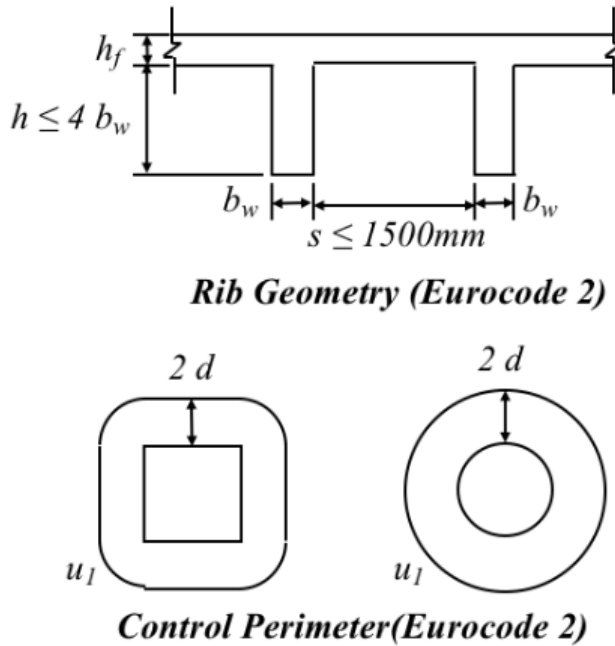


Figure 2. Rib geometry and control perimeter according to Eurocode 2 [6]

### 2.3 NBR 6118 [5]

According to the Brazilian code, the estimated punching shear load ( $V_{NBR,p}$ ), for slabs without shear reinforcement, is given by Equation 7.

$$V_{NBR,p} = 0.18 \xi (100 \rho_l f_{ck})^{\frac{1}{3}} u_l d \tag{7}$$

Where:

$f_{ck}$  = compressive strength of concrete in MPa;

$\rho_l$  = longitudinal reinforcement rate;

$\xi = (1 + \sqrt{200/d})$  ;

$d$  = section effective depth;

$u_l$  = control perimeter according to NBR 6118 [5] (Figure 3).

The NBR 6118 [5] does neither limit the size effect ( $\xi$ ) nor the longitudinal reinforcement rate ( $\rho_l$ ).

For waffle slabs, the Brazilian code recommends that the ribs should have a minimum width ( $b_w$ ) of 50 mm and if it has compression reinforcement, the minimum width ( $b_w$ ) should be 80 mm (Figure 3). The topping slab thickness must be at least 50 mm when there is conduit wiring of  $\phi 10$ mm, or at least  $(40 \text{ mm} + \phi)$  when conduit wiring inside the slabs has a diameter greater than  $\phi 10$ mm, or at least  $(40 \text{ mm} + 2\phi)$  when there is a conduit crossover inside the slabs.

If the spacing between axes of the ribs is less than or equal to 650 mm, checking the topping slab as an independent slab and the shearing of the ribs are not needed. When the spacing between the axes of the ribs is between 650 mm and 1100 mm, the bending behavior of the topping slab must be checked and the ribs must be dimensioned as beams, with verification of the shear. However, when the spacing between the axes of the ribs is up to 900 mm and the average width of the ribs is greater than 120 mm, checking the topping slab is not needed. In case the spacing between the axes is greater than 1100 mm, the topping slab must be checked as a solid slab, supported on a beam grid, and must meet the minimum thickness limits.

For ribs without shear reinforcement, NBR 6118 [5] requires the following checks:

Diagonal compression:

$$V_{NBR,dc} = 0.27\alpha_{v1}f_{ck}b_w d \tag{8}$$

$$\alpha_{v1} = 1 - f_{ck} / 250 \tag{9}$$

Diagonal tension:

$$V_{NBR,s} = V_{NBR,dt} = [\tau_R k (1.2 + 40 \rho_1)] b_w d \tag{10}$$

Where:

$$\tau_R = 0.05(f_{ck})^{2/3};$$

$k = |1.6 - d|$ , with a value of  $d$  in meters;

$\rho_1 = A_{s1} / (b_w d) \leq 0.02$ , where  $A_{s1}$  is the longitudinal reinforcement in the rib;

$b_w$  = minimum section width along effective depth  $d$ .

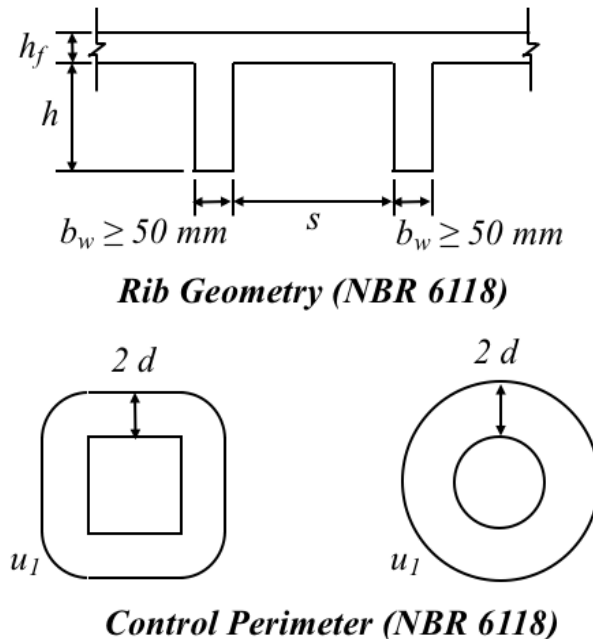


Figure 3. Rib geometry and control perimeter according to NBR 6118 [5]

### 3 METHODOLOGY

In this research, it was decided to analyze computationally, using the *ANSYS Workbench* program, 10 waffle slabs with several dimensions of the solid area around the column and different spacing of the ribs (Figure 4), by simulating panels with dimensions of 2220 mm x 2220 mm x 180 mm, with a cover layer (topping slab) of 60 mm and concrete beams (ribs) of 60 mm width, arranged in the X and Y orthogonal directions.

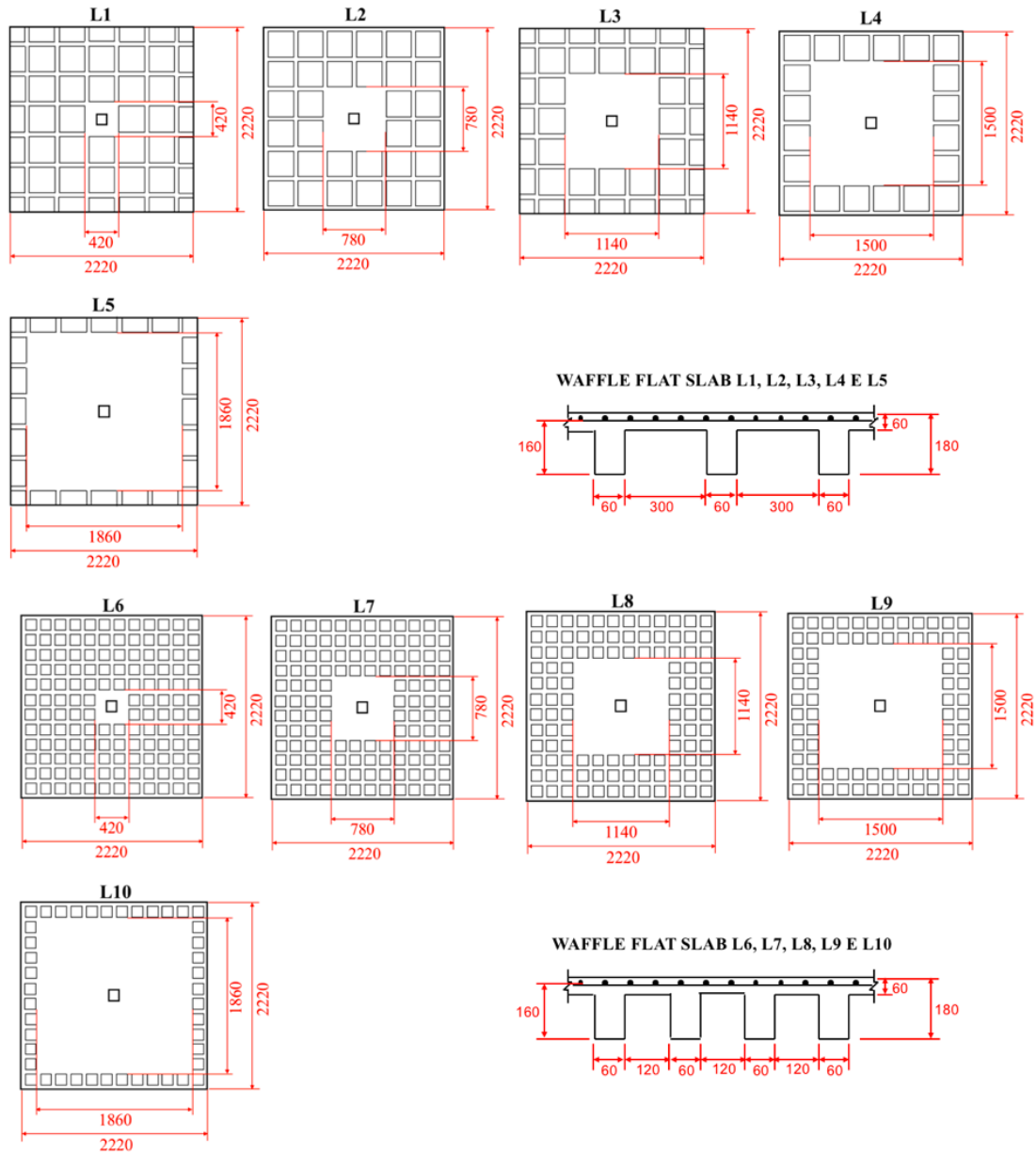


Figure 4. Waffle flat slabs (units in mm)

The methodology used in *ANSYS* was incremental, applying load/displacement step by step, through *substeps* until the failure of the slabs. Thus, simulating a possible experimental test, the dimensions of the waffle slabs were compatible with the reaction slab of the Structural Laboratory at UFPA. Figure 5 shows the assembly of the test, performed computationally using the *ANSYS* program [9], [10], showing the holes in the reaction slab, the ties, the load cell and the hydraulic cylinder.

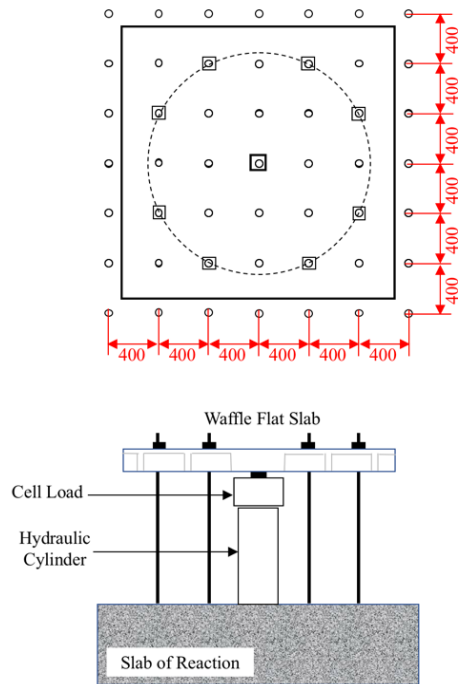


Figure 5. Scheme of the test (units in mm)

It is worth pointing out that, at no time, this research was interested in correlating the analyzed waffle slabs with a prototype in real scale, through a quantitative research. This research was purely qualitative, where the waffle slabs with different solid areas dimensions were compared with each other in order to estimate percentages of strength gains and losses among them.

A non-linear static analysis was defined on the *ANSYS Workbench platform*. *Solid65* elements were used for concrete and *Link180* for reinforcement. The *ANSYS* constitutive model for concrete was the concrete model, which uses the constitutive equations of Willam and Warnke [11] with five parameters for failure. This model predicts rupture of fragile materials and can work with failure modes by cracking (tensile) and crushing (compression), as shown in Figure 6. For steel, a bilinear model was adopted where the yield stress and the tangential module were required for the definition of the material, the reinforcement was considered to resist only axial forces. The bonding between concrete and steel was considered perfect. For the load and support application points, the *Solid185* element was defined and the same material as the reinforcement was used, however, without non-linearity properties.

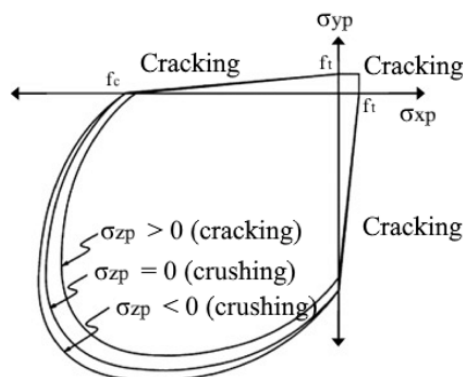


Figure 6. Constitutive model of concrete (adapted from ANSYS [10])

For the concrete, an average compressive strength of 30 MPa, an average tensile strength of 2.9 MPa and an elastic modulus equal to 31 GPa were adopted. The stress-strain graph of the compressed concrete was defined as recommended by fib [12] and is shown in Figure 7, with the maximum stress being reached at a strain of 2.3 ‰. After reaching the maximum stress, the stress-strain response was considered constant until the failure strain of 3.5‰ because ANSYS does not allow a negative slope.

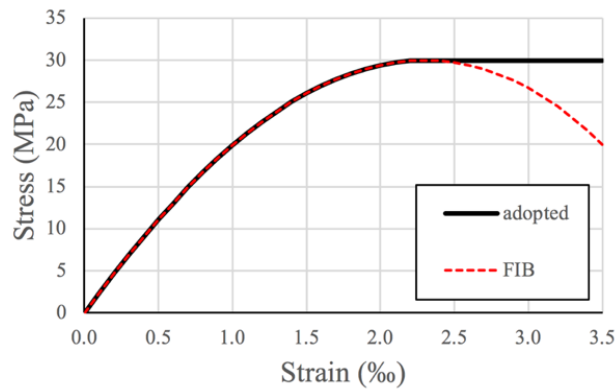


Figure 7. Stress-strain graph of compressed concrete

For the reinforcement steel, the CA-50 type was adopted, with yield stress equal to 500 MPa, modulus of elasticity equal to 210 GPa and tangential modulus equal to 0 after yielding, that is, a perfect elastoplastic bilinear model. The coefficients for the concrete with an open crack was equal to 0.3 and for a closed crack equal to 1.0. The Poisson's ratios adopted for concrete and steel were 0.2 and 0.3, respectively.

The *Solid65* element requires the use of a discrete reinforcement model, which requires the reinforcement to be positioned on the edges of the concrete elements so that their joints coincide. To avoid the formation of tetrahedral elements in the slab mesh, which would cause problems of convergence and compatibility with the reinforcement, the slabs were cut and separated into two parts: the topping slab (upper) and the ribs (lower), as shown in Figure 8. In this way, it was possible to generate a mesh with only hexahedral elements.

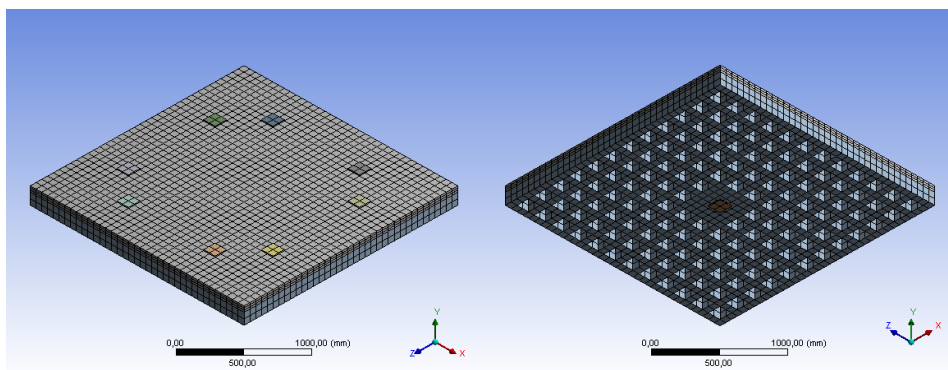


Figure 8. Slab model (Slab L6)

Between the two parts of the slabs, the *bonded contact* type was used, where the faces in contact cannot separate or move relative to each other, and the *pure penalty* formulation was adopted. This contact configuration was also adopted for the regions between the slabs and the load/support application points.

After a mesh convergence study for the slabs, the mesh was designed with 60 mm elements. In the topping slab the mesh was refined in the Y direction by 20 mm so that there was a coincidence of joints between the concrete and reinforcement elements (Figure 9).

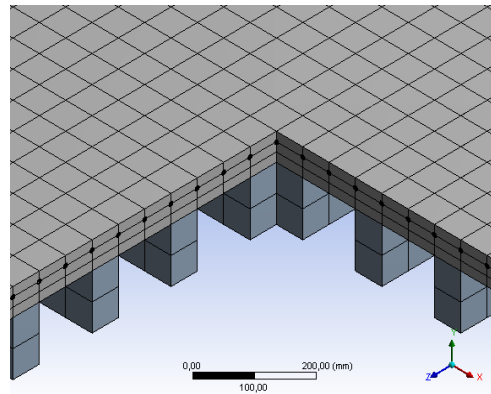


Figure 9. Detail of reinforcement positioning

The analyses used a convergence criterion based on displacements, where a tolerance of 1% was defined and the complete Newton-Raphson method was adopted. The loading was applied in a single *loading step* with 100 *substeps* and was applied as a vertical downward force on the upper face of the loading application points. Support reactions were defined as zero displacements on the Y axis on the underside of the support solid.

## 4 RESULTS AND DISCUSSIONS

### 4.1 Validation of the model

Validation tests of the computational model were carried out comparing the numerical results with the results of 2 slabs tested by Albuquerque and Oliveira [8]. The results of the validation are reported in Table 1. The results showed good agreement between the results of the experimental and computational failure loads, with identical failure modes also occurring. It was noted a loss of strength in the L3 because there is less solid area. It was also observed that the estimated punching shear loads, calculated using the codes provisions, for the L1 slab, were reasonably good, mainly that of NBR 6118 [5]. In addition, it was noted that all code estimated shear loads for the ribs were overly conservative.

Table 1. Computational, experimental and normative results for Albuquerque and Oliveira slabs [8]

Slab	$\frac{L_{SA}}{L_{NM}}$	$\rho$ (%)	$V_{comp}^{(A)}$ (kN)	Type of Failure	$V_u^{(B)}$ (kN)	$\frac{A}{B}$	Type of Failure	$V_{code,p}^{(C)}$ (kN)		$V_{code,s}^{(D)}$ (kN)		Type of Failure	Code
								$\frac{A}{C}$	$\frac{A}{D}$				
L1	0.500	0.50	280.0	PS	270.5	1.03	PS	229.5	1.22	93.5	3.00	SR	ACI
								237.4	1.18	91.0	3.02	SR	EC
								267.1	1.05	59.3	4.72	SR	NBR
L3	0.188	0.87	145.0	SR	150.5	0.96	SR	229.5	0.63	46.7	3.10	SR	ACI
								285.2	0.51	54.6	2.65	SR	EC
								320.9	0.45	29.7	4.89	SR	NBR

$L_{SA}$  = Solid area span (800 mm for L1 and 300 mm for L3);  $L_{NM}$  = Slab length with negative bending moment (1600 mm for L1 and L3);  $V_{comp}$  = Computational failure load via Ansys;  $V_u$  = Experimental failure load of the slabs of Albuquerque and Oliveira [8]; PS = Punching shear; SR = Shear in the ribs;  $V_{code,p}$  = Failure load by punching shear according to code;  $V_{code,s}$  = Failure load by shear in the ribs according to code.

### 4.2 Slab simulations

The results discussed here were calculated using data from the 10 waffle flat slabs analyzed computationally, which are presented in Table 2.

**Table 2.** Data from analyzed slabs

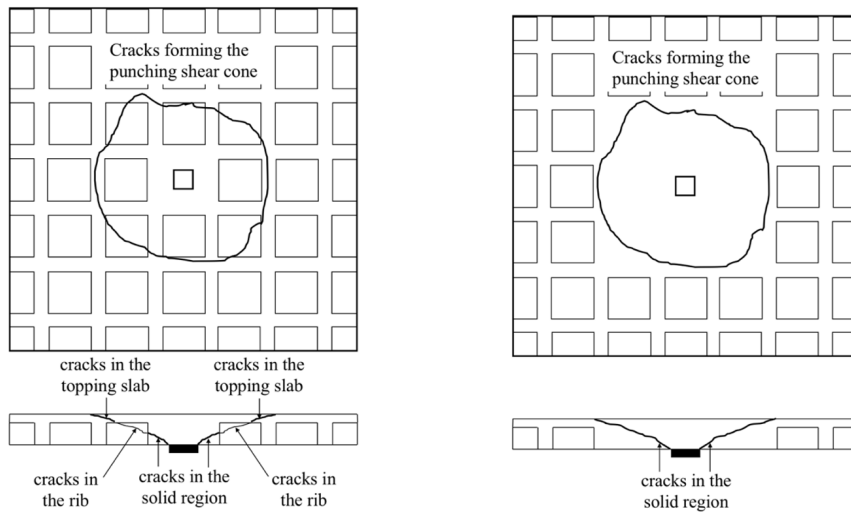
Slab	A <sub>s, Total</sub> (mm <sup>2</sup> )	A <sub>s, strip (c+6d)</sub> (mm <sup>2</sup> )	Empty, strip (c+6d) (mm <sup>2</sup> )	A <sub>c, strip (c+6d)</sub> (mm <sup>2</sup> )	ρ <sub>l</sub> (%)	Number of ribs converging with the solid area	
L1	2827	1376	72000	100800	1.36	8	
L2			36000	136800	1.01	12	
L3							16
L4			0	172800	0.80	20	
L5							24
L6			57600	115200	1.19	12	
L7			28800	144000	0.96	20	
L8							28
L9			0	172800	0.80	36	
L10							44
A <sub>s, strip (c+6d)</sub> is the cross section area of upper longitudinal steel distributed in a direction of the slab within the central strip (c + 6d); The area of concrete in the strip (c + 6d) is the area of concrete in this strip, discounting empties:				Average compressive strength of concrete: f <sub>c</sub> = 30 MPa; Steel yield stress: f <sub>y</sub> = 500 MPa;			
$A_{c, strip (c+6d)} = [(c+6d) \cdot d - \text{voids}]$				Square column width: c = 120 mm;			
The reinforced geometrical rate (ρ <sub>l</sub> ) for the central strip (c+6d), discounting voids:				Rib width: b = 60 mm;			
$\rho_l = A_{s, strip (c+6d)} / A_{c, strip (c+6d)}$				Effective depth: d = 160 mm;			
				Slab height: h = 180 mm.			

Table 3 shows the results of the slabs via computational analysis. For the waffle flat slabs L1 to L5, with ribs spaced each 300 mm, the slabs with smaller solid area (L1 and L2) failed with a much lower load than the others due to shearing of the ribs, while the slabs with greater solid area (L3, L4 and L5) failed by punching shear with very close loads. For the waffle flat slabs L6 to L10, with ribs spaced each 120 mm, the slab with smallest solid area (L6) failed with a much lower load than the others due to shearing of the ribs, while the slabs with greater solid area (L7, L8, L9 and L10) failed by punching shear with relatively close loads.

**Table 3.** Computational results and solid areas dimensions

Slab	L <sub>Solid Area</sub> (mm)	L <sub>Neg. Mom.</sub> (mm)	L <sub>Solid Area</sub> /L <sub>Neg. Mom.</sub>	V <sub>comp</sub> (kN)	Computational failure
L1	420	1600	0.26	220.0	Shear in the ribs
L2	780		0.49	392.0	
L3	1140		0.71	485.0	Punching Shear
L4	1500		0.94	478.0	
L5	1860		1.16	479.0	
L6	420		0.26	365.0	Shear in the ribs
L7	780		0.49	484.0	Punching Shear
L8	1140		0.71	459.0	
L9	1500		0.94	442.0	
L10	1860		1.16	439.0	

The occurrence of shear failures in the ribs in slabs L1, L2 and L6 was influenced by the formation of punching shear cones extending beyond the solid areas, unlike the other slabs that behaved as completely solid flat slabs (Figure 10).



**Figure 10.** Cracks forming the punching shear cone in waffle flat slab with smaller solid area and larger solid area

The shear on the ribs (Figure 11) for slabs L1, L2 and L6 show critical shear stresses (maximum and minimum) in the ribs, which caused failure by diagonal tension in the ribs with loads below the punching shear failure loads estimated by the design codes. The reduction in strength of slabs L1, L2 and L6 would not occur if the solid areas were larger.

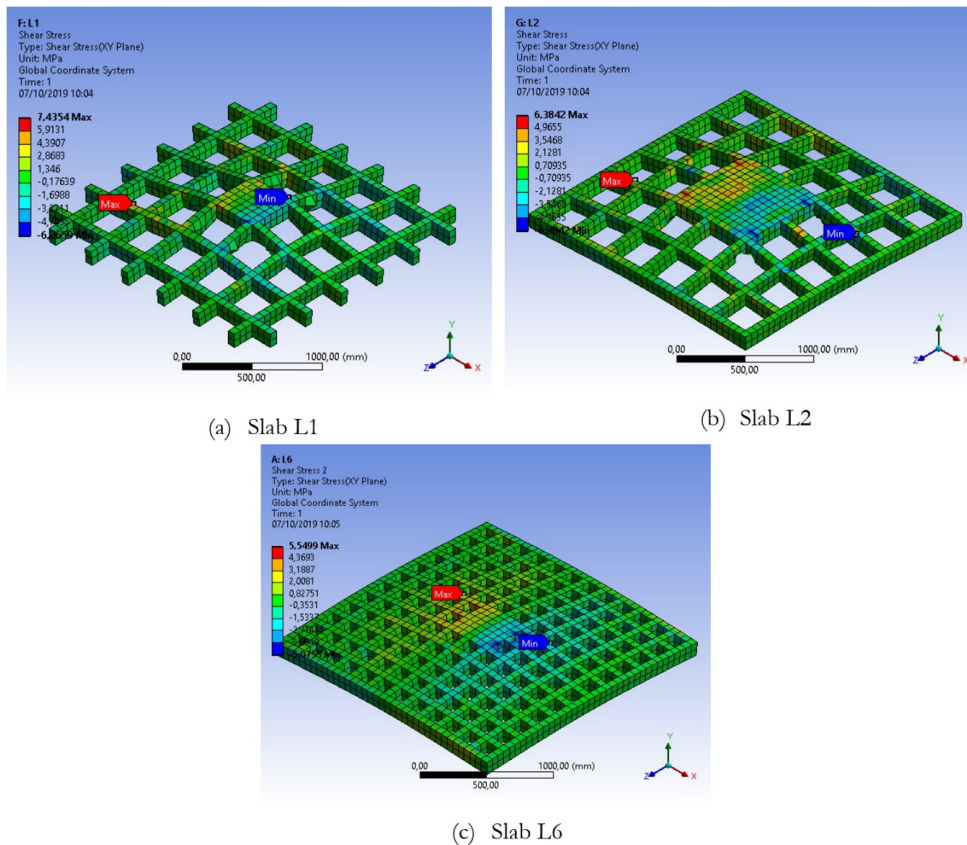


**Figure 11.** Shear stresses in the ribs of the slabs L1, L2 e L6

Figure 12 shows the load vs displacement curves for the slabs analyzed, deepening the critical evaluation of the variables through the range between maximum and minimum displacements recorded (a), as well as adding information on the yielding strains for ductility analysis (b). The slabs L1, L2, L3 and L4, with 300 mm internal spacing of the ribs, presented the greatest plastic strains before failure. From this first group of slabs, it is reasonable to consider that the ribs of the L5 slab had minimal influence on the general behavior, given that the location of the supports was coincident with the solid area limit, leading to a behavior similar to that of a solid slab.

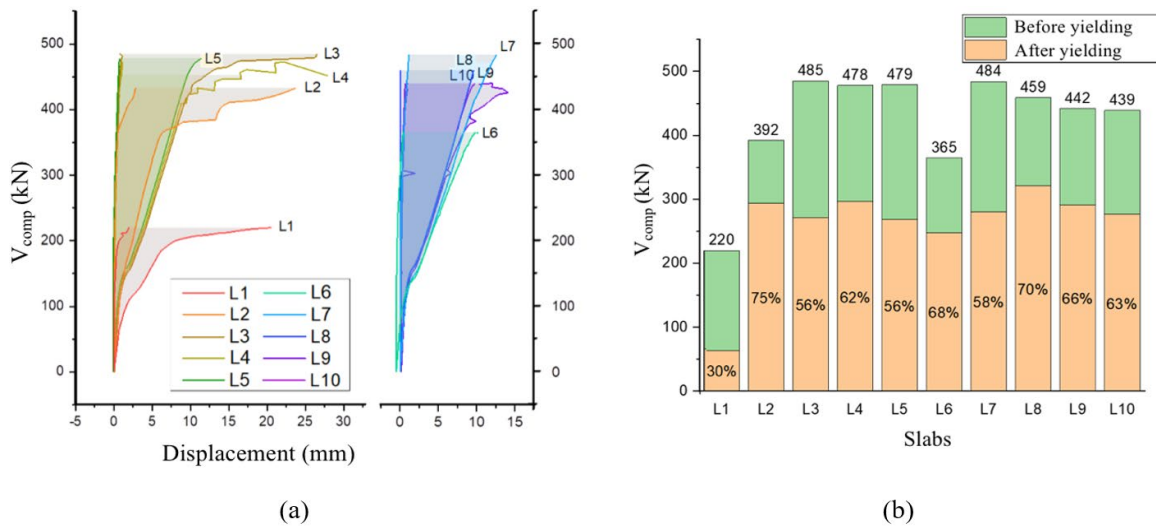


Figure 12. (a) Load x displacement curves and (b) Ductile behavior of the slabs

In these slabs, represented by warm colors, it was clear that, among all the slabs, L1 was the weaker. In terms of strength, the L2 slab had double the strength of L1, the range of maximum and minimum displacements has shown a similar trend. The L3 and L4 slabs deformed the most, and had similar magnitudes of strength and stiffness, although, apparently, L3 exhibited more stable behavior. As previously mentioned, the L5 slab had a more rigid behavior compared to the other slabs. Although slab L4 behaved in a similar way to slab L5 up to about 400 kN, for loadings close to failure, it deformed more reaching double the maximum displacement in amplitude. Slabs whose ribs were 120 mm internally spaced are represented by cool colors and reached less relevant values; L7 slab stands out slightly as the most ductile of the group, also having slightly higher bearing capacity than the others. The L6 slab experienced large displacement but it did not reach a strength comparable to the other slabs. Slab L8 was the stiffest slab among all slabs.

The L7, L9 and L10 slabs experienced similar minimum displacements, similar to those of the L5 slab, although it did not exceed it in relation to the maximum displacements. The behavior of the L10 slab was comparable to that of the L9 slab, both with regard to strength and stiffness, although it experienced greater maximum displacements. The L10 slab also behaved in a similar way to the L8 slab in terms of maximum displacement, but it had greater bearing capacity. This discussion confirms the grillage effect for slabs with shorter spacing between ribs, which allows a more uniform load distribution.

Considering the results of slabs L1 and L6, Figure 12 (b) shows that although the solid area has a predominant influence on the strength, when comparing the ductility of these models in relationship to the others, the quantity of ribs that reaches the solid area is of great importance to define the extension of it. For the models under analysis, the beginning of the reinforcement yielding is no longer proportional in slabs with a solid area with dimensions starting at 1140 mm, given as a reference of 15% of the span length, corroborated by the plateau in the bearing capacities and compatible with their stiffness. From such similarity in structural performance, the behavior of the waffle slabs with more advantageous solid areas is similar to that of solid slabs, without highlighting their effectiveness as a grid with movable supports at the intersections between ribs.

Tables 4, 5 and 6 contrast the strength of the slabs computationally estimated with the strength of the slabs estimated by the codes ACI 318 [7], Eurocode 2 [6] and NBR 6118 [5]. The computationally estimated failure loads were lower than the punching shear strength estimated by Eurocode 2 [6] and NBR 6118 [5] for slabs L1, L2 and L6. Indicating that the estimates by these codes, considering the waffle slab as if it were solid, lead to unconservative results.

Meanwhile, the estimates by ACI 318 [7], considering the waffle slab as if it were solid, were shown to be unconservative only for L1 slab.

**Table 4.** Computational and ACI 318 [7] results

Slab	$\rho$ (%)	$V_{comp}^{(A)}$ (kN)	$V_{ACI,p}^{(B)}$ (kN)	(A)/(B)	$V_{ACI,s}^{(C)}$ (kN)	(A)/(C)	Failure by ACI
L1	1.36	220.0		0.68	70.1	3.14	
L2	1.01	392.0		1.21	105.2	3.73	
L3		485.0		1.50	140.2	3.46	
L4	0.80	478.0		1.48	175.3	2.73	
L5		479.0	323.9		210.3	2.28	Shear in the ribs
L6	1.19	365.0		1.13	105.2	3.47	
L7	0.96	484.0		1.49	175.3	2.76	
L8		459.0		1.42	245.4	1.87	
L9	0.80	442.0		1.36	315.5	1.40	
L10		439.0			385.6	1.14	Punching Shear

**Table 5.** Computational and Eurocode 2 [6] results

Slab	$\rho$ (%)	$V_{comp}^{(A)}$ (kN)	$V_{EC,p}^{(B)}$ (kN)	(A)/(B)	$V_{EC,s}^{(C)}$ (kN)	(A)/(C)	Failure by EC
L1	1.36	220.0	494.4	0.44	95.3	2.31	
L2	1.01	392.0	446.6	0.88	129.1	3.04	
L3		485.0		1.17	159.2	3.05	
L4	0.80	478.0	413.1	1.16	199.0	2.40	
L5		479.0			238.8	2.01	Shear in the ribs
L6	1.19	365.0	472.9	0.77	136.7	2.67	
L7	0.96	484.0	439.0	1.10	211.5	2.29	
L8		459.0		1.11	278.7	1.65	
L9	0.80	442.0	413.1	1.07	358.3	1.23	
L10		439.0		1.06	437.90	1.00	Punching Shear

**Table 6.** Computational and NBR 6118 [5] results

Slab	$\rho$ (%)	$V_{comp}^{(A)}$ (kN)	$V_{NBR,p}^{(B)}$ (kN)	(A)/(B)	$V_{NBR,s}^{(C)}$ (kN)	(A)/(C)	Failure by NBR
L1	1.36	220.0	523.6	0.42	44.5	4.94	
L2	1.01	392.0	472.9	0.83	66.7	5.87	
L3		485.0		1.11	89.0	5.45	
L4	0.80	478.0	437.5	1.09	111.2	4.30	
L5		479.0		1.09	1335	3.59	Shear in the ribs
L6	1.19	365.0	500.8	0.73	66.7	5.47	
L7	0.96	484.0	464.9	1.04	111.2	4.35	
L8		459.0		1.05	155.7	2.95	
L9	0.80	442.0	437.5	1.01	200.2	2.21	
L10		439.0		1.00	244.7	1.79	

When compared to the estimated shear strengths of the ribs, only the L10 slab, via ACI 318 [7] and Eurocode 2 [6], failed by punching shear, indicating that the codes in general underestimate the ribs shear strength.

The waffle slabs with a greater solid area behaved like a completely solid flat slab and the codes estimates, regarding the punching shear, were reasonable. ACI 318 [7] was the one that presented the most conservative results and much greater than the computational results, while Eurocode 2 [6] and NBR 6118 [5] presented more assertive results. NBR 6118 [5], as it does not limit  $\xi$ , presented better results than Eurocode 2 [6]; mainly for slabs L7, L8, L9 and L10 with ribs spaced each 120 mm.

The rule of thumb, to consider 15% of the span to define the length of the solid area in the waffle flat slab would be equivalent to 71% of the negative bending moment of the analyzed slabs. Following this rule, the minimum size of 1136 mm ( $0.71 \cdot 1600 \text{ mm} = 1136 \text{ mm}$ ) would be indicated for the solid area of the analyzed waffle flat slabs. Thus, the slabs L3, L4, L5, L8, L9 and L10 would be conforming to this minimum value. In this way, the waffle flat slabs that conforming to this minimum size of solid area showed good results, compatible with the solid flat slab.

The finite element simulation allowed to clarify the effect of the parameters of variation of the solid area around a central column of waffle flat slabs, through the investigation of the change in failure mode. This discussion sought to warn that the use of punching shear formulations for solid flat slabs in waffle flat slabs can be extremely dangerous.

## 5 CONCLUSIONS

The conclusions of this work are limited only to the results of the 10 slabs analyzed here. Further analyses, computational and experimental, are necessary to validate these results. Thus, it can be concluded that:

- Waffle flat slabs with small solid areas had reduced strength compared to waffle flat slabs with larger solid areas;
- Waffle flat slabs with the largest solid areas behaved like solid flat slabs;
- Punching shear cones on waffle flat slabs with small solid areas exceeded these areas, causing shear failures by diagonal tension in the ribs of the slabs.
- Regarding the computational results, NBR 6118 [5] best estimated the punching shear results, while the ACI [7] had the worst estimation, being quite conservative.
- Still in relation to computational results, ACI [7], Eurocode 2 [6] and NBR 6118 [5] underestimate the shear strengths of the ribs of the waffle flat slabs.
- The practical rule for determining the solid area dimensions corresponding to 15% of the span length showed good results compared to the computational results.

## 6 ACKNOWLEDGMENTS

The authors would like to thank the Federal University of Pará (UFPA), the State University Vale do Acaraú (UVA) and the Federal University of Rio Grande (FURG) for the interaction for the development of this research.

## 7 REFERENCES

- [1] A. F. Al-Bayati, L. T. Leong, and L. A. Clark, "Concentric punching shear of waffle slab," *ACI Struct. J.*, vol. 112, no. 5, pp. 533–542, Aug 2015.
- [2] A. F. Al-Bayati, T. L. Lau, and L. A. Clark, "Eccentric punching shear of waffle slab," *ACI Struct. J.*, vol. 115, no. 1, pp. 163–174, Jan 2018.
- [3] C. Arunkumar, K. Saketh, S. S. Senthil, and T. M. Jeyashree, "Behaviour of punching shear in normal RC slab and waffle slab," *Asian J. Civ. Eng.*, vol. 19, no. 1, pp. 27–33, Jan 2018.
- [4] P. V. P. Sacramento, M. S. Picanço, and D. R. C. Oliveira, "“Lajes nervuradas de concreto armado com viga-faixa”, *RIEM - Rev. IBRACON Estrut. Mater.*, vol. 11, no. 5, pp. 981–996, Oct 2018. <http://dx.doi.org/10.1590/s1983-41952018000500005>.
- [5] Associação Brasileira de Normas Técnicas, *Design of Concrete Structures – Procedure*, NBR 6118, 2014.
- [6] European Committee for Standardization, *Design of Concrete Structures, Part 1, General Codes and Codes for Buildings*, Eurocode 2, 2010.
- [7] American Concrete Institute, *Building Code Requirements for Structural Concrete and Commentary*, ACI 318M-19, 2019.
- [8] N. G. B. Albuquerque and D. R. C. Oliveira, "Análise experimental de lajes lisas nervuradas de concreto armado com região maciça de geometria variável," in *An. 51º Congr. Bras. Concr.*, Oct., 2009, pp. 1-17.
- [9] ANSYS Inc., *ANSYS Composite PrepPost User's Guide, Release 15.0*, 2013.
- [10] ANSYS Inc., *ANSYS Mechanical APDL Material Reference, Release 15.0*, 2013.
- [11] K. J. Willam and E. P. Warnke, "Constitutive model for the triaxial behaviour of concrete", in *Proc. Int. Assoc. Bridge Struct. Eng.*, May, 1974, pp. 1-30.
- [12] Fédération Internationale du Béton, *fib Model Code for Concrete Structures 2010*, Model Code 2010, 2012.

---

**Author contributions:** RJCS: conceptualization, writing, methodology; DRCO: supervision; FESSJ: software; NGBA and FSL: formal analysis.

**Editors:** Fernando Fonseca, José Luiz Antunes de Oliveira e Sousa, Guilherme Aris Parsekian.



ORIGINAL ARTICLE

# Numerical analysis of the influence of block geometry on the behavior of piled foundations

*Análise numérica da influência da geometria do bloco no comportamento de fundações estacadas*

Jean Rodrigo Garcia<sup>a</sup> Paulo José Rocha de Albuquerque<sup>b</sup> <sup>a</sup>Universidade Federal de Uberlândia – UFU, Faculdade de Engenharia Civil, Uberlândia, MG, Brasil<sup>b</sup>Universidade de Campinas – UNICAMP, Faculdade de Engenharia Civil, Campinas, SP, Brasil

Received 23 March 2020

Accepted 25 May 2020

**Abstract:** In recent years, engineering has significantly increased the use of numerical modeling, mainly applied in studies of solutions and analysis of the behavior of the soil - structure and foundation element interaction. In this sense, this paper analyzes the behavior of blocks foundations made up of one, two, three and four piles with 25 cm in diameter (d) and 5 m in length (L) and with unusual spacing between the piles, equal to 5d in a three-dimensional finite element numerical model (MEF-3D). The results of the numerical analyzes demonstrated an average contribution of 36% due to the block-to-ground contact in relation to the total capacity of the system. The geometry of the block influences the response in terms of load capacity and stiffness of the foundation element. These results demonstrate an opportunity to reevaluate traditional calculation requirements, with the aim of rationalizing the design of foundations, thus improving the safety of the structural system.

**Keywords:** numerical analysis, block geometry, load-settlement curve, piled raft.

**Resumo:** Nos últimos anos, a engenharia tem aumentado significativamente o uso da modelagem numérica, principalmente aplicada em estudos de soluções e análise do comportamento da interação solo - estrutura e elemento de fundação. Nesse sentido, este trabalho analisa o comportamento de fundações de blocos constituídos por uma, duas, três e quatro estacas com 25 cm de diâmetro (d) e 5 m de comprimento (L) e com espaçamentos não usuais entre as estacas, igual a 5d em um modelo numérico de elemento finito tridimensional (MEF-3D). Os resultados das análises numéricas demonstraram uma contribuição média de 36% devido ao contato bloco-solo em relação à capacidade total do sistema. A geometria do bloco influencia a resposta em termos de capacidade de carga e rigidez do elemento de fundação. Estes resultados demonstram uma oportunidade de reavaliar os requisitos tradicionais de cálculo, com o objetivo de racionalizar o dimensionamento das fundações, melhorando assim a segurança do sistema estrutural.

**Palavras-chave:** análise numérica, geometria do bloco, curva carga vs recalque, radier estacado.

**How to cite:** J. R. Garcia and P. J. R. Albuquerque, “Numerical analysis of the influence of block geometry on the behavior of piled foundations,” *Rev. IBRACON Estrut. Mater.*, vol. 14, no. 1, e14107, 2021, <https://doi.org/10.1590/S1983-41952021000100007>

## 1 INTRODUCTION

The first studies that considered the contribution of the support capacity arising from the liquid area, between the piles, in piled foundations occurred in the 1950s, from the studies developed by Zeevart [1], Katzenbach and Reul [2], Burland et al. [3], Davis and Poulos [4]. The study of Katzenbach and Reul [2] is considered as one of the first to consider the contact of the piled foundation in the ground. Piled foundations contribute significantly to normalizing settlements [5], increasing the load capacity of the system and improving efficiency when compared to traditional foundations [6]–[9] in addition to reducing costs associated with the foundation [10]. Optimization occurs by reducing

Corresponding author: Jean Rodrigo Garcia. E-mail: [jean.garcia@ufu.br](mailto:jean.garcia@ufu.br)

Financial support: Fundação de Amparo à Pesquisa do Estado de São Paulo (grant nº 11/17959-3).

Conflict of interest: Nothing to declare.



This is an Open Access article distributed under the terms of the Creative Commons Attribution License, which permits unrestricted use, distribution, and reproduction in any medium, provided the original work is properly cited.

the required number of piles when the block contributes to this additional capacity [8], [5]. However, for a long time the contribution of the shallow foundation surface close to the soil was neglected, regardless of whether the block was in contact with the soil or not.

One of the main benefits of the contact block is to avoid the collapse of this foundation system., i.e., this contact causes an increase in the horizontal stress acting on the pile shaft, concomitantly with the stress effect caused by its action close to the ground [11]–[13]. The capacity gain of an unpiled and piled raft foundation was linearly dependent on the load distribution when embedded in a uniform soil [14]. The magnitude of the spacing influences greatly the development of the behavior of piled foundations (piled raft). According to Brand et al. [15] and Koizumi and Ito [16], the influence of the block is only significant for blocks with sufficiently spaced piles, from a spacing of three times the diameter of the piles, making the block-ground contact support about 20% of the ultimate load.

It is common for conventional foundation designs to consider that the entire design load is assumed by the piles, thus neglecting the contribution of the block-to-ground contact [7]. This traditional design approach (design approach based on load capacity, CBD) conflicts with the experimental results obtained by several authors [17]–[21]. For groups of piles with a small proportion of  $s/d$  spacing ( $\sim 3$  to  $4$ ) and which cover the entire block area, the percentage of the load supported by the block is not less than approximately 20%, and this value increases up to 60 – 70% with the increase in the  $s/d$  ratio [21].

There are several interactions that govern the behavior of pile foundations, such as those of (Figure 1): group dimensions, subsoil conditions, the method of installing the piles, the level of stresses applied, among other factors [22].

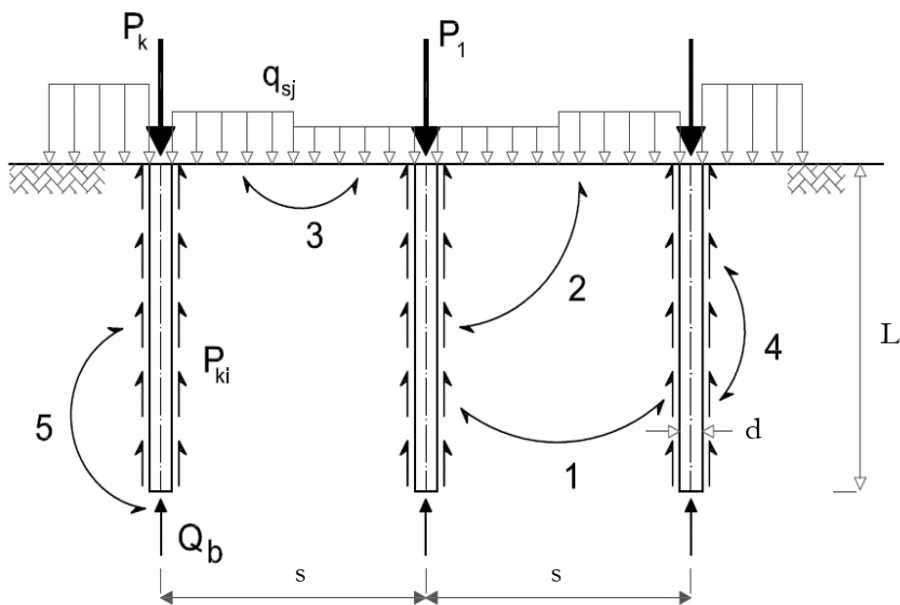
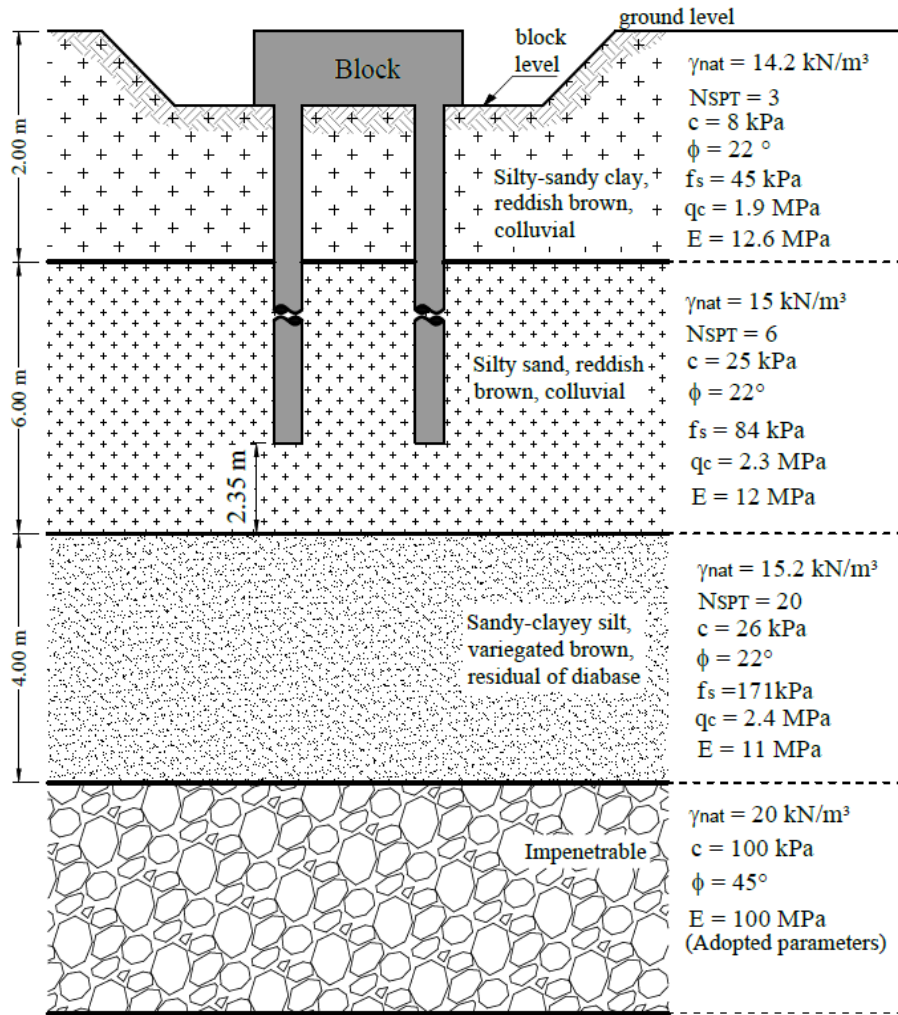


Figure 1. Different interactions that affect piled raft behavior [22]

Papers on the analysis of piled foundations using numerical models, based on three-dimensional finite elements [17], [23]–[25], can be found in the literature. The methods for analyzing the behavior of piled foundations are complex due to the large number of factors involved in the soil-pile block interaction [7] and [26].

## 2 STRUCTURAL AND GEOTECHNICAL CHARACTERIZATION

All the properties of the soil layers were obtained through in-situ and laboratory tests, as well as for the concrete of the piles and blocks (Figure 2 and Table 1). These parameters used of this study was obtained at Unicamp Experimental Site II, located the School of Civil Engineering, Architecture and Urban Planning (FEC) at Unicamp, Campinas, SP, Brazil. The crowning blocks were simulated with a height that results in a strut inclination angle between  $40^\circ$  and  $55^\circ$ , that is, rigid block (Figure 3).



**Figure 2.** Geological-geotechnical profile and position of the piled foundations, modified from Garcia and Albuquerque [27];  $\gamma_{nat}$  - Unit weight;  $N_{SPT}$  - Blow of SPT test; c - Cohesion;  $\phi$  - Friction angle;  $f_s$  - Sleeve friction;  $q_c$  - Tip resistance; E - Young's modulus.

The Young's modulus obtained for both concrete and steel were used to estimate the composite modulus.

$$E_{composite} = \frac{A_a \cdot E_a + A_c \cdot E_c}{A_a + A_c}$$

$A_a$  – Useful cross-sectional area of steel;  $E_a$  – Young's modulus of steel (MN/m<sup>2</sup>);  $A_c$  – Useful cross-sectional area of concrete;  $E_c$  – Young's modulus of concrete (MN/m<sup>2</sup>).

**Table 1.** Strength and strain parameters of concrete

Material	E	$\gamma$	$R_c$	$R_t$	$\nu$
	[MPa]	[kN/m <sup>3</sup> ]	[MPa]	[MPa]	[-]
Concrete	25,000	25.0	36.7	3.67	0.2

$R_c$ : Compression strength;  $R_t$ : Tensile strength; E: Young's Modulus

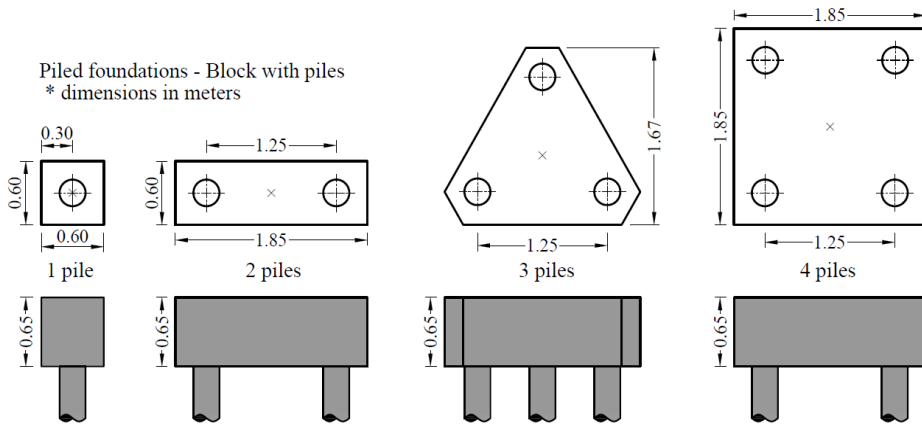


Figure 3. Plan view and elevation details of piled foundations [27]

### 3 NUMERICAL MODELING

The numerical model of the piled foundations analyzed was made from a quarter ( $\frac{1}{4}$ ) of the problem, due to the existing symmetry for the foundations composed of one, two, three and four piles (Figure 4, Figure 5, Figure 6 and Figure 7). For the analysis of the foundation made up of three piles, the constructed model represents half ( $\frac{1}{2}$ ) of the problem (Figure 6).

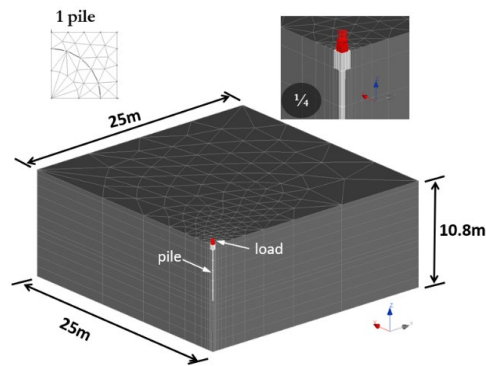


Figure 4. Perspective of the finite element mesh of the piled foundation with one pile [10]

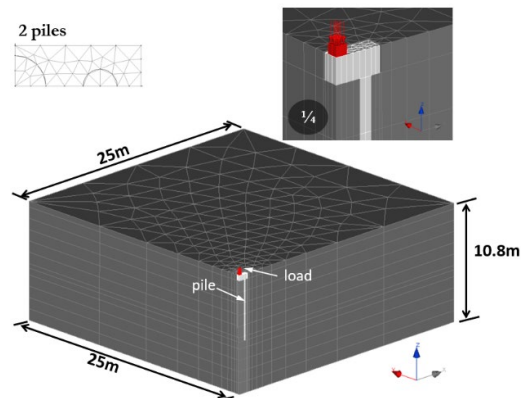


Figure 5. Perspective of the finite element mesh of the piled foundation with two piles [10]

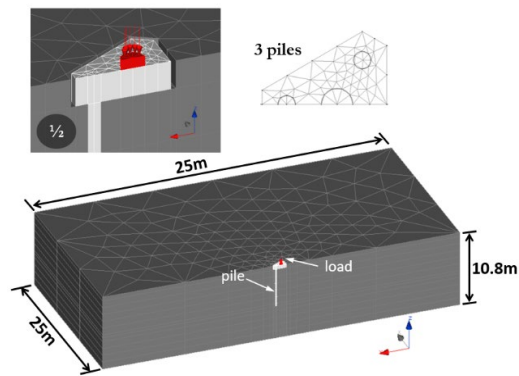


Figure 6. Perspective of the finite element mesh of the piled foundation with three piles [10]

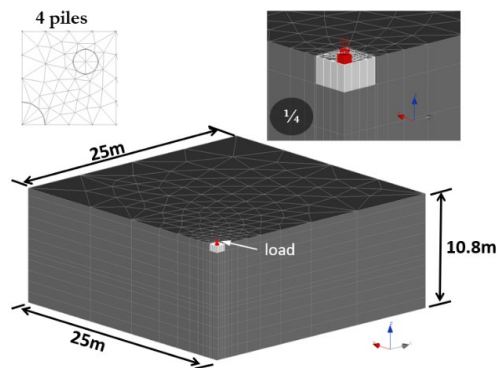


Figure 7. Perspective of the finite element mesh of the piled foundation with four piles [10]

The boundary conditions attributed to the model are important factors observed in several studies [28]–[32], among others. The dimensions adopted for the numerical model were assigned in order to ensure that the boundary conditions at the ends of the problem resulted in zero displacement, consequently, they did not affect the results of the analyzes with the foundation and soil element. Therefore, the limits of the numerical model were defined to minimize the influence of stresses on the limits of the problem. The sides of the model were fixed for horizontal movement ( $dx = 0$ ) and kept free in the vertical direction. The lower limit of the model was fixed against vertical and horizontal movements ( $dx = dy = 0$ ). Therefore, the geometry of the model was determined by means of convergence tests, which involve verifying whether the responses of the boundary conditions are in accordance with the boundary limits defined in the pre-processing step.

### 3.1 Constitutive model

The finite element mesh is composed of triangular elements of quadratic interpolation, which were extruded every meter in depth, resulting in a volumetric element of the pentahedral type composed of 15 nodes. Numerical analyzes were performed using the software LCPC-CESAR v.5.04, developed at the Laboratoire Central des Ponts et Chaussées. This software is a 3D Finite Element Method tool. The Mohr -Coulomb model, perfectly elastic-plastic, was used to simulate the nonlinear behavior of the soil in terms of stress-strain and adopted failure criteria: unit weight ( $\gamma$ ); cohesion ( $c$ ); friction angle ( $\phi$ ); Young's modulus ( $E$ ) and Poisson's ratio ( $\nu$ ). These parameters had been previously obtained by Gon [33], except for Poisson's ratio, which was adopted because of the soil behavior as assessed by the tests. For materials with brittle behavior, a linear elastic parabolic model was used, i.e., concrete of the piles and raft/block. These parameters were determined in the laboratory by Garcia [10], such as compression strength ( $R_c$ ),  $E_c$  and  $\nu_c$ , and values for tensile strength ( $R_t = 10\% \cdot R_c$ ) and  $\gamma_c$ .

### 3.2 Convergence test

The convergence test, which consists of verifying whether the boundary conditions provide results that are in accordance with the pre-established definitions, was performed in the preprocessing step to validate the half-space dimensions, i.e., the model geometry. Comparisons with available results were made to ensure the applicability of the program to the problems addressed in this study.

The dimensions of the model and the respective number of nodes and elements were checked. The evaluated geometries were: 10 x 10 m<sup>2</sup>, 15 x 15 m<sup>2</sup>, 20 x 20 m<sup>2</sup> and 25 x 25 m<sup>2</sup>. The boundary conditions imposed by the problem were verified at each simulation of the validation process, therefore the boundary conditions of the 25 x 25 m<sup>2</sup> mesh showed deformations of less than one tenth of a millimeter, as such these were considered insignificant for the type of problem under analysis.

The convergence tests resulted in a “block/raft” measuring 25 x 25 m<sup>2</sup> and 10.8 m deep. An elastoplastic model was used that varies according to the applied stresses, and thus follows a non-linear behavior.

The problem composition resulted (on average) in a finite element mesh comprising of 6,500 elements and 20,000 nodes.

In addition, analyzes were carried out to validate the model, tests of finite element mesh refinement. Thus, we analyzed the responses to the displacement at the edge compared to other forms of refinement, with lower density in terms of elements and nodes.

The refinement of the mesh, by increasing the density of the mesh of finite elements, caused the initially obtained displacement to increase in the successive stages until they were practically stable in the 3rd stage. Therefore, the option was to maintain the mesh with the same number of elements and nodes as in the previous phase (2nd stage), as there would be no improvement through further refinement of this mesh.

To ensure the reliability of the numerical analysis results, verifications have been performed before initiating the analyses: comparison with available published results, convergence test to ensure that the boundary conditions did not influence the analysis results and comparison of the soil parameters used in the analysis with the experimental results.

After completing the steps, the finite element model was calibrated by comparing the results of a load test on a single pile (L=5 m and  $\phi=0.25$  m) that was evaluated by Schulze [34] at the FEC-Unicamp experimental site for the same pile, using the properly adjusted soil parameters that were originally obtained by Gon [33]. The numerical analyses performed in this study were subdivided into two stages. The first stage was the calibration of the geotechnical parameters in the Mohr-Coulomb constitutive model. The second stage a comprised numerical analysis of the piled rafts.

## 4 RESULTS AND DISCUSSIONS

From the numerical simulations, load vs settlement curves of the piled foundations analyzed in this paper were obtained by use of the previously calibrated model (Figure 8). The behavior of the curves does not demonstrate the occurrence of failure of the foundation system. This is due to the contact effect of the block on the ground, which the behavior of this foundation to approach that of a shallow foundation, where failure is difficult to ascertain. In these cases, it is necessary to agree on the load failure, in order to obtain the allowable load that can be used in the design of foundations or in the verification of the supporting capacity of the foundation element in relation to the safety of the structure. In this aspect, the evaluation can be made of the degradation of the safety factor in relation to the maximum load (Q<sub>max</sub>), in such a way that displacement caused by the load of the respective stage and the resulting safety factor of this design condition can be evaluated together (Figure 9). In this type of result evaluation, displacement (settlement) tends to be the limiting factor in establishing the allowable design load, which depends on the characteristics of the superstructure.

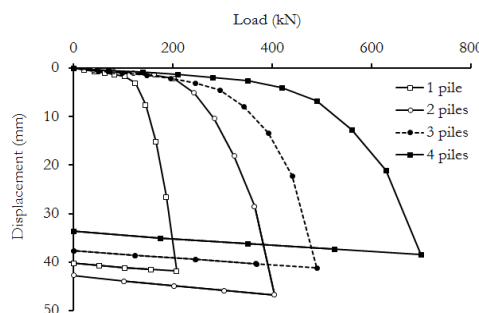


Figure 8. Results for load–displacement curve of piled foundations.

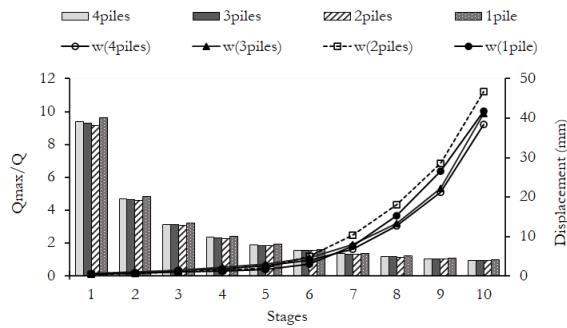


Figure 9. Variation of the  $Q_{max}/Q$  relationship by stage increment and displacement.

The ultimate load was then established by well-known criteria, the Van der Veen [35] method, the stiffness method [36] and the Eurocode criterion. The results of the load vs settlement curve for each of the numerically tested foundations were reprocessed by each of the methods mentioned, so that each of these methods generated a curve through retroanalysis. For the blocks of one pile, it was found that there existed less agreement between the curves in relation to the other pile blocks (Figure 10), since this type of foundation approaches the behavior of an isolated pile, due to the small net area of block-contact with the ground. The results of this analysis demonstrate that there is good agreement between the numerical results and those obtained by the Van der Veen and the stiffness method, mainly for blocks composed of two, three and four piles (Figure 11, Figure 12 and Figure 13).

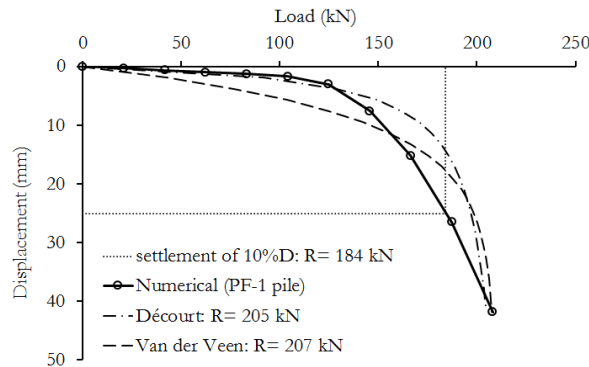


Figure 10. Extrapolation of the curve for the piled foundation using one pile.

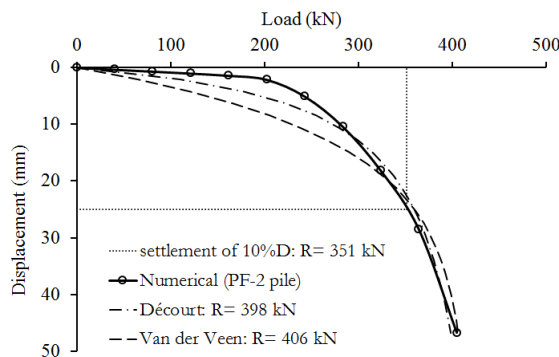


Figure 11. Extrapolation of the curve for the piled foundation using two piles.

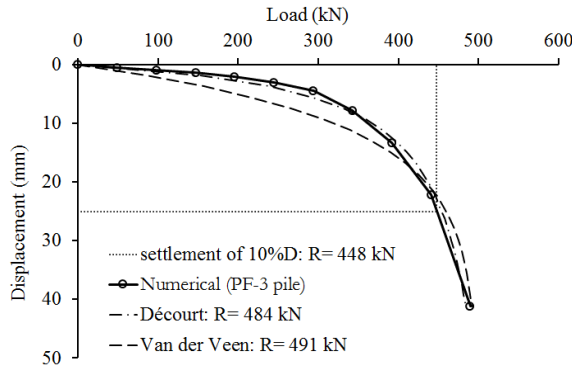


Figure 12. Extrapolation of the curve for the piled foundation using three piles.

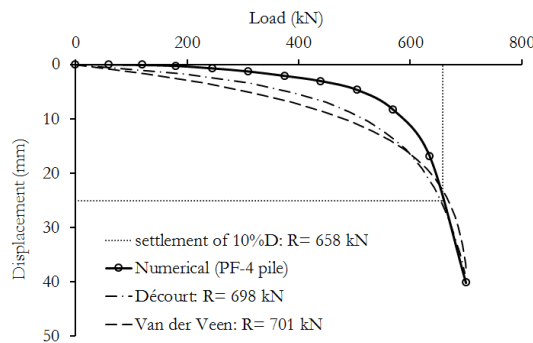


Figure 13. Extrapolation of the curve for the piled foundation using four piles.

Once the ultimate load was decided, due to the different extrapolation and displacement fixation criteria, the allowable load (for a safety factor of two [37]) of the pile foundations was obtained, consisting of one, two, three and four piles (Table 2).

Table 2. Extrapolated failure load (R), maximum settlement load (P<sub>max</sub>), load corresponding to the 10% settlement φ (P<sub>10%</sub>) and allowable foundation loads (P<sub>ai</sub>) via distinct failure criteria.

Piled Foundation	Van der Veen		Stiffness (Décourt)		10%·φ (Eurocode)	
	R (kN)	P <sub>ai</sub> (kN)	R (kN)	P <sub>ai</sub> (kN)	P <sub>10%</sub> (kN)	P <sub>ai</sub> (kN)
1 pile	207	103.5	205	102.5	184	92.0
2 piles	406	203.0	398	199.0	351	175.5
3 piles	491	245.5	484	242.0	448	224.0
4 piles	701	350.5	698	349.0	658	329.0

Although it is fundamental to understand the behavior of the foundation system, it is equally important to understand how load distribution occurs, since the behavior of foundations supported on piles and soil is analyzed. Therefore, the loads absorbed at the top of the piles in each foundation system were determined (Figure 14 and Figure 15). This compression measure was performed considering the average from a total of 16 points distributed in the cross section of each pile. Thus, it was possible to determine the load distribution between the surface and deep foundation elements, i.e., the load absorbed by the pile or pile group and the block-to-ground contact at each loading stage.

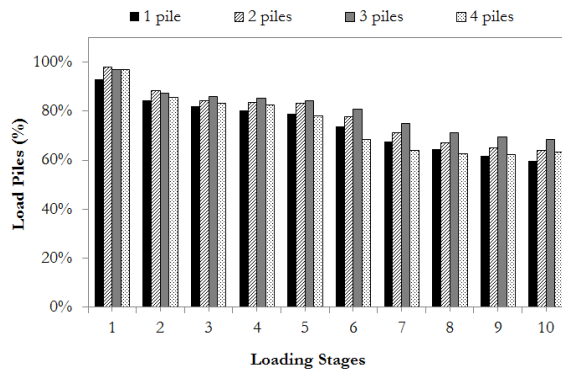


Figure 14. Load born by piles.

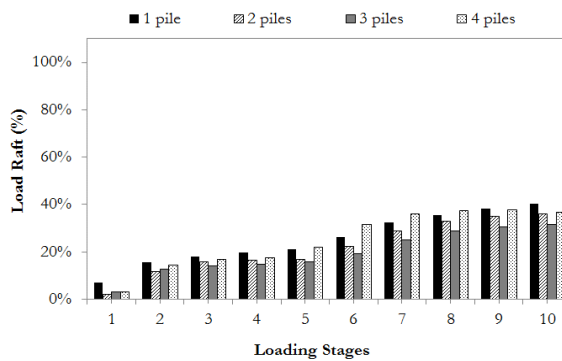


Figure 15. Load born by the shallow element.

The average load mobilized by the piles of the triangular block of three piles, is higher in practically all loading stages, mainly from the sixth loading stage, predominating up to the maximum test load (Figure 14). The increased compression of the block-to-ground contact does not seem to be as effective, due to its triangular geometry, and thus, a greater portion of load is observed acting on the piles. In blocks composed of two and four piles, there is a tendency toward an average load behavior in the piles, which remains more significant until the eighth stage, losing intensity until it is equalized in the maximum loading stage. On the other hand, the opposite behavior is observed for the average load that is absorbed by the block-ground contact, in which the three-pile block is the one with the lowest participation (Figure 15).

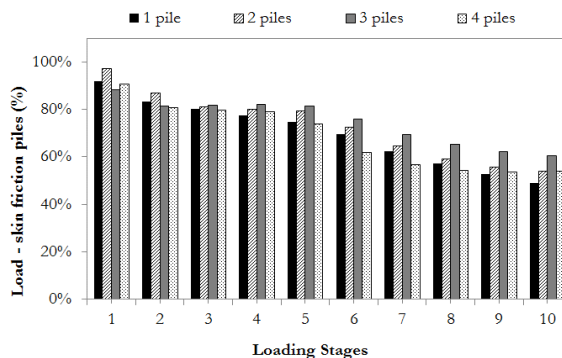


Figure 16. Load born by the skin friction.

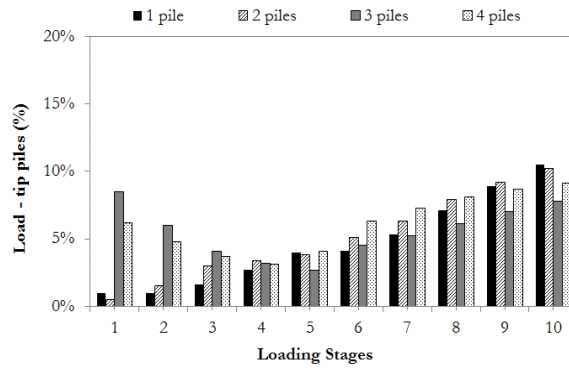


Figure 17. Load born by the tip of piles.

Through the transfer of the load from the top to the tip of the pile (Figure 16 and Figure 17), one notes that for blocks containing a group of piles, these somehow confine the soil between themselves (three and four piles). These also tend to mobilize greater tip resistance from the first stages of loading, which decreases until reaching the allowable load and then initiates an increase that continues until the maximum test load. The blocks of one and two piles, have low tip resistance in the first stages that gradually increases until the maximum test load. In all pile blocks, the skin friction resistance of the piles is higher in the first stages and decreases continuously with the increase of the tip resistance (Figure 17).

The difference in behavior of the foundation systems analyzed in this paper, may have been influenced by several factors, such as: the geometry of the block in contact with the underlying soil and the arrangement of the pile group (Figure 3). This could be explained by analyzing the initial stiffness of the load vs displacement curves separately. (Figure 18 to Figure 21). This seems to be related to the irregular geometry of the triangular block in contact with the ground, causing the increase in stresses not uniformly under the block, as well as in the other blocks.

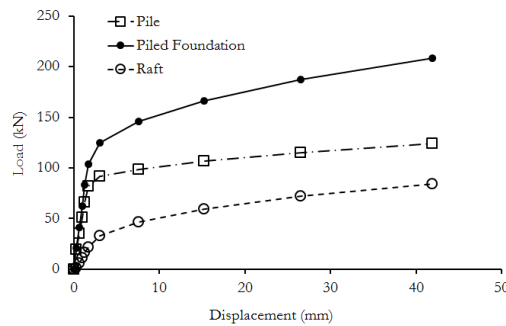


Figure 18. Load–displacement curve of piled foundation using one pile.

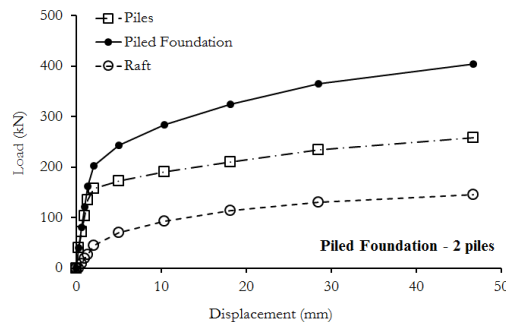


Figure 19. Load–displacement curve of piled foundation using two piles.

The stiffness of the piled foundation and the respective foundation elements (piles and block) were determined from the initial tangent of its load vs settlement curves (Table 3).

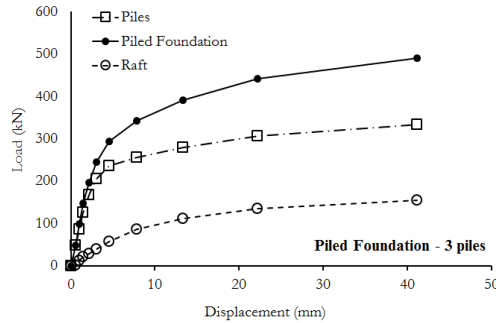


Figure 20. Load–displacement curve of piled foundation using three piles.

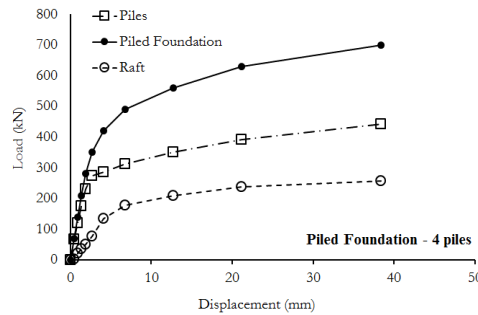


Figure 21. Load–displacement curve of piled foundation using four piles.

The obtained values of stiffness are higher for the foundation systems (piled foundation) in relation to the isolated elements (piles and blocks). The geometry of the surface foundation element (block) significantly influences the stiffness results, where the block composed of a pile is predominantly influenced by the pile stiffness and is very small when compared to the block, since its net area of block-soil contact is insignificant (Table 3). Similar behavior is observed in the block of four piles, where the stiffness of piles also predominates in relation to the block. In the case of two piles, the opposite occurs, since the block stiffness is greater than that of the piles, which may be justified by the resistant moment of this block. The block composed of three piles is the one that presents the most discrepant behavior in relation to the others and even though it is composed of several piles, the values of piles and block stiffness are low, as well as the system stiffness (Table 3). Regarding the stiffness of the foundation systems, there is a tendency to increase with the increase in the number of piles and the geometry of the block for all cases, except for the block containing three piles that do not follow this trend (Table 3 and Figure 22).

Table 3. Stiffness of piles ( $K_p$ ), rafts ( $K_r$ ) and piled foundations ( $K_{pr}$ ).

Piled Foundation	$K_p$ (kN/mm)	$K_r$ (kN/mm)	$K_{pr}$ (kN/mm)
1 pile	87	2	87
2 piles	90	142	169
3 piles	42	34	104
4 piles	116	69	283

From the results of the stiffness for the foundation system and the elements individually, trend lines were generated to find an equation that describes the behavior for the analyzed cases (Figure 22). From this analysis, we obtained the equations that describe the stiffness behavior of these foundations and their respective values of the determination

coefficient ( $R^2$ ), as presented on Table 4. In this analysis, the block composed of three piles showed the greatest discrepancy among all the cases analyzed, this is quite possibly due to the influence of the geometry of the block.

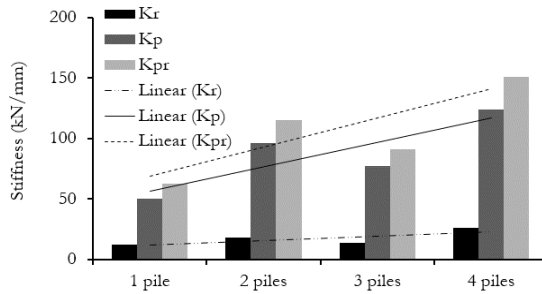


Figure 22. Results of stiffness for piles ( $K_p$ ), rafts ( $K_r$ ) and piled foundations ( $K_{pr}$ ).

When analyzing the stiffness results in a scenario with all piled foundations and removing the triangular shaped block, it is found that the equations start to represent, in a more adequate manner, the behavior due to the increase in the number of piles, since the  $R^2$  values increase significantly, remaining above 0.90 for blocks composed of 1, 2 and 4 piles (Table 4).

Table 4. Stiffness of piles ( $K_p$ ), rafts ( $K_r$ ) and piled rafts ( $K_{pr}$ ) depending on the number of piles.

Stiffness*	Piled foundation of 1, 2, 3 and 4 piles		Piled foundation of 1, 2, and 4 piles	
Raft	$K_r = 3.8 \cdot n + 8$	$R^2 = 0.63$	$K_r = 4.6 \cdot n + 8$	$R^2 = 0.99$
Pile(s)	$K_p = 20.3 \cdot n + 36$	$R^2 = 0.71$	$K_p = 23.1 \cdot n + 36$	$R^2 = 0.90$
Piled Raft	$K_{pr} = 24 \cdot n + 45$	$R^2 = 0.69$	$K_{pr} = 27.7 \cdot n + 45$	$R^2 = 0.92$

Where n is the number of piles. \*Values for guidance only, due to the small number of results.

For the adequate foundation design, it is necessary to establish the displacement that the structure may be subjected to, in order that the allowable settlement is the factor that determines the allowable design load, since the allowable load obtained for a safety factor restricts travel to levels acceptable by the superstructure. When analyzing the relationship between normalized displacement ( $w/D$ ) and normalized load ( $Q_{max}/Q$ ), it appears that for all piled foundations, limiting the settlement between 5% and 10% of the pile diameter, the maximum load which would define the permissible design load, is in the range between 0.73 and 0.93. This confirms that the foundation design must be carried out through the control of settlement and not by the load capacity (as noted by [5], [38], [8], [4]), as is usually the case (Figure 23). In an analysis in terms of the safety factor ( $\approx Q_{max}/Q$ ), it appears that this reduces from 2 to 1 for a settlement between 5% and 10% of the pile diameter, proving that the loss of safety and stability of the pile superstructure by the foundation support occurs for low displacement levels (Figure 23).

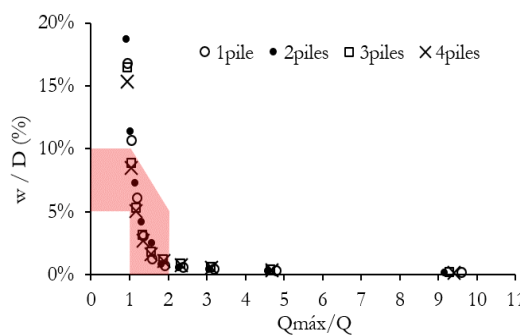


Figure 23. Mean normalized displacement and normalized load of the piled foundations.

The participation of piles in the load capacity of the piled foundation showed that the interaction factor ( $\alpha_{pr}$ ), influenced the load transfer model in the cases analyzed, either by the geometry of the block-ground contact or due to the magnitude of this area (Figure 24). The Figure 25, it is possible to evaluate the variation of the  $\alpha_{PR}$  according to the loading evolution.

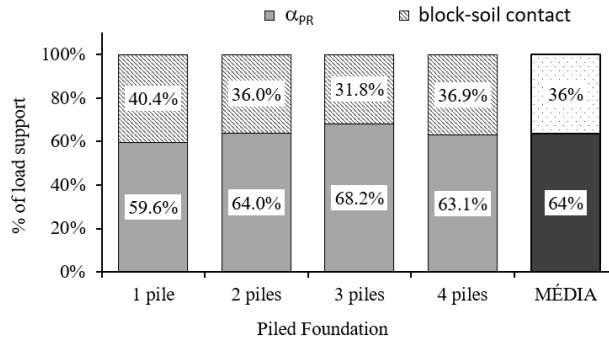


Figure 24. Contribution of piles group ( $\alpha_{PR}$ ) and raft–soil contact.

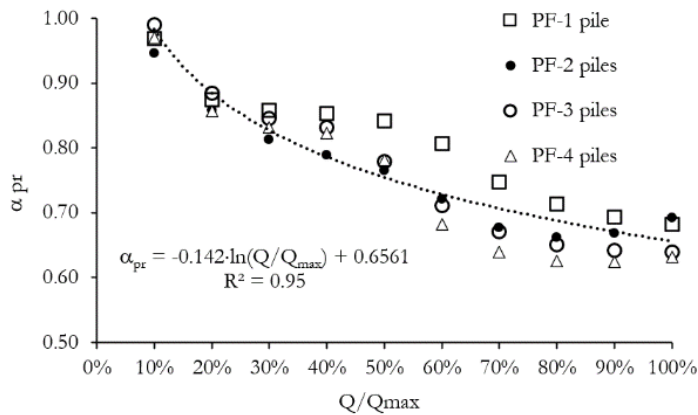


Figure 25. Variation of  $\alpha_{PR}$  and  $Q/Q_{max}$ .

The highest value of the observed interaction factor occurred in the pile block composed of three piles (68.2%), and the lowest, for the piled foundation composed of 1 pile (59.6%), with an overall average of 64%. The participation due to the block-to-ground contact was 36%, a value close to those observed in some works in the literature (Figure 24), as verified by Mandolini et al. [21].

The pile contribution to the load capacity of the piled raft can be seen in Figure 25. It is noted that at the beginning of the loading ( $Q/Q_{max} = 10\%$ ) the piles were responsible for receiving the entire load. During the loading, the raft increases to contribute to the load capacity, ending with an average of 36% (Figure 24). When the applied load represented half of the applied load ( $Q/Q_{max} = 50\%$ ), the raft was responsible, on average, for 25% of the load. In general, this effect is disregarded in foundation design, which can be interesting when evaluating the performance of the foundation in the structure. According to Brand et al. [15] and Koizumi and Ito [16], the influence of the block is only significant for blocks with sufficiently spaced piles, from a spacing of three times the diameter of the piles, making the block-ground contact support about 20% of the ultimate load.

## 5 CONCLUSIONS

Considering the analyses and discussions of this study, the following conclusions can be drawn:

The consideration of the block-to-ground contact effect can optimize the design of foundations with significantly positive impacts technically and economically, as the application of this technique allows one to take advantage of the

availability of the surface resistance of the soil adjacent to the block and between the group of piles, promoting greater stability and security of the structure.

Regarding the load capacity, it was found that the greatest relative difference occurred when analyzing the ultimate load given from ratio between the block composed by one pile and two piles, which showed an increase in strength of the order of 100%. Evaluating the ratio with blocks of three and four piles, there was an increase of 150% and 250%, respectively. In these sets, there is no direct relationship between ultimate load and number of piles in the block.

The modeling demonstrated that the contact effect in piled rafts, with pile spacing equal to  $5 \phi$  of average net area, accounts for 36% of the ultimate load applied to the piled raft, compared to 64% due pile load.

In the ultimate load, the piles showed frictional behavior with a tip load of around 10%. Behavior already expected in view of the subsoil resistance along the depth.

The stiffness of piled foundations must be analyzed from the perspective of reduced settlement values that the structure can support. It is also suggested which consideration, when designing the foundations, is given to the stiffness obtained by the initial tangent of the characteristic curves of these foundations. The suitable range for analyzing the capacity of the foundation system should be between 5% and 10% of the pile diameter.

The stiffness retroanalysis showed a good approximation considering all the cases analyzed (one pile, two piles, three piles and four piles) in this paper and according to the characteristics considered. When considering only piled foundations composed of 1 pile, 2 piles and 4 piles, the retroanalysis showed significantly important results with  $R^2$  above 0.9. However, the correlations presented in Table 4 was obtained for the foundation's geometry analyses (number of piles, diameter, length etc) and geotechnical profile for specific case this article.

## ACKNOWLEDGEMENTS

The authors would like to thank the São Paulo Research Foundation (Fundação de Amparo à Pesquisa no Estado de São Paulo – FAPESP), the National Council for Scientific and Technological Development (Conselho Nacional de Desenvolvimento Científico e Tecnológico - CNPq) and the Foundation for Research and Extension Support (Fundação de Apoio à Pesquisa e Extensão – FAEPEX - Unicamp) for the financial support necessary for research development.

## CITATIONS

- [1] L. Zeevart, "Compensated friction-pile foundation to reduce the settlement of buildings on highly compressible volcanic clay of Mexico City," in *Proc. 4th Int. Conf. Soil Mech. Found. Eng.*, 1957.
- [2] R. Katzenbach and O. Reul, "Design and performance of piled rafts," in *Proc. XIV Int. Conf. Soil Mech. Found. Eng.*, 1997, pp. 6–12.
- [3] J. B. Burland, B. B. Broms, and V. F. B. De Mello, "Behaviour of foundations and structures," in *Proc. IX ICSMFE*, 1977, pp. 495–545.
- [4] E. H. Davis and H. G. Poulos, "Rate of settlement under two-and three-dimensional conditions," *Geotechnique*, vol. 22, no. 1, pp. 95–114, Mar 1972.
- [5] M. F. Randolph, "Design Methods for pile groups and pile rafts," in *Proc. XIII Int. Conf. Soil Mech. Found. Eng.*, 1994, pp. 61–82.
- [6] M. M. Sales, *Behavior Analysis of Piled Rafts*. Brasília: Civ. Environ. Eng. Dep., Univ. Brasília, 2000.
- [7] H. G. Poulos, "Piled raft foundations: design and applications," *Geotechnique*, vol. 51, no. 2, pp. 95–113, Mar 2001.
- [8] J. E. Bezerra, "Estudo do comportamento de fundações em radier estaqueado: conceitos e aplicações," M.S. thesis, Univ. Brasília, Brasília, 2003.
- [9] P. Deb and S. K. Pal, "Analysis of load sharing response and prediction of interaction behaviour in piled raft foundation," *Arab. J. Sci. Eng.*, vol. 44, no. 10, pp. 8527–8543, Oct 2019.
- [10] J. R. Garcia, "Análise experimental e numérica de radiers estaqueados executados em solo da região de Campinas/SP," Ph.D. dissertation, Univ. Est. Campinas, Campinas, 2015.
- [11] L. Phung, "Piled raft – a cost-effective foundation method for high-rises," *Geotech. Eng. J. SEAGS AGSSEA*, vol. 41, pp. 1–12, 2010.
- [12] M. Ottaviani, "Three-dimensional finite element analysis of vertically loaded pile groups," *Geotechnique*, vol. 25, no. 2, pp. 159–174, Jun 1975.
- [13] L. Jinli and Y. Zhenlong, "Comportement et problemes de calcul des groupes de pieux dans le limon," *Bull. Liaison Lab. Ponts Chaussees*, vol. 3, no. 160, pp. 21–35, 1989.
- [14] B. Sheil, "Numerical simulations of the reuse of piled raft foundations in clay," *Acta Geotech.*, vol. 12, no. 5, pp. 1047–1059, Oct 2017.
- [15] E. W. Brand, C. Muktabhant, and A. Taechathummarak, "Load tests on small foundation in soft clay," in *ASCE Conf. Perform. Earth and Earth Support. Struct.*, 1972, pp. 903–928.

- [16] Y. Koizumi and K. Ito, "Field tests with regard to pile driving and bearing capacity of piled foundations," *SOILS Found.*, vol. 7, no. 3, pp. 30–53, 1967.
- [17] A. Mandolini, "Design of piled raft foundations: practice and development," in *BAP IV, Int. Geotech. Semin. Deep Found. Bored and Auger Piles*, 2003, pp. 59–80.
- [18] G. Conte, A. Mandolini, and M. F. Randolph, "Centrifuge modelling to investigate the performance of piled rafts," in *BAP IV, Int. Geotech. Semin. Deep Found. Bored and Auger Piles*, 2003, pp. 359–366.
- [19] C. Viggiani, A. Mandolini, and G. Russo, "Piles and pile groups," in *Applied Soil Mechanics*, J. A. Hemsley, Ed., 1st ed. Hoboken, NJ, USA: John Wiley & Sons, 2012, pp. 286–331.
- [20] L. De Sanctis and A. Mandolini, "Bearing capacity of piled rafts on soft clay soils," *J. Geotech. Geoenviron. Eng.*, vol. 132, no. 12, pp. 1600–1610, 2006.
- [21] A. Mandolini, R. Di Laora, and Y. Mascarucci, "Rational design of piled raft," *Procedia Eng.*, vol. 57, pp. 45, 2013.
- [22] Y. El-Mossallamy and E. Franke, "Piled rafts: numerical modelling to simulate the behaviour of piled raft foundations," in *Design Applications of Raft Foundations*, J. A. Hemsley, Ed., Darmstadt, Germany, 1997.
- [23] L. de Sanctis and G. Russo, "Analysis and performance of piled rafts designed using innovative criteria," *J. Geotech. Geoenviron. Eng.*, vol. 134, no. 8, pp. 1118–1128, Aug 2008.
- [24] M. F. Randolph and O. Reul, "Piled rafts in overconsolidated clay: comparison of in situ measurements and numerical analyses," *Geotechnique*, vol. 53, no. 3, pp. 301–315, 2003.
- [25] O. Reul and M. F. Randolph, "Design strategies for piled rafts subjected to nonuniform vertical loading," *J. Geotech. Geoenviron. Eng.*, vol. 130, no. 1, pp. 1–13, Jan 2004.
- [26] J. Lee, Y. Kim, and S. Jeong, "Three-dimensional analysis of bearing behavior of piled raft on soft clay," *Comput. Geotech.*, vol. 37, no. 1–2, pp. 103–114, Jan 2010.
- [27] J. R. Garcia and P. J. R. Albuquerque, "Analysis of the contribution of the block-soil contact in piled foundations," *Lat. Am. J. Solids Struct.*, vol. 16, no. 6, pp. e211, 2019.
- [28] R. B. J. Brinkgreve, W. M. Swolfs, and E. Engine, *Plaxis User's Manual*. Rotterdam: Balkema, 2002.
- [29] J. Cho, J.-H. Lee, S. Jeong, and J. Lee, "The settlement behavior of piled raft in clay soils," *Ocean Eng.*, vol. 53, pp. 153–163, Oct 2012.
- [30] A. Alnuaim, H. Nagggar, and M. H. El Nagggar, "Performance of piled-raft system under axial load," in *Proc. 18th Int. Conf. Soil Mech. Geotech. Eng.*, 2013.
- [31] B. El-Garhy, A. A. Galil, A. F. Youssef, and M. A. Raia, "Behavior of raft on settlement reducing piles: Experimental model study," *J. Rock Mech. Geotech. Eng.*, vol. 5, no. 5, pp. 389–399, 2013.
- [32] Z. M. Omeman, "Load sharing of piled-raft foundations in sand subjected to vertical loads," Ph.D. dissertation, Concordia University, Montreal, 2012.
- [33] F. S. Gon, "Caracterização geotécnica através de ensaios de laboratório de um solo de diabásio da região de Campinas/SP," M.S. thesis, Fac. Eng. Civ. Arquit. Urban., Univ. Est. Campinas, Campinas, 2011.
- [34] T. Schulze, "Análise da capacidade de carga de estaca escavada instrumentada de pequeno diâmetro por meio de métodos semiempíricos," M.S. thesis, Univ. Est. Campinas, Campinas, 2013.
- [35] C. Van Der Veen, "Bearing capacity of a pile," in *Int. Conf. Soil Mech. Found. Eng.*, 1953, pp. 84–90.
- [36] L. Décourt, "Ruptura de fundações e coeficientes de segurança a luz do conceito de rigidez," in *An. XI COBRAMSEG*, 1998, pp. 1599–1606.
- [37] Associação Brasileira de Normas Técnicas, *Projeto e Execução de Fundações*, ABNT NBR 6122, 2019.
- [38] M. M. Sales, *Análise do Comportamento de Sapatas Estaqueadas*. Brasília: Univ. Brasília, 2000.

---

**Author contributions:** JRG: conceptualization, formal analysis, methodology, writing, review and supervision; PJRA: funding acquisition, supervision and review.

**Editors:** Fernando Fonseca, José Luiz Antunes de Oliveira e Sousa, Guilherme Aris Parsekian.



## ORIGINAL ARTICLE

# Numerical analysis of RC wall with opening and strengthened with CFRP

## *Análise numérica de parede de concreto armado com abertura e reforçada com CFRP*

Marcos Alves da Silva<sup>a</sup> Rafael Andrés Sanabria Díaz<sup>a</sup> Luiz Carlos de Almeida<sup>a</sup> Leandro Mouta Trautwein<sup>a</sup> <sup>a</sup>Universidade Estadual de Campinas – UNICAMP, Departamento de Estruturas, Campinas, SP, Brasil

Received 12 February 2020

Accepted 30 May 2020

**Abstract:** The present work simulates and analyzes numerically two one-way walls (OW) with a central unforeseen cut-out-opening, which were previously tested experimentally. The models are based in the Finite Element Method and consider nonlinear behavior of the concrete material, such as hardening/softening and fracture. The first wall model was analyzed without any type of strengthening whereas the second one was strengthened using externally bonded CFRP along the opening edges. The strengthening modeling process was discussed through three different approaches suitable for unidirectional CFRP wrap. Load results were presented with load-displacement and load-strain curves that evidenced the flexural behavior of these structures. The crack pattern and failure mode observed showed good agreement with reported literature. The CFRP strengthening presented a small influence in the load capacity for big opening size.

**Keywords:** strengthening, CFRP, concrete, opening, wall.

**Resumo:** O presente trabalho simula e analisa numericamente duas paredes de uma direção (UD) com abertura não prevista, as quais foram testadas previamente de forma experimental. Os modelos se baseiam no Método de Elementos Finitos e consideram o comportamento não linear do concreto, como o endurecimento/amolecimento e fratura. O primeiro modelo de parede foi analisado sem reforço estrutural, enquanto o segundo foi reforçado com PRFC colado externamente envolvendo a abertura. O processo de modelagem do reforço é discutido através de três diferentes abordagens que são adequadas a tecidos unidirecionais de PRFC. Os resultados de carga são apresentados em gráficos carga-deslocamento e carga-deformação que evidenciam o comportamento a flexão desses elementos. O padrão de fissuração e modo de ruptura observado mostra boa concordância com o reportado na literatura. O reforço com PRFC apresentou uma pequena influência na capacidade de carga para a maior abertura.

**Palavras-chave:** reforço, PRFC, concreto, abertura, parede.

**How to cite:** M. A. Silva, R. A. S. Díaz, L. C. Almeida, and L. M. Trautwein, “Numerical analysis of RC wall with opening and strengthened with CFRP,” *Rev. IBRACON Estrut. Mater.*, vol. 14, no. 1, e14108, 2021, <https://doi.org/10.1590/S1983-41952021000100008>

## 1 INTRODUCTION

Reinforced concrete structures are subjected to the creation of openings for different purposes. When this change in the element's continuity is foreseen on the original project, it is usually employed additional steel bars near the openings, intended to strengthen the structure. However, there are cases in which the openings are not anticipated. The cut-out openings are referred to the removal of both concrete and reinforcement after the wall was casted, thus limiting its strengthening possibility.

Corresponding author: Marcos Alves da Silva. E-mail: [marcosasilva@live.com](mailto:marcosasilva@live.com)

Financial support: Coordenação de Aperfeiçoamento de Pessoal de Nível Superior (CAPES).

Conflict of interest: Nothing to declare.



This is an Open Access article distributed under the terms of the Creative Commons Attribution License, which permits unrestricted use, distribution, and reproduction in any medium, provided the original work is properly cited.

In general, cut-out openings are a result of incompatibilities between projects (mechanical, electrical, and plumbing), construction faults and architectural modifications to adapt existing structures to the users' needs and current standards. According to Popescu et al. [1], in recent years, there has been increasing interest in enlarging spaces by connecting adjacent rooms through creating openings in existing solid walls.

Walls can be constructed with various support conditions that influence its deflected shape, crack pattern and strength when an axial load is applied. There are two wall types related to the support condition (see Figure 1). The panel can be restrained at the top and bottom only, behaving in one way (OW), or it can also have lateral side restrains, behaving in two-way (TW). Ho et al. [2] described OW walls as elements that deform along the loading direction showing a single curvature. In contrast, TW walls deform along with both the horizontal and vertical directions with double curvature, commonly encountered in core walls of high-rise buildings.

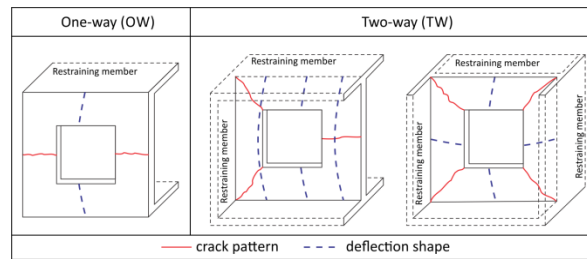


**Figure 1.** One-way and two-way behavior of axially loaded RC walls. Adapted from Popescu et al. [11].

The structural behavior of wall panels has been subject of numerous experimental and numerical studies. Saheb and Desayi [3] and Doh and Fragomeni [4] focused in provide more reliable and accurate wall design equations based in experimental tests. Robinson et al. [5] evaluated design methodologies applicable to pre-cast RC panels and concluded that current design equations underestimated the load capacity of slender RC walls. Fragomeni et al. [6] showed that the RC wall design equation given in the ACI 318 [7] code fails to recognize any contribution to load capacity from the side restrains in TW walls.

There are two main methods of designing reinforced concrete walls (RC walls) found in standards codes: (1) a simplified design method and (2) column-theory based method. The simplified methods are based on empirical formulations obtained through experimental tests and are found in CSA A23.3 [8]; AS 3600 [9]; ACI 318 [10]. Although the easy and direct application, this method lacks a more generalized scope once it results from experimental adjustments. The methods based in the column theory comprises a more refined calculation considering stress-strain compatibilities and the equilibrium of the element cross-section. The column-theory based method represents a viable alternative that provides more accurate results according to Popescu et al. [11] and can be found in ABNT NBR 16055 [12] and EN 1992 [13]. In the case of RC walls with cut-out opening, no straightforward methods to evaluate the ultimate capacity was found in standards codes.

Saheb and Desayi [14] reported the first systematic study of concrete walls with openings, tested in OW and TW action that investigated the influence of various parameters on the ultimate load. In their study, the authors introduced Equation 1 to calculate the new load capacity  $P_{uoc}^c$  after the creation of an opening. This equation considers the position and size of an opening in the wall by means of the coefficient  $\alpha$ , which is obtained according Figure 2. The constants  $k_1$  and  $k_2$  advent from the linear adjustment of experimental results, whereas  $P_{uc}^c$  is the ultimate load of an identical panel without opening computed following the ACI318 [10].

$$P_{uoc}^c = (k_1 - k_2 \cdot \alpha) \cdot P_{uc}^c \tag{1}$$

Recent research has shown that the strength of these panels can decrease dramatically as a function of the size of the opening (Guan et al. [15]; Doh et al. [16], Popescu et al. [1]). Consequently, modifications have been made in empirical formulas to consider the presence of the opening that assumes a linear relationship between the reduction in the wall strength and the opening size.

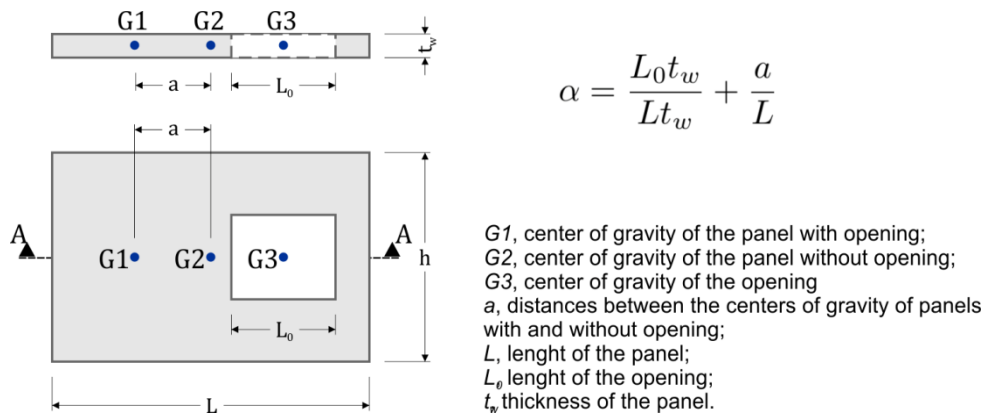


Figure 2. Opening parameter  $\alpha$  for the method proposed by Saheb and Desayi [14].

Strengthening methods have been employed to recover load capacity in cut-out opening walls. There are traditional methods to strengthen wall panels, such as increase element thickness and to create a frame around the opening using reinforced concrete [5]. The difficulty of execution associated with the materials weight and time consuming are the main disadvantages of these two methods. Carbon fiber reinforced polymers (CFRP) have presented as alternative strengthening material and become common in civil engineering as available rehabilitation method on several types of structures. Hansen et al. [17] highlight that CFRP advantages lie on the low weight to high strength ratio, good mechanical properties, and the easy application techniques.

Nowadays, we evidence a lack of procedures about how calculating the amount of CFRP needed to strengthen cut-out opening walls and predict its update load capacity. Enochsson et al. [18] introduced a rational method to obtain the CFRP cross-section area to strengthening RC walls with cut-out opening. The method was originally proposed to strengthen RC slab and is based on BBK04 [19] recommendations. However, it has been used in experimental studies of RC walls (Lima et al. [20], Mohammed et al. [21]).

Mohammed et al. [21] performed a series of experimental tests in OW wall panels to predict the ultimate load of strengthened walls. As the outcome of their research, the authors presented a formulation to predict the ultimate load adjusted to CFRP strengthened walls with opening. Additionally, they noted that when CFRP was placed on 45° at the opening corners, load capacity was higher than when it was placed along the opening corners. Also, the strengthening efficiency was reduced when the opening size increase.

Numerical studies have assisted in understanding the behavior of strengthened wall panels better. However, they considered a perfect rigid connection between concrete and CFRP. This paper presents different aspects of numerical modeling strengthening, considering the interface between materials. In addition, it contributes to showing the structural behavior of strengthened OW wall through load-displacement and load-strain curves. The developed models used as reference the experiments reported by Mohammed et al. [21].

## 2 EXPERIMENTAL

The studied RC walls were tested by Mohammed et al. [21] and their dimension was 800x400x40 mm (height:length:thickness), supported by two hinged steel plates with 20x400x40 mm located at its top and bottom edges. In the walls center was created an unforeseen cut-out-opening without additional reinforcement bars. Two tested specimens were identified by WO4a and WO4b (strengthened) in which the nomenclature refers to the opening size and the belonging wall series. One layer of reinforcement was placed centrally within the wall cross-section mainly to avoid offset creep and shrinkage effects in the concrete. It was composed of 5 mm diameter steel bars in each direction with a spacing of 60 mm. The average yield strength was 478 MPa and elastic modulus of 205 GPa.

In the wall WO4b, strengthening was provided by externally bonded (EB) CFRP unidirectional wrap bonded along the opening in both faces. The average value of concrete strength was measured at the age of testing the wall panels using cube specimens. For these walls, the concrete compressive strength was 19.73 MPa on WO4a and 18.83 MPa on WO4b. The cylinder compressive strength was assumed 80% of cube compressive strength. Tensile strength ( $f_t$ ) was estimated by the mean value of the three cylinder splitting tests and adopted equal 1.46 MPa. Modulus of elasticity ( $E$ ) and Poisson ( $\nu$ ) ratio of the concrete cylinder were 21 GPa and 0.21, respectively. The wall panels were tested using

one 30-ton hydraulic jack that transmitted a uniformly distributed load across the top support plate through a 20 mm diameter steel bar at an eccentricity of  $t/6$ .

Figure 3 illustrates the RC walls studied in this paper. The experimental tests provided the load capacity, crack pattern and failure mode of the wall panels. Full details of the reference models can be found in Mohammed et al. [21].

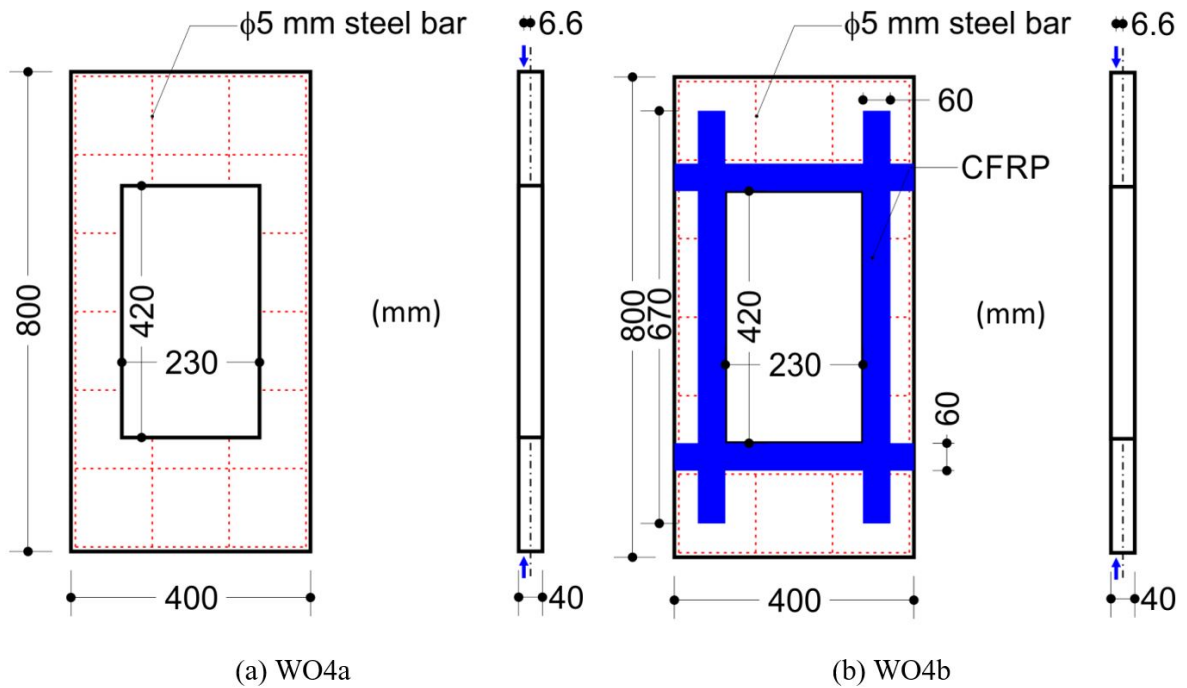


Figure 3. Dimensions, rebar layout and CFRP strengthening of the experimental RC walls.

### 3 NUMERICAL MODEL

The nonlinear finite element software ATENA Studio (version 5) and GiD (version 10) were used in the present study to investigate the behavior and ultimate strength of two RC wall structures. In these finite element programs, the constitutive relationships implemented can simulate the behavior of reinforced concrete structures, including cracking, crushing and reinforcement yielding. GiD was used as a pre-processor of the numerical simulation where the models were built and input files for ATENA were created. Afterward, post-processing analysis was carried out in ATENA, which provided deformed shape, stress and strain diagrams.

The present study is based on the two experimental wall panels: WO4a and WO4b (strengthened). Nomenclature adopted in the developed models was kept equal experimental, but information about the employed mesh type was added as suffix part.

Loading and support plates of 20 mm thickness and 400 mm width were modeled at the load application and reaction lines. Elements *CCIsoTetra* simulated the steel profiles employed to prevent premature failure due to high stress concentration in the concrete. Maximum element dimension was set 40 mm. Contact connection between plates and the concrete was considered perfect bond without the possibility of slip.

The wall geometry was equal to experimental and the model was divided into *CCIsoBrick* elements. This element combined with constitutive material allows for plastic deformation, cracking in three orthogonal directions, and crushing. The most important aspect of this element is the treatment of nonlinear material properties Pizzocchero [22].

Reinforcement was modeled as discrete elements (*CCIsoTruss*) positioned in the wall middle plane. The bars presented uniaxial behavior in their own direction governed by a bi-linear stress-strain curve with mechanical properties set equal to the experimental test. The bars diameter was 5 mm with average proof yield strength of 478 MPa and modulus of elasticity of 205 GPa. A perfect bond condition was considered between the concrete and the reinforcement, so dowel effect was neglected.

For the solution of the nonlinear iteration problem, an iterative Newton-Raphson method was chosen, where the load was applied incrementally. Convergence parameters used to obtain the solution for each load increment was set

1%, 1% and 0.01% corresponding to the displacement, residual force, and energy errors, respectively. A controlled vertical displacement (0.8 mm) was divided into load steps (100), which acted on an eccentric line in the top plate. Monitoring points measured displacements and strains at points of interest that are presented in the results.

Figure 4 illustrates a typical wall model and its boundaries conditions. These conditions and the loading scheme were imposed in accordance with the experimental test. The bottom plate had a support line that prevented  $z$  and  $y$  displacements and kept free rotation around the  $x$ -axis, whereas the top plate had a loading line that prevented  $z$  displacement. The positions of the loading line and bottom support line were set to match the eccentricity associated with the experimental tests.

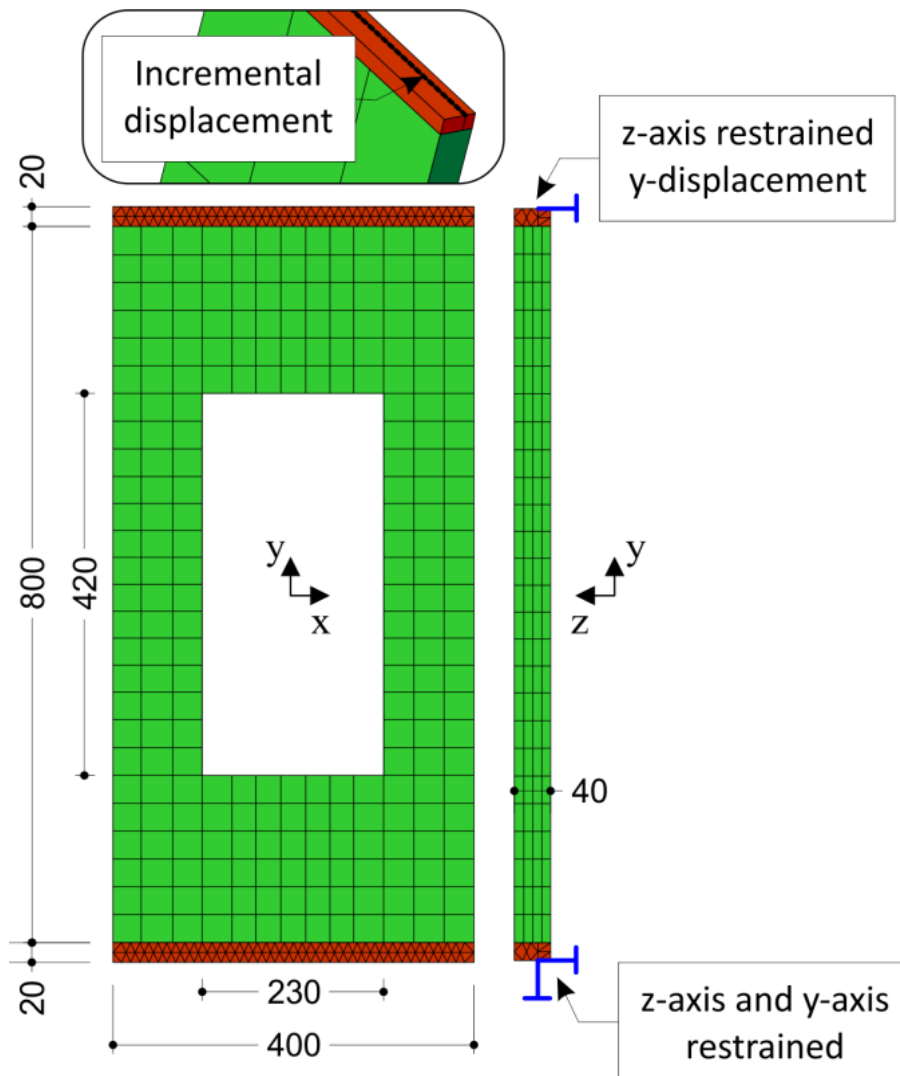
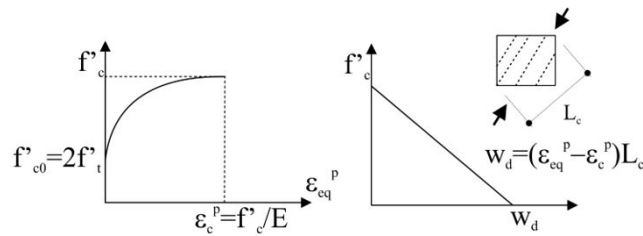


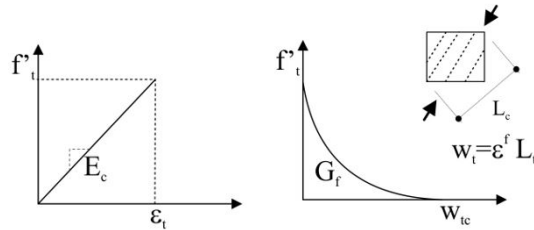
Figure 4. Typical model developed of OW wall.

The constitutive model that simulated the concrete was *CC3DNonLinCementitious2*, which is fully incremental and capable of reproducing material and geometrical nonlinearities, both considered. It combines constitutive models for tensile (fracturing) and compressive (plastic) behavior illustrated in Figure 5. The fracture model is based on the classical orthotropic smeared crack formulation and crack band model. It employs the Rankine failure criterion, exponential softening, and it can be used as rotated or fixed crack model. The hardening/softening plasticity model is based on Mentrey-Willam failure surface Cervenka et al. [23].

Some parameters that were not determined experimentally were calculated using the *fib* Model Code 2010 (2013) equations and GiD recommendations (see Table 1.) Basic parameters were maintained equal to experimental values.



(a) Compressive hardening/softening and compressive characteristic length. Based on experimental observations by VAN MIER



(b) Stress-Strain curve for concrete in tension

Figure 5. Fracture-plastic constitutive model of the concrete. Adapted from Cervenka et al. [23].

Table 1. Constitutive relation of the concrete material.

Basic	Compressive strength (MPa)	$f_c = -0.85 f_{cu}$
	Tensile strength (MPa)	$f_t = 0.3 f_c^{2/3}$
	Elastic modulus (MPa)	$E = 21500 (f_c/10)^{1/3}$
General	Onset nonlinear behavior (MPa)	$f_{c0} = -2.1 f_t$
	Plastic strain	$\epsilon_{cp} = f_c / E$
	Fracture energy (N/m)	$G_F = 73 f_c^{0.18}$
	Critical compressive displacement (mm)	$w_d = 0.5$
	Compressive strength reduction	$F_{c,red} = 0.8$

### 3.1 Mesh models

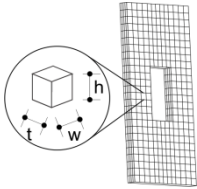
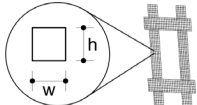
Initially, the concrete mesh was investigated on the non-strengthened wall (WO4a) using 12 different meshes that were divided into linear and quadratic groups, each one with six models with particular solid elements in the analysis. Linear group was discretized by *CCIsoBrick* elements of eight nodes, while quadratic group used the same elements but with 20 nodes. Six mesh configurations were tested in each group, which were named A (fine mesh) to F (coarse mesh). As an example, the model WO4a-F corresponds to the non-strengthened wall where mesh type F is adopted in the concrete.

Taking the WO4a-C model as reference, a second analysis was performed for the strengthened model (WO4b) using three different mesh types of mesh for the CFRP discretization, varying between meshes 1 (fine), 2 (medium) and 3 (coarse). As an example, the model WO4b-C2 indicates the strengthened wall where mesh type C is adopted in the concrete and mesh type 2 in the CFRP. Table 2 presents the geometric properties of the meshes analyzed.

The use of solid elements with linear approximations is susceptible to the so-called locking effect that arises mainly in bending-dominated situations and in the limit of incompressibility Reese et al. [24]. Thus, the developed models

used four elements along the wall thickness to reproduce properly the bending/buckling through vertical load and to reduce the locking effect.

**Table 2.** Finite element model meshes.

Element	Mesh type	$l_t$	$w$	$h$
	WO4a-A	10	10	10
	WO4a-B	10	20	20
	WO4a-C	10	30	30
	WO4a-D	10	40	40
	WO4a-E	10	50	50
	WO4a-F	10	60	60
	WO4b-C1	-	10	10
	WO4b-C2	-	20	20
	WO4b-C3	-	30	30

<sup>l</sup> finite element dimension in millimeter;  $t$ , thickness;  $w$ , width;  $h$ , height

### 3.2 Strengthening modeling

#### 3.2.1 CFRP

Three strengthening approaches were studied in this paper, all of them can represent the orthotropic nature of CFRP wrap with unidirectional fibers correctly. Experimental results were used to validate numerical models in terms of ultimate strength, crack pattern and failure mode. The ultimate strength represented the maximum load that the model was able to resist.

The first approach modeled CFRP as 2D membrane elements with composite material properties. This type of element works in-plane stress state and can reproduce compression and tension effects. However, it did not consider strengthening flexural stiffness. The material *CCCombinedMaterial* allows combining a brittle material with internal reinforcement. This is exactly the situation in the CFRP wrap, which consists of a brittle epoxy resin and a carbon fiber reinforcing net. The carbon fibers are considered as smeared, thus only its average effect is treated.

The second approach used 2D shell elements that accounts for the bending stiffness of CFRP wrap. Nevertheless, a major contribution of this effect was not expected due to the small thickness of the wrap (1mm). Epoxy resin can use the fracture-plastic material *CC3DNonLinCementitious2* as the basic shell material and the carbon fibers are included as special reinforcement layers. This approach requires the carbon fibers position, which in this case, was in the middle of the element thickness.

Finally, 3D shell elements were used to model CFRP. These elements are particularly useful for structures that combine solid 3D elements and shell elements because they do not imply any additional shell kinematic constraint that would harm an adjacent 3D solid element. They are designed for bent shells and to analyze these structures. They require far fewer finite elements compared to a similar analysis using standard hexahedral elements.

All the above cases need mechanical properties of epoxy resin and carbon fibers that may be difficult to find. Tables 3 and 4 contain the wrap parameters used in this paper. Some of them were found in manufacturer catalog Mapei [25] while others estimated according to Sajdlov [26].

#### 3.2.2 Interface

A possible failure mode of a reinforced concrete element strengthened in flexure with externally CFRP occurs in the boundary area between fiber and matrix, a so-called peeling failure, which causes the fiber to slip from the

surrounding matrix Taljsten [27]. In this case, it is necessary to include interface connection on strengthened models considered as contact volume with zero thickness.

**Table 3.** Mechanical properties of epoxy resin.

Epoxy resin			
$f_c$ (MPa)	65	$G_F$ (MN/m)	100
$f_t$ (MPa)	30	$\epsilon_{cp}$ (%)	0.084
$E$ (MPa)	2500	$f_{c0}$ (MPa)	40

**Table 4.** Mechanical properties of CFRP.

Epoxy resin			
$f_y$ (MPa)	4800	$\epsilon_{cu}$ (%)	2.1
$E$ (GPa)	230	$\rho$ (%)	0.167

The present work used *CCIsoGap* elements to simulate the interface between the concrete and the CFRP. The discretization of these elements required compatible finite element meshes, therefore the boundary surfaces (concrete/CFRP) need to have coincident nodes to make interface use possible. The strengthened models had elements with different mesh sizes at the interface edges. Thus, it was necessary to create an auxiliary surface with identical structure as the CFRP to match the nodes. A perfectly rigid connection was admitted between the concrete and this auxiliary surface while interface connected the auxiliary surface and the CFRP wrap. This procedure is illustrated in Figure 6.

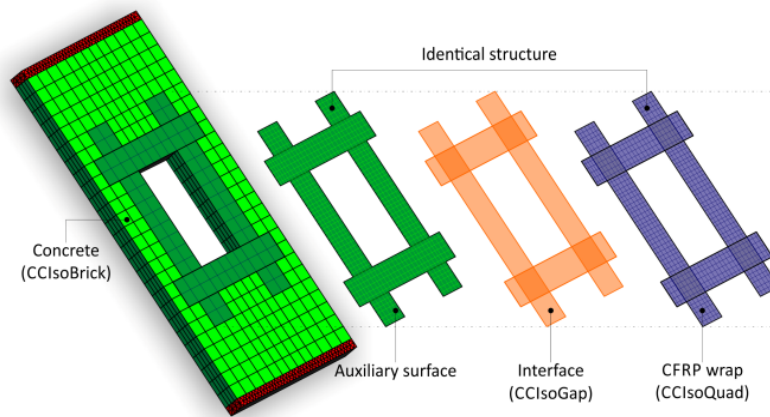


**Figure 6.** Strengthening process of the developed models.

The constitutive material for interface element (*CC3DInterface*) is illustrated in Figure 7, which is based on Mohr-Coulomb criterion with tension cut-off. The relation for a general two-dimensional case is given in terms of tractions on the interface planes, relative sliding and the opening displacements. Parameters as tensile strength ( $f_t$ ), shear cohesion ( $c$ ) and friction ( $m_u$ ) describe real physical properties and can be obtained by pull-off tests, single and double direct shear tests, among others. Otherwise, they may be estimated according to Sajdlov [26].

The coefficients  $K_{nn}$  and  $K_{tt}$  denote the initial elastic normal and shear stiffness, respectively. Normal and tangential stiffness can be estimated based on the stiffness of the adjacent finite elements. There are two additional stiffness values that need to be specified in the ATENA input denoted as  $K_{n,min}$  and  $K_{t,min}$  that are required for numerical purpose. These values are used only after the failure of the element to preserve the positive definiteness of the global system of equations. Theoretically, after the interface failure, the interface stiffness should be zero, which would mean that the global stiffness would become undefined. This minimal stiffness is recommended to be about 0.01-0.001 times the initial stiffness according to Gholamhoseini (2018). The values of interface parameters adopted in developed models are presented in Table 5.

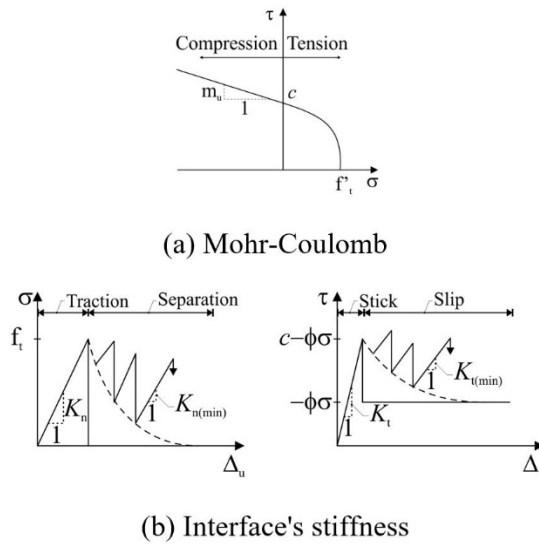


Figure 7. Constitutive model of interface element. Adapted from Gholamhoseini [28]

Table 5. Interface constitutive parameters.

Real	Cohesion, $c$ (MPa)		
			0.110
Numerical	Friction, $m_u$		0.300
	Tensile strength, $f_t$ (MPa)		0.370
	Normal stiffness, $K_n$ (MN/m <sup>3</sup> )		$7 \cdot 10^6$
	Tangential stiffness, $K_t$ (MN/m <sup>3</sup> )		$7 \cdot 10^6$
	Normal residual stiffness, $K_{n,min}$ (MN/m <sup>3</sup> )		$7 \cdot 10^4$
Tangential residual stiffness, $K_{t,min}$ (MN/m <sup>3</sup> )		$7 \cdot 10^4$	

## 4 RESULTS

### 4.1 Mesh sensitivity

Non-strengthened wall (WO4a): Table 6 presents a summary of the ultimate load obtained from the finite element mesh analysis ( $P_u^{num}$ ) and the comparison with ultimate experimental load ( $P_u^{exp}$ ) and theoretical prediction ( $P_{uoc}^c$ ) using Equation 1. The structural behavior was investigated through load-displacement and load-strain curves obtained from monitor points. Figure 8 shows the displacements and strain measured in linear (8-nodes) and quadratic (20-nodes) models before the ultimate load is reached.

Table 6. Ultimate loads obtained from non-strengthened models with 8 and 20 nodes elements.

Model	8-nodes element			20-nodes element		
	$P_u^{num}$ (kN)	$\frac{P_u^{num}}{P_u^{exp}}$	$\frac{P_u^{num}}{P_{uoc}^c}$	$P_u^{num}$ (kN)	$\frac{P_u^{num}}{P_u^{exp}}$	$\frac{P_u^{num}}{P_{uoc}^c}$
WO4a-A	53.44	0.73	1.01	49.93	0.68	0.94
WO4a-B	55.21	0.75	1.04	49.18	0.67	0.93
WO4a-C	57.53	0.78	1.08	48.63	0.66	0.92
WO4a-D	59.78	0.81	1.13	48.32	0.66	0.91
WO4a-E	64.33	0.87	1.21	47.83	0.65	0.90
WO4a-F	68.25	0.93	1.28	47.66	0.65	0.90
Mean	59.75	0.81	1.13	48.59	0.66	0.92
Std. dev.	5.62	0.08	0.11	0.85	0.01	0.02

$P_u^{exp} = 73.7 \text{ kN}$  ;  $P_{uoc}^c = 53.1 \text{ kN}$  , calculated according Equation 1.

It is noted in Table 6 linear elements had load capacity ranged between 73% and 93% of experimental results. However, when the numerical result was compared with theoretical, computed with Equation 1, the ratio of the ultimate loads was non-conservative and varied between 1% and 28%. In general, linear models also obtained higher loads when compared with quadratic elements models. Model type WO4a-F (coarse mesh) was the one which most fitted experimental result and achieved 68.25 kN. Besides that, ultimate load increased proportionally to element dimension in linear models. Figure 8a shown finer meshes had the out-of-plane displacement (D1) increased which resulted in less stiffness models. On the other hand, coarser meshes presented a brittle behavior caused by the crack opening inside the element. Due to high mesh dependence obtained, linear models (8-nodes elements) were dismissed for the other analyses.

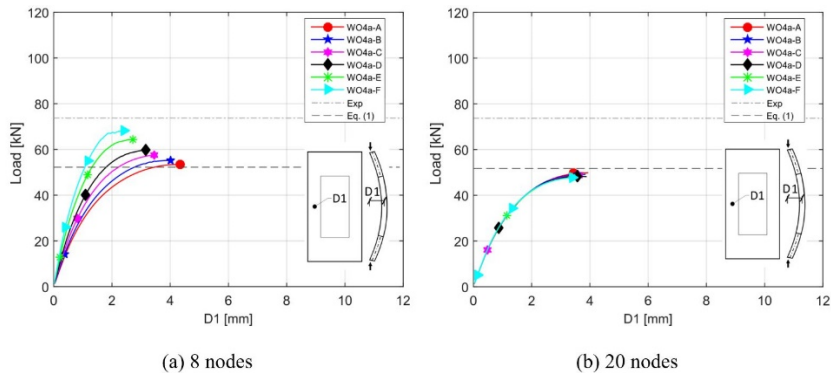


Figure 8. Out-of-plane displacement of non-strengthened models for different mesh sizes.

Quadratic models (20-nodes) presented low dependence of the element discretization on the structural behavior. The ultimate loads of the numerical models were practically constant and ranged 65-68% of experimental. Furthermore, the numerical models' results showed reasonable agreement with theoretical load (Equation 1), in which the ratios varied between 90-94%. The behavior was different of linear group because the fine mesh (WO4a-A) obtained higher capacity.

Despite of the lack of experimental data regarding the stiffness of the wall in Mohammed et al. [21] and Mohammed et al. [31], the out-of-plane displacement (D1) of the numerical models was approximately 4 mm and all models showed similar stiffness (Figure 8b). The mesh type of WO4a-C with quadratic elements was chosen for the strengthened models analysis, when considering the reasonable agreement between the ultimate load of numerical models and theoretical prediction, and also the crack pattern by the time ultimate load was reached in the numerical models.

The Table 7 presents the load results of strengthened models (WO4b). CFRP mesh discretization did not cause a significant influence on model strength. It was possible to have a better understanding of stress and strain distribution on CFRP when fine mesh type WO4b-C1 was used, provided by the elevated number of elements. Besides that, the computational cost, in this case, was significantly increased and took approximately four hours to complete analysis, whereas coarse mesh consumed a few minutes. The coarse mesh WO4b-C3, however, violated conditional break criteria of force equilibrium when modeled with membrane and 3D shell elements. The ultimate load remained among 61-63% of experimental. Lima et al. [29] obtained similar results (64%) using software ABAQUS, however, the authors used a perfectly rigid connection instead of interface elements in contact with concrete/CFRP.

Table 7. Ultimate load results of the three approaches used to model CFRP strengthening.

Model	Membrane	2D shell	3D shell
	$P_{uo}^{num} (kN)$	$P_{uo}^{num} (kN)$	$P_{uo}^{num} (kN)$
WO4b-C1	51.73	50.15	50.23
WO4b-C2	51.51	50.17	50.15
WO4b-C3	35.98	50.17	50.27

<sup>2</sup> $P_{uo}^{exp} = 82 \text{ kN}$

Figure 9 shows the load-strain curve of different approaches used to simulate strengthening. Monitoring points G1, G2 and G3 used to record strain were placed 5 mm inside the wall to avoid interference with external CFRP. In general, all strengthened models presented similar behavior and load capacity. Monitor G1 recorded the horizontal strain in the opening middle span. Figure 9a shows the load interval (30-35 kN) where two vertical cracks appeared near the opening edges and caused a reduction of the horizontal tension strain. Monitors G2 and G3 were fixed at the same localization but on opposite faces of the wall, in a way that one should be in tension and the other in compression, respectively. The vertical strain recorded by these two monitors are presented in Figure 9b and 9c. It is possible to note that, by the time the ultimate load was reached, the horizontal cross-section of 3D shell model was predominantly compressed. The G2 monitor of 3D shell model showed 0.07 tension strain which is small when compared with the membrane and 2D shell models, 0.20 and 0.30, of tension strain, respectively. Hence, the compression in the 3D shell model was higher than in the other two models and the neutral axis was near the tension face, which could be explained by the admission of the flexural stiffness of these elements. The G3 monitor showed that when the ultimate load was reached, the maximum compression strain was 0.15%; thus, the concrete did not crushed at this point.

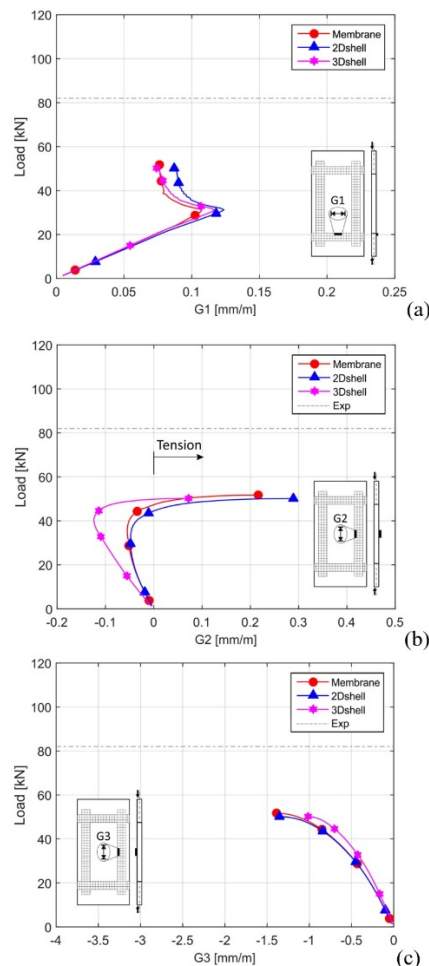
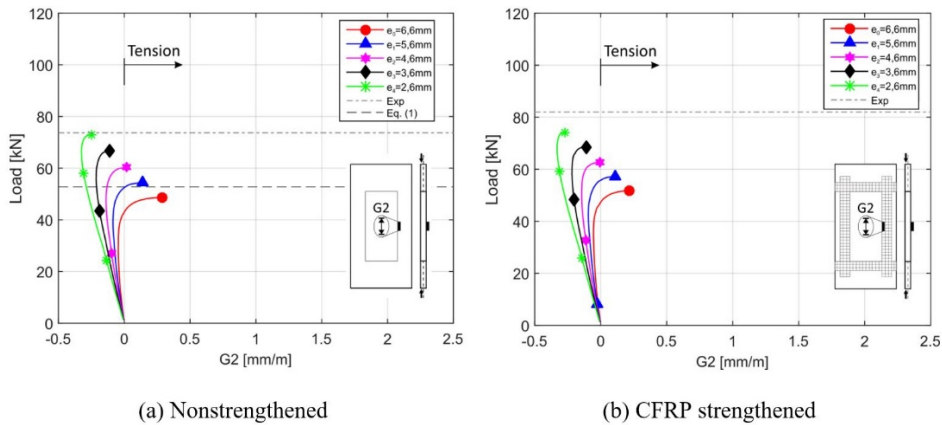


Figure 9. Load-strain behavior of strengthened models.

#### 4.2 Assessment of eccentricity in the ultimate load

The load eccentricity has a significant influence on the strength capacity of RC walls affecting the ultimate load and failure mode (ElMetwally et al. [30], Doh and Fragomeni [4]). Experimental tests reproduced in this paper handled eccentricity in the order of millimeters, which may be difficult to control. Using its experimental value (6.66 mm), the developed models obtained the ultimate loads presented in Tables 6 and 7. These results were lower than ones in experimental tests, therefore a parametric study was made with varying load eccentricity to investigate its influence on load capacity.

New numerical models were executed, varying the load eccentricity of WO4a-C and WO4b-C1 (CFRP strengthened, membrane elements). The eccentricity was varied from 2.6 mm to 6.6 mm (experimental), with increments of one millimeter. The load-strain behavior of these models is presented in Figure 10.



(a) Nonstrengthened (b) CFRP strengthened

**Figure 10.** Effect of eccentricity on the structural behavior of the models.

As the loading line approximates the wall middle-plane, compression overcomes flexural behavior in models with and without CFRP strengthening. In the present work, the eccentricity  $e_2$  (4,6mm) was the limit in which, below it, the cross-section was entirely compressed at ultimate load.

The best fit of ultimate load (99% of experimental) occurred when eccentricity was equal to 2.6 mm ( $e_4$ ), which means 4 millimeters change of experimental report. Thus, the horizontal cross-section in the wall center was entirely compressed for small eccentricity ( $e_4=2.6$  and  $e_3=3.6$  mm) and showed also tensile strain for larger eccentricity ( $e_1=5.6$  and  $e_2=6.6$  mm) (see Figure 10).

To investigate the divergence in the final load, an analytical approach based on ultimate limit state was applied. The two column strips were joined, and the resulting cross-section used to evaluate the resistance of the wall WO4a. It was assumed that the resulting cross-section is mostly subjected to the normal force and uniaxial bending. Thus, a moment-force interaction diagram (see Figure 11) was constructed with the resistances of the materials obtained in the tests and a parabolic-rectangular for stress concrete distribution in compression. In addition, Figure 11 shows the bending moment due to the numerical ultimate load ( $P_u^{num}$ ) considering the initial eccentricity 6.6mm (1st order effect) and the deflection D1 (2nd order effect); and also the rupture point that occurred in the post-peak. Despite the ultimate load and the bending moment due to the 2nd order effect is near the cross-section's strength limit, the numerical model did not fail at this point. The collapse of the numerical wall model happened due to concrete crushing without yielding of the rebars at the post-peak regime. Therefore, it shows that the numerical model agrees with the analytical results.

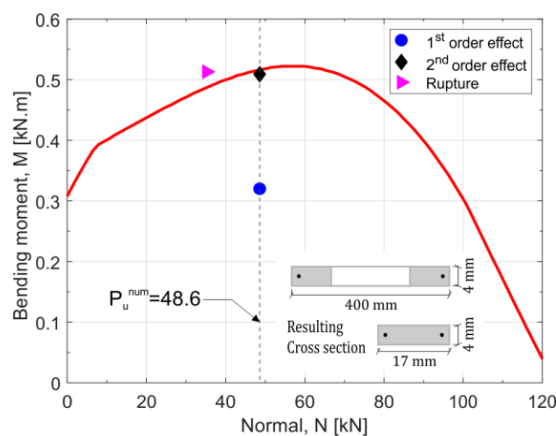
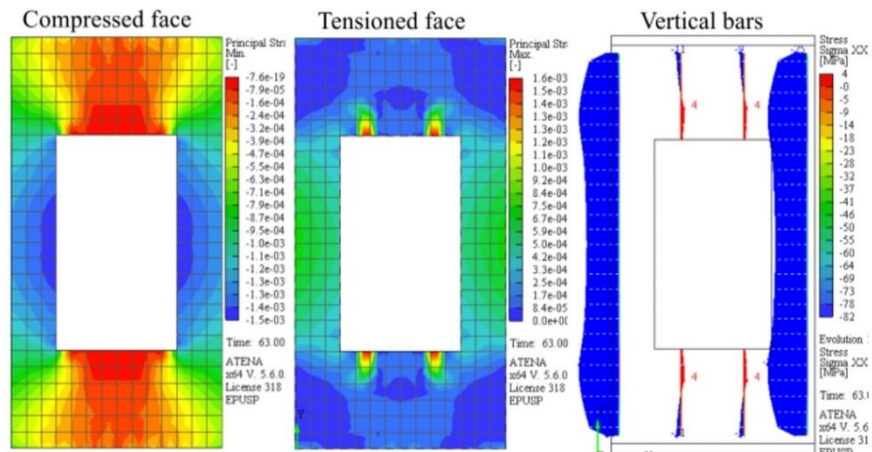


**Figure 11.** Cross section strength in the column strips.

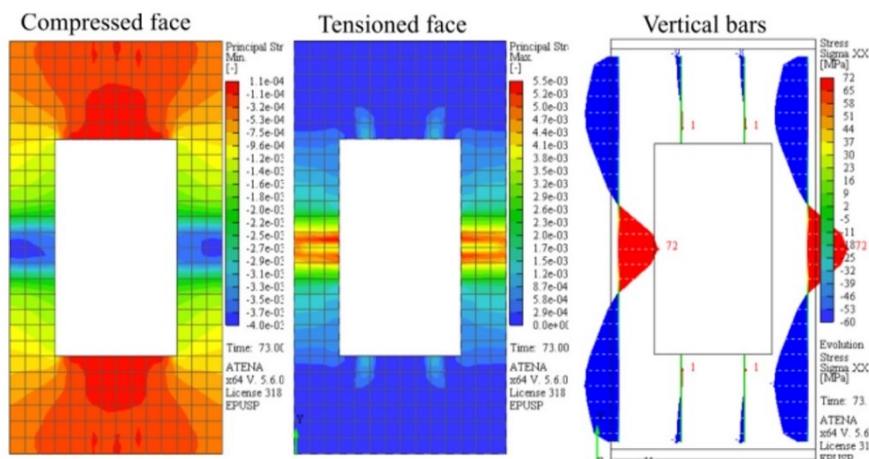
### 4.3 Failure mode

The failure of the models did not occur immediately after reaching the ultimate load. Numerical models showed softening regime where out-of-plane increased as the load decreased. At certain point, it was observed that major horizontal cracks in the tension face cause concrete crushing in the compression face of the wall, therefore causing the failure. The progression until failure is depicted in Figure 12 for the model WO4a-C with original eccentricity (6.6 mm). As it can be seen in Figure 12a by the time ultimate load was reached, typical flexural strains were concentrated in the column strips next to the opening and the vertical steel bars were predominantly compressed.

Furthermore, the principal tensile strains were in the span near the opening edges where vertical cracks appeared. Following Figure 12b, the out-of-plane displacement continued to increase and most of the tensile strains moved from the opening span to the column strips center causing major horizontal cracks in this area. Consequently, the rebars experienced tension and the concrete crushing, thus identifying failure in the column strips.



(a) Strain and stress distribution in peak load



(b) Strain and stress distribution in the rupture

Figure 12. Collapse of non-strengthened numerical models WO4a-C.

The experimental crack patterns of these walls were described in Mohammed et al. [21]. The authors reported that cracks before failure were not evident in wall panels with big openings, which was the case of WO4a and WO4b

(strengthened). They reported those two specimens collapsed due to horizontal cracks initiation near the opening edge in column strip. Strengthened wall WO4b also presented CFRP peeled off before the structural collapsed happened.

Figure 13 illustrates a typical crack evolution until the rupture of the numerical models with crack opening filter of 0.01 mm. The crack started vertical near the opening edges and advanced in the direction of the support plates. Afterward, the wall deflection increased, and horizontal cracks appeared in the two-column strips. Although there are horizontal cracks near the opening edges, the critical crack which caused rupture occurred in the center of column strips. The critical crack in the experimental test was also horizontal in the column strip but it appeared close to the opening edge (see Figure 14).

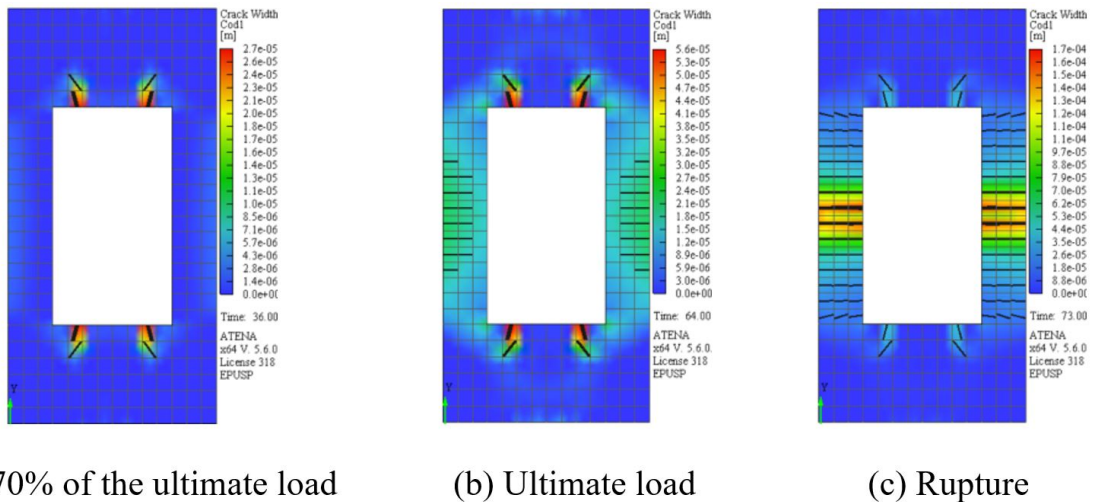


Figure 13. Crack pattern of model WO4a-C.

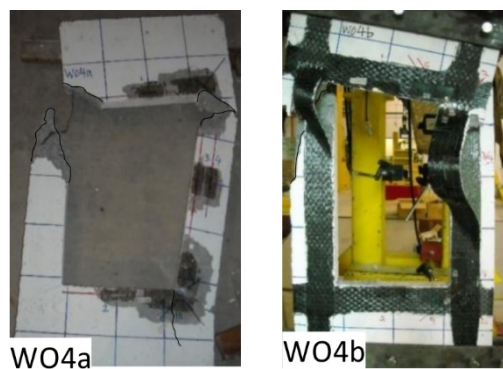
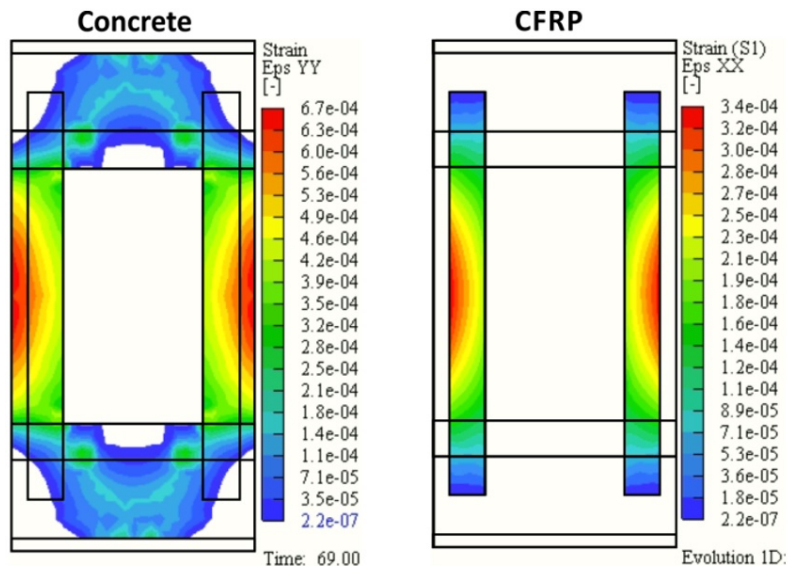


Figure 14. Failure mode in the experimental test. Adapted from Mohammed et al. [21].

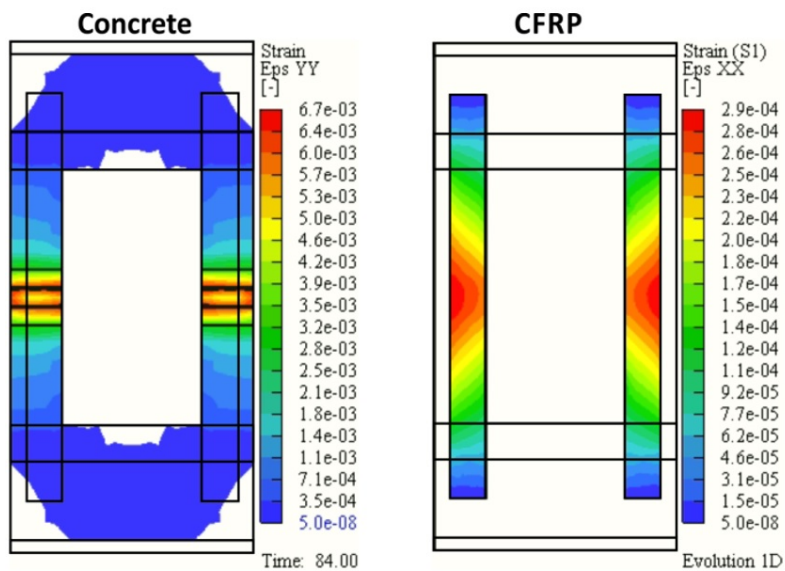
The strengthened model (WO4b-C1) showed a primary failure caused by CFRP debonding. This phenomenon was indirectly observed comparing the vertical strain in models with membrane and 2D shell elements. Figure 15 illustrates the vertical strain in the concrete and strain in the fiber's direction of the CFRP wrap. The difference between concrete strain ( $\epsilon_c=0.067\%$ ) and CFRP strain ( $\epsilon_{cfrrp}=0.034\%$ ) was small at the peak load (see Figure 15a). However, as the out-of-plane deflection increased, this strain difference was approximately 23 times between the concrete and the CFRP (see Figure 15b). The stiffness of CFRP is higher than the concrete; hence it presents small deformation, which indicates a reduction of adherence forces. After this primary failure, the structural collapse occurred like the non-strengthened model (WO4a-C).

In the strengthened model using 3D shell elements, it was possible to visualize the relative displacement between the materials when primary failure was initiated. Figure 16 shows the debonding process of WO4b-C1 (3D shell). The

structural collapse occurred when out-of-plane deflection significantly increased after reaching the ultimate load, similar to the non-strengthened model (WO4a-C).



(a) Ultimate load



(b) Rupture

**Figure 15.** Vertical strain in the concrete and the CFRP material.

## 5 CONCLUSIONS

The present work showed three different approaches of modeling strengthening with externally bonded CFRP in case of OW with openings. Additionally, it provides stiffness curves, obtained numerically, that help to understand better the structural behavior of these elements, which were not provided in recent and limited number of studies (Mohammed et al. [31], Mohammed et al. [21]; Lima et al. [29]) found regarding a strengthened wall with openings.

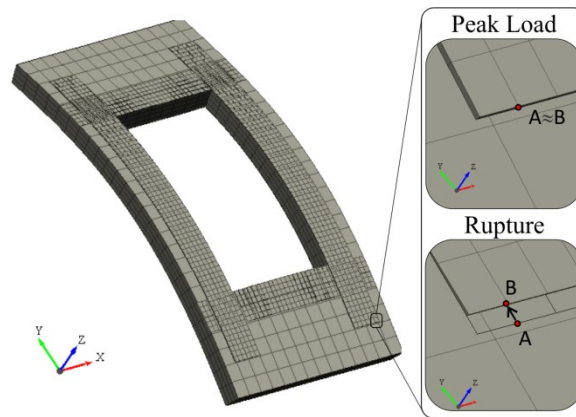


Figure 16. Relative displacement between the concrete and CFRP using 3D shell elements.

### 5.1 Nonstrengthened models (WO4a)

The load capacity of the non-strengthened developed model was not influenced by the mesh discretization when quadratic elements were used. The models presented similar stiffness through all loading stage. Regarding the lack of experimental data published about this test, the model behaved as a typical OW wall showing a single curvature in the panel due to a flexural pattern, with horizontal cracks propagating in the middle of the column strips which lead the structure to failure. The numerical models could reproduce properly the structural behavior of experimental test. Besides that, the ultimate load corresponding to WO4a-C (quadratic) model was 66% of the experimental. The comparison with theoretical prediction presented reasonable results, in which the ultimate load of the developed model achieved 92% of theoretical. As the dimension involved in the tests made by Mohammed et al. [21] was small, a parametric study made in this paper shows the relevance of eccentricity in load capacity. The model strength increased by 24% and 50% when load eccentricity was reduced 2 and 4 millimeters, respectively.

### 5.2 Strengthened models (WO4b)

In general, CFRP discretization had a small influence on the load capacity that remained between 61-63% of experimental. The walls tested in this paper had small ductility due to their reduced dimension; therefore, debonding of CFRP was less relevant to loading capacity. Similar results can be obtained by adopting fixed contact between CFRP and concrete as presented by Lima et al. [29] using ABAQUS (64% of experimental). The membrane elements provided a higher load capacity to the wall model. However, it is still below experimental and as non-strengthened case a small change on eccentricity could provide better results in terms of load capacity. The collapse of the model occurred after the failure of the bond between CFRP and concrete, which was noted in the post-peak stage. At this stage, the vertical strain in the wall face was about 10 times bigger than in CFRP which may indirectly indicate slipping in membrane and 2D shell elements approaches. Furthermore, the 3D shell elements approach was capable of directly reproducing slipping process between CFRP and concrete. In this case, higher compression of horizontal cross-section in the model center was noted. For future works, experimental measures are required to compare strains in CFRP and the bond-slip relation between materials. In addition, larger scale tests and structures that are more ductile may show the relevance of interface modeling and externally bond strengthening.

### ACKNOWLEDGEMENTS

The authors would like to express their gratitude to the Coordenação de Aperfeiçoamento de Pessoal de Nível Superior (CAPES) and the Structural Modeling and Monitoring Laboratory (LABMEM) of the University of Campinas (UNICAMP) for supporting this research. Website: <http://www.fec.unicamp.br/~labmem/>

### REFERENCE

- [1] C. Popescu, G. Sas, C. Sabău, and T. Blanksvärd, "Effect of cut-out openings on the axial strength of concrete walls," *J. Struct. Eng.*, vol. 142, pp. 2–6, 2016, [http://dx.doi.org/10.1061/\(ASCE\)ST.1943-541X.0001558](http://dx.doi.org/10.1061/(ASCE)ST.1943-541X.0001558).

- [2] N. M. Ho, J. H. Doh, and S. Fragomeni, "Instability analysis of reinforced concrete walls with various support conditions," *Struct. Des. Tall Spec. Build.*, vol. 26, no. 7, pp. e1353, 2017., <http://dx.doi.org/10.1002/tal.1353>.
- [3] S. M. Saheb and P. Desayi, "Ultimate Strength of RC wall panels in one way in plane action," *J. Struct. Eng.*, vol. 115, no. 10, pp. 2617–2630, 1989, [http://dx.doi.org/10.1061/\(ASCE\)0733-9445\(1989\)115:10\(2617\)](http://dx.doi.org/10.1061/(ASCE)0733-9445(1989)115:10(2617)).
- [4] J. H. Doh and S. Fragomeni, "Evaluation of experimental work on concrete walls in one and two-way action," *Aust. J. Struct. Eng.*, vol. 6, no. 1, pp. 37–52, 2005, <http://dx.doi.org/10.1080/13287982.2005.11464943>.
- [5] G. P. Robinson, A. Palmeri, and S. A. Austin, "Design methodologies for one way spanning eccentrically loaded minimally or centrally reinforced pre-cast RC panels," *Eng. Struct.*, vol. 56, pp. 1945–1956, 2013, <http://dx.doi.org/10.1016/j.engstruct.2013.07.041>.
- [6] S. Fragomeni, P. Mendis, and W. Grayson, "Review of reinforced-concrete wall design formulas," *ACI Struct. J.*, vol. 91, pp. 521–529, 1994.
- [7] American Concrete Institute, *Building Code Requirements for Structural Concrete*, ACI 318, 2019.
- [8] Canadian Standards Association, *Design of Concrete Structures*, CSA A23.3, 2004.
- [9] Australian Standard, *Concrete Structures*, AS 3600, 2001.
- [10] American Concrete Institute, *Building Code Requirements For Structural Concrete*, ACI 318, 2019.
- [11] C. Popescu, G. Sas, T. Blanksvard, and B. Taljsten, "Concrete walls weakened by openings as compression members: A review," *Eng. Struct.*, vol. 89, pp. 172–190, 2015, <http://dx.doi.org/10.1016/j.engstruct.2015.02.006>.
- [12] Associação Brasileira de Normas Técnicas, *Parede de Concreto Moldada no Local para a Construção de Edificações – Requisitos e Procedimentos*, NBR 16055, 2012.
- [13] European Standard, Eurocode 2 – Design of Concrete Structures – Part 1-1: General Rules and Rules for Buildings, *EN 1992*, 2004
- [14] S. M. Saheb and P. Desayi, "Ultimate strength of RC wall panels with openings," *J. Struct. Eng.*, vol. 116, no. 6, pp. 1565–1577, 1990.
- [15] H. Guan, C. Cooper, and D. J. Lee, "Ultimate strength analysis of normal and high strength concrete wall panels with varying opening configurations," *Eng. Struct.*, vol. 32, no. 5, pp. 1341–1355, 2010.
- [16] J. Doh, Y. Loo, and S. Fragomeni, "Concrete walls with and without openings supported on three sides," in *Incorporating Sustainable Practice in Mechanics and Structures of Materials*, S. Fragomeni, Ed., CRC Press, 2010, pp. 209–214.
- [17] C. S. Hansen, G. Sas, and B. Taljsten, "FRP strengthening of RC walls with openings," in *IV Int. Conf. Adv. Compos. Constr.*, 2009, pp. 202–213.
- [18] O. Enochsson, J. Lundqvist, B. Taljsten, P. Rusinowski, and T. Olofsson, "CFRP strengthened openings in two-way concrete slabs - an experimental and numerical study," *Constr. Build. Mater.*, vol. 21, no. 4, pp. 810–826, 2007.
- [19] Svensk Byggtjänst, *Boverkets Handbok om Betongkonstruktioner – BBK04 [The Swedish Building Administrations Handbook of Concrete Structures]*. Swedish, 2004
- [20] M. M. Lima, J. H. Doh, and M. N. Hadi, "Experimental study on RC walls with opening strengthened by externally bonded CFRP," *J. Compos. Constr.*, vol. 23, no. 2, 2019.
- [21] B. Mohammed, L. Ean, and M. Malek, "One way RC wall panels with openings strengthened with cfrp," *Constr. Build. Mater.*, vol. 40, pp. 575–587, 2013.
- [22] A. Pizzocchero, "Calibration and validation of ATENA concrete material model with respect to experimental data," Ph.D. dissertation, Univ. Studi Padova, Padova, 2015.
- [23] V. Cervenka, L. Jendele, and J. Cervenka, *ATENA Program Documentation, Part 1: Theory*. Prague: Cervenka Consulting, 2016.
- [24] S. Reese, P. Wriggers, and B. Reddy, "A new locking-free brick element technique for large deformation problems in elasticity," *Comput. Struc.*, vol. 75, no. 3, pp. 291–304, 2000.
- [25] Mapei. "Design guide." <https://cdnmedia.mapei.com/docs/global-technical-specification/application-of-composite-materials.pdf> (accessed Jan. 5, 2019).
- [26] T. Sajdlov, *ATENA Program Documentation, Part 4-9*. Prague: Cervenka Consulting, 2006.
- [27] B. Taljsten, *FRP Strengthening of Existing Concrete Structures*. Lulea: Lulea University of Technology, 2006.
- [28] A. Gholamhoseini, "Experimental and finite element study of ultimate strength of continuous composite concrete slabs with steel decking," *Int. J. Adv. Struct. Eng.*, vol. 10, no. 1, pp. 85–97, 2018.
- [29] M. Lima, J. Doh, M. Hadi, and D. Miller, "The effects of cfrp orientation on the strengthening of reinforced concrete structures," *Struct. Des. Tall Spec. Build.*, vol. 25, no. 15, pp. 759–784, 2016.
- [30] S. E. ElMetwally, F. Ashour, and W. F. Chen, "Instability analysis of eccentrically loaded concrete walls," *J. Struct. Eng.*, vol. 116, no. 10, pp. 2862–2880, 1990.

- [31] B. S. Mohammed, L. W. Ean, and K. Hossain, "M. CFRP Composites for strengthening of reinforced concrete walls with openings," *Int. J. Eng. Res. Appl.*, vol. 1, pp. 1841–1852, 2011.

---

**Author contributions:** MAS: conceptualization, methodology, investigation, validation, writing-original; RASD: writing - review and editing, visualization; LCA: supervision, validation, writing - review; LMT: writing - review and editing.

**Editors:** Maurício de Pina Ferreira, José Luiz Antunes de Oliveira e Sousa, Guilherme Aris Parsekian.



ORIGINAL ARTICLE

# Influence of recycled concrete aggregates on the shear strength of reinforced concrete beams

## *Influência dos agregados reciclados de concreto na resistência ao cisalhamento de vigas de concreto armado*

Allan Carvalho Cardoso<sup>a</sup>

Isaque Guerreiro Lima<sup>a</sup>

Maurício de Pina Ferreira<sup>a</sup>

Rafael Alves de Souza<sup>b</sup>

<sup>a</sup>Universidade Federal do Pará – UFPA, Instituto de Tecnologia, Belém, PA, Brasil

<sup>b</sup>Universidade Estadual de Maringá – UEM, Departamento de Engenharia Civil, Maringá, PR, Brasil

Received 21 January 2019

Accepted 26 May 2020

**Abstract:** This research evaluates the influence of the replacement of natural coarse aggregates (NCA) by recycled concrete aggregates (RCA) on the shear strength of reinforced concrete beams. Experimental tests on six reinforced concrete beams with RCA replacement ratios of 0%, 30%, and 100% are presented. Furthermore, a database with results of 170 tests on beams with RCA is used to discuss adjustments in the recommendations presented by ABNT NBR 6118 to estimate the shear strength of reinforced concrete beams. According to the Demerit Points Classification (DPC) proposed by Collins, 80% of the theoretical results obtained using models I and II from the Brazilian code fall in an appropriate safety condition range, showing that the substitution of NCA by RCA has a low impact on the shear strength reinforced concrete beams.

**Keywords:** shear, recycled concrete aggregates, reinforced concrete.

**Resumo:** Esta pesquisa avaliou a influência da substituição de agregados graúdos naturais (AGN) por agregados reciclados de concreto (ARC) na resistência ao cisalhamento de vigas de concreto armado. Ensaios experimentais em seis vigas de concreto armado com taxas de substituição de ARC de 0%, 30% e 100% são apresentados. Além disso, um banco de dados com resultados de 170 ensaios em vigas com ARC é utilizado para discutir os ajustes nas recomendações apresentadas pela ABNT NBR 6118 para estimar a resistência ao cisalhamento de vigas de concreto armado. Segundo o *Demerit Points Classification* (DPC), proposto por Collins, 80% dos resultados teóricos obtidos com os modelos I e II da norma brasileira caem dentro de uma faixa considerada de segurança apropriada, mostrando que a substituição dos AGN por ARC tem baixa influência na resistência ao cisalhamento de vigas de concreto armado.

**Palavras-chave:** cisalhamento, agregados reciclados de concreto, concreto armado.

**How to cite:** A. C. Cardoso, I. G. Lima, M. P. Ferreira, and R. A. Souza, “Influence recycled concrete aggregates on the shear strength of reinforced concrete beams,” *Rev. IBRACON Estrut. Mater.*, vol. 14, no. 1, e14109, 2021, <https://doi.org/10.1590/S1983-41952021000100009>

## 1 INTRODUCTION

Civil construction is one of the leading industrial sectors and contributes significantly to economic growth and social development. In this context, the aggregate industry is an important segment, as according to Langer et al. [1], on a global level, it involves the exploration of significant quantities of non-renewable natural resources. The civil construction industry is also considered a relevant waste generating agent. Pinto [2] presents and discusses the high numbers of construction and demolition waste (CDW) production in Brazil. More recent data (see [3]), provided by the Brazilian Association of Public Cleaning and Special Waste Companies (ABRELPE), indicate that in 2018, the total

Corresponding author: Maurício de Pina Ferreira. E-mail: mpina@ufpa.br

Financial support: None.

Conflict of interest: Nothing to declare.



This is an Open Access article distributed under the terms of the Creative Commons Attribution License, which permits unrestricted use, distribution, and reproduction in any medium, provided the original work is properly cited.

quantity of CDW collected by the cities in the country was of 122,012 tonnes/day, resulting in a per capita generation of 0.585 kg/inhabitant/day.

The use of CDW in non-structural or structural concrete production has been the focus of intense scientific studies. This theme is also relevant considering the expected increase of concrete consumption and, therefore, of coarse aggregate, as highlighted by Arezoumandi et al. [4]. Rahal and Alrefaei [5] investigated the effect of replacing natural coarse aggregate (NCA) by RCA and did not observe any damaging effects in the shear strength of reinforced concrete beams for replacement rates until 16%. For beams with shear reinforcement, Ignjatović et al. [6] did not observe significant changes in both behaviour and shear strength for NCA to RCA replacement rates of 0, 50, and 100%.j

From a theoretical point of view, it is expected that the change of aggregates will affect the shear strength since it may alter the roughness of the failure plane, reducing the contribution of concrete through aggregate interlock. For structural elements with high flexural reinforcement ratio ( $\rho_l$ ), these effects may be even more significant because crack widths are wider at failure. These variables (aggregate interlock and  $\rho_l$ ) were the target of some classic shear investigations, such as those carried by Taylor [7] to Poli et al. [8], or more recent research, such as those presented by Ulaga [9] and Sagaseta and Vollum [10].

This paper presents an experimental and theoretical investigation about the influence of the replacement of NCA by RCA on the shear strength of reinforced concrete beams without and with shear reinforcement. These results are used to evaluate the need for adjustments in the current recommendations presented by ABNT NBR 6118 [11], in case it is used to predict the shear strength of reinforced concrete beams with the replacement of NCA by RCA.

## 2 LITERATURE REVIEW

The impact of the replacement of NCA by RCA in the compressive strength of concrete can vary significantly. Studies from [7] and [12] to [13] indicate a 30% reduction in the concrete strength due to the replacement of NCA by RCA. On the other hand, according to [14] and [15], the reduction can reach up to 76%. The loss of strength is more pronounced if recycled concrete aggregates from an unknown source are used. The use of RCA produced from the waste of high-strength concrete ( $f_c \geq 50$  MPa) will result in a compressive strength comparable with those obtained with NCA, that according to Schubert et al. [16], is related to the aggregate's water absorption. Cordeiro et al. [17] describe that it is possible to optimize RCA characteristics by incorporating reactive and non-reactive fines, improving the performance of concretes made with RCA.

In structural terms, [6] and [18] concluded that there is a similarity in both the crack pattern and the cracking load for reinforced concrete beams without stirrups, regardless of whether the concrete was produced with NCA or RCA. [6] also reports that no significant reductions in the shear strengths were measured. However, according to Rahal and Alrefaei [5], replacements of 23% and 35% led to a shear strength reduction of 10% and 21%, respectively. In the case of beams with shear reinforcement, these authors did not measure significant reductions in the shear strength, regardless of the amount of RCA. The shear-span can be another parameter to be investigated, as Choi et al. [19] observed pronounced reductions in the shear strength due to RCA's use in beams with a lower  $a/d$  ratio. Regarding the design standards, González-Fonteboa and Martínez-Abella [20] observed a better correlation between theoretical estimates of shear strength and experimental results for beams without shear reinforcement, which is not allowed in practice, than for those with stirrups, pointing that this is a topic that deserves more scientific efforts.

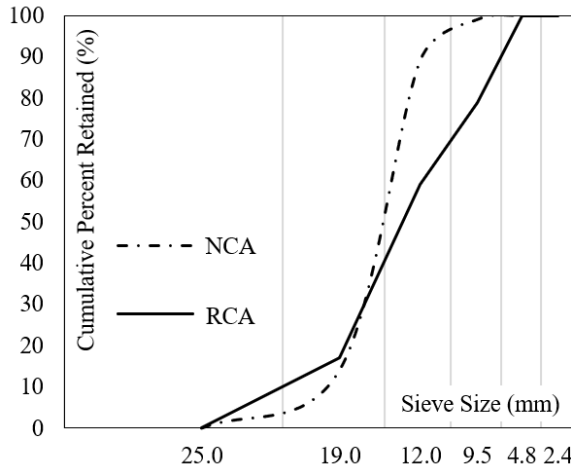
## 3 MATERIALS AND METHODS

### 3.1 Experimental program

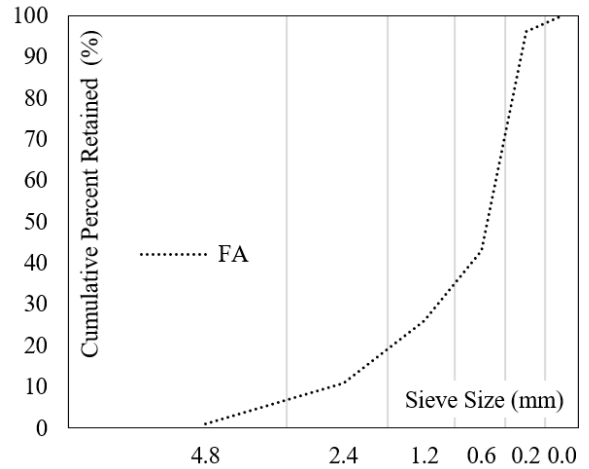
The concrete used to cast the tested beams was produced with 0, 30, and 100% replacement rates of NCA by RCA. Basaltic gravel with a maximum size of 25 mm was used as a natural coarse aggregate. As a fine aggregate, medium natural sand was used. The coarse recycled concrete aggregates were produced at the Civil Engineering Laboratory of the Federal University of Pará. For their production, the laboratory's structural concrete wastes were carefully selected to guarantee that only regular strength concrete ( $f_c < 50$  MPa) was used as origin material.

The RCA production process consisted of grinding the wastes with a jaw crusher. After this procedure, all the material was sieved, following the recommendations of ABNT NBR NM 248 [21], and separated into different granulometric ranges. The methods adopted by the Brazilian and international standards, used for

natural aggregates, can be unsuitable for RCA. For this reason, the methodology proposed by Leite [22] was used to determine the aggregate specific gravity of the RCA. Figure 1 shows the granulometric composition of the aggregates and their main characteristics.



a) The granulometric curve of coarse aggregate



b) The granulometric curve of fine aggregate

	<b>FA</b>	<b>NCA</b>	<b>RCA</b>
<b>Fineness Modulus</b>	2.61	7	6.96
<b>Maximum Size</b>	4.8 mm	25 mm	25 mm
<b>Specific Gravity</b>	2.61 g/cm <sup>3</sup>	2.62 g/cm <sup>3</sup>	2.66 g/cm <sup>3</sup>
<b>Unit Weight</b>	1.67 g/cm <sup>3</sup>	1.34 g/cm <sup>3</sup>	1.11 g/cm <sup>3</sup>

c) Properties of coarse and fine aggregates

**Figure 1.** Aggregates characterization.

The concrete proportioning was set to achieve a C30 strength class and was based on the design curves presented by Santos et al. [23], using high early strength Portland cement CP-V ARI RS. The concrete's workability was measured by slump tests, following the recommendations presented by ABNT NBR NM 67 [24]. The slump values were defined as  $15 \pm 2$  cm for both concrete with NCA and RCA. The wet curing of the concrete beams and specimens was initiated after the concrete's surface hardening. The beams and the cylindrical samples used to characterize the concrete's mechanical properties were wet-cured for seven days.

Six reinforced concrete beams with a 2,200 mm length and rectangular section (180 mm width and 280 mm height) were tested. Two beams served as reference and were cast with NCA concrete, one without shear reinforcement and the other with closed stirrups. The rest of the beams were cast with concrete with 30% and 100% replacement of NCA by RCA, having or not shear stirrups. All the beams had  $\rho_1$  equal to 2.13%, about half of the maximum value allowed by the ABNT NBR 6118 [11]. The beams with stirrups had a shear reinforcement ratio of 0.10%. Table 1 and Figure 2 show the main characteristics of the tested beams.

**Table 1.** Characteristics of the tested beams.

Specimen	% of RCA	$d$ (mm)	$a$ (mm)	$a/d$	$\theta_f$ (mm)	$\theta_w$ (mm)	$\rho_l$ (%)	$\rho_w$ (%)
V0	0	246	620	2.52	20	0	2.13	0
W0						4.2		0.10
V30	30	246	620	2.52	20	0	2.13	0
W30						4.2		0.10
V100	100	246	620	2.52	20	0	2.13	0
W100						4.2		0.10

Note:  $b_w = 180$  mm;  $h = 280$  mm;  $L = 2200$  mm;  $c = 20$  mm;  $f_c = 30$  MPa;  $f_{ys} = 500$  MPa;  $\alpha = 90^\circ$ ;  $\rho_w = A_{sw} / (b_w \cdot s)$ ;  $\rho_l = A_{sl} / (b_w \cdot d)$

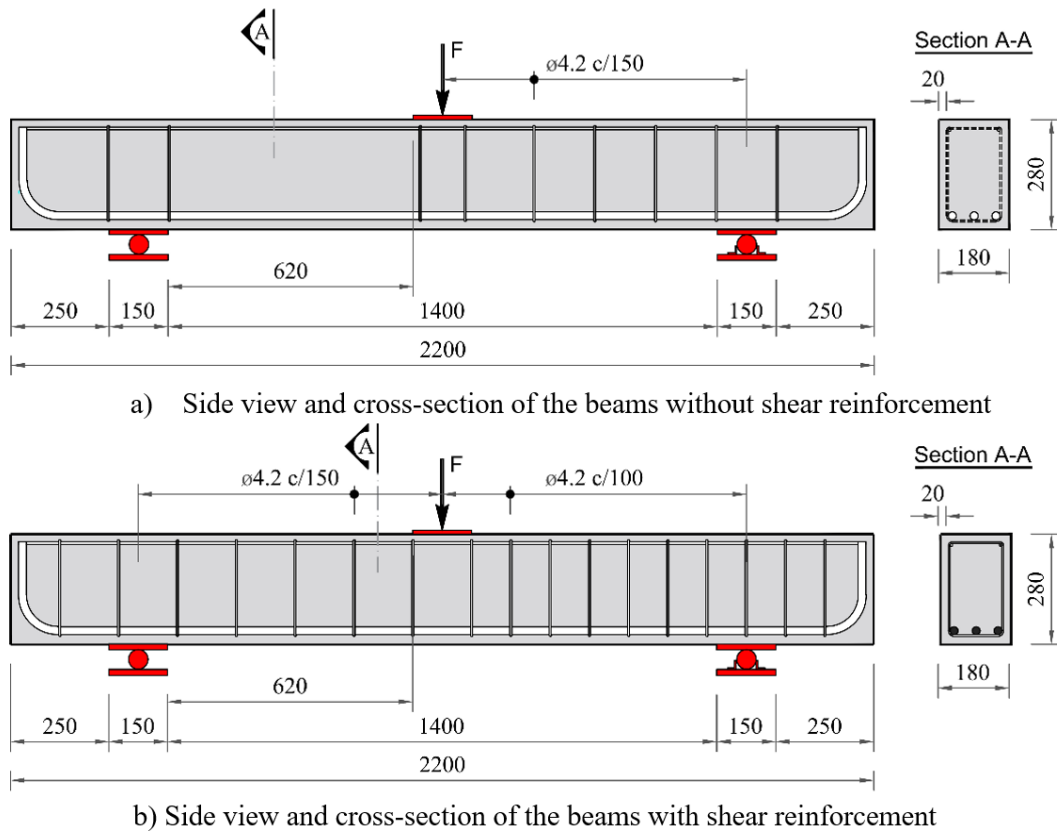


**Figure 2.** Flexural and shear reinforcement of the tested beams

The tested beams had two symmetrical spans with different amounts of shear reinforcement to guarantee that failure would occur in the weaker side where the strain gauges were placed. Figure 2 shows that the beams' left span is the weak side and was the focus of this experimental investigation. The beams denominated as “V” do not have stirrups on the left span and the beams denominated as “W” had closed stirrups made with 4.2 mm bars spaced at each 150 mm. For the flexural reinforcement, three steel bars with 20 mm of diameter distributed on a single layer were used, as shown in Figure 2.

Simply supported beams with three-point loading were tested. The supports were made with double “I” steel profiles in which two steel plates (150 mm wide and 20 mm thick) and one roller (40 mm diameter) were attached. The load was applied using a testing machine in 5 kN load steps, and its intensity was continuously measured by a load cell connected to an electronic acquisition data system. Figure 3 shows the testing system.

A potentiometric linear displacement transducer attached to a yoke was used to measure the vertical displacements (see Figure 4a). One pair of strain gauges was used to measure the flexural reinforcement strains, as shown in Figure 4b. Strains in the shear reinforcement were also measured by pairs of strain gauges attached to 3 layers of stirrups, as shown

in Figure 4c. The results presented for the flexural and shear reinforcement strains refer to the mean values of the pairs of strain gauges.

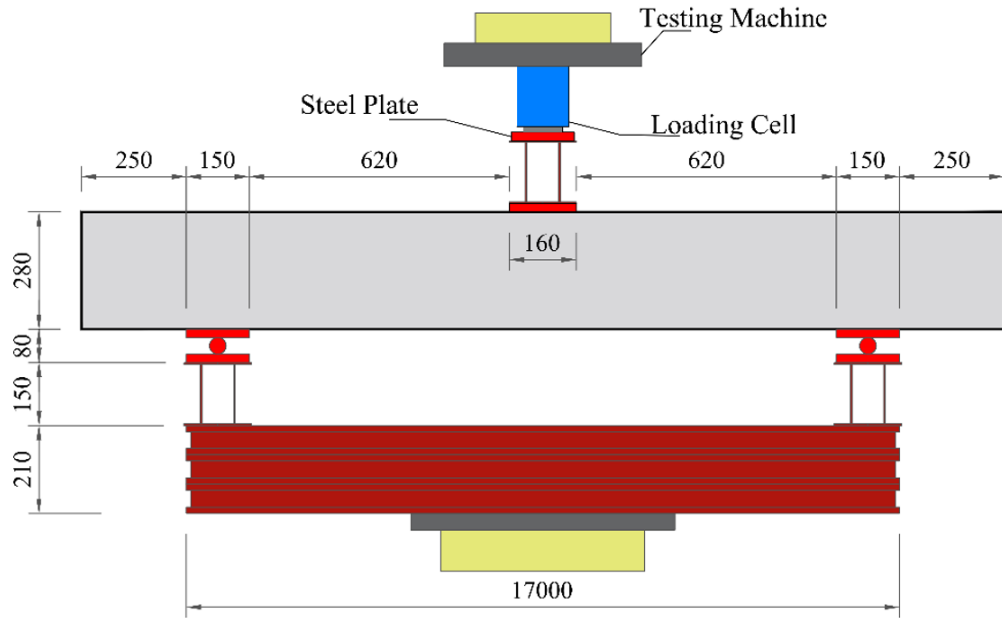


Figure 3. Testing setup

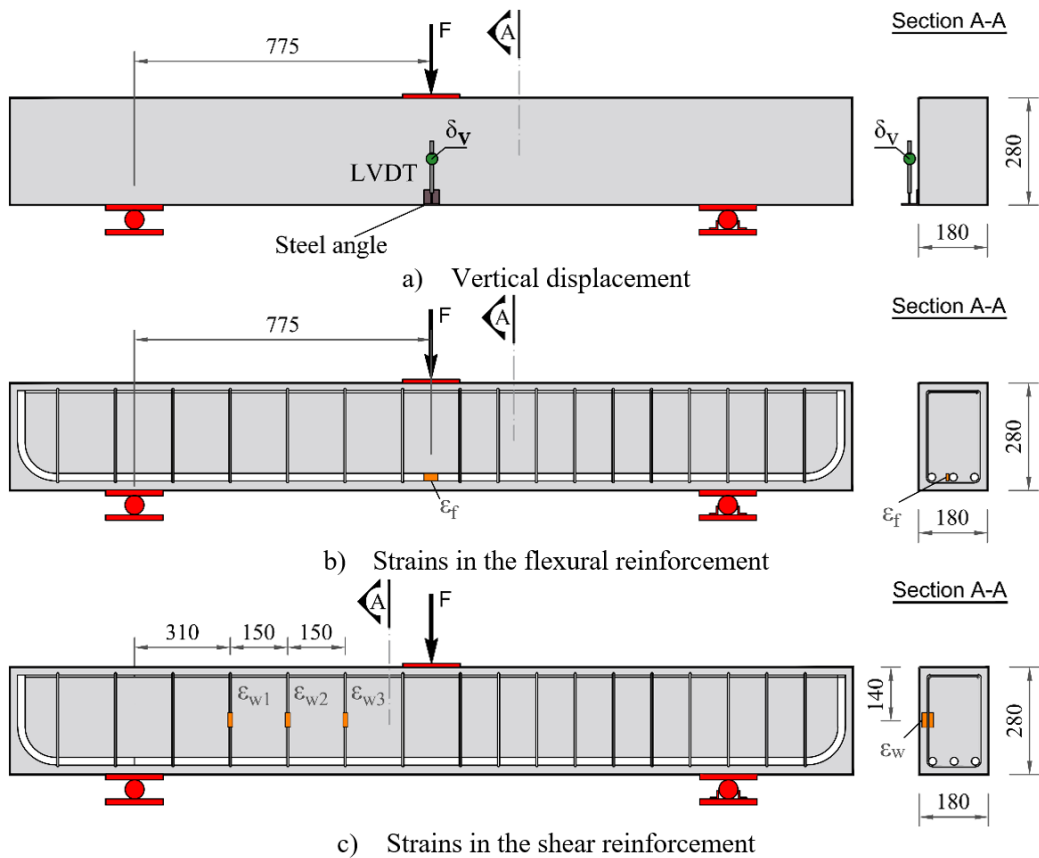


Figure 4. Instrumentation of the tested beams.

### 3.2 Shear strength of beams according to ABNT NBR 6118

ABNT NBR 6118 [11] considers that the shear strength of a beam ( $V_R$ ) can be computed as the sum of the contributions given by the concrete shear resistant mechanisms ( $V_{Rc}$ ) and the steel activated up to failure ( $V_{Rs}$ ), as expressed in Equation 1. The Brazilian code presents two different models to calculate the contributions from concrete ( $V_{Rc}$ ), shear reinforcement ( $V_{Rs}$ ), and the maximum resistance due to concrete strut's crushing ( $V_{Rmax}$ ). Model I assume that the concrete struts have an angle of  $\theta = 45^\circ$ , and the shear strength can be calculated considering Equations 1-4. Model II admits that the concrete strut angle can vary between  $30^\circ$  to  $45^\circ$  in relation to the beam's longitudinal axis. Thus, the shear strength can be obtained by using Equation 1 and Equations 5-7.

$$V_R = V_{Rc} + V_{Rs} \leq V_{R,max} \quad (1)$$

$$V_{Rc,I} = 0.6 \cdot f_{ctd} \cdot b_w \cdot d \quad (2)$$

$$V_{Rs,I} = \frac{A_{sw}}{s} 0.9 \cdot d \cdot f_{ywd} \cdot (\sin \alpha + \cos \alpha) \quad (3)$$

$$V_{R,max I} = 0.27 \cdot \left(1 - \frac{f_{ck}}{250}\right) \cdot f_{ck} \cdot b_w \cdot d \quad (4)$$

$$V_{Rc,II} = V_{Rc,I} \cdot \frac{V_{R,maxII} - V}{V_{R,maxII} - V_{Rc,I}} \leq V_{Rc,I} \quad (5)$$

$$V_{Rsw,II} = \frac{A_{sw}}{s} 0.9 \cdot d \cdot f_{yw} \cdot (\cot \alpha + \cot \theta) \cdot \sin \alpha \quad (6)$$

$$V_{R,maxII} = 0.54 \cdot \left(1 - \frac{f_{ck}}{250}\right) \cdot f_{ck} \cdot b_w \cdot d \cdot \sin^2 \cdot (\cot \alpha + \cot \theta) \quad (7)$$

Where:

$b_w$  is the smallest cross-sectional width;  $d$  is the effective depth of the beam;  $s$  is the spacing of the stirrups;  $f_{ctd} = \frac{f_{ctk,inf}}{\gamma_c}$ ;  $f_{ctk,inf} = 0.7 \cdot f_{ctm}$ ;  $f_{ctm} = 0.3 \cdot f_c^{2/3}$  for concrete strength class varying from C20 to C50;  $f_{ctm} = 2.12 \ln(1 + 0.11 \cdot f_{ck})$  for concrete C55 until C90;  $f_{yw}$  is the yield strength of the shear reinforcement, limited to 500 MPa in this paper.

### 3.3 Database

A database containing results of shear tests on reinforced concrete beams with the replacement of NCA by RCA. An extensive literature review was carried, and the following criteria were considered during the selection of the test results:

- Only beams with shear span-to-depth ratio ( $a/d$ ) greater than or equal to 2.5 were used, restricting the analyses and conclusions of this study to the case of slender beams;
- Only beams made of concrete with compressive strength ranging from 20 MPa to 90 MPa were used to respect the scope of the ABNT NBR 6118 [11];
- Only beams with  $\rho_l$  and  $\rho_w$  within the minimum and maximum limits prescribed by ABNT NBR 6118 [11] were used.

Following these ideas, a database with 170 beams (see Annex A) was developed. For the analyses and discussions, these beams were classified into three groups:

- Group 1 contained beams with NCA to RCA replacement rates of less than 11%. There were 22 beams without shear reinforcement and 20 beams with closed stirrups;

- b) Group 2 had beams with RCA replacement rates ranging from 11% to 50%. There were 32 beams without stirrups and 20 beams with stirrups.
- c) Group 3 had beams with RCA replacement rates greater than 50%. There were 46 beams without shear reinforcement and 30 beams with stirrups.

This database, formed by results from tests presented in references [4], [5], [6], [16], [19], [20], [25], [26], [27], [28], [29], [30], [31] and [32], allows a comprehensive evaluation of the influence of the values of  $\rho$ ,  $\rho_w$ , and the NCA to RCA replacement on the shear strength of reinforced concrete beams.

## 4 RESULTS AND DISCUSSION

### 4.1 Experimental tests

Tests on cylindrical specimens, 100 mm of diameter and 200 mm of length, were performed to determine the compressive strength of concrete, following the recommendations of the ABNT NBR 5739 [33]. Diametral compression tests on 100 x 200 mm cylindrical specimens were carried to determine the concrete's tensile strength, following the recommendations of the ABNT NBR 7222 [34]. The modulus of elasticity of the concrete was also measured, following the recommendations of ABNT NBR 8522 [35], in tests on cylindrical specimens with 150 mm of diameter and 30 mm of height.

The concrete's compressive and tensile strength's presented values represent the highest strength measured in a pair of specimens. For the modulus of elasticity, the results presented are the mean of the results obtained in three cylindrical samples. The results of the characterization tests are presented in Figure 5.

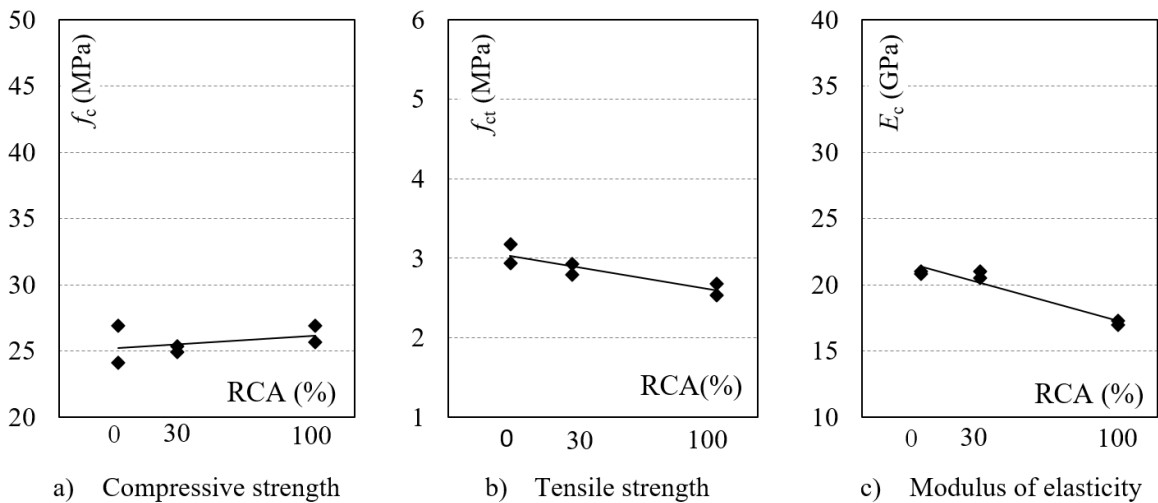


Figure 5 – Results of characterization tests.

The compressive strength results show that the concrete proportioning was successful, and the mean resistance was maintained regardless of the replacement ratio of NCA by RCA. The same was not observed for either the tensile strength or the modulus of elasticity of the concrete. Concerning the tensile strength, a reduction trend is noted for both replacement ratios of 30% and 100%. In general, an average reduction of 15% was measured in the tensile strength due to 100% replacement ratio of NCA by RCA. The substitution of 30% of RCA did not affect the modulus of elasticity results, but a replacement ratio of 100%, an average reduction of 20% was observed.

Three samples of each rebar size were submitted to axial tensile tests, following the recommendations of ABNT NBR ISO 6892 [36], to obtain the mechanical properties of the flexural and shear reinforcement. These results are summarized in Table 2 and are on the expected range of the steel bars commercialized in Brazil.

**Table 2** – Mechanical properties of reinforcement bars

$\phi$ (mm)	$f_{ys}$ (MPa)	$\epsilon_{ys}$ %	$E_s$ (GPa)
4,2	610	3,02	202
20	546	2,80	194

Figure 6 presents the tested beams' response, measured by the relation between the applied shear force ( $V$ ) and the vertical displacements ( $\delta$ ) in mid-span. The behaviour of the beams without shear reinforcement was fragile, and the shear failure occurred abruptly, with low displacement levels. For these beams, it was not observed relevant reductions of their flexural stiffness due to the replacement of the NCA by RCA. The beams with shear reinforcement reached significantly higher loading levels before the ruin, allowing the observation of a reduction in flexural stiffness due to the replacement of NCA by RCA.

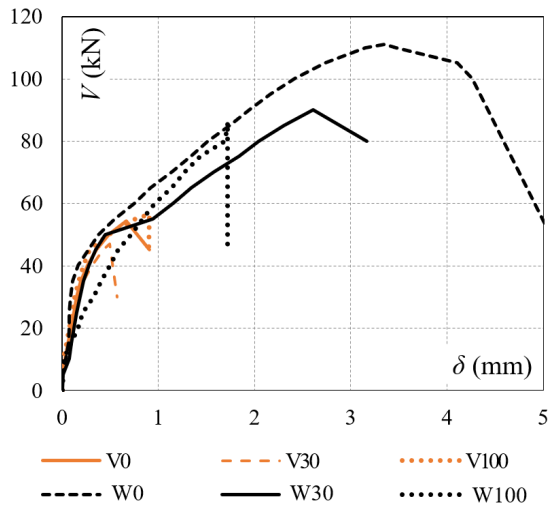


**Figure 6** –  $V - \delta$  response of the tested beams.

Table 3 shows the beams' measured strengths and compares the experimental results with theoretical predictions using models I and II from [11]. For beams without shear reinforcement, a significant reduction of the shear resistance was observed with the replacement of 30% of NCA by RCA. The same was not observed for a 100% replacement ratio, as V100 strength was almost the same as the reference beam (V0). For tests on beams with stirrups, a trend of strength reductions was experimentally observed. The substitution of NCA by RCA led to a 19% reduction of the shear strength of beam W30 and 22% for beam W100.

**Table 3** – Experimental relations with design codes.

Beams	Experimental values $V_u$ (kN)	$V_{Res}$ (kN)		$V_u / V_{Res,I}$	$V_u / V_{Res,II}$
		I	II		
V0	54.33	53.6	53.6	1.01	1.01
V30	46.74	53.7	53.7	0.87	0.87
V100	56.57	58.6	58.6	0.96	0.96
W0	110.97	76.6	83.9	1.45	1.32
W30	90.07	72.3	79.3	1.25	1.14
W100	86.08	73.4	80.5	1.17	1.07
	Mean			1.12	1.06
	SD			0.21	0.16
	COV (%)			19.11	14.75

Figure 7 graphically presents the ratio between the experimentally measured shear strengths ( $V_u$ ) and the theoretical results obtained according to NBR 6118 [11] ( $V_{Rcs,I}$  and  $V_{Rcs,II}$ ). In Figure 7, the tests on beams without shear reinforcement reveal that the theoretical models overestimate the concrete contribution in the shear strength, regardless of the replacement ratio of NCA by RCA. On the other hand, for beams with stirrups, the theoretical models presented by NBR 6118 [11] produced conservative estimates of the shear strength, even for beams with RCA, with model II presenting a better correlation between the estimates and theoretical results. It should also be highlighted that the theoretical calculations' safety levels decreased within the increase of the RCA content.

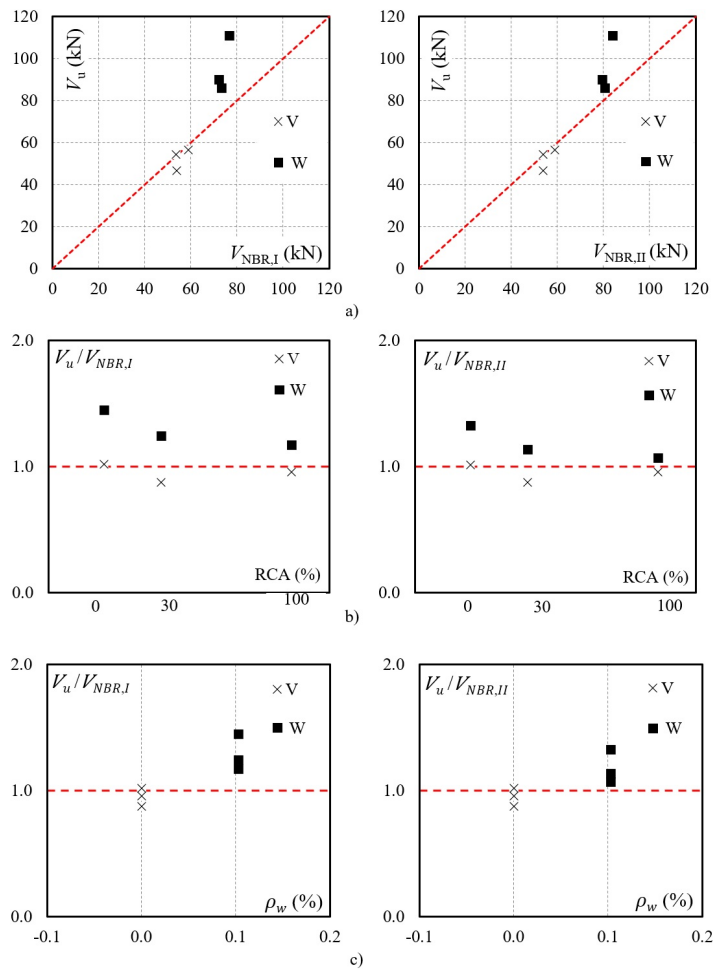


Figure 7 – Comparison between the experimental and theoretical for the tested beams.

#### 4.2 Database

Figure 8 presents comparisons between the experimental shear strengths ( $V_u$ ) and the theoretical estimates obtained using models I and II ( $V_{NBR,I}$  and  $V_{NBR,II}$ ) from [11] for the beams with shear reinforcement. These analyses are carried in general terms in Figure 8a and as a function of the percentage of replacement of NCA by RCA (Figure 8b) and the flexural and shear reinforcement ratio (Figures 8c and 8d). Figure 8a shows that, for both models, most of the theoretical estimates were conservative.

Figures 8b, 8c, and 8d evidence that, regardless of the replacement percentage of NCA by RCA, the safety of the theoretical estimates, measured by the ratio between experimental and theoretical results, is mainly affected by the flexural reinforcement ratio of the beams. In this context, if any adjustments in NBR 6118 [11] would have to be recommended, they would not be motivated by using recycled concrete aggregates instead of natural coarse aggregates.

Similar analyses are carried in Figure 9 but considering the results of tests on beams without shear reinforcement. These analyses are carried to check the performance of the theoretical models presented by NBR 6118 [11] to account for the

contribution of concrete to the shear resistance of reinforced concrete beams and if this performance is affected by the replacement of natural coarse aggregates by recycled concrete aggregates. In general, the dispersion between experimental and theoretical estimates is significantly smaller in this situation (see Figure 9a). However, for a significant number of results, the theoretical models overestimate the shear resistance of the tested beams. No correlation between the replacement ratio of NCA by RCA is observed (see Figure 9b), and the safety level of the theoretical estimates slightly increases with the growth of the flexural reinforcement ratio of the beams, regardless of the use or not of recycled concrete aggregates.

Table 4 evaluates the performances of theoretical models according to the Demerit Points Classification (DPC) proposed by Collins [37]. For beams with shear reinforcement (see Figure 10a), the model I from [11] showed better performance, with 80% of results falling into the appropriate safety and conservative classes. The worst performance from model II resulted from 18% of their results being classified in the dangerous class. Considering the results of beams without shear reinforcement, both models had similar performance, as shown in Figure 10b.

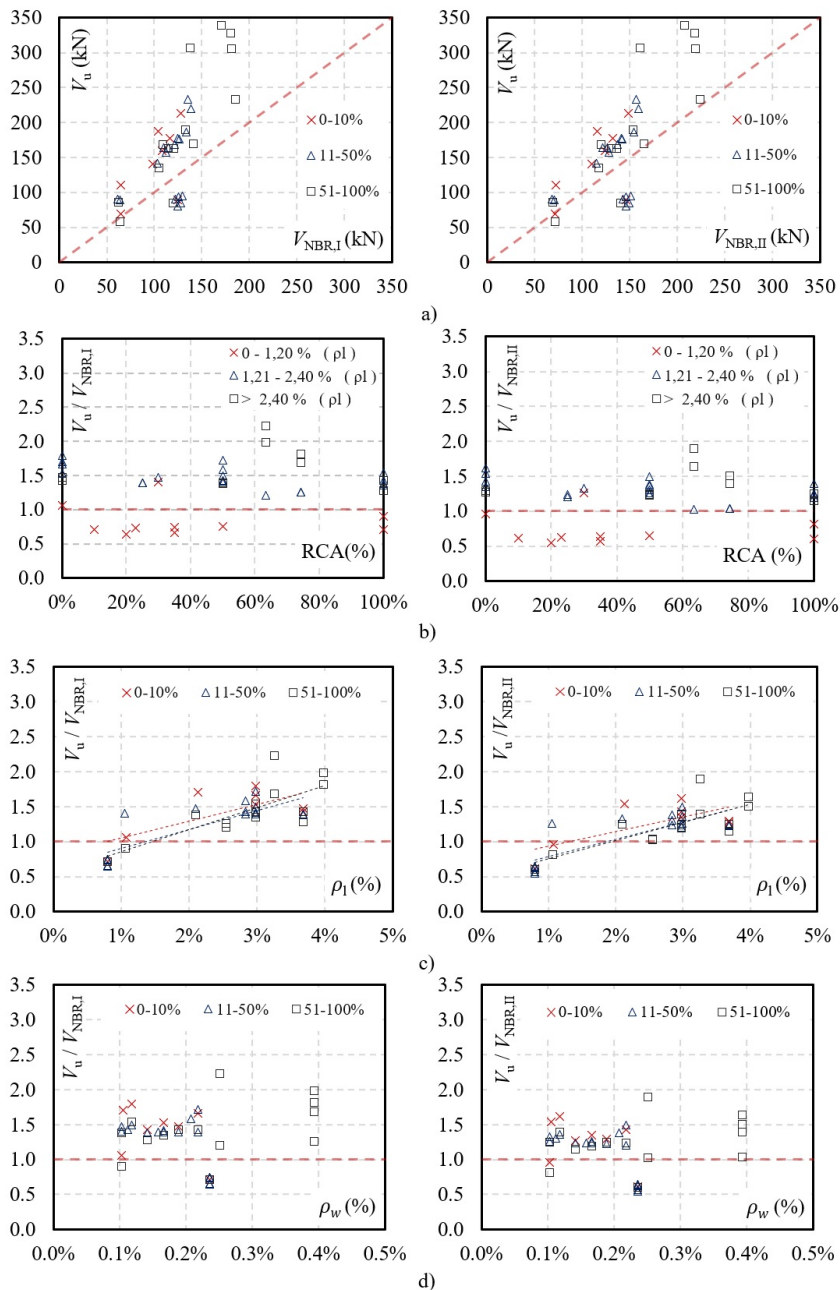


Figure 8. Comparison between the experimental and theoretical for the database of beams with stirrups

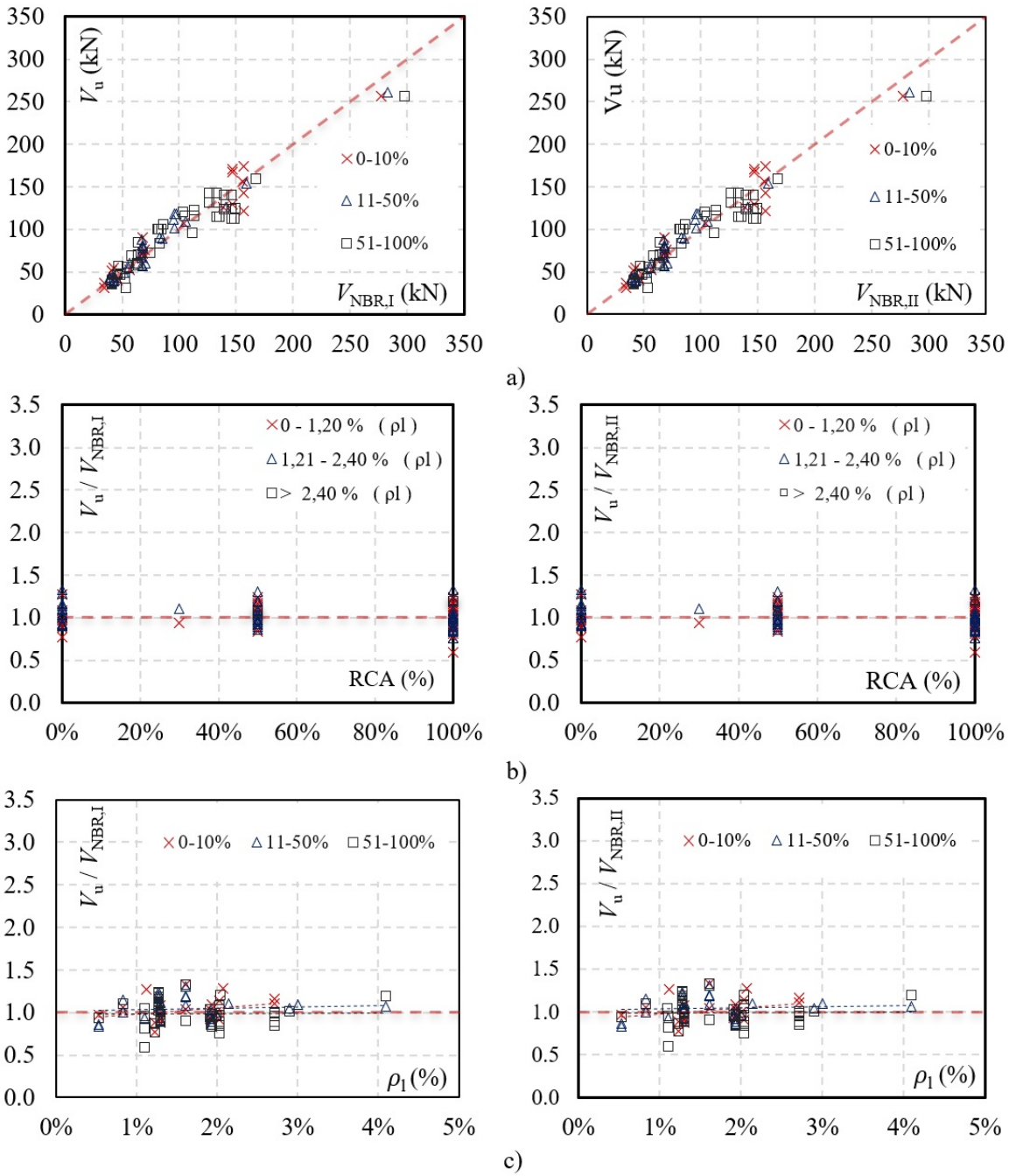


Figure 9. Comparison between the experimental and theoretical for the database of beams without stirrups

Table 4. Performance of theoretical estimates as proposed by Collins [37].

$V_u/V_{teo}$	Score	Classification
$< 0.50$	10	Extremely dangerous
$[0.50 - 0.65[$	5	Dangerous
$[0.65 - 0.85[$	2	Low safety
$[0.85 - 1.30[$	0	Appropriate safety
$[1.30 - 2.00[$	1	Conservative
$\geq 2.00$	2	Overconservative

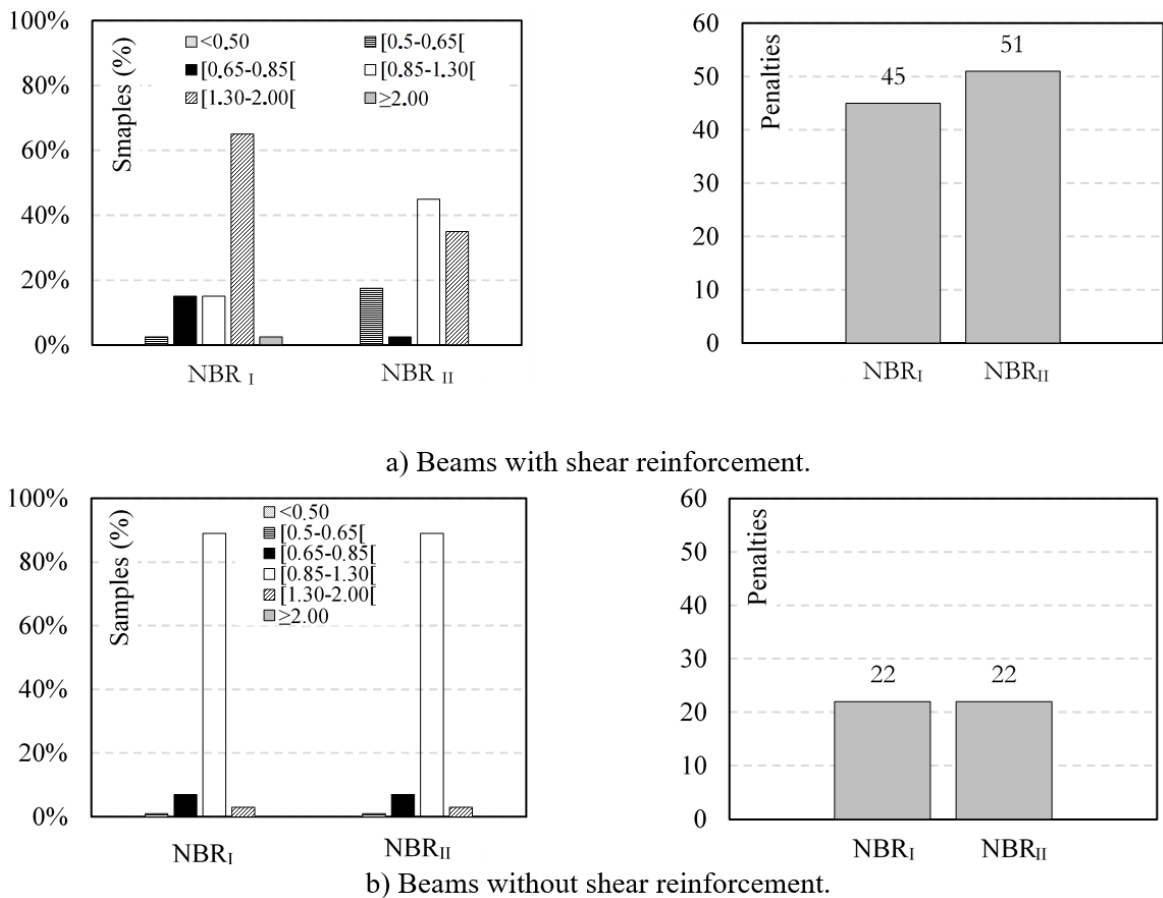


Figure 10. Result of the DPC for the beams within the database.

## 5 CONCLUSIONS

The main conclusions obtained were:

- The replacement of natural coarse aggregates by recycled concrete aggregates was not associated with reductions in concrete's compressive strength, considering the materials and the concrete proportioning used in the experimental program.
- The concrete's tensile strength and modulus of elasticity were slightly affected by the substitution of natural aggregates by recycled concrete aggregates. For the tensile strength, an average reduction of 15% was measured, and for the modulus of elasticity, mean reductions of 20% were observed, both for 100% replacement of NCA by RCA.
- Small reductions in the flexural stiffness and the shear resistance were observed in the tested beams due to the replacement of NCA by RCA. Those with shear reinforcement showed a conservative correlation between experimental and theoretical resistance estimates. On the other hand, those without shear reinforcement presented ultimate shear capacity below the theoretical expectation, regardless of the replacement of NCA by RCA.
- The extensive analyses allowed by the database with tests on beams without and with shear reinforcement do not show significant shear strength reductions associated with the substitution of natural coarse aggregates by recycled concrete aggregates. Considering the safety levels of the theoretical shear strengths obtained by following models I and II from the Brazilian code, these analyses show that the unsafe predictions are not associated with the use of recycled concrete aggregates but with the consideration of the contribution given by the flexural reinforcement ratio of the reinforced concrete beams.

## REFERENCES

- [1] W. H. Langer, L. J. Drew, and J. S. Sachs. *Aggregate and the Environment*. American Geological Institute, 2004.
- [2] T. P. Pinto, "Metodologia para a gestão diferenciada de resíduos sólidos da construção urbana," Ph.D. dissertation, Esc. Politéc., Univ. São Paulo, 2009.
- [3] Associação Brasileira das Empresas de Limpeza Pública e Resíduos Especiais, *Panorama dos Resíduos Sólidos no Brasil 2018/2019*, 2019. [Online]. Available: <http://abrelpe.org.br/download-panorama-2018-2019/>
- [4] M. Arezoumandi, J. Drury, J. S. Volz, and K. H. Khayat, "Effect of recycled concrete aggregate replacement level on shear strength of reinforced concrete beams," *ACI Mater. J.*, vol. 112, no. 4, 2015.
- [5] K. N. Rahal and Y. T. Alrefaei, "Shear strength of longitudinally reinforced recycled aggregate concrete beams," *Eng. Struct.*, vol. 145, pp. 273–282, 2017.
- [6] I. S. Ignjatović, S. B. Marinković, and N. Tošić, "Shear behaviour of recycled aggregate concrete beams with and without shear reinforcement," *Eng. Struct.*, vol. 141, pp. 386–401, 2017.
- [7] H. P. J. Taylor. *Investigation of the Forces Carried Across Cracks in Reinforced Concrete Beams in Shear by Interlock of Aggregate*. Cement and Concrete Association, 1970.
- [8] S. D. Poli, M. di Prisco, and P. G. Gambarova, "Cover and stirrup effects on the shear response of Dowel bar embedded in concrete," *ACI Struct. J.*, vol. 90, pp. 441–450, 1993. <http://dx.doi.org/10.14359/3962>.
- [9] T. Ulaga, "Reinforced concrete elements with reinforcement composed of bars and strips: bond and tension modelling," M.S. thesis, ETHZ, Zurich, 2003.
- [10] J. Sagaseta and R. L. Vollum, "Influence of aggregate fracture on shear transfer through cracks in reinforced concrete," *Mag. Concr. Res.*, vol. 63, no. 2, pp. 119–137, 2011.
- [11] Associação Brasileira de Normas Técnicas, *Projeto de Estruturas de Concreto – Procedimento*, NBR 6118, 2014.
- [12] S. W. Tabsh and A. S. Abdelfatah, "Influence of recycled concrete aggregates on strength properties of concrete," *Constr. Build. Mater.*, vol. 23, no. 2, pp. 1163–1167, 2009.
- [13] M. J. McGinnis, M. Davis, A. De La Rosa, B. D. Weldon, and Y. C. Kurama, "Quantified sustainability of recycled concrete aggregates," *Mag. Concr. Res.*, vol. 69, no. 23, pp. 1203–1211, 2017., <http://dx.doi.org/10.1680/jmacr.16.00338>.
- [14] N. K. Bairagi, K. Ravande, and V. K. Pareek, "Behaviour of concrete with different proportions of natural and recycled aggregates," *Resour. Conserv. Recycling*, vol. 9, no. 1, pp. 109–126, 1993.
- [15] K. Yanagibashi, K. Inoue, S. Seko, and D. Tsuji, "A study on cyclic use of aggregate for structural concrete," in *SB05 Tokyo: Action for Sustainability*, 2005.
- [16] S. Schubert, C. Hoffmann, A. Leemann, K. Moser, and M. Motavalli, "Recycled aggregate concrete: experimental shear resistance of slabs without shear reinforcement," *Eng. Struct.*, vol. 41, pp. 490–497, 2012.
- [17] L. N. P. Cordeiro, A. B. Masuero, D. C. C. D. Molin, P. S. L. Souza, and I. N. L. Paes, "Avaliação de processos de misturas de concretos com agregados graúdos reciclados," *Ambient. Constr.*, vol. 17, no. 3, pp. 255–265, 2017.
- [18] M. Arezoumandi, A. Smith, J. S. Volz, and K. H. Khayat, "An experimental study on shear strength of reinforced concrete beams with 100% recycled concrete aggregate," *Constr. Build. Mater.*, vol. 53, pp. 612–620, 2014.
- [19] H. B. Choi, C. K. Yi, H. H. Cho, and K. I. Kang, "Experimental study on the shear strength of recycled aggregate concrete beams," *Mag. Concr. Res.*, vol. 62, no. 2, pp. 103–114, 2010.
- [20] B. González-Fonteboia and F. Martínez-Abella, "Shear strength of recycled concrete beams," *Constr. Build. Mater.*, vol. 21, no. 4, pp. 887–893, 2007.
- [21] Associação Brasileira de Normas Técnicas, *Agregados – Determinação da Composição Granulométrica*, NBR NM 248, 2003.
- [22] M. B. Leite, "Avaliação de propriedades mecânicas de concretos produzidos com agregados reciclados de resíduos de construção e demolição," Ph.D. dissertation, Univ. Fed. Rio Gd. do Sul, Porto Alegre, 2001.
- [23] I. L. Santos, F. S. Salgado Neto, L. H. S. Martins, and L. N. P. Cordeiro, "Dosagem de concretos produzidos com agregado graúdo reciclado de concreto," in *An. 57 Cong. Bras. Concr.*, 2015.
- [24] Associação Brasileira de Normas Técnicas, *Concreto – Determinação da Consistência pelo Abatimento do Tronco de Cone*, NBR NM 67, 1998.
- [25] M. Etxeberria Larrañaga, "Experimental study on microstructure and structural behaviour of recycled aggregate concrete," M.S. thesis, Univ. Politècnica Catalunya, Barcelona, 2004.
- [26] A. C. Cardoso, "Efeito da adição de agregados reciclados na resistência ao cisalhamento de vigas de concreto armado," M.S. thesis, Univ. Fed. Pará, Belém, 2018.
- [27] G. Fathifazl, A. G. Razaqpur, O. B. Isgor, A. Abbas, B. Fournier, and S. Foo, "Shear strength of reinforced recycled concrete beams with stirrups," *Mag. Concr. Res.*, vol. 62, no. 10, pp. 685–699, 2010., <http://dx.doi.org/10.1680/macr.2010.62.10.685>.

- [28] A. M. Knaack and Y. C. Kurama, "Behavior of reinforced concrete beams with recycled concrete coarse aggregates," *J. Struct. Eng.*, vol. 141, no. 3, 2015.
- [29] H. Katkhuda and N. Shatarat, "Shear behavior of reinforced concrete beams using treated recycled concrete aggregate," *Constr. Build. Mater.*, vol. 125, pp. 63–71, 2016., <http://dx.doi.org/10.1016/j.conbuildmat.2016.08.034>.
- [30] S. W. Kim, C. Y. Jeong, J. S. Lee, and K. H. Kim, "Size effect in shear failure of reinforced concrete beams with recycled aggregate," *J. Asian Archit. Build. Eng.*, vol. 12, no. 2, pp. 323–330, 2013.
- [31] S. Sadati, M. Arezoumandi, K. H. Khayat, and J. S. Volz, "Shear performance of reinforced concrete beams incorporating recycled concrete aggregate and high-volume fly ash," *J. Clean. Prod.*, vol. 115, pp. 284–293, 2016.
- [32] I. Ignjatović "Ultimate strength of reinforced recycled concrete beams," PhD thesis, Univ. of Belgrade, Belgrade, 2013.
- [33] Associação Brasileira de Normas Técnicas, *Concreto – Ensaio de Compressão de Corpos de Prova Cilíndricos*, NBR 5739, 2007.
- [34] Associação Brasileira de Normas Técnicas, *Concreto e Argamassa – Determinação da Resistência à Tração por Compressão Diametral de Corpos de Prova Cilíndrico*, NBR 7222, 2011.
- [35] Associação Brasileira de Normas Técnicas, *Concreto – Determinação do Módulo Elástico de Elasticidade à Compressão*, NBR 8522, 2008.
- [36] Associação Brasileira de Normas Técnicas, *Materiais Metálicos – Ensaio de Tração. Parte 1: Método de Ensaio à Temperatura Ambiente*, NBR ISO 6892, 2013.
- [37] M. P. Collins, *Evaluation of Shear Design Procedures for Concrete Structures*. CSA Technical Committee on Reinforced Concrete Design, 2001.

---

**Authors contribution:** CARDOSO, C. A.: conceptualization, data analysis, bibliographic research, experimental analysis; LIMA, I. G.: experimental analysis, conceptualization, methodology, drafting; FERREIRA, M. P.: conceptualization, supervision, drafting and formal analysis, SOUZA, R. A.: writing and formal analysis.

**Editors:** Jose Tadeu Balbo, José Luiz Antunes de Oliveira e Sousa, Guilherme Aris Parsekian.

ANNEX A

Table A1. Database of tests on reinforced concrete beams with shear reinforcement.

Author	Beam	RCA (%)	$b_w$ (mm)	$d$ (mm)	$a$ (mm)	$a/d$	$A_s$ (mm <sup>2</sup> )	$A_{sw}$ (mm <sup>2</sup> )	$\rho_l$ (%)	$\rho_w$ (%)	$V_u$ (kN)	$V_{flex}$ (kN)	$f_{ck}$ (MPa)	$f_{yw}$ (MPa)
Larrañaga [25]	HC-2	0	200	304	1.000	3,3	1.810	57	3,0	0,2	213	214	32	495
	HC-3	0	200	304	1.000	3,3	1.810	57	3,0	0,2	177	214	32	495
	HC-4	0	200	304	1.000	3,3	1.810	57	3,0	0,1	188	214	32	495
Cardoso [26]	VAW0	0	180	254	620	2,4	491	28	1,1	0,1	69	98	23	554
	VBW0	0	180	255	620	2,5	942	28	2,1	0,1	111	166	23	554
Ignjatović et al. [6]	NAC-2	0	200	261	1.000	3,8	1.923	57	3,7	0,1	141	214	35	391
	NAC-3	0	200	261	1.000	3,8	1.923	57	3,7	0,2	160	214	35	391
Rahal and Alrefaei [5]	35-A-0-10	10	150	388	1.162	3,0	462	57	0,8	0,2	89	94	30	455
	35-A-0-20	20	150	388	1.162	3,0	462	57	0,8	0,2	80	94	30	455
	35-S-0-23(50)	23	150	388	1.162	3,0	462	57	0,8	0,2	95	95	33	455
Larrañaga [25]	HR25-2	25	200	304	1.000	3,3	1.810	57	3,0	0,2	187	220	35	495
	HR25-3	25	200	304	1.000	3,3	1.810	57	3,0	0,2	169	220	35	495
Cardoso [26]	VAW30	30	180	260	620	2,4	491	28	1,0	0,1	89	99	21	554
	VBW30	30	180	250	620	2,5	942	28	2,1	0,1	90	158	21	554
Rahal and Alrefaei [5]	35-A-0-35	35	150	388	1.162	3,0	462	57	0,8	0,2	90	94	29	455
	35-S-0-35(75)	35	150	388	1.162	3,0	462	57	0,8	0,2	85	94	32	455
	35-A-0-50	50	150	388	1.162	3,0	462	57	0,8	0,2	94	94	30	455
González-Fonteboa and Martínez-Abella [20]	V24RC	50	200	303	1.000	3,3	1.810	57	3,0	0,1	164	241	35	455
	V17RC	50	200	303	1.000	3,3	1.810	57	3,0	0,2	177	245	37	455
	V13RC	50	200	303	1.000	3,3	1.810	57	3,0	0,2	234	244	36	455
Larrañaga [25]	HR50-2	50	210	304	1.000	3,3	1.810	57	2,8	0,2	220	223	35	495
	HR50-3	50	210	304	1.000	3,3	1.810	57	2,8	0,2	176	223	35	495
	HR50-4	50	210	304	1.000	3,3	1.810	57	2,8	0,1	164	223	35	495
Ignjatović et al. [6]	RAC50-2	50	200	261	1.000	3,8	1.923	57	3,7	0,1	142	222	38	391
	RAC50-3	50	200	261	1.000	3,8	1.923	57	3,7	0,2	157	222	38	391
Fathifazl et al. [27]	EM-3S-R	63,5	200	309	800	2,6	1.571	101	2,5	0,3	170	235	33	482
	EM-6S-R	63,5	200	302	800	2,6	1.963	101	3,3	0,3	307	342	33	482
	EM-6S-D	63,5	200	301	800	2,7	2.395	157	4,0	0,4	339	374	33	482
	EV-3S-R	74,3	200	309	800	2,6	1.571	157	2,5	0,4	233	242	40	482
	EV-3S-R*	74,3	200	309	800	2,6	1.571	157	2,5	0,4	233	242	40	482
	EV-6S-R	74,3	200	302	800	2,6	1.963	157	3,3	0,4	306	365	40	482
Rahal and Alrefaei [5]	EV-6S-D	74,3	200	301	800	2,7	2.395	157	4,0	0,4	328	409	40	482
	35-A-0-100	100	150	388	1.162	3,0	462	57	0,8	0,2	85	93	27	455
Larrañaga [25]	HR100-2	100	200	304	1.000	3,3	1.810	57	3,0	0,2	190	219	34	495
	HR100-3	100	200	304	1.000	3,3	1.810	57	3,0	0,2	163	219	34	495
	HR100-4	100	200	304	1.000	3,3	1.810	57	3,0	0,1	168	219	34	495
Cardoso [26]	VAW100	100	180	258	620	2,4	491	28	1,1	0,1	58	99	22	554
	VBW100	100	180	250	620	2,5	942	28	2,1	0,1	86	160	22	554
Ignjatović et al. [6]	RAC100-2	100	200	261	1.000	3,8	1.923	57	3,7	0,1	135	225	40	391
	RAC100-3	100	200	261	1.000	3,8	1.923	57	3,7	0,2	163	225	40	391

**Table A2.** Database of tests on reinforced concrete beams without shear reinforcement.

Author	Beam	RCA (%)	$b_w$ (mm)	$d$ (mm)	$a$ (mm)	$a/d$	$A_s$ (mm <sup>2</sup> )	$\rho_1$ (%)	$V_u$ (kN)	$V_{flex}$ (kN)	$f_{ck}$ (MPa)
Choi et al. [19]	NANAC-L2.5	0	200	360	900	2,5	382	0,5	66	75	21
	NANAC-M2.5	0	200	360	900	2,5	598	0,8	72	106	21
	NANAC-H2.5	0	200	360	900	2,5	1.159	1,6	91	178	21
	NANAC-H3.5	0	200	360	1.170	3,3	1.159	1,6	71	137	21
Knaackand Kurama [28]	S0-1a	0	150	200	760	3,8	390	1,3	31	51	27
	S0-1b	0	150	200	760	3,8	390	1,3	37	51	27
	S0-2a	0	150	200	760	3,8	390	1,3	40	54	42
	S0-2b	0	150	200	760	3,8	390	1,3	42	54	42
Katkhuda [29]	NC-3	0	200	267	800	3,0	1.018	1,9	53	130	24
Arezoumandi et al. [4]	CC-NS-4.1	0	300	400	1.200	3,0	1.810	1,2	121	228	33
	CC-NS-4.2	0	300	400	1.200	3,0	1.810	1,2	130	226	30
	CC-NS-6.1	0	300	400	1.200	3,0	1.810	2,0	143	228	33
	CC-NS-6.2	0	300	400	1.200	3,0	1.810	2,0	167	226	30
	CC-NS-8.1	0	300	400	1.200	3,0	1.810	2,7	174	228	33
	CC-NS-8.2	0	300	400	1.200	3,0	1.810	2,7	171	226	30
Kim et al. [30]	NA-S2	0	200	300	750	2,5	1.161	1,9	76	204	28
	NA-M2	0	200	450	1.125	2,5	1.734	1,9	107	305	28
	NA-L2	0	200	600	1.500	2,5	2.323	1,9	126	408	28
	NA-M3	0	300	450	1.125	2,5	2.694	2,0	157	471	28
	NA-L4	0	400	600	1.500	2,5	4.645	1,9	256	816	28
Cardoso [26]	VA0	0	180	244	620	2,5	491	1,1	52	92	20
	VB0	0	180	253	620	2,5	942	2,1	54	159	20
	VA30	30	180	248	620	2,5	491	1,1	41	95	21
	VB30	30	180	245	620	2,5	942	2,1	47	155	21
Choi et al. [19]	RARAC30-L2.5	50	200	360	900	2,5	382	0,5	57	75	21
	RARAC30-M2.5	50	200	360	900	2,5	598	0,8	78	106	21
	RARAC30-H2.5	50	200	360	900	2,5	1.159	1,6	81	178	21
	RARAC30-H3.5	50	200	360	1.170	3,3	1.159	1,6	81	137	21
	RARAC50-L2.5	50	200	360	900	2,5	382	0,5	58	75	20
	RARAC50-M2.5	50	200	360	900	2,5	598	0,8	67	106	20
	RARAC50-H2.5	50	200	360	900	2,5	1.159	1,6	88	178	20
	RARAC50-H3.5	50	200	360	1.170	3,3	1.159	1,6	73	137	20
Ignjatovic (2013) [32]	RAC50-1b	50	200	235	1.000	4,3	1.922	4,1	60	160	29
Knaackand Kurama [28]	S50-1a	50	150	200	760	3,8	390	1,3	44	53	38
	S50-1b	50	150	200	760	3,8	390	1,3	39	53	38
	S50-2a	50	150	200	760	3,8	390	1,3	44	53	33
	S50-2b	50	150	200	760	3,8	390	1,3	41	53	33
Katkhuda [29]	R50-3	50	200	267	800	3,0	1.018	1,9	49	127	21
	T50-3	50	200	267	800	3,0	1.018	1,9	55	130	24
Sadati et al. [31]	RAC50-1	50	200	303	1.000	3,3	1.818	3,0	91	237	36
	RAC50-2	50	200	303	1.000	3,3	1.757	2,9	89	233	37
	RAC50-3	50	150	200	760	3,8	390	1,3	44	51	38
	RAC50-4	50	150	200	760	3,8	390	1,3	39	51	38
	RAC50-5	50	150	200	760	3,8	390	1,3	44	51	33
	RAC50-6	50	150	200	760	3,8	390	1,3	41	51	33
Kim et al. [30]	RH-S2	50	200	300	750	2,5	1.161	1,9	61	205	29
	RH-M2	50	200	450	1.125	2,5	1.734	1,9	109	307	29
	RH-L2	50	200	600	1.500	2,5	2.323	1,9	126	410	29
	RH-M3	50	300	450	1.125	2,5	2.694	2,0	154	473	29
	RH-L4	50	400	600	1.500	2,5	4.645	1,9	262	820	29

**Table A2.** Database of tests on reinforced concrete beams without shear reinforcement (cont.).

Author	Beam	RCA (%)	$b_w$ (mm)	$d$ (mm)	$a$ (mm)	$a/d$	$A_s$ (mm <sup>2</sup> )	$\rho_t$ (%)	$V_u$ (kN)	$V_{flex}$ (kN)	$f_{ck}$ (MPa)
Schubert et al. [16]	RC-M-1 Q1	50	500	170	560	3,3	1.080	1,3	118	159	28
	RC-M-1 Q2	50	500	170	560	3,3	1.080	1,3	118	159	27
	RC-M-2 Q1	50	500	170	560	3,3	1.080	1,3	112	159	27
	RC-M-2 Q2	50	500	170	560	3,3	1.080	1,3	102	159	27
	RC-C-1	100	500	170	560	3,3	1.080	1,3	116	161	31
	RC-C-2 Q1	100	500	170	560	3,3	1.080	1,3	123	163	34
	RC-C-2 Q2	100	500	170	560	3,3	1.080	1,3	116	163	34
	RC-C-3	100	500	170	560	3,3	1.080	1,3	121	161	30
	RC-M-3 Q1	100	500	170	560	3,3	1.080	1,3	101	154	21
	RC-M-3 Q2	100	500	170	560	3,3	1.080	1,3	101	154	21
	RC-M-4 Q1	100	500	170	560	3,3	1.080	1,3	100	155	22
	RC-M-4 Q2	100	500	170	560	3,3	1.080	1,3	106	156	23
Cardoso [26]	VA100	100	180	250	620	2,5	491	1,1	48	96	23
	VB100	100	180	257	620	2,4	942	2,0	57	168	23
Arezoumandi et al. [4].	RAC-NS-4.1	100	300	400	1.200	3,0	1.810	1,2	115	222	26
	RAC-NS-4.2	100	300	400	1.200	3,0	1.810	1,2	113	226	30
	RAC-NS-6.1	100	300	400	1.200	3,0	1.810	2,0	143	222	26
	RAC-NS-6.2	100	300	400	1.200	3,0	1.810	2,0	124	226	30
	RAC-NS-8.1	100	300	400	1.200	3,0	1.810	2,7	131	222	26
	RAC-NS-8.2	100	300	400	1.200	3,0	1.810	2,7	140	226	30
Kim et al. [30]	RF-S2	100	200	300	750	2,5	1.161	1,9	73	208	31
	RF-M2	100	200	450	1.125	2,5	1.734	1,9	96	311	31
	RF-L2	100	200	600	1.500	2,5	2.323	1,9	125	416	31
	RF-M3	100	300	450	1.125	2,5	2.694	2,0	160	479	31
	RF-L4	100	400	600	1.500	2,5	4.645	1,9	257	831	31
Sadati et al. [31]	RAC100-1	100	170	270	594	2,2	505	1,1	60	116	36
	RAC100-2	100	170	270	810	3,0	505	1,1	43	83	27
	RAC100-3	100	305	400	1.240	3,1	3.306	2,7	115	433	26
	RAC100-4	100	305	400	1.240	3,1	2.477	2,0	113	364	30
	RAC100-5	100	305	375	1.219	3,3	1.453	1,3	143	216	26
	RAC100-6	100	305	375	1.219	3,3	2.322	2,0	131	316	26
	RAC100-7	100	305	375	1.219	3,3	3.100	2,7	124	404	30
	RAC100-8	100	305	375	1.219	3,3	3.100	2,7	140	404	30
	RAC100-9	100	200	303	1.000	3,3	1.757	2,9	84	231	36
	RAC100-10	100	150	200	760	3,8	390	1,3	36	51	35
	RAC100-11	100	150	200	760	3,8	390	1,3	38	51	35
	RAC100-12	100	150	200	760	3,8	390	1,3	40	51	35
	RAC100-13	100	150	200	760	3,8	609	2,0	36	75	35
	RAC100-14	100	170	270	1.080	4,0	505	1,1	32	62	28
Katkhuda [29]	R100-3	100	200	267	800	3,0	1.018	1,9	46	125	19
	T100-3	100	200	267	800	3,0	1.018	1,9	56	128	23
Knaackand Kurama [28]	S100-1a	100	150	200	760	3,8	390	1,3	36	53	35
	S100-1b	100	150	200	760	3,8	390	1,3	38	53	35
	S100-2a	100	150	200	760	3,8	390	1,3	40	53	35
	S100-2b	100	150	200	760	3,8	390	1,3	36	53	35
Ignjatovic (2013) [32]	RAC100-1b	100	200	235	1.000	4,3	1.922	4,1	69	163	31
Choi et al. [19]	RARAC100-L2.5	100	200	360	900	2,5	382	0,5	60	75	19
	RARAC100-M2.5	100	200	360	900	2,5	598	0,8	70	105	19
	RARAC100-H2.5	100	200	360	900	2,5	1.159	1,6	85	175	19
	RARAC100-H3.5	100	200	360	1.170	3,3	1.159	1,6	58	135	19



## ORIGINAL ARTICLE

# Numerical evaluation of the slab effective width in steel-concrete composite box girder bridges

*Determinação via simulação numérica da largura efetiva de lajes de pontes mistas de aço e concreto em seção caixão*

Renato Silva Nicoletti<sup>a</sup> Alex Sander Clemente de Souza<sup>a</sup>

<sup>a</sup>Universidade Federal de São Carlos – UFSCar, Departamento de Engenharia Civil – DECiv, São Carlos, SP, Brasil

Received 21 January 2019

Accepted 26 May 2020

**Abstract:** Bridges are structures built to overcome obstacles and allow continuity of transport routes. In the search for efficient construction systems, steel-concrete composite structures, especially box girder bridges, emerged. The American AASHTO and European EN 1994-2-2 standards present design procedures for this type of bridge, but there are still doubts about which portion of the concrete slab contributes to each web strength in composite section (effective width). The present paper aims to evaluate, by numerical analysis in the Abaqus® software, the concrete slab effective width and to verify whether the expressions for its calculation in composite I-girder bridges are valid for box girder sections. After analyzing the results, it was found that the standards recommendations for composite I-girder cannot be applied directly to box girders. Finally, based on the numerical analysis, an equation was proposed to calculate the effective width of steel-concrete composite box girder bridges.

**Keywords:** effective width, steel-concrete composite bridges, box section, numerical analysis.

**Resumo:** Pontes são estruturas construídas para vencer obstáculos e permitir a continuidade de vias de transporte. Na busca por sistemas construtivos eficientes, vieram à tona as estruturas mistas de aço e concreto, em especial as pontes em seção caixão. As normas americanas AASHTO e europeias EN 1994-2-2 procedimentos de projeto para essa tipologia de pontes, porém ainda há dúvidas sobre qual parcela do tabuleiro contribui para a resistência de cada alma da seção mista (largura efetiva). O presente trabalho busca avaliar numericamente no software Abaqus®, a largura efetiva da laje de concreto e verificar se as expressões existentes perfis tipo “I” são válidas para perfis do tipo caixão. Após a análise dos resultados, constatou-se que as recomendações normativas para vigas mistas com seções tipo “I” não podem ser aplicadas diretamente para seções do tipo caixão. Por fim, com base nos resultados, propôs-se uma equação para o cálculo da largura efetiva de pontes mistas de aço e concreto em seção caixão.

**Palavras-chave:** largura efetiva de laje, pontes mistas de aço e concreto, seção caixão, análise numérica.

**How to cite:** R. S. Nicoletti and A. S. C. Souza. “Numerical evaluation of the slab effective width in steel-concrete composite box girder bridges,” *Rev. IBRACON Estrut. Mater.*, vol. 14, no. 1, e14110, 2021, <https://doi.org/10.1590/S1983-41952021000100010>

## INTRODUCTION

The association between steel and concrete has been an efficient solution for the formation of steel-concrete composite structural elements, such as beams, slabs and columns. Several authors have dedicated themselves to the study of steel-concrete composite elements and defended their advantages and applications. Of these, it is worth mentioning Veríssimo [1], De Nardin and Souza [2], Kotinda [3] and Souza et al. [4].

The use of composite structures can bring important advantages in relation to reinforced concrete structures and steel structures, such as dispensing formwork and shoring; reduction of own weight and volume of the structure; reduction of foundation costs; increased dimensional accuracy of construction, reduced consumption of structural steel

**Corresponding author:** Renato Silva Nicoletti. E-mail: [renato\\_nicoletti@hotmail.com](mailto:renato_nicoletti@hotmail.com)

**Financial support:** CNPq, process 120583/2017-8.

**Conflict of interest:** Nothing to declare.



This is an Open Access article distributed under the terms of the Creative Commons Attribution License, which permits unrestricted use, distribution, and reproduction in any medium, provided the original work is properly cited.

and less need for protection against fire and corrosion in steel profiles. In Brazil, the most common applications are for building construction. However, steel-concrete composite structures can be applied with advantages in the construction of bridges, enabling the construction of large spans, adding speed and rationalization in construction and also reducing costs and environmental impacts.

A steel-concrete composite system is called one in which a steel profile (laminated, welded or cold formed) resists together with concrete, forming a composite element - beam, column, slab or even a connection. The interaction between the concrete and the steel profile can take place through mechanical means (connectors, dents, projections, etc.), by friction or, in some cases, by simple adhesion and load sharing. With regard to steel-concrete composite bridges, the most common structural systems are in I-girders and in box girders (simple or double).

In particular, the composite box section consists of a closed section in which the sides (webs) and the lower part (bottom flange) are made of steel, constituting a closed section through the connection of the top box flange with the concrete slab, using shear connectors. In other words, the box section is formed with the union of a steel box girder interconnected with the concrete slab. Rectangular or trapezoidal sections are the most common. The bridge can have its cross section with only one box or multiple boxes depending on the width, span and loads. As advantages of the box section, mention is made of the greater torsional rigidity, facilities in terms of construction and maintenance, durability and aesthetic factors. Some alternatives for the design of steel-concrete composite box girder bridges are presented in Figure 1 together with a detail of the steel-concrete interface, highlighting the position of the shear connectors.

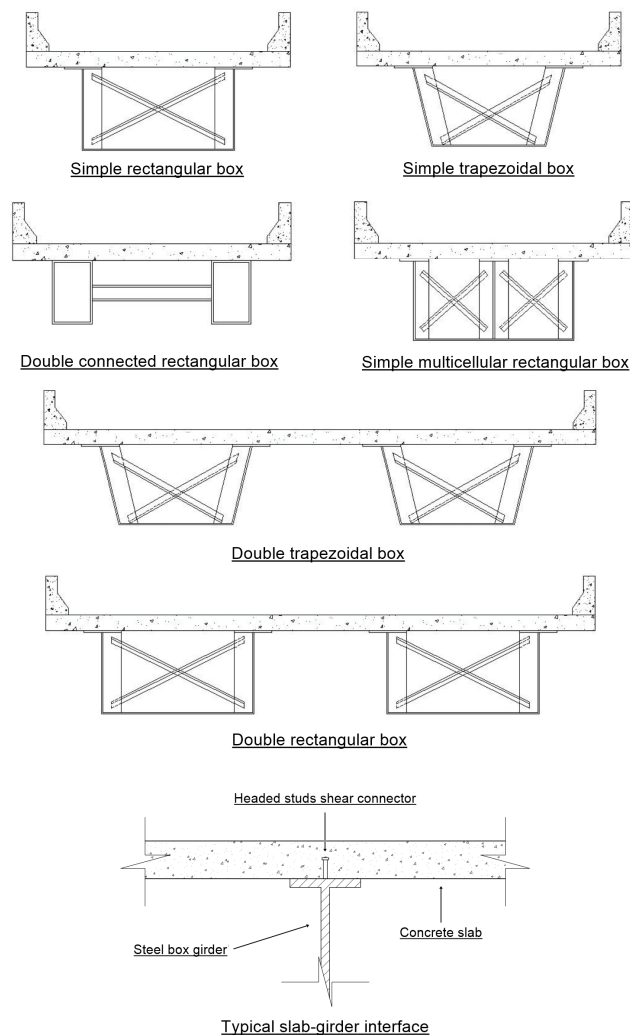


**Figure 1.** Examples of steel-concrete composite box girder bridges. Adapted from Pinho and Bellei [5].

In the construction of buildings, the use of steel-concrete composite elements is already established and consolidated in Brazil, with national technical standards that establish the parameters of design and construction. However, for the construction of bridges, the potential of composite structures is still little explored due to several factors, such as, for example, the lack of specific technical standards, design tools and limited technical knowledge.

The availability of national bibliography for steel-concrete composite bridges is limited and is out of date. It is worth mentioning the work of Pinho and Bellei [5], which presents an overview of typologies and design criteria for steel and steel-concrete composite bridges based on foreign standards.

Orlando et al. [6] and Souza [7] present studies on the behavior, analysis and design of steel-concrete composite bridges, however the emphasis is bridges focuses on I-girders. Faria and Pravia [8] synthetically present the design procedures of the American standard for steel-concrete composite box girder bridges.

In foreign countries, technical and scientific paper about steel-concrete composite box girder bridges are more abundant and can be classified into: development of new construction and design technologies [9], [10]; development of codes, manuals, practical examples of design and analysis and design procedures [11], [12].

With regard to design codes, in Brazil there is no specific standard for the design of steel-concrete composite box girder bridges. The American standards AASHTO [13] and European EN 1994-2-2 [14] present design procedures for this type of bridge, however there are still doubts and uncertainties about which portion of the board that really contributes to the resistant capacity of the composite section, that is, about the effective width of the concrete slab.

The need to improve Brazil's road infrastructure is very important for the country's economic development. In addition to political and economic issues, difficulties in meeting this demand are also affected by technical factors. In this context, it is urgent to develop constructive systems for bridges and road and rail viaducts that are capable of meeting the need for infrastructure quickly, economically and with the least possible environmental impact.

Undoubtedly the steel-concrete composite box bridges are among the most promising construction technologies, requiring more investment in scientific and technological research, design tools and transfer of knowledge to the technical environment to make this construction system viable.

In this context, one of the problems that must be faced in the design of steel-concrete composite box girder bridges is the definition of the effective width of the concrete slab that contributes to the joint steel-concrete behavior in the web region. There are no specific recommendations in the Brazilian standard ABNT NBR 8800: 2008 [15], which deals with steel and steel-concrete composite structures in buildings, nor in the American standards AASHTO [13] and European EN 1994-2-2 [5]. For this reason, the effective width of the steel-concrete composite box girder section is determined with the recommendations for composite I-girders. In this context, the present paper aims to determine, through numerical analyzes, the effective slab width in steel-concrete box girder bridges.

## Objectives

Determine, by numerical analyzes, the effective width of the slab that contributes to the cross section of the web in steel-concrete composite box girder bridges.

The specific objectives are to:

- Analyze the validity and adapt, if necessary, the expressions presented by AASHTO [13], EN 1994-2-2 [14] and ABNT NBR 8800: 2008 [15] for steel-concrete composite girders with I-profiles to be applied to box girders;
- Study the influence of the slab height, the length of the longitudinal span, the distance between box (in double box girder configuration) and the distance between webs (in simple box girder configuration) on the effective slab width of steel-concrete composite box girder bridges.

## Effective width

In steel-concrete composite beams, the stresses in the slab are not uniform, so that they present maximum stresses close to the beams, producing a non-flat section after loading. Such a phenomenon is called the shear lag effect.

To exemplify, it is assumed a simply supported composite beam with a concentrated load applied in the middle of the span - see Figure 2a. In this situation, the shear diagram on the slab is linear and, as a result, the displacements due to deformations in the longitudinal direction are parabolic in the transversal direction. On the left side of the beam, the shear is positive. The right side of the beam, in turn, is subjected to negative shear. Figure 2b shows the displacement distribution in both cases. For geometric compatibility to be maintained in the middle of the span, changes in the distribution of bending stresses as well as in the shear distribution are necessary. These stress changes result in the shear lag effect.

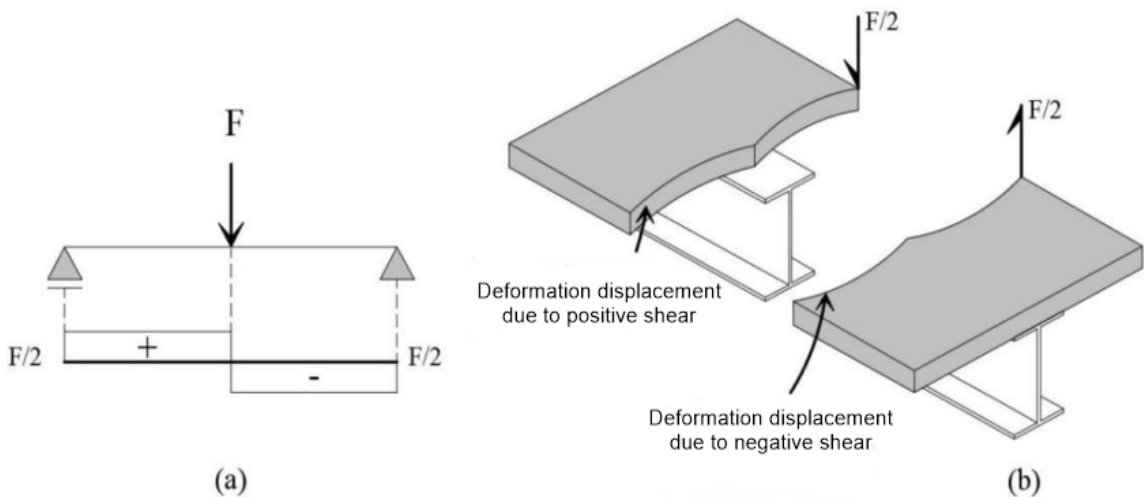


Figure 2. Displacements due to incompatible deformations. Adapted from Reginato [16].

To consider this effect, there is the effective width concept, reducing the width of the slab and allowing the hypotheses of flat section to be maintained, within acceptable limits for design routines. In other words, only a portion of the slab is considered effective in contributing to the resistant capacity of the composite elements and, therefore, it becomes unnecessary to consider the non-uniform stress distribution. Figure 3 summarizes the concept of effective width.

In Figure 3, the effective width ( $b_{ef}$ ) is determined when the stress distribution area ABCDEFG is equal to an abcd area, delimiting the width in which stresses are maximum and uniform. It is also observed that the maximum normal stress occurs at the point of connection of the steel beam with the concrete slab, due to the greater existing rigidity of this region, and decreases as it moves away from the center of the beam.

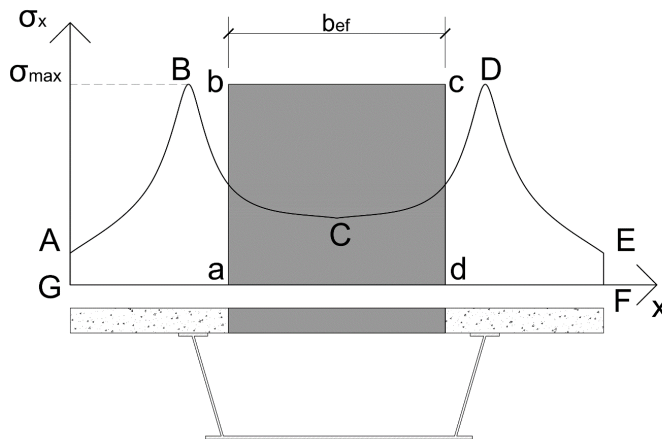


Figure 3. Effective width concept.

The effective width phenomenon has been investigated by several researchers in the literature, and it is worth highlighting the work of Patel [17], Amadio and Fragiaco [18], Salama and Nassif [19], Abbu, Ekmekyapar and Ozakça [20], Zhu et al. [21] and Yuan et al. [22].

In general, two main approaches are found in the literature for the assessment of effective width. The first is related to the state of stress on the slab. In this situation, the effective width is conceptualized as the width of the slab that supports efforts equal to that of the real slab, assuming that the normal stresses are constant in the effective width of

the slab and equivalent to the maximum stress ( $\sigma_{xmax}$ ) on the center line of the beam steel. Equation 1 summarizes this concept mathematically.

$$b_{ef} = \frac{I}{\sigma_{xmax}} \int_{-\frac{b}{2}}^{+\frac{b}{2}} \sigma_x dy \tag{1}$$

Where  $b_{ef}$  denotes the effective width,  $\sigma_x$  the normal longitudinal stresses,  $\sigma_{xmax}$  the maximum normal stress, and  $b$  the geometric width of the concrete slab of the composite section.

In turn, a second approach is specialized in the stiffness of the steel-concrete section. In this case, the deflection of the composite beam must be calculated and, subsequently, by means of analytical expressions, obtain the derivation of the second moment corresponding to the area that would result in the same deformation value of the idealized beam. Finally, based on the second equivalent moment of area, the effective width is estimated. In the present work, the first method was used.

For steel-concrete composite beams with I-profiles, mainly for building beams, an effective slab width is already in use in standards. Table 1 presents the requirements of Brazilian and European standards for calculating the effective width of steel-concrete composite simply supported beams with I-profiles.

**Table 1.** Recommendations for calculating the effective width in simply supported beams in buildings.

ABNT NBR 8800 [15]	EN 1994-2-2 [14]
The effective width must be less than or equal to:	When the slab extends to both sides of the beam, the effective width must be less than or equal to:
<ul style="list-style-type: none"> <li>• <math>\frac{l}{8}</math> of the span of the composite beam;</li> </ul>	<ul style="list-style-type: none"> <li>• <math>\frac{l}{4}</math> of the span of the composite beam;</li> </ul>
<ul style="list-style-type: none"> <li>• Half the distance between the center of the analyzed beam and the adjacent beam;</li> </ul>	<ul style="list-style-type: none"> <li>• Average distance between axes of adjacent beams.</li> </ul>
<ul style="list-style-type: none"> <li>• Distance from the center line of the beam to the edge of a cantilevered slab.</li> </ul>	In turn, when the slab extends to only one side, the effective width is limited to:
	<ul style="list-style-type: none"> <li>• <math>\frac{l}{8}</math> of the span of the composite beam;</li> </ul>
	<ul style="list-style-type: none"> <li>• Half the distance between the center of the analyzed beam and the adjacent beam.</li> </ul>

For steel-concrete composite bridges with I-girders, the American standard AASHTO [13] defines what the effective calculation width of the area must not exceed:

- One-fourth of the span length of the girder;
- The distance center to center of girders;
- Twelve times the least thickness of the slab.

However, for box girders, there is no specific standardization and the validity of the expression recommended for I-girders is not known.

**METHODOLOGY**

In analyses, 35 numerical models were developed, 19 with single box configuration and 16 with double box configuration, in the Abaqus® software [23], varying geometric parameters such as the slab height, span length, the distance between box (double box configuration) and the distance between webs (simple box configuration) - the main parameters that determine the effective width in normalizations.

The geometric design of the elements was performed according to the recommendations of AASHTO [13]. On all models, set the cross-section width to 12.80 m. As for the steel box girder: for the models in the simple box configuration, a height of 3.50 m and a thickness of the profiles of 41.28 mm were adopted; and for the models in the

double box configuration, a height of 2.00 m and a thickness of 41.28 mm were adopted. Trapezoidal box girders were used.

In all models, normal stresses were collected in the middle of the span and at the loading step at the beginning of the slab's plastic behavior. With such data, a non-uniform distribution curve was drawn up and the effective width was calculated using the quotient of the area below the curve by the maximum normal stress. Finally, the results found numerically were compared with the effective analytical width prescribed by the normalizations for steel-concrete composite I-girder bridges.

### Numerical analysis and model conception

To discretize the steel and concrete components of the girder and slab, respectively, the solid element C3D8R was used, which has 8 nodes with 3 degrees of freedom per node (translations in the x, y and z directions), as this element supports the analysis plastic with high deformations and displacements.

The steel girder could be discretized by means of shell elements, requiring less processing time. However, the use of shell elements is more usual when the thickness of the component can be disregarded. Thus, given that the best finite element to discretize concrete is the hexahedral element and this element provides more accurate results also for the steel profile, the choice of finite element C3D8R is justified.

The modeling of the shear connectors was not performed and total interaction between the two materials was admitted through the “Tie constraint” tool of the Abaqus® software [23], which couples the nodes of the steel-concrete interface, making both materials resist together to efforts, totally preventing relative slipping between the two contact surfaces. Figure 4 shows a scheme of the surfaces where the Tie constraint was applied.

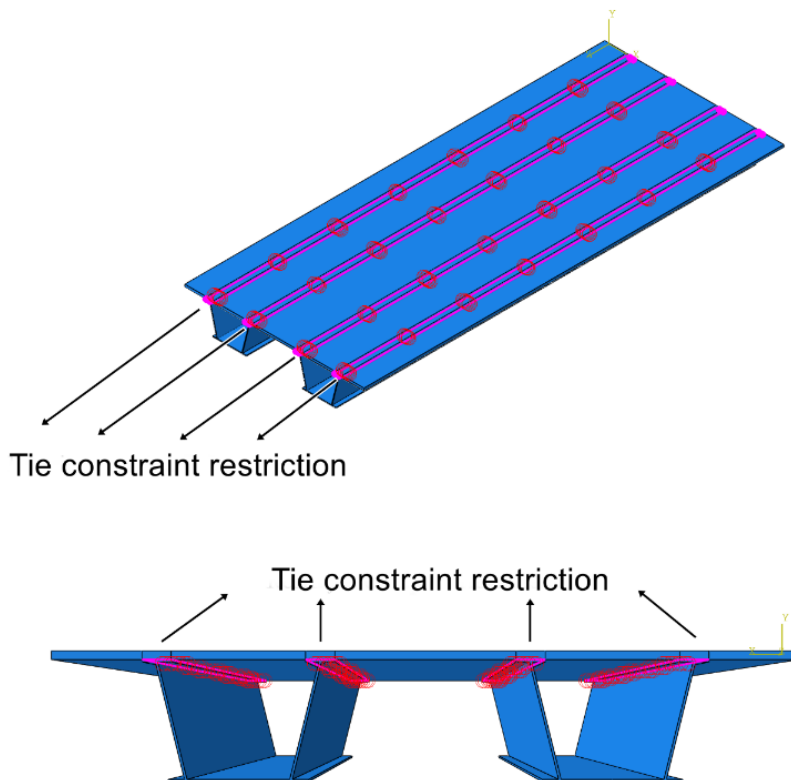


**Figure 4.** Relative interface displacement restricted by the Abaqus® [23] “tie constraint” tool.

For all models simply supported restrictions was adopted. Thus, the movement in the y and z directions was restricted along the lower table on both steel box girder supports. Figure 5 shows such boundary conditions imposed on Abaqus® [23].

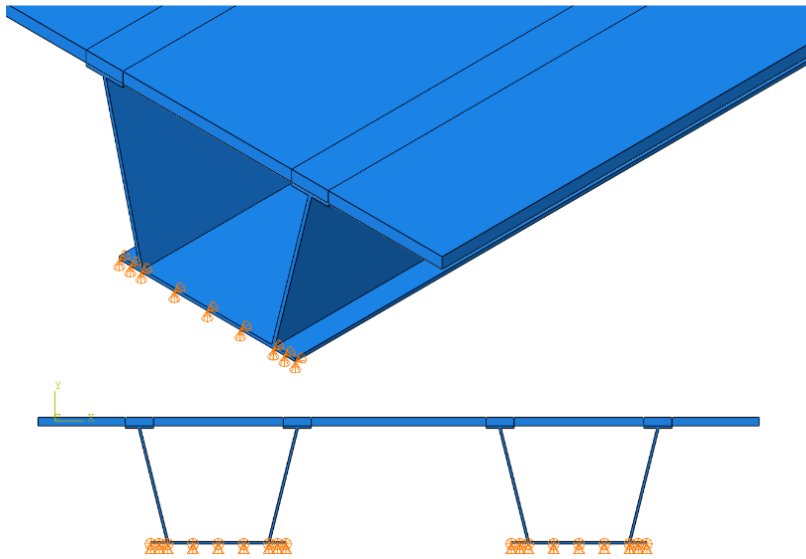


**Figure 5.** Boundary conditions of the models.

The loading, in turn, was defined for the composite section to reach the plastic behavior and applied with maximum loading steps of 2.5% of the total value, as a pressure distributed over the entire upper surface of the board. Figure 6 shows the loading and restriction of a model in the double box configuration.

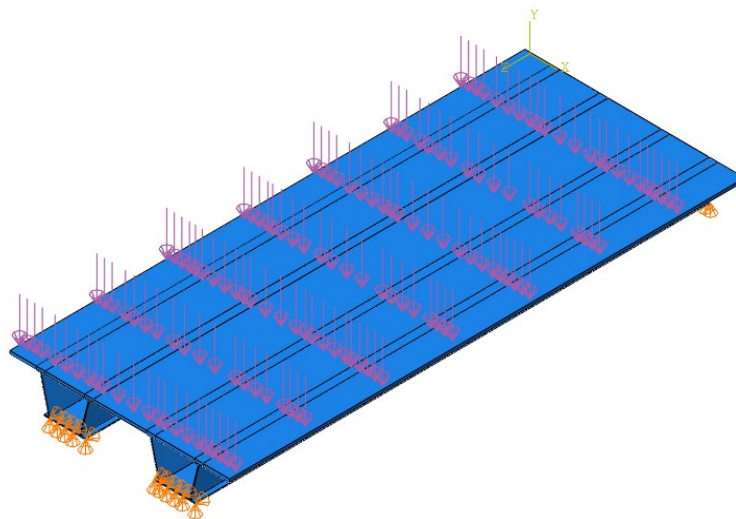


**Figure 6.** Application of loading models.

As for the mechanical properties of steel and concrete materials, both were satisfactorily described by a constitutive stress-strain relationship with perfect elastoplastic behavior. For steel, the Kirchhof model [24] was adopted, in which the yield strength of steel ( $f_y$ ) is 229.8 MPa. As for the longitudinal elastic modulus ( $E$ ) and the Poisson's ratio in elastic regime ( $\nu$ ), the values of 200 GPa and 0.3 were used, respectively. In turn, the compressive cylinder strength ( $f_{ck}$ ) of 30 MPa was adopted for concrete, culminating in an elasticity module of 30,672.46 MPa. The value of the Poisson's ratio in elastic regime of the admitted concrete was 0.2. Table 2 presents the properties of the materials. As the neutral plastic axis of all models are located in the steel box girder, the concrete was modeled considering only your compression behavior. Figure 7 shows a stress-strain curves used for steel and concrete, respectively.

**Table 2.** Materials mechanical properties for parametric study.

MATERIAL	E [MPa]	$\nu$	YIELD STRENGTH [MPa]
Steel	200,000	0.3	229.8
Concrete	30,672.46	0.2	30.0

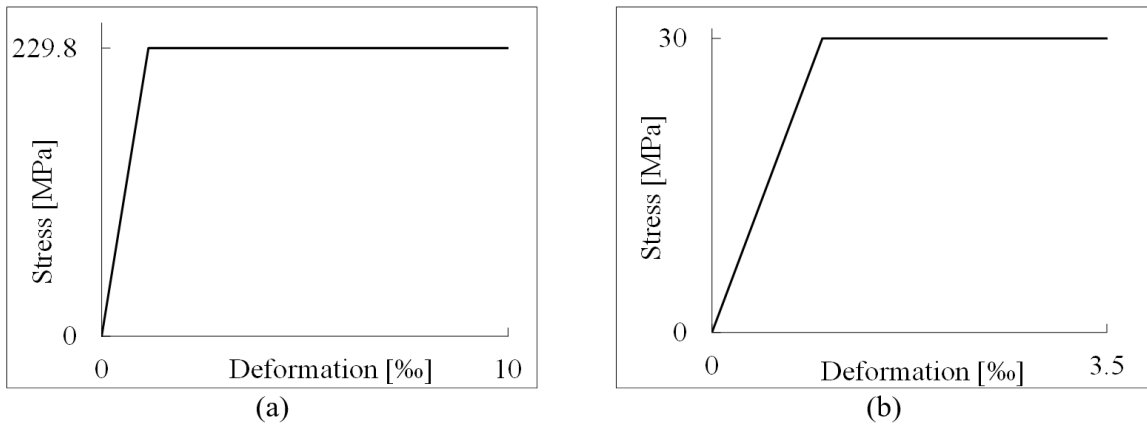


**Figure 7.** Stress-strain curve of steel (a) and concrete (b). Adapted from Kirchof [24].

The most suitable mesh to discretize the model was defined after analyzing the influence of its level of refinement on the results, culminating in a mesh of 10 cm in the x direction, 10 cm in the y direction and 50 cm in the z direction, which presents coherent results for adequate processing time. Figure 8 shows a detail of the models' mesh.

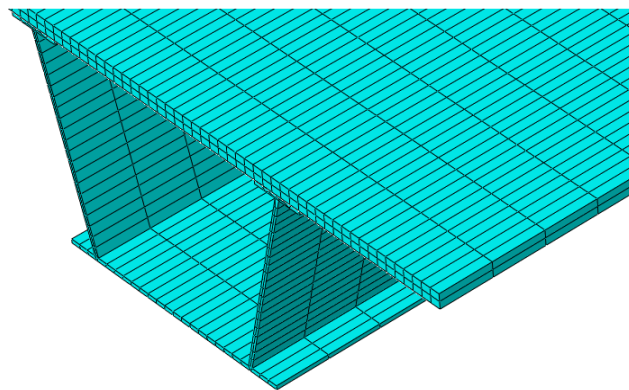


**Figure 8.** Detail of the typical mesh of the models.

In addition, to reduce processing time, the models were made with a condition of transversal and longitudinal symmetry.

## RESULTS AND DISCUSSIONS

The results were divided for the simple box configuration and double box configuration.

The analysis of normal stresses was performed in the middle of the span and at the interface between the steel box girder and the concrete slab. Specifically, the stress collection was carried out in the loading step of the start of the plastic behavior of the concrete of the slab because the effective width cannot be measured when such element is plasticized, as this would cause a uniform stress distribution and it would not be possible to analyze the effect of shear lag. Thus, the collection of stresses was made in the loading step where the first finite element of the slab was plasticized, that is, in the imminence of plasticization to start on the concrete slab.

To determine the effective numeric width, the following steps were followed:

1. Measurement of the normal stresses on the half slab height, in the middle of the span;
2. Creation of the stress distribution curve along the cross section;
3. Calculation of the area under the curve using the finite sum method, in which 1000 points were used;
4. Calculation of the effective width using Equation (01), which was approximated to Equation (02), using this method.

Figure 9 illustrates the variables in Equation (02).

$$b_{ef} = \frac{\text{Area under the curve}}{\sigma_{max}} \quad (02)$$

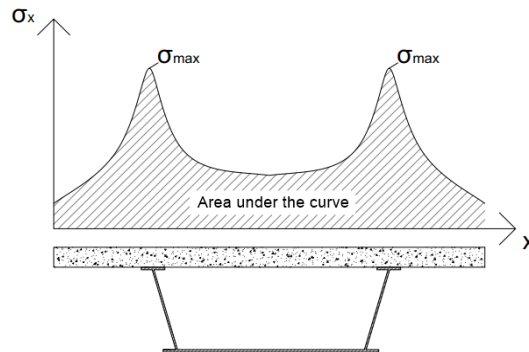


Figure 9. Variables for calculating the effective numeric width.

For all models, the stress distribution curve has the same typical configuration (with maximum stresses in the region of the beam webs). This demonstrates coherence with the curves found in the literature, in which the highest stress values are in the web region, showing the slab's contribution to the strength of the composite section. Figure 10 shows the normal stress distribution found in the models of simple and double box configuration, respectively.

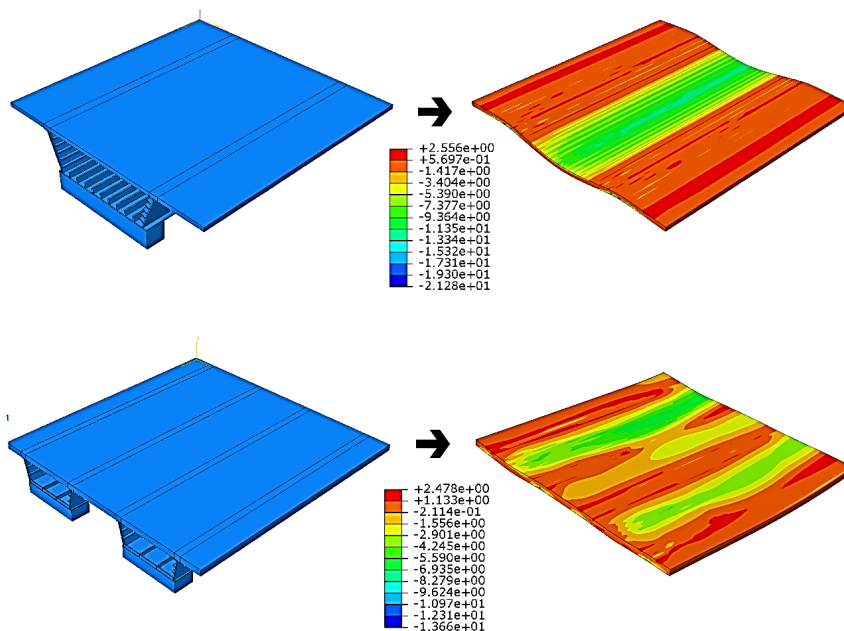
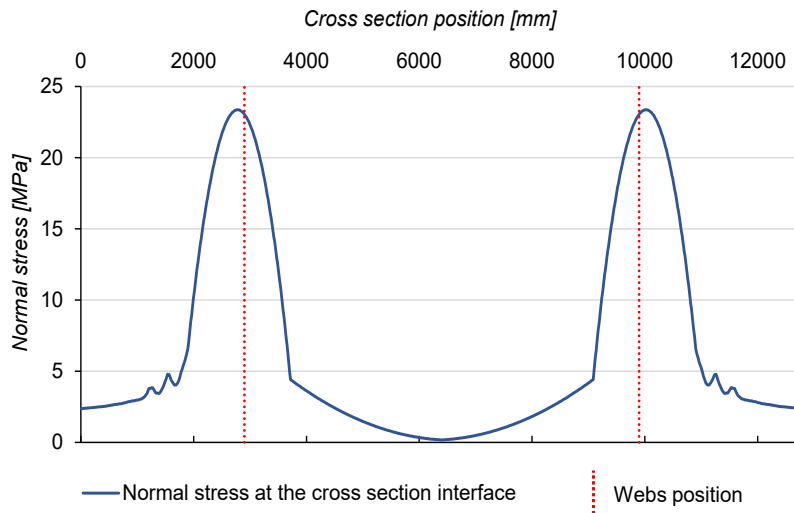
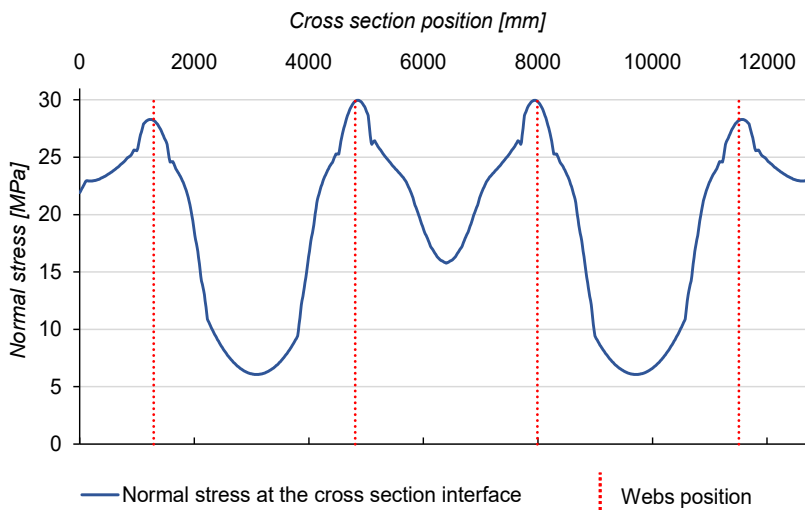


Figure 10. Stress distribution typical of models in single and double box configurations. [N/mm<sup>2</sup>].

It is worth noting that the maximum normal stresses occur where the concrete slab rests on the steel girder due to the greater rigidity of that location in the composite section and, as a consequence, there is the shear lag effect. Figures 11 and 12 illustrate, respectively, the occurrence of maximum stresses at the support points and the typical shape of the stress distribution curve for simple and double box girder configurations.



**Figure 11.** Occurrence of maximum normal stresses in the region of the webs in models with simple box configuration.



**Figure 12.** Occurrence of maximum normal stresses in the region of the webs in models with double box configuration.

### Simple box section

#### Influence of slab height

In order to analyze the influence of the slab height in the calculation of the effective width, for a span of 3,000 cm and distance between webs of 620.0 cm, eight numerical models with slab heights of 15.0 cm; 20.0 cm; 22.5 cm; 25.0 cm; 27.5 cm; 30.0 cm; 35.0 cm; and 50.0 cm, were analyzed. Table 3 summarizes the results obtained in calculating the effective width by varying the

slab height. The results of Table 3 are expressed in the graph of Figure 13 in a comparison with the effective width calculated using the standards AASHTO [13], ABNT NBR 8800 [15] and EN 1994-2-2 [14].

**Table 3.** Numeric effective width versus slab height for single box configuration.

MODEL	SLAB HEIGHT ( $h_i$ ) [cm]	EFFECTIVE WIDTH ( $b_{ef}$ ) [cm]
1	15.0	201.2
2	20.0	257.8
3	22.5	270.7
4	25.0	289.7
5	27.5	309.3
6	30.0	322.0
7	35.0	325.2
8	50.0	320.9

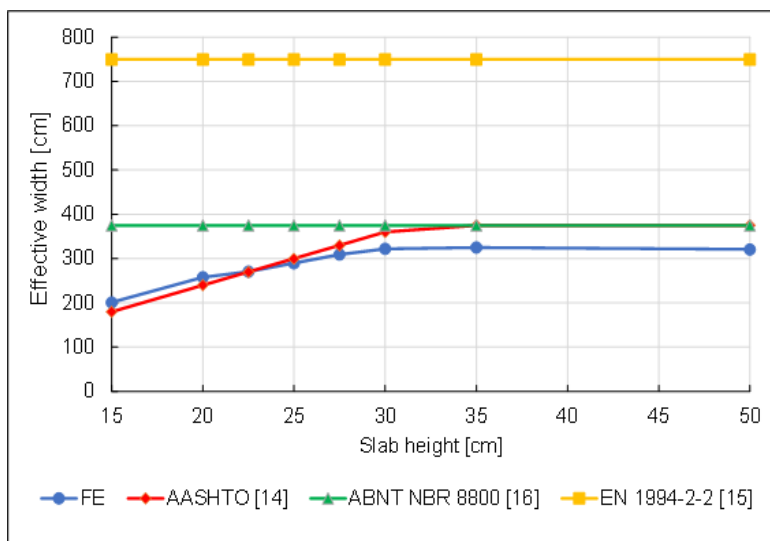


**Figure 13.** Effective width versus slab height for single box configuration.

It is possible to observe that the effective width curve as a function of the slab height has an increase that grows proportionally to the usual slab values, that is, up to a height of 30.0 cm. Discarding models 7 and 8 - which have unusual slab heights - there is an average ratio between the effective width and the slab height of 11.98, which is very close to that described by the AASHTO standard [13]. Such results can be seen in Table 4. Comparing the numerical effective width with that recommended by ABNT NBR 8800 [15] and EN 1994-2-2 [14], great divergences were observed, especially in relation to the European standard, which presented effective width values considerably higher than those found in numerical analyzes.

**Table 4.** Relationship between the effective numerical width and the slab height for simple box configuration.

MODEL	SLAB HEIGHT ( $h_i$ ) [cm]	EFFECTIVE WIDTH ( $b_{ef}$ ) [cm]	$\frac{b_{ef}}{h_i}$
1	15.0	201.2	13.42
2	20.0	257.8	12.89
3	22.5	270.7	12.03
4	25.0	289.7	11.59
5	27.5	309.3	11.25
6	30.0	322.0	10.73
<i>Average</i>			<b>11.98</b>

### Influence of span length

In the study of the influence of span length, five numerical models were developed. For a slab height of 25.0 cm and a distance between webs of 620.0 cm, the span length was modeled with: 1,000.0 cm; 2,000.0 cm; 3,000.0 cm; 4,000.0 cm; and 5,000.0 cm. Table 5 summarizes the results obtained in calculating the effective width for the five models described.

**Table 5.** Relationship between the effective numerical width and the longitudinal span length for the simple **box configuration**.

MODEL	SPAN [cm]	EFFECTIVE WIDTH ( $b_{ef}$ ) [cm]	$\frac{SPAN}{b_{ef}}$
9	1000.0	259.9	3.85
10	2000.0	275.5	7.26
11	3000.0	289.7	10.36
12	4000.0	288.8	13.85
13	5000.0	286.5	17.45

Observing the results, it is noted that the span length influences the effective width calculation up to 3,000 cm. After this limit, the models showed a practically constant result for the effective width (possibly due to the effective width being governed by the height of the slab and not by the span anymore). This shows that higher span values do not have much influence on this calculation. This fact becomes even clearer when looking at the graph shown in Figure 14, which makes a comparison of the numerical effective width with that calculated by the AASHTO [13], ABNT NBR 8800 [15] and EN 1994-2-2 [14] standards.

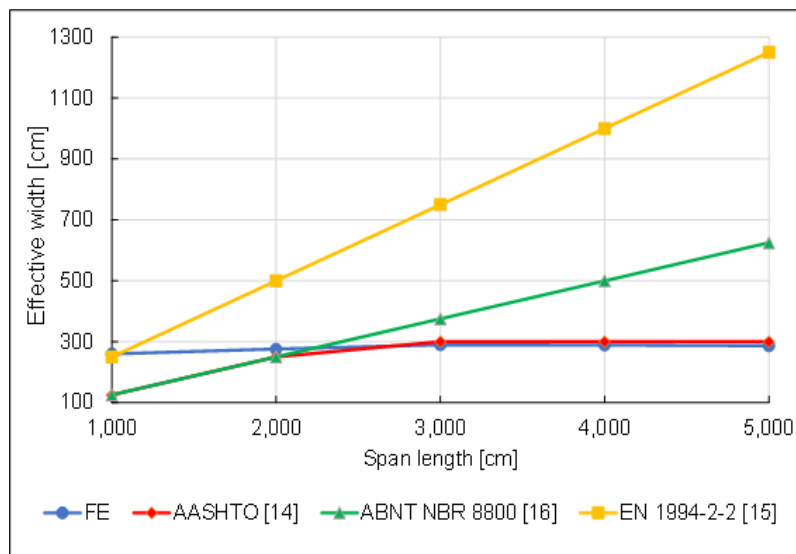


**Figure 14.** Effective width versus span length for single box configuration.

AASHTO's recommendations [13] approached the numerical effective width for spans greater than 3,000 cm. Furthermore, the requirements of ABNT NBR 8800 [15] and EN 1994-2-2 [14] showed considerable divergences - especially the European standard, which again provided values of effective width greater than those found.

### Transversal cantilever influence (distance between webs)

In the analysis of the influence of the transversal cantilever distance, fixing the slab height at 20.0 cm and the span length at 5,000 cm, the cantilever distances were: 350.0 cm; 340.0 cm; 330.0 cm; 320.0 cm; 310.0 cm; and 300.0 cm. Table 6 shows the results obtained.

**Table 6.** Relationship between the effective numerical width and the distance between webs for the simple **box** configuration.

MODEL	CANTILEVER [cm]	DISTANCE AMONG WEBS ( $w$ ) [cm]	EFFECTIVE WIDTH ( $b_{ef}$ ) [cm]	$\frac{b_{ef}}{w}$
14	350.0	580.0	216.3	0.37
15	340.0	600.0	205.0	0.34
16	330.0	620.0	192.4	0.31
17	320.0	640.0	174.0	0.27
18	310.0	660.0	130.9	0.20
19	300.0	680.0	124.0	0.18
<i>Average</i>				<b>0.28</b>

Figure 15 shows the behavior of the effective width as a function of the distance between the girder webs and those calculated by the normalizations AASHTO [13], ABNT NBR 8800 [15] and EN 1994-2-2 [14]. The numerical analyzes provided results closer to the recommendations of AASHTO [13], while ABNT NBR 8800 [15] and EN 1994-2-2 [14] resulted in higher  $b_{ef}$  values.

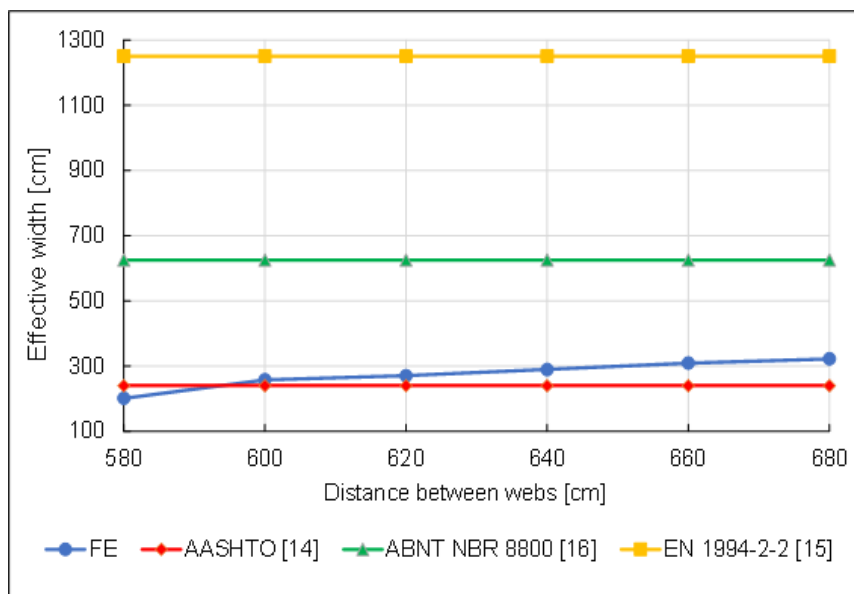


**Figure 15.** Effective width versus distance between webs for simple box configuration.

In addition, it is noted that the effective width decreases as the webs are separated. This phenomenon is explained by the fact that the rigidity of one web is not able to maintain the “absorption” of normal stresses until the other. It is also worth noting that the average quotient of the width between webs for the effective width is  $0.28 \cong 1/4$ .

**Comparison between the effective numerical width and that established by the standards**

In all parameterizations, a large discrepancy is noticed between the effective numerical width calculated numerically in Abaqus® [23] and those prescribed by ABNT NBR 8800 [15] and EN 1994-2-2 [14]. The reason for this is that such normalizations limit the effective width only by the length of the span and the distance between girders. As in the simple box configuration there is only one box girder, the effective width found is greater than that found numerically.

Overall, numerical results were closer to the recommendations of AASHTO [13], especially in the variation of slab height and span length. However, when the distance between webs was varied, AASHTO [13] provided values of effective width greater than those found numerically.

Finally, for the simple box configuration, it is noted that the standards have values of effective width higher (in most cases) than those calculated numerically - especially when compared with ABNT NBR 8800 [15] and EN 1994-2-2 [14].

## Double box section

### Influence of slab height

For models in a double box section, the influence of the slab height on the effective width calculation was analyzed by simulating six numerical models with the following heights: 15.0 cm; 20.0 cm; 22.5 cm; 25.0 cm; 27.5 cm and 30.0 cm. The span length was set at 3,000 cm and the distance between the center of steel box girders at 620,0 cm. Table 7 shows the results obtained in the calculation of the effective width by varying the slab height and Figure 16 expresses these results graphically in a comparison with the effective width established by the codes AASHTO [13], ABNT NBR 8800 [15] and EN 1994 - 2-2 [14].

**Table 7.** Relationship between the effective numerical width and the slab height for the double **box configuration**.

MODEL	SLAB HEIGHT ( $h$ ) [cm]	EFFECTIVE WIDTH ( $b_{ef}$ ) [cm]	$\frac{b_{ef}}{h}$
20	15.0	210.7	14.05
21	20.0	215.3	10.77
22	22.5	217.4	9.66
23	25.0	223.1	8.92
24	27.5	224.5	8.16
25	30.0	219.1	7.30
<i>Average</i>			<b>9.81</b>

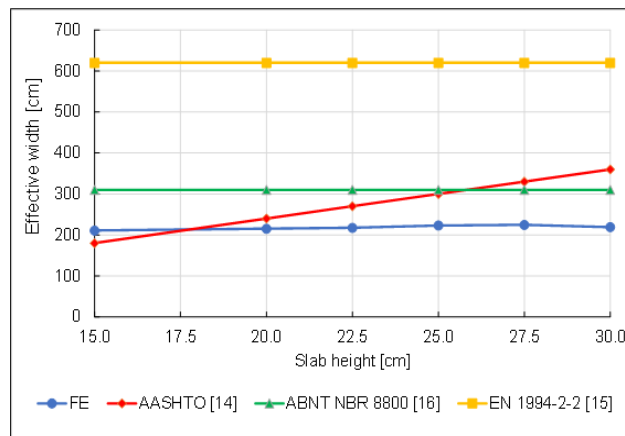


**Figure 16.** Effective width versus slab height for double box configuration.

Analyzing the stress distribution, it was found that as the slab height increased, the maximum stress in the central webs became smaller. This is explained by the fact that the plastic neutral axis goes up to the concrete slab as the height of the slab increases. Furthermore, the drop in the effective width value in the model with a slab height of 30.0 cm is explained by the slab's height no longer being the limiting factor of the shear lag effect. Finally, it appears that the average quotient of the effective width by the height of the slab is approximately 10.

With the exception of the model with a 15.0 cm slab height, the recommendations of AASHTO [13], ABNT NBR 8800 [15] and EN 1994-2-2 [14] presented higher effective width values - especially EN 1994-2-2 [14].

### Influence of span length

In the analysis of the influence of the span length for the calculation of the effective width in a double box section, five numerical models were simulated. For a slab height of 25.0 cm, distance from center to center of box girders of 620.0 cm, the span length was designed with: 1,000.0 cm; 2,000.0 cm; 3,000.0 cm; 4,000.0 cm; and 5,000.0 cm. Table 8 presents the results obtained. Figure 17 presents these results graphically compared to the effective width of the AASHTO [13], ABNT NBR 8800 [15] and EN 1994-2-2 [14] standards.

**Table 8.** Relationship between the effective numerical width and the longitudinal span length for the double **box configuration**.

MODEL	SPAN [cm]	EFFECTIVE WIDTH ( $b_{ef}$ ) [cm]	$\frac{SPAN}{b_{ef}}$
26	1,000.0	248.4	4.03
27	2,000.0	275.5	7.26
28	3,000.0	277.1	10.83
29	4,000.0	277.9	14.39
30	5,000.0	279.2	17.91

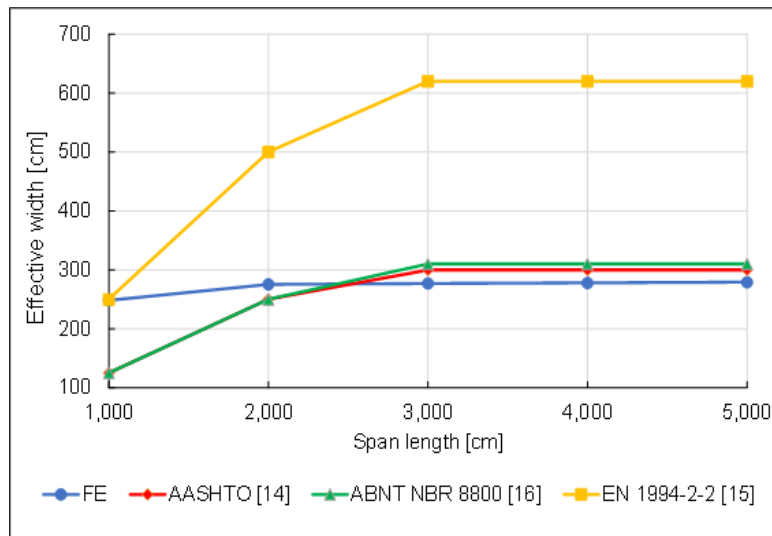


**Figure 17.** Effective width versus span length for double box configuration.

With the exception of the model with a span of 1,000 cm, the effective numerical width remained practically constant. Similar to the simulations for simple box configuration, it is explained that the effective width was being limited by the height of the slab and no longer by the span.

The  $b_{ef}$  values recommended by EN 1994-2-2 [14] were considerably higher than all numerical results. As for the recommendations of AASHTO [13] and ABNT NBR 8800 [15], with the exception of the model with a span length of 1,000 cm, the results showed greater agreement.

**Transversal cantilever influence (distance between girders)**

In assessing the influence of the effective width against the variation in the distance between box girders ( $a$ ), fixing the slab height at 22.5 cm and the span length at 3,000 cm, five models were simulated for the following distance values between girders: 580.0 cm; 600.0 cm; 620.0 cm; 640.0 cm; and 660.0 cm. Table 9 shows the results obtained.

**Table 9.** Relationship between the effective numerical width and the distance between girders for the double **box configuration**.

MODEL	DISTANCE BETWEEN GIRDERS ( $a$ ) [cm]	EFFECTIVE WIDTH ( $b_{ef}$ ) [cm]	$\frac{b_{ef}}{a}$
31	580.0	255.7	0.44
32	600.0	249.4	0.42
33	620.0	235.2	0.38
34	640.0	217.4	0.34
35	660.0	213.3	0.32
<i>Average</i>			<b>0.38</b>

Figure 18 represents the numerical effective width distribution for such models and compares the results with the effective widths calculated by AASHTO [13], ABNT NBR 8800 [15] and EN 1994-2-2 [14]. The effective numerical width was smaller than that recommended by all methods, with emphasis on EN 1994-2-2 [14], which presented much higher values.

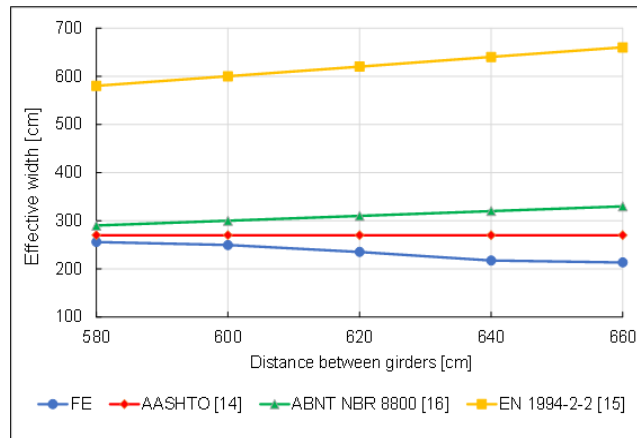


Figure 18. Effective width versus distance between girders for double box configuration.

It is also noted that the effective width has its value reduced as the box girders are moved away. This variation is explained by the girders contributed together to maintain high tensions in the region between them. Analyzing an average relationship between the effective width and the distance between the girders, it is recommended that the effective width is not less than 30% of the distance from the center to the center of box girders.

Finally, it is worth mentioning that for the analysis of the influence of the span length and the influence of the transversal cantilever distance in double box configuration, a mesh refinement twice higher than that used in the others was necessary. This is attributed to the difference in the value of the effective numerical width between models 23 and 28 and 22 and 23, which have the same geometry.

### Comparison between the effective numerical width and that established by the standards

Comparing the curves of the effective numerical width with those prescribed by the standards for the double box configuration, there is a great disparity in relation to that established by EN 1994-2-2 [14].

In addition, the effective numerical width and those calculated by AASHTO [13] and ABNT NBR 8800 [15] showed similar values. The reason for this is that the Brazilian standard limits the effective width to half the distance between center to center between adjacent girders - different from EN 1994-2-2 [14], which limits the effective width in relation to the span and the average of the center distance between the girder analyzed and the adjacent girders.

In general, the technical standards have values of effective width higher (in most cases) than those calculated numerically - especially EN 1994-2-2 [14].

### Suggestion of formulation

Based on the results presented, for steel-concrete composite box girder bridges in simple box configuration, it is recommended that the effective width of the slab must not exceed: (for each web):

- One-fourth of the span length of the girder;
- Half the distance from center to center of girders;
- 12 times the least thickness of the slab.

In turn, for steel-concrete composite bridges in double box configuration, it is recommended that the effective width of the slab must not exceed: (for each box girder):

- One-fourth of the span length of the girder;
- 30% of the distance from center to center of girders;
- 10 times the least thickness of the slab.

## CONCLUSIONS

A numerical analysis was developed to determine the effective width in steel-concrete composite box girder bridges with simple and double box section. For this purpose, the influence of the span, the height of the slab and the distance between webs (simple box configuration) and girders (double box configuration) were evaluated. The numerical values of effective width were compared with those obtained by the AASHTO [13], ABNT NBR 8800 [15] and EN 1994-2-2 [14] standards for beams with I-profiles.

Among the analyzed parameters, the height of the slab was the one that most influenced the calculation of the effective width, showing a proportional increase with the increase in the height of the slab in the range from 15.0 cm to 30.0 cm.

The span length, in turn, influenced the effective width value for spans up to 3,000 cm. For larger spans, the effective width has not been significantly changed, due to the fact that the effective width is being limited by the height of the concrete slab and no longer by the span.

Finally, it is noted that the effective width decreases as the webs and girders are separated. This phenomenon is explained by the rigidity of a single web not being able to maintain the “absorption” of normal stresses in the section until the other.

In general, AASHTO [13] was the technical standard that most converged with the results found numerically. The recommendations of ABNT NBR 8800 [15] and, mainly, of the European standard EN 1994-2-2 [14], presented values of effective width higher than those of numerical analysis.

More specifically about AASHTO [13], which resulted in the best concordances, comparing the effective width values obtained numerically with those recommended by the American standard, it is clear that the relationship  $b_{ef} \leq \frac{Span}{4}$  is confirmed. However, the limitation of 12 times the thickness of the slab for the double box configuration and the limitation of the effective width as being less than or equal to the distance between girders or webs, overestimates the contribution of the slab to the strength of the composite section.

Therefore, based on the numerical results discussed above, it is concluded that the recommendations prescribed by the AASHTO [13], ABNT NBR 8800 [15] and EN 1994-2-2 [14] standards for steel-concrete composite bridges with I-girders, should not be applied directly to box girder sections. Thus, for the calculation of the effective width of steel-concrete composite box girder bridges, it is recommended to use the formulation presented in item 4.3 of this work. It is also worth noting the need for additional numerical and experimental studies to prove and rectify the formulation.

## ACKNOWLEDGMENTS

The authors would like to thank CNPq, process 120583/2017-8 and the entire team of IBRACON Structures and Materials Journal for the opportunity to publicize the work.

## REFERENCES

- [1] G. S. Veríssimo, “Desenvolvimento de um conector de cisalhamento em chapa dentada para estruturas mistas de aço e concreto e estudo do seu comportamento,” M.S. thesis, Univ. Fed. Minas Gerais, Belo Horizonte, 2007.
- [2] S. de Nardin and A. S. C. Souza, “Sistemas de vigas mistas contínuas e semicontínuas para edifícios,” in *An. XXXIII Jorn. Sudam. Ing. Estructural*, Santiago, Chile, 2008, pp. 1-10.
- [3] I. T. Kotinda, “Modelagem numérica de vigas mistas aço-concreto simplesmente apoiadas: ênfase ao estudo da interface laje-viga,” M.S. thesis, Esc. Eng. São Carlos, Univ. São Paulo, São Carlos, 2006.
- [4] A. S. C. Souza, W. F. Maia, and S. de Nardin, “Análise numérica de vigas mistas de aço e concreto protendidas,” *Rev. Estrutura Aco*, vol. 4, pp. 1–15-1, 2015.
- [5] F. Pinho and I. H. Bellei, *Pontes e Viadutos em Vigas Mistas*, 1. ed. Rio de Janeiro: IBS/CBCA, 2007.
- [6] D. Orlando, Z. M. C. Pravia, and G. A. Drehmer “Análise de pontes mistas de aço e concreto pelo método dos elementos finitos,” in *An. XVII Cong. Reg. Iniciaç. Cient. Tec.*, Porto Alegre, 2003.
- [7] V. J. L. Souza, “Contribuição ao projeto e dimensionamento da superestrutura de pontes rodoviárias em vigas mistas de aço e concreto,” M.S. thesis, Dep. Eng. Civ., Univ. Fed. São Carlos, São Carlos, 2006.

- [8] H. P. Faria and Z. M. C. Pravia, "Metodologia de cálculo de uma ponte em caixão metálico com laje em concreto," in *An. VII Cong. Bras. Pontes e Estrut.*, Rio de Janeiro, 2014.
- [9] J. Brozzetti, "Design development of steel-concrete composite bridges in France," *J. Construct. Steel Res.*, vol. 55, no. 1-3, pp. 229–243, 2000.
- [10] S. Nakamura, Y. Momiyama, T. Hosaka, and K. Homma, "New technologies of steel/concrete composite bridges," *J. Construct. Steel Res.*, vol. 58, no. 1, pp. 99–130, 2002.
- [11] D. C. Iles, *Design Guide for Composite Box Girder Bridges*, 2th ed. Ascot, England: SCI, 1994.
- [12] B. Chavel and J. Rivera, *Steel Bridge Design Handbook Design – Example 5 – Three-Span Continuous Horizontally Curved Composite Steel Tub-Girder Bridge*, 1th ed. USA: FHWA, 2015.
- [13] American Association of State Highway and Transportation Officials, *LRFD Bridge Design*, 2017.
- [14] European Committee for Standardization, *Eurocode 4 – Design of Composite Steel and Concrete Structures – Part 2: General Rules and Rules for Bridges*, EN 1994-2-2, Brussels, Belgium, 2005.
- [15] Associação Brasileira de Normas Técnicas, *Design of Steel and Composite Structures for Buildings*, NBR 8800, 2008.
- [16] L. G. Reginato, "Estudo da largura efetiva de vigas mistas de aço-concreto em carregamento de serviço: método dos elementos finitos versus códigos de projeto," M.S. thesis, Dep. Eng. Civ., Univ. Fed. Rio Grande do Sul, Porto Alegre, 2017.
- [17] P. Patel, "LRFD design of double composite box girder bridges," M.S. thesis, Univ. South Florida, Florida, USA, 2009.
- [18] C. Amadio and M. Fragiocomo, "Effective width evaluation for steel-concrete composite beams," *J. Construct. Steel Res.*, vol. 58, no. 3, pp. 373–388, 2002.
- [19] T. Salama and H. H. Nassif, "Effective flange width for composite steel beams," *J. Eng. Res.*, vol. 8, no. 1, pp. 28–43, 2011.
- [20] M. Abbu, T. Ekmekyapar, and M. F. E. Ozakça, "Analysis of stresses in composite box girder bridges," in *Proc. Int. Civ. Eng. Architecture Symposium for Academicians*, Antalya, Turkey, 2014.
- [21] L. Zhu, J. G. Nie, F.-X. Li, and W.-Y. Ji, "Simplified analysis method accounting for shear-lag effect of steel-concrete composite decks," *J. Construct. Steel Res.*, vol. 115, pp. 62–80, 2015.
- [22] H. Yuan, H. Deng, Y. Yang, Y. Weijian, and Z. Zhenggeng, "Element-based effective width for deflection calculation of steel-concrete composite beams," *J. Construct. Steel Res.*, vol. 121, pp. 163–172, 2016.
- [23] Abaqus®. Dassault Systèmes Simulia. Abaqus 6.18. 2016.
- [24] L. D. Kirchhof, "Uma contribuição ao estudo de vigas mistas aço-concreto simplesmente apoiadas em temperatura ambiente e em situação de incêndio," M.S. thesis, Esc. Eng. São Carlos, Univ. São Paulo, São Carlos, 2004.

---

**Author contributions:** RSN: conceptualization, methodology, numerical analysis, writing; ASCS: formal analysis, methodology, supervision, review.

**Editors:** Leandro Mouta Trautwein, José Luiz Antunes de Oliveira e Sousa, Guilherme Aris Parsekian.



## ORIGINAL ARTICLE

# Reinforced concrete flat slabs with openings at different distances from the column

*Lajes lisas de concreto armado com aberturas em diferentes distâncias do pilar*

Diego da Silva Lourenço<sup>a</sup>

Elyson Andrew Pozo Liberati<sup>b</sup>

Marília Gonçalves Marques<sup>c</sup>

Luiz Carlos de Almeida<sup>a</sup>

Leandro Mouta Trautwein<sup>a</sup>

<sup>a</sup> State University of Campinas - UNICAMP, School of Civil Engineering, Architecture and Urban Design, Campinas, São Paulo, Brazil

<sup>b</sup> State University of Maringá - UEM, Civil Engineering Department, Maringá, Paraná, Brazil

<sup>c</sup> Federal University of Viçosa - UFV, Rio Paranaíba, Brazil, Brazil

Received 08 March 2020

Accepted 11 June 2020

**Abstract:** The increase in the use of flat slabs and the need of the openings for the passage of installations, such as hydraulic and electrical, which significantly reduces the punching shear resistance capacity of the slab, makes the understanding of the influence of openings in this type of structure extremely necessary. The influence in the structural behaviour of flat slabs with openings at different distances from the column was investigated through five square slabs (1,800 mm x 1,800 mm x 130 mm) supported on square columns (150 mm x 150 mm) tested until failure. The results obtained experimentally were compared with results available in the literature, as well as with responses predicted from the normative instructions. The results confirm high stresses concentration in the region between the column and the opening and that opening situated at  $3d$  from the column have no influence on the failure load for the tested slabs.

**Keywords:** Reinforced concrete, flat slabs, punching, openings.

**Resumo:** Com o aumento da utilização de lajes lisas e a necessidade da presença de aberturas para a passagem de instalações hidráulicas e elétricas, que reduzem de forma acentuada a capacidade resistente à punção, o entendimento da influência de aberturas nesse tipo de estrutura se torna extremamente necessária. A influência no comportamento estrutural de lajes lisas com aberturas em diferentes distâncias do pilar foi investigada por meio de cinco lajes quadradas (1.800 mm x 1.800 mm x 130 mm), apoiadas sobre pilares quadrados (150 mm x 150 mm) e testadas até a ruptura. Os resultados obtidos experimentalmente foram comparados com resultados disponíveis na literatura, bem como com respostas previstas por meio de instruções normativas. Os experimentos mostram concentração elevada de tensões na região crítica entre o pilar e a abertura e que a partir de  $3d$  a abertura passa a não ter mais influência na carga de ruptura da laje.

**Palavras-chave:** Concreto armado, lajes lisas, punção, aberturas.

**How to cite:** D. S. Lourenço, E. A. P. Liberati, M. G. Marques, L. C. Almeida, and L. M. Trautwein, "Reinforced concrete flat slabs with openings at different distances from the column," *Rev. IBRACON Estrut. Mater.*, vol. 14, no. 1, e14111, 2021, <https://doi.org/10.1590/S1983-41952021000100011>

## 1 INTRODUCTION

Reinforced concrete flat slabs without shear reinforcement are commonly used in many structural systems, such as flat slabs of buildings and parking garages. Although simple in appearance, the flat slab system presents a complex behavior, especially in the slab-column connection. Failures in punching of flat slabs without shear reinforcement develop in a brittle manner with limited deflections and are followed by an almost complete loss of the load carrying capacity (Figure 1).

**Corresponding author:** Elyson Andrew Pozo Liberati. E-mail: eapliberati@uem.br

**Financial support:** None.

**Conflict of interest:** Nothing to declare.



This is an Open Access article distributed under the terms of the Creative Commons Attribution License, which permits unrestricted use, distribution, and reproduction in any medium, provided the original work is properly cited.

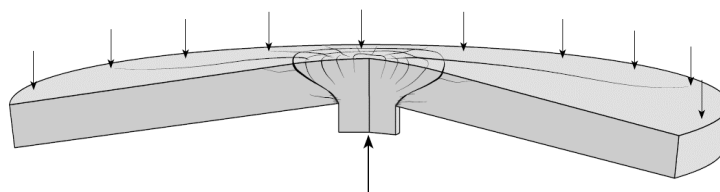


Figure 1. Punching shear failure of flat slab.

Among the problems that may decrease the resistance to punching of flat slabs is the existence of openings in the regions near the column. This is due to the decrease in shear strength caused by the removal of concrete and reinforcement at the opening, reducing the critical slab perimeter. Therefore, it is important to estimate accurately the punching shear strength of flat slabs with openings.

Several researchers studied the punching shear behavior of slabs with openings, including Elstner and Hognestad [5], Moe [6], and Regan [7] and later by Gomes and Andrade [8] and El-Salakawy et al. [9]. Recently, Teng et al. [10], Borges et al. [11], Anil et al. [12], Ha et al. [13], Balomenos et al. [14] and Liberati et al. [15] carried out studies on this topic. Despite the significant advances achieved, all these experimental findings have shown that when the openings are located near the column it may be critical to significantly reduce the punching shear strength of the connection. However, these experimental efforts consider only cases with openings located at a certain distance from column's face that is next to the column or within the control perimeter.

The current design codes for punching shear try to relate the effect of opening on slab's ultimate capacity based on its size and location by reducing the control perimeter. The ACI 318 [3] and *fib* Model Code [4] adopt the critical shear perimeter at distance  $d/2$  from the loaded area (column), while the NBR 6118 [2] and Eurocode 2 [1] consider the control perimeter, at distance  $2d$  from the column's face, where  $d$  is the effective depth of the slab. The Eurocode 2 [1], *fib* Model Code [4] and NBR 6118 [2] assume the control shear perimeter with circular ends, while ACI 318 [3] adopts rectangular shape for the critical shear perimeter. All design codes reduce the critical shear perimeter based on the size and the location of the opening, where a part of the control perimeter contained between two tangents drawn to the outline of the opening from the center of the column is considered ineffective. In such cases, the control perimeter will be reduced only if the distance between the column perimeter and the edge of the opening meets the values stipulated for each design code as shown in Figure 2.

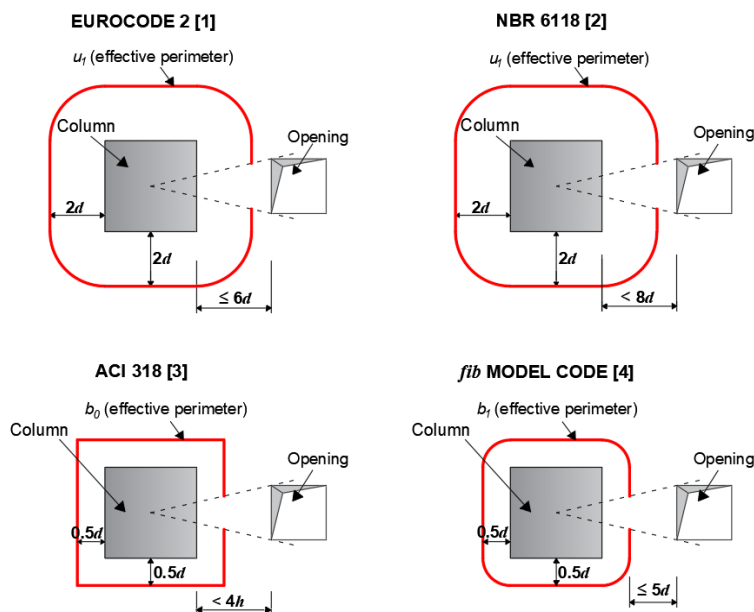


Figure 2. Effective control perimeters.

In this context, this study presents the results of the experimental program involving reinforced concrete flat slabs without shear reinforcement subjected to concentric punching shear. The influence of openings near the column is analysed. The displacements, collapse loads values, and failure modes are analysed and compared with design code provisions, which is the main contribution of this study.

## 2 DESIGN CODES

According to Eurocode 2 [1] and NBR 6118 [2], the punching shear strength ( $V_{EC}$  and  $V_{NBR}$ , respectively) for slabs without shear reinforcement is defined in the Equation 1.

$$V_{EC}, V_{NBR} = \gamma \cdot k \cdot (100 \cdot \rho \cdot f_c)^{1/3} \cdot u_1 \cdot d \quad (1)$$

where  $\gamma$  is equal to 0.18 for Eurocode 2 [1] and 0.13 for NBR 6118 [2],  $u_1$  is the control perimeter positioned at a distance  $2d$  from the face of the column (Figure 2). The factor  $k$  is accounting for size effect (decreasing nominal shear strength with increasing size of the member), whose value is obtained as follows:

$$k = 1 + \sqrt{\frac{200}{d}} \quad (2)$$

The Eurocode 2 [1] limits the value of this effect in  $k \leq 2.0$  whereas in the Brazilian standard this is not limited.

The code provision of ACI 318 [3] regarding punching of slabs without shear reinforcement is rather simple and straightforward. The area at the control perimeter is multiplied by admissible shear stress. Thus, the punching strength ( $V_{ACI}$ ) is obtained as the minimum of the following Equation 3.

$$V_{ACI} = \min \begin{cases} 0.33 \cdot \lambda_s \cdot \sqrt{f_c} \cdot b_0 \cdot d \\ 0.17 \cdot \left(1 + \frac{2}{\beta}\right) \cdot \lambda_s \cdot \sqrt{f_c} \cdot b_0 \cdot d \\ 0.08 \cdot \left(2 + \frac{\alpha_s d}{b_0}\right) \cdot \lambda_s \cdot \sqrt{f_c} \cdot b_0 \cdot d \end{cases} \quad (3)$$

where,  $\alpha_s$  is equal to 40 for internal columns, 30 for edge columns, and 20 for corner columns;  $\beta$  is the ratio between the largest and smallest side of the column;  $b_0$  is the control perimeter (Figure 2). The parameter  $\lambda_s$  is the size effect factor giving by Equation 4.

$$\lambda_s = \sqrt{\frac{2}{1 + 0.004 d}} \leq 1 \quad (4)$$

The *fib* Model Code [4] is based on the Critical Shear Crack Theory (CSCT). For slabs without shear reinforcement, this code enables the punching strength ( $V_{MC}$ ) assessment as follows:

$$V_{MC} = k_\psi \cdot \sqrt{f_c} \cdot b_1 \cdot d \quad (5)$$

where,  $b_1$  is the control perimeter (Figure 2),  $k_\psi$  depends on the rotations of the slab ( $\psi$ ) is defined by Equation 6.

$$k_\psi = \frac{1}{1.5 + 0.9 \cdot k_{dg} \cdot \psi \cdot d} \leq 0.6 \quad (6)$$

In Equation 6  $k_{dg}$  is a factor that takes into account the maximum aggregate size  $d_g$ . If the value of  $d_g$  is not less than 16 mm, the value of this parameter can be set equal to 1.0. Otherwise,  $k_{dg}$  can be estimated according to the Equation 7.

$$k_{dg} = \frac{32}{16 + d_g} \geq 0.75 \tag{7}$$

Another speciality of the *fib* Model Code [4] is that different levels of approximation exist. In this research, Level II approximation is used for the prediction of the tested specimens. The following expression for the second level of approximation (LoA II) can be used in the majority of cases according to the Equation 8.

$$\psi = 1.5 \cdot \frac{r_s}{d} \cdot \frac{f_y}{E_s} \cdot \left( \frac{m_s}{m_R} \right)^{1.5} \tag{8}$$

where,  $r_s$  defines where the radial bending moment is equal to zero,  $m_R$  is the moment capacity of the slab,  $m_s$  is the average acting moment in the column strip, that for interior columns in slabs with sufficiently regular geometry can be approximated as  $m_s = V/8$ , and  $V$  is characteristic shear force.

Assuming a perfectly plastic behavior of the reinforcement after yielding, a rectangular stress block for concrete in the compression zone and neglecting compression reinforcement, the moment capacity  $m_R$  of the section is then:

$$m_R = \rho \cdot f_y \cdot d^2 \cdot \left( 1 - \frac{\rho \cdot f_y}{2 \cdot f_c} \right) \tag{9}$$

### 3 EXPERIMENTAL PROGRAM

The present study aims to reproduce the structural behavior of reinforced concrete flat slabs in the region around internal columns. Thus, the slabs and the experimental scheme adopted represent the region of negative bending moment, delimited by points of inflection with the length of approximately 1,800 mm, i.e., two-fifths of the total span between columns (4,500 mm), according to Figure 3.

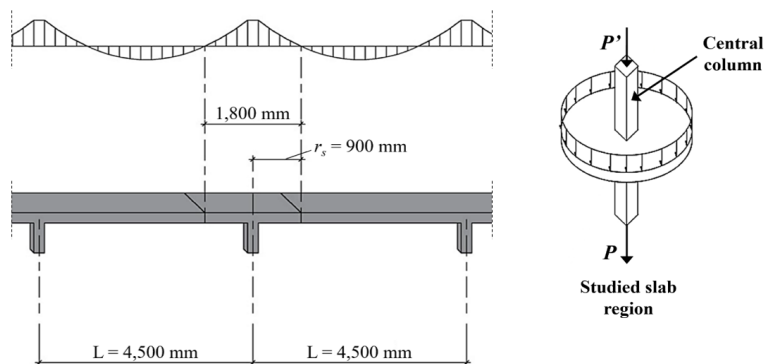


Figure 3. Idealized interior panel characterizing the situation studied (Lourenço [17]).

The experimental analyses performed in this study include tests until failure of 5 square flat slabs with 1,800 mm side and 130 mm thickness. The main variables accounted are the existence or not of openings near the column and the flexural reinforcement ratio, which is a function of the openings. The other test variables such as the size of the column (150 mm x 150 mm) and the size of the openings (150 mm x 150 mm) were kept constant. The size of the openings was adopted to represent the supply of gas, water, electricity and air conditioning systems. Slab openings can also be located very close to or far away from vertical load resisting columns.

The experimental program was carried out at the Laboratory of Structures of the School of Civil Engineering, Architecture and Urban Design of the State University of Campinas, Brazil.

### 3.1 Slab characteristics

The specimens were divided into slab without opening or also named reference slab (LR) and slabs with openings (LF1, LF2, LF3 and, LF4). All the slabs from the LF group had only one square opening of 150 mm x 150 mm positioned adjacent to the column (LF1) or at certain distance ( $s$ ) from the face of the column as follow: LF2 with  $s = 90$  mm ( $\approx d$ ); LF3 with  $s = 180$  mm ( $\approx 2d$ ) and LF4 with  $s = 270$  mm ( $\approx 3d$ ). All five specimens were manufactured without punching shear reinforcement. Figure 4 illustrates the characteristics of the slabs tested in this research.

The slabs were cast with normal strength concrete composed mainly by granite aggregate with maximum size ( $d_g$ ) of 16 mm. Cylindrical specimens (100 mm x 200 mm) were molded at the same time and from the same batch of concrete as the test slabs to determine the mechanical properties of the concrete (compressive strength -  $f_c$ ; splitting tensile test -  $f_t$  and Young's modulus -  $E_c$ ). Table 1 shows the average material properties of concrete determined at the age of testing for each specimen.

The flexural reinforcement ratio provided ( $\rho$ ) was set higher than the normal value to ensure clear punching shear failures. Thus, the effect of opening on punching shear strength can be observed clearly, with minimum interference from flexure. The values of the reinforcement ratio were calculated according to the NBR 6118 [2] as  $\rho = (\rho_x \rho_y)^{1/2}$ . For the calculation of  $\rho_x$  and  $\rho_y$  in this equation, the bars oriented on the  $x$  and  $y$  axes, respectively, were placed in a region between the column faces plus a  $3d$  length from each column face. The bars that intercepted the opening in these slabs were cut and were not considered in the calculation of the reinforcement ratio ( $\rho$ ), as shown in Table 1.

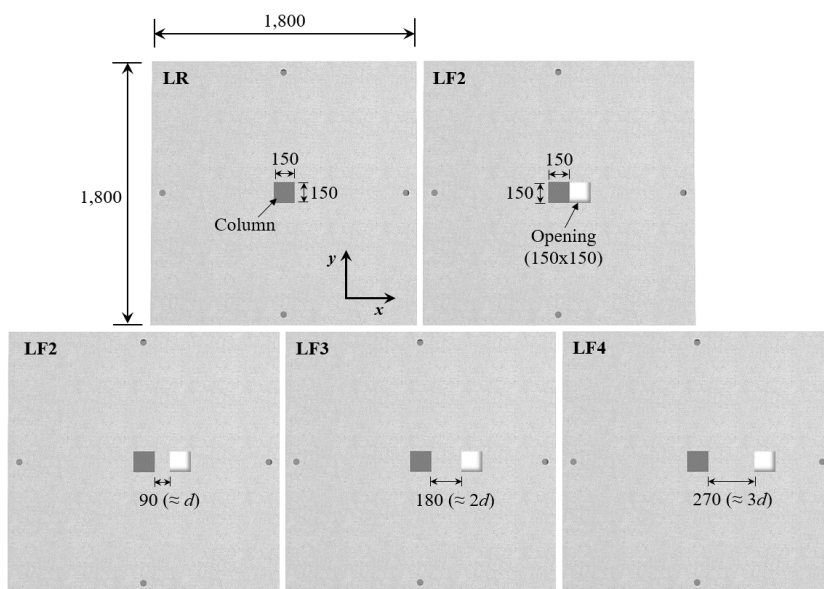


Figure 4. Slab characteristics (units in mm).

Table 1. Properties of specimens.

Slab	Openings [mm]	$s$ [mm]	Column [mm]	$\rho$ [%]	$d$ [mm]	$f_c$ [MPa]	$f_t$ [MPa]	$E_c$ [GPa]
LR	-	-	150 x 150	1.58	90	39.8	3.4	32.0
LF1	150 x 150	0	150 x 150	1.23	92	46.0	3.8	37.5
LF2	150 x 150	90	150 x 150	1.26	91	46.3	3.8	37.8
LF3	150 x 150	180	150 x 150	1.23	92	45.9	3.8	37.4
LF4	150 x 150	270	150 x 150	1.49	93	41.2	3.6	31.3

The flexural reinforcement was uniformly distributed over the whole slab. The diameter of top surface reinforcing bars was 12.5 mm bars on all slabs and the spacing was 90.0 mm in both directions. This spacing has been designed for providing the same flexural strength in both directions. The bottom reinforcement consisted of 6.3 mm reinforcing bars

at 150 mm spacing. This reinforcement layer was utilized for avoiding cracks during the slabs transportation. In the slabs with openings, this basic pattern of flexural reinforcement was modified locally.

To ensure anchorage of the negative reinforcement, U-shaped hooks composed of 6.3 mm diameter bars were were utilized at the slab ends and at the region of the openings. Mechanical properties of reinforcement were determined by tension testing three samples of each diameter bars and the results are presented in Table 2. Figure 5 presents the distribution of the top and bottom reinforcement of the slabs tested.

**Table 2.** Mechanical properties of reinforcement.

Local	Slab	Bar size [mm]	$f_y$ [MPa]	$\epsilon_y$ [mm/m]	$f_u$ [MPa]	$\epsilon_u$ [mm/m]	$E_s$ [GPa]
Top reinforcement	LR	12.5	576	3.2	735	15.4	180
	LF4						
	LF1						
	LF2						
Bottom reinforcement	LF3	6.3	563	2.85	728	15.5	198
	All slabs						
			569	3.1	724	9.9	184

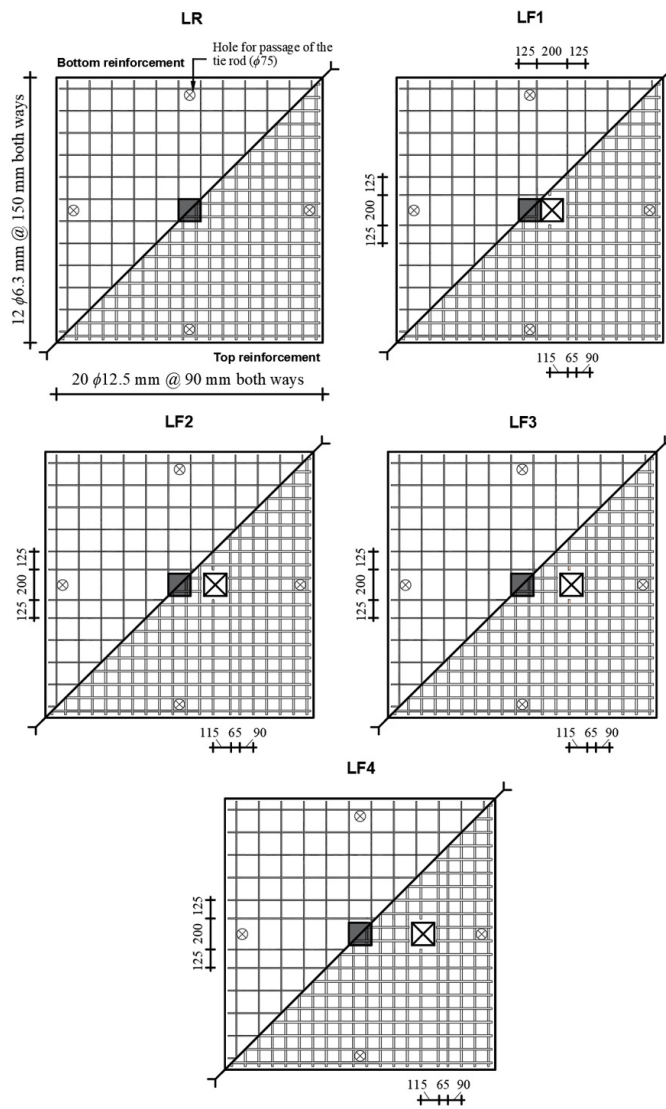


**Figure 5.** Slabs flexural reinforcements (units in mm).

### 3.2 Test setup

In the main series of the test program, 5 slabs were 130 mm thick and 1,800 mm square on plan. A square steel plate of 150 mm x 150 mm was used to simulate a rigid column in all specimens. Upward loading was applied incrementally by a hydraulic jack below this plate and measured by a load cell between the jack and plate. Loading was applied on a load-controlled basis. Reactions were provided by steel beams from the slab edges supported by eight equidistant points positioned at a circumference of radius equal to 900 mm ( $r_q$ ). These reactions were transmitted to the strong laboratory floor by tie rods ( $\phi 40$  mm), as shown in Figure 6.

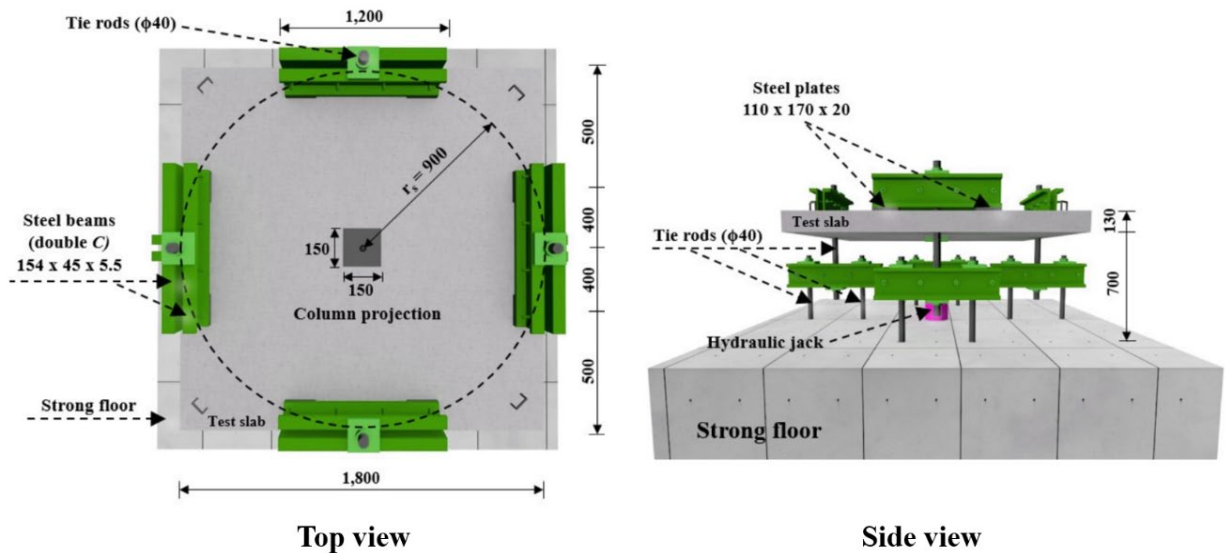


Figure 6. Typical test slabs (units in mm).

The vertical displacements of the specimens were measured at the 9 points along the slab (Figure 7) using linear variable displacement transducers (LVDTs), positioned at the tensioned face of the slabs. Transducers D2 and D3 were used to measure the displacement of the tested slab in relation to the reaction slab and were positioned in the line of the bending moment inflection points. The LVDTs were placed on a metal structure (C-dual profile) supported on tripods, as shown in Figure 8.

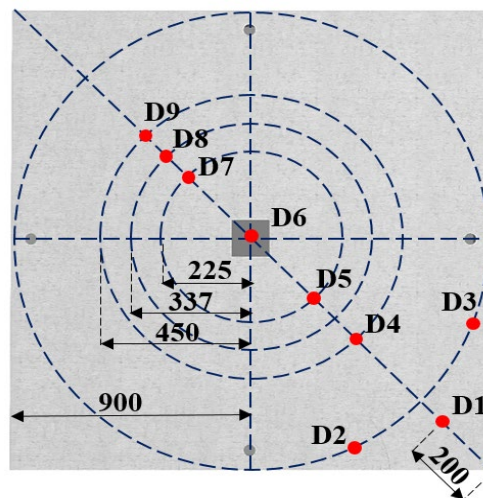


Figure 7. Location of the deflection measurements (units in mm).

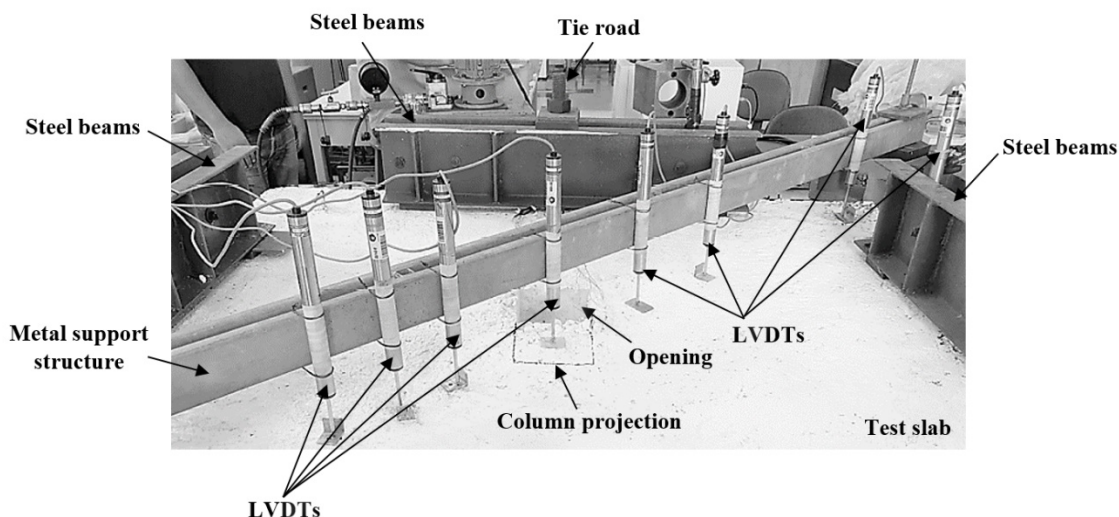


Figure 8. Setup of digital indicators for measuring vertical displacements.

Strains on the flexural reinforcement were measured on one side of the slab in both directions. Gauges were placed only on the flexural reinforcement bars that were located near the center of gravity of the column and around the opening. Typical locations of steel strain measurements are illustrated in Figure 9.

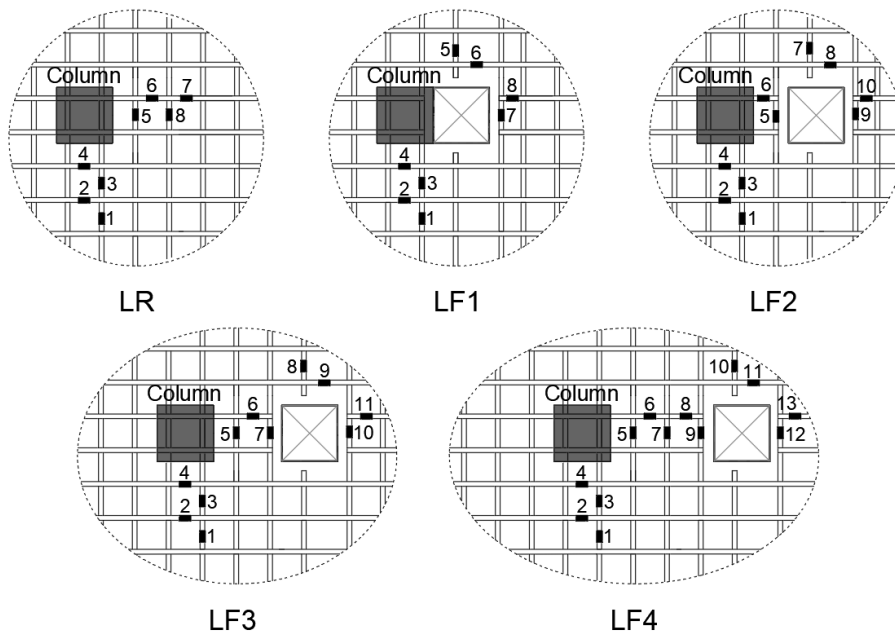


Figure 9. Location of the steel strain measurements.

## 4 RESULTS AND DISCUSSIONS

### 4.1 Vertical slab displacements

The displacements measured at different points increased with the increase in the load (Figure 10). The specimen LR presented a symmetrical profile for the vertical displacements obtained in both directions. As for the slabs with opening, the vertical displacements obtained around the opening were not symmetrical with the respective points

equidistant from the column. The opening reduces the slab stiffness and leads to a higher deflection of the slab area near the opening.

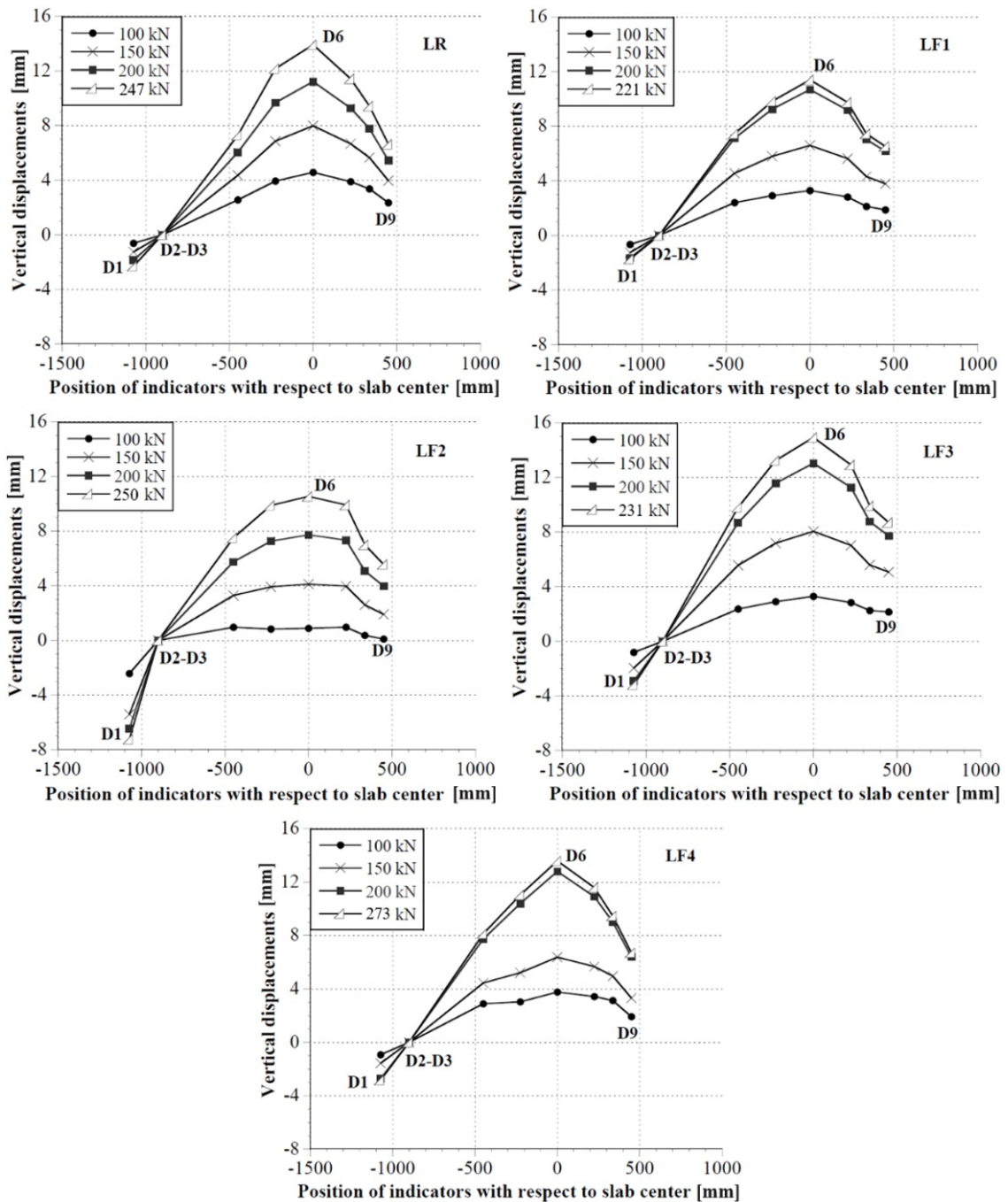


Figure 10. Vertical displacements vs position of indicators in the slabs.

All tested slabs experienced punching failure and their post-punching responses were recorded up to the point at which no meaningful data were recorded by the measurement instrumentations. It was generally observed that after the punching failure had occurred, the deflection increased and the load decreased rapidly. In Figure 11, the vertical displacements measured at the center of slabs are plotted against the test.

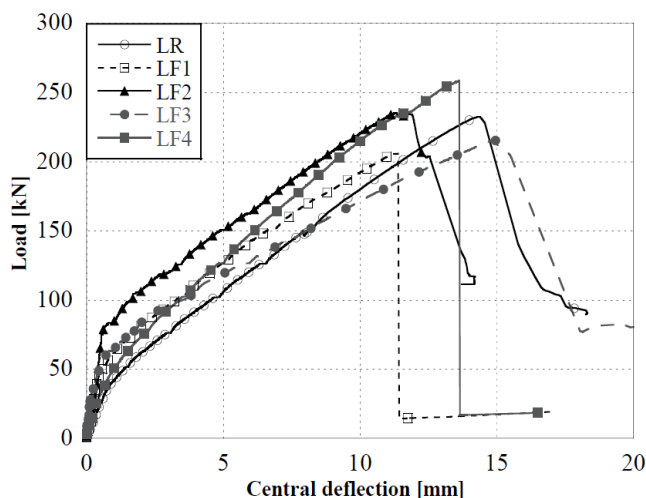


Figure 11. Load-deflection response of all test specimens.

LR showed greater displacements among all the slabs until around 150 kN. From this point, LF3 slab became the model that obtained larger displacements for smaller loads, reaching its maximum value of 14.9 mm, slightly larger than LR (14.3 mm). On the other hand, the lowest displacement is verified in LF2 (11.3 mm), very close to the maximum displacement of 11.4 mm in LF1.

In general, it is possible to observe that all the slabs with openings started their non-linear behavior with a load higher than the reference, except for LF4 that beginning to crack with a load nearby to LR. The higher values of concrete compressive strength ( $f_c$ ) obtained for slabs with openings may have influenced this behavior in the first load increments during the tests.

The presence of the openings led the tested models to present smaller displacements. However, for the final stages of loading, the LF3, with the opening positioned at  $2d$  from the column face, presented higher displacements in comparison to the other specimens, surpassing even the LR.

Figure 12 demonstrates that the presence of the openings results in the decreased in the maximum rotations approximately 20% for LF1 and LF2, as compared with LR. The slab LF2 showed higher rigidity, which justifies the lowest rotation obtained in the test in comparison with other slabs. One of the factors for this behavior can be explained by the late cracking in this slab in relation to the others. The tested slabs LF3 and LF4 presented marginally differences in comparison with the slab without openings LR, with variations around 5%. The values of the rotations were calculated from the difference between the central displacement and the displacement at the anchored perimeter.

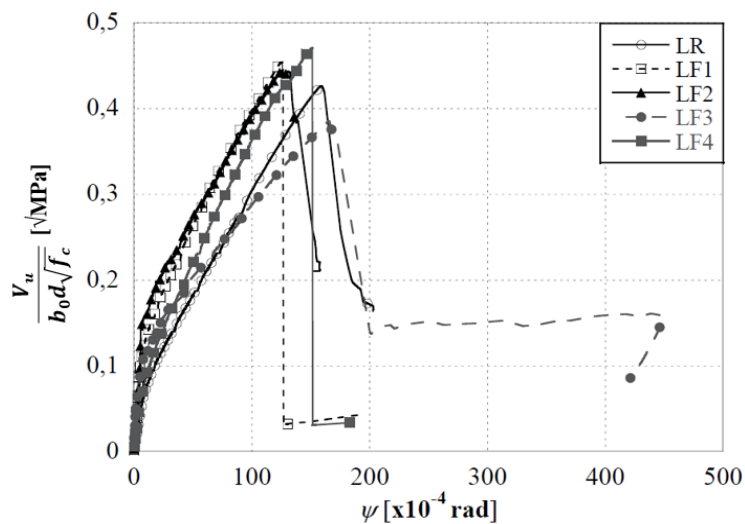


Figure 12. Load-rotation relationships.

### 4.2 Ultimate strengths and failure modes

The load application on the slabs occurred incrementally. The load value for the slab failure is the maximum value reached in the load cell reader. All the measurement readings were set to zero before starting the test, assuming that the slab deformations under self-weight of the slabs and the testing equipment were negligible (approximately 15 kN, added later to the measured load). Due to the different values of compressive concrete strengths ( $f_c$ ) of the models tested, the values of failure loads of slabs with openings were normalized ( $V_{u, norm}$ ) as a function of the variable  $f_c$ , as shown in Table 3.

**Table 3.** Experimental results.

Slab	$f_c$ [MPa]	$d$ [mm]	$V_u^a$ [kN]	$V_u^a/V_{flex}^b$	$V_{u, norm}^c$ [kN]	Energy Dissipation Capacity [kNmm]	Failure Mode
LR	39.8	90	247	0.51	-	1,945.78	Punching
LF1	46.0	92	221	0.64	206	1,505.88	Punching
LF2	46.3	91	250	0.64	232	1,761.34	Punching
LF3	45.9	92	231	0.59	215	2,105.93	Punching
LF4	41.2	93	273	0.57	268	2,126.35	Punching

<sup>a</sup>  $V_u$ : ultimate shear force including self-weights of slabs and loading system; <sup>b</sup>  $V_{flex}$ : shear force associated with flexural capacity of slab; <sup>c</sup>  $V_{u, norm}$ : normalized failure load given by  $V_{u, norm} = V_u \sqrt{f_{c, LR} / f_{c, LF}}$ , where  $f_{c, LR}$  is the compressive strength of the concrete of the reference slab and  $f_{c, LF}$  is the compressive strength of the slab concrete with opening.

The flexural resistance of the slabs ( $V_{flex}$ ) was calculated through the Yield Line Method, according to Gosav et al. [16]. The configuration of the yield lines adopted for the slabs was according to the cracking pattern observed during the tests. It was considered that part of the slab after the opening did not contribute to the flexural strength due to the absence of cracks. Table 3 shows the characteristics of the slabs and the ultimate load and the flexural resistance values obtained.

Table 4 presents the results of the failure load of the tested specimens and similar sized slabs tested by other researchers. The relationship  $V_u/(b_0 d \sqrt{f_c})$  was calculated in this table due to the different values of compressive concrete strengths ( $f_c$ ), effective depth ( $d$ ) and control perimeter ( $b_0$ ) of the analyzed slabs. In this equation,  $b_0$  is the perimeter of the critical shear failure surface taken at a distance  $d/2$  away from the column face, determined according to the ACI 318 [3].

**Table 4.** Slab data.

Authors	Slab	Openings [mm]	$s$ [mm]	$d$ [mm]	$f_c$ [MPa]	$b_{0, ACI}$ [mm]	$V_u$ [kN]	$V_u/(b_0 d \sqrt{f_c})$ [ $\sqrt{MPa}$ ]
Test results	LR	-	-	90	39.8	960	247	0.453
	LF1	1x(150 x 150)	0	92	46.0	726	221	0.488
	LF2	1x(150 x 150)	90	91	46.3	855	250	0.472
	LF3	1x(150 x 150)	180	92	45.9	898	231	0.413
	LF4	1x(150 x 150)	270	93	41.2	920	273	0.497
Teng et al. [10]	OC11	-	-	105	36.0	1,224	423	0.548
	OC11H30	1x(400 x 200)	0	108	33.9	924	349	0.601
	OC11V20	1x(200 x 400)	0	105	38.6	765	207	0.415
	OC13H50	1x(400 x 200)	0	110	36.3	1,803	443	0.371
	OC13V40	1x(200 x 400)	0	109	43.0	1,485	340	0.320
Borges et al. [11]	1	-	-	100	20.8	1200	193	0.352
	2	1x(300 x 300)	0	100	20.6	800	99	0.273
	4	1x(500 x 500)	0	100	19.6	720	77	0.241
	6	1x(300 x 300)	300	100	20.0	1200	135	0.251
	8	1x(500 x 500)	300	100	20.1	1200	116	0.215
Balomenos et al. [14]	SB1-0	2x(70 x 70)	0	90	44.0	1,114	182	0.274
	SB-0	2x(150 x 150)	0	90	44.0	660	145	0.368
	SB1-1	2x(70 x 70)	90	90	44.0	1,180	198	0.281
	SB-1	2x(150 x 150)	90	90	44.0	1,020	180	0.296
	SB1-2	2x(70 x 70)	180	90	44.0	1,229	213	0.290
	SB-2	2x(150 x 150)	180	90	44.0	1,126	197	0.293
	SB1-3	2x(70 x 70)	270	90	44.0	1,253	218	0.291
SB-3	2x(150 x 150)	270	90	44.0	1,177	212	0.302	

Based on the results presented in Tables 3 and 4, it is observed that the openings created in existing reinforced concrete flat slabs reduced the punching shear strength of the slabs and the amount of this reduction is affected by the opening size and opening location from the column's face. In the LF1 slab there was a decrease of 17% of the normalized failure load ( $V_{u,norm}$ ) compared to the LR slab (247 kN). The LF2 and LF3 specimens showed a failure loads 6% and 13% lower, respectively, than the reference slab when the load is normalized according to the values of the concrete resistances obtained in the tests. For LF4, where the opening was positioned at  $3d$  from the column face, the increase in the failure load was 10% compared to LR.

Some researches, such as Teng et al. [10], Borges et al. [11], Anil et al. [12] and Balomenos et al. [14] presented results which the openings nearest to the columns reduce the punching shear resistance of flat slabs. However, the slab LF2 that has the opening closer to the column in comparison to the LF3 showed failure load 8% higher. This result obtained, therefore, differs from the results found in the literature for slabs with similarly arranged openings.

The difference between the flexural resistance of the slabs LR and LF1 was significant with 481 and 345 kN, respectively. The  $V_u/V_{flex}$  ratio ranged from 0.51 to 0.64 with the lowest ratio corresponding to LR and the highest to LF1 and LF2, with openings closer to the column. The lower values of flexural reinforcement rate due to the cutting of bars influenced the flexural capacity of slabs with openings. The tested strength lower than its calculated flexural strength for all slabs shows that flexural capacity was not the main factor in any of the specimens. According to the  $V_u/V_{flex}$  ratio, the failure mode for the tested slabs would be classified as punching. However, in the case of openings in the slab, the analysis of the behavior of the reinforcement bars and the cracking pattern of the slab must be observed together with the  $V_u/V_{flex}$  relation because of the critical zone between the column or the loaded area and the opening.

The energy dissipation capacity of the slabs (were obtained by calculating the area under the load-deflection curves), is also provided in Table 3. The reference slab was 1.29 times larger than LF1 slab and 1.10 times larger than LF2 slab. The slabs LF3 ( $s = 2d$ ) and LF4 ( $s = 3d$ ) presented energy dissipation capacity values 8% and 9%, respectively higher than the LR slab. The effects of the opening variables on stiffness were similar to the effects on punching shear strength.

The value of the slab control perimeter is inversely proportional to the value of the normalized failure load. This can be verified by the results of slabs LF1, LF2 and LF4, with  $V_u/(b_0d\sqrt{f_c})$  values higher than the normalized load value of LR slab. Increasing the opening dimension or its orientation with respect to the center of gravity of the column promotes a marked reduction in the shear strength of the slab. This can be verified by comparing the results of the OC11H30 and OC11V20 slabs studied by Teng et al. [10].

### 4.3 Strain at the flexural reinforcement

The radial and circumferential strains of the slab flexural reinforcement are presented in Figure 13 and 14, respectively. The LR results are corresponding in both directions, as demonstrated by comparing the radial (1-7 and 3-6) and the circumferential (2-8 and 4-5) strain gauges results. The cracks and reinforcement strains similarities in LR demonstrate a resembling stress distribution in every direction, as expected for a reference slab.

According to Figure 13 and 14, it is possible to observe that the most requested reinforcement bar in LF1 was the one that passes through the column (strain gauge 1), even reaching the yield value ( $\varepsilon_y = 3.20$  mm/m). For the bars positioned beyond the column, the Figure 14 shows a minor strain for the strain gauge 6 compared to strain gauge 7. This bars behavior as well as the absence of cracks after the opening indicate a change in stress distribution due to presence of the opening.

For LF2, Figure 13 presents that the deformations in the bar perpendicular to the column were higher in the direction without opening (strain gauge 3), in comparison with the bars between the column and the opening (strain gauge 6) and bar after the opening (strain gauge 10). The small strains in the interrupted bars show that there is no stress transfer and therefore these bars do not contribute to the shear strength through the dowel action.

Regarding the bars positioned parallel to the column in LF2, the graph shows a sharp deformation for the bar between the column and the opening (strain gauge 5) indicating a high concentration of stresses present in this region. The strain gauges also show similar strain values for the side with no opening (strain gauges 2 and 4) and the bars positioned around the opening (strain gauges 8 and 9).

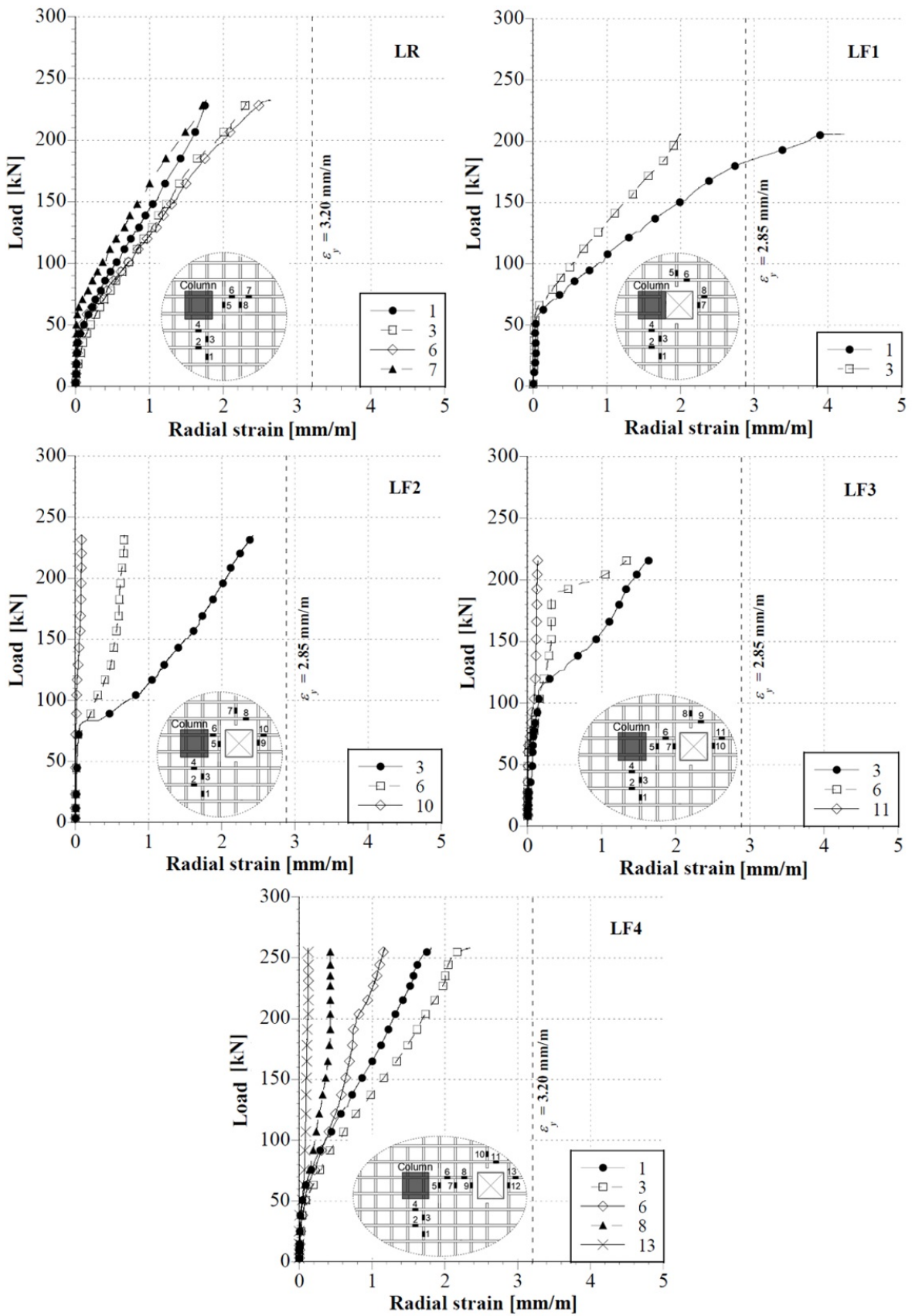


Figure 13. Load-radial strain flexural reinforcement in the slabs.

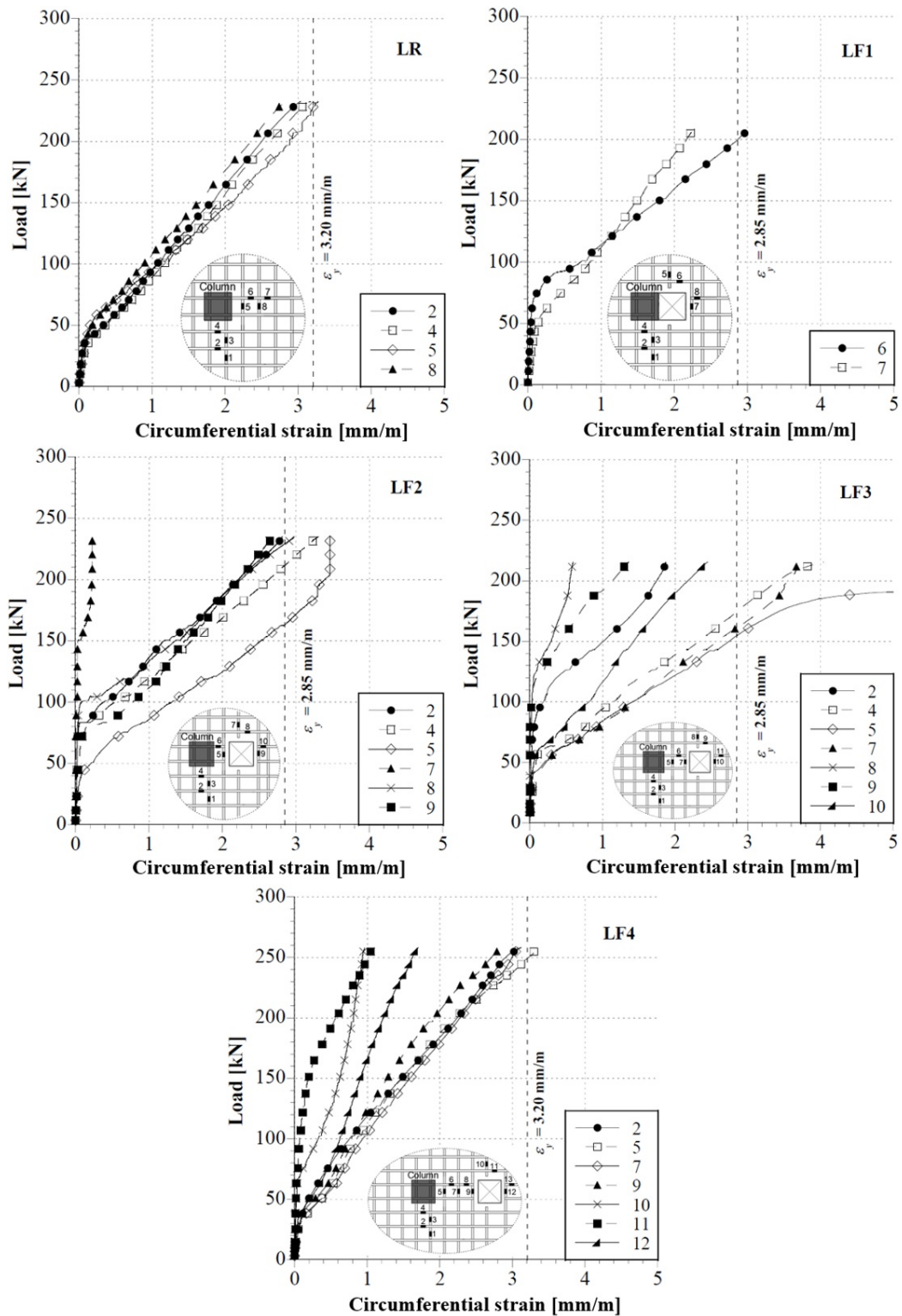


Figure 14. Load-circumferential strain flexural reinforcement in the slabs.

The results for LF3 illustrate that the deformation in the bars perpendicular to the column are quite similar in the direction without opening (strain gauge 3) and the region between the column and the opening (strain gauge 6). The

circumferential strains show that the largest values are presented in the region between the column and the opening (strain gauges 5 and 7).

The observation of the graphs in Figure 13 evidences that the greater deformations for LF4 are in the bars in the direction without the opening. Furthermore, Figure 14 imply that the deformation in the direction without opening is very similar to the direction in the presence of the opening. LF4 slab presents a structural behavior closer to the reference slab than the other slabs with the opening.

#### 4.4 Cracking patterns

Figure 15 shows the cracking pattern of all specimens. The presence of the opening conduces to the smaller number of cracks in the direction of the opening and the concentration of cracks in the  $y$ -direction, changing the slab behavior from a bidirectional action to an unidirectional action.

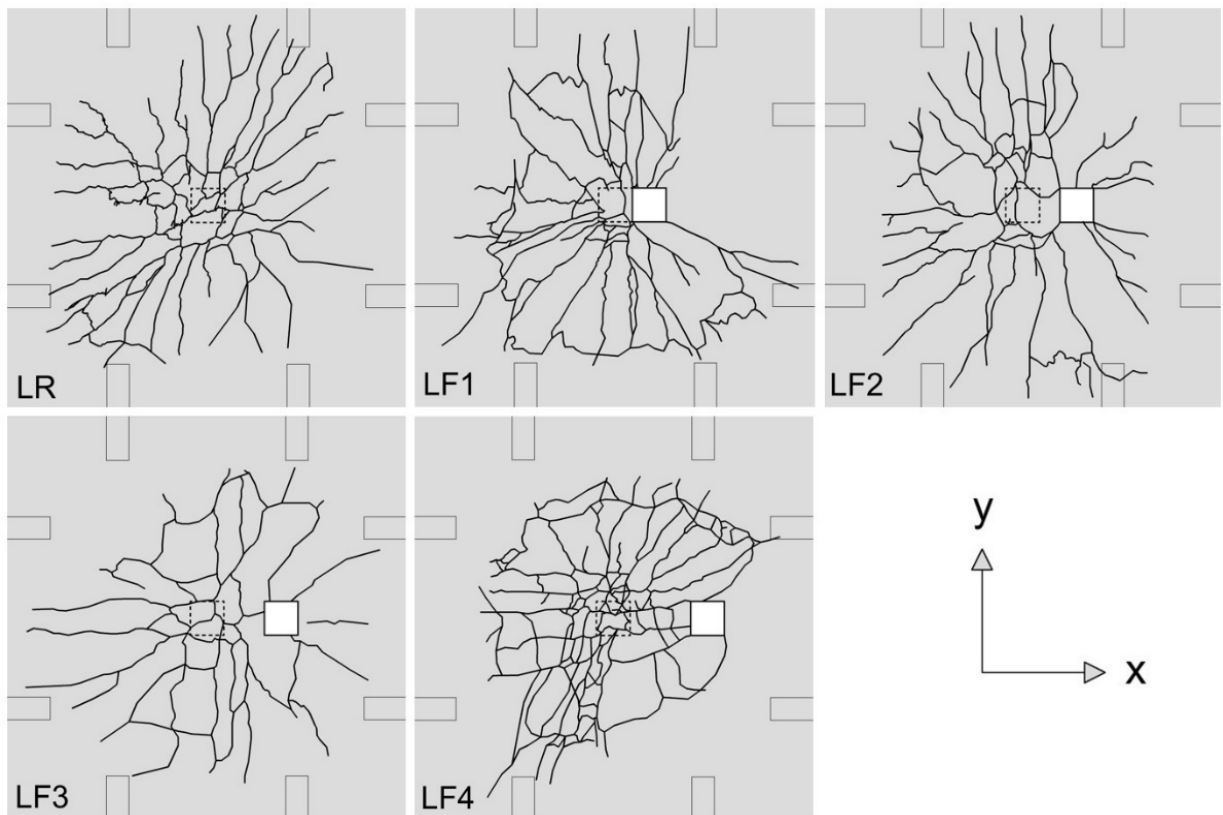


Figure 15. Crack pattern after failure at top surface of slabs.

As the distance between the opening and the column increase, a greater amount of cracks in the  $y$ -direction could be observed in LF2, LF3, and LF4. The crack patterns indicated that the stresses started in the column and outlined the openings for those specimens. For slab LF3 ( $s = 2d$ ) and LF4 ( $s = 3d$ ), the cracks beginning in the column and reached the opening. This illustrates that as the opening is positioned farthest from the column, there is a stress concentration in the region between the column and the opening.

#### 4.5 Comparison between experimental and predicted strengths

The control perimeter values suggested for each code are in Table 5 (control perimeters calculated according to Figure 2). Table 6 reports the punching shear loads of the code's predictions compared to experimental results. The ultimate shear force ( $V_u$ ) in Table 6 including self-weights of slabs and loading system. The safety coefficients specified in each standard were not considered in these analyses.

**Table 5.** Effective control perimeter lengths.

Slab	Eurocode 2 [1] [mm]	NBR 6118 [2] [mm]	ACI 318 [3] [mm]	fib Model Code [4] [mm]
LR	1,731	1,731	960	883
LF1	1,318	1,318	726	667
LF2	1,514	1,514	855	776
LF3	1,606	1,606	898	819
LF4	1,658	1,658	920	840

**Table 6.** Comparison of analytical punching capacity with experimental results.

Slab	$V_u$ [kN]	$V_{EC}$ [kN]	$V_u/V_{EC}$	$V_{NBR}$ [kN]	$V_u/V_{NBR}$	$V_{ACI}$ [kN]	$V_u/V_{ACI}$	$V_{MC}$ [kN]	$V_u/V_{MC}$
LR	247	223	1.11	278	0.89	180	1.37	207	1.19
LF1	221	168	1.32	207	1.07	150	1.47	165	1.34
LF2	250	192	1.30	239	1.05	175	1.43	190	1.32
LF3	231	204	1.13	253	0.91	185	1.25	202	1.14
LF4	273	219	1.25	270	1.01	181	1.51	206	1.33
<i>Average</i>			<b>1.22</b>		<b>0.99</b>		<b>1.41</b>		<b>1.26</b>
<i>CV (%)</i>			<b>7.9</b>		<b>8.1</b>		<b>7.2</b>		<b>7.0</b>

The ACI 318 [3] was more conservative with the average value higher than 42%, 16% and 12% in relation to NBR 6118 [2], Eurocode 2 [1] and *fib* Model Code [4], respectively. In addition, the ACI 318 [3] resulted in a low correlation coefficient (7.2%), surpassed only by the *fib* Model Code [4] (7.0%). The main reason for the  $V_{ACI}$  value of the LF4 slab was 1.9% lower than the LF3 slab was its lower concrete strength value ( $f_c = 10.2\%$  lower LF4-LF3). This occurred even with an increase in the critical perimeter value of the LF4 slab relative to the LF3 slab ( $b_{o,ACI} = 2.4\%$  higher LF4-LF3).

The standard NBR 6118 [2] recommends the minimum thickness of 16 cm for flat slabs in order to limit the size effect according to the design equation through  $(1 + \sqrt{(200/d)})$ . The specimens thick were 13 cm due to the equipment available in the laboratory. Therefore, the  $V_u/V_{NBR}$  ratio resulted average in value less than 1.0, therefore against the safety.

The Eurocode 2 [1] limits the portion  $(1 + \sqrt{(200/d)})$  to a maximum of 2.0, resulting in  $V_u/V_{EC}$  ratio in favor of safety. For LR and LF3 slabs, the estimated values were very close to the tested. For the other specimens, the European standard predicts resulted 25% to 32% above the experimental results. When the openings are located near the column ( $s = 0$  to  $s = 2d$ ), the Eurocode 2 [1] and *fib* Model Code [4] predictions show similar  $V_u/V_{EC,MC}$  ratios, while this ratio changes for the LR and LF4 slabs.

The second level of approximation (LoA II) was used in and *fib* Model Code [4] predictions, since level I results were rather conservatives. The  $V_u/V_{MC}$  ratio varied from 14% to 33%, in every case in favor of safety.

## 5 CONCLUSIONS

This paper summarises the test program of five reinforced concrete flat slabs with opening positioned at different distances from the column. Future studies may evaluate the behavior of reinforced concrete flat slabs with openings oriented at the corners of the column associated or not with shear reinforcement. The results obtained from the tests are provided, compared between each other and with previsions from different codes and discussed. The results obtained experimentally were compared with results available in the literature, as well as with responses predicted from the normative instructions.

The five specimens had punching failure, presenting brittle failures in concrete, typical failure mode in flat slabs without shear reinforcement. The punching resistance of the slabs with openings was not always lower than the reference slab without openings. The slabs LF2 and LF4 presented failure loads 1% and 11% larger than LR, respectively. However, when analyzing the influence of the compressive strength of the concrete ( $f_c$ ) of the slabs with opening, the values of  $V_{u,norm}$  were lower than that of the reference slab, except for the LF4 slab with opening distant 3d from the column face.

The displacements at the center of the slabs with openings are smaller than LR. This ensures that they presented a more rigid behavior than the slab LR, except after the load of 150 kN, in which the slab LF3 had greater displacements until the failure.

The energy dissipation capacity of flat slabs was affected due to the presence and arrangement of openings in the slab. The presence of the opening adjacent to the column in LF1 slab resulted in a reduction of 23.6% of this capacity, while for the slabs LF3 ( $s = 2d$ ) and LF4 ( $s = 3d$ ) presented energy dissipation capacity values 8% and 9%, respectively higher than the LR slab. Thus, the openings leads to the concentrated mechanical damage. Then, the energy dissipation before collapse is restricted in comparison with references slabs.

Design codes do not have a way to consideration of reinforcement ratio for the verification of the punching phenomenon in reinforced concrete flat slabs with openings. From the results obtained in this work it can be indicated that for the calculation of the flexural reinforcement ratio in the prediction models of these codes the sectioned bars located within the punching region are not considered and the concrete volume is kept constant.

The flexural reinforcement cut bars that were positioned after the openings showed insignificant deformations. For cut bars between the column and the opening, it can be noted an increase in the deformations as the opening is distanced from the column. However, for all LF slabs, the deformations in these bars were smaller than reference slab bars. This evidences that the cut of bars interferes with the continuity of the stresses flow in these bars.

The ACI 318 [3] showed the most conservative code among all studied codes, with the average expected failure load 41% higher than the tested. The Eurocode 2 [1] was the code that best estimates the punching resistance with previsions average 22% smaller than the tested loads. The estimated results using the NBR 6118 [2] design method was against the safety as they surpass the experimental results. This can be explained by the thickness of specimens smaller than the minimum thickness recommendation for the Brazilian standard. The predictions by *fib* Model Code [4] were average around 26% higher than the experimental loads. It is worth noting that the safety coefficients specified in each standard were not considered in these analyses.

## LIST OF NOTATIONS

$b_0, b_1, u_1$	is the punching perimeters
$d$	is the average effective height of two-way slab in two directions
$d_g$	is the maximum diameter of aggregate
$k$	is the size effect factor by Eurocode 2 [1] and NBR 6118 [2]
$E_c$	is the Young's modulus of concrete
$E_s$	is the Young's modulus of longitudinal reinforcement steel
$f_c$	is the compressive strength of concrete (cylinder)
$f_t$	is the tension strength of concrete
$f_u$	is the tensile strength of reinforcement
$f_y$	is the yield strength of reinforcement
$r_q$	is the radius of load introduction at perimeter
$r_s$	is the radius of the slab.
$s$	is the distance between the face of the column and the opening
$V_{NBR}$	is the nominal punching shear strength according to NBR 6118 [2]
$V_{EC}$	is the nominal punching shear strength according to Eurocode 2 [1]
$V_{ACI}$	is the nominal punching shear strength according to ACI 318 [3]
$V_{MC}$	is the nominal punching shear strength according to <i>fib</i> Model Code [4]
$V_{flex}$	is the shear force associated with flexural capacity of slab
$V_u$	is the experimental punching shear strength
$V_{u,norm}$	Is the normalized failure load
$P$	is the flexural reinforcement ratio
$\epsilon_y$	is the yield strain of reinforcement
$\epsilon_u$	is the ultimate strain of reinforcement
$\lambda_s$	is the size effect factor by ACI 318 [3]

## REFERENCES

- [1] European Committee for Standardization, *EN 1992-1-1: Design of Concrete Structures, Part 1-1: General Rules and Rules for Buildings*. Brussels, Belgium: CEN, 2010.
- [2] Brazilian Association of Technical Standards, *NBR 6118: Design of Concrete Structures – Procedures*. Rio de Janeiro, Brazil, 2014.
- [3] American Concrete Institute, *ACI 318R-19: Building Code Requirements for Structural Concrete and Commentary*. Farmington Hills, MI, USA: American Concrete Institute, 2019.
- [4] Federation Internationale Du Béton, *Model Code for Concrete Structures*. Germany: Ernst & Sohn, 2010.

- [5] R. C. Elstner and E. Hognestad, "Shear strength of reinforced concrete slabs," *ACI Struct. J.*, vol. 53, no. 2, pp. 29–57, 1956.
- [6] J. Moe, *Shearing Strength of Reinforced Concrete Slabs and Footings Under Concentrated Loads* (Bulletin D47). Skokie, IL, USA: Portland Cement Association, 1961.
- [7] P. E. Regan, "Design for punching shear," *Struct. Eng.*, vol. 52, no. 6, pp. 197–207, 1974.
- [8] R. B. Gomes and M. A. S. Andrade, "Punching in reinforced concrete flat slabs with holes," in *Proc. Develop. Comput. Aided Des. Model. Struct. Eng.*, Endinburgh, UK, 1995, pp. 185–193.
- [9] E. F. El-Salakawy, M. A. Polak, and M. H. Soliman, "Reinforced concrete slab-column edge connections with shear studs," *Can. J. Civ. Eng.*, vol. 27, pp. 338–348, 2000.
- [10] S. Teng, H. K. Cheong, K. L. Kuang, and J. Z. Geng, "Punching shear strength of slabs with openings and supported on rectangular columns," *ACI Struct. J.*, vol. 101, no. 5, pp. 678–687, 2004.
- [11] L. L. J. Borges, G. S. Melo, and R. B. Gomes, "Punching shear of reinforced concrete flat plates with openings," *ACI Struct. J.*, vol. 110, no. 4, pp. 1-10, 2013.
- [12] Ö. Anil, T. Kina, and V. Salmani, "Effect of opening size and location on punching shear behaviour of two-way RC slabs," *Mag. Concr. Res.*, vol. 66, no. 18, pp. 955–966, 2014., <http://dx.doi.org/10.1680/mac.14.00042>.
- [13] T. Ha, M. Lee, J. Park, and D. Kim, "Effects of openings on the punching shear strength of RC flat-plate slabs without shear reinforcement," *Struct. Des. Tall Spec. Build.*, vol. 24, pp. 895–911, 2015., <http://dx.doi.org/10.1002/tal.1217>.
- [14] G. P. Balomenos, A. S. Genikomsou, and M. A. Polak, "Investigation of the effect of openings of interior reinforced concrete flat slabs," *Struct. Concr.*, vol. 19, pp. 1–10, 2018., <http://dx.doi.org/10.1002/suco.201700201>.
- [15] E. A. P. Liberati, M. G. Marques, E. D. Leonel, L. C. Almeida, and L. M. Trautwein, "Failure analysis of punching in reinforced concrete flat slabs with openings adjacent to the column," *Eng. Struct.*, vol. 182, pp. 331–343, 2019., <http://dx.doi.org/10.1016/j.engstruct.2018.11.073>.
- [16] A. V. Gosav, Z. I. Kiss, T. Onet, and D. V. Bompa, "Failure assessment of flat slab-to-column members," *Mag. Concr. Res.*, vol. 68, no. 17, pp. 887–901, 2016., <http://dx.doi.org/10.1680/jmacr.15.00405>.
- [17] D. S. Lourenço, "Punção em lajes lisas de concreto armado com aberturas: análise experimental," M.S. Thesis, State Univ. Campinas, School of Civil Eng. Arch. Urb. Design, Campinas, Brazil, 2018. [Online]. Available: <http://repositorio.unicamp.br/jspui/handle/REPOSIP/331186>

---

**Author contributions:** LIBERATI and MARQUES: conceptualization, writing, data curation, formal analysis, methodology, writing, data curation; ALMEIDA and TRAUTEWIN: funding acquisition, supervision.

**Editors:** Maurício de Pina Ferreira, José Luiz Antunes de Oliveira e Sousa, Guilherme Aris Parsekian.



ORIGINAL ARTICLE

# Shear failure in reinforced concrete members without transverse reinforcement: analysis of model error of NBR6118:2014

*Cisalhamento unidirecional de peças em concreto armado sem armadura transversal: análise do erro de modelo da NBR6118:2014*

Vinicius Paes de Barros<sup>a,b</sup>   
André Teófilo Beck<sup>c</sup>   
Túlio Nogueira Bittencout<sup>a</sup>

<sup>a</sup>Universidade de São Paulo – USP, Escola Politécnica, São Paulo, SP, Brasil

<sup>b</sup>Instituto Federal de Educação, Ciência e Tecnologia de Mato Grosso – IFMT, Cuiabá, MT, Brasil

<sup>c</sup>Universidade de São Paulo – USP, Escola de Engenharia de São Carlos, São Carlos, SP, Brasil

Received 06 February 2020  
Accepted 04 June 2020

**Abstract:** This article presents an analysis of NBR6118:2014 models used to determine the one-way shear strength in reinforced concrete members without transversal reinforcement. The study compares model predictions with 751 experimental results, taken from the 2015 ACI-DAFStb database and from Quach. Model errors are quantified. Mean values observed are around unity, indicating models with no bias, but coefficients of variation are large. Model error trends are identified with respect to cross-section depth and longitudinal reinforcement rate. In elements with low rate of longitudinal reinforcement and/or large cross-section depths, the normative models provide results with low safety. This shows the need for revision of the normative models. By means of non-linear regression analysis, two correction terms are proposed to consider the longitudinal reinforcement rate and the size effect (decrease in shear strength with increase in section depth). With the proposed corrections, the observed trends are eliminated, and the design equation becomes more accurate with respect to cross-section shear.

**Keywords:** shear, building code, database, model error, size effect.

**Resumo:** Este artigo apresenta um estudo do modelo da NBR6118:2014 para determinação da contribuição de resistência do concreto no cisalhamento unidirecional em elementos de concreto armado sem armadura transversal. O estudo é feito a partir da comparação entre previsões normativas e 751 resultados experimentais, provenientes do banco de dados ACI-DAFStb de 2015 e Quach. A variável erro de modelo é quantificada. Verifica-se uma média próxima da unidade (modelo sem bias), porém com elevado coeficiente de variação. São observadas tendências dos resultados principalmente em relação aos parâmetros altura útil e taxa de armadura longitudinal. Em elementos com baixa taxa de armadura longitudinal e/ou grandes alturas, o modelo normativo fornece resultados inseguros, o que enseja a necessidade de revisão. A partir da regressão não-linear, são propostas neste trabalho duas correções para o modelo de cálculo da NBR6118:2014. Uma considera a taxa de armadura longitudinal, e outra endereça o efeito de escala (diminuição de resistência ao cisalhamento com aumento da altura útil). Utilizando as correções propostas, observa-se eliminação das tendências, em termos de taxa de armadura longitudinal e altura útil, e melhora na previsão do modelo.

**Palavras-chave:** cisalhamento, norma, banco de dados, erro de modelo, efeito de escala.

**How to cite:** V. P. Barros, A. T. Beck, and T. N. Bittencout, “Shear failure in reinforced concrete members without transverse reinforcement: analysis of model error of NBR6118:2014,” *Rev. IBRACON Estrut. Mater.*, vol. 14, no. 1, e14112, 2021, <https://doi.org/10.1590/S1983-41952021000100012>

Corresponding author: Vinicius Paes de Barros. E-mail: [vinicius.barros@cba.ifmt.edu.br](mailto:vinicius.barros@cba.ifmt.edu.br)

Financial support: None.

Conflict of interest: Nothing to declare.



This is an Open Access article distributed under the terms of the Creative Commons Attribution License, which permits unrestricted use, distribution, and reproduction in any medium, provided the original work is properly cited.

## 1 INTRODUCTION

Designing procedures provided by regulatory codes must be safe, correct in concept, simple to understand, and should not increase design and construction costs unnecessarily. Such procedures are more effective, therefore, when based on relatively simple models instead of complex empirical equations [1].

While in bending strength prediction there are widely accepted models, such as the Euler-Bernoulli hypothesis, in one-way shear of reinforced concrete members, code provisions are usually based on empirical equations calibrated on the basis of available test data [1]–[4]. The reason for this is that, although researchers agree on which mechanisms influence the determination of the shear strength of reinforced concrete members, there is no consensus on whether, or under which circumstances, one mechanism is more important than others [1], [4], [5]. Despite this, the significant amount of research in this topic in the last decades, is evident. Such studies allowed a better understanding of the different mechanisms of shear transfer in concrete, as follows [1], [2]: (a) shear transfer at the crack interface, as a result of the resistance to the sliding of the sections, due to the roughness of cracked concrete and aggregate interlock ( $V_a$ ); (b) dowelling action, related to the shear resistance of the longitudinal reinforcement crossing the crack ( $V_d$ ); (c) arc effect, when the compressed chord inclines towards the support, absorbing part of shear strength and decreasing the traction in the web ( $V_c$ ); (d) residual tensile stresses after cracking the concrete, transferred directly through the cracks ( $V_t$ ). Such mechanisms are shown in Figure 1 and can be seen in more detail in the scientific literature [1], [5].

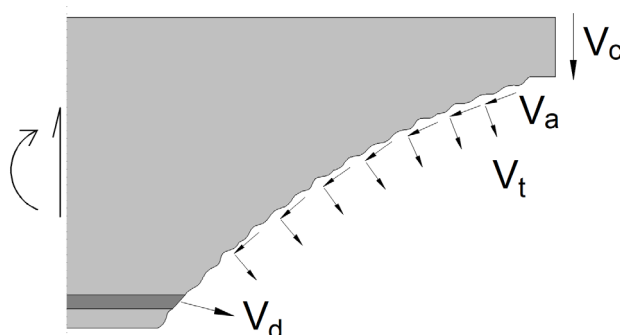


**Figure 1.** Shear transfer mechanisms in concrete members without transversal reinforcement: aggregate-interlock ( $V_a$ ), dowel action ( $V_d$ ), arc effect ( $V_c$ ) and residual tensile strength in cracked concrete ( $V_t$ ).

Regarding the main parameters that influence the shear strength, we can mention: the tensile strength of concrete, an increase of which leads to increase in shear strength; the relationship between the shear span ( $a$ ) – defined as the distance from the center of the support to the center of the load causing the shear – and the cross-section effective depth ( $d$ ): the higher the  $a/d$  ratio, the lower the average shear stress at rupture; the longitudinal reinforcement rate ( $\rho_l$ ), where higher longitudinal reinforcement rates imply greater shear strength; axial forces, where compression forces increase and tensile forces decrease shear strength; the maximum size of aggregates, which has a direct effect on the shear transfer at the crack interface; and the cross-section effective depth ( $d$ ), the increase of which causes a reduction in the shear strength (known as *size effect*). Detailed explanation of these parameters can be found elsewhere [1], [4]–[8].

Due to the difficulty in quantifying the contribution of each shear transfer mechanism, mainly because of the influence of several parameters, different models for shear design have been proposed. As examples: Truss Model; Modified Compression Field Theory (MCFT) [9]; Critical Shear Crack Theory (CSCT) [5] and the Size Effect Law (SEL) [10].

As a result of the presented theories, experimental studies and recent structural accidents, there is a concern in the scientific community for updating the design procedures of regulatory codes, in order to properly consider the mechanisms mentioned, taking into account the various parameters, especially the size effect [11]. As a recent example, the American code ACI 318/2019 [12] updated the one-way shear model for concrete members without transverse reinforcement to address the size effect, and revised the longitudinal reinforcement rate approach, using SEL [10]. Other codes also sought to adopt theoretical models in their texts. Model Code 2010 [13] (for one-way shear design), as well as the Canadian code CSA.A23 2014 [14], use MCFT [9] as the basis for their formulations. The Swiss code [15] and the Model Code 2010 [13] (for punching shear) adopted the CSCT [5]. However, several other codes, such as the

Brazilian code (NBR 6118/2014) [16] and EUROCODE 2/2004 [17], use purely empirical formulations to determine the contribution of shear transfer mechanisms [18].

## 2 OBJETIVE

In view of the above, it is evident the need to verify the NBR 6118:2014 [16] model for linear members without transverse reinforcement (model for slabs and linear members with  $b_w \geq 5d$ ), since this could result in low safety results. For this purpose, this paper proposes to make a comparison between the model of NBR 6118:2014 [16] for one-way shear design of elements without transversal reinforcement and results of shear tests from the ACI-DAFStb database [19] and from Quach [20], evaluating the statistical parameters relevant to the problem. Corrections of the model are also proposed, based on a regression analysis of test results.

## 3 THE NBR 6118:2014 MODEL

For designing linear concrete members without transverse reinforcement, the Brazilian Code, NBR 6118:2014 [16], has a model for slabs and linear elements with  $b_w \geq 5d$ , these being the only elements that do not have mandatory transverse reinforcement. The resistance contribution of cracked concrete to tensile forces, when there is no axial force, is given by  $\tau_{Rd1}$  (Equation 1):

$$\tau_{Rd1} = \frac{V_{Rd1}}{b_w d} = \tau_{Rd} k (1.2 + 40 \rho_l) \quad (1)$$

where  $b_w$  is the member width,  $d$  is the cross-section effective depth and  $f_{ctd}$  is the design value of concrete tensile strength.  $\tau_{Rd}$  is the tensile resistance stress in the concrete (Equation 2).

$$\tau_{Rd} = 0.25 f_{ctd} \quad (2)$$

$\rho_l$  is the longitudinal reinforcement rate (Equation 3):

$$\rho_l = \frac{A_{s1}}{b_w d} \leq 0.02 \quad (3)$$

and  $k$  is a coefficient, with values:

- for elements where 50% of the longitudinal reinforcement does not reach the support,  $k = 1$ .
- for other cases  $k = |1.6 - d| \geq 1$ ,  $d$  in meters.

The Technical Committee CT 301 IBRACON/ABECE [21] makes two recommendations on the use of this model: limit  $\tau_{Rd}$  to the value corresponding to a characteristic concrete compressive strength of 60MPa, and do not use this equations for elements with cross-section effective depth greater than 600mm (suggesting, in this case, the use of EUROCODE 2 formulations).

## 4 THE MODEL ERROR

To determine the resistance of a structural member, we use calculation models, which intend to represent its real behavior, especially close to failure or collapse situations. Due to the enormous complexity of structural behavior, the models have approximations from different origins: arising from physical and geometric linearities, to make models simpler or operational, or even when the nature of the behavior is not completely known [22]. Because of this, it is evident that the models are not 100% accurate, that is, the predictions of the models differ from results in real structures.

The evaluation of model accuracy, ideally, should be carried out based on the real resistance of the structure or constructed members. However, it is quite complicated to carry out this measurement *in loco* in a non-destructive way,

which makes such an approach unfeasible [22]. Thus, it is common to compare the model's prediction with experimental tests, which attempt to replicate a structure or its members in a real-life situation [22].

To make such a comparison, we can use a random variable  $\varepsilon$ , called model error, determined from Equation 4:

$$\varepsilon_i = \frac{(R_{exp})_i}{(R_{mod})_i} \tag{4}$$

where  $R_{exp}$  are the resistances obtained experimentally in the laboratory and  $R_{mod}$  are the resistances obtained from the model.

The main statistics for the random variable  $\varepsilon$  are the mean value  $\mu_\varepsilon$ , the variance  $\sigma_\varepsilon^2$  and the coefficient of variation  $\delta_\varepsilon = \sigma_\varepsilon / \mu_\varepsilon$  (COV). The statistical sampling error is reduced as the number of tests increases. An ideal model would have unitary mean ( $\mu_\varepsilon = 1$ ) and zero variance ( $\sigma_\varepsilon^2 = 0$ ); but in practice, a good structural model has a coefficient of variation  $\delta_\varepsilon$  less than 0.1 [22].

Collins [23] proposed a demerit scale classifying normative procedures for different mean values of  $\varepsilon$ , as shown in Table 1. In this paper, this demerit scale will be used to classify the model safety, together with variance and coefficient of variation data.

**Table 1.** Demerit scale for model classification

$\varepsilon$	Classification
< 0.50	Extremely Dangerous
0.50  -- 0.65	Dangerous
0.65  -- 0.85	Low Safety
0.85  -- 1.30	Proper Safety
1.30  -- 2.00	Conservative
> 2.00	Extremely Conservative

## 5 METHODOLOGY

The model error was computed based on results taken from the database of shear tests on reinforced and prestressed concrete members, organized by ACI-DAfstb, in 2015. In this database, 784 tests are on reinforced concrete members without transverse reinforcement, the subject of this article. From those, 34 tests used concretes with strength greater than 90 MPa and were removed, since NBR 6118:2014 [16] is limited to class C90 concrete. In addition, the test performed by Quach [20] was included – a test with a 4 meters high beam – due to the small number of pieces with great depth. Therefore, a total of 751 experiments were used in this paper. In total, 40 flexion tests were performed with uniformly distributed loads, and the remaining 711 with concentrated load, of which 607 flexions at 4 points and 104 flexions at 3 points. Database detailed information can be seen in Reineck et al. [24] and Dunkelberg et al. [19]

For each test in the database, the prediction of shear strength was calculated using the NBR 6118:2014 model (Equation 1). From the results, mean value, variance, standard deviation, coefficient of variation and maximum and minimum values were obtained. The safety coefficients were not included in this study, but the percentage of samples with  $\varepsilon < \frac{1}{1.4} \cong 0.71$  was indicated, where 1.4 represents the most usual partial factor for loading combination in the ultimate limit state (ULS).

To address the well-known size effect, the database was divided into effective depth intervals, as done by Bažant and Yu [7]. In this division, the value of the highest effective depth  $d_f$  is twice the initial value  $d_i$ , that is, the variation in each interval is equal to the interval's  $d_i$ . In this way, 7 intervals from  $d_i$  to  $d_f$  (in millimeters) were obtained: less than 75, 75 to 150, 150 to 300, 300 to 600, 600 to 1200, 1200 to 2400 and 2400 to 4800. The data of mean value, variance, standard deviation, coefficient of variation (COV) and maximum and minimum values were generated for each effective depth range. It should also be noted that most of the tests were carried out on small members ( $d < 500mm$ ). With this division, a reduction in the variations of the other parameters of influence is also obtained, within each interval  $d_i$ .

Finally, from the results of the tests, a non-linear regression was performed with the objective of understanding the observed trends.

### 6 ANALYSIS OF MODEL ERROR OF NBR6118/2014 FOR SHEAR IN MEMBERS WITHOUT TRANSVERSE REINFORCEMENT

For the 751 experimental results, the shear resistance prevision of NBR6118:2014 was determined. The calculated results were compared with the experimental ones through the model error ( $\varepsilon$ ), Equation 5, according to section 4.

$$\varepsilon_i = \frac{(\tau_{exp})_i}{(\tau_{mod})_i} \tag{5}$$

$\varepsilon$  values were compared to the Collins demerit scale (Table 1). This analysis includes the mean, median, variance, standard deviation, minimum and maximum values, and coefficient of variation, shown in Table 2. A first analysis shows that the model obtained a mean value slightly higher than the unit, indicating a model with appropriate safety, according to the Collins scale [23]. However, the standard deviation of the sample and, consequently, the coefficient of variation (COV) are large, which indicates that this is not a “good” model, according to Beck [22].

**Table 2.** Statistics of the model error for the NBR6118 model.

$\varepsilon$ Statistics	NBR6118 Model
Mean Value ( $\mu$ )	1.034
Variance ( $\sigma^2$ )	0.091
Standard Deviation ( $\sigma$ )	0.301
COV ( $\delta$ )	0.291
Minimum	0.292
Maximum	2.835
$\varepsilon < 0.71$	8.79%

In order to verify how the problem variables influenced the result, graphs were constructed to demonstrate the impact of four variables on the model error results: the effective depth, the longitudinal reinforcement rate, the  $a/d$  ratio and concrete strength.

The impact of the effective depth on the model error is shown in Figure 2. Note that most tests are with beams smaller than 600 mm. In addition, there is a tendency for the model error to result in less conservative values with increasing depth.

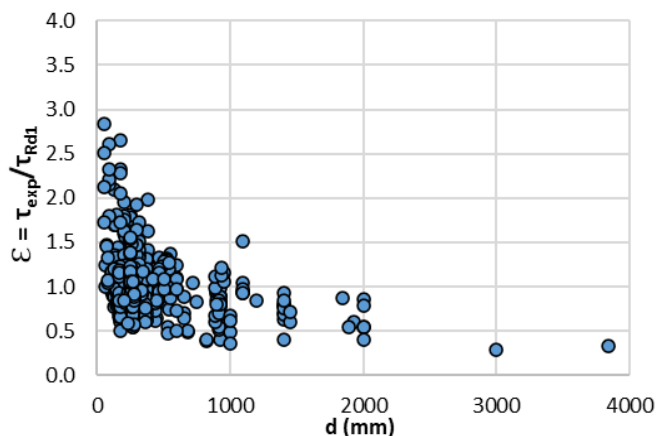


**Figure 2.** Impact of effective depth on model error

Figure 3 shows the influence of the longitudinal reinforcement rate on the model error. In this case, the database does not have a large concentration of tests around a specific value; however, it is possible to observe a certain variation depending on the longitudinal reinforcement rate: members with low rate of longitudinal reinforcement tend to have less conservative responses, which indicates that the models may have a tendency in relation to this variable, which was not adequately considered.

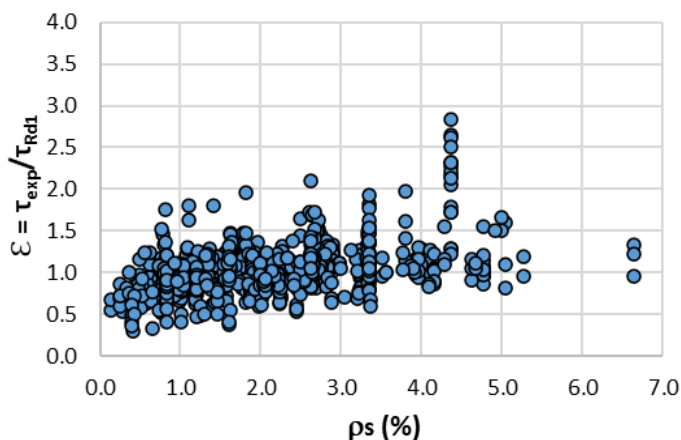


Figure 3. Impact of longitudinal reinforcement rate on model error

Figure 4 shows the influence of  $a/d$  ratio and the average compressive strength of concrete. In both cases, there is no visible trend due to these parameters. However, there is a great dispersion for values of  $a/d$  ratio around 3, and average compressive strength around 30MPa.

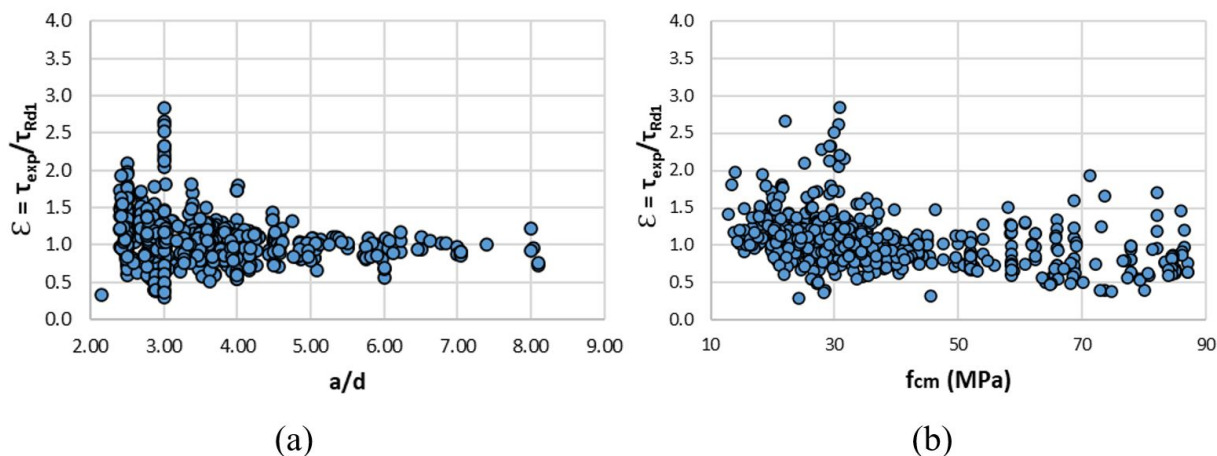


Figure 4. (a) Impact of  $a/d$  ratio on model error, (b) Impact of average compressive concrete strength on model error

Due to the trend observed in the prediction of shear strength and the non-uniform distribution of samples on the effective depth, the methodology of Bažant and Yu [7], presented in section 5, was introduced, dividing the database into 7 different ranges of effective depth. Figure 5 illustrates the percentage distribution of each effective depth range. Note, again, the great concentration of results of small beam heights, mainly between 150 and 300 mm.

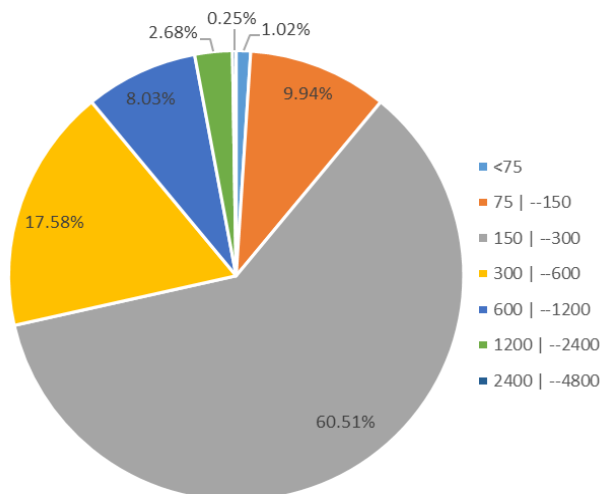


Figure 5. Distribution of the database in relation to the effective depth (in mm).

Table 3 presents the results of the statistics of the model error variable by effective depth range. It is observed that the average decreases considerably with the increase of the effective depth.

Table 3. Statistics of model error by effective depth range for NBR6118 model.

Interval – d (mm)	< 75	75 - 150	150 - 300	300 - 600	600 - 1200	1200 - 2400	2400 - 4800
Mean Value ( $\mu$ )	1.797	1.215	1.042	1.006	0.823	0.696	0.309
Variance ( $\sigma^2$ )	0.411	0.126	0.069	0.053	0.061	0.022	0.001
Standard Deviation ( $\sigma$ )	0.641	0.356	0.263	0.231	0.248	0.150	0.024
COV ( $\delta$ )	0.357	0.293	0.253	0.229	0.301	0.216	0.078
Minimum	0.993	0.772	0.506	0.472	0.364	0.405	0.292
Maximum	2.835	2.610	2.656	1.982	1.509	0.921	0.326
Number of tests	8	76	457	132	55	21	2
$\epsilon < 0.71$	0.0%	0.0%	5.9%	8.3%	34.6%	47.6%	100.0%

Considering the Collins classification (Table 1), we can conclude that:

- for effective depth less than 75 mm, the mean value greater than 1.3 indicates a “conservative” model, and there are no test results with  $\epsilon < 0.71$ . In this range we obtained the highest mean value, standard deviation and coefficient of variation;
- for effective depths between 75 to 150mm, the average indicates a model with “appropriate safety” and, despite the high standard deviation, there are no values with  $\epsilon < 0.71$ ;
- for the ranges of effective depth between 150 and 300 mm and 300 and 600 mm, the mean value is close to unity, therefore classified as “appropriate safety”. There are just a few cases of  $\epsilon < 0.71$  (6.45%), even though these are the groups with the largest number of tests (more than 78% of the total samples). These are the ranges with the most usual members depths, and it is also where the model predictions best represented the experimental results;
- for effective depths between 600 and 1200 mm, the mean value is less than 0.85, which indicates a model with “low safety”. More than a third of the results showed  $\epsilon < 0.71$ , which corroborates the classification from the Collins demerit scale;
- for effective depths greater than 1200 mm and less than 2400 mm, the model has a mean value smaller than 0.70 (“low safety”) and 47.7% of the results with values  $\epsilon < 0.71$ . In addition, none of the code model's predictions had  $\epsilon > 1$ , which indicates a strong tendency for the model to overestimate shear strength;
- for the range effective depth greater than 240mm and less than 480mm, the model resulted in values much higher than the experimental results (all samples resulted in  $\epsilon < 0.71$ ), in which the mean value indicates an “extremely dangerous” model.

The effective depth range division shows a strong trend of the normative model to result in less conservative predictions with the increase of effective depth; that is, the size effect is not addressed. However, for members with effective depth smaller than 600mm, the model presents satisfactory predictions of the experimental results, confirming the observation of IBRACON [21].

### 7 PROPOSITION OF A NEW EQUATION FOR NBR6118:2014

In Section 6 the model error obtained from comparing NBR6118:2014 [16] model for shear design of reinforced concrete members without transverse reinforcement and experimental results of the 2015 ACI-DAfStb shear database [19] and by Quach [20] revealed trends with respect to cross-section depth and longitudinal reinforcement rate. Therefore, two changes to the normative equation (Equation 1) are proposed:

- Change the  $k$  coefficient (which is a function of effective depth) so that it addresses the size effect;
- Change the term  $(1.2 + 40\rho_l)$ , which includes the longitudinal reinforcement rate, to improve the representation of this variable, reducing the observed trend.

The  $k$  coefficient is replaced by a non-linear expression in the variable  $d$ :  $(c_1/d)^{c_2}$ , with  $c_1$  and  $c_2$  constants to be determined. The term  $(1.2 + 40\rho_l)$  is replaced by  $c_3\rho_l^{c_4}$ , with  $c_3$  and  $c_4$  constants to be determined. The proposed expression (Equation 6) considers the formats of the trend graphs (Figures 2 and 3), as well as the formulations of the Canadian and American codes.

$$\tau_{Rl} = \tau_R \left( \frac{c_1}{d} \right)^{c_2} c_3 \rho_l^{c_4} \tag{6}$$

The four constants,  $c_1$  to  $c_4$ , are determined from non-linear regression with the test data, using the Least Squares Method. In this way, the results are obtained as:  $c_1 = 0.6; c_2 = 0.4; c_3 = 1.35; c_4 = 1/3$ . Equation 7 is the new proposed equation:

$$\tau_{Rl} = 1.35 \left( \frac{0.6}{d} \right)^{0.4} (\rho_l)^{1/3} \tau_R \tag{7}$$

where  $d$  is the effective depth, in meters;

$\rho_l = \frac{A_{sl}}{b_w d}$  is the longitudinal reinforcement rate, in %;

$\tau_R$  is the tensile resistance stress of concrete, obtained from Equation 3, in MPa.

Based on Equation 7, the model error statistics are recalculated, as shown in Table 4. A lower COV and a reduction to 5.6% of results where the model error is less than 0.71 are observed. The mean value remained close to the previous: 1.092, but COV decreased to 0.235.

**Table 4.** Statistics of the model error for the proposed equation.

$\varepsilon$ Statistics	Proposed Equation
Mean Value ( $\mu$ )	1.092
Variance ( $\sigma^2$ )	0.066
Standard Deviation ( $\sigma$ )	0.256
COV ( $\delta$ )	0.235
Minimum	0.506
Maximum	2.084
$\varepsilon < 0.71$	5.19%

In Figure 6, the model is no longer biased in relation to the effective depth or in relation to the longitudinal reinforcement rate, the two issues pointed out in the current model of NBR6118:2014. It is also verified that the large dispersions for  $a/d$  (shear span per effective depth) ratios close to 3 and for the average compressive strength of 30MPa were reduced. In addition, when observing the values by effective depth range (Table 5), it is possible to observe that the size effect is addressed, since results previously classified as “dangerous” or “extremely dangerous” for large values of  $d$ , no longer exist.

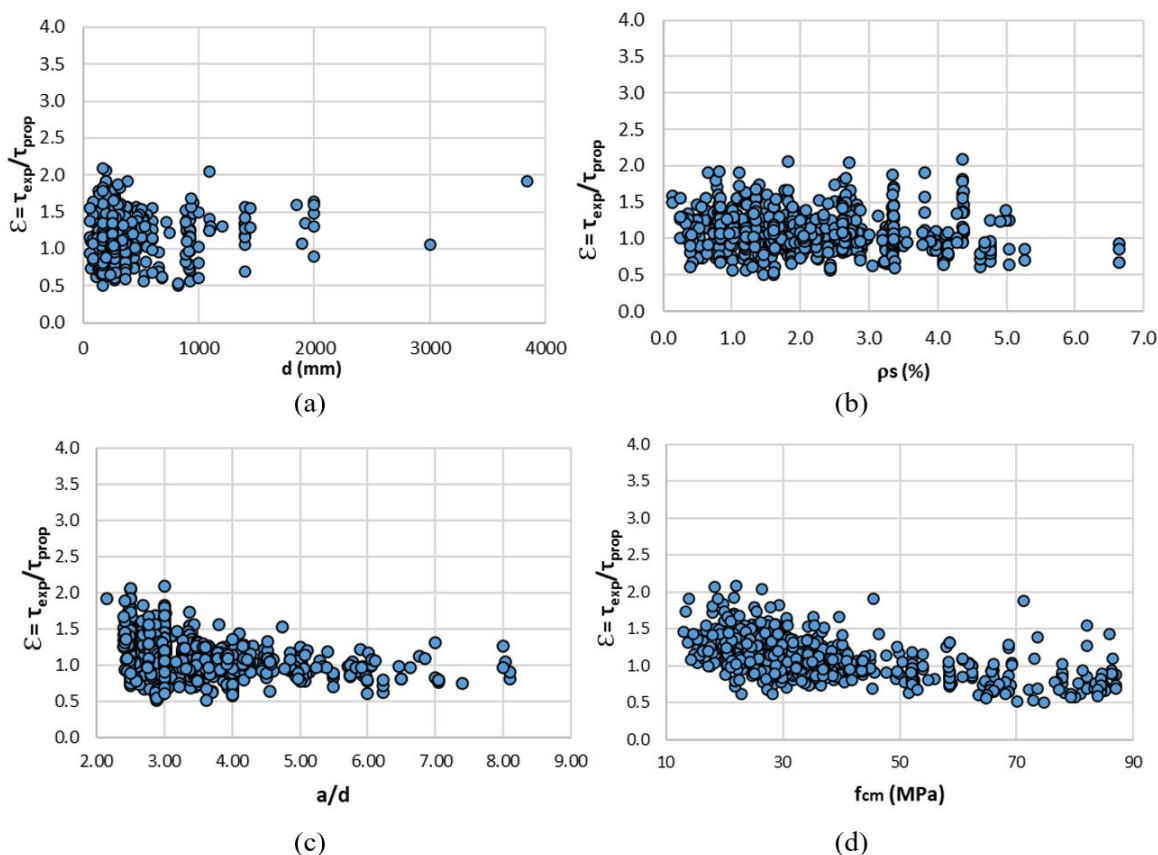


**Figure 6.** Impact of (a) effective depth, (b) longitudinal reinforcement rate, (c) a/d ratio and (d) average concrete strength on model error for the proposed equation.

**Table 5.** Statistics of model error by effective depth range for the proposed equation.

Interval – d (mm)	< 75	75 - 150	150 - 300	300 - 600	600 - 1200	1200 - 2400	2400 - 4800
Mean Value ( $\mu$ )	1.112	1.015	1.068	1.160	1.131	1.305	1.485
Variance ( $\sigma^2$ )	0.067	0.056	0.060	0.054	0.113	0.058	0.362
Standard Deviation ( $\sigma$ )	0.259	0.237	0.244	0.233	0.335	0.240	0.602
COV ( $\delta$ )	0.233	0.233	0.228	0.201	0.297	0.184	0.405
Minimum	0.735	0.615	0.510	0.563	0.506	0.686	1.060
Maximum	1.548	1.785	2.084	1.911	2.042	1.634	1.911
Number of tests	8	76	457	132	55	21	2
$\epsilon < 0.71$	0.0%	2.6%	5.7%	3.0%	14.5%	4.7%	0.0%

## 8 CONCLUSIONS

The scientific community does not fully understand all the mechanisms and parameters that govern the problem of shear strength on reinforced concrete members, which incurs in many design codes using empirical equations in their provisions, including the Brazilian code (NBR 6118:2014). Recent experimental results have shown, however, that

those models could provide unsafe design. To verify the model's safety, this paper presented a comparison between model predictions of NBR6118:2014 [16] for one-way shear strength of reinforced concrete members without transversal reinforcement and experimental results compiled from the ACI-DAfStb database [19] and Quach [20], through the analysis of model error variable. From this study, it was concluded that:

- a) The current NBR6118:2014 model does not address the size effect; it shows considerable reduction in model error mean, with the increase in effective depth, especially for members with depth greater than 600mm. In addition, it is biased in relation to the longitudinal reinforcement rate, whose decrease implies in less conservative results (Figures 2 and 3);
- b) For values of effective depth between 75mm and 600mm, the model of NBR 6118:2014 gives satisfactory predictions. For effective depths greater than 1200mm, the predictions are classified as "dangerous" or "extremely dangerous", according to the Collins demerit scale (Table 1);

By means of non-linear regression analysis, this paper proposed an amendment for the NBR6118:2014 model. Results shown that the new equation is not biased with respect to the effective depth or longitudinal reinforcement rate. Mean values are still close to unity, but the coefficient of variation was reduced, from 0.291 to 0.235, which indicates an improvement in the model. Specimens with  $\varepsilon < 0.71$  were diminished to 5.19% of total, pointing to a safer model. Size effect is addressed in the new formulation, a fact observed by safer results for large-scaled specimens. Large dispersions observed for  $a/d$  ratio close to 2 and average compressive strength close to 30MPa were also reduced.

## REFERENCES

- [1], ASCE ACI Committee 445, "Recent approaches to shear design of structural concrete," *J. Struct. Eng.*, vol. 124, no. 12, pp. 1375–1417, Dec 1998, [http://dx.doi.org/10.1061/\(ASCE\)0733-9445\(1998\)124:12\(1375\)](http://dx.doi.org/10.1061/(ASCE)0733-9445(1998)124:12(1375)).
- [2] F. Cavagnis, M. Fernández Ruiz, and A. Muttoni, "An analysis of the shear-transfer actions in reinforced concrete members without transverse reinforcement based on refined experimental measurements," *Struct. Concr.*, vol. 19, no. 1, pp. 49–64, Nov 2018, <http://dx.doi.org/10.1002/suco.201700145>.
- [3] F. Cavagnis, M. F. Ruiz, and A. Muttoni, "Shear failures in reinforced concrete members without transverse reinforcement: an analysis of the critical shear crack development on the basis of test results," *Eng. Struct.*, vol. 103, pp. 157–173, 2015, <http://dx.doi.org/10.1016/j.engstruct.2015.09.015>.
- [4] P. Huber, T. Huber, and J. Kollegger, "Investigation of the shear behavior of RC beams on the basis of measured crack kinematics," *Eng. Struct.*, vol. 113, pp. 41–58, Apr 2016, <http://dx.doi.org/10.1016/j.engstruct.2016.01.025>.
- [5] A. Muttoni and M. Fernández Ruiz, "From experimental evidence to mechanical modeling and design expressions: the critical shear crack theory for shear design," *Struct. Concr.*, vol. 20, no. 4, pp. 1464–1480, Jun 2019, <http://dx.doi.org/10.1002/suco.201900193>.
- [6] Z. P. Bažant and J. Kim, "Size effect in shear failure of longitudinally reinforced beams," *ACI J.*, vol. 81, no. 5, pp. 456–468, 1984.
- [7] Z. P. Bažant and Q. Yu, "Minimizing statistical bias to identify size effect from beam shear database," *ACI Struct. J.*, vol. 105, no. 6, pp. 685–691, Oct 2008.
- [8] D. A. Kuchma, S. Wei, D. H. Sanders, A. Belarbi, and L. C. Novak, "Development of the one-way shear design provisions of ACI-319 for reinforced concrete," *ACI Struct. J.*, vol. 116, no. 4, pp. 285–295, Jul 2019, <http://dx.doi.org/10.14359/51716739>.
- [9] M. P. Collins and D. Mitchell, *Prestressed Concrete Basics*, 1st ed. Ottawa: Canadian Prestressed Concrete Institute, 1987.
- [10] Z. P. Bažant, "Size effect in blunt fracture: concrete, rock, metal," *J. Eng. Mech.*, vol. 110, no. 4, pp. 518–535, Apr 1984, [http://dx.doi.org/10.1061/\(ASCE\)0733-9399\(1984\)110:4\(518\)](http://dx.doi.org/10.1061/(ASCE)0733-9399(1984)110:4(518)).
- [11] Q. Yu, J. Le, M. H. Hubler, R. Wendner, G. Cusatis, and Z. P. Bažant, "Comparison of main models for size effect on shear strength of reinforced and prestressed concrete beams," *Struct. Concr.*, vol. 17, no. 5, pp. 778–789, Dec 2016, <http://dx.doi.org/10.1002/suco.201500126>.
- [12] American Concrete Institute, *Building Code Requirements for Structural Concrete*, ACI 318, 2019.
- [13] Fédération Internationale du Béton, *fib Model Code for Concrete Structures 2010*, MC2010, 2013.
- [14] Canadian Standards Association, *Design of Concrete Structures*, A23.3, 2014.
- [15] Swiss Society of Engineers and Architects, *SIA Code 262 for Concrete Structures*, SIA 262, 2003.
- [16] Associação Brasileira de Normas Técnicas. *Projeto de Estruturas de Concreto – Procedimento*, NBR 6118, 2014.
- [17] European Standard, *Eurocode 2 – Design of Concrete Structure – General rules and rules for buildings*, EN 1992-1-1, 2004.
- [18] A. Dönmez and Z. P. Bažant, "Critique of critical shear crack theory for fib Model Code articles on shear strength and size effect of reinforced concrete beams," *Struct. Concr.*, vol. 20, no. 4, pp. 1451–1463, May 2019, <http://dx.doi.org/10.1002/suco.201800315>.

- [19] D. Dunkelberg, L. H. Sneed, K. Zilch, and K. Reineck, "The 2015 ACI-DAfStb database of shear tests on slender prestressed concrete beams without stirrups – overview and evaluation of current design approaches," *Struct. Concr.*, vol. 19, no. 6, pp. 1740–1759, Mar 2018, <http://dx.doi.org/10.1002/suco.201700216>.
- [20] P. T. Quach, "Understanding and safely predicting the shear response of large-scale reinforced concrete structures," M.S. thesis, Dept. Civ. Eng., Univ. Toronto, Toronto, 2016.
- [21] Instituto Brasileiro do Concreto, *ABNT NBR 6118:2014 – Comentários e Exemplos de Aplicação*, 1st ed. São Paulo: Ibracon, 2015.
- [22] A. T. Beck, *Confiabilidade e Segurança das Estruturas*, 1st ed. Rio de Janeiro: Elsevier, 2019.
- [23] M. P. Collins, *Evaluation of Shear Design Procedures for Concrete Structures*. Canada: CSA Technical Committee on Reinforced Concrete Design, 2001, pp. 29-37.
- [24] K. Reineck, E. C. Bentz, B. Fitik, D. A. Kuchma, and O. Bayrak, "ACI-DAfStb database of shear tests on slender reinforced concrete beams without stirrups," *ACI Struct. J.*, vol. 110, pp. 867–876, Sep 2013.

---

**Author contributions:** VPB: conceptualization, formal analysis, methodology, writing; A.T.B: writing, proofreading, supervision; TNB: data curation, supervision, proofreading.

**Editors:** Sérgio Hampshire de Carvalho Santos, José Luiz Antunes de Oliveira e Sousa, Guilherme Aris Parsekian.



ORIGINAL ARTICLE

## Current condition of the exposed concrete façades reinforcement of the Vilanova Artigas building: modern architectural heritage

*Avaliação do estado de conservação das armaduras das empenas de concreto aparente do edifício Vilanova Artigas: patrimônio cultural da arquitetura moderna*

Adriana de Araujo<sup>a</sup> Claudia de Andrade Oliveira<sup>b</sup> Tatiana Regina da Silva Simão<sup>b,c</sup> <sup>a</sup>Instituto de Pesquisas Tecnológicas do Estado de São Paulo – IPT, São Paulo SP, Brasil<sup>b</sup>Faculdade de Arquitetura e Urbanismo – FAU, Universidade de São Paulo – USP, São Paulo, SP, Brasil<sup>c</sup>Instituto Federal São Paulo – IFSP, São Paulo, SP, Brasil

Received 04 March 2020

Accepted 12 June 2020

**Abstract:** The heritage of modern architecture in exposed reinforced concrete has been shown pathological manifestations affecting the structural safety and functionality of the buildings. The manifestations are, primarily, associated with the steel corrosion; however published data obtained from site surveys, on the Brazilian architectural heritage and related to the issue, are still scarce in the literature. Thus, the aim of the study is to assess the current condition of the exposed concrete façades reinforcement of the Vilanova Artigas building, a Brazilian architectural heritage, opened in 1969. Legal restrictions limited the destructive tests and sampling areas. The history of the interventions, environmental aggressiveness and preliminary inspection (in the parent concrete and patch repairs) provided qualified information for analyzing in situ testing results. In the sampling areas physical, chemical and electrochemical tests were carried out. The façades surfaces are naturally porous, irregular, with concrete segregation and corrosion products stains; 24% of the concrete was replaced with proprietary mortar repair. In patch repairs, the average carbonation depth ranged from 3 to 29 mm, in concrete it ranged from 15 to 30 mm. The reinforcement cover ranged from 8 to 33 mm. Corrosion potential maps, with equipotential lines drawn at 50 mV intervals, indicated the corrosion-prone areas, where there is a concentration of lines with a variation equal to or greater than 150 mV. The presence of corrosion products, detected in the visual examination of the reinforcement under the patch repairs, validated the active corrosion state. The rough surface of the concrete, the low cover to depassivated reinforcement and the active corrosion state emphasize the need for monitoring the façades and the urgency of implementing a preventive maintenance plan, along with a conservation project in order to preserve the heritage values of the building.

**Keywords:** heritage conservation, exposed concrete, carbonation, corrosion, electrochemical measurements.

**Resumo:** O patrimônio da arquitetura moderna de concreto armado aparente tem apresentado manifestações patológicas que afetam a sua segurança estrutural e funcionalidade. As manifestações estão, principalmente, vinculadas à corrosão do aço, entretanto dados de levantamentos de campo, realizados no patrimônio arquitetônico brasileiro e vinculados ao tema, ainda são escassos na literatura. Portanto, o objetivo do estudo é avaliar o estado de conservação das armaduras das empenas de concreto aparente do edifício Vilanova Artigas, patrimônio cultural da arquitetura brasileira, inaugurado em 1969. Restrições legais limitaram os ensaios destrutivos e áreas de amostragem. O histórico de intervenções, a agressividade ambiental e a inspeção preliminar (do concreto original e das áreas recuperadas com argamassa de reparo) compuseram a base para a análise dos resultados. Nas áreas de amostragem foram feitos ensaios físicos, químicos e eletroquímicos. A superfície do concreto é naturalmente porosa, irregular, com segregação e manchas de produtos de corrosão; 24% do concreto foi substituído por argamassa de reparo. Nos reparos a profundidade média de carbonatação variou de 3 a 29 mm, no concreto variou de 15 a 30 mm. O cobrimento da armadura variou de 8 a 33 mm. Mapas de potencial de

Corresponding author: Tatiana Regina da Silva Simão. E-mail: [simao.tatiana@usp.br](mailto:simao.tatiana@usp.br)

Financial support: The Getty Foundation (Keeping It Modern architectural conservation grant), IPT - Institute for Technological Research and IFSP - Federal Institute of São Paulo.

Conflict of interest: Nothing to declare.



This is an Open Access article distributed under the terms of the Creative Commons Attribution License, which permits unrestricted use, distribution, and reproduction in any medium, provided the original work is properly cited.

corrosão, com linhas equipotenciais traçadas em intervalos de 50 mV, indicaram as regiões mais propensas à corrosão onde há concentração de linhas com variação igual ou superior a 150 mV. O estado ativo da corrosão foi confirmado pela presença de produtos de corrosão, detectados no exame visual das armaduras sob a argamassa de reparo. O aspecto irregular da superfície do concreto, o baixo cobrimento da armadura - já despassivada - e o estado de corrosão ativo evidenciam a necessidade de monitoramento das empenas e a urgência da implementação de um plano de manutenção preventiva, combinado a um projeto de conservação para a salvaguarda dos valores patrimoniais do edifício.

**Palavras-chave:** conservação do patrimônio, concreto aparente, carbonatação, corrosão, medidas eletroquímicas.

---

**How to cite:** A. Araujo, C. A. Oliveira, and T. R. S. Simão, “Current condition of the exposed concrete façades reinforcement of the Vilanova Artigas building: modern architectural heritage,” *Rev. IBRACON Estrut. Mater.*, vol. 14, no. 1, e14113, 2021, <https://doi.org/10.1590/S1983-41952021000100013>

## 1 INTRODUCTION

Samples of the heritage of modern architecture in exposed reinforced concrete, built in the second half of the 20th century, have been shown pathological manifestations affecting the structural safety and functionality of the buildings. The scarcity of systemic studies on the major degradation processes that affect them – corrosion of reinforcement, associated to the lack of deeper knowledge about these buildings, have resulted in unsuccessful interventions, with patch repairs made by using the conventional process adopted in engineering, which mischaracterize the architectural surfaces to be preserved [1].

In Brazil, the preservation of the architectural heritage has been consolidating as an academic field of research and professional practice over the last few decades. Several research centers and laboratories, both among the traditional ones and the ones recently established, have promoted the approach of the several agents involved in preservation of the buildings, providing a multidisciplinary and multidimensional approach.

In spite of the consistent contributions of the abovementioned research centers and laboratories, in addition to the significant production of heritage-oriented graduate programs at universities throughout the country, the researches on the materiality of the built heritage are aimed, in their most part, to the colonial, baroque, eclectic, art nouveau, and art décor architectures. Although some groups are focusing their studies to the modern architecture materials, there are still scarce published works on the review of interventions in exposed reinforced concrete in terms of the methodological aspect and impact on the heritage values [2]–[6], as well as experimental researches [7], [8] that relate the concrete and patch repair and finish mortar technologies to the conservation of these structures.

In the international scenario, professionals working in research and practice of patch repair of concrete of the modern architecture already discussed, in the end of 1990s, the corrosion of reinforcements of these structures, as indicated by the papers published in the proceedings entitled “The fair face of concrete” of the Documentation and conservation of buildings, sites and neighborhoods of the Modern Movement - Docomomo International Seminar [9]. The articles express the tacit knowledge acquired in restoration, especially for buildings constructed after World War II. The interventions made in the 1980s and 1990s, based on the current engineering practices, were proved as ineffective, both technically and esthetically, according to studies reported in several articles [10]–[13].

In Brazil, despite the significant collection of modern architecture concrete structures, the discussion about the practice of conservation of the exposed reinforced concrete has not been consolidated yet, even that we can find qualified forums in the Docomomo Brasil Seminars – and in the Regional Chapters Seminars - covering the preservation of this architecture.

A review of the recent bibliography [14] on the conservation of exposed concrete in modernist buildings points the lack of researches about long-term performance of patch repairs, and that the existing assessments of the patch repairs are based on laboratory analyses, which are far from the actual performance of these repairs.

A phenomenon known and checked in the practice is the electrochemical incompatibility between repair material and concrete, described by Gu et al. [15] as a unbalance of the electrochemical potential between several sections of the reinforcement, caused by differences between the aqueous phases (in repair and concrete). This phenomenon may affect the exposed concrete of modern architecture buildings due to their specific characteristics (concrete totally carbonated, carbonation front reaching the reinforcement, high electric resistivity, variation of the reinforcement covering, among others), starting a corrosive process in the areas adjacent to the patch repair. Also, in spite of the scientific and technological mastering of the corrosion mechanisms, there are few studies reported in the literature about exposed concrete buildings, with 50-year service, presenting history of corrosion caused by carbonation of the concrete cover [16]–[19].

Within this context, this study has the aim of assessing the current condition of the exposed concrete façades reinforcement of Vilanova Artigas building, an icon of the Brazilian modern architectural heritage, opened in 1969. The investigation carried out had the purpose of deepening the knowledge of the structure and providing data to the future conservation plan for the building.

## 2 VILANOVA ARTIGAS BUILDING AND THE INSERTION ENVIRONMENT

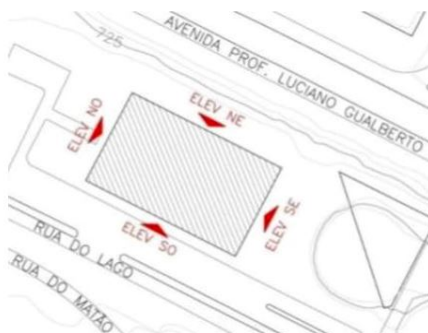
Vilanova Artigas building was built from the end of 1966 to early 1969, at Cidade Universitária, Universidade de São Paulo, metropolitan region of the city of São Paulo. It has 18,600 m<sup>2</sup> of built area distributed in a set of eight floors.

The major constructive material is cast-in-place exposed reinforced concrete. The board-formed concrete blind façades, object of this study, are important elements in the composition of the building. Both the modular pattern of the boards and wood grain texture are imprinted on the outer surface of the walls and extend to the intersection of the pyramidal base of the outer pillars. In addition to other attributes, the esthetic and formal characteristics of the building resulted in its listing in 1982 and in 1991 by state and municipal preservation institutions, respectively, as quoted in Oliveira et al. [20].

Figure 1a shows the building placement (rectangular block with plan measures of 110.20 m x 66.20 m). Figure 1b shows the partial view of the main façade of the building. The façades are identified according to their orientation. The main SW façade and the NE façade have length of 110.20 m; NW and SE façades, 66.20 m. Walls' height is 8.15 m, except for NE wall, which height is 7.25 m. Thickness of walls is 200 mm. The analysis of available original blueprints indicates cracking control reinforcement with 8 mm diameter, arranged in orthogonal mesh with inter-bar spacing of 100 mm or 200 mm, and 10 mm concrete cover according to the structural design [21].

### 2.1 Brief history of interventions

The building turned 50 years of service in 2019. There are no records about any preventive maintenance performed on its façades within the 4 decades that succeed its inauguration (1969-2012). There are punctual records of replacement of the walls-bearing pad system: in 1981 (Pillar P3, NE façade) and 2000 (Column P48, SW façade -). In 2009-2010, flashings were installed on the top of wall to prevent rain water penetration. Signs of deterioration of the exposed concrete, stemming from reinforcement corrosion, were reported in 1999, during inspection that preceded the replacement of the wall-bearing pad system on pillar P48. The inspection report was the first document containing recommendation for structural patch repairs on the façades. In 2004, Simões [22] performed visual inspection in the building and identified several regions of the façades with disaggregation, pathological manifestation characterized by detachment of the concrete cover, indicating worsening deterioration of the reinforcement. In November 2012, an extensive intervention campaign started to repair the outer surface of the façades, together with other repair services in the roof and interior of the building. The campaign was completed in April 2015. Figure 1b shows the patch repairs of the main façade, performed in 2013-2014.



(a)



(b)

**Figure 1.** (a) Building placement with direction of Northeast (NE), Southeast (SE), Southwest (SO) and Northwest (NO) façades; (b) and partial view of the main façade (SW). (Photo: Authors' collection, 2016).

In restoration of the exposed concrete built heritage, regardless on the listed or not listed status, the patch repairs should be designed to visually match the original material and to have compatible physical and mechanical properties to the parent concrete.; the purpose is to minimize visual fragmentation of the surfaces, maintaining the building uniformity. Aesthetics issues arising from the interventions carried out in 2012-2015, which cover the façade restoration, can be found in other publications [23], [24].

The technical specification for execution of the patch repairs was based on the standard engineering procedure for rehabilitation of reinforced concrete structures, by using industrialized cement-based mortar, modified with polymers and reinforced with fibers, followed by application of solvent based silane-siloxane water repellent, and a finish coat of pure acrylic varnish (without styrene) dispersed in solvent. The lack of in-depth studies on the visual impact of varnish led the board of the institution to decide for not applying this finish coat; other technical reasons also supported that decision, such as lack of studies on the full-scale application method and on the efficiency of the system in protecting such a porous and irregular surface, which should not be plaster-finished, in addition to implications, still unknown, on the maintenance of this protection without affecting the original concrete characteristics.

Figure 2 shows the aspect of the exposed concrete surface of the façades at the onset of the 2012-2015 intervention campaign (Figure 2a) and the disaggregated concrete areas with exposure of the corroded reinforcement (skin rebar), and with small covering thickness (Figure 2b).



**Figure 2.** Partial view of NE façade: (a) area with concrete disaggregation on pillar P3 and (b) exposure of corroded reinforcement steel (Photos: authors' collection, 2013).

The photographic records taken during the intervention suggest that the skin rebar of the façades is more prone to corrosion, presenting concrete cover with variable thicknesses.

## 2.2 Environmental condition

According to previous study on the atmospheric corrosivity [25], the building surroundings can be classified as urban environment, with moderate concentration of pollutants. This environment is defined by ABNT NBR 6118:2014 [26] standard as Class II, moderate aggressiveness for reinforced concrete structures.

Monitoring of the atmospheric air between 2006 and 2017, presented in Companhia Ambiental do Estado de São Paulo [27], registered gradual decrease of atmospheric pollutant concentration in the State of São Paulo. The exception was carbon dioxide (CO<sub>2</sub>), decreasing in the last years after strong trend of gradual increase. In regard to sulfur dioxide (SO<sub>2</sub>), typical gas of industrial and vehicle emission environments, the decrease was very significant, and within the metropolitan region of São Paulo, the atmospheric concentration of SO<sub>2</sub> was reduced from 16 µg/m<sup>3</sup> in 2000 to 3 µg/m<sup>3</sup> in 2017 [27].

Climate in São Paulo, with tropical characteristics, favors the development of corrosion process on concrete structures, as it provides conditions for frequent humidification of the concrete (reducing the concrete resistance to the current corrosion flow) and access of oxygen in the concrete/steel interface (oxidizing agent of the corrosion reactions) [25]. The trend for increase of the humidification condition can be verified by the total rainfall in 2017, amounting to 1648.8 mm in

187 rainy days, 16.7% above the average value from time series. The highest temperature registered in 2017 was 36.1 °C (October) and the lowest one 5.6 °C (June). Although the annual relative humidity (RH) mean in 2017 has been 79.5%, slightly above the average value from time series (81.2%) [28], the trend for higher frequency and rain intensity within the last decades have been confirmed by studies of time series for the metropolitan region of São Paulo (RMSP) [29].

The driving-rain index (DRI), presented in Simões [21], was estimated based on 2016 data, for January and February (summer), and July and August (winter), which are representative of the highest and lowest annual rainfall, respectively. In the DRI graphical representation for each cardinal direction, the SE façade is the most affected by driving-rain in summer; and SE and NW façades are the most affected in winter.

### 3 METHOD

Preliminary inspection was carried out along the whole extension of the façades, combined with review of documents containing results of characterization tests of the repair areas and the original concrete. Next, a detailed inspection was conducted in the sampling areas delimited on each one of the four façades, including physical, chemical and electrochemical tests. From the interpretation of the data and results of these inspections and tests, combined with review of the precedent interventions and local environment conditions, we concluded on the conservation conditions of the reinforcements, and provided considerations on new interventions in this heritage asset to extend its residual service life and preserve its the ascribed heritage values.

#### 3.1 Preliminary inspection and document review

Upon the general inspection, we have the aim of identifying the key singularities of the concrete surface, such as porosity and natural irregularity, as well as void areas, resulting from the constructive process of the structure. This phase also determined sampling areas for detailed inspection.

As it is a listed building, the detailed inspection, which would require the conduction of destructive tests, was preceded by preparation of detail project approved by advisory councils for historic preservation. Scarifications were authorized on the façades, for potential and corrosion rate measurements, in the repaired areas only. By considering these restrictions, we selected areas for detailed inspection, one for each façade. The selection was made based on the following criteria: accessibility in function of the building dimensions and proximity of the trees; areas with lower surface heterogeneity and that permitted fitting of two or three patch repairs, areas close to the selected locations for extracting concrete cores.

It must be emphasized that the preservation councils also limited the number of cores to four (diameter 50 mm and length 200 mm). Therefore, two samples were extracted from the NE façade and two from the NW façade, as they were the façades with largest and smallest repaired areas, respectively.

Data from other surveys and tests presented in Simões [21] were reviewed to support result interpretation and analysis:

- Area and positioning of the structural patch repairs, determined by laser scanning, complemented with photos and onsite inspections; the scanning methodology adopted can be found in Balzani et al. [30];
- Corrosion products deposits (corrosion spots) identified by direct visual observation and use of binoculars;
- Dampened areas detected after moderate rainfall during the day; moisture stains were identified by photographic records taken in early evening, once finished the rain.
- Concrete cover measured with metal detector (Bosch D-TECT 150) in 393 positions distributed on four façades;
- Concrete compressive strength of cores samples extracted from NE and NW façades, according to ABNT NBR 7680-1: 2015 [31];
- Mixture proportion reconstitution of the original concrete based on methods presented in Quarcioni [32] and Instituto de Pesquisas Tecnológicas [33].

#### 3.2 Detailed inspection

Detailed inspection of the concrete surface was conducted in the areas selected in each façade, by using articulated lifting platform, in January-February 2017, at time when building turned 49 year old.

Each area was delimited with reference grid drawn on the concrete surface, with white chalk, 15 cm x 15 cm intervals, following the existing board-marking on the surface (planks with height 30 cm). The grid makes easier the registration of pathological manifestations and is suitable for mapping the gradient of corrosion potential values. Each

value range is represented by one color or contour line. Regions with significant variation of colors or concentration of contour lines are potentially considered as more prone to corrosion.

The visual observation was performed to identify the key surface characteristics of concrete: segregated concrete/segregation, disaggregated concrete/disaggregation, exposed reinforcement, local corrosion spot/stain, surface air voids, cracking and hollow sound, according to the method described in Araujo and Panossian [34].

By using common scale, vernier caliper and crack gauge, the dimensions of surface air voids and the crack openings were determined.

Regions with hollow sound were located by using geologist's percussion hammer. The location of these regions is of interest of research, as it indicates voids in poorly compacted areas or inner cracking of the repair concrete or mortar.

Visual examination of the reinforcement was made after fracture in the repaired areas. The surface of the section newly exposed of the rebars (near-surface reinforcement) and the original concrete beneath it, and the original concrete/repair mortar interface were examined by naked eye. The major purpose of this examination was to evaluate the passive or active corrosion condition, with the active condition being usually characterized by the presence of corrosion products on the reinforcement/cementitious material interface [34].

The diameter of exposed rebars was measured with vernier caliper after mechanical cleaning for removal of the major part of corrosion products. The carbonation depth was measured by using a solution of phenolphthalein indicator, according to DIN EN 14630 [35].

To minimize the interference of the water repellent impregnant on the corrosion potential measurements, the concrete surface was strongly sanded, followed by moistening by period longer than that usually required for non-impregnated concrete. The corrosion rate measurements required an additional phase: brushing with nylon bristle brush, water and mild soap, followed by water spray during 45 minutes.

The corrosion potential ( $E_{corr}$ ) of the reinforcement was determined by a series of measures, on the reference grid, providing a gradient map with 50 mV intervals. The corrosion rate ( $i_{corr}$ ) was determined in some sections of the reinforcement, previously delimited within the reference grid limits. The electrochemical measurements were carried out with CorrMap equipment using Ag/AgCl reference electrode - EPCP (209 mV vs. standard hydrogen electrode), adopting a procedure similar to that used in Araujo et al. [36].

To determine the surface moisture content (up to 30mm depth), we used Moist 210B equipment, based on the microwave emission and reception, frequency range from 300 MHz to 300 GHz.

## 4 RESULTS

### 4.1 Preliminary inspection and document review

Several concrete segregation regions were identified on the construction joints and along the line between planks that composed the mold of the outer face of façades. In addition to the relief already mentioned produced by the wood grain imprinted on the concrete surface, other characteristics of the façade surfaces must be highlighted, such as air voids on the surface, resulting from entrapment air, bubbles as shown in Figure 3.

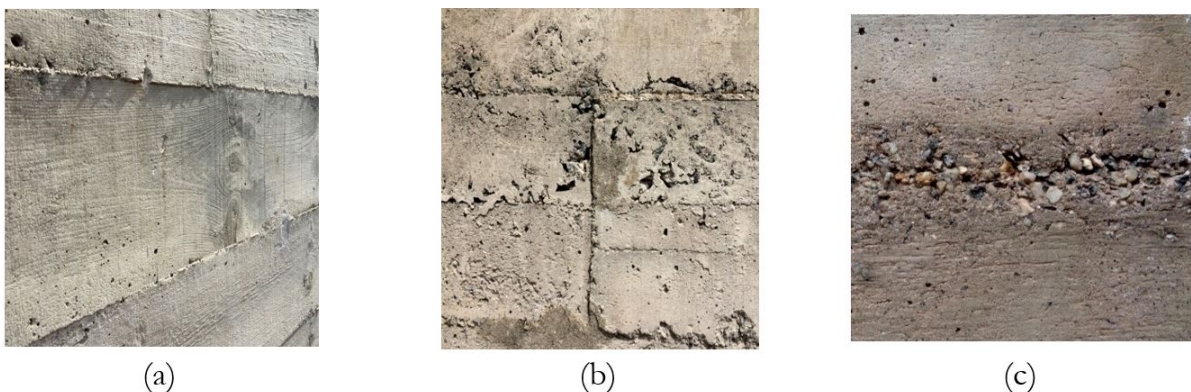


**Figure 3.** Characteristics of the exposed concrete of façades in Artigas building: (a) wood grain pattern on the surface (width 30cm); (b) rough surface texture and air voids; (c) segregation in construction joint. (Images: Collection of ConservaFAU, 2016).

These characteristics favor the deposition of particulate material, penetration of water and aggressive agents, which can be evidenced by dirt stains (carry of particulate material by storm water) and stains of steel corrosion products present throughout the façade extension.

The number of patch repairs and corrosion spots is shown in Table 1. Repairs are randomly dispersed on the façade surfaces, in several shapes and dimensions. Although the visual heterogeneity of concrete is a building characteristic since its inauguration, the repaired areas add variations to the façade surfaces in terms of texture, chromaticity and brightness, different from the parent concrete, which gains proper nuances with aging (Figure 1 and Figure 4).

NE façade had the greatest percentage of patch repairs, followed by SE façade. A total area of 727 m<sup>2</sup> was repaired, which is equivalent to replacement of approximately 24% of the original concrete.

**Table 1.** Number and total area of patch repairs and respective fraction of area repaired in each façade; number of corrosion spots. Inspections made in 2016.

Description	Façades				Total
	SW	SE	NE	NW	
Façade area (m <sup>2</sup> )	993	588	901	589	3071
Total number of repairs	295	146	305	194	940
Fraction of repaired area (%)	16	24	37	16	24
Repair area (m <sup>2</sup> )	159	141	333	94	727
Total number of corrosion spots	153	58	71	131	413
Fraction of corrosion spots (%)	15	10	8	22	----

Moisture stains are present on all the façades with the most significant dimensions on the NE façade, although more dispersed on the SW façade. Figure 4 shows typical moisture stains, suggesting water repellent impregnation failure. The surface moistening also makes cracks in the patch repairs noticeable.

The cover depth, measured in 393 positions by metal detector, results in the distribution shown in Figure 5. Note the predominance cover within the range up to 10 mm.

For cores extracted from the two façades, the average compression strength was 38 MPa, above 32 MPa, which is indicated as characteristic concrete compressive strength in original structural design. Observation of the samples reveals a well compacted concrete, but with outer end (outer surface of the façade) more porous. For core extracted from NW façade, the carbonation depth ranged from 1 to 2 mm on the outer surface, and 14 to 18 mm on the inner face. For core extracted from NE façade, the carbonation depth ranged from 20 to 25 mm on the outer face, and 30 mm on the inner face. Concrete strength is greater than the values achieved for concretes in buildings with similar characteristics, in urban environments, 50 year service life (24 MPa [16]; 22 MPa [17]; 11.3 to 24.1 MPa [18]); the carbonation depths measured are equivalent or less than the maximum values measured by other researchers (76 to 102 mm [16]; 31 mm [17]; 43.5 mm [18]; 5 to 95 mm [19]).



**Figure 4.** Partial views of SW façade: (a) typical moisture stains and (b) noticeable patch repair cracking after rain water penetration (Photos: Authors’ collection, 2017).

According to the mixture proportion reconstitution the average consumption of cement and the cement: aggregates ratio were estimated as 409 kg/m<sup>3</sup> and 1:4.1 for NE façade, and 424 kg/m<sup>3</sup> and 1:3.9 for NW façade. The reconstitution

method assumes water/cement ratio of 0.50, consistent with the values adopted at the building construction time, as indicated in the specialized literature of the engineer Abílio Azevedo Caldas Branco apud Thomaz [37].

According to the Brazilian standard for design of reinforced concrete structures, ABNT NBR 6118: 2014 [26], the building is located in a class II (moderate) aggressiveness environment, condition that requires the use of concrete with compressive strength equal or greater than 25 MPa, w/c ratio equal or less than 0.6, and nominal concrete cover of 30mm. The results suggest that the façade concrete provides properties compatible with the guidelines for durability of concrete structures in line with referred standard. Exception is made for the concrete cover, which, according to the measurements taken (Figure 5 and Table 2), has large variation, with predominance of values less than the ones defined in ABNT NBR 6118 [26].

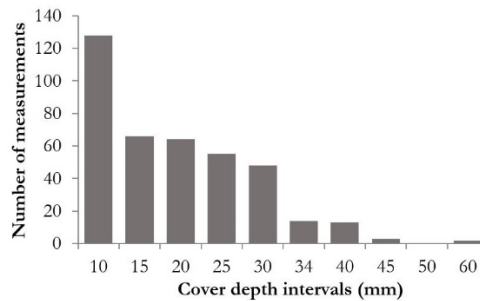


Figure 5. Distribution of cover depth measured on the façades of the Artigas building.

#### 4.2 Detailed inspection

Figure 6 shows the general aspect of two areas inspected with location of patch repairs and numerical grid. Although not clearly visible in the figure, some of the concrete characteristics mentioned are indicated with white chalk, with predominance of concrete segregation regions (S) and surface air voids (AV). Black arrow in Figure 6b indicates the place where two cores were extracted in NW façade. Cracks (C) with variable opening (most  $\leq 2$  mm) were observed on the repair mortar; these fissures affect adversely the performance of concrete by favoring the water ingress.

Regions with hollow sound were located in all the areas inspected (in repair mortar and in concrete). Finally, some sections of the exposed reinforcement were related to stains of corrosion products (corrosion spots) observed in the preliminary inspection. Some of these spots correspond to devices (steel pin or bar) probably used for fastening wall form elements. Measurements made directly on the exposed reinforcement suggest nominal rebar diameter of 8 mm, as indicated in the review of the original design.

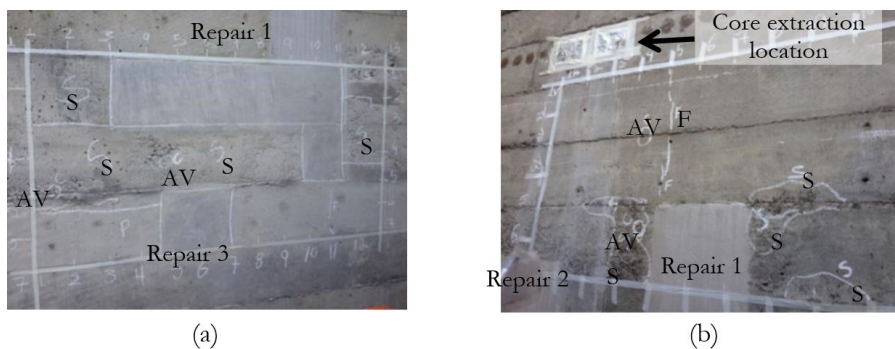


Figure 6. General aspect of the area inspected with identification of repairs: (a) on SW façade and (b) on NW façade (Photos: Authors' collection, 2017).

Table 2 shows the results achieved in the evaluation of repairs, and of the concrete around these repairs, in the areas inspected.

The cover, after fracture of the repair, ranged from 8 to 33 mm, which are values compatible with the intervals of the previous survey (Figure 5). The visual examination of sections newly exposed of the reinforcement indicated active corrosion state, checked by the presence of stains with typical colors of corrosion or accumulation of its products. In

most of the repairs inspected, the reinforcement is not totally surrounded by the repair mortar, but by carbonated concrete. The only reinforcement section wrapped by repair mortar was the exposed one in Repair 2 of SE façade, however the repair mortar presented a well-defined map cracking, a typical failure mode that favors water penetration. Figure 7 shows sections of exposed reinforcement in the repairs inspected. In Figure 7b, we can observe the carbonation depth in the repair mortar, and in the underlying concrete as well. The average carbonation depth in mortar was very variable (4 to 29 mm), and some values are close or greater than the concrete cover, indicating that the corrosion was caused by pH reduction.

**Table 2.** Results of inspection of the reinforcement newly exposed in the repair area of the façades; measurements of the cover and carbonation depth.

Description		Southwest			Northwest		Northeast		Southeast		
		Repair 1	Repair 2	Repair 3	Repair 1	Repair 2	Repair 1	Repair 2	Repair 1	Repair 2	
Reinforcement	Cover (mm)	Individual value	29	30	33	14	15	11	12	7	20
		Average	29	30	33	15	15	8	12	8	20
	Surface color	Brown/orange	Brown/orange	Brown/black/orange	Gray/orange	Brown/orange	Gray/orange	Brown/orange	Gray/orange	Gray/orange	Gray/orange
		Electrochemical state assigned	Active	Active	Active	Active	Active	Active	Active	Active	Active
Carbonation depth (mm)	Repair mortar	Individual value	16	3	30	4	5	3	15	5	9
		Individual value	8	3	34	7	5	15	15	7	10
		Individual value	7	3	24	5	3	10	12	5	8
		Individual value	4	-	27	4	8	7	11	8	8
		Individual value	11	-	28	-	6	-	-	10	7
	Average	9	3	29	5	5	9	13	7	8	
	Concrete	Individual Value (*)	17	34	33	16					
		Individual Value (*)	15	38	34	19	17 (**)	22 (**)	22 (**)	15 (**)	> 26 (***)
		Individual Value (*)	22	17	26	11					
		Individual Value (*)	14	32	25	25					
Average		17	30	30	18	17	22	22	15	-	

(\*) Depth of concrete analyzed beneath the mortar; (\*\*) Single measurement; (\*\*\*) Carbonation front not detected to scarification of 26mm

Upon repair evaluation, the measurements suggest the carbonation depth reaches approx. 20 mm, which affects durability of exposed concrete façade given the corrosion-related pathological manifestations. The carbonation progression in the mortar - within 4 years - may have been influenced by lack of varnish coat, not applied by the reasons indicated in 2.1. The reinforcement sections with cover less than 20 mm shall be depassivated and in an active corrosion process.

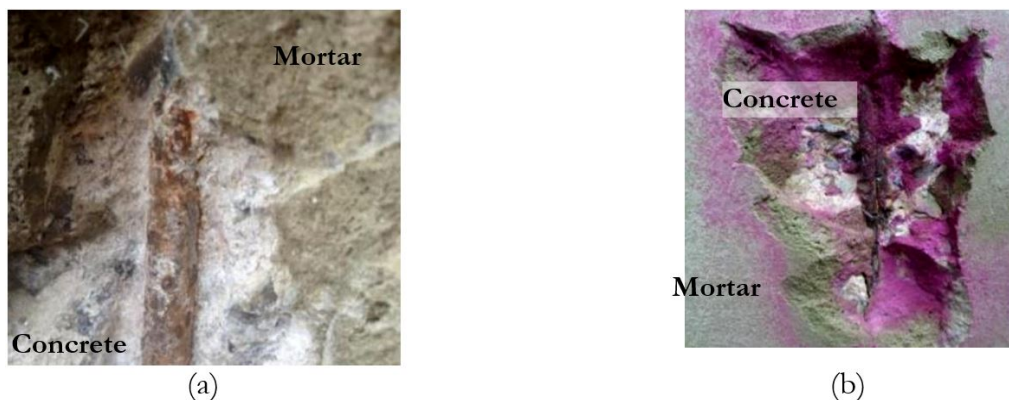


**Figure 7.** Exposed reinforcement during inspection: (a) on Repair 3 of SW façade and (b) on Repair 2 of NW façade (Photos: Authors' collection, 2017).

Figure 8 shows that the gradient of surface moisture, down to 30 mm depth, was not significant, prevailing the range 4 to 6% on SW façade (Figure 8a) and 6 to 7% on NW façade (Figure 8b). In addition, no change was observed in the moisture content in localized repair regions, and neither any correlation of the moisture content maps vs. corrosion potential maps (see Figures 8c and 8d) in the same inspection area.

Each corrosion potential range is represented by a color in Figures 8b and 8c. The concentration of contour lines, with potential variation equal or greater than 150 mV, indicates regions more prone to corrosion [38]. The location and frequency of these regions in the structural elements are the bases for decision-making on interventions. For both maps of Figures 8c and 8d, we observe regions with significant potential variation.

The positive values of potential for carbonated concrete of Figure 8c and 8d corroborate the results of Elsener et al. [39] and Araujo et al. [36], and enforce the importance of potential mapping in the assessment corrosion risk of the reinforcement under these conditions. Data in Figures 8c and 8d indicates significant variation of values in the repair region, which present higher risk of corrosion, i.e. electrochemical cells locations. This activity was checked by examining the reinforcement beneath the repair, which evidenced accumulation of corrosion products on its surface. Most of the values achieved for the corrosion rate were greater than  $1.0 \mu\text{A}/\text{cm}^2$  (section loss  $\geq 10 \mu\text{m}/\text{year}$ ), indicating severe corrosion [40]. However, it must be considered that values above  $1.0 \mu\text{A}/\text{cm}^2$  are typical of concrete exposed to relative humidity (RH) above 90%, which is a condition not verified locally, where the average value from time serie is 81.2%. Considering the local RH between 70% and 90%, the reinforcement corrosion rate must vary, and may increase significantly only under conditions of high relative humidity content, or in periods of intense and frequent rainfall.

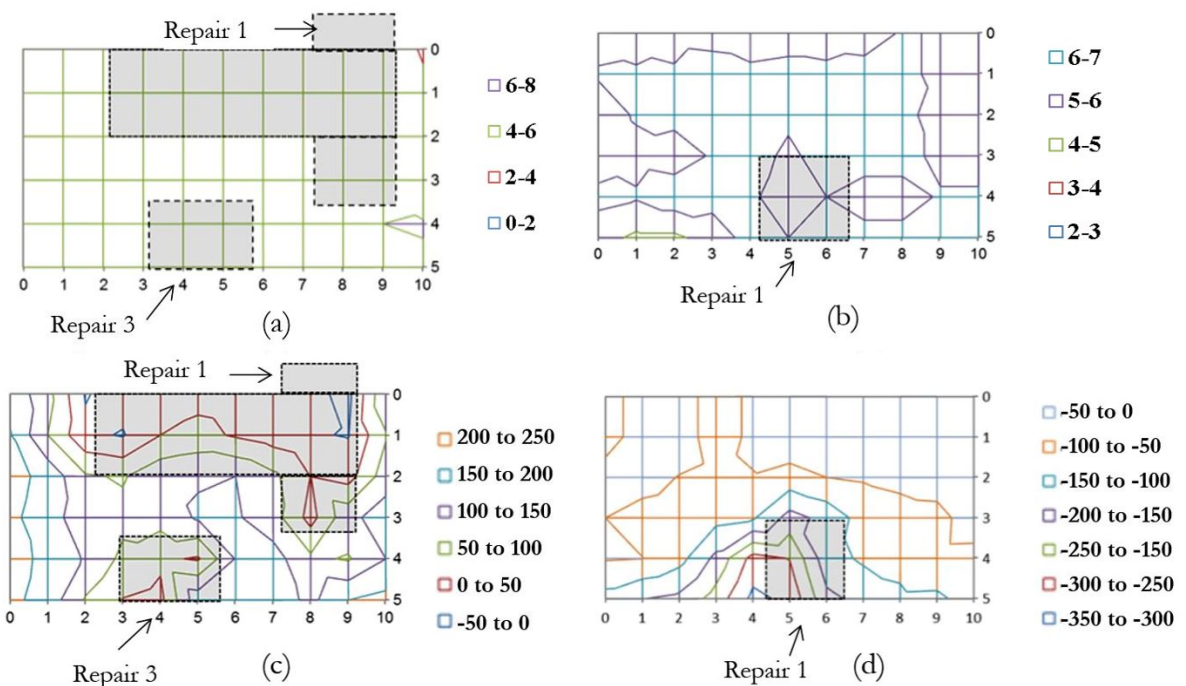


**Figure 8.** Surface moisture content map (%) in inspected area: (a) on SW façade and (b) on NW façade. Corrosion potential map (EPCP electrode) in inspected area: (c) on SW façade and (d) on NW façade. Corrosion potential values (mV).

### 5 RESULT ANALYSIS

The limit imposed by advisory councils for historic preservation for extraction of materials and destructive tests is a challenge faced during investigations, and also reported by other researchers [41]. In the present study, these restrictions limited the investigation to few localized areas, and the fracture in repaired areas only, which are inappropriate conditions for evaluation of large-size structure and extensive surface exposed to weathering.

In this scenario, the result analysis is based on uncertainties, which however could be overcome due to the methodological approach adopted. The differential of the methodology used in this research was the combination of

several techniques, which were evidenced as effective for assessment of the reinforcement current conditions. The past interventions, local conditions, environmental aggressiveness and preliminary inspection composed the reference basis for result analysis, and were essential for deepening the understanding of the structure performance. Among the techniques, we highlight the corrosion potential mapping, which combined to the reinforcement observation, evidenced the active corrosion conditions of the rebars in the areas inspected. The investigations also proved the need for uniform wetting to reduce interference on the corrosion potential measurements, caused by the residual water repellent impregnation and the high electric resistivity of carbonated concrete.

Visual examinations of the newly fractured reinforcement, combined to the thickness of its cover and the carbonation depth, suggest that the corrosion in progress was due to carbonation of the concrete cover, which presented very variable thickness, in addition to cracks, air voids and surface irregularities. The inefficacy of the water repellency effect also contributes for the scenario. Although this inefficacy can be partially assigned to flaws in the application process of the water repellent, upon the present study the product re-application term was already expired, according to the maintenance manual provided by the company in charge of the intervention. Additionally, the lack of efficacy of the water repellent is also related to segregation, cracks, air voids of the concrete surface, which exceed the maximum opening limits (0.3mm), not requiring filling before application of the product [42].

Onsite measurements suggest that the carbonation depth is equal or greater than the concrete cover in virtually the whole extension of façades, and considering the corrosion history of the building, the current condition fits within the propagation period, according to Tuuti [43] model. Within this period, the extension of the residual service life depends on the corrosion rate and its consequences over time. Thus, the reduction of the corrosion rate is the major focus of the strategy for façade conservation.

In Alonso and Andrade apud Bertolini [44] the definition is clear: in the corrosion by carbonation, once the carbonation front has reached the reinforcement and the steel is depassivated, the corrosion rate is controlled by water and oxygen availability on the reinforcement surface. Oxygen availability is very low only in the condition where the concrete is fully and permanently saturated with water [44]. Under other exposure conditions, the corrosion rate of steel in carbonated concrete is ruled by the electric resistivity of concrete. Therefore, for the structure in question, exposed to intermittent period of wetting, the moisture content of concrete is the prevailing parameter of the electric resistivity of the material, and consequently of the corrosion rate of the reinforcement.

By considering that the active corrosion state of the reinforcement, the environmental condition and the characteristics of the outer face of the façades investigated, the conservation plan shall consider a systemic approach focused on the 3 principles of BSI EN 1504-9 [45] (1) preservation or restoration of passivity; (2) control of the anodic area, and (3) protection against penetration /control of humidity.

The first principle is related to the identification of patch repairs that should be redone due to onsite conditions (carbonation front and map cracking, and active corrosion of reinforcement), as well as the new repairs, especially in zones with corrosion deposits and hollow sound. The system that combines industrialized mortar (thixotropic, Portland cement-based, modified with polymer and corrosion inhibiting admixture) and anti-corrosion primer applied on the exposed reinforcement is the proper option. But in this specific case, it would be beneficial a new approach for the mix design of repair mortars together in association with the manufacturers interested in supplying a product custom-made aiming to meet the aesthetic requirements.

The second principle guides the general treatment of the façade surfaces with impregnation of outer surfaces with migration corrosion inhibitor, compatible with the one adopted in the repair system. Impregnation shall be made after removal of the residual water repellent. The application of the corrosion inhibiting agent has the purpose of restricting the natural electrochemical incompatibility between the repair mortar and the original carbonated concrete. Although the use of migration corrosion inhibitor has been reported by Gaudette et al. [46] and MacDonald [47], due to the slight visual impact on the exposed concrete of the architectural heritage, published performance assessments of this protection over time are scarce. As the migration corrosion inhibitor efficiency depends on the final concentration of the product surround the reinforcement, previous studies are required on the migration corrosion inhibitor application method, as well as on the product penetration depth in aged carbonated concrete.

To meet the third principle, we shall proceed with surface protection of the concrete with high-performance water repellent impregnant, silane-based, with high concentration of solids, as reported in Edelson [16], aiming to prevent corrosion or to reduce the corrosion rate by controlling the concrete moisture content. This system has been used in the protection of exposed concrete architectural heritage, as reported in Slaton et al. [48]. As already highlighted in this text, the application method of water repellent and the number of layers shall be supported by previous studies before the concrete surface characteristics. In addition, impregnation does not provide protection against penetration of gases (CO<sub>2</sub> and water vapor), and also may contribute for progress of the carbonation front. To minimize the penetration of

these gases and extend the protection effect of the corrosion inhibitor impregnant, and also the water repellency effect, we have the option for superficial application of alkaline silicate-based solution, which also provides greater resistance to water penetration to the surface [16].

## 6 CONCLUSIONS

The present article presented the results from inspections for assessment of the current conditions of reinforcement in the exposed concrete façades of Vilanova Artigas building. Since it is an architectural heritage, destructive tests were restricted to predefined areas, approved by the advisory councils for historic preservation. The visual inspection of the concrete surfaces evidenced the typical characteristics of exposed concrete structures produced in the Modern Movement, reported in the literature. Many of these characteristics, such as surface air voids, segregation in the construction joints and small and variable concrete cover of the reinforcement, are related to the constructive method. The corrosion deposits identified on the original concrete surfaces are evidences that the concrete cover associated to concrete surface roughness and irregularities, and also to the lack of surface protection system, were determinant for the progress of the corrosion process. In the fractured repaired areas we observed that the carbonation depth was significant in this mortar. The corrosion potential map presented significant variation of values, indicating the active corrosion state of the reinforcement. Under the surface intensely moistened condition, the corrosion rate of the reinforcement was high. As evidenced in this article, detailed study of samples of the Modern Architecture also contributes for documentation of technical aspects, related to the design and materials used in the exposed reinforced concrete production, which impacted the performance of the structure over its service life.

The chronological milestone of 50-year service life, completed in 2019, without significant damage to the structural safety and functionality, provides evidence that the performance of the concrete/reinforcement system of the building façades under study is acceptable, considering the intervention campaign of 2012-2015. However, the rough surface and segregation of the concrete, the low concrete cover to depassivated reinforcement, and the verified active corrosion state of the reinforcement, point out the need for monitoring the façades and the urgency of implementing a preventive maintenance plan, along with a conservation project in order to preserve the heritage values of the building.

## ACKNOWLEDGEMENTS

Authors thank The Getty Foundation, IPT and IFSP for the support provided to the research.

## REFERENCES

- [1] C. S. R. Carvalho, "Preservação da arquitetura moderna: edifícios de escritórios construídos no Rio de Janeiro entre 1930 e 1960," Ph.D. dissertation, Fac. Arquit. Urban., Univ. São Paulo, São Paulo, 2005.
- [2] M. O. Guimarães, "Cinquenta tons de cinza: escalas de ação e de valorização do concreto aparente na Universidade de Brasília," in *Sem. Docomomo Brasil*, 2019. [Online]. Available: <http://docomomo.org.br/course/130-seminario-docomomo-brasil-salvador/>
- [3] F. H. Pinto and F. D. Moreira, "Intervenções em superfícies de concreto aparente e os valores da arquitetura moderna: o caso do edifício sede da CELPE – Companhia Energética de Pernambuco," *Rev. CPC*, no. 21, pp. 119–139, Jan./Jul. 2016, <https://doi.org/10.11606/issn.1980-4466.v0i21p119-139>.
- [4] F. L. H. Pinto, "O concreto aparente como atributo na conservação da arquitetura moderna," M.S. thesis, Prog. Pós-grad. Desenvolv. Urban., Cent. Artes Comun., Univ. Fed. Pernambuco, Pernambuco, 2012.
- [5] M. P. Rocha, "Patrimônio arquitetônico moderno: do debate às intervenções," M.S. thesis, Prog. Pós-grad. Arquit. Urban., Univ. Fed. Paraíba, Pernambuco, 2011.
- [6] C. T. A. Oliveira et al., "O restauro do moderno: o caso do edifício Vinanova Artigas da FAUUSP," in *An. 7º Sem. Docomomo Brasil*, 2007, 12 p.
- [7] C. S. S. M. Castro, "Para além das aparências: contribuição ao estudo da conservação de superfícies arquitetônicas de concreto aparente," M.S. thesis, Fac. Arquit. Urban., Univ. São Paulo, São Paulo, 2018.
- [8] D. C. V. B. C. Oliveira, "Restauração do concreto aparente: estudo tecnológico para salvaguarda de edificações com tendências modernistas," M.S. thesis, Progr. Pós-grad. Arquit. Urban., Inst. Tecnol., Univ. Fed. Pará, Belém, 2013.
- [9] International Docomomo Seminar, *The Fair Face of Concrete: Conservation and Repair of Exposed Concrete. Proceedings*. Eindhoven: DOCOMOMO International, Eindhoven University of Technology, 1998, p. 151. [Online]. Available: [https://issuu.com/docomomoisctechnology/docs/dossier\\_2\\_-\\_the\\_fair\\_face\\_of\\_concre](https://issuu.com/docomomoisctechnology/docs/dossier_2_-_the_fair_face_of_concre)

- [10] P. E. Gaudette and H. J. Hunderman, "Multiphased Approach – Promontory Apartments, Chicago (Mies Van der Rohe, 1949). Eindhoven: DOCOMOMO International, Eindhoven University of Technology, 1998, pp. 127–134. [Online]. Available: [https://issuu.com/docomomoisctechnology/docs/dossier\\_2\\_-\\_the\\_fair\\_face\\_of\\_concre](https://issuu.com/docomomoisctechnology/docs/dossier_2_-_the_fair_face_of_concre)
- [11] J. P. Oudot, *A Delay of Decay – Notre Dame de Royam (Guillaume Gille, 1955)*. Eindhoven: DOCOMOMO International, Eindhoven University of Technology, 1998, pp. 105–111. [Online]. Available: [https://issuu.com/docomomoisctechnology/docs/dossier\\_2\\_-\\_the\\_fair\\_face\\_of\\_concre](https://issuu.com/docomomoisctechnology/docs/dossier_2_-_the_fair_face_of_concre)
- [12] R. Pörtner, *Patch Repair Leaves Architectural Integrity – The Beethoven Hall of the Stuttgart Liederhalle*. Eindhoven: DOCOMOMO International, Eindhoven University of Technology, 1998, pp. 121–126. [Online]. Available: [https://issuu.com/docomomoisctechnology/docs/dossier\\_2\\_-\\_the\\_fair\\_face\\_of\\_concre](https://issuu.com/docomomoisctechnology/docs/dossier_2_-_the_fair_face_of_concre)
- [13] K. A. Van der Zanden, *Brilliant Match? Pumping Station Parksluizen, Rotterdam (1968)*. Eindhoven: DOCOMOMO International, Eindhoven University of Technology, 1998, pp. 95–98. [Online]. Available: [https://issuu.com/docomomoisctechnology/docs/dossier\\_2\\_-\\_the\\_fair\\_face\\_of\\_concre](https://issuu.com/docomomoisctechnology/docs/dossier_2_-_the_fair_face_of_concre)
- [14] S. Macdonald and A. P. A. Gonçalves, "Concrete conservation: outstanding challenges and potential ways forward," *Int. J. Build. Pathol. Adaptation*, vol. 38, no. 4, pp. 607–618, 2020, <http://dx.doi.org/10.1108/IJBPA-12-2018-0100>.
- [15] P. Gu et al., "Electrochemical incompatibility of patches in reinforced concrete," *Concr. Int.*, vol. 19, no. 8, pp. 68–72, 1997.
- [16] R. Edelson, "The Pentagon lightwell walls: repair, rehabilitation and protection for the next 50 years," *Struct. Mag.*, pp. 34–36, Jan., 2007.
- [17] L. N. Buchner and R. M. Pepi, "Restoration of the cast-in-place concrete at the New York Hall of Science," *APT Bull. The J. Preserv. Technol.*, vol. 46, no. 2–3, pp. 54–63, 2015.
- [18] E. E. Maldonado-Bandala, D. Nieves-Mendoza, J. L. Vela-Jiménez and P. Castro-Borges, "Avaliação de problemas patológicos associados à carbonatação e sulfatos em uma torre de concreto com mais de 50 anos de serviço," *ALCONPAT J.*, vol. 8, no. 1, pp. 94–107, 2017, <http://dx.doi.org/10.21041/ra.v8il.284>.
- [19] S. L. Pagliolico, R. Doglione, and J. M. Tulliani, "Diagnosis of the surface layer damage in a 1960s reinforced concrete building," *Case Stud. Constr. Mater.*, vol. 1, pp. 77–82, 2014, <http://dx.doi.org/10.1016/j.cscm.2014.04.006>.
- [20] C. T. A. Oliveira et al., "O restauro do moderno: o caso do edifício Vilanova Artigas da FAUUSP," in *An. 7º Sem. Docomomo Brasil*, 2007, 12 p. [Online]. Available: <http://docomomo.org.br/course/7-seminario-docomomo-brasil-porto-alegre/>
- [21] J. R. L. Simões, "Patologias – origens e reflexos no desempenho técnico-constructivo de edifícios: análise das origens das patologias e seus reflexos no desempenho técnico-constructivo de edifícios universitários da CUASO-USP/SP utilizando-se de edifícios da ISO-6241 e procedimentos da APU - avaliação pós-uso," Ph.D. dissertation, Fac. Arquit. Urban., Univ. São Paulo, São Paulo, 2004.
- [22] C. S. S. M. Castro, A. P. A. Gonçalves, R. A. C. Vergili, R. C. Campioto, C. T. A. Oliveira, and M. L. B. Pinheiro, "Edifício Vilanova Artigas: obra de intervenção em patrimônio moderno," in *Atas Cong. Ibero-Am. Patrimônio: Suas Matér. Imatér.*, 2016, pp. 1–20.
- [23] A. P. A. Gonçalves and C. S. Saraiva, "Intervenção em concreto aparente histórico: o caso das empenas do edifício Vilanova Artigas," in *An. 5º Sem. Docomomo SP*, 2017, pp. 166–181.
- [24] M. L. B. Pinheiro et al., *Subsidies for a Conservation Management Plan: Vilanova Artigas Building*. São Paulo: Sch. Architec. Urban., Univ. São Paulo, 2017. Technical Report. Keeping It Modern, The Getty Foundation. [Online]. Available: [https://www.getty.edu/foundation/initiatives/current/keeping\\_it\\_modern/report\\_library/vilanova\\_artigas.html?q=%7B%7D](https://www.getty.edu/foundation/initiatives/current/keeping_it_modern/report_library/vilanova_artigas.html?q=%7B%7D)
- [25] N. L. Almeida and P. Panossian, *Corrosão Atmosférica 17 Anos*. São Paulo: Secretaria da Ciência e Desenvolvimento Econômico do Estado de São Paulo, 1999, p. 130.
- [26] Associação Brasileira de Normas Técnicas, *Projeto de Estruturas de Concreto – Procedimento*, ABNT NBR 6118, 2014.
- [27] Companhia Ambiental do Estado de São Paulo. "Qualidade do ar no estado de São Paulo 2017." CETESB, 2018. <https://cetesb.sp.gov.br/ar/wp-content/uploads/sites/28/2018/05/relatorio-qualidade-ar-2017.pdf> (accessed Jan. 30, 2019).
- [28] Universidade de São Paulo. Instituto de Astronomia Geofísica e Ciências Atmosféricas, *Boletim Climatológico Anual da Estação Meteorológica do IAG/USP*. IAG, 2017. [Online]. Available: <http://www.estacao.iag.usp.br/Boletins/2017.pdf>
- [29] J. A. Marengo, L. M. Alves, T. Ambrizzi, A. Young, N. J. C. Barreto, and A. M. Ramos, "Trends in extreme rainfall and hydrogeometeorological disasters in the Metropolitan Area of São Paulo: a review," *Ann. N. Y. Acad. Sci.*, vol. 1472, no. 1, pp. 1–16, 2020, <http://dx.doi.org/10.1111/nyas.14307>.
- [30] M. Balzani, F. Maietti, and B. M. Köhl, "Point cloud analysis for conservation and enhancement of modernist architecture," *Int. Arch. Photogramm. Remote Sens. Spatial Inf. Sci.*, vol. XLII-2/W3, pp. 71–77, 2017. <http://dx.doi.org/10.5194/isprs-archives-XLII-2-W3-71-2017>.
- [31] Associação Brasileira de Normas Técnicas, *Concreto - Extração, Preparo, Ensaio e Análise de Testemunhos de Estruturas de Concreto - Parte 1: Resistência à Compressão Axial*, NBR 7680-1, 2015.
- [32] V. A. Quarcioni, "Reconstituição de traço de argamassas simples e mistas de cimento Portland e cal hidratada: atualização do método do IPT," M.S. thesis, Esc. Politéc., Univ. São Paulo, São Paulo, 1998.
- [33] Instituto de Pesquisas Tecnológicas, *Método Reconstituição do Traço do Concreto* (Boletim 25). São Paulo: IPT, 1940, pp. 75–84.

- [34] A. Araujo and Z. Panossian, "Inspeção rotineira de estruturas de concreto armado expostas a atmosferas agressivas," *Techne*, vol. 19, pp. 58–64, 2011.
- [35] Deutsches Institut für Normung, *Products and Systems for the Protection and Repair of Concrete Structures - Test Methods - Determination of Carbonation Depth in Hardened Concrete by the Phenolphthalein Method*, DIN EN 14630, 2007, 10 p.
- [36] A. Araujo, Z. Panossian, T. G. Rosa, and M. C. Braga, "Comportamento eletroquímico do aço-carbono em concreto: potencial de eletrodo e densidade de corrente elétrica," *Téchne*, no. 247, pp. 29–39, 2017.
- [37] E. C. S. Thomaz. "Notas de aula: concreto: traços – fabricação – 1967 – eng. Abílio A. Caldas Branco." [http://aquarius.ime.eb.br/~webde2/prof/ethomaz/cimentos\\_concretos/pad\\_cimentos.htm](http://aquarius.ime.eb.br/~webde2/prof/ethomaz/cimentos_concretos/pad_cimentos.htm) (accessed Nov. 5, 2018).
- [38] Nace International, *Use of Reference Electrodes for Atmospherically Exposed Reinforced Concrete Structures* (Publication 11100). Houston, 2000, 11 p.
- [39] B. Elsener, C. Andrade, J. Gulikers, R. Polder, and M. Raupach, "RILEM TC 154-EMC Half-cell potential measurements – potential mapping on reinforced concrete structures," *Mater. Struct.*, vol. 36, no. 7, pp. 461–471, 2003., <http://dx.doi.org/10.1007/BF02481526>.
- [40] C. Andrade and C. Alonso, "RILEM TC 154-EMC Test methods for on-site corrosion rate measurement of steel reinforcement in concrete by means of the polarization resistance method," *Mater. Struct.*, vol. 37, no. 11, pp. 623–643, 2004.
- [41] G. Crevello, N. Hudson, and P. Noyce, "Corrosion condition evaluations of historic concrete icons," *Case Stud. Constr. Mater.*, vol. 2, pp. 2–10, 2015., <http://dx.doi.org/10.1016/j.cscm.2014.12.005>.
- [42] S. J. Meier and F. H. Wittmann, "Water repellent surface impregnation of concrete: guidelines and recommendations," in *ASMES Int. Workshop – Basic Research on Concrete and Applications Proc.*, W. Folker H. and M. Olivier, Eds., Germany: Aedificatio Publishers Freiburg, 2011, pp. 49–66. <http://dx.doi.org/10.1515/rbm-2011-6476>.
- [43] K. Tuuti, *Corrosion Steel in Concrete*. Swedish: Cement and Concrete Research Institute, 1982, 469 p.
- [44] L. Bertolini, "Steel corrosion and service life of reinforced concrete structures," *Struct. Infrastruct. Eng.*, vol. 4, no. 2, pp. 123–137, 2008, <http://dx.doi.org/10.1080/15732470601155490>.
- [45] British Standards Institution, *Products and Systems for the Protection and Repair of Concrete Structures - Definitions, Requirements, Quality Control and Evaluation of Conformity - Part 9: General Principles for the Use of Products and Systems*, BS EN 1504-9, 2008, p. 32.
- [46] P. E. Gaudette, H. J. Hunderman, and D. Slaton, "The repair of Mies van der Rohe's Promontory Apartment Building, Chicago: a multi-phased approach," in *Concrete: Building Pathology*, S. MacDonald, Ed., Oxford: Blackwell Science Ltd., 2003, pp. 269–281.
- [47] S. MacDonald, Ed., "University of Sussex: developing repair methods for the listed buildings," in *Concrete: Building Pathology*. Oxford: Blackwell Science Ltd., 2003, pp. 285–288.
- [48] D. Slaton, P. E. Gaudette, and D. Patterson, "Morse and Ezra Stiles Colleges Yale University, New Haven, Connecticut," in *International Specialist Committee/Technology Dossier 14 - Concrete and Modernism: Technology and Conservation*, T. Prudon and K. Normandin, Eds., New York: Docomomo, 2018, pp. 32–37.

---

**Author contributions:** CAO: conceptualization, methodology, data collection, formal analysis, writing, supervision; AA e TRSS: conceptualization, methodology, data collection, formal analysis and writing.

**Editors:** Edna Possan, José Luiz Antunes de Oliveira e Sousa, Guilherme Aris Parsekian.



ORIGINAL ARTICLE

# Influence of cement type, air-entrained admixture and hydration stabilizing admixture on mortars' setting time

*Influência do tipo de cimento e dos aditivos incorporador de ar e estabilizador de hidratação no tempo de pega de argamassas*

Juliana Pippi Antoniazzi<sup>a</sup>

Gihad Mohamad<sup>b</sup>

Juliana Machado Casali<sup>c</sup>

<sup>a</sup>Universidade Federal de Santa Maria – UFSM, Departamento de Expressão Gráfica, Santa Maria, RS, Brasil

<sup>b</sup>Universidade Federal de Santa Maria – UFSM, Departamento de Estruturas e Construção Civil, Santa Maria, RS, Brasil

<sup>c</sup>Instituto Federal de Santa Catarina – IFSC, Departamento Acadêmico de Construção Civil, Florianópolis, SC, Brasil

Received 09 September 2019

Accepted 12 June 2020

**Abstract:** Ready mix mortar is a ready to use mixture that uses hydration stabilizing (HSA) and air-entrained (AEA) admixtures in its composition, which modify its properties, especially the setting times. HSA extends the setting time of mortars for a long period, while AEA promotes a greater workability to the mixture. The study determined the temperature of the mortars with the evaluation of the setting times obtained by a semi-adiabatic calorimeter. Two types of cement (CPII-F-40 e CPII-Z-32) and varied contents of HSA (0.0%, 0.6% e 0.9%) and AEA (0.0%, 0.2% e 0.4%) were used. The results showed that the use of HSA decreased the amplitude of the temperature peaks and increased the setting times with cement CPII-Z-32 in relation to cement CPII-F-40. The setting time of the mortars was influenced by the type of cement used and by the contents of the admixtures.

**Keywords:** air-entrained admixture, hydration stabilizing admixture, ready mix mortar, setting time.

**Resumo:** A argamassa estabilizada é uma mistura pronta que faz uso dos aditivos estabilizador de hidratação (AEH) e incorporador de ar (AIA) em sua composição, os quais modificam suas propriedades, principalmente, os tempos de pega. O AEH prorroga o tempo de pega das argamassas por um longo período, enquanto o AIA promove maior trabalhabilidade à mistura. O estudo determinou a temperatura de argamassas com a avaliação dos tempos de pega obtidos em calorímetro semi-adiabático. Foram utilizados dois tipos de cimento (CPII-F-40 e CPII-Z-32) e variados os teores de AEH (0.0%, 0.6% e 0.9%) e AIA (0.0%, 0.2% e 0.4%). Os resultados mostraram que o uso de AEH diminuiu a amplitude dos picos de temperatura e aumentou os tempos de pega das argamassas com o cimento CPII-Z-32 em relação ao cimento CPII-F-40. O tempo de pega das argamassas foi influenciado pelo tipo do cimento utilizado e pelos teores de aditivos.

**Palavras-chave:** aditivo incorporador de ar, aditivo estabilizador de hidratação, argamassa estabilizada, tempo de pega.

**How to cite:** J. P. Antoniazzi, G. Mohamad, and J. M. Casali, "Influence of cement type, air-entrained admixture and hydration stabilizing admixture on mortars' setting time," *Rev. IBRACON Estrut. Mater.*, vol. 14, no. 1, e14114, 2021, <https://doi.org/10.1590/S1983-41952021000100014>

## 1 INTRODUCTION

The use of ready mix mortar as a coating has been increasing in construction sites of big cities. These mortars arrive ready at the site for its use, and remain workable for up to 72 hours. These characteristics are due to the use of admixtures in the composition of the mixtures; the most common ones being hydration stabilizing admixture (HSA) and air-entrained admixture (AEA).

Corresponding author: Juliana Pippi Antoniazzi. E-mail: [juliana.antoniazzi@ufsm.br](mailto:juliana.antoniazzi@ufsm.br)

Financial support: None.

Conflict of interest: Nothing to declare.



This is an Open Access article distributed under the terms of the Creative Commons Attribution License, which permits unrestricted use, distribution, and reproduction in any medium, provided the original work is properly cited.

Air-entrained admixtures (AEA) are organic materials that belong to the class of the surfactants, usually of a cation-anion characteristic, being constituted with an (apolar) hydrophobic extremity and another (polar) hydrophilic one [1]. These admixtures decrease the superficial tension and modify the rheology of the mortars through the insertion of small air bubbles, offering a better plasticity [2]. The improvement in the workability of the mixtures is the main effect of the air-entrained admixture when used in mortars [2], [3], but it can also contribute to the delay of the reactions, since its molecules join the cement particles through its polar part (attraction through opposing charges), with the apolar tail focused towards the water [3]. This way, a layer of surfactants is formed around the cement particles which repels the water and may retard the reactions of hydration, depending on the quantity of admixture employed [4]. The permeability of the mortars may also increase with great quantities of entrained air, provided by the excess of AEA [3], and a decrease of the compressive strength may occur [4].

Hydration stabilizing admixtures (HSA) are substances composed by an aqueous salt solution, hydrocarboxylated acids and carbohydrates, that form long-lasting hydration delaying admixtures [5], which promote an increase of the plasticity of the mortar for a greater period of time [6], [7]. When added to mortars they act over all of the minerals of the clinker, reducing the concentration of calcium sulphate in the solution and forming a semipermeable layer around the cement particles, which extends the time of its reactions and of the setting time [7]–[9]. In ready mix mortars they are added together with kneading water, inhibiting the nucleation and formation of hydrated calcium silicates [8], [10], the main responsible for the compressive strength in hardened mortars. This way, HSA increases the period of induction and alters the rate of hydration of the compounds [11], [12]. However, the effects of the admixture on the process of Portland cement may vary according to its chemical basis, occurring in an isolated or simultaneous way [13]. This way, the formation of the hydrates may suffer delay, due to the adsorption of the molecules of the admixture through the surface of the cement particles [11]. Besides this, the chelating property of the molecules of the admixture may also hinder the precipitation and stabilize the dissolved calcium ions [14].

When the effect of the admixture disappears and the barrier formed is dissolved, the cement starts spontaneously to hydrate, and the mortar tends to start its setting process [4], [10].

The rate of HSA employed interferes directly in the time of the blocking of the reactions [15], being even able to act in such a way that the setting process does not occur or that an unwanted setting process ends up occurring. Besides this, when used in excessive quantities, the stabilizing admixture reduces expressively the compressive strength of the mortar [15]–[17].

This way, the employment and the dosage of the admixture in stabilized mortars requires specific studies and domain of the variables involved in the process. Many factors may affect the performance of these mortars, with the possibility of compromising its properties in the fresh and hardened states. The period of time and the procedure of the mixture, the type and the rate of the admixtures used, the compatibility of the admixtures with the cement employed, the consumption of the cement, the temperature and humidity, the type and granulometry of the aggregates, the quality of the water and the form of storage of the ready mix mortar are some of these factors [3], [18]–[20].

The setting times of the ready mix mortars are important factors during its dosage, once it is these mortars that are precisely commercialized with the objective of increasing the time of workability, therefore being necessary to increase the initial time of the reactions. These times depend, among other factors, on the quantity of admixtures employed. Campos [21] determined the setting time of the mortars with HSA, verifying a direct relationship with the admixture content, as well Ruppenthal and Pelisser [22], Pivetta et al. [23]. Calçada et al. [19] also found this relationship, whereas Guindani [13] verified one for stabilized pastes.

The initial setting times obtained by Campos [21] by the method of strength to penetration, according to NBR NM 9 [24], were superior to the ones obtained by a semi-adiabatic calorimeter and by ultrasound, which were also found by Macioski [20] in their analysis with batches of ready-mix mortars. Barbosa et al. [25] evaluated admixtures pastes and mortars with only one rate of HSA by verifying the direct influence of the water over the setting time of the pastes, while the presence of HSA increased the setting time of both. The setting time of the mortars with a HSA were inferior to the pastes with HSA, for the same relations of water/cement, demonstrating the quantity of water available in the system. According to Viécili et al. [26], the method of semi-adiabatic calorimetry proved to be adequate for the determination of the setting times of the pastes made with different types of cement, when comparing them with the results of the method of Vicat. The authors obtained the most coherent results for the setting times by the analysis of the derivatives method.

Other factors that may affect the speed and the quantity of heat liberated in the reactions of hydration are the type and the fineness of the cement. The finer the cement, the faster it will tend to react, once the hydration occurs from the surface to the interior of the grain [27]. With a greater quantity of particles per unit of mass, and, therefore, a greater area of surface in contact with the water, the rate of reactivity tends to be greater [28], [29]. However, none of the

studies mentioned evaluated the influence of HSA and AEA in different dosages and combinations over the setting times of the mortars. The effect of these admixtures over different types of cement was also not evaluated.

In view of the still existent gaps and the absence of specific norms for the employment of admixtures in ready-mix mortars, this study monitored the temperature of the mortars during the process of hydration, using two distinct types of cement (CPII-F-40 e CPII-Z-32) and different rates of air entrained (AEA) and hydration stabilizing admixtures (HSA). Therefore, the objective was to establish comparatives related to the setting times of the mortars for each type of cement, estimated by different methods of calculus (tangent, direct fraction and derivatives method), evaluating the conjunct and isolated action of each admixture.

## 2 MATERIALS AND EXPERIMENTAL PROGRAM

### 2.1 Materials

The study evaluated the temperature in the initial ages of the mortars using two types of Portland cement, varying the dosages of hydration stabilizing (HAS) and air entrained admixtures (AEA), in order to obtain the initial and final setting times of these. The mortars were made in laboratory, with the materials employed supplied and chosen due to their use by manufacturers of ready-mix mortar of the south region of the country.

The cements used in this research were a Portland cement composed with carbonate material (CPII-F-40) and a Portland cement composed with pozzolanic material (CPII-Z-32), both from the same manufacturer, denominated in this research as cement F and cement Z, respectively. The tests of characterization of Portland cement are found in Table 1 and Table 2.

**Table 1.** Physical characteristics of cements CPII F-40 and CP II Z-32.

Property	Cement F	Cement Z	Method
Specific mass (g/cm <sup>3</sup> )	3.10	3.06	ABNT NBR 16605 [30]
Fineness index (#0.075mm) (%)	0.12	0.51	ABNT NBR 11579 [31]
Percentage of water for normal consistency (%)	29.00	28.71	ABNT NBR 16606 [32]
Initial setting (h:min)	4:00	4:10	ABNT NBR 16607 [33]
Final setting (h:min)	5:20	5:44	ABNT NBR 16607 [33]
Surface area (m <sup>2</sup> /g)	1.2592	1.2844	BET
Pore volume (cm <sup>3</sup> /g)	0.004791	0.004190	BET
Pore dimension (nm)	20.0047	17.7925	BJH/BET

**Table 2.** Chemical, physical, and mechanical characteristics of cements CPII F-40 and CP II Z-32.

Chemical Tests					
	Cement F	Cement Z	Code Limit	Normative	
Ignition loss (%)	4.86	5.26	≤ 6.5	ABNT NBR NM 18 [34]	
Magnesium oxide (%)	5.90	5.52	≤ 6.5	ABNT NBR NM 14 [35]	
Sulfur trioxide (%)	3.56	2.83	≤ 4.0	ABNT NBR NM 16 [36]	
Insoluble residue (%)	0.82	13.17	≤ 2.5 / ≤ 16	ABNT NBR NM 22 [37]	
Physical and Mechanical Tests					
Blaine (cm <sup>2</sup> /g)	4521.50	3657.50	≥ 2800 / ≥ 2600	ABNT NBR 16372 [38]	
Hot expansibility (mm)	0.38	0.55	≤ 5.0	ABNT NBR 11582 [39]	
	1 day	23.73	12.51		N/A
Compression strength	3 days	34.47	22.89	ABNT NBR 7215 [40]	
	7 days	40.25	28.17		≥ 15.0 / ≥ 10.0
	28 days	47.68	37.13		≥ 25.0 / ≥ 20.0
			≥ 40.0 / ≥ 32.0; ≤ 49.0		

Source: Portland Cement Manufacturer

The fine aggregate employed (sand) is natural, from the river of the city of Santa Maria/RS, with its characteristics specified on Table 3. The choice of this aggregate was due to the study conducted by Antoniazzi [45]. In this study

statistically significant differences were not found related to the entrainment of air for mortars made with different granulometries. Therefore, the material with greater viability and easiness of access was chosen.

**Table 3.** Properties of the small aggregate.

Propriety	Sand	Method
Maximum characteristic dimension (mm)	1.20	ABNT NBR NM 248 [41]
Fineness module	1.73	ABNT NBR NM 248 [41]
Specific mass(g/cm <sup>3</sup> )	2.64	ABNT NBR NM 52 [42]
Unit mass (g/cm <sup>3</sup> )	1.63	ABNT NBR NM 45 [43]
Content of pulverulent material (%)	4.94	ABNT NBR NM 46 [44]
Surface area (m <sup>2</sup> /g)	0.5424	BET
Pore volume (cm <sup>3</sup> /g)	0.001156	BET
Pore dimension (nm)	8.4833	BJH/BET

Source: Author.

The granulometry of the aggregate was conducted according to NBR NM 248 [41] and may be verified in Figure 1. Before the preparation of the mortars, the aggregates were dried in an oven during 24 hours.

Meshes opening (mm)	Sand	
	% Retained	% Cumulative Retained Percentage
9.50	0.00%	0.00%
4.80	0.08%	0.08%
2.40	0.40%	0.47%
1.20	1.78%	2.25%
0.60	15.19%	17.45%
0.30	51.31%	68.76%
0.15	15.33%	84.08%
Bottom	15.92%	100.00%

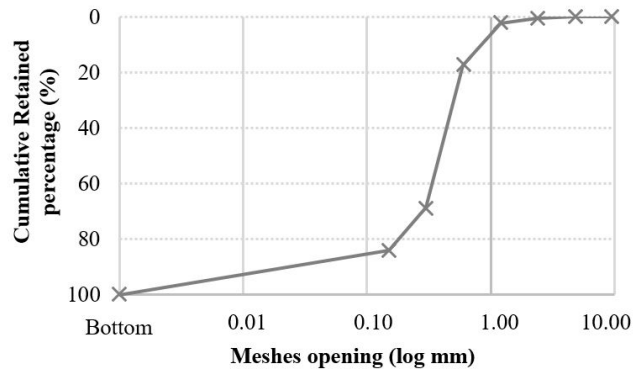


**Figure 1.** Particle size of Sand.

The mortars were prepared using two types of admixtures, an air entrained admixture (AEA) and a hydrating stabilizing (HAS). The technical data, supplied by the manufacturer, is found on Table 4.

**Table 4.** Technical data of the air-entrained admixture (AEA) and hydration stabilizing admixture (HSA).

Characteristics	AEA	HSA
Chemical base	Sulfated ethoxylated fatty alcohol salt	-
Aspect	Liquid	Liquid
Color	Yellow	Brown
Density (g/cm <sup>3</sup> )	1.00	1.17
Solids content (%)	3	45
pH	9	6
Solubility	Soluble in water (20°C)	Soluble in water
Dosages (% cement weight)	0.1 – 0.5	0.2 – 1.5

Source: Admixtures manufacturer.

## 2.2 Experimental Program

All of the tests were conducted in the Civil Engineering and Material Laboratory – CEML – and in the Environmental Processes Laboratory – EPL – both of Federal University of Santa Maria (UFSM).

Eighteen mortars were prepared with the same proportion in mass of 1:6.5, relation of water/cement of 1.0 and fine aggregate. The dosages of the admixtures used were varied, with the rates of 0.0%, 0.6% e 0.9% of HAS and of 0.0%, 0.2% e 0.4% of AEA being employed, related to the cement mass. Of the eighteen mortars prepared, nine used Cement F and nine used Cement Z Table 5 presents the mortars studied in this research with its respective denominations.

**Table 5.** Mortar mixtures with cements F and Z.

Mortar	HSA (%)	AEA (%)	Type of cement	Nomenclature
A1(0.0/0.0)	0.0	0.0	Cement F	A1F(0.0/0.0)
			Cement Z	A1Z(0.0/0.0)
A2(0.6/0.0)	0.6	0.0	Cement F	A2F(0.6/0.0)
			Cement Z	A2Z(0.6/0.0)
A3(0.9/0.0)	0.9	0.0	Cement F	A3F(0.9/0.0)
			Cement Z	A3Z(0.9/0.0)
A4(0.0/0.2)	0.0	0.2	Cement F	A4F(0.0/0.2)
			Cement Z	A4Z(0.0/0.2)
A5(0.0/0.4)	0.0	0.4	Cement F	A5F(0.0/0.4)
			Cement Z	A5Z(0.0/0.4)
A6(0.6/0.2)	0.6	0.2	Cement F	A6F(0.6/0.2)
			Cement Z	A6Z(0.6/0.2)
A7(0.6/0.4)	0.6	0.4	Cement F	A7F(0.6/0.4)
			Cement Z	A7Z(0.6/0.4)
A8(0.9/0.2)	0.9	0.2	Cement F	A8F(0.9/0.2)
			Cement Z	A8Z(0.9/0.2)
A9(0.9/0.4)	0.9	0.4	Cement F	A9F(0.9/0.4)
			Cement Z	A9Z(0.9/0.4)

The mortars were prepared in a mixer of 5 liters, with planetary movement. The procedure of mixture was performed based on recommendations described in NBR 7215 [40] with adaptations for the use of admixtures and within the time of rest as described below. Initially all of the water was inserted (in the mortars with admixtures, these were added at this moment and mixed in low speed with the water during 20 seconds for homogenization) and, afterwards, all of the Portland cement. With the mixer in low speed, the materials were mixed during 30 seconds. Afterwards, without paralyzing the equipment, the sand was introduced gradually, during a period of 30 seconds. After the sand was inserted, the speed was altered to high and the materials were mixed for another 30 seconds. The mixer was turned off during 15 seconds for the withdrawal of mortar adhered to the walls with the help of a shovel. The mixer was then turned on again in high speed for 180 more seconds, totalizing a full time of 270 seconds, as established by Antoniazzi [45], for a maximum entrainment of air.

For each mixture of mortar three samples were evaluated, which were placed in distinct semi-adiabatic calorimeters. Figure 2 presents a scheme of the system performed, in cut, which consists in an expanded cup of polypropylene (Styrofoam) with a lid, and an internal diameter of 8 cm and a useful height of 11 cm. This cup was inserted in a box of the same material with a lid, with dimensions of 20 x 25 x 28 cm. Both were coated with aluminum paper internally and externally for a better thermal isolation. The cup received the sample of mortar in its interior and had a thermocouple “type t” wire submerged. The space between the two boxes was filled with small spheres of expanded polypropylene (Styrofoam), which were confined by a sheet of expanded polypropylene (Styrofoam) on the superior part. The thermocouple wire was connected to the data collector (Fieldlogger Novus), which was interconnected to a computer with Novus Fieldchart software, for data plotting. This way, each mixture was placed in a calorimeter, where the evolution of the temperature for 336 hours (14 days) was followed up. The collection of the data was programmed to be registered every ten minutes.

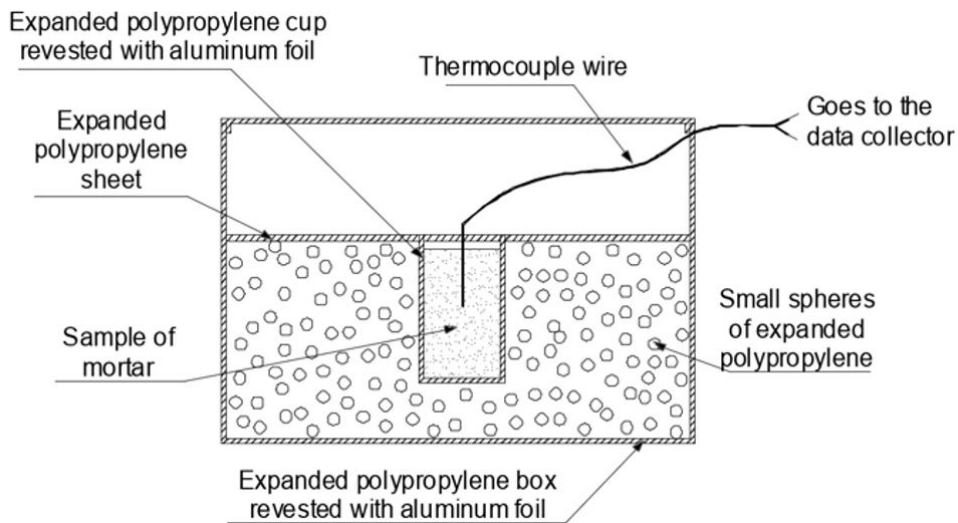


Figure 2. Scheme of the semi-adiabatic calorimeter in section.

The sequence of assembly of the boxes for the rehearsal occurred in the following way: first, a hole was made on the lid of the cup, where the thermocouple wire type T (Figure 3a) was inserted, with the depth, that should penetrate in the box in order for it to remain always in the same position (half height) inside the samples, being marked. Small spheres of expanded polypropylene were placed (Figure 3b) around the cup containing the sample of mortar in its interior, which was inserted inside a plastic bag to make the reutilization of the cups possible (Figure 3c). The filling of the sample was performed in two layers, with 20 blows of metallic socket and 3 falls of approximately 3 cm in each one, with a volume of mortar of approximately 553 cm<sup>3</sup>. The cup with the sample was closed with a lid (Figure 3d), surrounded by spheres of isopropylene and fit into the hole of the plate. The box was also perforated on its side for the passage of the thermocouple wire to the external space (Figure 3e), closing the holes with liquid silicone where the thermocouple wire passed. The thermocouple wire was connected to the data collector (Figure 3f). Based on the data obtained, three distinct methods were used for the analysis and determination of the initial and final setting times: the tangent method [46], direct fraction method [26], [47] and the derivatives method [48]. In each of the methods the times considered for each mixture was the arithmetic mean between the three samples tested.

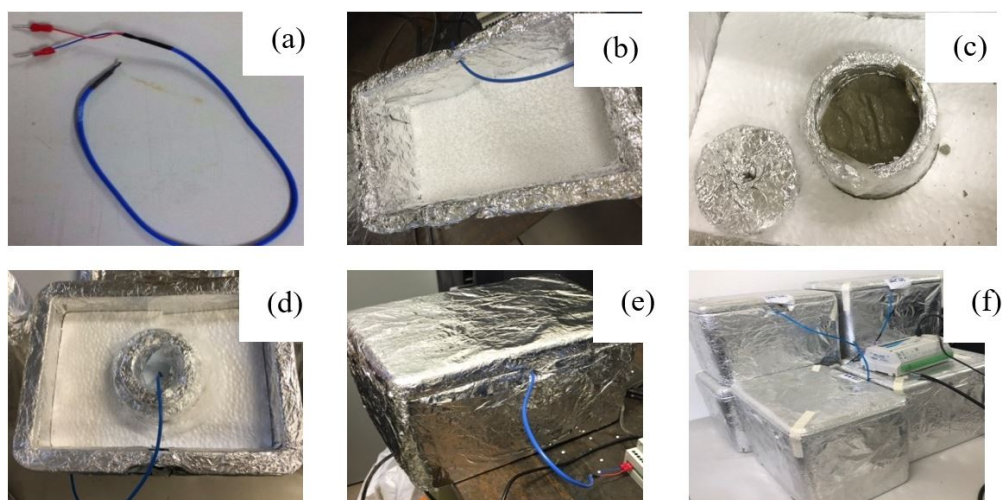


Figure 3. Sequence of the assembly of the boxes for the initial setting time test. (a) thermocouple type T; (b) expanded polypropylene box with cradle for small expanded polypropylene spheres; (c) expanded polypropylene cup positioned inside the box, embedded in expanding polypropylene plate, receiving the mortar sample within; (d) thermocouple positioned within the sample, properly capped and sealed with silicone; (e) closed box with the sample inside and thermocouple exiting the external medium, connecting to the data collector; (f) system ready and connected to the data collector.

The tangent method, as demonstrated on Figure 4 [46], estimates, based on the values of temperature versus time, the time of the beginning of the setting process through the trace of horizontal lines that tangent the curve in the maximum and minimum temperature points. The tangent lines, by turn, are intercepted by a third line superimposed to the curve in the period of acceleration and reaction to hydration. The points of intersection between the traced lines correspond to the initial and final setting times.

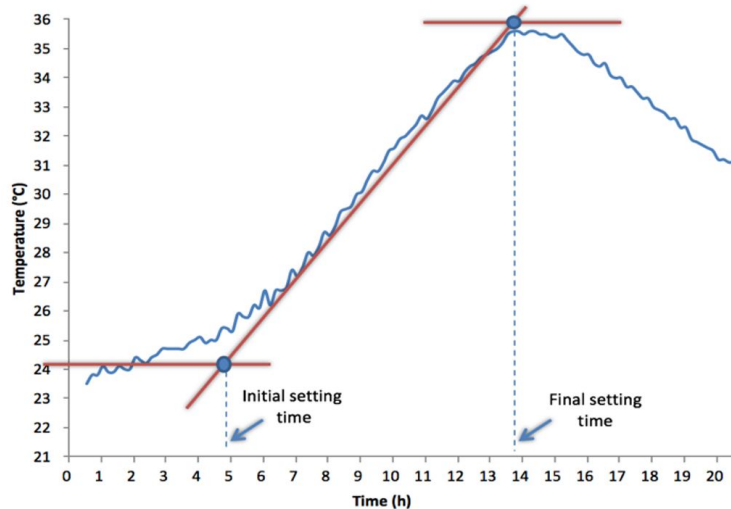


Figure 4. Scheme representing the determination of the initial and final setting times by the tangent method.

Through the direct fraction method [26], [47] the initial and final setting times are determined by percentages of the total increase of the temperature. This way, in controlled environment conditions, the initial setting time is equivalent to 21% of the difference between the temperature of the beginning of the induction and superior peak of the temperature reached, while the final time is equivalent to 42%, as shown in Figure 5.

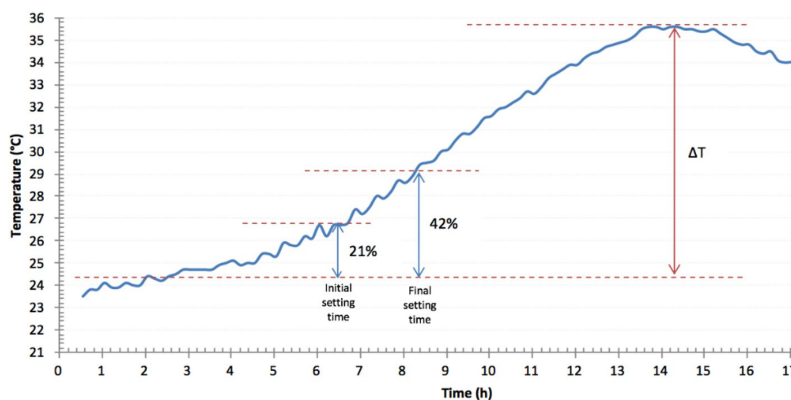
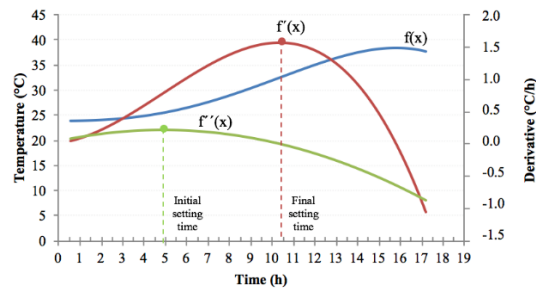


Figure 5. Scheme representing the determination of the initial and final setting times by the direct fraction method.

The derivatives method [48] is based on studies that demonstrated that the initial setting time is equivalent to the maximum peak of temperature of the second derivative of the temperature versus time curve, while the final setting time is obtained through the peak of the first derivative, according to the demonstration on Figure 6.

To allow the analysis of the mortars under the same conditions of molding, testing and temperature (24°C), the mortars of the same trace and same rate of admixture were simultaneously molded, varying only the type of Portland cement (Cement F and Cement Z). The monitoring of the mortars started 20 min after the confection of the samples due to the assembly, transportation to the air-conditioned location and connection to the field logger.



**Figure 6.** Scheme representing the determination of the initial and final setting times by the derivatives method.

The data of the research was analyzed with the help of the SPSS (Statistical Package for Social Sciences, version 20.0) program, using T Tests and ANOVA with the Tukey Post Hoc Test ( $p < 0.05$ ) for the comparison of the results between the different mixtures and between mortars with the two types of Portland cement. The determination coefficient ( $R^2$ ) was used to classify the adjustment of the data to a regression model, and also Pearson’s linear correlation coefficient ( $r$ ) was calculated, which expresses the intensity and the sense of linear relation existent between the two numeric variables. In data analysis, when ( $p < 0.05$ ), it is considered that there is a significant statistic difference between the results, otherwise there are no significant differences. When there were differences, the Post Hoc Tukey Test was applied to evaluate which groups are different and which are similar, with superscript letters for identification. When the results receive the same superscript letter this indicates that there are no differences between them, whereas, when the letters are different, they are statistically different.

### 3 RESULTS AND DISCUSSIONS

The curves of the temperature versus time, for each one of the mortars studied are presented in Figure 7, with (a) the mortars prepared with cement F and (b) the mortars prepared with cement Z in its composition.

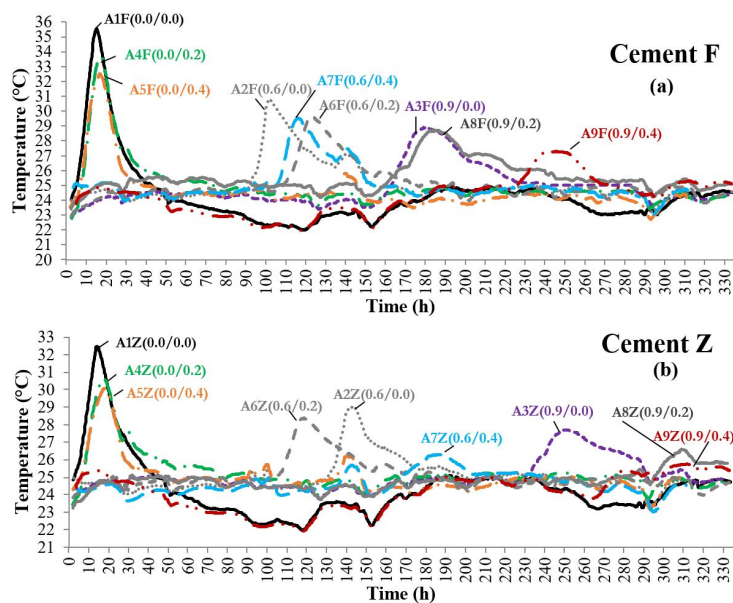


**Figure 7.** Evolution of the mortar temperatures over time, for cement F (a) and cement Z (b).

It is observed in Figure 7 that the type of Portland cement employed influenced in the process of hydration and in the formation of the hydrated compounds. This behavior was verified because, for a same trace and same rate of admixture, the type of cement used altered almost all of the setting times and peaks of temperature reached. Through the curves of evolution of the temperature with time (Figure 7) it is perceived that the mortars with cement F reached greater temperatures than the ones with cement Z, probably due to the greater liberation of heat during its reactions of

hydration. This may be attributed to the greater fineness of the cement (values of fineness obtained through the method of air entrainment – the Blaine method – Table 2) and also to the fact that cement Z contains a greater quantity of pozzolans (rate of insoluble residues – Table 2), where the quantity of clinker is greater in cement F, influencing the rate of hydration of the particles [12]. Like cement F, besides being finer (Table 2), it has a greater rate of anhydrous compounds, such as, for example, tricalcium aluminate (C<sub>3</sub>A) and tricalcium silicate (C<sub>3</sub>S), increasing the temperature in the first ages due to the liberation of heat through the exothermic reaction of hydration of these components.

A great influence of the HSA admixture in the setting times was observed in the mortars studied. For the two types of cement, the reactions of hydration of Portland cement began during the first hours for mortars A1(0.0/0.0), A4(0.0/0.2) e A5(0.0/0.4); in other words, for all that did not have HSA in its composition. The other mixtures suffered an increase of time during the beginning of the setting process, possibly due to the water repellent layer that HSA forms over the particles of cement [7], [8]. The increase of the initial setting time was influenced directly by the rate of HSA used, through the type of cement and by the combination with AEA. It is also possible to observe that, the greater the quantity of HAS in the composition of the mortar, smaller was the amplitude of the peak of temperature reached, as evidenced in Figure 7 and Figure 8, indicating a greater dissipation of the heat and delay in the rate of hydration of the compounds [13], [15].

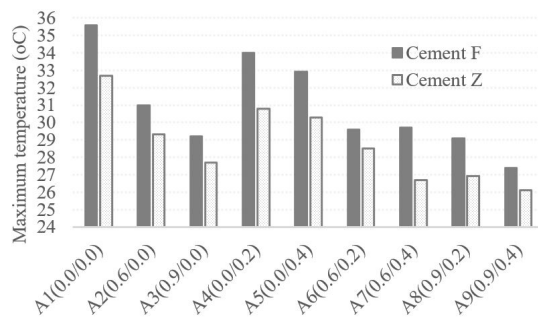


Figure 8. Maximum temperatures reached by mortars with cement F and cement Z.

### 3.1 Comparison between the methods of determination of the setting times

Through the data of the temperature due to the time, the initial and final setting times were determined through three methods: of the tangents, direct fractions and of the derivatives. The mean results, followed by the standard deviations, are presented in Tables 6, 7 and 8 for the mortars analyzed.

Through the analysis of data of Table 6, it is observed that there was no statistically different difference between the setting times obtained by the two types of cement, both for mortar A4(0.0/0.2), as well as A5(0.0/0.4). As for mortar A1(0.0/0.0), there were considerable differences ( $p^{**}=0.024$ ) for the initial setting time; however, the final setting times were similar ( $p^{**}=0.230$ ).

Table 6. Mortar setting time (M±SD) using cements F and Z, by the tangent method.

Mixture (HSA/AEA)	Initial setting time (h)			Final setting time (h)		
	Cement F	Cement Z	P**	Cement F	Cement Z	P**
A1 (0.0/0.0)	4.17±0.29 <sup>A</sup>	3.33±0.29 <sup>A</sup>	0.024	13.00±0.29 <sup>A</sup>	12.83±0.29 <sup>A</sup>	0.230
A2 (0.6/0.0)	93.17±1.26 <sup>B</sup>	132.00±1.00 <sup>C</sup>	<0.001	100.50±0.50 <sup>B</sup>	140.17±0.76 <sup>C</sup>	<0.001
A3 (0.9/0.0)	155.50±1.32 <sup>E</sup>	227.83±0.29 <sup>E</sup>	<0.001	175.50±0.87 <sup>E</sup>	246.83±0.29 <sup>E</sup>	<0.001
A4 (0.0/0.2)	5.33±0.29 <sup>A</sup>	4.50±0.50 <sup>A</sup>	0.067	13.83±0.29 <sup>A</sup>	14.00±0.50 <sup>A</sup>	0.643
A5 (0.0/0.4)	5.00±0.50 <sup>A</sup>	4.50±0.50 <sup>A</sup>	0.288	14.67±0.76 <sup>A</sup>	14.50±0.50 <sup>A</sup>	0.768
A6 (0.6/0.2)	110.17±0.76 <sup>D</sup>	106.00±1.73 <sup>B</sup>	0.019	121.67±0.76 <sup>D</sup>	117.50±1.32 <sup>B</sup>	0.009
A7 (0.6/0.4)	105.00±0.50 <sup>C</sup>	153.33±0.76 <sup>D</sup>	<0.001	114.17±0.29 <sup>C</sup>	182.83±1.26 <sup>D</sup>	<0.001
A8 (0.9/0.2)	154.00±1.00 <sup>E</sup>	290.00±0.50 <sup>G</sup>	<0.001	183.00±1.00 <sup>F</sup>	386.00±5.67 <sup>G</sup>	<0.001
A9 (0.9/0.4)	223.00±1.00 <sup>F</sup>	264.33±0.29 <sup>F</sup>	<0.001	237.83±0.76 <sup>G</sup>	278.17±2.52 <sup>F</sup>	<0.001
<b>p*</b>	<0.001	<0.001	-	<0.001	<0.001	-

p\* ANOVA with Tukey com Post Hoc: comparison between the setting times of the nine different mixtures with the same cement; p\*\* T Test of independent samples: comparison between the setting times obtained by the same mixture with different types of cement.

**Table 7.** Mortar setting time (M±SD) using cements F and Z, by the direct fraction method.

Mixture (HSA/AEA)	Initial setting time (h)			Final setting time (h)		
	Cement F	Cement Z	P**	Cement F	Cement Z	P**
A1 (0.0/0.0)	5.76±0.21 <sup>A</sup>	5.44±0.49 <sup>A</sup>	0.353	8.91±0.17 <sup>A</sup>	7.45±0.46 <sup>A</sup>	0.007
A2 (0.6/0.0)	94.17±0.65 <sup>B</sup>	133.36±0.67 <sup>C</sup>	<0.001	95.56±0.94 <sup>B</sup>	135.30±0.59 <sup>C</sup>	<0.001
A3 (0.9/0.0)	159.54±1.10 <sup>E</sup>	231.50±0.60 <sup>E</sup>	<0.001	164.09±0.85 <sup>E</sup>	236.53±0.64 <sup>E</sup>	<0.001
A4 (0.0/0.2)	7.11±0.22 <sup>A</sup>	6.35±0.40 <sup>A</sup>	0.053	8.90±0.33 <sup>A</sup>	8.44±0.43 <sup>A</sup>	0.214
A5 (0.0/0.4)	7.16±0.40 <sup>A</sup>	6.69±0.34 <sup>A</sup>	0.196	8.89±0.40 <sup>A</sup>	8.28±0.30 <sup>A</sup>	0.099
A6 (0.6/0.2)	112.51±1.02 <sup>D</sup>	108.43±1.32 <sup>B</sup>	0.013	114.97±0.98 <sup>D</sup>	110.73±1.28 <sup>B</sup>	0.010
A7 (0.6/0.4)	106.50±0.82 <sup>C</sup>	160.54±0.98 <sup>D</sup>	<0.001	108.56±0.66 <sup>C</sup>	166.36±1.04 <sup>C</sup>	<0.001
A8 (0.9/0.2)	160.28±0.72 <sup>E</sup>	294.55±0.67 <sup>G</sup>	<0.001	167.44±0.58 <sup>F</sup>	298.16±1.00 <sup>G</sup>	<0.001
A9 (0.9/0.4)	224.65±0.12 <sup>F</sup>	266.69±0.21 <sup>F</sup>	<0.001	228.34±0.06 <sup>G</sup>	270.20±0.65 <sup>F</sup>	<0.001
<b>p*</b>	<0.001	<0.001		<0.001	<0.001	

p\* ANOVA with Tukey com Post Hoc: comparison between the setting times of the nine different mixtures with the same cement; p\*\* T Test of independent samples: comparison between the setting times obtained by the same mixture with different types of cement.

It is perceived, on Table 7, that the values found also indicate a similarity among the results of the setting time of mortar A4(0.0/0.2) for the two types of cement, also verified for A5(0.0/0.4). In the mixture A1(0.0/0.0), the initial setting times were statistically similar (p\*\*=0.353) and the final setting times divergent (p\*\*=0.007).

**Table 8.** Mortar setting time (M±SD) using cements F and Z, by the derivative method.

Mixture (HSA/AEA)	Initial setting time (h)			Final setting time(h)		
	Cement F	Cement Z	P**	Cement F	Cement Z	P**
A1 (0.0/0.0)	6.31±0.27 <sup>A</sup>	5.67±0.70 <sup>A</sup>	0.216	8.36±0.18 <sup>A</sup>	8.26±0.25 <sup>A</sup>	0.774
A2 (0.6/0.0)	94.26±0.70 <sup>B</sup>	132.56±0.80 <sup>C</sup>	<0.001	98.45±0.76 <sup>C</sup>	134.30±1.22 <sup>D</sup>	<0.001
A3 (0.9/0.0)	166.31±0.85 <sup>F</sup>	229.74±0.70 <sup>E</sup>	<0.001	179.80±0.86 <sup>G</sup>	239.77±0.50 <sup>F</sup>	<0.001
A4 (0.0/0.2)	7.05±0.12 <sup>A</sup>	7.09±0.30 <sup>A</sup>	0.840	10.07±0.55 <sup>AB</sup>	15.74±0.55 <sup>B</sup>	<0.001
A5 (0.0/0.4)	6.63±0.39 <sup>A</sup>	7.40±0.53 <sup>A</sup>	0.113	11.37±0.35 <sup>B</sup>	9.27±0.39 <sup>A</sup>	0.002
A6 (0.6/0.2)	113.85±1.25 <sup>D</sup>	105.28±0.01 <sup>B</sup>	<0.001	115.91±1.06 <sup>E</sup>	110.45±0.01 <sup>C</sup>	0.001
A7 (0.6/0.4)	106.58±0.69 <sup>C</sup>	155.52±0.75 <sup>D</sup>	<0.001	109.60±0.84 <sup>D</sup>	163.94±0.75 <sup>E</sup>	<0.001
A8 (0.9/0.2)	152.30±0.93 <sup>E</sup>	296.29±0.71 <sup>G</sup>	<0.001	168.25±0.66 <sup>F</sup>	301.69±0.71 <sup>H</sup>	<0.001
A9 (0.9/0.4)	227.36±1.26 <sup>G</sup>	267.48±1.02 <sup>F</sup>	<0.001	230.65±0.36 <sup>H</sup>	273.57±1.02 <sup>G</sup>	<0.001
<b>p*</b>	<0.001	<0.001		<0.001	<0.001	

p\* ANOVA with Tukey com Post Hoc: comparison between the setting times of the nine different mixtures with the same cement; p\*\* T Test of independent samples: comparison between the setting times obtained by the same mixture with different types of cement.

Through the derivatives method (Table 8) the initial setting times between cement F and cement Z were statistically equal for mortars A1(0.0/0.0), A4(0.0/0.2) e A5(0.0/0.4). For the final setting time there was only a similarity for A1(0.0/0.0).

Figure 9 presents a comparison between the initial setting times obtained with cement F (Figure 9a) with cement Z (Figure 9b), estimated by the tangent, direct fraction, and derivatives methods. In general, the results obtained by the three methods of calculus employed demonstrated coherence and proximity with one another.

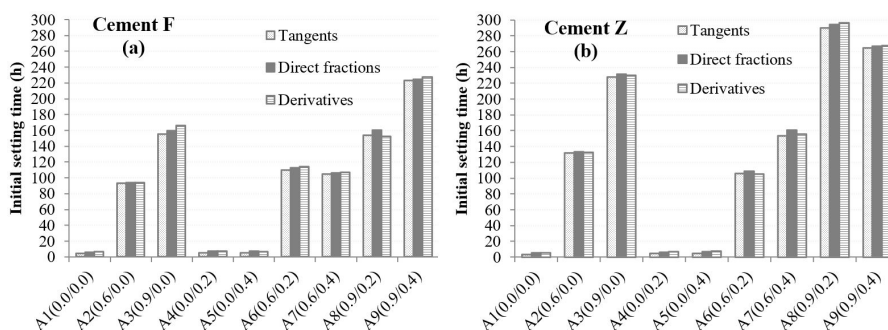


**Figure 9.** Initial setting times obtained by different methods for mortars with cements F and Z.

This way, Figure 10 presents the correlations obtained for the initial setting time obtained by the three methods employed, together with the determination coefficients ( $R^2$ ), and Pearson's correlation ( $r$ ), of the equation of linear tendency. Excellent correlation coefficients between all of the methods were obtained, with the best correlation obtained between the tangent and direct fraction methods ( $r=0.9998$ ) (Figure 10a).

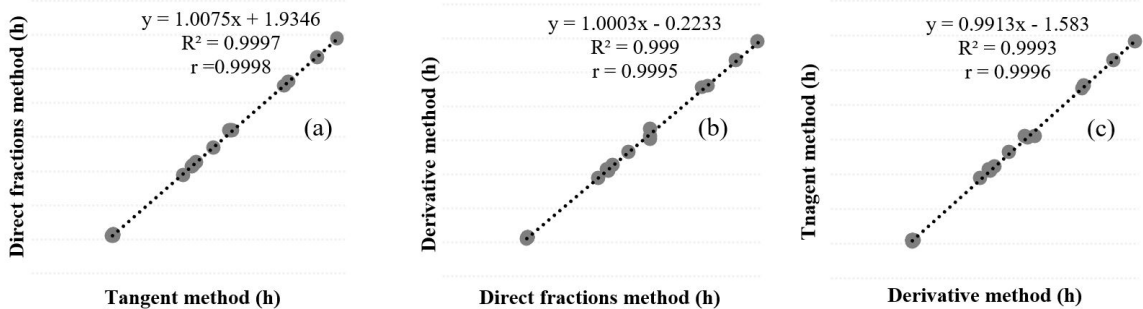


Figure 10. Correlation between the initial setting times obtained by the tangent, direct fraction, and derivatives methods, for mortars with cement F and cement Z.

Figure 11 presents the final setting times obtained through the tangent, direct fraction and derivatives methods for cement F (Figure 11a) and for cement Z (Figure 11b). The greatest differences between the three methods evaluated were obtained for the final setting times, as shown in Figure 11. These differences are due to the fact that the tangent method consider the end of the setting process only when the temperature reaches the maximum peak after the period of induction [27], [29], [49], while in the other methods the end is considered before, being located close to the half of the period of acceleration [26], [50], [51].

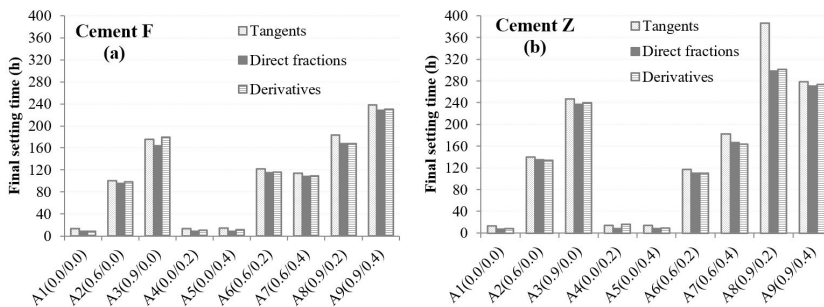


Figure 11. Final setting times obtained by different methods for mortars with cements F and Z.

Figure 12 presents the correlations found for the final setting times for the three methods together with the determination coefficients ( $R^2$ ) and Pearson's correlation ( $r$ ), of the equation of line of linear tendency.

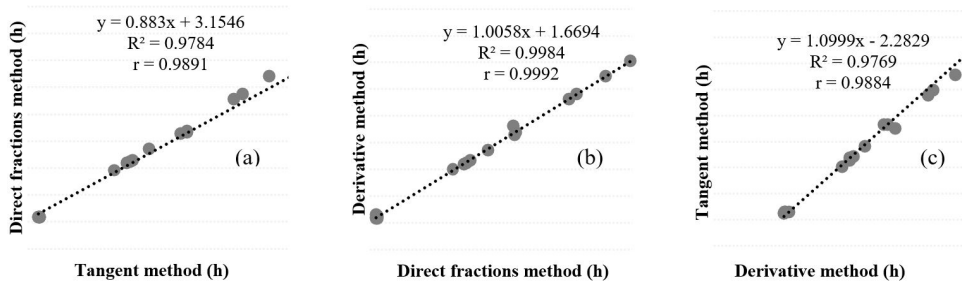


Figure 12. Correlation between the final setting times obtained by the tangent, direct fraction, and derivative methods.

In all of the correlations for final setting times, coefficients (r) very close to 1.0 were obtained, demonstrating and excellent correlation between the different methods. The greatest correlation coefficient (r) was obtained for the final setting time between the direct fraction and derivatives methods( $r=0.9992$ ) (Figure 12b).

Considering the initial and final setting times, the method that best correlated with the other was the one of direct fractions. Therefore, the times established by the direct fraction method were used for the data analysis of this study of the mortars of this study.

### 3.2 Analysis of the setting times – Direct fraction method

As demonstrated on Table 7, for the mixtures without HSA, that is, A1(0.0/0.0), A4(0.0/0.2) and A5(0.0/0.4), the initial and final setting times were statistically equal ( $p^{**}>0.05$ ) between each other and for the two types of cement, demonstrating that the presence and the rate of admixture did not influence the setting time. Romano [3] also observed that the AEA admixture did not influence the hydration of the Portland cement. Numerically, for these mixtures, the initial setting time of cement Z was smaller than the one of cement F. In the mixtures that contained HSA, the initial and final setting times of the mortars with cement Z were very superior ( $p^{**}<0.001$ ) to the ones obtained with cement F, being up to 84% superior in A8(0.9/0.2). The exception was for mixture A6(0.6/0.2), which had the initial setting time with cement F delayed in 4 hours when compared to cement Z ( $p^{**}=0.013$ ). This behavior may be explained by the particles of fly ash (contained in cement Z) being able to absorb the molecules of the HSA admixture, with a continuous poisoning of the growth of the hydrates, slowing down and prolonging the reaction, resulting in peaks of temperature with lower levels and of greater amplitude of base (the mortars with cement F reached higher temperatures than the mortars with cement Z, for the same composition of the mortar – Figure 8). Similar results were obtained by Guindani [13] in admixture pastes.

Figure 13 presents the results of the initial and final setting times obtained for the mortar with HSA and AEA with cement F and cement Z by the direct fraction method.

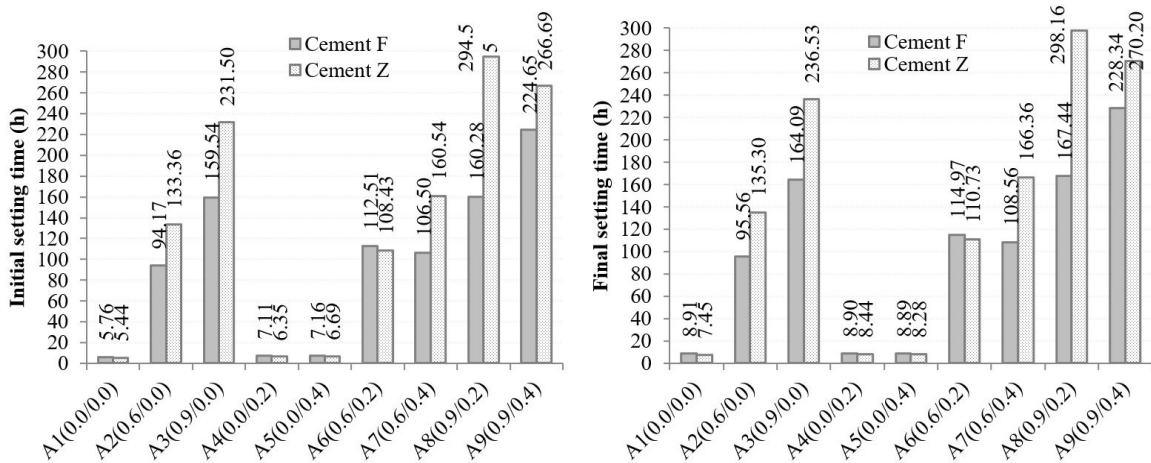


Figure 13. Initial and final setting times for mortars with cements F and Z, by the direct fraction method.

By comparing the initial setting time of the same mixtures prepared with the different cements, an increase in the setting time of the mortars with cement Z in relation to the ones with cement F was verified of approximately 39 h of difference in A9(0.9/0.4). In the mortars without AEA the setting times obtained with the two types of cement were similar between one another, that is, they did not present statistically significant differences between their values (Table 7). With the use of HSA, the mortars with cement Z had a delay in the potentialized setting time. Once the hydration processes from the surface to the inside of the grain, a bigger grain of cement (cement Z) would, naturally, take longer to hydrate than a smaller one (cement F).

According to Trevisol [7] and Souza [9], the admixture forms a film around the grain of cement, which repels the particles of water; therefore, the greater the grain, greater the quantity of molecules of the admixture adhered to cover its surface. On the other hand, it is likely that that the dissolution of this hydro repellent layer may be more difficult with a greater quantity of molecules of admixture adhered; therefore, the greater would be the effect of the delay of the

setting time. Besides this, cement Z is a Portland cement composed with pozzolanic material, containing approximately 13.17% of fly ash, obtained through the test of insoluble residue (Table 2), and, consequently, a greater quantity of clinker, which also influences the speed of the reactions of hydration and consequently the setting time. According to Mehta and Monteiro [4], pozzolanic cement has a slow reaction, consequently the rates of liberation of heat and the development of resistance also occur in a slower way, consuming calcium hydroxide instead of producing it.

By analyzing the mortars of each type of cement, it is observed that, when only HSA is added in the mixtures in its smallest rate studied, the initial setting time is already greater in 88 h for cement F - A2(0.6/0.0) and in 128h for cement Z - A3(0.9/0.0), when related to A1(0.0/0.0). This behavior may be explained by the influence of the HAS both in the setting time as well as the heat of hydration of the cement [52].

Figure 14 presents, for the mortars with cement F (a) and with cement Z (b), the effect of the increase in the rate of HSA from 0.0% to 0.6% and 0.9% for the mortars with only HAS, mortar with HAS associated with 0.2% of AEA and mortars with HAS associated with 0.4% of AEA. In Figure 14a, it is perceived that, for the mortars with cement F, by adding 0.6% of HSA only – A2(0.6/0.0), the initial setting time increased in 88 h related to the same mixture with 0.0% of HSA – A1(0.0/0.0). By increasing the HSA from 0.6% to 0.9% - A3 (0.9/0.0), the initial setting time was elevated to 65 more hours, totalizing a delay in 154 hours when related to the reference- A1(0.0/0.0). In the mortars that associated HSA to 0.2% of AEA, the increase of the time of the beginning of the setting process with 0.6% HSA, increasing 48 hours to the delay when used 0.9% of HSA – A8(0.9/0.2). In the mortars that associated HSA to 0.4% of AEA, there was a delay in the time of the initial setting time of 99 hours with the adding of 0.6% of HSA- A7(0.6/0.4) in relation to the mortar with 0.0% of HSA A5 (0.0/0.4). By increasing the rate HSA of 0.6% - A7 (0.6/0.4) to 0.9% - A9 (0.9/0.4), this delay increased in more 118 hours, totalizing a delay of 217 hours in comparison to the mortar without HSA - A5(0.0/0.4).

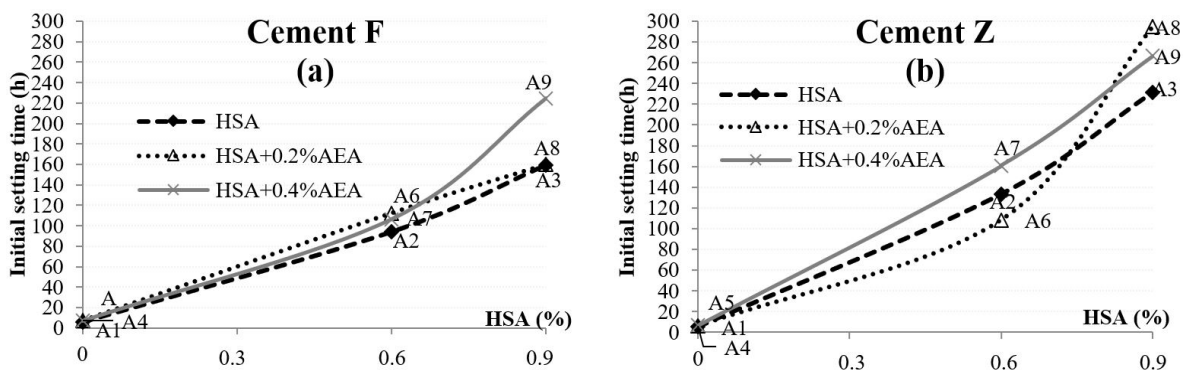


Figure 14. Effect of the increase in the content of HSA at the initial setting time of the mortar.

In Figure 14b the results obtained for the mortars with cement Z are exposed, where 128 hours more in the initial setting time were obtained when adding only 0.6% of HAS -A2(0.6/0.0), in comparison to the reference – A1(0.0/0.0). When increased to 0.9% of HSA – A3(0.9/0.0) the initial setting time was amplified in 98 more hours, that is, a delay of 226 hours related to A1(0.0/0.0). When combined to 0.2% of AEA, the rate of 0.6% of HAS – A6(0.6/0.2) offered 102 more hours to the initial setting time in relation to A4(0.0/0.2). Whereas with the rate of 0.9% of HAS – A8(0.9/0.2) a delay of 168 more hours in the initial setting time was verified. For the mortars of 0.4% of AEA, 145 more hours were obtained during the setting time of A7(0.6/0.4), in relation to A5(0.0/0.4), increasing in 106 more hours when employed 0.9% of HSA - A9(0.9/0.4). This represents a total increase in the setting time of 260 hours, comparing A9(0.9/0.4) with A5(0.0/0.4). These results demonstrate how the adding of HSA, increases the initial setting time of the mortars [13], with more effects for the mortars with cement Z being perceived, as previously discussed.

Observing the action of the AEA in the setting time of the mortars through Table 7, a small increase in the setting time of the mortars admixture with only AEA is observed, in relation to A1(0.0/0.0), for both cements. Statistically the initial setting times of A4(0.0/0.2) and A5(0.0/0.4) are not different from A1(0.0/0.0) (Tukey Post Hoc = A), however, numerically, a small increase in the time only by the use of AEA (up to 1.4hrs) is observed, with no directly proportional relation with the rate employed being observed.

However, when combined to HSA, the evidence of action of the AEA becomes evident, over the reactions of hydration of cement, as observed both in Table 7 as well as Figure 14. When comparing A2(0.6/0.0) with A6(0.6/0.2)

and A7(0.6/0.4), it is verified that all of the mixtures have the same rate of HAS; however, when AEA is added, 18 and 12 hours more are obtained, respectively, in the initial setting time for cement F (Figure 14a). Whereas with cement Z (Figure 14b), mortar A6 (0.6/0.2) started the setting process 25 hours before A2(0.6/0.0), while A7(0.6/0.4) delayed 27 hours. When comparing A3(0.9/0.0) with A8(0.9/0.2), no differences were found for the initial setting time of cement F (Figure 14a); whereas for cement Z, there were 63 hours of delay (Figure 14b). Still, when comparing A3(0.9/0.0) with A9(0.9/0.4), there is, for cement F, 65 hours of increase (Figure 14a) and 35 hours for cement Z (Figure 14b). The molecules of AEA may possibly join the molecules of HSA, due to the attraction by opposite charges [3], in such a way that its apolar tail may contribute to a hydro repellent barrier formed around the grains of cement, increasing even more the initial setting time. This way, a distinct behavior when the admixtures are used simultaneously is clearly observed, influencing the initial setting time.

Trevisol and Koman [53] smaller values for the setting times with cement Z, in comparison to the ones obtained in this study. The authors obtained 98 hours for the initial setting time of the mortar with 0.6% of HSA, while in the present study, for this same rate of HAS, 108 to 160 hours were obtained, depending on the rate of AEA associated. However, Trevisol and Koman [53] prepared mortars in factory, with a trace 1:6 (a/c=1.05), which may cause differentiated effects on the properties.

Schackow et al. [15] also evaluated the temperature of the ready-mix mortars with CII Z-32 in a semi-adiabatic calorimeter, obtaining initial setting times close to 50 hours. Besides the traces of distinct admixtures, it was expected that the setting process would occur faster than the similar traces studied in this research, once the authors decreased the quantity of water of the mixtures according to the rates of admixtures employed.

Campos et al. [46] found an initial setting time of 70 hours for the mortar with cement F - 32 (1:6 e a/c=0.87) with 0.9% of HSA, a value very inferior to the one obtained in the present study for the same rate of isolated HSA (159 hours). However, besides the distinct proportion, there are quite different characteristics for the HAS employed and the cement and aggregates, altering the properties of the mixture.

It is worth pointing out that the chemical basis of the HSA admixture combined with the AEA admixture, with distinct rates and compositions, may have influenced the setting time by demonstrating distinction of the results obtained for each study. This way, it is recommended that an evaluation of the interaction of these admixtures with Portland cement, which will be used in the dosage of the ready-mix mortars, be conducted.

For cement F, the following sequence for the beginning of the reactions of hydration, in growing order of the events, was observed: A1(0.0/0.0)  $\approx$  A4(0.0/0.2)  $\approx$  A5(0.0/0.4) < A2(0.6/0.0) < A7(0.6/0.4) < A6(0.6/0.2) < A3(0.9/0.0)  $\approx$  A8(0.9/0.2) < A9(0.9/0.4). Whereas for cement Z, the sequence suffered some alterations and happened in the following order: A1(0.0/0.0)  $\approx$  A4(0.0/0.2)  $\approx$  A5(0.0/0.4) < A6(0.6/0.2) < A2(0.6/0.0) < A7(0.6/0.4) < A3(0.9/0.0) < A9(0.9/0.4) < A8(0.9/0.2).

These results demonstrated that the AEA may also influence the setting time of the mortars, with significant effects observed when associated to the employment of HSA. However, a direct relationship was only verified between the setting time and the rate of AEA in the mortars with cement F that employed AEA associated to 0.9% of HSA and for cement Z with AEA associated to 0.6% of HSA.

In relation to HSA, the initial setting time of the mortars demonstrated having a direct relationship with the rate employed for all cases studied, as shown in Figure 14.

## 5 CONCLUSIONS

With the results obtained, it was verified that the three methods of determination used to estimate the setting times of the mortars demonstrated having a very strong correlation between them. For the analysis conducted, the direct fraction method was chosen because it presented a better correlation with the other methods.

During the period evaluated, a greater temperature in the mortars with Cement F was verified than with the ones with Cement Z, once cement F is finer and has a smaller quantity of additions. In the mixtures without admixtures or only with AEA, there were no significant differences found between the setting times with the different types of cement. When HSA was added the effect of the fineness of the cement and the use of admixture in the Portland cement (pozzolanic material) potentialized the increase of the setting time due to the use of the admixtures, with a greater setting time of the mortars prepared with cement Z being verified.

The initial setting time of the mortars demonstrated having a direct relation with the rate of HSA employed for all of the cases studied, in both cements. The employment of AEA also offered a delay in the setting time of the mortars when associated to the employment of HSA.

Therefore, it is possible to conclude in this research that for ready-mix mortars, the type of cement and the rate of the admixtures employed, HSA and AEA, influence the setting time, demonstrating clearly the need of a study for the dosage of the ready-mix mortar, once it is commercialized based on its period of time of workability.

## ACKNOWLEDGEMENTS

The authors thank the UFSM for the support, location and resources for the conduction of the research and Supermix and Supertex companies for the supply of materials.

## REFERENCES

- [1] R. Rixon and N. Mailvaganam, *Chemical Admixtures for Concrete*, 3th ed. London: E & FN SPON, 1999.
- [2] H. Carasek, "Argamassas," in *Materiais de Construção Civil e Princípios de Ciência e Engenharia de Materiais*, G. C. Isaia, Ed., São Paulo: IBRACON, 2010, ch. 28, pp. 893-943.
- [3] R. C. O. Romano, "Incorporação de ar em materiais cimentícios aplicadas em construção civil," M.S. thesis, Esc. Poli, Univ. São Paulo, São Paulo, 2013.
- [4] P. K. Mehta and P. J. M. Monteiro, *Concrete: Microestrutura, Propriedades e Materiais*, 2nd ed. São Paulo: IBRACON, 2014.
- [5] American Society for Testing and Materials, *Standard Specification for Chemical Admixtures for Concrete*, C494, 2004.
- [6] R. L. Nelson et al. "Ready mix mortar in the United States," in 8th Int. Brick Block Mason. Conf., 1988, pp. 150-161.
- [7] L. A. Trevisol Jr., "Estudo comparativo entre as argamassas: estabilizada dosada em central, industrializada e produzida em obra por meio de ensaios físicos nos estados fresco e endurecido", Ph.D. dissertation, Inst. Eng. Paraná, Curitiba, 2015.
- [8] J. Rickert, *Influence of Retarders on the Hydration of Clinker and Cement*, *Concrete Technology Reports 2001-2003*. Duesseldorf: Verlag Bau+Technik, 2004.
- [9] A. F. Souza, "Otimização do uso de aditivo estabilizador de hidratação do cimento em água de lavagem dos caminhões-betoneira para produção de concreto," Ph.D. dissertation, Univ. Fed. Santa Catarina, Florianópolis, 2007.
- [10] M. Paolini and R. Khurana, "Admixtures for recycling of waste concrete," *Cement Concr. Compos.*, vol. 20, no. 2-3, pp. 221-229, 1998, [http://dx.doi.org/10.1016/S0958-9465\(97\)00066-8](http://dx.doi.org/10.1016/S0958-9465(97)00066-8).
- [11] J. Cheung et al., "Impact os admixtures on the hydration kinetics of portland cement," *Cement Concr. Res.*, vol. 41, no. 12, Dec 2011, <http://dx.doi.org/10.1016/j.cemconres.2011.03.005>.
- [12] W. N. Wczelik and Z. Pytel, "Heat evolution in hydrated cementitious systems admixed with different set controlling components," *J. Therm. Anal. Calorim.*, vol. 77, no. 1, pp. 159-164, Jul 2004., <http://dx.doi.org/10.1023/B:JTAN.0000033199.47106.72>.
- [13] E. N. Guindani, "Argamassa estabilizada para revestimento: avaliação da influência da adição de finos nas propriedades do estado fresco e endurecido," Ph.D. dissertation, Prog. Pós-grad. Eng. Civ., Univ. Fed. Santa Catarina, Florianópolis, 2018.
- [14] J. Dransfield, "Admixtures for concrete, mortar and grout," *Adv. Concr. Technol.*, vol. 3, pp. 3-36, 2003., <http://dx.doi.org/10.1016/B978-075065686-3/50280-9>.
- [15] A. Schackow, A. K. Ferrari, C. Effting, V. O. Alves, and I. R. Gomes, "Stabilized mortar with air incorporator agent and plasticizer set retarder: performance measurement," *Rev. IBRACON Estrut. Mater.*, vol. 12, no. 6, pp. 1248-1259, Dec 2019., <http://dx.doi.org/10.1590/s1983-41952019000600002>.
- [16] L. G. Couto, *Admixture Handout, disciplina de Civ 361 - Materiais de Construção Civil II*. Viçosa: Universidade Federal de Viçosa, 2011.
- [17] D. Lootens and D. P. Bentz, "On the relation of setting and early-age strength development to porosity and hydration in cement-based materials," *Cement Concr. Compos.*, vol. 68, pp. 9-14, 2016., <http://dx.doi.org/10.1016/j.cemconcomp.2016.02.010>.
- [18] J. M. Casali et al., "Avaliação das propriedades do estado fresco e endurecido da argamassa estabilizada para assentamento e revestimento," in *An. IX SBTA*, 2011.
- [19] L. M. L. Calçada, A. E. Gaio, and M. G. Ramos, "Estudo da influência da dosagem no tempo de início de pega da argamassa estabilizada," in *Sem. Pesq. Inov. IFSC*, 2013.
- [20] G. Macioski, "Avaliação do comportamento de argamassas estabilizadas para revestimento," Undergraduate thesis, Univ. Fed. Paraná, 2014.
- [21] G. M. Campos, "Estudo do tempo de início de pega de argamassas com aditivo estabilizador de hidratação," Specialization thesis, Univ. Tecnol. Fed. Paraná, Curitiba, 2012.
- [22] S. M. Ruppenthal and F. Pelisser, "Estudo de argamassas de revestimento com inibidores de hidratação", Undergraduate thesis, Univ. Ext. Sul Catarin., Criciúma, 2012. [Online]. Available: <http://repositorio.unesc.net/bitstream/1/1158/1/Suellem%20Michels%20Ruppenthal.pdf>

- [23] D. M. Pivetta et al., “Desempenho de argamassas estabilizadas: influência do aditivo estabilizador de hidratação no estado fresco” in *An. 58º Cong. Bras. Concr.*, 2016.
- [24] Associação Brasileira de Normas Técnicas, *Concreto e Argamassa – Determinação dos Tempos de Pega por Meio de Resistência a Penetração*, NBR NM 9, 2003.
- [25] C. S. Barbosa et al., “Estudo da influência da quantidade de água no tempo de pega em pastas e em argamassas estabilizadas” in *An. XIII Simpósio Bras. Tecnol. Argamassas*, 2019.
- [26] M. J. C. Viecili, D. Hastenpflug, and R. Girardi, "Comparativo entre o teste de Vicat e a calorimetria semi-adiabática para determinação do tempo de início e fim de pega em cimentos Portland," *Rev. Materia*, vol. 23, no. 3, 2018., <http://dx.doi.org/10.1590/s1517-707620180003.0506>.
- [27] P. K. Mehta and P. J. M. Monteiro, *Concreto: Estrutura, Propriedades e Materiais*, 2nd ed. São Paulo: Ed. Pini, 1994.
- [28] E. G. R. Petrucci, *Concreto de Cimento Portland*, 13th ed. São Paulo: Globo, 1998.
- [29] A. M. Neville and J. J. Brooks, *Tecnologia do Concreto*, 2nd ed. Porto Alegre: Bookman, 2013.
- [30] Associação Brasileira de Normas Técnicas, *Cimento Portland e Outros Materiais em Pó – Determinação da Massa Específica*, ABNT NBR 16605, 2017.
- [31] Associação Brasileira de Normas Técnicas, *Cimento Portland – Determinação do Índice de Finura por Meio da Peneira 75µm (no 200)*, ABNT NBR 11579, 2013.
- [32] Associação Brasileira de Normas Técnicas, *Cimento Portland – Determinação da Pasta de Consistência Normal*, ABNT NBR 16606, 2018.
- [33] Associação Brasileira de Normas Técnicas, *Cimento Portland – Determinação dos Tempos de Pega*, ABNT NBR 16607, 2018.
- [34] Associação Brasileira de Normas Técnicas, *Cimento Portland – Análise Química – Determinação de Perda ao Fogo*, ABNT NBR NM 18, 2012.
- [35] Associação Brasileira de Normas Técnicas, *Cimento Portland – Análise Química – Método de Arbitragem para Determinação de Dióxido de Silício, Óxido Férrico, Óxido de Alumínio, Óxido de Cálcio e Óxido de Magnésio*, ABNT NBR NM 14, 2012.
- [36] Associação Brasileira de Normas Técnicas, *Cimento Portland – Análise Química – Determinação de Anidrido Sulfúrico*, ABNT NBR NM 16, 2012.
- [37] Associação Brasileira de Normas Técnicas, *Cimento Portland com Adições de Materiais Pozolânicos – Análise Química – Método de Arbitragem*, ABNT NBR NM 22, 2012.
- [38] Associação Brasileira de Normas Técnicas, *Cimento Portland e Outros Materiais em Pó – Determinação da Finura pelo Método de Permeabilidade ao Ar – Método de Blaine*, ABNT NBR 16372, 2015.
- [39] Associação Brasileira de Normas Técnicas, *Cimento Portland – Determinação da Expansibilidade Le Chatelier*, ABNT NBR 11582, 2016.
- [40] Associação Brasileira de Normas Técnicas, *Cimento Portland – Determinação da Resistência à Compressão de Corpos de Prova Cilíndricos*, ABNT NBR 7215, 2019.
- [41] Associação Brasileira de Normas Técnicas, *Agregados – Determinação da Composição Granulométrica*, ABNT NBR NM 248, 2003.
- [42] Associação Brasileira de Normas Técnicas, *Agregado Miúdo – Determinação da Massa Específica e Massa Específica Aparente*, ABNT NBR NM 52, 2009.
- [43] Associação Brasileira de Normas Técnicas, *Agregados – Determinação da Massa Unitária e do Volume de Vazios*, ABNT NBR NM 45, 2006.
- [44] Associação Brasileira de Normas Técnicas, *Agregados – Determinação do Material Fino que Passa Através da Peneira 75 µm, por Lavagem*, ABNT NBR NM 46, 2003.
- [45] J. P. Antoniazzi, “O efeito dos aditivos incorporador de ar e estabilizador de hidratação nas propriedades das argamassas estabilizadas”, M.S. thesis, Univ. Fed. Santa Maria, Santa Maria, 2019.
- [46] G. M. Campos, G. Macioski, and J. M. Casali, “Estudo do tempo de início de pega de argamassas com aditivo estabilizador de hidratação” in *Anais 55º Cong. Bras. Concr.*, 2013.
- [47] R. W. Weakley, “Evaluation of semi-adiabatic calorimetry to quantify concrete setting”, M.S. thesis, Fac. Auburn Univ., Auburn, Alabama, USA, 2010. [Online]. Available: <http://hdl.handle.net/10415/1981>
- [48] P. Sandberg and S. Liberman, “Monitoring and evaluation of cement hydration by semi-adiabatic Field calorimetry,” in *Concrete Heat Development – Monitoring, Prediction and Management*, K. Wang and A. K. Schindler, Eds., Georgia, NY: Curran Associates, 2007.
- [49] H. F. W. Taylor, *Cement Chemistry*, 2nd ed. London: Academic Press, 1997. <http://dx.doi.org/10.1680/cc.25929>.
- [50] V. S. Ramachandran, *Concrete Admixtures Handbook*, 2nd ed. New York: Noyes Publications, 1984.

- [51] I. Jawed, J. Skalny, and J. F. Young, "Hydration of Portland cement," in *Structure and Performance of Cement*, P. Barbes, Ed., London: Applied Science Publishers, 1983.
- [52] B. E. Watts and C. Ferraro, "Prediction of setting for admixture modified mortars using the VCCTL," *Cement Concr. Compos.*, vol. 78, pp. 63–72, 2017.
- [53] L. A. Trevisol Jr. and D. F. Koman, "Estudo da interferência do uso de cal hidratada no tempo de estabilidade em argamassas estabilizadas dosadas em central" in *An. XIII SBTA*, 2019.

---

**Author contributions:** Antoniazzi: experimental results, data analysis and discussion, writing. Mohamad and Casali: conceptualization, methodology, supervision.

**Editors:** Edgar Bacarji, José Luiz Antunes de Oliveira e Sousa, Guilherme Aris Parsekian.



## ORIGINAL ARTICLE

# Monolithic equivalent stiffness of precast columns with grouted splice sleeve connections

## *Equivalência monolítica de rigidez em pilares pré-moldados com emendas com luvas grauteadas*

Marcelo de Araujo Ferreira<sup>a</sup> Luís Augusto Bachega<sup>a</sup> Bruna Catoia<sup>a</sup> <sup>a</sup>Universidade Federal de São Carlos – UFSCar, Departamento de Engenharia Civil, São Paulo, Brasil

Received 24 October 2019

Accepted 23 April 2020

**Abstract:** The aim of this paper is the validation of monolithic equivalent stiffness applied to precast columns with grouted splice sleeve connections, wherein spliced precast elements have been compared with continuous monolithic elements. The experimental investigation has been carried out with bending tests for two spliced elements (L1 and L2), comparing the deflections along these elements with the results obtained from two monolithic elements (M1 and M2). The grouted splice sleeve connections have been characterized by their rotational stiffness (moment-rotation relationship), ultimate strength, and ductility, allowing the calibration of the equation for the secant stiffness according to ABNT NBR9062:2017. Based on the experimental results, the effective deformation length within the connection zone obtained was  $L_{ed} = 20\phi$ , corresponding to a secant stiffness of  $R_{sec} = 77,785 \text{ kN}\cdot\text{m}/\text{rad}$ . Although relative rotations have been observed at the grouted splice joint, the deflections along the precast spliced elements were very close to the deflections along the monolithic elements. A strong convergence for all phases of the load x displacement curves has been observed, as well as good approximation in terms of rotational stiffness, strength and ductility. Therefore, based on the analysis of the experimental results, the requirement to define the monolithic equivalent stiffness for the precast columns has been met.

**Keywords:** precast concrete structures, equivalent connection, monolithic, secant stiffness.

**Resumo:** O propósito deste trabalho é a verificação da equivalência monolítica de rigidez de pilares pré-moldados com emendas por meio de luvas mecânicas grauteadas, onde os deslocamentos ao longo de protótipos pré-moldados segmentados foram comparados com deslocamentos obtidos ao longo de protótipos monolíticos contínuos. Para tal, realizou-se um estudo experimental com ensaios de flexão simples para modelos pré-moldados com ligações (L1 e L2), cujos resultados experimentais foram comparados com os resultados de ensaios em modelos monolíticos contínuos (M1 e M2). Adicionalmente, as ligações por meio de luvas grauteadas foram caracterizadas quanto à sua rigidez (relação momento-rotação), resistência e ductilidade, possibilitando a calibração da equação da rigidez secante para relação momento-rotação definida na ABNT NBR9062:2017. O comprimento efetivo de deformação da barra tracionada na região da junta atingiu um valor médio de  $L_{ed} = 20\phi$ , correspondente a uma rigidez média de  $R_{sec} = 77,785 \text{ kN}\cdot\text{m}/\text{rad}$ . Com base na comparação experimental entre os modelos com ligações e os modelos monolíticos, observou-se que embora tenha havido uma descontinuidade na região da junta grauteada, com liberação de rotações relativas entre os elementos de pilares pré-moldados, os deslocamentos apresentados ao longo dos protótipos segmentados foram muito próximos aos deslocamentos obtidos nos elementos monolíticos, tendo-se uma boa convergência para todas as fases da curva força x deslocamento, com equivalência de rigidez, resistência e ductilidade para as curvas analisadas, caracterizando-se assim a equivalência monolítica do pilar pré-moldado.

**Palavras-chave:** estruturas pré-moldadas, ligação equivalente, monolitismo, rigidez secante.

**How to cite:** M. A. Ferreira, L. A. Bachega, and B. Catoia, “Monolithic equivalence of precast columns with grouted splice sleeve connections,” *Rev. IBRACON Estrut. Mater.*, vol. 14, no. 1, e14115, 2021, <https://doi.org/10.1590/S1983-41952021000100015>

**Corresponding author:** Bruna Catoia. E-mail: [bcatoia@yahoo.com.br](mailto:bcatoia@yahoo.com.br)

**Financial support:** Leonardi Industrialized Construction Company and Splice-Sleeve Japan.

**Conflict of interest:** Nothing to declare.



This is an Open Access article distributed under the terms of the Creative Commons Attribution License, which permits unrestricted use, distribution, and reproduction in any medium, provided the original work is properly cited.

## 1 INTRODUCTION

In addition to the influence of the semirigid behavior of beam-column connections, lateral sway in precast structures is highly affected by the actual stiffness of the precast columns, which is also affected by premature cracking during the transitory phases of production and during the assembly of structural precast members, as well as affected by crack formation within the serviceability limit state.

Column connections can be positioned either at the bottom or at mid-height of the column, which is the case in multistory buildings. For precast columns consisting of spliced members, the actual lateral stiffness of the whole column can be affected by relative displacements within the joints, either at the mid-height column-to-column joint or at the bottom of column-to-foundation joints. As such, these localized deformations in the joints will increase the lateral sway of the building, especially in industrial buildings with cantilevered columns. Figure 1 shows typical solutions of column-to-column connections used in Brazil.

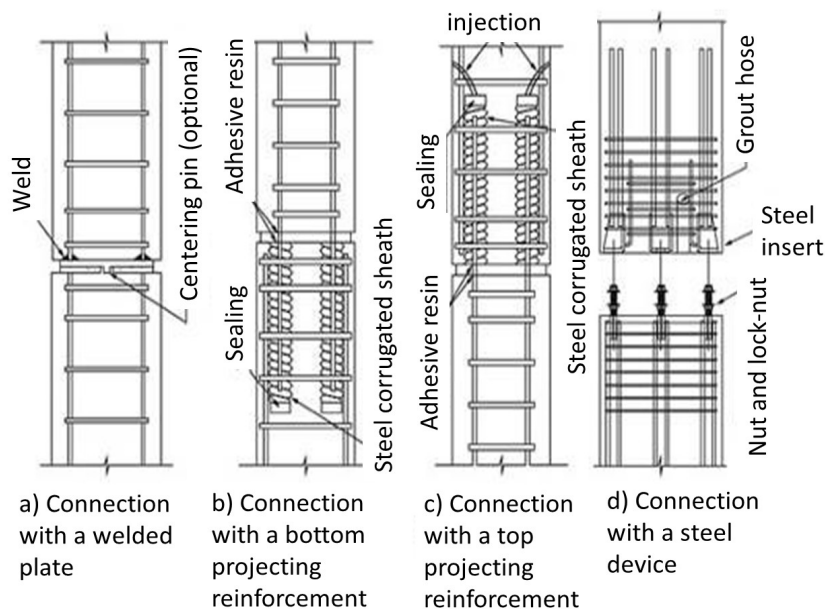


**Figure 1.** Typical column-to-column connections according to ABNT NBR 9062:2017 [1].

Depending on the moment-rotation relationship of a column-to-column connection, which characterizes its semirigid behavior, spliced precast columns can behave as continuous or discontinuous columns (equivalent monolithic columns). Therefore, for multistory buildings, with joints at mid-height of the columns, the structural continuity of precast columns is highly dependent on the connection behavior itself.

The existing studies on columns with grouted splice sleeves are mostly addressed to the structural behavior in seismic zones, wherein the main research interest is related to the ultimate plastic strength and ductility of the rebars crossing the joints. However, there is no monitoring of the moment-rotation relationship in the joints, which is needed to determine the secant rotational stiffness of the connections according to [1].

### 1.1 Scope

The aim of this paper is the hypothesis verification of the monolithic equivalence applied to precast columns with grouted splice sleeve connectors. An experimental investigation with four bending tests has been conducted for two spliced models (L1 and L2), wherein the deflection along these models were confronted against the results obtained from two monolithic models (M1 and M2). Additionally, the grouted splice sleeve connections have been experimentally characterized by their stiffness (moment-rotation relationship), strength and ductility. Therefore, the level of restriction in the relative displacements between the connected elements within the precast models could be evaluated.

According to ABNT NBR 9062:2017 [1], it is possible to use any building technology for precast structures based on demonstrated performance with conclusive tests in order to evaluate the connections as specified in the design. On the other hand, designers cannot rely on technologies with demonstrated performance based on tests carried out in other countries, without considering local conditions for materials and production processes applied in Brazil.

Column-to-column connectors comprising mechanical sleeves filled with grout are widely used in Brazil. However, grouted splice sleeves require shorter anchorage lengths, it is very important to study the actual anchorage performance of the bars as well as the efficiency of the high strength grout that is used to fill the splice sleeve.

## 2 LITERATURE REVIEW

### 2.1 Previous research

Einea et al. [2] investigated the effect of confinement on the bond strength between the rebar and the surrounding grout within mechanical sleeves. Grout-filled steel sleeves with different parameters and geometrical design were loaded for axial tension until failure. The experimental results were discussed and analysed in the light of the design criteria based on tensile strength and ductility. The results strongly indicate that precast members can be safely connected when using standard steel sleeves filled with field grout. The investigation focused on a typical splice sleeve that was capable of developing a minimum strength of 125% of the bar's yield strength with the potential of reaching the ultimate strength of the bar.

The research presented in Ahn et al. [3] also had the purpose of studying the effect of confinement on the bond strength between the rebar and the surrounding grout within the mechanical sleeves. A total of 6 full-scale prototypes were tested under monotonic loads, using strain gauges at 12 locations within the sleeve and along the reinforcing bar. The experimental variables were the embedment length and the diameter of reinforcing bars. Ahn et al. [3] concluded that under the ultimate strength condition, the confining pressure within the grouted splice sleeve improved the connector performance, allowing a reduction of the embedment length of the reinforcing bar.

In Hua et al. [4], 35 specimens were tested under incremental tensile force. These specimens varied in terms of configurations and were assessed for feasibility in the aspects of bond strength, ductility response and failure modes. According to Hua et al. [4], the typical modes of failure were bar tensile failure, grout-bar bond failure, grout-sleeve bond failure, and sleeve tensile failure. These failures revealed the parameters to be considered in the design of a splice connector. Hua et al. [4] concluded that under confinement, the required anchorage length of the bars can be shortened to nearly nine times the diameter of the spliced bar.

In addition to the studies on related to the maximum capacity of grouted splice sleeves, the major concern regarding this connection, especially in countries such as the USA and Japan, is related to the guarantee of high ductility, wherein the studied connection should be able to absorb deformations without failure when subjected to seismic actions. Thus, many column-to-column connections have been studied with the purpose to act as assembly connections or as connections with sufficient ductility required to resist against seismic actions.

Belleri & Riva [5] investigated the suitability of grouted sleeve connections as column-to-foundation connections for precast concrete structures in seismic regions. Experiments on the cyclic behavior of column-to-foundation subassemblies compared the response of grouted sleeve connections with cast-in-place and pocket-foundation connections. The results demonstrated that grouted sleeves ensure a ductility and energy dissipation capacity similar to those of traditional connections. According to Belleri & Riva [5], the confinement provided by the grouted sleeves inhibits buckling of the longitudinal reinforcement and increases the compressive strength of the grout. As a consequence, the damage associated with this kind of connection is localized to the column base, allowing easier post-seismic column repair compared to traditional connections.

Ameli et al. [6] investigated the seismic performance of grouted splice sleeve connections with the connectors placed in the column or footing of bridge subassemblies and intentional debonding of the footing dowel bars. In this research, quasi-static cyclic loads were used to test three half-scale precast column-to-footing specimens and one cast-in-place control specimen. The precast concrete specimens incorporated grouted splice sleeve connectors in which two bars were grouted at both ends. According to Ameli et al. [6], experimental results showed that the precast subassemblies had lower ductility capacity than the control cast-in-place specimen. On the other hand, an improved seismic response was observed when the splice sleeve connectors were located inside the footing rather than the column end. An intentional debonded reinforcing bar zone was used to further improve the displacement ductility capacity of the assembly.

Kinnunen [7] presents the results of tests carried out for precast column connections with column shoes and anchor bolts. There were 24 precast column connections tested with different column dimensions and different types of column shoes for bending resistance, rotational stiffness, shear capacity and fire resistance. The experimental results have confirmed that the stiffness of the column-to-column connection is at least as rigid as a continuously reinforced cast-in-situ column connection.

Kinnunen [7] presented a test set up corresponding to a four-point bending test who is the aim was to verify the design rules of EN 19921-1 [8], recommended for slender cast-in-situ columns. In this particular case, the equivalent stiffness of the precast unit was measured without any axial force in order to have a conservative evaluation. Figure 2 illustrates the different zones for relative flexural stiffness in precast and cast-in-situ columns.

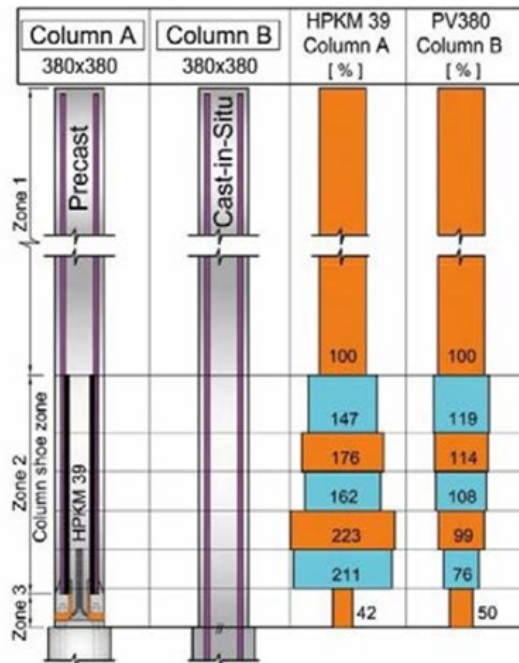


Figure 2. Relative bending stiffness of subzones (Kinnunen [7]).

The precast column A was compared with a reference column B, which was cast-in-situ and continuously reinforced with the same main longitudinal reinforcement as for the precast column. According to Kinnunen [7], the intention in this research was to compare the stiffness of a precast column with that of the reference column. In Zone 1 of the precast column A, the column shoes did not affect the column stiffness. In Zone 2, the flexural stiffness was very high due to the overlapping of the anchor bars of the column shoes and the main reinforcement of the column. In Zone 3, the flexural stiffness was quite low due to the reduction of the effective concrete section at the end of the column with an eccentric tensile force in the column shoes. Based on the experimental results, Kinnunen [7] concluded that the relative stiffness of precast column A and cast-in-situ column B in Zone 1 were naturally the same. In Zone 2, and especially in its lowest subzone, the relative stiffness of precast column A was significantly higher (229% and 211%) than that of the cast-in-situ column B (102% and 76%). The relative stiffness of the cast-in-place column B and its zone 3 was lower than zone 2. The relative stiffness of the column shoe connection in zone 3 was lower than in upper zone 2. Although the relative stiffness of zone 3 of the precast column A was lower than that of the cast-in-situ column B, the difference was minor. When compared with column B, the higher stiffness in zone 2 of column A will compensate for the lower stiffness in zone 3. The calculated deflections at the top of the columns were 380.7 mm and 450.2 mm for HPKM 39 and PV380, respectively. Thus, the column A with column shoes was stiffer than the column B and the tests confirmed that the connection with a grouted joint between the precast column and base structure behaves in the same way as a corresponding monolithic reinforced cast-in-place column.

Tullini and Minghini [9] present the results of full-scale tests on precast reinforced concrete column-to-column connections made with grouted sleeve splices. The precast column units had a square cross-section of 500 mm wide.

Eight bars with 20 mm diameter protruding from one unit were grouted into corrugated steel sleeves encased in the other unit. The column-to-column connections were subjected to three monotonic tests (axial tension and four-point bending with and without axial compression) and two cyclic tests (four-point bending and shear). According to Tullini and Minghini [9], the tension test failure took place far from the interface between the precast units and highlighted the effectiveness of the stress transfer along the splice region. Tullini and Minghini [9] showed that in all other tests, damage developed at the interface between the precast units, the rotation that concentrated at the interface led to a moderate reduction of the global bending stiffness. In the case of the shear test, the pure shear capacity of the bars crossing the joint was achieved. Furthermore, the cyclic bending test resulted in a ductile and stable hysteretic behavior in the connection.

Although grouted sleeves have been widely studied in the international literature, all these studies focused on the evaluation of the strength and ductility of the connections, while considering their application in the seismic regions such as the United States and Japan. However, the information that allows one to evaluate the secant stiffness of connections to be considered in the stability analysis has not been fully addressed within the technical literature.

In this context, this paper contributes to the improvement of practical design applications of precast columns in Brazil, addressing new recommendations in ABNT NBR 9062:2017 [1], regarding strength, stiffness and ductility in column-to-column connections based on the research carried out by Bachega [10], wherein the behavior of this connection with grouted splice sleeves was studied, concerning the performance characterization of the relative stiffness of the precast spliced column. According to Bachega [10], special attention was given to the behavior within the column-to-column interface after cracking, to identify a possible occurrence of bond-slip between grout and steel bars prior but close to the yielding while considering the secant rotational stiffness of moment-rotation relationship according to ABNT NBR 9062:2017 [1]. Figure 3 presents a schematic layout of the grouted steel sleeve used in this paper (Splice Sleeve System) [11]. This paper presents the experimental results from a PhD research carried out by Bachega [10].

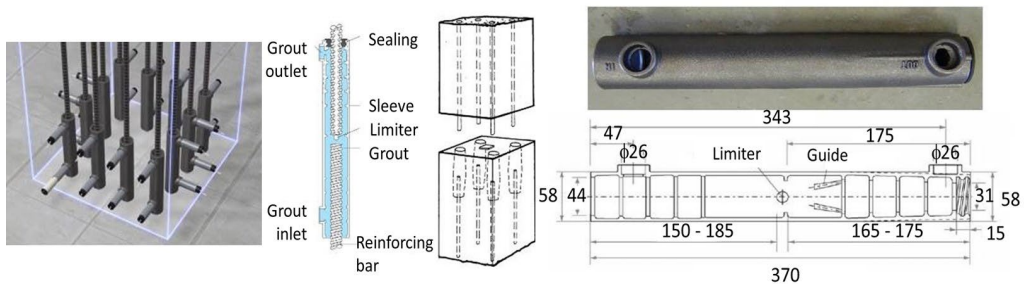


Figure 3. Grouted splice sleeve according to Splice Sleeve Japan [11].

## 2.2 Monolithic equivalence of precast columns

Since the studied connection was originally developed to be applied in buildings in seismic zones, most of the previous experimental studies limited their focus on the structural behavior of the connections related to their ultimate plastic strength and ductility (wherein the plastic rotational stiffness is given by  $R_{plast} = M_u / \theta_u$ ). Therefore, in most cases, there was no interest of studying the rotational stiffness for the column-to-column connection within the serviceability limit state (after crack begins but before the steel bars start yielding).

According to the design criteria for structures in seismic zones recommended by ACI Committee 550 [12], applying the so called Emulative Design, precast elements can emulate the behavior of monolithic elements in design provided that their connections are capable to achieve the ultimate strength and ductility (plastic deformation higher than 2.5 times the yielding deformation), wherein the concept of Emulative Design is restricted to the emulation in terms of ductility. On the other hand, the concept of the monolithic equivalent stiffness comprises the monolithic emulation for all stages of the force-displacement relationship along the precast members. For the stability analysis of precast structures in non-seismic regions, it is essential to know the secant stiffness of the moment-rotation relationship of the connections in order to properly evaluate the lateral stiffness of the precast structure. In addition, it is also important to know the rotational stiffness of the connection within the serviceability limit state in order to obtain the effective

stiffness of a spliced precast column, in order to decide if there is equivalence with the relative stiffness of a monolithic element.

According to Bachega [10], a precast column can be considered equivalent to a monolithic column if the criteria described hereafter is met:

- When lateral deflections (sideways) in the precast columns do not exceed 10% of the displacements in the equivalent monolithic columns.
- When the connection behaves as rigid (fixity factor  $\alpha_R \geq 0.85$ ), the presence of the connection does not affect the continuous behavior of the precast column.

In order to characterize the structural behavior of a connection in a precast column, which is related to its rotational stiffness, flexural strength and ductility, Bachega [10] proposed a procedure that comprises a trilinear diagram based on the limit moment ( $M_{y,lim}$ ) and the secant stiffness ( $R_{sec}$ ), as presented in Figure 4 and comprising Equations of 1 to 9.

$$R_{sec} = \frac{M_{y,lim}}{\theta_{y,lim}} \tag{1}$$

$$R_{ini} = 1.5 R_{sec} \tag{2}$$

$$R_u = 0.4 R_{sec} \tag{3}$$

$$M_{y,lim} = 0.9 f_{yk} A_s d \tag{4}$$

$$M_{ini} = 0.5 M_{y,lim} \tag{5}$$

$$M_u = 1.1 M_{y,lim} \tag{6}$$

$$\theta_u = 2.5 \theta_{y,lim} \tag{7}$$

$$\alpha_R = \left[ 1 + \frac{3(EI)_{ef}}{R_{sec} L} \right]^{-1} \tag{8}$$

Considering the simplified equation proposed by Ferreira et al. [13] and adopted in [1].

$$R_{sec} = k \frac{E_s A_s d^2}{L_{ed}} \tag{9}$$

Therefore, the effective deformation length can be directly determined from experimental secant stiffness by the following Equation 10.

$$L_{ed} = k \frac{E_s A_s d^2}{R_{sec}} \tag{10}$$

where  $R_{sec}$  = secant stiffness;  $M_{y,lim}$  = bending moment at the start of yielding of the flexural bar;  $\theta_{y,lim}$  = rotation in the start of yielding of the flexural bar;  $R_{ini}$  = initial stiffness (it refers to the serviceability limit state);  $R_u$  = ultimate stiffness (plastic stiffness, it refers to the ultimate limit state);  $k$  = coefficient of adjustment that varies between 0.75 to 1.0;  $L_{ed}$  = deformation effective length of the flexural bar;  $M_{ini}$  = initial moment (it refers to the serviceability limit state);  $M_u$  = ultimate moment (plastic moment, it refers to the ultimate limit state);  $\theta_u$  = ultimate rotation (plastic rotation, it refers to the ultimate limit state);  $d$  = effective height of the effective cross-section;  $A_s$  = the cross-sectional area of the steel longitudinal bar;  $E_s$  = steel elastic modulus;  $f_{yk}$  = characteristic yielding tension strength of steel;  $\alpha_R$  = fixity factor of connections;  $(EI)_{ef}$  = effective stiffness coefficient of the element.

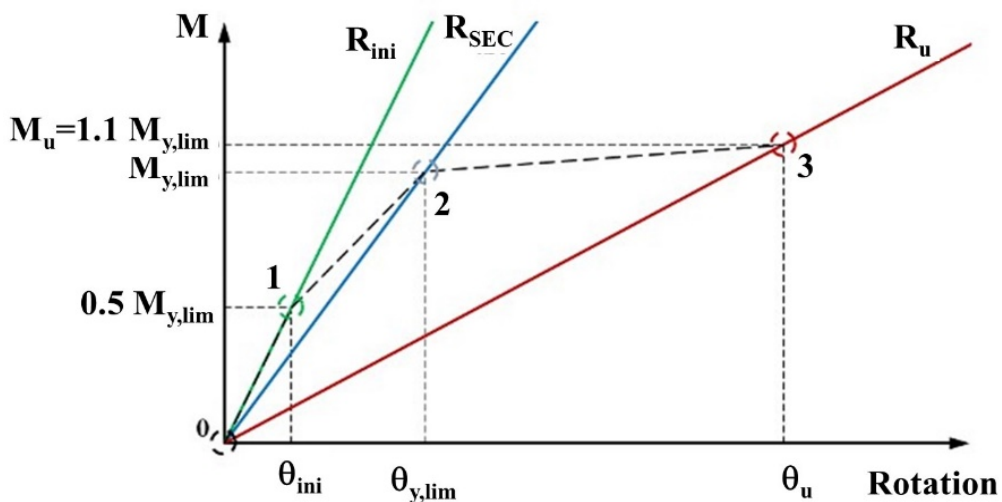


Figure 4. The proposed trilinear diagram in [10] for the characterization of the Monolithic equivalent behavior of precast jointed elements

The curve stretch 0-1 is related to the initial deformation connector at the Serviceability Limit State (SLS) for bending moments lower than the limit given by  $0.5M_{y,lim}$ . The curve stretch 1-2 is related to the design combination considered in the global stability analysis of the precast structures. In the case of precast structures, the consideration of connection secant stiffness aims to take into account the effects of cracking adding possible bond slippage within the connection region until prior the yielding of the steel bars. For the stretch 1-2, the secant stiffness represents the minimum rotational stiffness, wherein the design criteria of strength-stiffness is considered. For the last curve stretch, after the steel bars start yielding, the criteria design of strength-ductility is then considered. Therefore, the secant rotational stiffness of the connection is considered within the SLS.

### 3 EXPERIMENTAL INVESTIGATION

The experimental study carried out in Bachega [10] was intended to verify if a precast column with the studied grouted splice sleeve connector can be considered to possess equivalent stiffness of a monolithic column. The experimental investigation included four full-scale bending tests, with two specimens comprising monolithic elements (M1 and M2) and two models comprising of spliced columns with grouted splice sleeve connections (L1 and L2). The studied connection was also characterized in terms of rotational stiffness, flexural strength and ductility. Furthermore, the experimental results were used for adjustment of analytical models to represent the connection behavior according to the design criteria. It is worth mentioning that the simple bending test set up showed in Figure 5 does not apply any axial compression force on the column unit. Nevertheless, in the case of industrial buildings columns (cantilever posts), it is common to have a design combination of loads that leads to high bending moments at the base with low values for the axial compressive forces. As such, most precast industrial columns are designed as cantilever beams. Therefore, the four-point bending tests represent a good approximation for the behavior of a precast industrial building column (acting

as a post). The connection studied in this research, showed in Figure 3, can be applied for different types of precast concrete elements when full continuity is required, including column-to-column, column-to-foundation and beam-to-beam.

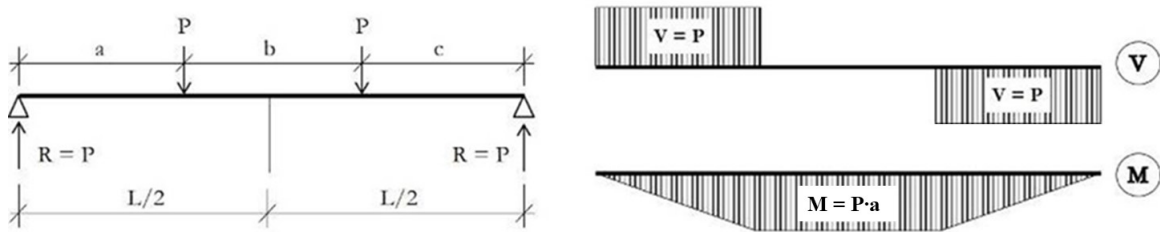


Figure 5. The structural layout of the four points bending test with bending moment (M) and shear force (V) diagrams.

### 3.1 Design Model

As previously said, two monolithic models (named M1 and M2, Figure 6) were used as a reference for comparison and verification of Monolithic equivalence of two models with grouted splice sleeve (named L1 and L2).

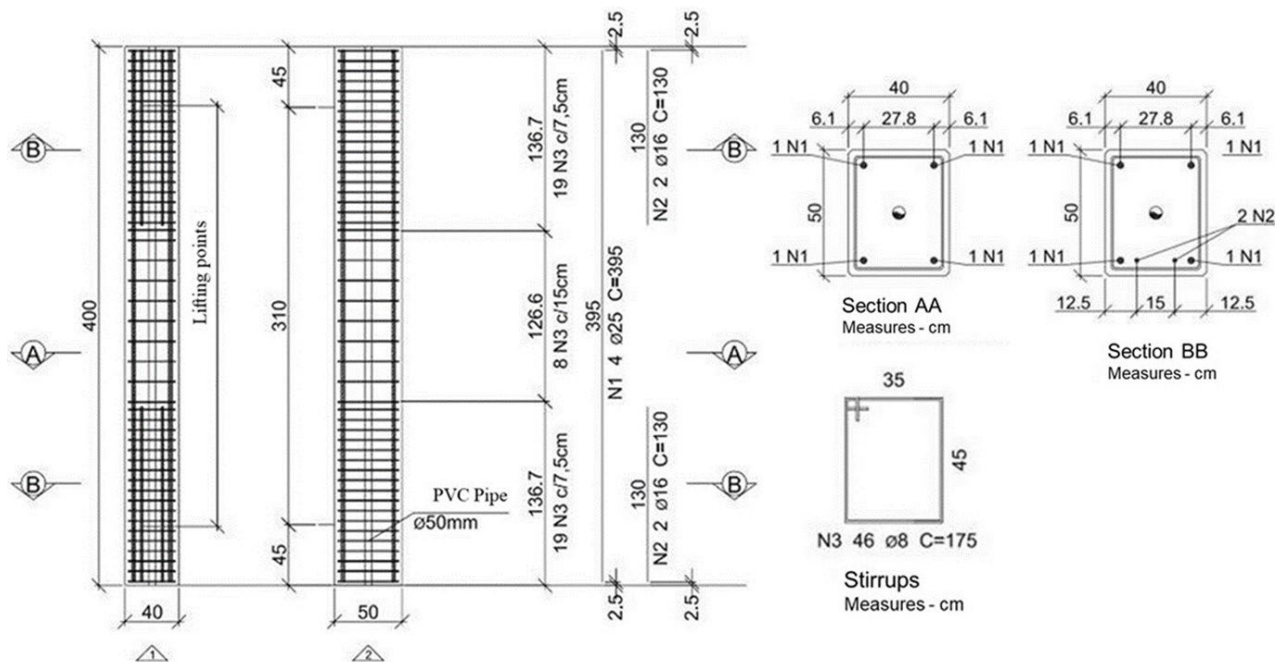


Figure 6. Design of the monolithic models (M) [10].

The dimensions of precast elements and the longitudinal bars were defined according to the maximum hydraulic actuator capacity of the laboratory NETPre, resulting in elements with a width of 40 cm and a height of 50 cm and with two longitudinal bars with a 25 mm diameter.

In the case of M models, the column elements were cast as a single element and in the case of L models (with connection), the elements were cast in two parts (Figure 7 and 8).

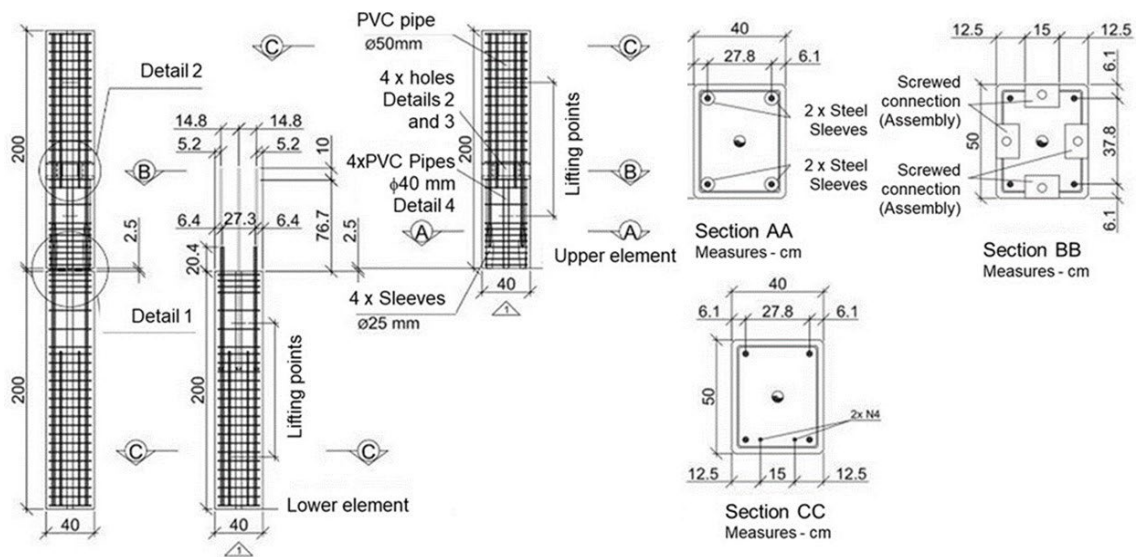


Figure 7. Design of the models with connections (L) [10].

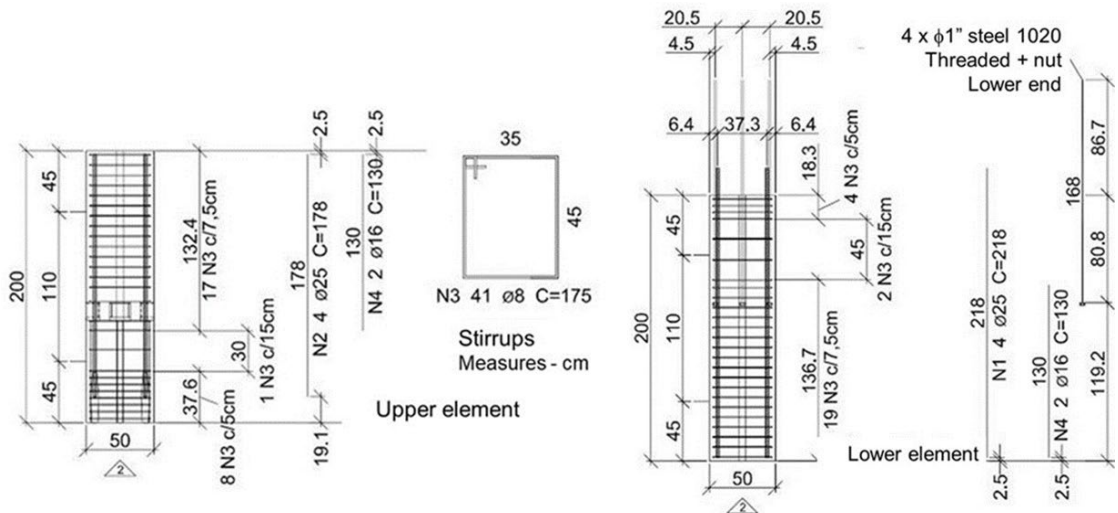


Figure 8. Detailing of the precast elements with connections (model L) [10].

All elements were prefabricated using steel molds at the Leonardi Industrialized Construction Company that donated all models to be tested.

The two monolithic elements were commonly cast because they had no specific details for their prefabrication. So, each monolithic element is 4 m in length. It is important to emphasize the concentration of stirrups at the end of the elements to control cracking in this region, inducing the failure to happen within the joint. Self-compacting concrete (SCC) with a compressive strength of 50 MPa has been used. Furthermore, complementary bars (16 mm of diameter) were placed at one of the 400 mm faces with the dual purpose of strengthening this region while increasing the probability of failure at the central region.

Special care was taken for casting the elements with connections. The main difference between the M and L models was that, in L, there were two separate elements connected with grouted splice sleeves. In this case (L), each unit presented a length of 2 m plus a joint thickness of 25 mm that corresponded to 1% less than the length of the model M. It was considered that all the models had the same length, ignoring this small difference. Bars with a diameter of 25 mm were also used in each edge of the 2 m units but with different lengths: bars with a length of 2.18 m for the lower element (a length of 2 m for the element plus the bonding length of reinforcing bars within the grouted sleeves plus the joint length of 25 mm, resulting in bar lengths of 2.18 m) bars with a length of 1.78 m for the upper element (a length of 2 m for the

element minus the bonding length of a steel reinforcement within the grouted sleeves in the lower element). All lengths considered a concrete cover of 25 mm.

To the design and conception of the models the following aspects were considered:

- The connection device used, corresponding to the bar with a 25 mm diameter, had a total length of 370 mm and a maximum internal diameter of 44 mm. This large opening allowed the adjustment in the assembly of the concrete elements. However, they were interfered in the concrete cover of the main bars (the bars inside the sleeves had a concrete cover that considered the stirrups concrete cover that surrounds the sleeves and sleeves' diameter, as illustrated in Figure 9);
- From studies of connections with steel devices, further detailed in Bachega [10], it is possible to observe that it is common to use a concentration of stirrups over the sleeves in the design of this kind of connection. As the connection corresponds to a discontinuity region of the element, when there is the confinement in this region with stirrups, the connection performance allows that the reinforcement achieves the steel yielding, ensuring the structural safety and making possible the structural design in the domain 2 of deformation.
- In this study is also given concerning the assembly with the purpose to represent a real column. Thus, was needed to predict a connection also be capable to guarantee the balance, plumb and safety before the grouting of connection.

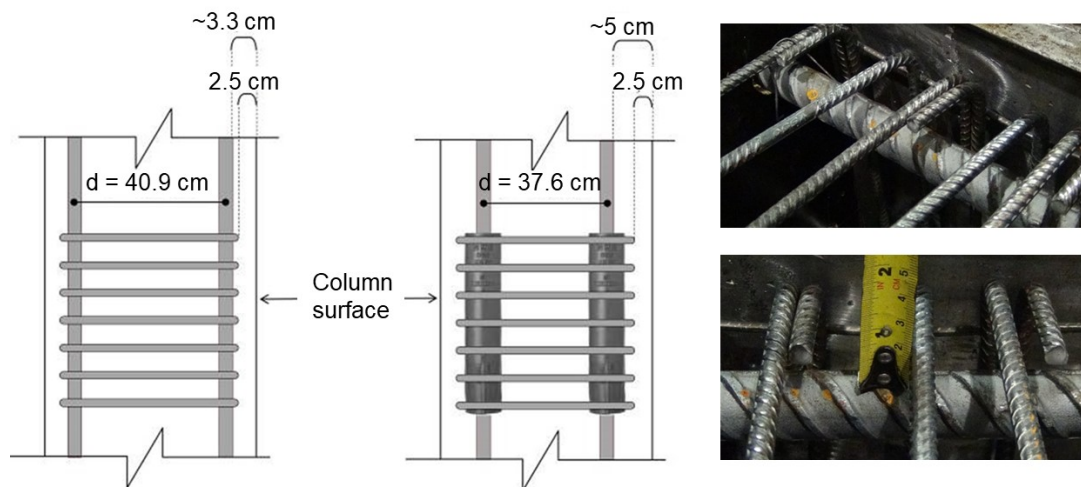


**Figure 9.** Change of the concrete cover and the effective height in the cross-section, indicating spaces between stirrups and the longitudinal reinforcements [10].

### 3.2 Details of test specimens

The assembly of rebar and the embedment of sleeves at the end of the test specimens are illustrated in Figure 10. The fitting of the rebar within the steel sleeves was simple to perform by just pressing it against the rebar until the limiter to position it. A threaded rubber seal was used at one end of the sleeve to avoid the penetration of cement neat into the device. Before to place the rebar within the metallic mold, the metallic sleeves were fixed on a positioning jig, providing accuracy during the vertical assembly between the lower rebar within the upper metallic sleeves. After the sleeves were fixed onto the wooden jig, transversal stirrups were fixed surrounding the metallic sleeves. Four threaded bars were used to assure the temporary fixing between the lower and upper parts of the column specimen.

The monolithic models were cast at the factory and lifted after curing. Differently from M models, L models were assembled at the factory and needed other phases after the lifting. The lower unit was temporarily placed and plumbed in a pocket foundation. The upper unit was placed over the lower unit to verify if the length of the anchor bolts and the projecting bars were correct. After this verification, steel support plates and other needed devices (such as springs and sealing caps with the purpose to avoid the filling of the sleeve by the joint grout) were used to assemble the upper element.

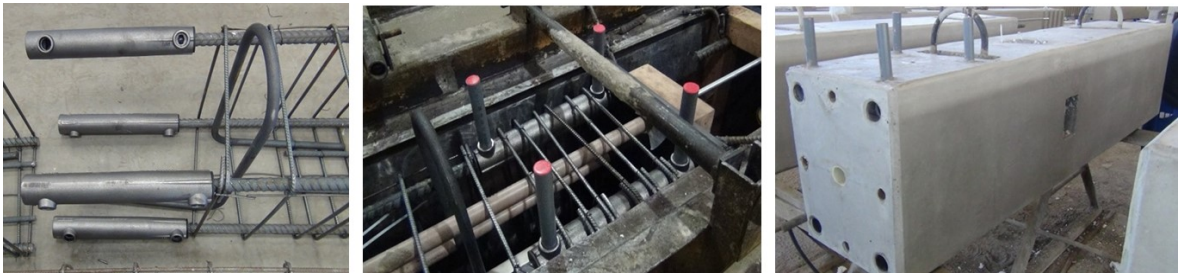


Figure 10. Fabrication of the models [10].

Among possible grouting methods for filling the steel sleeves, the manual filling method by suction pump was adopted. In this method, it is necessary to fill the joints with mortar before the assembly of the upper element. The compressive strength of this mortar should be equal to, or even greater than the lower compressive strength of the connected elements, to maintain the continuity of the concrete elements.

The same grout that filled the steel sleeves was used as the mortar, adding less water to the mixture (1,500 ml) so that the mortar would be more cohesive and moldable. The compressive strength of the grout at 28 days was 70 MPa. Then, the mortar was placed on the lower element and the upper element was fitted. The anchor bolts were screwed, and the plumb of the element was adjusted. Three hours after making the mortar (enough time for the grouted joints to reach sufficient strength) the sleeves were grouted. The process started with the cleanliness of the sleeves inserting water through the upper opening with the same hand pump employed to grout the joint. Rubber seals were placed into the sleeves' holes to prevent waste and also to make the grouting process cleaner. The grout was made with the same mixture used in the mortar. However, 2,100 ml of water (instead of 1,500 ml) was added to produce a grout with greater fluidity.

After this process, to measure the grout workability, the slump flow test was carried out, resulting in a slump of 16.5 cm. According to the manufacturer specifications, the grout slump should be between 15.5 cm and 23.5 cm. Thus, the measured value was close to the lower limit. This occurred due to the lower ambient temperature, around 19°C. With the acceptance of the slump test, cylindrical and cubic specimens were made to verify the compressive strength. Then, the grouting was carried out with a manual pump by filling the sleeves from the upper one to the lower one to avoid the appearance of air bubbles. Grouting was completed when the indicator placed in the upper hole moved to its maximum limit. To fill the eight metallic sleeves, one bag of the grout mixture was enough (four for each model).

After assembly, the M and L models were transported to the NETPre laboratory to be tested. Thus, according to Figure 11, the assembly sequence was: 1 Fixation of the lower element; 2 Placing the mortar of the joint; 3 Guaranteeing the plumbs of the upper element; 4 Tightening the anchor bolts of the assembly connection (temporary stability); 5 Grouting of steel sleeves.



Figure 11. Assembly of the models with connections (L) [10].

### 3.3 Test setup

To measure the moment-rotation relationship within a consistent range of accuracy, bending tests were carried out by applying static concentrated loads at two points according to the test setup shown in Figure 12.

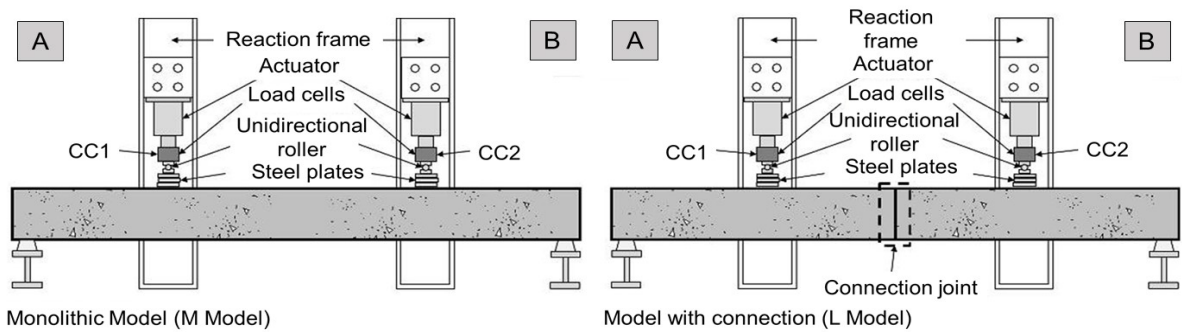


Figure 12. Bending tests carried out in [10].

As aforesaid, this test setup represents an approximation of the column behavior of an industrial building, with the column base embedded in the foundation and a free top or with simple roofs. This configuration usually causes large bending moments at the base of the column and small normal forces, which can still be compression or tension. The test simulates an unfavorable situation for the design of elements subjected to bending.

Hydraulic actuators with the loading capacity of 500 kN were used for continuous application of load (monotonic test). Load cells (LC) were used to measure the applied force, and under the load cell, unidirectional roller supports were used to allow the movement of the models without possible damage. The rectangular metal plates were placed under the roller supports to ensure full transfer of load from the actuator to the concrete.

The models' supports were composed of a Steel "I" profile under a trapezoidal wooden profile (with a rubber tape fixed to the upper face).

### 3.4 Experimental instrumentation

The instrumentation is shown in Figure 13. Ten linear displacement transducers (TD) were used to measure displacements: 08 in the vertical direction (02 in the supports, 02 in the position of force application and 04 in the central region) and 02 in the horizontal direction (for calculation of the rotation in the central region, TD9 (top) and TD10 (bottom), see Figure 13), positioned as far as possible from each other.

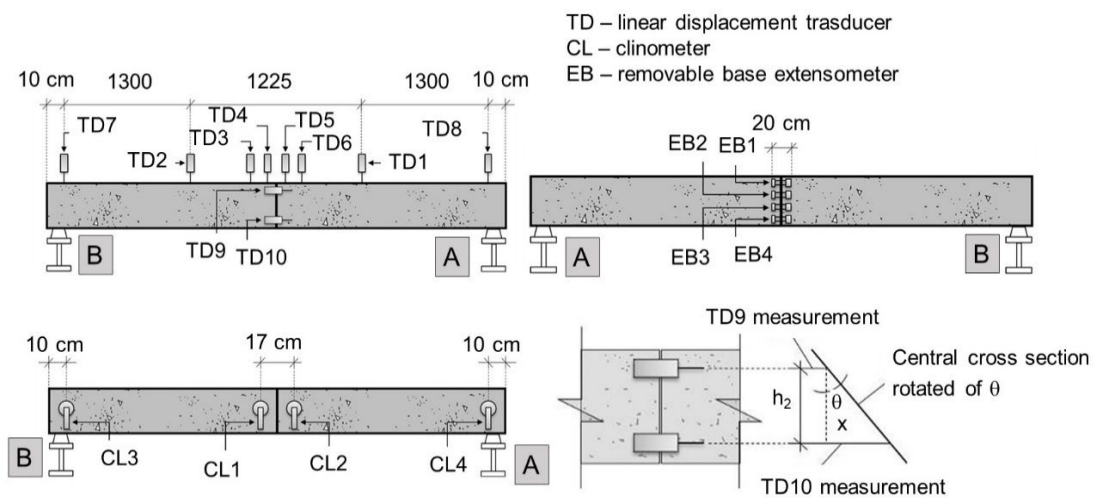


Figure 13. Layout for the test instrumentation in [10].

Rotations in supports and the central region of the models were measured using clinometers (CL). Two (02) clinometers were positioned towards the central transducers, spaced 170 mm apart and two (02) clinometers at the extreme edges, one on each support, positioned 10 cm from the end. Four (04) removable base extensometers (EB) were also used to obtain the concrete deformation and the average plane of deformation in the central region cross-

section to calculate the neutral line. The base length of the extensometer was 200 mm and an average crack opening was measured along it. These instruments were removed from the models before the end of the test to avoid damage to them. The tests are illustrated in Figure 14.



Figure 14. Models instrumentation [10].

### 3.5 Mechanical properties of materials

The compressive strength of concrete and grout was determined in cylindrical specimens with the dimensions of 100 x 200 mm for the concrete and 50 x 100 mm for the grout. The specimens were molded according to ABNT NBR 5738:2015 [14] and were tested according to ABNT NBR 5739:2007 [15] and according to ABNT NBR 7215:1996 [16], while considering concrete and grout respectively. Cubic grout specimens with 5 cm edges also were tested to determine the compressive strength. Thus, the average compressive strength of concrete (51.80 MPa) was determined while considering the average value of seven specimens, and the average compressive strength of grout (92.79 MPa) was calculated while considering the average value of three cylindrical specimens. (see Table 1).

The diametrical compression tests were carried out to determine the concrete tensile strength according to ABNT NBR 7222:2010 [17], which allowed the obtaining of the average value of  $f_{ct,med} = 3.724$  MPa (Table 2). The initial elasticity modulus ( $E_{ci}$ ) was determined using concrete cylindrical specimens according to ABNT NBR 8522:2008 [18]. The average value of initial elasticity modulus ( $E_{ci,med} = 44,959$ ) was obtained from the average value of three specimens with the stress of  $\sigma_n = 13$  MPa. So, the average of secant elasticity modulus according to ABNT NBR 6118:2014 [19] was  $E_{cs,med} = 41,853$  MPa. In all the tested models, steel class CA-50 was used for the main reinforcements and stirrups, with the mean yield limit being  $f_{yk} = 600$  MPa (value provided by the manufacturer) and the elasticity modulus of  $E_s = 205$  GPa (Table 3).

Table 1. Compressive strength of concrete and grout [9].

Concrete	$f_c$ (N/mm <sup>2</sup> )	$f_{c,med}$ (N/mm <sup>2</sup> )	Grout	$f_c$ (N/mm <sup>2</sup> )	$f_{c,med}$ (N/mm <sup>2</sup> )
CP1	51.48			CP1	104.44
CP2	51.34		cylindrical	CP2	89.20
CP3	53.91			CP3	84.72
CP4	52.76	51.80		CP4	116.43
CP5	49.16		cubic	CP5	75.58
CP6	38.41*	CP6		94.15	
CP7	52.12				

\*value disregarded in the calculation of average value

**Table 2.** Tensile strength of concrete  $f_{ct}$  from the diametral compression test ( $f_{ct,sp}$ ) according to ABNT NBR 7215:1996 [16].

Specimen	d (mm)	I (mm)	F (N)	$f_{ct,sp}$ (N/mm <sup>2</sup> )	$f_{ct}$ (N/mm <sup>2</sup> )	$f_{ct,med}$ (N/mm <sup>2</sup> )
CP1	100	200	106,300	3.384	3.045	3.724
CP2	100	200	141,800	4.514	4.062	
CP3	100	200	141,900	4.517	4.065	

**Table 3.** Summary of the concrete characteristics used in the tested models.

Compression $f_{c,med}$ (N/mm <sup>2</sup> )	Initial Elasticity Modulus $E_{ci,med}$ (N/mm <sup>2</sup> )	Secant Modulus $E_{cs,med}$ (N/mm <sup>2</sup> )	Tension (NBR 7222:2010) [17] $f_{ct,med}$ (N/mm <sup>2</sup> )	Cracking Bending Moment $M_r$ (kN·m)	Moment of Inertia (Stage II) $I_{II}$ (mm <sup>4</sup> )
51.80	44,959	41,853	3.724	53.0	67,781.77·10 <sup>-4</sup>

### 4 EXPERIMENTAL RESULTS

Bachega [10] presents the strain measurements by observing tensile strain on the bottom fibers and compressive strain on the top fibers (Figure 15). Moreover, it was observed that the models with connections presented initial strain values higher than the monolithic models. Thus, it was possible to trace the average strain plane of each model while considering the measurement variations of the extensometers until the value of 160 kN at both points of the loading application.

The positioning of the neutral line is evident when the cracking pattern of the models is analyzed, so that in the monolithic models the cracking spread out from the cross-section of the middle of the span, while in the models with connections the cracking started in intermediate sections between the middle of the span and the load application point (Figure 15).

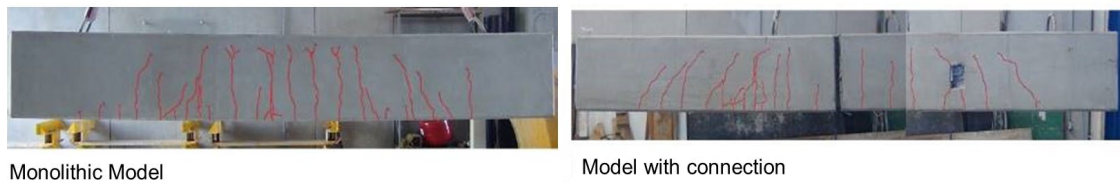


**Figure 15.** Cracking pattern for the models obtained in [10].

Figure 15 shows the applied force versus vertical displacement curves (deflection) for the four models tested, and it is possible to observe that the four models showed very similar behavior, and even after cracking, all models presented a very similar stiffness gradient and a significant reduction in the vicinity of the applied force of 180 kN, showing the reinforcement yielding. Figure 16 shows the applied force versus rotation curves on the supports for the four models, making it possible to observe a very similar behavior between the four models, showing that all of them presented a variation of the effective stiffness very similar for the different stages of the applied load.

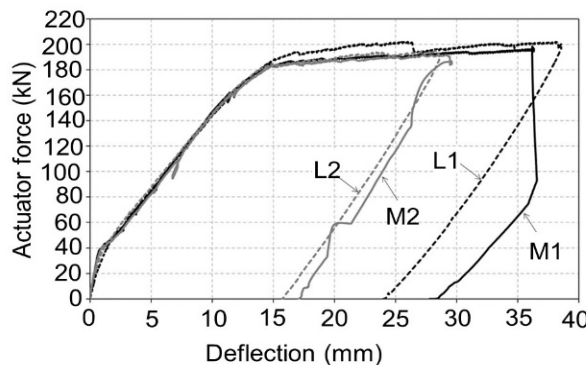


**Figure 16.** Actuator force vs deflection curves obtained in [10].

### 5 EQUIVALENT STIFFNESS OF THE PRECAST COLUMNS

The equivalent stiffness of precast columns with grouted splice sleeves was confronted against the actual relative stiffness obtained for the monolithic elements, taking into account the force-deflection relationship along the columns as well as the force-rotation relationship at the supports, as shown in Figures 16 and 17, respectively. It was possible to observe that after the crack begins ( $P = 40$  kN at each point of load application) until the limit of elastic behaviour, prior the steel bars reach their yield strength (around  $P = 180$  kN), the relative stiffness along the structural elements was very similar for all the test results.

Based on Figure 17a, while considering the beginning of the yield strength of the steel bars (for the applied  $P$  force) and the rotation  $\theta$  at the support considered as the average from the measurements taken from clinometers CL3 and CL4, positioned at the supports, it was possible to determine  $EI_{ef}$  (effective stiffness) according to Equation 11, as follows:

$$EI_{ef} = \frac{P \cdot a \cdot \left(\frac{L}{2}\right) \cdot \left(1 - \frac{a}{L}\right)}{\theta_{support}} \tag{11}$$

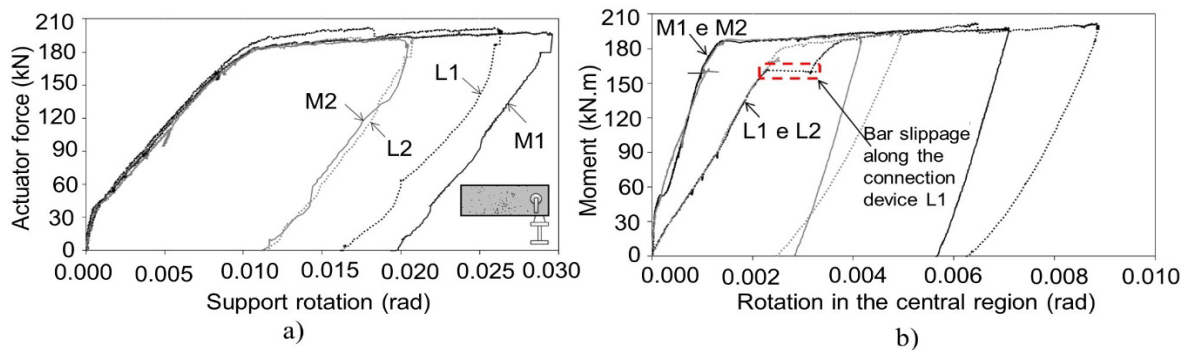


**Figure 17.** a) Curves force x rotation at support measured by clinometers; b) Curves moment x rotation at the center [10].

Table 4 shows the values of the effective stiffness coefficient  $(EI)_{ef}$  corresponding to the secant stiffness obtained at the beginning of the yielding in the experimental curves illustrated in Figure 17b). The cracking moment  $M_r$  obtained for  $f_{ct} \leq 1.2 \cdot f_{ctk,inf} = 1.2 \cdot 0.7 \cdot f_{ctm} = 0.8 \cdot f_{ctm}$  ( $f_{ctm} = 3.74$  MPa) was of  $M_r = 53$  kN·m. This value is compatible with the moment reached for an applied force  $P_r = 40.8$  kN.

**Table 4.** Coefficient of effective stiffness  $(EI)_{ef}$  for the tested models.

Model	P (kN)	L (mm)	a (mm)	$(EI)_{ef}$ Deflection (kN·m <sup>2</sup> )	$(EI)_{ef}$ Rotation (kN·m <sup>2</sup> )	$(EI)_{ef}$ Average (kN·m <sup>2</sup> )	$E_{cs,med} \cdot I_2$ (kN·m <sup>2</sup> )
M1	180.8	3783	1283	28,916	28,073	28,471	28,400
M2	179.0	3797	1298	28,808	28,088		
L1	178.0	3827	1304	32,554	30,613	30,904	28,400
L2	177.1	3820	1310	30,903	29,546		

All models reached  $EI_2$  (stiffness of the cracked section) around 180 kN referring to the acting moment at the beginning of the reinforcement yielding  $M_a = 234$  kN·m. The  $EI_2$  value was obtained as follows:

$$E_{cs} I_2 = 41,850 \cdot 6.78 \cdot 10^8 = 2.84 \cdot 10^{13} \text{ N} \cdot \text{mm}^2 = 28,400 \text{ kN} \cdot \text{m}^2$$

### 6 SECANT STIFFNESS OF THE COLUMN-TO-COLUMN CONNECTION

To evaluate the secant stiffness ( $R_{sec}$ ) performance of the connection, defined by the secant of the moment-rotation curve (relative rotation between the column elements), the secant stiffness ( $R_{sec}$ ) was determined by Equation 1, as shown in Figure 4. Therefore, the limit-moment that defines the beginning of the yielding, given by Equation 4, was

$M_{y,lim} = 231.94 \text{ kN}\cdot\text{m}$ , corresponding to the rotation of the models shown in Table 5. It was observed that the central region of the model with connection presented a secant stiffness ( $R_{sec} = 77,785 \text{ kN}\cdot\text{m}/\text{rad}$ ) 58.3% the secant stiffness ( $R_{sec} = 186,497 \text{ kN}\cdot\text{m}/\text{rad}$ ) obtained while considering the corresponding rotation of the monolithic model. In fact, it was expected that there would be a loss of stiffness in the connection region. In this case, a dry joint was made before filling the grout in the mechanical sleeves.

**Table 5.** Value of secant stiffness  $R_{sec}$  for the central region.

Model	$\theta_{y,lim}$ * (rad)	$\theta_{y,med}$ (rad)	$R_{sec}$ (kN·m/rad)	Dif. (%)
M1	1.245E-03	1.244E-03	186,497	---
M2	1.242E-03			
L1	3.480E-03	2.982E-03	77,785	-58.3
L2	2.484E-03			

\*rotation obtained as defined in Figure 13

Based on the moment-rotation relationship obtained experimentally while considering only the local section of the column-to-column connection, the comparison of the secant stiffness obtained for the two types of models (L and M model) showed a discontinuity located in the joint. In this case, if only the stiffness of the connection section was considered, the connection could be considered as semirigid. However, the effective region of the connection, in this case, is much larger, because it includes the ends of each segment, which correspond to the sections with more stirrups, with additional threaded bars used for assembly and also with an increase in the steel area in the region of the mechanical sleeves (an increase of around 30%), which provided greater confinement of the longitudinal reinforcements, with better crack control.

Therefore, it is possible to observe that there was a stiffness compensation in the segmented model, where the loss of rotational stiffness within the column-to-column joint was compensated by the increase of the relative stiffness within the connection zone (wherein there is a concentration of stirrups surrounding the steel sleeves). In other words, it is believed that the single crack opening at the joint between the precast units was equivalent to the sum of cracks within the corresponding region in the cracked monolithic models.

Considering the experimental secant stiffness  $R_{SEC} = 77,785 \text{ kN}\cdot\text{m}/\text{rad}$ , while taking into account the use of grout with a resistance much higher than the concrete strength of the precast models, and adopting  $k = 1.0$ , it was possible to obtain an effective deformation length corresponding to  $L_{ed} = 20\varnothing_b$ , as follows:

$$L_{ed} = k \frac{E_s A_s d^2}{R_{sec}} = (1.0) \cdot \frac{205 \cdot 982 \cdot 436.5^2}{77,785,000} \cong 20\varnothing_b, \text{ where } \varnothing_b = 25 \text{ mm}; A_s = 982 \text{ mm}^2; E_s = 205 \text{ kN} / \text{mm}^2; d = 437.5 \text{ mm}$$

Therefore, the secant stiffness of the studied connection can be represented by the following expression:

$$R_{sec} = \frac{E_s A_s d^2}{20\varnothing_b}$$

Based on the values of  $M_{y,lim}$  and  $\theta_{y,lim}$ , using Equations 1 to 9, it was possible to predict a trilinear diagram to represent the connection behavior, as shown in Figure 18, considering the effective deformation length of  $L_{ed} = 20\varnothing_b$ .

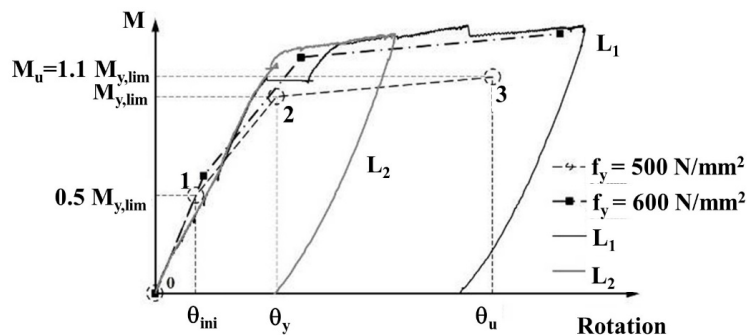


**Figure 18.** Trilinear diagram for the connection characterization [10].

## 7 CONCLUSIONS

Based on the analysis and interpretation of the experimental results, it has been evidenced that the precast members with grouted splice sleeve connections presented relative stiffness that was equivalent to the monolithic members. Therefore, precast columns with this type of connection can be considered in design as a continuous column.

Applying the equations for the secant stiffness and the fixity factor, it was possible to validate a design procedure using a trilinear diagram to predict the structural performance of the column-to-column connection, wherein the connectors were classified as rigid.

Furthermore, the higher concentration of stirrups surrounding the splice sleeves within the connection zone, with the addition of longitudinal reinforcement (from threaded bars used in the assembly and the steel area in the sleeve region) in the segmented models promoted higher confinement for the longitudinal reinforcements and, consequently, better crack control within the connection zone when comparing with the monolithic elements.

Therefore, it is possible to conclude that there was a compensation of the relative stiffness along the spliced member, wherein the loss of rotational stiffness located at the column-to-column joint was compensated by a higher relative stiffness in the connection region.

The authors highlight that the bending test setup used by Bachega [10] was first meant to evaluate a precast column in a single-story building, taking into account a critical design situation under lateral loads. Therefore, carrying out new bending tests combining compressive axial forces, to simulate the load combination in multi-story buildings, can lead to a situation far less critical, wherein the relative stiffness of the precast columns are similar to the behaviour the monolithic ones.

Although the results were satisfactory for the effective behaviour of the connection, it is noteworthy that the connection performance can be improved by enhancing some of the connection details. For instance: improving the confinement within the connection region by adding more stirrups; improving the method of column-to-column joint filling by exploring other alternatives besides the use of dry joints; and improving the distribution of the steel area across the cross-section.

## ACKNOWLEDGEMENTS

The authors acknowledge UFSCar and NETPre for providing laboratory facilities, ABCIC for Institutional support, Leonardi Industrialized Construction Company for the donation of precast elements, and Splice-Sleeve Japan for financial assistance.

## REFERENCES

- [1] Associação Brasileira de Normas Técnicas, *Projeto e Execução de Estruturas de Concreto Pré-moldado*, ABNT NBR 9062:2017, 2017.
- [2] A. Einea, T. Yamane, and M. K. Tadros, "Grout-filled sleeve splices for precast concrete Construction", *Prec. Prestr. Concr. Inst. J.*, vol. 40, no. 1, pp. 82–93, 1995.
- [3] B. Ahn, H. Kim, and B. Park, "Confining effect of mortar grouted splice sleeve on reinforcing bar," *J. Korea Concr. Inst.*, vol. 15, no. 1, pp. 102–109, 2003.
- [4] L. J. Hua, A. B. A. Rahman, I. S. Ibrahim, and Z. A. Hamid, "Feasibility study of grouted splice connector under tensile load," *Constr. Build. Mater.*, vol. 50, pp. 530–539, 2014.
- [5] A. Belleri and P. Riva, "Seismic performance and retrofit of precast concrete grouted sleeve connections", *Prec. Prestr. Concr. Inst. J.*, vol. 57, no. 1, pp. 97–109, 2012.
- [6] M. J. Ameli, D. N. Brown, J. E. Parks, and C. P. Pantelides, "Seismic column-to-footing connections using grouted splice sleeves," *ACI Struct. J.*, vol. 87, no. 113-S, pp. 1021–1030, 2016.
- [7] J. Kinnunen, "ETA tests and design of HPKM Column Shoe Connections," *Proc. Eng.*, vol. 172, pp. 521–528, Feb 2017.
- [8] European Committee for Standardization. *Eurocode 2: Design of Concrete Structures. Part 1-1: General Rules and Rules for Buildings*, EN 1992-1-1:2004, 2004.
- [9] N. Tullini and F. Minghini, "Grouted sleeve connections used in precast reinforced concrete construction – Experimental investigation of a column-to-column joint," *Eng. Struct.*, vol. 127, pp. 784–803, 2016.
- [10] L. A. Bachega, "Equivalência monolítica em pilares com ligações por meio de luvas metálicas grauteadas", PhD dissertation, Univ. Fed. de São Carlos, 2016.
- [11] Splice Sleeve Japan, *Engineering Datasheet*, Tokyo, Japan: Splice Sleeve Japan, 1990.
- [12] American Concrete Institute, *Guide to Emulating Cast-in-place Detailing for Seismic Design of Precast Concrete Structures*, ACI 550.1R-09, 2012.

- [13] M. A. Ferreira, K. S. Elliott, and S. Hasan, *State-of-Art Research Report: Precast Concrete Framed Structures with Semi-rigid Connections*, Nottingham, UK: School of Civil Engineering, University of Nottingham, 2010
- [14] Associação Brasileira de Normas Técnicas, *Concreto - Procedimento para Moldagem e Cura de Corpos de Prova*, ABNT NBR 5738:2015, 2015.
- [15] Associação Brasileira de Normas Técnicas, *Concreto - Ensaio de Compressão de Corpos de Prova Cilíndricos - Método de Ensaio*, ABNT NBR 5739:2007, 2007.
- [16] Associação Brasileira de Normas Técnicas, *Cimento Portland: Determinação da Resistência à Compressão*, ABNT NBR 7215:1996, 1996.
- [17] Associação Brasileira de Normas Técnicas, *Concreto e Argamassa: Determinação da Resistência à Tração por Compressão Diametral de Corpos de Prova Cilíndricos*, ABNT NBR 7222:2010, 2010.
- [18] Associação Brasileira de Normas Técnicas, *Concreto - Determinação dos Módulos Estáticos de Elasticidade e Deformação*, ABNT NBR 8522:2008, 2008.
- [19] Associação Brasileira de Normas Técnicas, *Projeto de Estruturas de Concreto: Procedimentos*, ABNT NBR 6118:2014, 2014.

---

**Author contributions:** MAF: supervision, writing conceptualization, funding acquisition, supervision, writing and formal analysis; LAB: conceptualization, experimental analysis, methodology and experimental tests; BC: data curation, experimental tests, methodology, conceptualization, writing and text formatting.

**Editors:** José Marcio Calixto, José Luiz Antunes de Oliveira e Sousa, Guilherme Aris Parsekian.